

Gaetan Kerschen *Editor*

Nonlinear Dynamics, Volume 1

Proceedings of the 36th IMAC, A Conference and Exposition
on Structural Dynamics 2018



Conference Proceedings of the Society for Experimental Mechanics Series

Series Editor

Kristin B. Zimmerman, Ph.D.
Society for Experimental Mechanics, Inc.,
Bethel, CT, USA

More information about this series at <http://www.springer.com/series/8922>

Gaetan Kerschen

Editor

Nonlinear Dynamics, Volume 1

Proceedings of the 36th IMAC, A Conference and Exposition
on Structural Dynamics 2018

Editor

Gaetan Kerschen
Mechanical Engineering, S3L, Quartier Polytech
University of Liege, Department of Aerospace
Liege, Belgium

ISSN 2191-5644 ISSN 2191-5652 (electronic)
Conference Proceedings of the Society for Experimental Mechanics Series
ISBN 978-3-319-74279-3 ISBN 978-3-319-74280-9 (eBook)
<https://doi.org/10.1007/978-3-319-74280-9>

Library of Congress Control Number: 2018940866

© The Society for Experimental Mechanics, Inc. 2019

This work is subject to copyright. All rights are reserved by the Publisher, whether the whole or part of the material is concerned, specifically the rights of translation, reprinting, reuse of illustrations, recitation, broadcasting, reproduction on microfilms or in any other physical way, and transmission or information storage and retrieval, electronic adaptation, computer software, or by similar or dissimilar methodology now known or hereafter developed.

The use of general descriptive names, registered names, trademarks, service marks, etc. in this publication does not imply, even in the absence of a specific statement, that such names are exempt from the relevant protective laws and regulations and therefore free for general use.

The publisher, the authors and the editors are safe to assume that the advice and information in this book are believed to be true and accurate at the date of publication. Neither the publisher nor the authors or the editors give a warranty, express or implied, with respect to the material contained herein or for any errors or omissions that may have been made. The publisher remains neutral with regard to jurisdictional claims in published maps and institutional affiliations.

Printed on acid-free paper

This Springer imprint is published by the registered company Springer International Publishing AG part of Springer Nature.
The registered company address is: Gewerbestrasse 11, 6330 Cham, Switzerland

Preface

Nonlinear Dynamics represents one of nine volumes of technical papers presented at the 36th IMAC, A Conference and Exposition on Structural Dynamics, organized by the Society for Experimental Mechanics, and held in Orlando, Florida, February 12–15, 2018. The full proceedings also include volumes on Dynamics of Civil Structures; Model Validation and Uncertainty Quantification; Dynamics of Coupled Structures; Special Topics in Structural Dynamics; Structural Health Monitoring, Photogrammetry and DIC; Rotating Machinery, Vibro-Acoustics and Laser Vibrometry; Sensors and Instrumentation, Aircraft/Aerospace and Energy Harvesting; and Topics in Modal Analysis and Testing.

Each collection presents early findings from experimental and computational investigations on an important area within structural dynamics. Nonlinearity is one of these areas.

The vast majority of real engineering structures behave nonlinearly. Therefore, it is necessary to include nonlinear effects in all the steps of the engineering design: in the experimental analysis tools (so that the nonlinear parameters can be correctly identified) and in the mathematical and numerical models of the structure (in order to run accurate simulations). In so doing, it will be possible to create a model representative of the reality which, once validated, can be used for better predictions.

Several nonlinear papers address theoretical and numerical aspects of nonlinear dynamics (covering rigorous theoretical formulations and robust computational algorithms) as well as experimental techniques and analysis methods. There are also papers dedicated to nonlinearity in practice where real-life examples of nonlinear structures will be discussed.

The organizers would like to thank the authors, presenters, session organizers, and session chairs for their participation in this track.

Liege, Belgium

Gaetan Kerschen

Contents

1	Interface Reduction on Hurty/Craig-Bampton Substructures with Frictionless Contact	1
	Patrick J. Hughes, Wesley Scott, Wensi Wu, Robert J. Kuether, Matthew S. Allen, and Paolo Tiso	
2	Experimental Path Following of Unstable Static Equilibria for Snap-Through Buckling	17
	T. van Iderstein and R. Wiebe	
3	Direct Detection of Nonlinear Modal Interactions and Model Updating Using Measured Time Series	23
	Keegan Moore, Mehmet Kurt, Melih Eriten, D. Michael McFarland, Lawrence A. Bergman, and Alexander F. Vakakis	
4	Pareto Optimization of a Nonlinear Tuned Mass Damper to Control Vibrations in Hand Held Impact Machines	27
	Seyed Milad Mousavi Bideleh and Viktor Berbyuk	
5	Inverse Methods for Characterization of Contact Areas in Mechanical Systems	45
	Matthew Fronk, Kevin Eschen, Kyle Starkey, Robert J. Kuether, Adam Brink, Timothy Walsh, Wilkins Aquino, and Matthew Brake	
6	Experimental Characterization of a New Benchmark Structure for Prediction of Damping Nonlinearity ...	57
	Aabhas Singh, Matteo Scapolan, Yuta Saito, Matthew S. Allen, Daniel Roettgen, Ben Pacini, and Robert J. Kuether	
7	Nonlinear System Identification for Joints Including Modal Interactions	79
	Alexander H. Haslam, Gaurav Chauda, Nalik Kenia, Esther S. Rufat-Meix, Matthew S. Allen, Robert M. Lacayo, Malte Krack, and Matthew R. W. Brake	
8	Performance of Nonlinear Modal Model in Predicting Complex Bilinear Stiffness	101
	Benjamin R. Pacini, Wil A. Holzmann, and Randall L. Mayes	
9	Low Order Nonlinear Dynamic Modelling of Fuel Supply Pipes	113
	Alberto Sanchez and Christoph W. Schwingshackl	
10	System Identification to Estimate the Nonlinear Modes of a Gong	121
	Daniel Piombino, Matthew S. Allen, David Ehrhardt, Tim Beberniss, and Joseph J. Hollkamp	
11	An Enhanced Static Reduction Algorithm for Predictive Modeling of Bolted Joints	137
	Iman Zare, Matthew S. Allen, and Emily Jewell	
12	Time-varying Spectral Submanifolds: Analytic Calculation of Backbone Curves and Forced Response	141
	Thomas Breunung and George Haller	
13	Operational Modal Analysis Based Stress Estimation in Friction Systems	143
	Marius Tarpø, Tobias Friis, Bruna Nabuco, Sandro Amador, Evangelos Katsanos, and Rune Brincker	
14	Damping Estimation of Friction Systems in Random Vibrations	155
	Tobias Friis, Evangelos Katsanos, Sandro Amador, and Rune Brincker	

15	System Identification of Jointed Structures: Nonlinear Modal Testing Vs. State-Space Model Identification	159
	Maren Scheel, Gleb Kleyman, Ali Tatar, Matthew R. W. Brake, Simon Peter, Jean-Philippe Noël, Matthew S. Allen, and Malte Krack	
16	Effect of Boundary Conditions on Finite Element Submodeling	163
	Michael W. Sracic and William J. Elke	
17	On Euler Buckling and Snap-Through	171
	Richard Wiebe, Mihaela Nistor, and Ilinca Stanciulescu	
18	Solitons in Cyclic and Symmetric Structures	175
	Filipe Fontanela, Aurelien Grolet, Loic Salles, and Norbert Hoffmann	
19	Experimental and Numerical Nonlinear Modal Analysis of a Beam with Impact: Part I – Numerical Investigation	179
	F. Schreyer, S. Peter, and R. I. Leine	
20	Experimental and Numerical Nonlinear Modal Analysis of a Beam with Impact: Part II – Experimental Investigation	183
	S. Peter, F. Schreyer, and R.I. Leine	
21	The Effect of Non-Flat Interfaces On System Dynamics	187
	I. Lawal, S. Shah, M. Gonzalez-Madrid, T. Hu, C. W. Schwingshackl, and M. R. W. Brake	
22	Investigating Modal Contributions Using a Galerkin Model	199
	A. J. Elliott, A. Cammarano, and S. A. Neild	
23	Acoustic Excitation of a Flanged Joint	211
	Trevor W. Jerome, Micah R. Shepherd, and Stephen A. Hambric	
24	In Situ Measurements of Interfacial Contact Pressure During Impact Hammer Tests	225
	B. Seeger, P. Butaud, M. V. Baloglu, F. Du, M. R. W. Brake, and C. W. Schwingshackl	
25	An Improved Shape Reconstruction Methodology for Long Rod Like Structures Using Cosserat Kinematics- Including the Poisson’s Effect	237
	Mayank Chadha and Michael D. Todd	
26	Computing Nonlinear Normal Modes of Aerospace Structures Using the Multi-harmonic Balance Method	247
	Christopher I. VanDamme, Ben Moldenhauer, Matthew S. Allen, and Joseph J. Hollkamp	
27	Nonlinear Identification of an Aero-Engine Component Using Polynomial Nonlinear State Space Model ...	261
	Samson B. Cooper, Koen Tiels, and Dario DiMaio	
28	Curved Structures That Can Elastically Snap-Through	275
	Lawrence N. Virgin, Yue (Susan) Guan, Raymond H. Plaut	
29	Experimental Analysis of Non-Linear Damping Performance in Composites Materials Thanks to Local Transduction-Dissipation Phenomenon	279
	Mathieu Chevalier, Camille Bessaguet, Luis Quiroga-Cortès, Eric Dantras, and Guilhem Michon	
30	Subspace-Based Identification of a Distributed Nonlinearity in Time and Frequency Domains	283
	D. Anastasio, S. Marchesiello, J. P. Noël, and G. Kerschen	
31	Reduced Order Modelling for Non-linear Rotating Systems in ALE Formulation with Contact	287
	Tim Weidauer and Kai Willner	
32	Damage Precursor Indicator for Aluminum 7075-T6 Based on Nonlinear Dynamics	303
	Robert A. Haynes, Ed Habbour, Todd C. Henry, Daniel P. Cole, Volker Weiss, Antonios Kotsos, and Brian Wisner	
33	Application of Control-Based Continuation to a Nonlinear System with Harmonically Coupled Modes	315
	L. Renson, D. A. W. Barton, and S. A. Neild	

34 Numerically Assessing the Relative Significance of Nonlinear Normal Modes to Forced Responses	317
T. L. Hill, S. A. Neild, and A. Cammarano	
35 Direct Frequency Domain Identification of Time Varying Systems	327
Lee Mazurek and Richard Christenson	
36 Reduced-Order Modelling for Investigating Nonlinear FEM Systems	335
I. Tartaruga, S. A. Neild, T. L. Hill, and A. Cammarano	
37 Nonlinear Forced Response of a Composite Fan Blade Actuated by Piezoelectric Patches: Simulation and Testing	351
Antoine Mabilia, Claude Gibert, Fabrice Thouverez, and Edouard De Jaeghere	
38 Locating Nonlinearity in Mechanical Systems: A Dynamic Network Perspective	363
J. P. Noël, M. Schoukens, and P. M. J. Van den Hof	
39 Tracing a Prescribed Force-Displacement Curve Using Topology Optimization	369
Jongsuh Lee, Thibaut Detroux, and Gaetan Kerschen	
40 Model Updating of a Wing-Engine Structure with Nonlinear Connections	373
Mingming Song, Ludovic Renson, Jean-Philippe Noël, Babak Moaveni, and Gaetan Kerschen	
41 Modal Analysis of Axially Deforming Rods with Isolated Lap Joints	375
D. Dane Quinn	
42 Identification of Nonlinear Viscoelastic Parameters Based on an Enhanced Oberst Beam Method	379
Kévin Jaboviste, Emeline Sadoulet Reboul, Nicolas Peyret, Gaël Chevallier, C. Arnould, and E. Collard	
43 A General Framework for Time Domain Finite Element Analysis of Viscoelastically Damped Structures ...	383
J.-F. Deü and L. Rouleau	
44 Nonlinear Structural, Inertial and Damping Effects in an Oscillating Cantilever Beam	387
Michal Raviv Sayag and Earl H. Dowell	
45 Reduced Order Modeling of Structures with Preloaded Bolted Joints by the Use of Trial Vector Derivatives	401
Wolfgang Witteveen and Florian Pichler	
46 Towards the Development of a Model for Nonlinear Elements in Machine Tools	405
Steven M. Whithican, Charles Van Karsen, and Jason Blough	
47 Nonlinear Characterization of a Machine Tool Energy Absorber	419
Steven M. Whithican, Charles Van Karsen, and Jason Blough	
48 Tutorial: Bolted Joints and Tribomechadynamics	427
M. R. W. Brake	



Chapter 1

Interface Reduction on Hurty/Craig-Bampton Substructures with Frictionless Contact

Patrick J. Hughes, Wesley Scott, Wensi Wu, Robert J. Kuether, Matthew S. Allen, and Paolo Tiso

Abstract Contact in structures with mechanical interfaces has the ability to significantly influence the system dynamics, such that the energy dissipation and resonant frequencies vary as a function of the response amplitude. Finite element analysis is commonly used to study the physics of such problems, particularly when examining the local behavior at the interfaces. These high fidelity, nonlinear models are computationally expensive to run with time-stepping solvers due to their large mesh densities at the interface, and because of the high expense required to update the tangent operators. Hurty/Craig-Bampton substructuring and interface reduction techniques are commonly utilized to reduce computation time for jointed structures. In the past, these methods have only been applied to substructures rigidly attached to one another, resulting in a linear model. The present work explores the performance of a particular interface reduction technique (system-level characteristic constraint modes) on a nonlinear model with node-to-node contact for a benchmark structure consisting of two c-shape beams bolted together at each end.

Keywords Component mode synthesis · Substructuring · Hurty/Craig-Bampton Method · Interface reduction · Mechanical joints · Contact

1.1 Introduction

Contact in structures with mechanical interfaces can have a significant influence on the dynamic response to time varying loads. The magnitude of clamping forces near the contact due to bolt preloads influences the overall stiffness in the system, while frictional effects in joints typically contribute to the overall structural damping [1]. A common approach in interface modeling is to approximate contact areas with linear springs and dashpots, or with nonlinear elements such as Jenkins elements [2] or Iwan elements [3]. These approaches are capable of simplifying the interface model at the expense of losing local kinematics and stresses at these locations. When higher interface fidelity is desired, the interfaces must be modeled in full detail with a fine mesh resolution to adequately resolve nonlinear contact and friction effects. Sophisticated models of this type are computationally expensive to run with transient solvers, due to the high number of degrees-of-freedom (DOF) required to accurately capture the local contact forces at the interface. Furthermore, the contact state can change in time, requiring continuous updating of internal force vectors and Jacobian operators within implicit integration schemes. This work seeks to address this issue by exploring model order reduction techniques to speed up transient simulations for structures with nonlinear contact. The current study focuses on the frictionless case such that there are no tangential loads due to friction.

P. J. Hughes
Department of Structural Engineering, University of California – San Diego, San Diego, CA, USA

W. Scott · M. S. Allen
Department of Engineering Physics, University of Wisconsin-Madison, Madison, WI, USA

W. Wu
School of Civil and Environmental Engineering, Cornell University, Ithaca, NY, USA

R. J. Kuether (✉)
Sandia National Laboratories, Albuquerque, NM, USA
e-mail: rjkueth@sandia.gov

P. Tiso
Institute for Mechanical Systems, Zurich, Switzerland

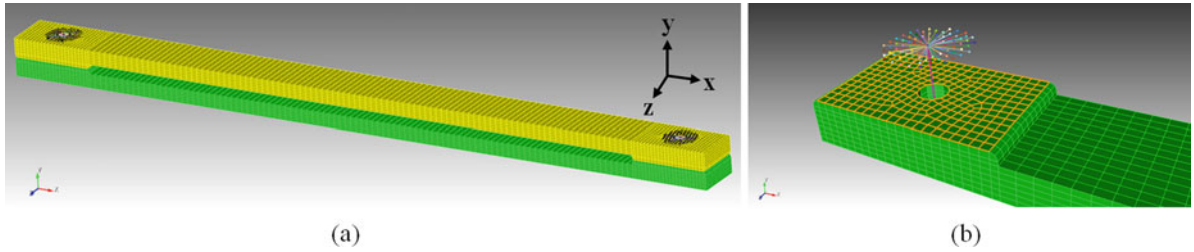


Fig. 1.1 (a) Finite element model of bolted C-beam assembly with coordinate axes. (b) Close-up view of interface surface with bolt DOF spider

Component mode synthesis (CMS) methods in structural dynamics are used to reduce the linear portion of a model, while preserving the physical DOF at interfaces containing nonlinear elements [4, 5]. One commonly used approach is the Hurty/Craig-Bampton (HCB) method, which was originally proposed by Hurty [6], and later simplified by Craig and Bampton [7]. The HCB method represents each subcomponent by a truncated set of dynamic fixed-interface modes, augmented with a static constraint mode for every physical interface DOF. For finite element models with a fine interfacial mesh, the number of constraint modes needed for the HCB method becomes excessively high and prohibits the effectiveness for applications involving contact. Furthermore, the critical time step for HCB models with explicit time solvers is dictated by the static constraint modes, which are localized in shape and therefore associated with high frequencies. As such, model reduction does little if anything to improve this [4].

The objective of this research is to further decrease the HCB model order by performing a secondary reduction on the interface DOF using a set of mode shapes describing the interface kinematics. Some of the authors have recently reviewed interface reduction methods for HCB models in [8], but these techniques were only applied to linear substructures with rigid compatibility enforced (i.e. linear assembly models). The review paper reveals that the system-level characteristic constraint mode method originally developed by Craig and Chang [9], and later elaborated by Castanier et al. [10] is most accurate for rigidly connected boundary DOF. This modal basis is slightly modified in this work to preserve some of the physical boundary DOF in the subspace. A few other works have explored interface reduction techniques on contacting interfaces. Becker and Gaul [5] applied component mode synthesis to structure with bolted joints, but the number and type of interface modes needed to resolve the local and global response remains an open research question.

In this research, the HCB method with a modified version of system-level interface reduction [9, 10] is used to model a system consisting of two C-shape beams bolted together at each end (see Fig. 1.1 in Sect. 1.3.1). Interface contact is considered frictionless here, modeled using node-to-node penalty springs [11] in the normal direction only. This work examines the necessary interface basis vectors to resolve the nonlinear kinematics at the frictionless contacting surfaces. Furthermore, this research examines the effect of interface reduction on transient solution accuracy and simulation time, relative to the full-interface HCB model.

1.2 Theory

1.2.1 Nonlinear Hurty/Craig-Bampton Method

Modern finite element models tend to have extremely fine meshes, with potentially hundreds of thousands of elements and millions of DOF. In models with substructures connected to one another via contacting boundary conditions, the interface DOF may control the dynamic response of the system, while the numerous interior (non-interface) DOF provide unnecessary model redundancy. As such, the interior DOF can be reduced through CMS methods, which approximate the substructure interior with a relatively small set of mode shapes, while leaving the interface DOF unchanged. One such method is the Hurty/Craig-Bampton technique, summarized below for the case when substructures are connected through nonlinear contact elements.

Consider an arbitrary substructure in an assembly with nonlinear elements at the interface. In discretized form, the equations of motion for the substructure are written as

$$\mathbf{M}\ddot{\mathbf{u}} + \mathbf{K}\mathbf{u} + \mathbf{f}_N = \mathbf{f}_{\text{ext}} \quad (1.1)$$

where \mathbf{M} and \mathbf{K} are respectively the mass and stiffness matrices, \mathbf{u} is the relative displacement vector, \mathbf{f}_N is the vector of displacement-dependent normal contact forces (discussed in Sect. 1.2.3), and \mathbf{f}_{ext} is the externally applied loading vector. The matrices are $n \times n$ and the vectors are $n \times 1$. Each dot placed over \mathbf{u} represents its derivative with respect to time. These equations can be partitioned into interior i and interface b DOF as

$$\begin{bmatrix} \mathbf{M}_{ii} & \mathbf{M}_{ib} \\ \mathbf{M}_{bi} & \mathbf{M}_{bb} \end{bmatrix} \begin{Bmatrix} \ddot{\mathbf{u}}_i \\ \ddot{\mathbf{u}}_b \end{Bmatrix} + \begin{bmatrix} \mathbf{K}_{ii} & \mathbf{K}_{ib} \\ \mathbf{K}_{bi} & \mathbf{K}_{bb} \end{bmatrix} \begin{Bmatrix} \mathbf{u}_i \\ \mathbf{u}_b \end{Bmatrix} + \begin{Bmatrix} \mathbf{0} \\ \mathbf{f}_{N,b} \end{Bmatrix} = \begin{Bmatrix} \mathbf{f}_{\text{ext},i} \\ \mathbf{f}_{\text{ext},b} \end{Bmatrix} \quad (1.2)$$

The mass and stiffness from the interior degrees of freedom are used to form the fixed-interface (FI) modes of the system through a partitioned eigenanalysis, i.e.

$$\left[\mathbf{K}_{ii} - (\omega_s^{\text{FI}})^2 \mathbf{M}_{ii} \right] \boldsymbol{\varphi}_s^{\text{FI}} = \mathbf{0} \quad (1.3)$$

The eigenvectors $\boldsymbol{\varphi}_s^{\text{FI}}$ ($s = 1, 2, \dots, n_{\text{FI}}$) form the FI modal matrix

$$\boldsymbol{\Phi}^{\text{FI}} = [\boldsymbol{\varphi}_1^{\text{FI}} \ \boldsymbol{\varphi}_2^{\text{FI}} \ \dots \ \boldsymbol{\varphi}_{n_{\text{FI}}}^{\text{FI}}] \quad (1.4)$$

where n_{FI} is an integer much smaller than the original number of DOF in set i . The truncation of modes in this step introduces the model reduction desired by the HCB process. The eigenshapes are combined with a set of static constraint modes that describe how the interior DOF respond when each interface DOF is moved independently. This is defined by the static condensation

$$\boldsymbol{\Psi}^{\text{HCB}} = -\mathbf{K}_{ii}^{-1} \mathbf{K}_{ib} \quad (1.5)$$

The combination of FI modes and constraint modes form a basis for the interior DOF of the substructure, and are arranged to form the HCB transformation matrix as

$$\mathbf{T}^{\text{HCB}} = \begin{bmatrix} \boldsymbol{\Phi}^{\text{FI}} & \boldsymbol{\Psi}^{\text{HCB}} \\ \mathbf{0} & \mathbf{I} \end{bmatrix} \quad (1.6)$$

which converts the interior DOF of the substructure to generalized HCB coordinates through the transformation

$$\mathbf{u} = \mathbf{T}^{\text{HCB}} \mathbf{v} \quad (1.7a)$$

$$\begin{Bmatrix} \mathbf{u}_i \\ \mathbf{u}_b \end{Bmatrix} = \begin{bmatrix} \boldsymbol{\Phi}^{\text{FI}} & \boldsymbol{\Psi}^{\text{HCB}} \\ \mathbf{0} & \mathbf{I} \end{bmatrix} \begin{Bmatrix} \mathbf{q}_i \\ \mathbf{u}_b \end{Bmatrix} \quad (1.7b)$$

The vector \mathbf{v} is the HCB generalized coordinate and \mathbf{q}_i is the modal representation of the interior partition of the substructure. The reduced mass and stiffness matrices, as well as the reduced load vectors, are computed via

$$\mathbf{M}^{\text{HCB}} = (\mathbf{T}^{\text{HCB}})^T \mathbf{M} \mathbf{T}^{\text{HCB}}, \quad \mathbf{K}^{\text{HCB}} = (\mathbf{T}^{\text{HCB}})^T \mathbf{K} \mathbf{T}^{\text{HCB}} \quad (1.8)$$

$$\mathbf{f}_N^{\text{HCB}} = (\mathbf{T}^{\text{HCB}})^T \mathbf{f}_N, \quad \mathbf{f}_{\text{ext}}^{\text{HCB}} = (\mathbf{T}^{\text{HCB}})^T \mathbf{f}_{\text{ext}}$$

where T is the transpose operator. The dimension of the problem after HCB reduction is $n_{\text{FI}} + n_b$, where n_{FI} is the number of retained fixed-interface modes, and n_b is the total number of interface DOF. The equations of motion for a substructure in HCB coordinates are

$$\mathbf{M}^{\text{HCB}} \ddot{\mathbf{v}} + \mathbf{K}^{\text{HCB}} \mathbf{v} + \mathbf{f}_N^{\text{HCB}} = \mathbf{f}_{\text{ext}}^{\text{HCB}} \quad (1.9a)$$

$$\begin{bmatrix} \mathbf{I}_{ii} & \mathbf{M}_{ib}^{\text{HCB}} \\ \mathbf{M}_{bi}^{\text{HCB}} & \mathbf{M}_{bb}^{\text{HCB}} \end{bmatrix} \begin{Bmatrix} \ddot{\mathbf{q}}_i \\ \ddot{\mathbf{u}}_b \end{Bmatrix} + \begin{bmatrix} \boldsymbol{\Lambda}_{ii}^{\text{FI}} & \mathbf{0} \\ \mathbf{0} & \mathbf{K}_{bb}^{\text{HCB}} \end{bmatrix} \begin{Bmatrix} \mathbf{q}_i \\ \mathbf{u}_b \end{Bmatrix} + \begin{Bmatrix} \mathbf{0} \\ \mathbf{f}_{N,b}^{\text{HCB}} \end{Bmatrix} = \begin{Bmatrix} \mathbf{f}_{\text{ext},i}^{\text{HCB}} \\ \mathbf{f}_{\text{ext},b}^{\text{HCB}} \end{Bmatrix} \quad (1.9b)$$

where \mathbf{I}_{ii} and $\boldsymbol{\Lambda}_{ii}^{\text{FI}}$ are the identity matrix and diagonal matrix of fixed-interface eigenvalues, respectively. This form arises from the orthogonality properties of the modal matrix $\boldsymbol{\Phi}^{\text{FI}}$ in the HCB coordinate transformation.

1.2.2 Interface Modal Basis

Any interface reduction basis must satisfy a number of criteria: (1) allow for realistic deformations in the contact area, (2) reproduce the distribution of contact forces, (3) match the overall dynamic response of the HCB model within a reasonable margin of error, and (4) be efficient enough to provide overall computational savings. This research attempts to meet each of these criteria by utilizing an interface reduction technique that is a modification of the system-level characteristic constraint modes [9, 10]. In addition to these mode shapes, the basis is augmented with the static deformation shape obtained from a nonlinear static preload analysis, as it is inefficient to resolve the interface kinematics with dynamic modes alone.

1.2.2.1 Extended System-Level Characteristic Constraint Modes About Preloaded State

The traditional method of system-level characteristic constraint modes, or SCC method, transforms all physical interface DOF in the HCB model into truncated modal DOF, such that the resulting model is defined entirely in the modal domain. In some cases, it is desirable to retain some portion of the interface as physical DOF. For example, it may be necessary to retain physical DOF when loads are applied near substructure boundaries (e.g. bolt preload force). A novel method to achieve this is introduced here, and referred to as the extended system-level characteristic constraint mode method, or SCCe method.

To reduce some of the interface DOF to modal DOF, and retain the rest as physical DOF, a given substructure must now be partitioned into three sets: the interior DOF i (i.e. fixed-interface mode partition), physical interface DOF p , and reduced interface DOF r . The HCB system mass and stiffness matrices, according to these partitions, are

$$\mathbf{M}^{\text{HCB}} = \begin{bmatrix} \mathbf{I}_{ii} & \mathbf{M}_{ir}^{\text{HCB}} & \mathbf{M}_{ip}^{\text{HCB}} \\ \mathbf{M}_{ri}^{\text{HCB}} & \mathbf{M}_{rr}^{\text{HCB}} & \mathbf{M}_{rp}^{\text{HCB}} \\ \mathbf{M}_{pi}^{\text{HCB}} & \mathbf{M}_{pr}^{\text{HCB}} & \mathbf{M}_{pp}^{\text{HCB}} \end{bmatrix}, \quad \mathbf{K}^{\text{HCB}} = \begin{bmatrix} \Lambda_{ii}^{\text{FI}} & \mathbf{0} & \mathbf{0} \\ \mathbf{0} & \mathbf{K}_{rr}^{\text{HCB}} & \mathbf{K}_{rp}^{\text{HCB}} \\ \mathbf{0} & \mathbf{K}_{pr}^{\text{HCB}} & \mathbf{K}_{pp}^{\text{HCB}} \end{bmatrix} \quad (1.10)$$

The contact state of the model about its preloaded state is important to capturing the correct dynamic response, and hence the SCCe modal basis must account for this. This is achieved by linearizing the preloaded HCB model to include stiffness contributions from the contact areas that form upon fastening/preloading substructures coming into contact. The static deformation due to the preload force (denoted as \mathbf{v}^e in HCB coordinates) is solved using a nonlinear static solver (see Sect. 1.2.2.2). A linearized stiffness matrix (denoted with $-c$ due to the added constraints) is formed by summing the linear HCB stiffness matrix and the Jacobian of the normal contact force, evaluated about the deformed state,

$$\mathbf{K}^{\text{HCB}-c} = \mathbf{K}^{\text{HCB}} + \left[\frac{\partial \mathbf{f}_N^{\text{HCB}}}{\partial \mathbf{v}} \right]_{\mathbf{v}=\mathbf{v}^e} \quad (1.11)$$

A set of SCCe mode shapes is computed from a second partitioned eigenanalysis, employing the linearized stiffness matrix and isolating the reduced interface DOF r

$$\left[\mathbf{K}_{rr}^{\text{HCB}-c} - (\omega^{\text{SCCe}-c})^2 \mathbf{M}_{rr}^{\text{HCB}} \right] \boldsymbol{\varphi}_s^{\text{SCCe}-c} = \mathbf{0} \quad (1.12)$$

A limited set of eigenvectors $\boldsymbol{\varphi}_s^{\text{SCCe}-c} = (s = 1, 2, \dots, n_s)$ are assembled into the columns of the constrained SCCe modal matrix

$$\boldsymbol{\Phi}^{\text{SCCe}-c} = \left[\boldsymbol{\varphi}_1^{\text{SCCe}-c} \quad \boldsymbol{\varphi}_2^{\text{SCCe}-c} \quad \dots \quad \boldsymbol{\varphi}_{n_s}^{\text{SCCe}-c} \right] \quad (1.13)$$

where n_s is a number smaller than the original number of DOF in set r .

The modes contained in $\boldsymbol{\Phi}^{\text{SCCe}-c}$ provide a good representation of the local interface dynamics when the interface is in contact due to the additional term in the contact stiffness, $\mathbf{K}^{\text{HCB}-c}$. If the interface loses contact during a vibration response, then these modes may be insufficient. In order to address this, the eigenanalysis can be repeated using the original stiffness matrix \mathbf{K}^{HCB} , such that a new set of *unconstrained* modes (denoted with $-u$) can be added to the reduction basis.

$$\left[\mathbf{K}_{rr}^{\text{HCB}} - (\omega^{\text{SCCe}-u})^2 \mathbf{M}_{rr}^{\text{HCB}} \right] \boldsymbol{\varphi}_s^{\text{SCCe}-u} = \mathbf{0} \quad (1.14)$$

The first n_s unconstrained eigenvectors are used to build the unconstrained SCCe modal matrix as

$$\Phi^{\text{SCCe-u}} = [\varphi_1^{\text{SCCe-u}} \varphi_2^{\text{SCCe-u}} \dots \varphi_{n_s}^{\text{SCCe-u}}] \quad (1.15)$$

Both sets of eigenmodes described in Eqs. (1.13) and (1.15) use the r - r partition of the system matrices, so they inherently fix the motion of the physical interface DOF (set p) to be zero. To alleviate this issue, static constraint modes are added to the interface reduction set, similar to those in original the HCB method

$$\Psi^{\text{SCCe}} = -(\mathbf{K}_{rr}^{\text{HCB-c}})^{-1} \mathbf{K}_{rp}^{\text{HCB-c}} \quad (1.16)$$

Combining the dual set of eigenmodes with the constraint modes, along with appropriately-sized zero and identity partitions, the SCCe transformation matrix is formed as

$$\mathbf{T}^{\text{SCCe}} = \begin{bmatrix} \mathbf{I} & \mathbf{0} & \mathbf{0} & \mathbf{0} \\ \mathbf{0} & \Phi^{\text{SCCe-c}} & \Phi^{\text{SCCe-u}} & \Psi^{\text{SCCe}} \\ \mathbf{0} & \mathbf{0} & \mathbf{0} & \mathbf{I} \end{bmatrix} \quad (1.17)$$

This transformation uses a combination of dynamic ($\Phi^{\text{SCCe-c}}$, $\Phi^{\text{SCCe-u}}$) and static (Ψ^{SCCe}) shapes to convert the r portion of the model to modal DOF, while retaining the p portion as physical DOF. The transformation between HCB coordinates and SCCe coordinates becomes

$$\mathbf{v} = \mathbf{T}^{\text{SCCe}} \mathbf{w} \quad (1.18a)$$

$$\begin{Bmatrix} \mathbf{q}_i \\ \mathbf{u}_r \\ \mathbf{u}_p \end{Bmatrix} = \begin{bmatrix} \mathbf{I} & \mathbf{0} & \mathbf{0} & \mathbf{0} \\ \mathbf{0} & \Phi^{\text{SCCe-c}} & \Phi^{\text{SCCe-u}} & \Psi^{\text{SCCe}} \\ \mathbf{0} & \mathbf{0} & \mathbf{0} & \mathbf{I} \end{bmatrix} \begin{Bmatrix} \mathbf{q}_i \\ \mathbf{q}_c \\ \mathbf{q}_u \\ \mathbf{u}_p \end{Bmatrix} \quad (1.18b)$$

where \mathbf{w} is the SCCe generalized coordinate vector, and \mathbf{q}_c and \mathbf{q}_u are the constrained and unconstrained modal DOF in the r partition, respectively.

1.2.2.2 Static Preload Deformation

The inclusion of the static preload shape \mathbf{v}^e in the reduction basis ensures that the SCCe model is exact for the initial preload analysis performed on the nonlinear HCB model in Eqs. (1.9a) and (1.9b). This shape is determined by solving the following equations for static equilibrium, stated in HCB coordinates

$$\mathbf{K}^{\text{HCB}} \mathbf{v}^e + \mathbf{f}_N^{\text{HCB}} = \mathbf{b}^e f^e \quad (1.19)$$

where \mathbf{b}^e is a mapping vector that positions and orients the scalar preload force amplitude f^e at the correct physical DOF. In partitioned form, the equations are

$$\begin{bmatrix} \Lambda_{ii}^{\text{FI}} & \mathbf{0} & \mathbf{0} \\ \mathbf{0} & \mathbf{K}_{rr}^{\text{HCB}} & \mathbf{K}_{rp}^{\text{HCB}} \\ \mathbf{0} & \mathbf{K}_{pr}^{\text{HCB}} & \mathbf{K}_{pp}^{\text{HCB}} \end{bmatrix} \begin{Bmatrix} \mathbf{q}_i^e \\ \mathbf{u}_r^e \\ \mathbf{u}_p^e \end{Bmatrix} + \begin{Bmatrix} \mathbf{0} \\ \mathbf{f}_{N,r}^{\text{HCB}} \\ \mathbf{f}_{N,p}^{\text{HCB}} \end{Bmatrix} = \begin{Bmatrix} \mathbf{0} \\ \mathbf{0} \\ \mathbf{b}_p^e f^e \end{Bmatrix} \quad (1.20)$$

Due to the nonlinearity introduced by the contact force $\mathbf{f}_N^{\text{HCB}}$, the displacement vector $\mathbf{v}^e = [\mathbf{q}_i^e \ \mathbf{u}_r^e \ \mathbf{u}_p^e]^T$ must be determined using an iterative solver. In this research, a damped Newton Raphson method was employed.

1.2.2.3 Total SCCe Transformation Matrix

The static deformation vector is concatenated at the end of \mathbf{T}^{SCCe} to build the final SCCe transformation matrix $\mathbf{T}^{\text{SCCe}+}$

$$\mathbf{T}^{\text{SCCe}+} = [\mathbf{T}^{\text{SCCe}} \mathbf{v}^e] \quad (1.21a)$$

$$\mathbf{T}^{\text{SCCe}+} = \begin{bmatrix} \mathbf{I} & \mathbf{0} & \mathbf{0} & \mathbf{0} & \mathbf{q}_i^e \\ \mathbf{0} & \Phi^{\text{SCCe}-c} & \Phi^{\text{SCCe}-u} & \Psi^{\text{SCCe}} & \mathbf{u}_r^e \\ \mathbf{0} & \mathbf{0} & \mathbf{0} & \mathbf{I} & \mathbf{u}_p^e \end{bmatrix} \quad (1.21b)$$

This matrix performs the same transformation as Eqs. (1.18a) and (1.18b), but adds one more DOF from the preload vector. The HCB coordinate \mathbf{v} is transformed to the new SCCe coordinates \mathbf{w}^+ via

$$\mathbf{v} = \mathbf{T}^{\text{SCCe}+} \mathbf{w}^+ \quad (1.22a)$$

$$\begin{Bmatrix} \mathbf{q}_i \\ \mathbf{u}_r \\ \mathbf{u}_p \end{Bmatrix} = \begin{bmatrix} \mathbf{I} & \mathbf{0} & \mathbf{0} & \mathbf{0} & \mathbf{q}_i^e \\ \mathbf{0} & \Phi^{\text{SCCe}-c} & \Phi^{\text{SCCe}-u} & \Psi^{\text{SCCe}} & \mathbf{u}_r^e \\ \mathbf{0} & \mathbf{0} & \mathbf{0} & \mathbf{I} & \mathbf{u}_p^e \end{bmatrix} \begin{Bmatrix} \mathbf{q}_i \\ \mathbf{q}_c \\ \mathbf{q}_u \\ \mathbf{u}_p \\ \mathbf{q}_e \end{Bmatrix} \quad (1.22b)$$

where \mathbf{q}_e is the scalar DOF introduced by the inclusion of \mathbf{v}^e .

The variety of shapes that make up $\mathbf{T}^{\text{SCCe}+}$ can lead to a basis set that is not necessarily linearly independent. The singular value decomposition (SVD) reforms $\mathbf{T}^{\text{SCCe}+}$ as

$$\mathbf{T}^{\text{SCCe}+} = \mathbf{U}^{\text{SCCe}+} \mathbf{\Sigma}^{\text{SCCe}+} \mathbf{V}^{\text{SCCe}+} \quad (1.23)$$

where $\mathbf{U}^{\text{SCCe}+}$ and $\mathbf{V}^{\text{SCCe}+}$ are the left and right singular vectors, respectively, and $\mathbf{\Sigma}^{\text{SCCe}+}$ is a diagonal matrix of singular values. The vectors in $\mathbf{U}^{\text{SCCe}+}$ form an orthonormal basis for the column space of $\mathbf{T}^{\text{SCCe}+}$, so they are taken as the final transformation matrix to convert between HCB and SCCe coordinates. Thus, the SCCe system matrices and load vectors are computed as

$$\begin{aligned} \mathbf{M}^{\text{SCCe}} &= (\mathbf{U}^{\text{SCCe}+})^T \mathbf{M}^{\text{HCB}} \mathbf{U}^{\text{SCCe}+}, \quad \mathbf{K}^{\text{SCCe}} = (\mathbf{U}^{\text{SCCe}+})^T \mathbf{K} \mathbf{U}^{\text{SCCe}+} \\ \mathbf{f}_N^{\text{SCCe}} &= (\mathbf{U}^{\text{SCCe}+})^T \mathbf{f}_N^{\text{HCB}}, \quad \mathbf{f}_{\text{ext}}^{\text{SCCe}} = (\mathbf{U}^{\text{SCCe}+})^T \mathbf{f}_{\text{ext}}^{\text{HCB}} \end{aligned} \quad (1.24)$$

The dimension of the problem is now $n_{\text{FI}} + 2n_{\text{S}} + n_{\text{p}} + 1$, where n_{FI} is the number of retained fixed-interface modes, n_{S} is the number of retained SCCe modes (one set of constrained, one set of unconstrained), n_{p} is the number of physical interface DOF, and the 1 accounts for the static preload shape.

The equations of motion for the system in SCCe coordinates are

$$\mathbf{M}^{\text{SCCe}} \ddot{\mathbf{w}}^+ + \mathbf{K}^{\text{SCCe}} \mathbf{w}^+ + \mathbf{f}_N^{\text{SCCe}} = \mathbf{f}_{\text{ext}}^{\text{SCCe}} \quad (1.25a)$$

$$\begin{bmatrix} \mathbf{I}_{ii} & \mathbf{M}_{ic}^{\text{SCCe}} & \mathbf{M}_{iu}^{\text{SCCe}} & \mathbf{M}_{ip}^{\text{SCCe}} & \mathbf{M}_{ie}^{\text{SCCe}} \\ \mathbf{M}_{ci}^{\text{SCCe}} & \mathbf{M}_{cc}^{\text{SCCe}} & \mathbf{M}_{cu}^{\text{SCCe}} & \mathbf{M}_{cp}^{\text{SCCe}} & \mathbf{M}_{ce}^{\text{SCCe}} \\ \mathbf{M}_{ui}^{\text{SCCe}} & \mathbf{M}_{uc}^{\text{SCCe}} & \mathbf{M}_{uu}^{\text{SCCe}} & \mathbf{M}_{up}^{\text{SCCe}} & \mathbf{M}_{ue}^{\text{SCCe}} \\ \mathbf{M}_{pi}^{\text{SCCe}} & \mathbf{M}_{pc}^{\text{SCCe}} & \mathbf{M}_{pu}^{\text{SCCe}} & \mathbf{M}_{pp}^{\text{SCCe}} & \mathbf{M}_{pe}^{\text{SCCe}} \\ \mathbf{M}_{ei}^{\text{SCCe}} & \mathbf{M}_{ec}^{\text{SCCe}} & \mathbf{M}_{eu}^{\text{SCCe}} & \mathbf{M}_{ep}^{\text{SCCe}} & \mathbf{M}_{ee}^{\text{SCCe}} \end{bmatrix} \begin{Bmatrix} \ddot{\mathbf{q}}_i \\ \ddot{\mathbf{q}}_c \\ \ddot{\mathbf{q}}_u \\ \ddot{\mathbf{u}}_p \\ \ddot{\mathbf{q}}_e \end{Bmatrix} + \begin{bmatrix} \Lambda_{ii}^{\text{FI}} & \mathbf{0} & \mathbf{0} & \mathbf{0} & \mathbf{0} \\ \mathbf{0} & \mathbf{K}_{cc}^{\text{SCCe}} & \mathbf{K}_{cu}^{\text{SCCe}} & \mathbf{K}_{cp}^{\text{SCCe}} & \mathbf{K}_{ce}^{\text{SCCe}} \\ \mathbf{0} & \mathbf{K}_{uc}^{\text{SCCe}} & \mathbf{K}_{uu}^{\text{SCCe}} & \mathbf{K}_{up}^{\text{SCCe}} & \mathbf{K}_{ue}^{\text{SCCe}} \\ \mathbf{0} & \mathbf{K}_{pc}^{\text{SCCe}} & \mathbf{K}_{pu}^{\text{SCCe}} & \mathbf{K}_{pp}^{\text{SCCe}} & \mathbf{K}_{pe}^{\text{SCCe}} \\ \mathbf{0} & \mathbf{K}_{ec}^{\text{SCCe}} & \mathbf{K}_{eu}^{\text{SCCe}} & \mathbf{K}_{ep}^{\text{SCCe}} & \mathbf{K}_{ee}^{\text{SCCe}} \end{bmatrix} \begin{Bmatrix} \mathbf{q}_i \\ \mathbf{q}_c \\ \mathbf{q}_u \\ \mathbf{u}_p \\ \mathbf{q}_e \end{Bmatrix} + \begin{Bmatrix} \mathbf{0} \\ \mathbf{f}_{N,c}^{\text{SCCe}} \\ \mathbf{f}_{N,u}^{\text{SCCe}} \\ \mathbf{f}_{N,p}^{\text{SCCe}} \\ \mathbf{f}_{N,e}^{\text{SCCe}} \end{Bmatrix} = \begin{Bmatrix} \mathbf{f}_{\text{ext},i}^{\text{SCCe}} \\ \mathbf{f}_{\text{ext},c}^{\text{SCCe}} \\ \mathbf{f}_{\text{ext},u}^{\text{SCCe}} \\ \mathbf{f}_{\text{ext},p}^{\text{SCCe}} \\ \mathbf{f}_{\text{ext},e}^{\text{SCCe}} \end{Bmatrix} \quad (1.25b)$$

Note that, although the normal contact force vector $\mathbf{f}_N^{\text{SCCe}}$ has been reduced to SCCe coordinates, it must still be computed in HCB coordinates, where all interface DOF are physically represented. In nonlinear dynamic simulations, this requires a

transformation from SCCe to HCB coordinates at every time step to evaluate the nonlinear forces. The advantage that comes from this reduction is twofold: (1) the size of the equations to solve is smaller compared to the HCB model and (2) the high frequency content has been truncated and thus improves the critical time step in explicit solvers.

1.2.3 Normal Contact Model

Contact in the normal direction is modeled using a node-to-node approach with the penalty method [11]. In this method, the normal gap g between a contacting node pair can be either negative (in contact) or positive (out of contact). For a particular node pair j , the normal gap is

$$g^j = \left(Y_1^j + \Delta Y_1^j \right) - \left(Y_2^j + \Delta Y_2^j \right) \quad (1.26)$$

where the Y 's are the undeformed normal coordinates, and the ΔY 's are the physical relative displacements in the normal direction. The subscripts 1 and 2 refer to the two nodes in node pair j . The penalty method states that the normal contact force at node j f_N^j can be written as

$$f_N^j = \begin{cases} k_{\text{pen}} g^j, & g^j < 0 \\ 0, & g^j \geq 0 \end{cases} \quad (1.27)$$

where k_{pen} is the penalty stiffness value. This defines the penalty force as proportional to the gap when the nodes are in contact ($g^j < 0$), and zero when the nodes are out of contact ($g^j \geq 0$). The node-to-node contact model assumes that relative tangential displacements are small, and thus node pairs do not change during dynamic simulation. Construction of the normal contact force vector \mathbf{f}_N is a matter of positioning and orienting each nodal force f_N^j using a corresponding mapping vector \mathbf{b}_N^j as

$$\mathbf{f}_N = \sum_{j=1}^{n_n} \mathbf{b}_N^j f_N^j \quad (1.28)$$

where n_n is the number of node pairs in all interfaces of the system.

1.2.4 Time Integration Schemes

The response time histories of the reduced order models are computed using one of two different 2nd order accurate methods: an explicit scheme from Chung and Lee [12], and the implicit Hilber-Hughes-Taylor α (HHT- α) method extended to nonlinear systems [13]. The implicit method is implemented with $\alpha = 0$, yielding the constant average acceleration method, which is unconditionally stable for linear systems. The Chung-Lee scheme is conditionally stable, with a critical time step requirement that is dependent on its single free parameter, β_{CL} ,

$$\Delta t_{\text{cr}} = \frac{2}{\omega_{\text{max}} \sqrt{4\beta_{\text{CL}} - 3}} \quad (1.29)$$

where Δt_{cr} is the critical time step length, and ω_{max} is the largest natural circular frequency in the system. The Chung-Lee parameter β_{CL} is chosen to be $28/27$, the maximum permissible value in the stability limit of $1 \leq \beta_{\text{CL}} \leq 28/27$. This selection improves stability by introducing slight numerical dissipation of high-frequency responses, which mitigates the amplification of numerical errors.

Table 1.1 Summary of material properties used in finite element model of C-beams

Symbol	Description	Numerical value	
E	Young's modulus	194	GPa
ν	Poisson's ratio	0.290	
ρ	Mass density	8000	Kg/m ³

1.3 Numerical Studies: Two-Beam Assembly with Frictionless Contact

1.3.1 Model Description

Figure 1.1a shows the benchmark finite element model under consideration, which consists of two identical C-beams bolted together at each end. Each individual C-beam is 50.8 cm long, 3.2 cm wide, 1.27 cm thick at its ends, and 0.95 cm thick at the mid-section. A total of 24,944 first order hexahedral elements are used to model each individual C-beam, and they are made of linear elastic structural steel. Table 1.1 provides a summary of material properties used for the C-beams.

These are connected by 5/16-inch diameter steel bolts at each end that are modeled with 25 discretized beam elements along the y-axis, as depicted in Fig. 1.1b. The bolt ends are connected rigidly to a circular patch of nodes on the C-beams to represent clamping boundary conditions through a nut-washer-bolt assembly. The C-beam assembly has simply supported boundary conditions at all DOF along the z-directional line on the lower beam ends. The full fidelity finite element model has a total of 94,244 physical DOF.

The model has two areas where the C-beams come into contact; each is 3.2 cm wide by 5.0 cm long, as indicated in Fig. 1.1b. The interface surfaces are meshed in such a way that their nodal locations are coincident and unmerged in the undeformed state, allowing for direct implementation of node-to-node contact elements. The Hurty/Craig-Bampton model is defined such that the boundary DOF include the nodes along these interface surfaces and the four nodes at each end of the beam elements (to apply the preload force); the remaining DOF are partitioned to interior DOF. Three different reduced order models are generated with fixed-interface mode frequencies cut off at 2, 3, and 4 kHz. The DOF count in the reduced model is dominated by the 3660 boundary DOF that account for the contacting surfaces, while 24 DOF pertain to the bolt DOF and 8–16 DOF for the fixed-interface modes, depending on the cutoff frequency (see Sect. 1.3.3). The HCB reduction is performed using the Sierra Structural Dynamics (Sierra/SD) [14] finite element code developed at Sandia National Laboratories.

Contact at the interface surfaces is considered through node-to-node penalty elements in the normal direction [11]. Selection of the penalty stiffness k_{pen} is critical in the accuracy and stability of the penalty method - using a stiffness value that is too small allows excessive and non-physical nodal interpenetration, while a value that is too high can cause numerical ill-conditioning or instability. Preliminary studies indicated that a value of 3.78×10^9 N/m was sufficient to avoid excessive node overlap, while retaining stability and convergence.

1.3.2 Static Preloading of Bolt Elements

A static preload force f^e is applied to the ends of the bolt elements, to simulate the effect of bolt torque clamping the C-beams together. The preload force is obtained via an artificial strain ϵ_{art} , which leads to the following expression.

$$f^e = EA\epsilon_{art} \quad (1.30)$$

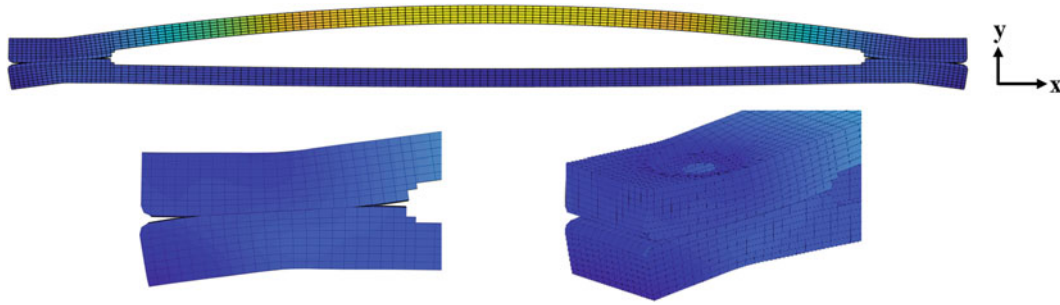
The cross-sectional area A of each bolt is 4.95×10^{-5} m², and the Young's modulus E is the same as that of the C-beams (194 GPa). To ensure that a physically reasonable preload force is applied, a target internal bolt force is obtained using the DIN 946 standard [15] equation to convert applied torque T to transmitted axial force f_{tr} .

$$f_{tr} = \frac{T}{0.159P + 0.578d\mu_T + 0.5D_f\mu_H} \quad (1.31)$$

where P is the bolt thread pitch, d is the nominal bolt diameter, D_f is the effective diameter in contact, μ_T is the thread friction coefficient, and μ_H is the head friction coefficient. Inputs for these variables are summarized in Table 1.2. For a typical applied torque of 18.5 ft-lb (25.1 N-m), the transmitted axial force is computed as 2.91 kN.

Table 1.2 Summary of bolt preload parameters

Symbol	Description	Numerical value	
T	Applied bolt torque	25.1	N-m
P	Bolt thread pitch	0.00106	m
d	Nominal bolt diameter	0.00794	m
D_f	Effective diameter in contact	0.0191	m
μ_T	Thread friction coefficient	0.600	
μ_H	Head friction coefficient	0.600	
f_{tr}	Transmitted axial force	2.91	kN
ε_{art}	Artificial preload strain	3.32E-04	
f^e	Preload force	3.19	kN

**Fig. 1.2** Amplified deformation after static preload, with close-up view of interface**Table 1.3** HCB model comparison for different cutoff frequencies

Cutoff FI frequency [Hz]	FI modes per substructure	Max FI frequency [Hz]	Max model frequency [Hz]	Model size [DOF]	Δt_{cr} [sec]	Δt_a [sec]
2000	4	1544	9.14E + 06	3692	3.25E-08	2.93E-08
3000	7	2534	9.13E + 06	3698	3.25E-08	2.93E-08
4000	8	3763	9.13E + 06	3700	3.25E-08	2.93E-08

The correct ε_{art} (and therefore f^e) is obtained through an iterative procedure that incrementally alters ε_{art} , and applies the corresponding f^e , until the resulting internal bolt axial force matches the theoretical transmitted force f_{tr} . This procedure indicates that an artificial strain of $3.32 \cdot 10^{-4}$ (corresponding to a preload force of 3.19 kN) is appropriate to produce an internal axial force equal to 2.91 kN.

A visualization of the preloaded deformation mapped to the full-field model is displayed in Fig. 1.2, along with a close-up view of the interface, showing how the preload force indents the C-beam surfaces and causes receding of the contact area.

1.3.3 Results: Full-Interface Model

A critical step in the Hurty/Craig-Bampton (HCB) reduction is determining the number of fixed-interface (FI) modes to retain, which is established by discarding FI modes with frequencies above a defined threshold. For a given loading bandwidth and pattern, the dynamic response of the system will converge to the “true” solution by increasing the frequency cut-off limit. The number of FI modes required for convergence is considered adequate to capture the important dynamic characteristics of the system. For this research, so-called “cutoff” frequencies of 2, 3, and 4 kHz are examined and summarized in Table 1.3. The lowest fixed-interface mode frequency in all cases is 288 Hz.

Critical time step lengths are computed for the Chung-Lee Scheme [12] using Eq. (1.29). The maximum natural circular frequency ω_{max} was determined using the regular HCB mass matrix and the linearized HCB stiffness matrix computed in Eq. (1.11). This method of computing the critical time step assumes a linear model, so the analysis time step Δt_a is taken as 90% of Δt_{cr} to ensure stability in the nonlinear case.

Table 1.3 demonstrates that the critical time step length is controlled by the HCB constraint modes computed in Eq. (1.5), and remains unchanged as fixed-interface modes are truncated. This suggests that HCB substructuring with nonlinear

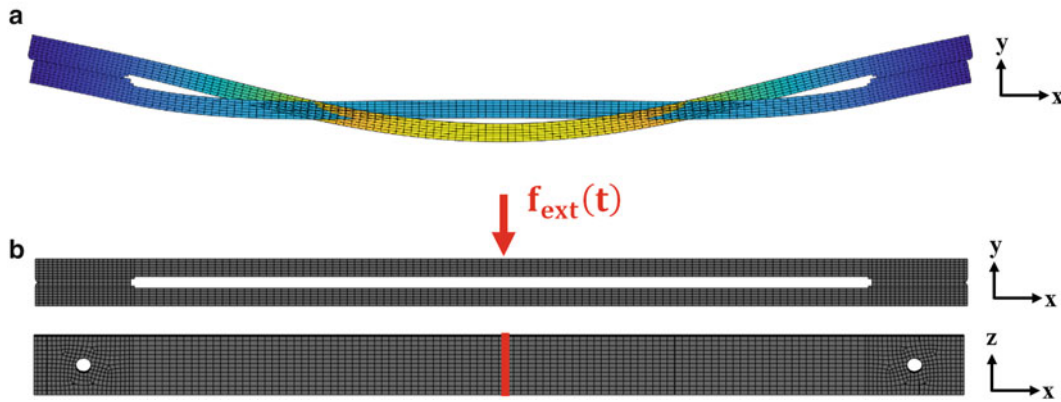


Fig. 1.3 (a) Fundamental mode shape of the HCB model. (b) Dynamic loading pattern

interface DOF does not gain any computational advantage directly from explicit time integration, except for the lower order of equations solved. In other words, the critical time step is determined by the constraint modes.

An externally applied loading pattern $f_{\text{ext}}(t)$ was designed to excite the fundamental mode of the C-beam model, which has the displacement field shown in Fig. 1.3a. This mode exhibits bending about the z -axis, with most of the deformation concentrated in the top beam. To excite this mode, a vertical haversine impulse was applied to a strip of nodes at center of the top C-beam. The impulse has a duration of 1 ms and was applied with various amplitudes. The loading pattern can be seen in Fig. 1.3b.

Dynamic simulation results are presented for the three HCB models described in Table 1.3, and for three loading amplitudes of 15, 100, and 500 N. These loading amplitudes are selected to elicit linear, moderately nonlinear, and strongly nonlinear responses, respectively. It is important to study different loading amplitudes to ensure that the HCB models retain accuracy for varying degrees of nonlinear response. A viscous damping matrix with 1% damping in all modes is included in the system to simulate a more realistic system.

Response convergence is determined based on system-level and interface-level outputs: the drive point displacement (vertical displacement at the loading point) is used to evaluate the global response convergence, while contact area and summation of normal contact forces determine local interface-level convergence. Time histories are computed out to 10 ms to adequately show the transient vibration response of the system subjected to a 1 ms haversine impulse.

A comparison of the different loading amplitudes and HCB models in Fig. 1.4 reveals that increasing the cutoff frequency from 2 to 3 kHz significantly alters the response at the system-level and interface-level. Drive point displacements, as well as contact area and interface forces, change dramatically in magnitude and frequency between the 2 and 3 kHz models. Furthermore, a visual comparison shows strong similarity between the 3 and 4 kHz results, indicating the reduced order models have converged. Similar to results from [4], the 2 kHz model is not accurate for this loading because the $2/\tau$ impulse frequency is 2000 Hz, but the model only kept frequencies up to 1544 Hz. Thus, the 2 kHz model cannot produce response frequencies in the range generated by the 1 ms impulse.

It is interesting to observe that for the 3 and 4 kHz models, the qualitative behavior of the drive point displacement does not change between different input levels (although the amplitude is scaled proportional to force). The contact area changes significantly with force level, and the total force at the interface oscillates considerably about the 2.91 kN preload force level. A seemingly linear global response in fact contains nonlinearities that are hidden in the interface-level outputs. This implies that, should friction be included, the damping characteristics of the system would change dramatically in time as the interfaces come in and out of contact.

The 3 and 4 kHz models provide satisfactory starting points for interface reduction, and both would be suitable for the dynamic loading considered here. Nonetheless, the 4 kHz model provides roughly 1200 Hz of increased frequency bandwidth over the 3 kHz model at the cost of only two more DOF, so the 4 kHz model is used for the following interface reduction studies.

1.3.4 Results: Interface-Reduced Model

The dynamic analysis from the full-interface studies in Sect. 1.3.3 is repeated here, but now using the interface-reduced models described by Eqs. (1.25a) and (1.25b). The base HCB model includes all fixed-interface frequencies up to 4 kHz,

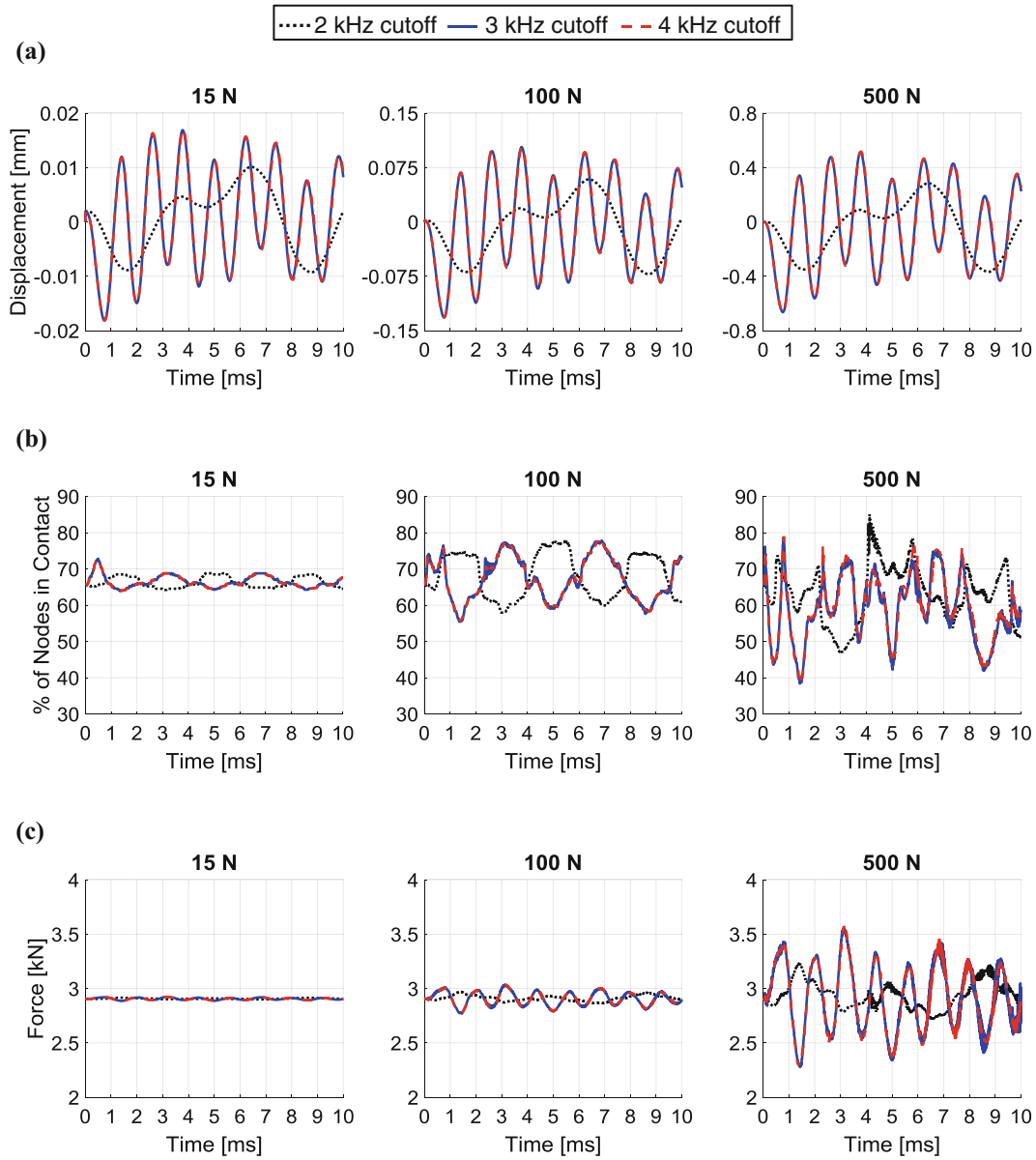


Fig. 1.4 Time history of (a) drive point displacement; (b) contact area (percentage of nodes in contact); (c) total normal contact force on one interface. Comparison between different HCB cutoff frequencies

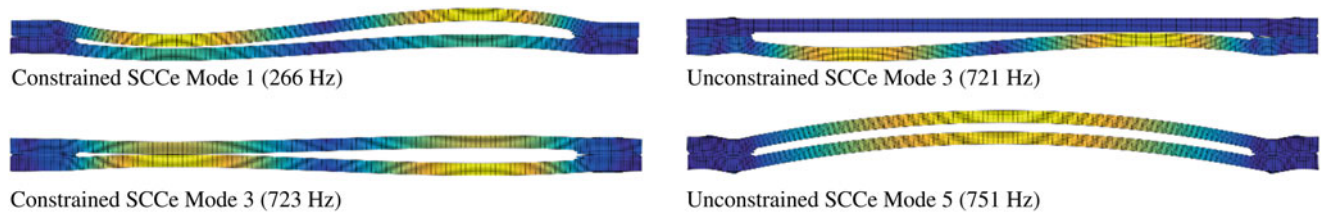


Fig. 1.5 Amplified SCCe mode shapes. Constrained modes are formulated in Eqs. (1.12) and (1.13). Unconstrained modes are formulated in Eqs. (1.14) and (1.15)

which equates to 16 FI modes. The effect of interface fidelity is considered through several reduction cases that retain between 20 and 3659 total SCCe modes (constrained + unconstrained). A few SCCe mode shapes with their corresponding frequencies are plotted in Fig. 1.5.

Table 1.4 Model comparison for various levels of SCCe interface reduction

SCCe modes retained	Max constrained SCCe frequency [Hz]	Max unconstrained SCCe frequency [Hz]	Max model frequency [Hz]	Model size [DOF]	Δt_{cr} [sec]	Δt_a [sec]
20	1.95E + 03	1.90E + 03	1.87E + 05	61	2.51E-07	2.26E-07
100	5.01E + 04	4.18E + 04	4.28E + 05	141	1.37E-07	1.23E-07
200	1.12E + 05	1.06E + 05	5.88E + 05	241	9.54E-08	8.59E-08
500	2.46E + 05	2.23E + 05	8.91E + 05	541	6.46E-08	5.81E-08
993*	3.77E + 05	3.48E + 05	1.19E + 06	1034	4.37E-08	3.93E-08
3659*	8.48E + 05	7.97E + 05	1.63E + 06	3700	3.26E-08	2.93E-08

Cases marked with * had some modes removed during the orthonormalization process

The same process shown in Sect. 1.3.3 is employed to determine ω_{max} and Δt_{cr} , but now the eigenvalue problem is formulated in the SCCe system using \mathbf{M}^{SCCe} and a linearized SCCe stiffness matrix \mathbf{K}^{SCCe-c} , obtained via

$$\mathbf{K}^{SCCe-c} = (\mathbf{U}^{SCCe+})^T \mathbf{K}^{HCB-c} \mathbf{U}^{SCCe+} \quad (1.32)$$

Similar to Sect. 1.3.3, the analysis time step Δt_a is obtained by multiplying the critical time step Δt_{cr} by a factor of 0.9. Table 1.4 summarizes the different SCCe models in terms of maximum frequency, number of DOF, and critical time step length. Note that the analysis time steps of the SCCe models are significantly larger than that of the HCB model (2.93E-08), which results in nearly an order of magnitude speed-up in explicit time solvers.

Drive point displacement, contact area, and normal contact force time histories for the different SCCe models are plotted against those of the 4 kHz HCB model, shown in Fig. 1.6.

Visual comparison of the drive point displacement histories in Fig. 1.6a shows that all SCCe solutions lie on top of the HCB solution, with no observable deviations. For 500 or more SCCe modes, the normal contact force in Fig. 1.6c also shows near-perfect agreement. The contact area (percentage of nodes in contact) in Fig. 1.6b is the slowest to converge to the HCB solution, with significant errors observed for the case of 20 and 100 SCCe modes. All results converge to the HCB solution when all SCCe modes (3659 + 1 augmentation vector) are retained and the transformation basis is not truncated.

Drive point displacements from the HCB and SCCe models match well because the loading excites vibrational modes with deformations concentrated away from the interfaces, regardless of loading amplitude. The contact area and contact force, however, show a strong dependence on the loading amplitude. Errors in these quantities are negligible for the linear excitation of 15 N, but become more significant as the loading increases to the nonlinear excitations of 100 and 500 N. This implies that the accuracy of the SCCe method not only depends on the number of modes in the reduction basis, but also on the degree of nonlinearity (and therefore the loading amplitude). If the only output of interest is some system-level displacement at a location sufficiently distant from the interfaces, then only a small number of SCCe modes is required. Still, the rapid changes in contact area (Fig. 1.6b) would have a significant effect on the system-level damping if friction was included at the interface. In that case, more SCCe modes would be necessary to accurately capture system-level response.

It is important to note that at certain levels of interface reduction, the total contact force (Fig. 1.6c) may be accurate, while the contact area (Fig. 1.6b) has significant errors. Interface forces in the SCCe model with 500 modes show near-perfect agreement with the HCB model, but the contact areas are in error by up to 20%. A relatively small number of SCCe modes are needed for convergence in overall contact forces, but more modes must be added to achieve suitably accurate interfacial stresses, which require accurate representation of the contact area.

This is confirmed by the distribution of contact forces plotted in Fig. 1.7. The spread of contact forces over one interface surface is plotted at single instant in time ($t = 3.10$ ms), and under the most severe loading (500 N). At this selected time, the structure is transitioning from low to high contact area, a phenomenon that seemingly requires a high number of included SCCe modes. The sum of instantaneous contact forces quickly converges to around 3500 N, but doesn't accurately represent the distribution of those forces within the interface until many more modes are added.

To the extent previously described, the interface reduction basis provides an acceptable level of accuracy relative to the full-interface HCB model. The final and arguably most important metric for gauging the effectiveness of the interface reduction is its potential for computational savings. The previous analyses were repeated using the implicit and explicit time integration schemes described in Sect. 1.2.4. Simulation run times for each of these cases are plotted in Figs. 1.8 and 1.9. The solve time reduction factor is the ratio of HCB solve time to SCCe solve time.

Explicit time integration is carried out using 90% of the critical time step as determined by Eq. (1.29). This resulted in a time step length of 2.93E-08 sec for the HCB model, and ranged from 2.26E-07 sec to 2.93E-08 sec for the SCCe models (see Table 1.4). The implicit scheme is unconditionally stable, so a time step length is chosen provide adequate resolution

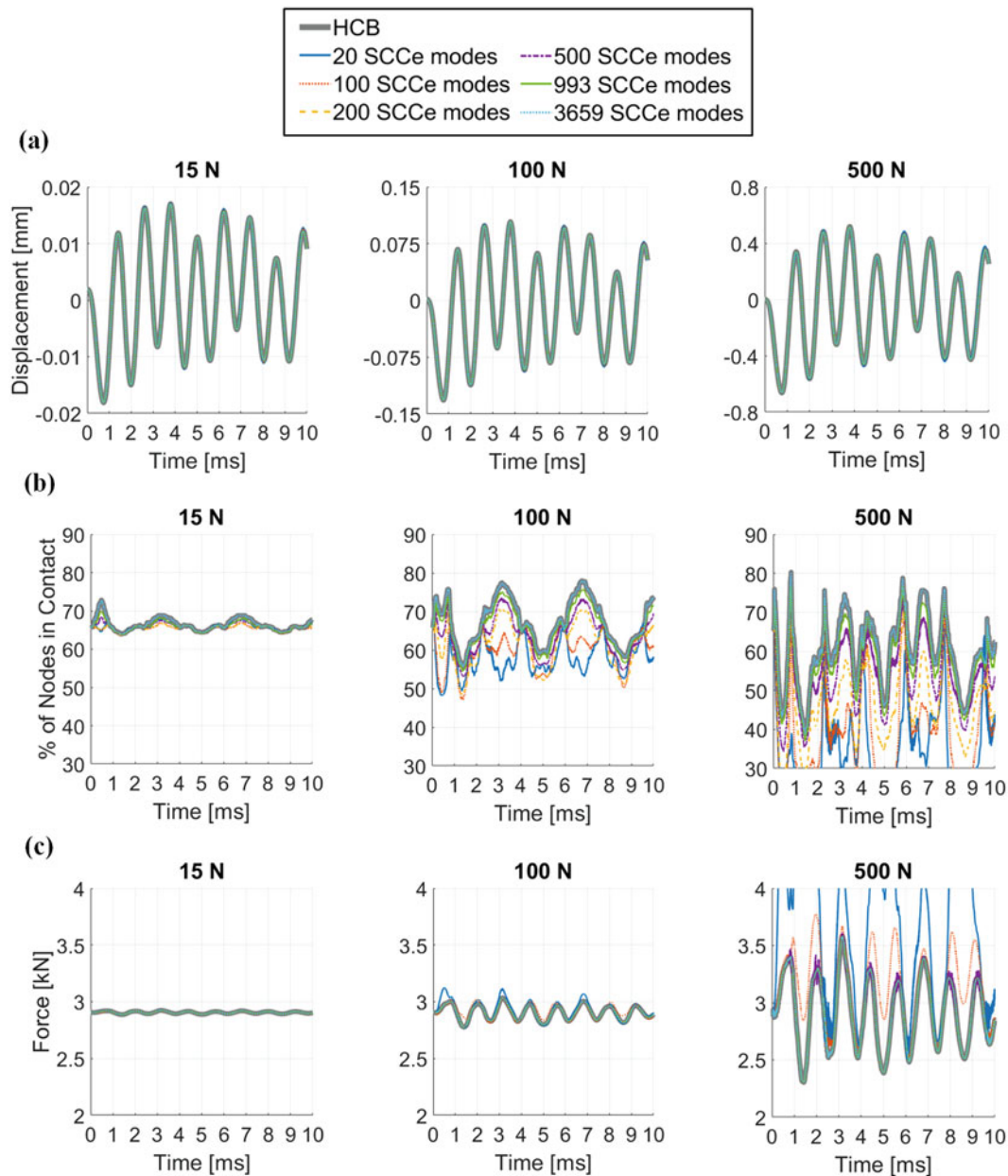


Fig. 1.6 Time history of (a) drive point displacement; (b) contact area (percentage of nodes in contact); (c) total normal contact force on one interface. Various levels of SCCe reduction compared to full-interface HCB model

over a simulation time of 10 ms. For this study, a time step of $1.00\text{E-}05$ sec was selected, such that the implicit scheme yields 1000 equally-spaced solution points.

Results from the implicit simulations in Fig. 1.8a, b show that the SCCe interface reduction provides a wide range of computational savings. The SCCe method reduces solve time by a factor of approximately 19 when 20 modes are included, but the savings decrease rapidly as more modes are added. With 100, 200, and 500 SCCe modes retained, the solve time is reduced by a factor of 8, 4, and 2, respectively. The 993 mode case provides almost no reduction for the 15 N loading (reduction factor of about 1), and increases solve time for the 100 N and 500 N loadings (reduction factor less than 1). The “exact” case of 3659 SCCe more than doubles the solve time for all loading amplitudes. This seemingly counterintuitive result comes from the fact that the implicit solver requires iterations at each time step to reach equilibrium with the nonlinear contact forces. The SCCe models require a costly coordinate transformation at every state determination, so eventually the cost of performing the transformation outweighs the savings from the reduced model size. Furthermore, higher-amplitude

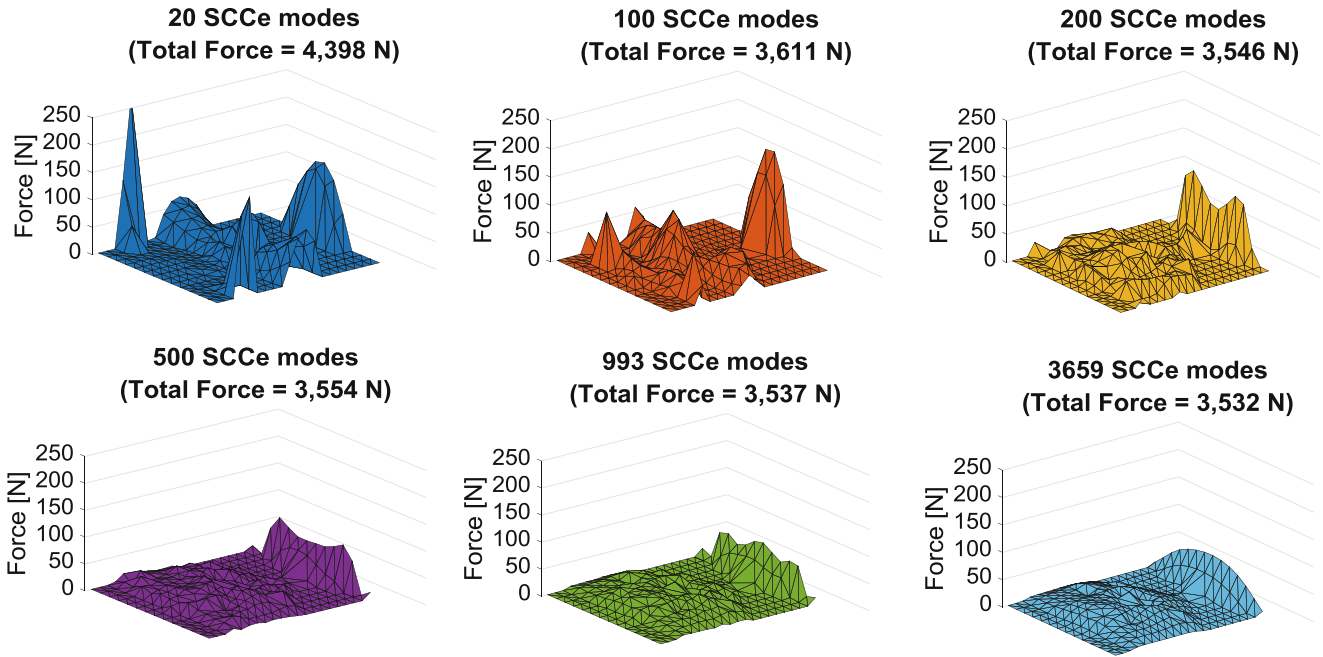


Fig. 1.7 Contact force distribution at one interface surface for full-interface HCB model and various levels of SCCe interface reduction. Snapshot is taken at $t = 3.10$ ms with loading amplitude 500 N

loadings are effected more by this phenomenon because the greater degree of nonlinearity inherently requires more iterations to reach equilibrium.

The explicit simulation results in Fig. 1.9a, b are drastically different than those of the implicit scheme. Firstly, the solve times are indifferent to the loading amplitude, which is due to the lower order of equations being solved relative to the implicit case. The cost savings are also much more significant, with reduction factors between 40 and 220 for the cases of 20, 100, and 200 SCCe modes. The 500 mode case reduced the computation time by a factor of 16, and the 993 mode case by a factor of 5. The cost reduction observed in the explicit results is due to the significant model size reduction (3700 reduced to 61, 141, 241, 541, or 1034), as well as the difference in time step length (see Table 1.4).

In the “exact” case, where 3659 modes are retained, the SCCe simulation ran about twice as long as the equivalent HCB analysis. This means that, somewhere between 993 and 3659 retained SCCe modes, the reduced model will complete a simulation in the same time as the full-interface model. At this critical reduction level, the benefit of a reduced model size is exceeded by the cost of the HCB-SCCe coordinate transformation that must be performed at each time step.

1.4 Conclusions

The Hurty/Craig-Bampton (HCB) method was applied to a system with frictionless contact, and a novel expansion of the system-level characteristic constraint mode method (SCC) method was defined and used to further reduce the model size and simulation time. The new interface reduction technique, deemed the SCCe method, reduced most of the interface DOF in the HCB model to modal DOF, while leaving some as physical DOF. Contact at the interfaces was modeled using node-to-node penalty elements in the normal direction, with the interfaces meshed such that the contact surfaces are conforming and node pairs are known a priori. The SCCe method was demonstrated on an assembly of two beams bolted together and subjected to a 1-ms haversine impulse applied at its midspan. The base HCB model used for interface reduction included 16 fixed-interface modes, with a maximum fixed-interface frequency of 3763 Hz.

Results from the SCCe reduced models indicate that only a small number of retained SCCe modes is required to reproduce system-level displacements and total contact force at the interfaces, but more SCCe modes are needed to converge to the HCB solution for contact area. Reduction in simulation time, relative to the HCB model, is most significant when using an explicit integration method. Use of an implicit scheme with the SCCe method yields much less computational savings, and even increases the simulation time where the explicit scheme would reduce it.

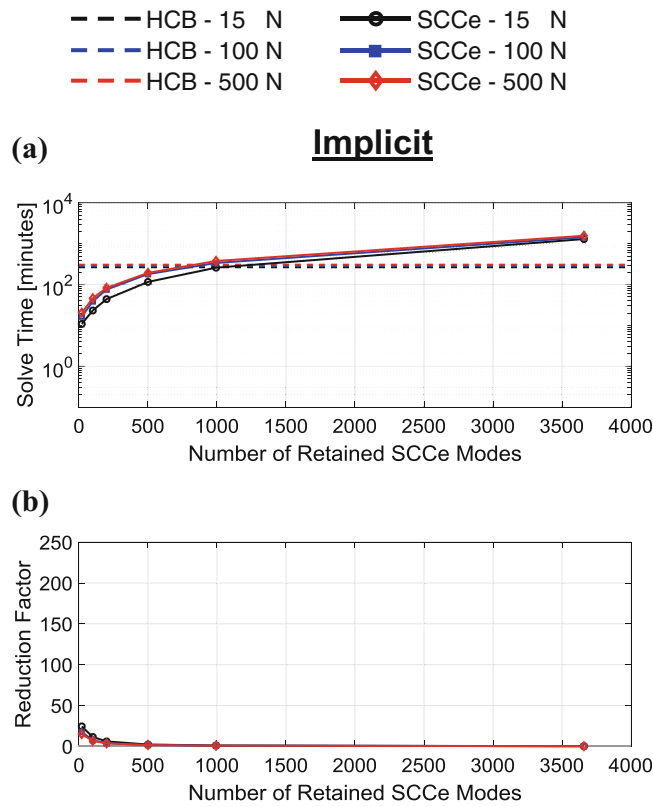


Fig. 1.8 (a) Solve time and (b) solve time reduction factor for implicit

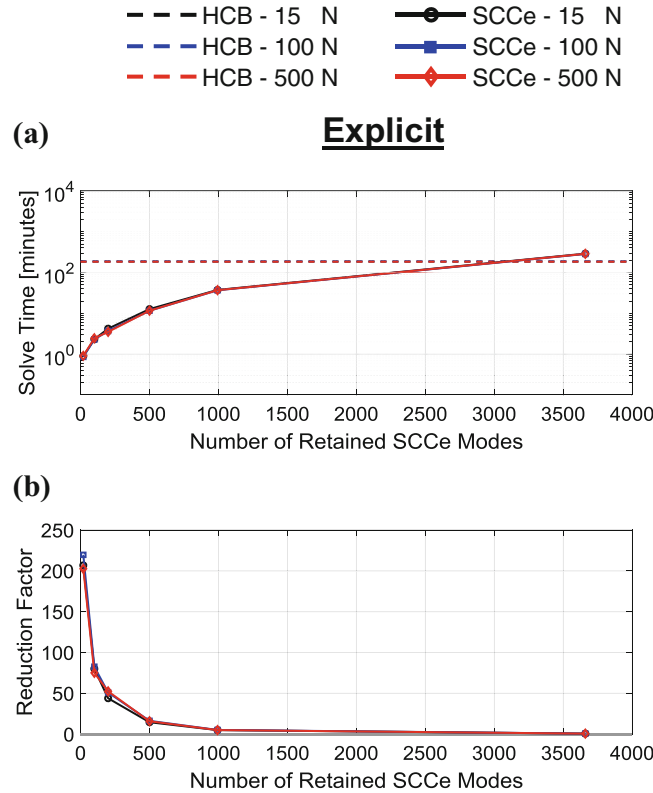


Fig. 1.9 (a) Solve time and (b) solve time reduction factor for explicit

This research serves as a numerical proof-of-concept, which explores the viability of interface reduction on contacting substructures when nonlinear elements are applied at the interface. Results from this work indicate moderate success of the reduction scheme, but more work is needed to determine the applicability of this method to other situations. Future work will examine different reduction bases, variation in dynamic loading patterns, more general contact models, non-conforming interfaces, and the inclusion of friction elements.

Acknowledgements This research was conducted at the 2017 Nonlinear Mechanics and Dynamics (NOMAD) Research Institute supported by Sandia National Laboratories. Sandia National Laboratories is a multi-mission laboratory managed and operated by National Technology and Engineering Solutions of Sandia, LLC., a wholly owned subsidiary of Honeywell International, Inc., for the U.S. Department of Energy's National Nuclear Security Administration under contract DE-NA-0003525. SAND2017-11361C.

References

1. Gaul, L.: Wave transmission and energy dissipation at structural and machine joints. *ASME Trans J Vib Acoust Stress Reliab Des.* **105**, 489–496 (1983)
2. Jenkins, G.M.: Analysis of the stress-strain relationships in reactor grade graphite. *Br. J. Appl. Phys.* **13**(1), 30 (1962)
3. Iwan, W.D.: A distributed-element model for hysteresis and its steady-state dynamic response. *ASME.* **33**, 893 (1966)
4. Kuether, R.J., Coffin, P.B., Brink, A.R.: On Hurty/Craig-Bampton substructuring with Interface reduction on contacting surfaces. *Proceedings of the ASME International Design Engineering Technical Conferences & Computers and Information in Engineering Conference* (2017)
5. Gaul, L., Becker, J.: Damping prediction of structures with bolted joints. *Shock. Vib.* **17**(4–5), 359–371 (2010)
6. Hurty, W.C.: Dynamic analysis of structural systems using component modes. *AIAA J.* **3**(4), 678–685 (1965)
7. Craig, R.R., Bampton, M.C.C.: Coupling of substructures for dynamic analysis. *AIAA J.* **6**(7), 1313–1319 (1968)
8. Krattiger, D., Wu, L., Zacharczuk, M., Buck, M., Kuether, R.J., Allen, M.S., et al.: Interface reduction for Hurty/Craig-Bampton substructured models: review and improvements. *Mech. Syst. Signal Process.* (in Review) (2017)
9. Craig, R., Chang, C.: Substructure coupling for dynamic analysis and testing. NASA, TR CR-2781, 1977
10. Castanier, M.P., Tan, Y.-C., Pierre, C.: Characteristic constraint modes for component mode synthesis. *AIAA J.* **39**(6), 1182–1187 (2001)
11. Wriggers, P.: *Computational contact mechanics.* Springer, Berlin, 2006
12. Chung, J., Lee, J.M.: A new family of explicit time integration methods for linear and non-linear structural dynamics. *Int. J. Numer. Methods Eng.* **37**(23), 3961–3976 (1994)
13. Crisfield, M.A.: *Non-linear Finite Element Analysis of Solids and Structures. Volume 2: Advanced Topics,* New York, John Wiley and Sons, pp. 455–456, 1991 *Engineering & Structural Dynamics* 5.3 (1977): 283–292
14. Sierra Structural Dynamics Development Team, *Sierra Structural Dynamics – User's Notes,* SAND2017–3553, Sandia National Laboratories, Albuquerque, NM (2017)
15. DIN 946 (1991–10). Determination of coefficient of friction of bolt/nut assemblies under specified conditions (1991)



Chapter 2

Experimental Path Following of Unstable Static Equilibria for Snap-Through Buckling

T. van Iderstein and R. Wiebe

Abstract Understanding the potential energy surface of bistable systems is critical for predicting dynamic snap-through response. Static equilibria create peaks, valleys, and saddle points, guiding a beam or plate through its vibration. Numerical methods allow detailed study of these points, but experimental work has been more limited in scope. Unstable equilibria are not possible to observe with current experimental methods. This paper presents the design and implementation of a control system and testing apparatus able to stabilize unstable equilibria and follow unstable equilibrium paths. The results for a buckled beam with a point load at midspan are presented.

Keywords Unstable equilibria · Snap-through buckling · Control system · Experimental · Nonlinear

2.1 Introduction

Snap-through buckling is a mainstay topic in nonlinear analysis and structural stability. Recent work, primarily in hypersonic aircraft and microelectromechanical devices, has brought practical significance to the topic. Snap-through buckling is characterized by complicated load-displacement behavior with many bifurcations and unstable regions. The system can behave chaotically under dynamic loading. Static equilibria form local maximums, minimums, and saddle points in the potential energy surface. Local minimums are stable, but local maximums and saddle points are both unstable. Stable configurations are easy to observe experimentally, but little work has been done to identify unstable equilibria in physical structures experimentally.

Numerous quasi-static experiments on snap-through buckling have been conducted under load control in [1], displacement control with contact only in [2, 3], displacement control with full attachment in [4], and rigid displacement constraints in [5]. These papers explored stable configurations under a single point load or continuous rigid constraint. In [6], a dynamic approach was taken to identify a single unstable static equilibrium, which required large datasets and significant post-processing.

A control system is needed to observe unstable static equilibria experimentally. The loading case considered in this paper, shown in Fig. 2.1a, is similar to previous experimental work: a transverse point load applied at the midspan of a buckled beam with pin-pin boundary conditions. Under load control, the structure snaps to a remote configuration when a limit or bifurcation point is encountered, skipping over parts of the curve at a lower load. The branch with the lowest load can be followed by controlling the displacement of one point, as seen in [4]. More control points are needed for higher-order branches. To stabilize the first symmetric branch, three control points are needed: a loaded control point at midspan and two unloaded control points at the one-quarter and three-quarter span locations, shown in Fig. 2.1b. At an equilibrium configuration, only the control point at the midspan carries a load. The side control points must have zero load to satisfy the load case, but their displacement determines whether the beam is in a symmetric or asymmetric configuration. Fig. 2.1a shows a displacement state on the first asymmetric branch, and Fig. 2.1b shows a higher-order configuration on the first symmetric branch.

T. van Iderstein (✉) · R. Wiebe

Department of Civil & Environmental Engineering, University of Washington, Seattle, WA, USA

e-mail: tvi@uw.edu

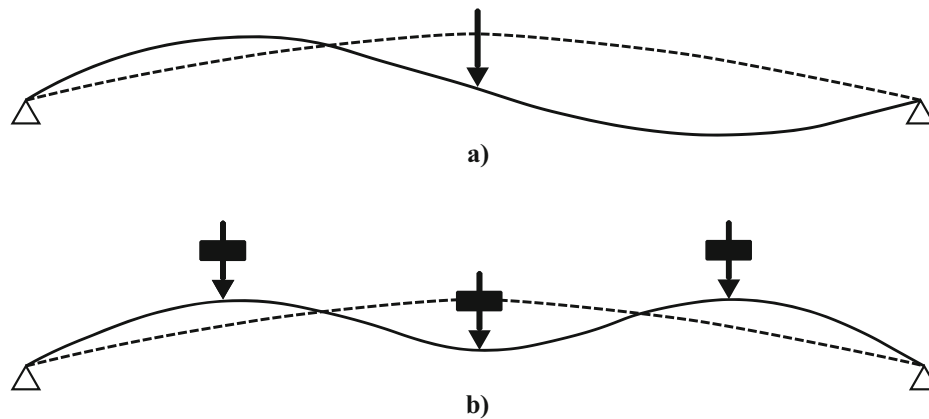


Fig. 2.1 Schematics of load case and control points used to stabilize a higher-order equilibrium path. (a) Load case considered in test showing unloaded shape (dashed) and deformed shape (solid). (b) Location of control points showing unloaded shape (dashed) and higher-order deformed shape (solid)

2.2 Experimental Design

2.2.1 Experimental Setup

For ease of testing, a beam with a low limit load and resistance to damage was needed. Carbon fiber composite was chosen, as it does not yield and is thin. This enables the use of cheaper equipment and repeated testing without damaging the beam. A beam with $E = 108\text{GPa}$, and dimensions $267\text{ mm} \times 30\text{ mm} \times 0.56\text{ mm}$ was used.

Load was monitored by three Honeywell Model 34 load cells [7], two with a capacity of 5 lb. (22.2 N) and one with a capacity of 10 lb. (44.5 N). The 10 lb. actuator was used at the center point, as the loading would be highest here and allowed for a larger range of limit loads. The 5 lb. load cells were used at the one-quarter and three-quarter points as the loads at these locations would be near zero for most of the test.

Displacement was controlled and measured by three Actuatorix L12-I micro linear actuators with a stroke of 50 mm [8]. At the selected gearing ratio of 210:1, these were rated to a tensile capacity 80 N, a compressive capacity of 45 N, and a repeatability error of 0.5 mm. The actuators contained integrated controllers and potentiometer feedback, making them simple to implement with analog voltage control. At loads above 15 N, the actuators had difficulty moving small increments due to friction in the screw drive. Because small movements were necessary in this experiment, this became the controlling limit load. In addition, the stroke limit on the actuators dictated the buckled rise on the beam.

The load frame was constructed out of OpenBeam [9], an extruded aluminum beam and plastic connection modular product. The test beam specimen was connected to the frame using small metal piano hinges, giving as close to an ideal pin connection as possible. The load cells were attached to the actuators by a threaded rod, and the beam was attached to the load cell via a threaded swivel-shaft rod end glued to the beam top surface. The swivel-shaft rod end allowed free rotation of the beam at the load-application point. The final testing apparatus is shown in Fig. 2.2 with a beam attached.

2.2.2 Control System

With three actuators, snap-through buckling experiments are impractical with manual control. An automated control system is needed for efficient and accurate testing. For the results presented, a control system implemented in LabVIEW was used. The midspan and side actuators operated independently from each other. Displacement control was used on the midspan actuator. A two-degree-of-freedom Newton Raphson scheme was used to control the side actuators since the load case required zero load at those two control points. A flowchart of the control system is shown in Fig. 2.3.

The local tangent stiffness was needed for every iteration in the Newton-Raphson scheme. This was approximated by the local secant stiffness measured by the side control points. A column of the stiffness matrix was calculated by moving one actuator a small displacement, measuring the change in load at both control points, and normalizing that change by the small displacement. This stiffness was used to calculate the displacement increment that would minimize the load in the

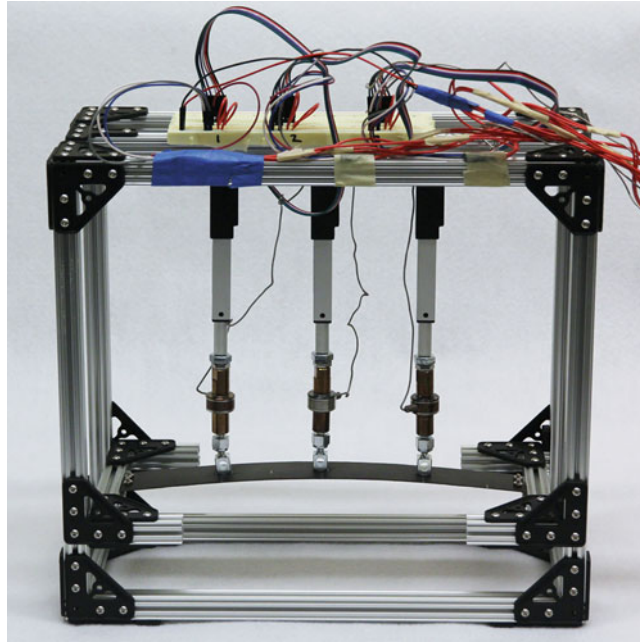


Fig. 2.2 Load frame with beam in unloaded configuration

side control points. Once convergence was achieved, the loads and displacements at the three control points were saved. By measuring the tangent stiffness experimentally, imperfections in the setup were accounted for.

Despite the power of this control system, it has its limitations. As the tangent stiffness becomes singular at limit and bifurcation points, the Newton-Raphson scheme breaks down, limiting where equilibrium points can be found on both the stable and unstable paths. In addition, by monotonically increasing the displacement of the center actuator, reversals along the force-displacement curve will be lost. Another numerical method commonly used in models for snap-through buckling—the arc length method—was investigated but was not suitable. It is able to follow reversals and traverse singular points, but it relies on being able to control load independently of displacement. With the current load frame, the two cannot be decoupled, so an alternative numerical method is needed.

2.3 Results

In Fig. 2.4, the force-displacement curve of a snap-through test is shown. The primary branch was obtained by displacement control of only the midspan control point, while the higher-order branch was obtained using the control system described above with three control points. One limit point for the higher-order branch occurs around $y_{\text{mid}} = -9$ mm. Since the control system was not able to converge near this point, the data here is missing. Experimentally following the higher-order branch stopped when the beam displaced into an asymmetric configuration around $y_{\text{mid}} = 4$ mm. Theoretically, the higher-order branch would continue downwards and loop around into other higher-order paths, but that would require more than three control points to stabilize. A reflection of the higher-order branch could be followed starting at $y_{\text{mid}} = 8$ mm and decreasing in displacement, but it was not followed in this experiment.

In Fig. 2.5, the displaced shapes at $y_{\text{mid}} = -0.75$ mm on the primary path and the higher-order symmetric path are shown. A second stable configuration coexists with a mirror-image displaced shape. From Fig. 2.4, the unstable configuration requires a higher load than the stable configuration. The curvature in the symmetric shape is higher, resulting in higher internal moments. Both of these things put the symmetric configuration at a higher energy state. In addition, any perturbation of the symmetric shape would result in convergence to an asymmetric shape if the control points were not present.

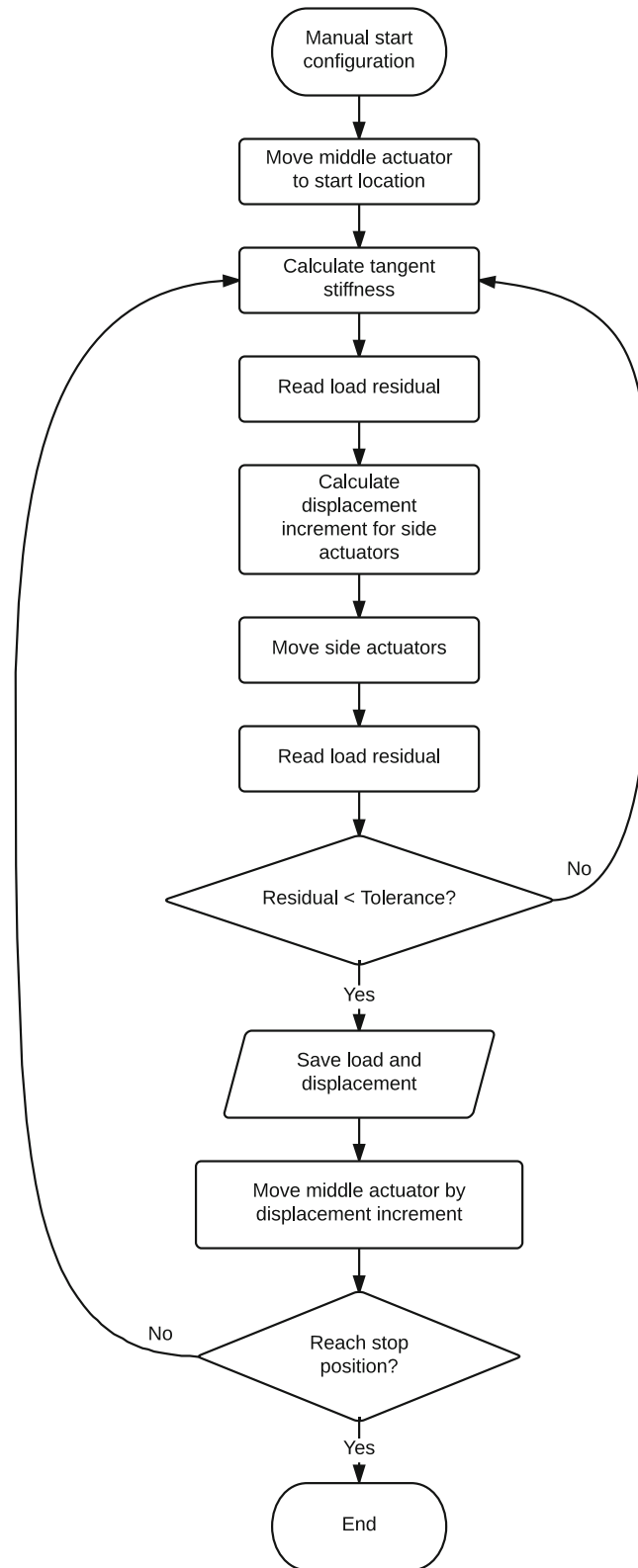


Fig. 2.3 Flowchart for a control system combining load and displacement control to find equilibrium configurations in a structure using multiple actuators

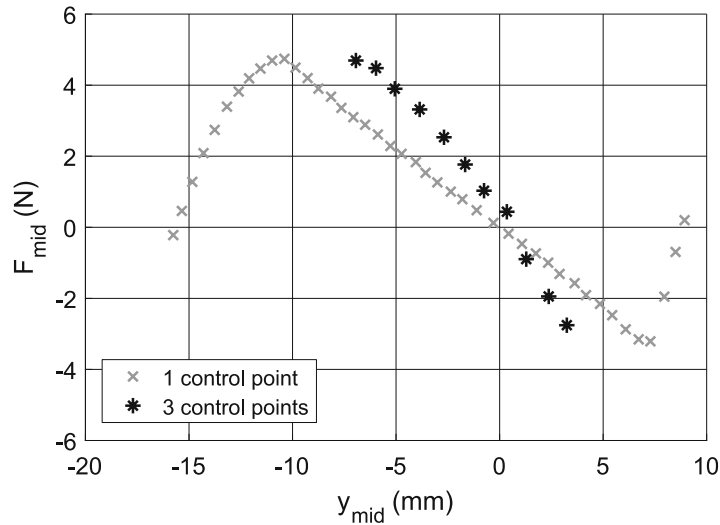


Fig. 2.4 Experimental force-displacement curve for two co-existing equilibrium paths

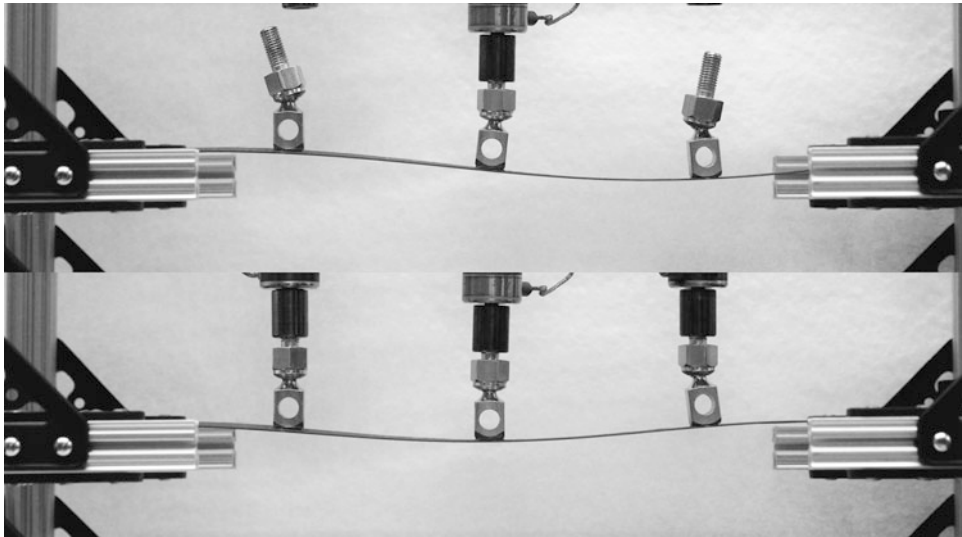


Fig. 2.5 Displaced shapes at $y_{mid} = -0.75$ mm, first asymmetric path using one control point (upper photo), first symmetric path using three control points (lower photo)

2.4 Conclusion

This work details an experimental method for finding and following unstable equilibrium paths in structures that exhibit snap-through buckling. The control system was unable to converge around a limit or bifurcation point because of numerical limitations (compounded by experimental error), but the majority of the first symmetric equilibrium path was accessible. Only one load case and initial configuration was considered, so further work is necessary to expand the experimental envelope of this experimental method.

The control method used requires accurate displacement control and measurement of displacement and load. The actuators in this setup were not intended for high-accuracy work, so the experiments had to be run at a coarser step size. For future experimental work, actuators with higher accuracy controllers and feedback are recommended.

While three control points were used in this work, the methodology scales to an arbitrary number of control points. The method for controlling the loaded control points can be modified to allow for other load cases. Specifying control points that must be unloaded at an equilibrium configuration allows for higher-order equilibrium paths to be stabilized. Future work for the authors includes finding the critical number of control points needed to stabilize these higher-order unstable configurations.

References

1. Fung, Y.C., Kaplan, A.: Buckling of low arches or curved beams of small curvature. NACA, Technical Note 2840 (1952)
2. Chen, J.-S., Hung, S.-Y.: Snapping of an elastica under various loading mechanisms. *Eur J Mech A Solids*. **30**(4), 525–531 (2011)
3. Harvey Jr., P.S., Virgin, L.N.: Coexisting equilibria and stability of a shallow arch: unilateral displacement-control experiments and theory. *Int. J. Solids Struct.* **54**, 1–11 (2015)
4. Camescasse, B., Fernandes, A., Pouget, J.: Bistable buckled beam and force actuation: experimental validations. *Int. J. Solids Struct.* **51**(9), 1750–1757 (2014)
5. Chai, H.: The post-buckling response of a bi-laterally constrained column. *J. Mech. Phys. Solids*. **46**(7), 1155–1181 (1998)
6. Wiebe, R., Virgin, L.N.: On the experimental identification of unstable static equilibria. *Proc. Royal Soc. A*. **472**(2190), 20160172 (2016)
7. <https://www.honeywell.com/>
8. <https://www.actuonix.com/>
9. <http://www.openbeamusa.com/>



Chapter 3

Direct Detection of Nonlinear Modal Interactions and Model Updating Using Measured Time Series

Keegan Moore, Mehmet Kurt, Melih Eriten, D. Michael McFarland, Lawrence A. Bergman, and Alexander F. Vakakis

Abstract We describe a new method for identifying mechanical systems with strongly nonlinear attachments using measured transient response data. The procedure is motivated by the desire to quantify the degree of nonlinearity of a system, with the ultimate goal of updating a finite-element or other mathematical model to capture the nonlinear effects accurately. Our method relies on the proper orthogonal decomposition to extract proper orthogonal mode shapes (POMs), which are inherently energy dependent, directly from the measured transient response. Using known linear properties, the system's frequencies are estimated using the Rayleigh quotient and an estimated frequency-energy plot (FEP) is created by them as functions of the system's mechanical energy. The estimated FEP reveals distinct linear and nonlinear regimes which are characterized by constant frequency (horizontal lines) and large frequency changes, respectively. The nonlinear regimes also contain spikes that connect different modes and indicate strongly nonlinear modal interactions. The nonlinearity is identified by plotting the estimated frequencies as functions of characteristic displacement and fitting a frequency equation based on the model of the nonlinearity. We demonstrate the method on the response of a cantilevered, model airplane wing with a nonlinear energy sink attached at its free end.

Keywords Proper orthogonal decomposition · Nonlinear system identification · Frequency-energy plot · Nonlinear normal modes · Nonlinear energy sink

3.1 Method

While the techniques to be presented are applicable to either discrete or continuous structures, it is most convenient to present them in the context of a discrete model. This is hardly a limitation in practice, considering that experimental data acquisition is inherently limited to discrete points in space, and that finite element analysis can produce a viable discrete model for most distributed systems of interest [1]. A large number of degrees of freedom can be accommodated, but it is often desirable to reduce the model dimension, either for computational efficiency or to avoid the need to infer quantities that are difficult to measure directly. An example of the latter is rotation about an in-plane axis at a point on a beam or plate undergoing bending. Such quantities can often be systematically eliminated from the equations of motion by an established technique such as Guyan reduction [2], with little effect on the behavior of the dynamical model.

Given the mass and linear stiffness properties of a system, represented by mass and stiffness matrices, we turn to the processing of time series obtained by measuring the response of the system following an input of known magnitude (typically an impulse applied to one degree of freedom). Using proper orthogonal decomposition [3], we construct a set of basis vectors which can be used to represent the response of the system over an interval when its total energy is nearly constant. Thus, the method applies to a damped system provided sufficient response is available at the energy of interest.

K. Moore (✉) · A. F. Vakakis
Department of Mechanical Science and Engineering, University of Illinois, Urbana, IL, USA
e-mail: kmoore14@illinois.edu

M. Kurt
Department of Mechanical Engineering, Stevens Institute of Technology, Hoboken, NJ, USA

M. Eriten
Department of Mechanical Engineering, University of Wisconsin, Madison, WI, USA

D. M. McFarland · L. A. Bergman
Department of Aerospace Engineering, University of Illinois, Urbana, IL, USA

Because of the nonlinearity of the system, the basis vectors obtained will, in general, depend on upon the energy in the system; they will evolve over time (albeit on a scale much slower than the system's vibration), or they will differ following inputs of different magnitudes. Combining the different sets of basis vectors with the constant coefficient matrices of the linear part of the system model, we obtain energy-dependent frequency estimates and thus *energy-dependent measures of the effects of nonlinearity*, which is reflected in the measured response although it is not found in the matrices used in the post-processing [4]. For each measurement, the characteristic displacement is defined as the temporal average of the absolute relative displacement between the system and the nonlinear attachment, which provides a single displacement value that is representative of the entire response. Finally, the nonlinearity is identified by plotting the estimated frequencies as functions of characteristic displacement to form a frequency-displacement plot (FDP) and fitting a frequency equation based on the characterization of the nonlinearity.

3.2 Example

We apply our method to a cantilevered, model airplane wing with a nonlinear energy sink attached to its free end. The wing is made of aluminum and its full dimensions are described in Fig. 3.1a. The finite element mesh used to model the wing is presented in Fig. 3.1b. The nonlinear energy sink is attached to the center of the wing's free end with both linear and nonlinear coupling. The linear coupling has stiffness 10 N/m and the nonlinear coupling is realized with a nonlinear spring possessing a pure cubic force-displacement relationship and a stiffness of $3 \times 10^9 \text{ Nm}^{-3}$. We excite the wing at the attachment point using a half-sine pulse with amplitude varying from 10^{-2} to 10^{12} N. The wing's transient response is simulated at 1000 force levels using a finite element model for 1 s. For each simulation, a set of basis vectors is extracted, the corresponding frequencies are estimated, and the characteristic displacements are computed as previously described. In Fig. 3.2a, we present the FDP for the NES, the wing's first four flexible modes, and the identified model. The nonlinearity is modeled as a polynomial nonlinearity of the form αz^β where z is the characteristic displacement. Using the identification procedure previously described, the parameters were identified as $\alpha = 3.047 \times 10^9$ and $\beta = 3.069$. Figure 3.2b presents the comparison of the predicted response using the identified model to the exact response for an impulse amplitude of 100 N.

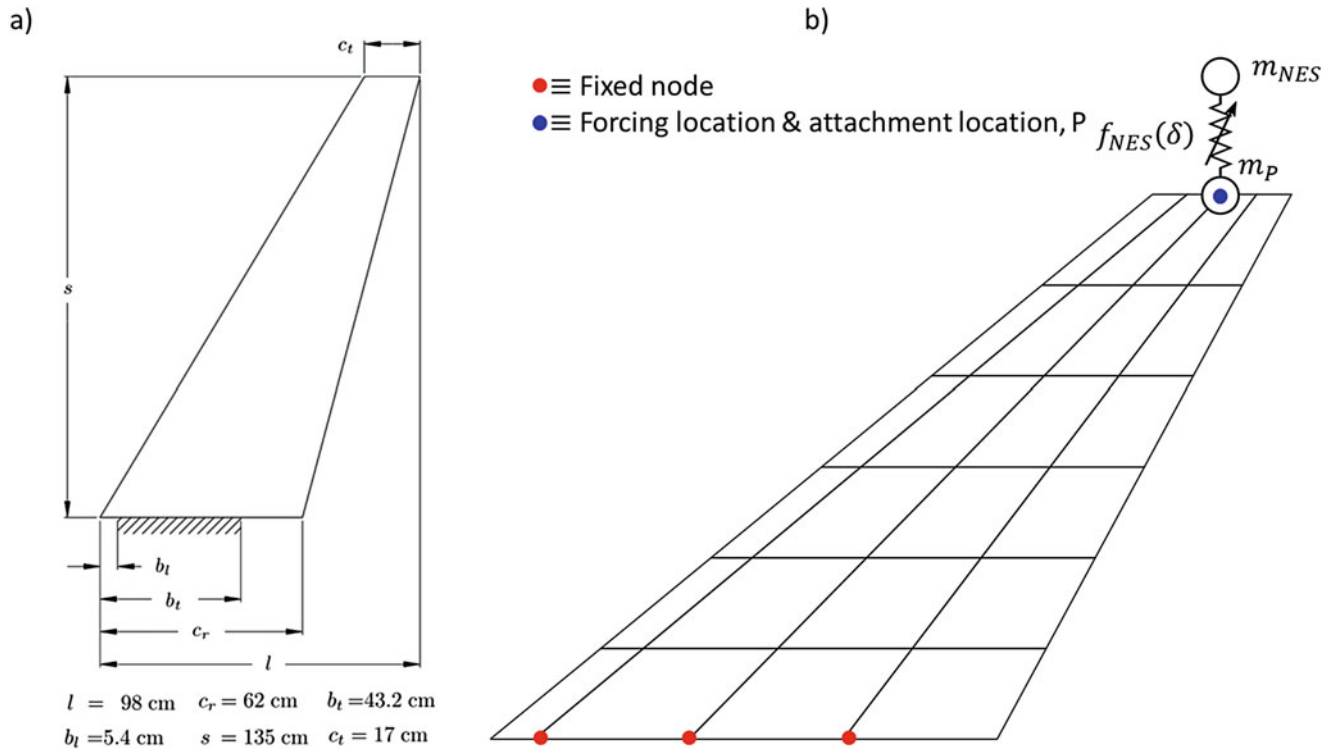


Fig. 3.1 (a) dimensions of the wing and (b) the FE model mesh used to model the wing

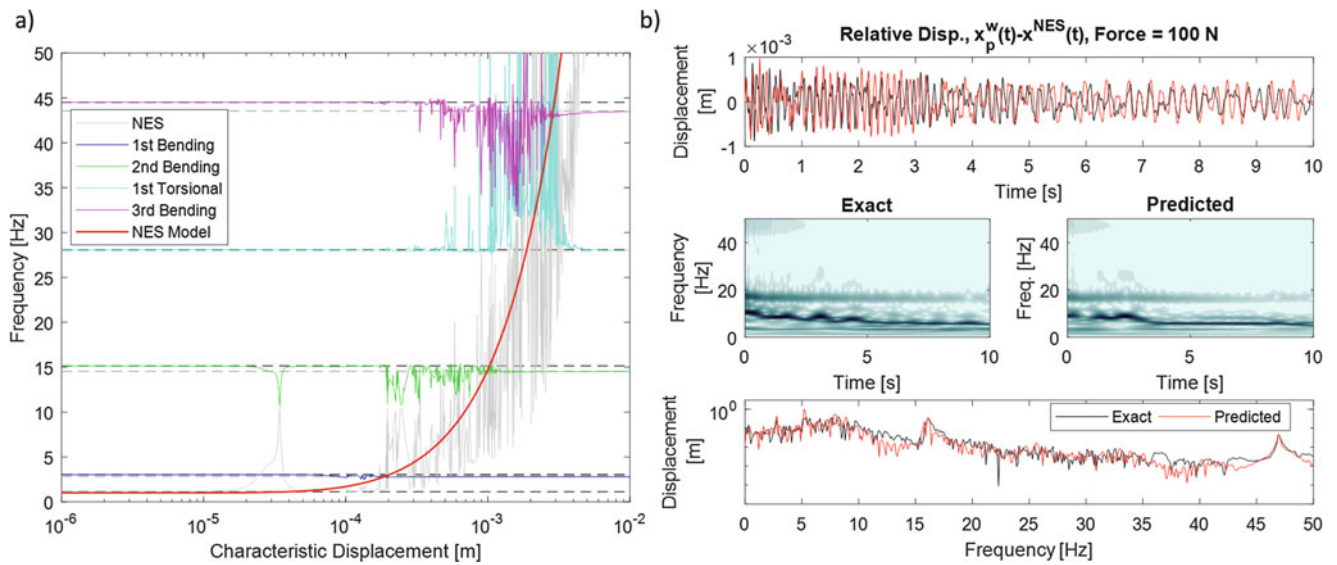


Fig. 3.2 (a) The estimated frequencies and identified model plotted as functions of characteristic displacement and (b) Comparison of the exact response and the response using the identified model for an impulse amplitude of 100 N

References

1. Friswell, M.I., Mottershead, J.E.: Finite Element Model Updating in Structural Dynamics. Springer, (1995)
2. Guyan, R.J.: Reduction of stiffness and mass matrices. AIAA J. **3**, 380 (1965)
3. Kerschen, G., Golinval, J.-C., Vakakis, A.F., Bergman, L.A.: The method of proper orthogonal decomposition for dynamical characterization and order reduction of mechanical systems: an overview. Nonlinear Dyn. **41**, 147–169 (2005)
4. Moore, K.J., Kurt, M., Eriten, M., McFarland, D.M., Bergman, L.A., Vakakis, A.F.: Direct detection of nonlinear modal interactions from time series measurements. Mech. Syst. Signal Process. <https://doi.org/10.1016/j.ymssp.2017.09.010>



Chapter 4

Pareto Optimization of a Nonlinear Tuned Mass Damper to Control Vibrations in Hand Held Impact Machines

Seyed Milad Mousavi Bideleh and Viktor Berbyuk

Abstract Large amplitude vibrations from hand held impact machines might bring serious health problems for users in long term. Here, a vibration absorber which works based on the nonlinear tuned mass damper concept is applied to mitigate unpleasant vibrations in a hand held impact machine. A global sensitivity analysis is carried out using multiplicative dimensional reduction method to scrutinize the effects of different components on the hand held impact machine dynamics response and attenuate the number of input parameters for optimization. Based on the global sensitivity analysis results, the nonlinear tuned mass damper components are chosen as the design parameters subject to optimization. A multiobjective optimization problem is formulated and solved using genetic algorithm to reduce vibrations and total weight of the machine. The Pareto optimized solutions are robust against the exciting force amplitude and frequency. The global sensitivity analysis results revealed that it is possible to run the simulations with a constant exciting force amplitude and extend the obtained solutions for the case with a variable exciting force amplitude while the same order of accuracy in the results can be observed. This significantly reduced the computational burden of the optimization. Closed form expressions for the optimal values of the tuned mass damper parameters as well as system response in terms of the auxiliary mass are developed by using the nonlinear least squares method. The results revealed that the proposed technique can significantly suppress the vibrations induced by the hand held impact machine. This makes it possible for users to operate the machine for a longer time period with lower health risks.

Keywords Nonlinear tuned mass damper · Hand held impact machine · Weight-vibration Pareto optimization · Global sensitivity analysis · M-DRM

4.1 Introduction

Efficiency, simplicity, and low maintenance cost are some of the most important features of tuned mass damper (TMD) technology which make it possible to employ this technique in a variety of engineering applications. Yang et al. [1] designed a two degrees of freedom (DOFs) TMD to damp the dominant mode of the workpiece/fixture assembly in milling process. The experimental results revealed around 80 percent reduction in the amplitude of the dominant mode using the two proposed techniques which was more efficient in comparison with to a single DOF and two single DOF TMDs with equal mass. Li and Tang [2] integrated a particle damping mechanism into a TMD configuration. Such a combination significantly magnified the energy dissipation capacity of the TMD especially when the host structure vibrates with low amplitudes. The proposed technique could also be used in harsh conditions such as high temperatures where ordinary fluid dampers might fail. Dinh and Basu [3] investigated the application of multiple TMDs in mitigating nacelle and spar vibrations of floating offshore wind turbines. The performance of the proposed multiple TMDs has been tested under different loading conditions. The results also showed that vibration reduction is not much improved by using more than two TMDs.

Optimization of TMD properties has been considered by many researchers, see e.g. [4–8]. Genetic algorithm (GA) is one of the most powerful tools in multiobjective design optimization of mechanical and structural systems, see e.g. [9–11]. Ok et al. [12] utilized a fast elitist non-dominated sorted GA to solve the multiobjective optimization problem of finding the optimal properties of a bi-tuned mass damper. The multiobjective optimization problem has been considered for different

S. M. Mousavi Bideleh
Multibody Dynamics, VETEC AB, Mölndal, Sweden
e-mail: milad.mousavi@vetec.se

V. Berbyuk (✉)
Department of Mechanics and Maritime Sciences, Chalmers University of Technology, Göteborg, Sweden
e-mail: viktor.berbyuk@chalmers.se

mass ratios to account for the respective effects on the control performance. By using the Pareto optimal solutions of each case and a nonlinear curve fitting technique, closed-form expressions for optimal tuning frequencies and damping ratios of bi-tuned mass dampers have been derived. Mohtat and Dehghan-Niri [13] utilized GA for robust design of TMD systems with application in multi-story buildings. The overall dynamics of the system has been modeled using a linear fractional transformation framework which isolated the TMD as a feedback controller. This approach made it possible to apply the active structural control concepts in passive design of TMDs. Greco et al. [14] employed GA to solve the multiobjective optimization design problem of a TMD to control the vibrations in buildings under low-moderate earthquakes. Cost and efficiency of the TMD device have been considered as two objective functions for optimization. The simulations showed that best TMD performance is achieved when the frequency of the main system is around the resonance region. Furthermore, the TMD yield higher performance for structures with a low damping. Detroux et al. [15] considered the performance, robustness, and sensitivity analysis of a nonlinear tuned vibration absorber. The effects of different design parameters and force amplitudes on the performance and operation region of the nonlinear tuned vibration absorber have been analyzed.

Multidisciplinary and multiobjective design optimization is basically a time costly procedure. Number of input design parameters can significantly affect the computational efforts for optimization. Therefore, as a preliminary stage in multidisciplinary design optimization of mechanical systems, it is necessary to carry out sensitivity analysis of the system response with respect to different design parameters. This makes it possible to narrow down the number of inputs for optimization and improve the computational efficiency of the algorithm. Zhang and Pandey [16] proposed an efficient algorithm for global sensitivity analysis (GSA) which worked based on a multiplicative dimensional reduction method (M-DRM). In the M-DRM, a given deterministic function is approximated by low dimensional functions which significantly simplifies high dimensional integrals required to calculate the sensitivity indices. The method has been applied to some simple mechanical and mathematical examples and the results showed excellent agreement with those associated with the Monte Carlo simulation. Mousavi Bideleh and Berbyuk employed this approach to study the effects of elastic suspension components of a high speed train on the overall performance of the vehicle, see e.g. [17, 18]. The results revealed that the proposed method is capable to accomplish the GSA for complex nonlinear systems with many DOFs in a computationally efficient manner.

Early it was shown that incorporation of a TMD into a hand held impact machine (HHIM) can significantly reduce the vibrations [19]. The present paper is a continuation of the work done in [19] and is focused on Pareto optimization of the TMD parameters in HHIMs. By using the M-DRM, the GSA is carried out for a 3 DOFs mechanical system which represents the HHIM with TMD. Then, a bi-objective optimization problem is considered to simultaneously reduce the weight and vibrations in the machine on a wide operation range of frequency and amplitude. The obtained results are analyzed and presented as Pareto front and Pareto set. The nonlinear least squares method is used to derive analytical expressions for relationships between the mass of the nonlinear TMD and optimized stiffness, gap, and preload values.

4.2 Engineering and Mathematical Models

The pneumatic HHIM comprises of a handle housing, an air inlet valve, a main body, a piston, an air outlet, a cylinder, a chisel, an auxiliary mass as well as several stiffness and damping components. The engineering model of the considered HHIM is depicted in Fig. 4.1a and is described more in detail in [19]. A 3 DOFs mechanical system is chosen to represent the HHIM with TMD. The sketch of the HHIM as a 3 DOFs system is shown in Fig. 4.1b. Parameters k_a , a , and F_0 represent the TMD stiffness, the half gap length, and the spring preload, respectively. Rest of the notations used to describe the HHIM model and respective values are given in Table 4.1. Vector $\mathbf{x}(t) = [x_1, x_2, x_3]^T$ is chosen as the vector of coordinates of the vibrating system as depicted in Fig. 4.1b.

The equations of motion for the 3 DOFs system shown in Fig. 4.1b are given [19]:

$$m_m \ddot{x}_1 + (c_m + c_h) \dot{x}_1 - c_h \dot{x}_3 + (k_m + k_h) x_1 - k_h x_3 = F_e(t) + F_k(\mathbf{x}) + F_c(\mathbf{x}, \dot{\mathbf{x}}) - m_m g \quad (4.1)$$

$$m_a \ddot{x}_2 = -F_k(\mathbf{x}) - F_c(\mathbf{x}, \dot{\mathbf{x}}) - m_a g \quad (4.2)$$

$$m_h \ddot{x}_3 - c_h \dot{x}_1 + (c_h + c_p) \dot{x}_3 - k_h x_1 + (k_h + k_p) x_3 = -m_h g \quad (4.3)$$

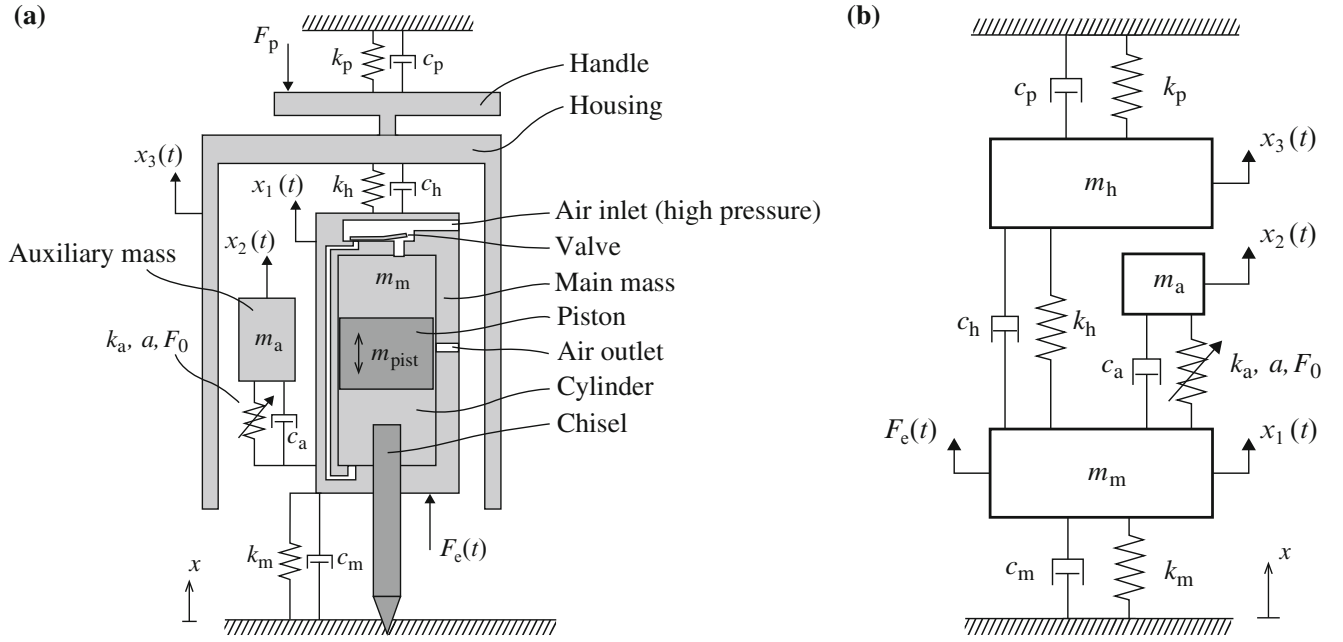


Fig. 4.1 Structure of the HHIM: (a) Engineering model; (b) 3 DOFs equivalent model [19]

Table 4.1 Structural parameters of the HHIM

Parameter	Nominal value	Description
m_m [kg]	2.7	The main body mass
m_a [kg]	1	The auxiliary mass
m_h [kg]	3.1	The housing mass
k_m [kN/m]	0.5	The stiffness between main mass and ground
k_h [kN/m]	14	The stiffness between main mass and housing
k_p [kN/m]	1	The hand arm stiffness
c_m [Ns/m]	100	The damping between main mass and ground
c_a [Ns/m]	1	The damping of the TMD
c_h [Ns/m]	20	The damping between main mass and housing
c_p [Ns/m]	60	The hand arm damping

In Eqs. (4.1, 4.2 and 4.3), functions $F_k(\mathbf{x})$ and $F_c(\mathbf{x}, \dot{\mathbf{x}})$ are stiffness and damping forces exerted by the TMD and function $F_e(t)$ is the periodic external excitation force acting on the HHIM.

In case when the functions $F_k(\mathbf{x})$ and $F_c(\mathbf{x}, \dot{\mathbf{x}})$ are given by the following expression.

$$F_k(\mathbf{x}) = k_a(x_2 - x_1), \quad (4.4)$$

$$F_c(\mathbf{x}, \dot{\mathbf{x}}) = c_a(\dot{x}_2 - \dot{x}_1), \quad (4.5)$$

the Eqs. (4.1, 4.2 and 4.3) with expressions (4.4 and 4.5) and the following initial states:

$$\begin{cases} \mathbf{x}(t_0) = \mathbf{x}_0 \\ \dot{\mathbf{x}}(t_0) = \dot{\mathbf{x}}_0 \end{cases}, \quad (4.6)$$

constitute the mathematical model of the HHIM equipped with linear TMD (L-TMD).

Alternatively, it is also assumed that the stiffness force exerting by the TMD is determined by the following nonlinear expression [19]:

$$F_k(\mathbf{x}) = \begin{cases} F_0 + k_a(x_2 - x_1 - a) & \text{if } x_2 - x_1 > a \\ -F_0 - k_a(-x_2 + x_1 - a) & \text{if } x_2 - x_1 < -a \\ 0 & \text{else} \end{cases} \quad (4.7)$$

The Eqs. (4.1, 4.2 and 4.3), expressions (4.5 and 4.7) together with the initial states (4.6) constitute the mathematical model of the HHIM with nonlinear TMD (N-TMD).

Some verification and experimental validation results of the presented mathematical models can be found in [19].

4.3 Objective Functions and Design Parameters

In what follows several problems on sensitivity analysis and optimization of the HHIM are considered within the L-TMD and N-TMD models.

To study the design of the HHIM as well as its performance several characteristics and objective functions are used. For both L-TMD and N-TMD models the following objective functions given by Eqs. (4.8 and 4.9) are introduced to measure the vibrations induced to the user by the HHIM

$$\Gamma_{\text{Dis}}(f) = \max_f \{ \text{RMS}(x_3(t)) \}, \quad (4.8)$$

$$\Gamma_{\text{Vol}} = \int_{F_{\text{eref}}^{\min}}^{F_{\text{eref}}^{\max}} \int_{f_{\min}}^{f_{\max}} \text{RMS}(x_3(t)) \, df \, dF_{\text{eref}}, \quad (4.9)$$

where $\text{RMS}(x_3(t)) = \sqrt{\frac{1}{t_f - t_0} \int_{t_0}^{t_f} (x_3(t))^2 dt}$.

Variables $f \in [f_{\min}, f_{\max}]$ and $F_{\text{eref}} \in [F_{\text{eref}}^{\min}, F_{\text{eref}}^{\max}]$ are the frequency and the reference value of amplitude of the harmonic external excitation force, respectively.

Objective function Γ_{Disp} indicates the maximum RMS value of $x_3(t)$ amplitude within the frequency range.

Objective function Γ_{Vol} is the volume below the surface surrounded by frequency, exciting force amplitude and RMS of the vibration. Indeed, in this case the aim is to minimize the RMS value of vibrations on a set of desired frequency and force amplitude ranges.

For the GSA and optimization of the HHIM different vectors of varying parameters are considered. Furthermore, the sensitivity of the natural frequencies and damping ratios will be study with respect to the vector of all structural parameters of the 3 DOFs HHIM with the L-TMD. The vector of input design parameters (\mathbf{d}_s) for GSA is given by Eq. (4.10).

$$\mathbf{d}_s = [m_m, m_a, m_h, k_m, k_a, k_h, k_p, c_m, c_a, c_h, c_p]^T. \quad (4.10)$$

The following vector of varying parameters will be used to study the sensitivity of the machine vibration level in case of utilization of the L-TMD in the HHIM:

$$\mathbf{d}_l = [m_a, k_m, k_a, k_h, k_p, c_m, c_a, c_h, F_{\text{eref}}]^T. \quad (4.11)$$

The GSA of vibration level of the HHIM equipped with the nonlinear TMD will be considered with respect to the following vector of varying parameters:

$$\mathbf{d}_n = [m_a, k_m, k_a, k_h, k_p, c_m, c_a, c_h, a, F_0, F_{\text{eref}}]^T. \quad (4.12)$$

In the case of multiobjective optimization problem, the vector of input design parameters for the HHIM with the linear TMD is considered as:

$$\mathbf{d}_{\text{pl}} = [m_a, k_a]^T. \quad (4.13)$$

For the Pareto optimization of the HHIM with the nonlinear TMD, the vector of varying parameters is chosen as:

$$\mathbf{d}_{pn} = [m_a, k_a, a, F_0]^T. \quad (4.14)$$

4.4 Global Sensitivity Analysis

Sensitivity analysis can be carried out either locally or globally. Local sensitivity is often measured by taking derivative of an objective function with respect to a particular design parameter around a fixed point in space. Therefore, the interaction of different design variables on an objective function is not properly reflected and the sensitivity highly depends on the chosen fixed point.

GSA is capable to thoroughly scan the domain of the input design variables and take into account the simultaneous effects of different design parameters on a particular objective function. However, large numbers of sample data required to achieve a satisfactory level of accuracy as well as evaluation of high dimensional integrals are some of the most important drawbacks within ordinary GSA methods.

Several approaches are developed to improve the computational efficiency of the GSA algorithms. Analysis of variance (ANOVA) decomposition, also known as high dimensional model representation (HDMR), decomposes a function into a set of sub functions and is a powerful tool in GSA, see, e.g., [20–22]. An efficient approximation of HDMR is cut-HDMR in which a particular function is decomposed around a set of points, planes, or hyper planes. Each objective function (Γ) can be expressed as functions of a set of n independent random variables $\mathbf{X} = [x_1, x_2, \dots, x_n]^T$, through the respective functional relationship $\Gamma = \mathcal{F}(\mathbf{X})$, with \mathbf{X} as the vector of design parameters. Based on the cut-HDMR concept, function $\mathcal{F}(\mathbf{X})$ is decomposed around the vector $\mathbf{c} = [c_1, \dots, c_n]^T$. This vector is known as cut center and contains nominal values of the design parameters. Finally, $\mathcal{F}(x_i, \mathbf{c}_{-i})$ denotes the function value for the case that all inputs except x_i , are fixed at their respective cut point coordinates.

Zhang and Pandey [16] used the cut-HDMR approach and proposed a M-DRM which simplifies the calculation of high dimensional integrals and yields the closed-form formulation for the global sensitivity index of an objective function with respect to the i th design parameter x_i :

$$S_i^T \approx \frac{1 - \alpha_i^2 / \beta_i}{1 - (\prod_{k=1}^n \alpha_k^2 / \beta_k)}, \quad (4.15)$$

here, S_i^T is the total sensitivity index.

Variables α_k and β_k are calculated using Gaussian quadrature integration method:

$$\begin{cases} \alpha_k \approx \sum_{l=1}^N w_{kl} \mathcal{F}(x_{kl}, \mathbf{c}_{-kl}) \\ \beta_k \approx \sum_{l=1}^N w_{kl} [\mathcal{F}(x_{kl}, \mathbf{c}_{-kl})]^2 \end{cases}, \quad (4.16)$$

here, N is the total number of integration points, x_{kl} and w_{kl} are the l th Gaussian integration abscissa and the corresponding weight, respectively. Note that α_i and β_i are also evaluated using Eqs. (4.16). Indeed, the numerator in Eq. (4.15) considers the effects of the i th design parameter (x_i), while the denominator takes into account the product of the effects of all the design parameters.

The total number of function evaluations required to calculate the sensitivity indices using this method is only $n \times N$. This approach is already verified against Monte Carlo simulation through some simple mathematical and mechanical examples [16]. The efficiency of this method for GSA of multibody systems is also shown in [17, 18]. More details on GSA and M-DRM approaches can be found in [16, 23, 24].

4.5 Multidisciplinary Design Optimization

The target of this study is to minimize vibrations and the weight of the HHIM. The multiobjective design optimization problem is then formulated as follows:

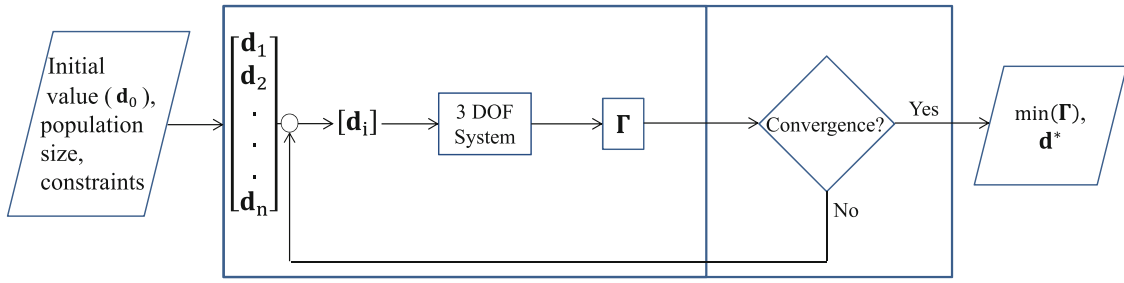


Fig. 4.2 Optimization flowchart

For the given HHIM model shown in Fig. 4.1 and prescribed structural parameters, it is required to determine the optimized vector of the design parameters (\mathbf{d}^*) such that the variational Eq. (4.17) is satisfied

$$\Gamma(\mathbf{d}^*) = \min_{\mathbf{d} \in \Omega} \Gamma(\mathbf{d}) \quad (4.17)$$

subject to differential constraints Eqs. (4.1, 4.2 and 4.3) and feasible initial states Eq. (4.6). Here, Γ is the vector of objective functions, and Ω is the domain of the input design variables (\mathbf{d}). The solution of Eq. (4.17) yields Pareto optimized vector of the design parameters (\mathbf{d}^*).

4.5.1 Optimization Algorithm

To solve the formulated problem, an evolutionary multiobjective optimization algorithm which works based on GA is implemented in MATLAB. For the initial values of the design parameters (\mathbf{d}_0), and based on the prescribed settings, the GA generates the vector of sample design parameters (\mathbf{d}_i). The dynamics response of the system and objective functions are evaluated based on the mathematical model of the HHIM. This procedure is continued until convergence or the maximum number of iterations is achieved. The flowchart of the multiobjective optimization procedure is depicted in Fig. 4.2.

4.5.2 Operational Scenarios

Two sets of operational scenarios (OS) are considered for the analysis:

1. Simulations run with a fixed reference force amplitude (F_{ref}) on a desired frequency range between 23–32 Hz. The vector of objective functions in this case is $\Gamma_{\text{OS1}} = [\Gamma_{\text{Disp}} / \Gamma_{\text{Disp}}^0, m_a / m_a^0]^T$. Here, Γ_{Disp} is determined by Eq. (4.8), the superscript “0” denotes the objective function value corresponding to the initial guess design parameters.
2. Simulations run with a variable reference force amplitude $0.8F_{\text{ref}} \leq F_{\text{ref}} \leq 1.2F_{\text{ref}}$ on the desired frequency range between 23 and 32 Hz. The vector of objective functions for the second OS is defined as $\Gamma_{\text{OS2}} = [\Gamma_{\text{Vol}} / \Gamma_{\text{Vol}}^0, m_a / m_a^0]^T$, where Γ_{Vol} is determined by Eq. (4.9).

4.6 Results

The GSA and multiobjective optimization results are presented in this section. The results of linear and nonlinear TMD systems are also analyzed and compared.

4.6.1 GSA Results

In all sections of this paper, a lognormal distribution of the input design parameters with $N = 20$ Gaussian quadrature abscissas for numerical integrations is considered to carry out the GSA. The mean values of the design parameters are given in Table 4.1. The coefficient of variation (COV) used in different GSA problems is chosen in a way that the respective variation is remained within the admissible ranges for each particular design parameter, see Table 4.2.

4.6.1.1 Linear System

The total global sensitivity indices of the natural frequencies ($S_{\omega_{n_i}}^T$) and corresponding damping ratios ($S_{\xi_{n_i}}^T$) with $i = 1, 2, 3$ as function of the design parameters are shown in Fig. 4.3 for the linear 3 DOFs system. Each color box represents the respective sensitivity index. The higher sensitivity index reflects the higher effect of a particular design parameter on an objective function.

It should be noted that all the six objective functions (natural frequencies and damping ratios) are simultaneously evaluated and the number of function evaluations to achieve the GSA results shown in Fig. 4.3 is merely $N \times n_d = 20 \times 11 = 220$.

As it follows from Fig. 4.3 the natural frequency of the first vibration mode (ω_{n_1}) is mostly sensitive with respect to the hand-arm and chisel stiffnesses (k_m and k_p). The damping ratio (ξ_1) at this vibration mode is mainly affected by the chisel mass m_m and linear TMD parameters (i.e. k_a and m_a). Therefore, the linear TMD mainly contributes in damping out the vibrations corresponding to the first vibration mode. The housing stiffness (k_h) together with the housing mass (m_h) and

Table 4.2 COVs used for GSA

m_m	m_a	m_h	k_m	k_a	k_h	k_p	c_m	c_a	c_h	c_p	a	F_0	F_{eref}
0.10	0.11	0.10	0.30	0.15	0.15	0.18	0.11	0.38	0.25	0.10	0.13	0.15	0.12

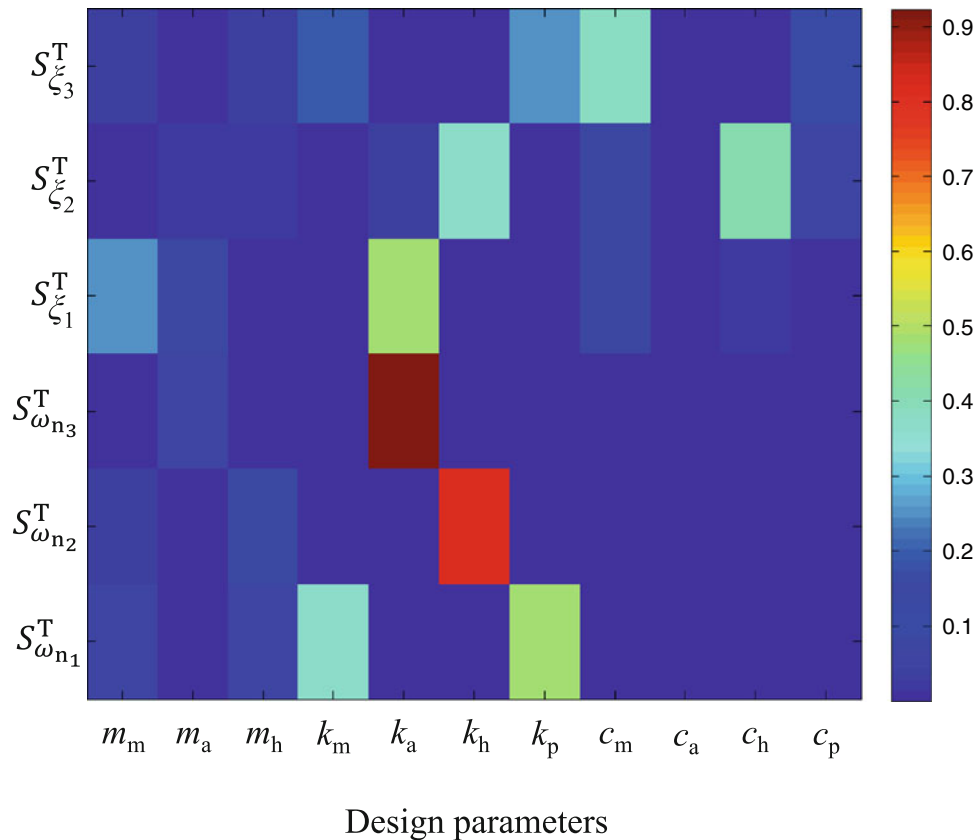


Fig. 4.3 Sensitivity indices of natural frequencies and damping ratios of the linear 3DOF system

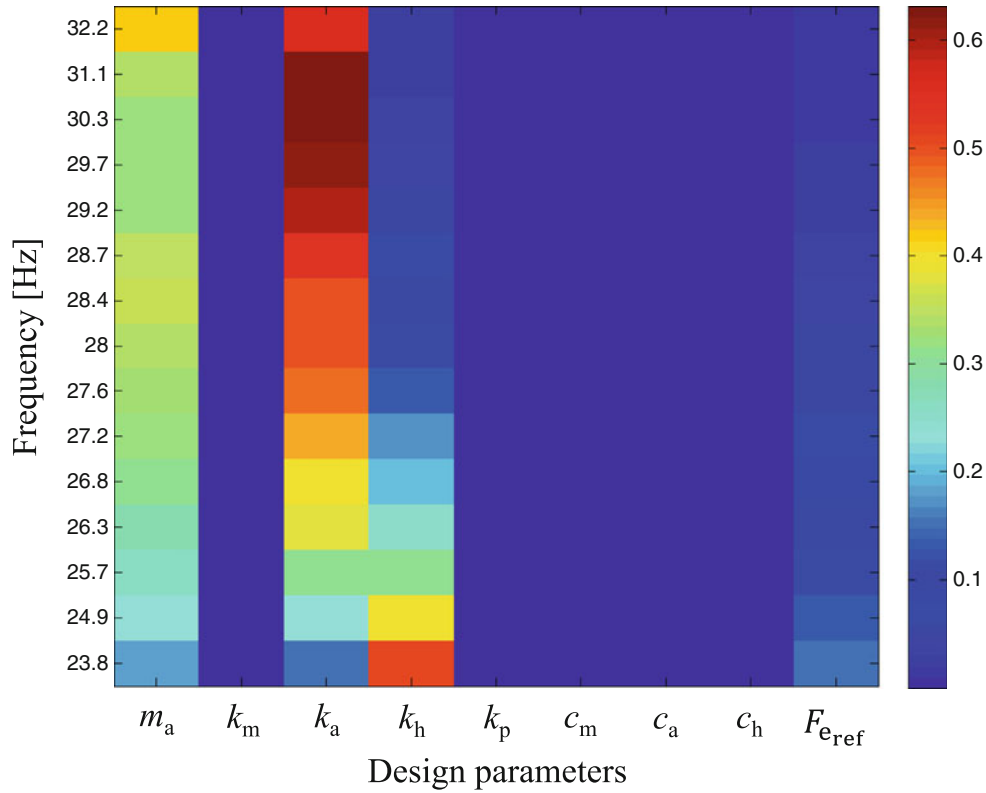


Fig. 4.4 Sensitivity of Γ_{Disp} at different exciting frequencies with respect to design parameters for the linear TMD

housing damping (c_h) are the most important parameters that can affect the second natural frequency (ω_{n_2}) and damping ratio (ξ_2), respectively. Finally, the third natural frequency of the system highly depends on the linear TMD parameters (i.e. k_a and m_a).

In order to use the 3 DOFs system given by Eqs. (4.1, 4.2, 4.3, 4.4, 4.5, 4.6 and 4.7) as a reference model for multidisciplinary design optimization of a HHIM, some practical design constraints have to be addressed. In this regard, the chisel mass (m_m), the housing mass (m_h), and the hand-arm damping (c_p) are considered constant during the subsequent sections inasmuch as those parameters are either fixed and/or already determined by the HHIM manufacturers. Therefore, the focus is on GSA and multiobjective optimization of the rest of the parameters.

The total global sensitivity indices of the maximum RMS value of x_3 , ($S_{\Gamma_{\text{Disp}}}^T$), at different exciting frequencies ($23.8 \text{ Hz} \leq f \leq 32.2 \text{ Hz}$) with respect to the design parameters are plotted in Fig. 4.4 for the linear TMD. It can be seen that the TMD parameters (i.e. m_a and k_a), the stiffness between the main mass and housing (k_h), and the reference force amplitude (F_{e_ref}) are the most important variables that can influence Γ_{Disp} in the desired frequency range.

The auxiliary mass m_a has almost a consistent effect on machine vibration estimated by the objective function given by Eq. (4.8). In lower frequencies the TMD parameters (m_a and k_a) have more or less similar effects on the vibration level. However, as long as the exciting frequency increases, the effects of the stiffness k_a becomes dominant. The sensitivity indices of parameters k_h and F_{e_ref} reflect an opposite behavior. In other words, k_h and F_{e_ref} have a more important influence on the machine vibration at lower exciting frequencies and by increasing the frequency, the respective effects become less important.

The values of total sensitivity index of the objective function Γ_{Vol} that estimates the machine vibration by using Eq. (4.9) on the prescribed range of the exciting force amplitude ($0.8F_{e_ref} \leq F_{e_ref} \leq 1.2F_{e_ref}$) and frequency ($23.8 \text{ Hz} \leq f \leq 32.2 \text{ Hz}$) are presented in Fig. 4.5. It can be seen that the volume below the exciting force amplitude (F_{e_ref}), frequency (f), and the maximum RMS value of x_3 is mostly sensitive with respect to the linear TMD parameters (i.e. auxiliary mass (m_a) and stiffness (k_a)) and the housing stiffness (k_h).

The GSA results of Γ_{Disp} and Γ_{Vol} showed that the linear TMD parameters have the most important influence on the machine vibrations. Therefore, the auxiliary mass (m_a) and stiffness (k_a) are considered as the design parameters for multiobjective optimization of the linear TMD. Indeed, the auxiliary mass (m_a) is simultaneously considered as one of the design parameters and objective functions.

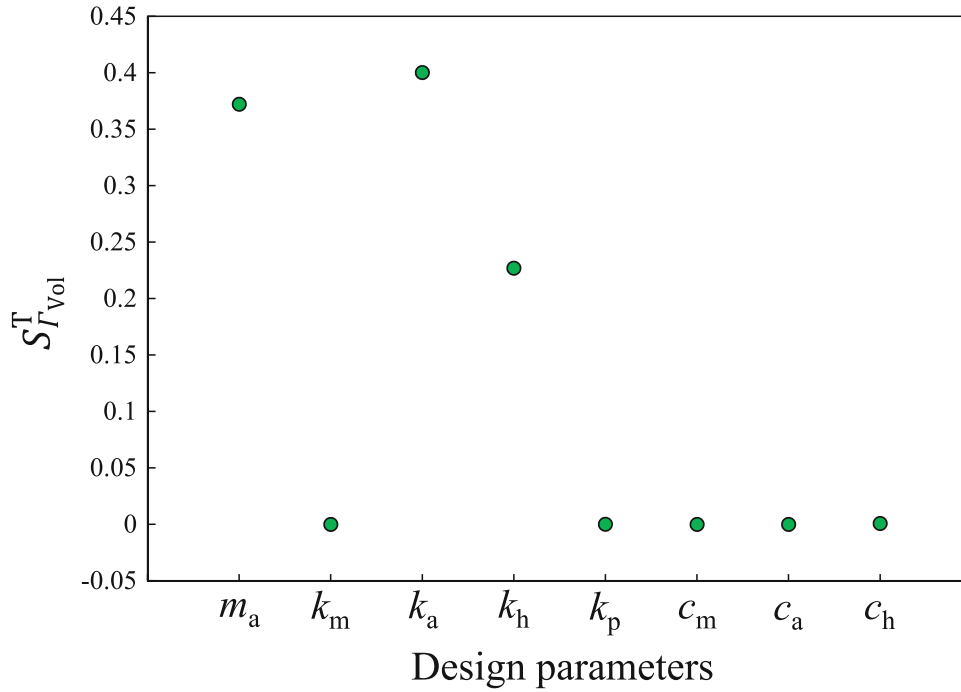


Fig. 4.5 Sensitivity of Γ_{Vol} with respect to the design parameters for the linear TMD

4.6.1.2 Nonlinear System

The values of the total global sensitivity index of the maximum RMS value of x_3 ($S_{\Gamma_{Disp}}^T$) at different exciting frequencies are presented in Fig. 4.6 for the nonlinear TMD.

It can be seen that the objective function Γ_{Disp} is mostly influenced by the nonlinear TMD parameters (i.e. auxiliary mass m_a , auxiliary stiffness k_a , gap a , and preload F_0). At lower exciting frequencies, all the nonlinear TMD parameters have to some extent similar impact on machine vibration estimated by using the objective function Γ_{Disp} . However, as long as the exciting frequency increases, the effects of the auxiliary mass (m_a) and stiffness (k_a) become dominant. From this point of view, m_a and k_a exhibit the same behavior for linear and nonlinear TMDs, see Figs. 4.4 and 4.6. In contrast, the effects of gap (a) and preload (F_0) decay as long as the exciting frequency increases.

The GSA results shown in Fig. 4.6 provide informative data regarding the influence of different design parameters on Γ_{Disp} at different exciting force frequencies which can be beneficial in formulating the multiobjective optimization problem. As an example, assume that only two design parameters can be considered for optimization due to the practical and/or cost constraints. Therefore, if the operational frequency of the HHIM is around 26 Hz, it is recommended to choose the auxiliary mass (m_a) and the gap (a) as the design parameters for optimization. While, if the operational frequency of the HHIM is around 29 Hz, it is recommended to choose the auxiliary mass and stiffness (m_a and k_a) as the design parameters, see Fig. 4.6.

The exciting force amplitude (F_{ref}) has a more important influence on Γ_{Disp} at lower exciting frequencies rather than higher frequencies. This behavior has also been observed in the linear TMD case, see Fig. 4.4. The GSA results shown in Figs. 4.4 and 4.6 revealed that the exciting force amplitude (F_{ref}) cannot significantly influence the system response (Γ_{Disp}) in either linear or nonlinear TMDs (especially for higher exciting frequencies). This might make it possible to run the multiobjective optimization with a constant exciting force amplitude (F_{ref}) and apply the obtained Pareto optimized solutions for cases with a variable F_{ref} . In other words, the GSA results reveal that it is possible to carry out multiobjective optimization for Γ_{OS1} and expect to achieve near optimal system behavior once utilizing the results obtained as the solutions to the multiobjective optimization problem with respect to Γ_{OS2} . This can significantly reduce the computational burden of optimization. Therefore, the GSA results can actively contribute in deciding the desired operational scenario for running the multiobjective optimization problems. The Pareto optimized solutions of the optimization problems with respect to Γ_{OS1} and Γ_{OS2} are compared and analyzed in Sect. 4.6.2 to better clarify the role of GSA on formulation of the multiobjective optimization problem.

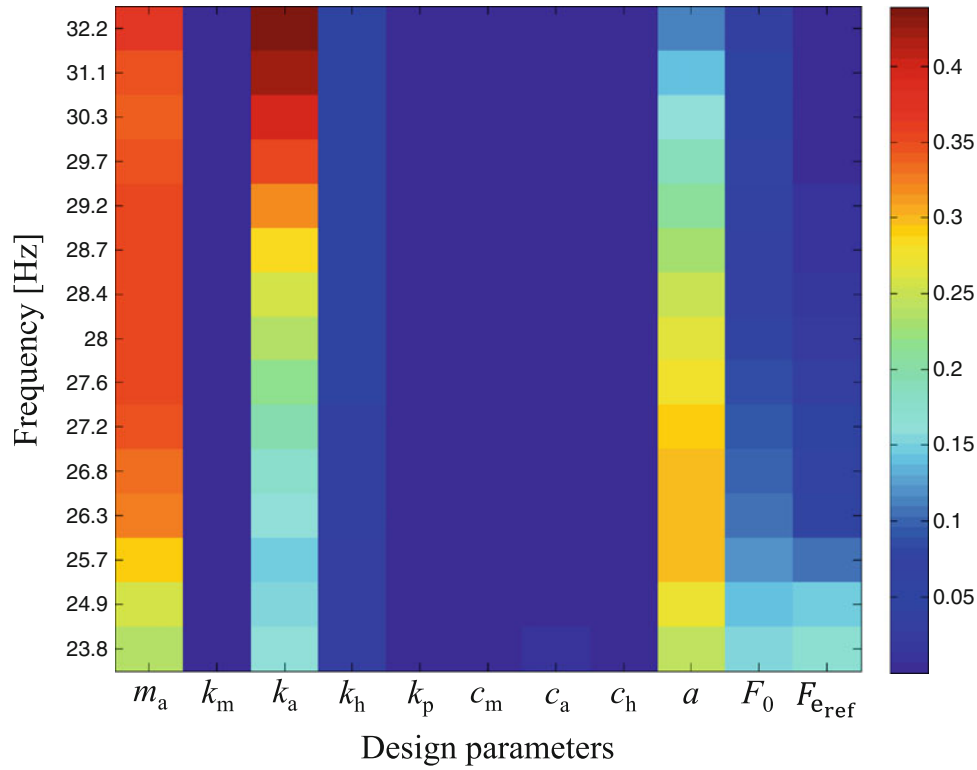


Fig. 4.6 Sensitivity of Max RMS of x_3 at different frequencies with respect to the design parameters for the nonlinear TMD

The values of the total sensitivity index of the objective function Γ_{Vol} for the nonlinear TMD in case that both the exciting force amplitude (F_{eref}) and frequency (f) are varying (i.e. OS2) are presented in Fig. 4.7.

It can be seen that the nonlinear TMD parameters i.e. the auxiliary mass (m_a) and stiffness (k_a), gap (a), and preload (F_0) have the most important effect on machine vibration estimated by the objective function Γ_{Vol} .

One interesting note is that although the housing stiffness (k_h) exhibit a remarkable influence on Γ_{Disp} or Γ_{Vol} for the linear TMD (Figs. 4.4 and 4.5), similar behavior is not observed for the nonlinear TMD. In this case, housing stiffness k_h does not reflect a remarkable influence on either Γ_{Disp} or Γ_{Vol} (see, Figs. 4.6 and 4.7). This shows one of the limitations of the linear TMD system.

Based on the GSA results, the TMD parameters (m_a and k_a for the linear case and m_a , k_a , a , and F_0 for the nonlinear case) are considered as the design parameters for optimization problems with respect to Γ_{OS1} and Γ_{OS2} . The Pareto optimized solutions are discussed in the next section.

4.6.2 Multiobjective Optimization Results

The GA is utilized to carry out the multiobjective optimization. Population size and number of generations are set to 50 which give the number of maximum iterations equal to 2551. Based on the chosen GA settings, the Pareto set and Pareto front include 25 Pareto optimal solutions to the multiobjective optimization problem. The Pareto sets associated with OS1 and OS2 are shown in Fig. 4.8 for the linear TMD.

The Pareto fronts for the linear and nonlinear TMDs associated with OS1 and OS2 are plotted in Fig. 4.9. It should be noted that there is a mapping between the linear TMD results shown in Figs. 4.8 and 4.9. Indeed, each point in the Pareto set (Fig. 4.8) corresponds to a point in the Pareto front given in Fig. 4.9.

It can be seen that vibration absorption capacity of the linear TMD is improved by increasing the auxiliary mass (m_a) and stiffness (k_a) in both operational scenarios (OS1 and OS2). In other words, the maximum RMS of x_3 (Γ_{Disp}) as well as the volume between frequency (f), reference force amplitude (F_{eref}), and maximum RMS of x_3 measured as Γ_{Vol} are reduced by choosing some stiffer k_a and a more massive m_a . However, increasing m_a deteriorates the other objective function i.e. the total weight of the HHIM.

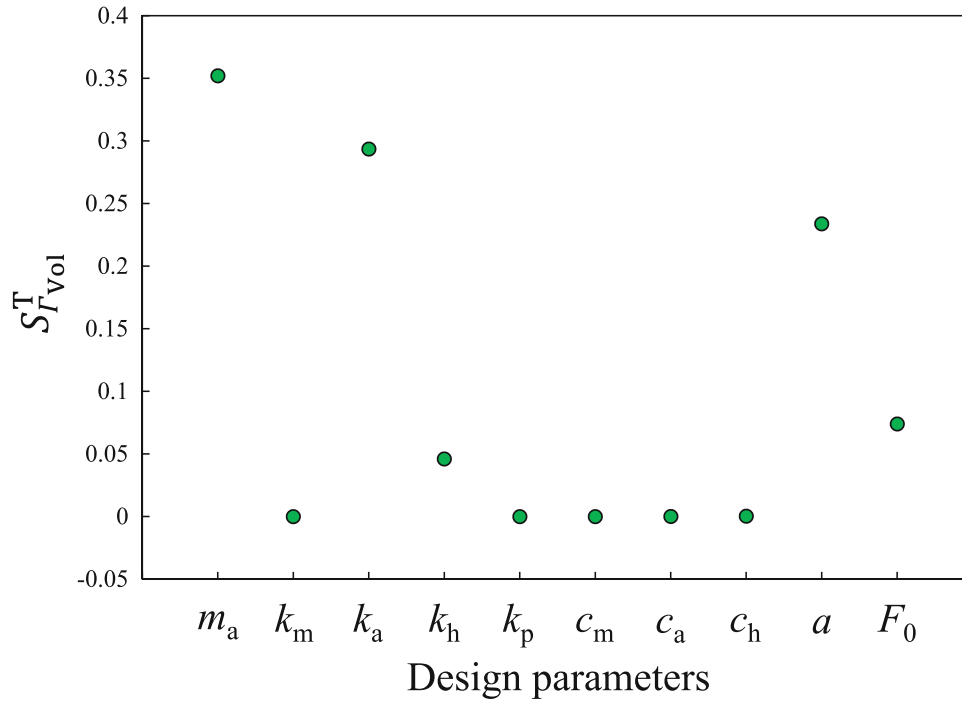


Fig. 4.7 Sensitivity of Γ_{vol} with respect to the design parameters for the nonlinear TMD

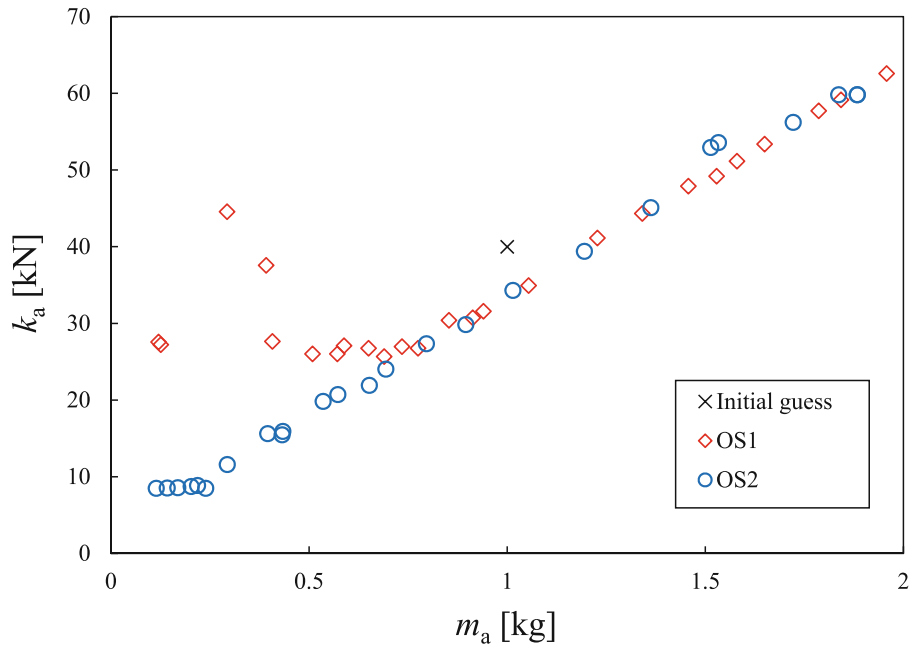


Fig. 4.8 Pareto sets for the linear TMD

According to the Pareto optimized results obtained for the linear TMD, the minimum auxiliary mass and stiffness required for which the vibration is reduced are $m_a \approx 0.8$ kg and $k_a \approx 30$ kN, respectively (see, Figs. 4.8 and 4.9). The interesting point is that both Pareto sets associated with OS1 and OS2 for the linear TMD follow almost the same linear trend given by Eq. (4.18).

$$k_a \approx 30000m_a + 3600, \quad m_a \geq 0.8 \text{ kg} \tag{4.18}$$

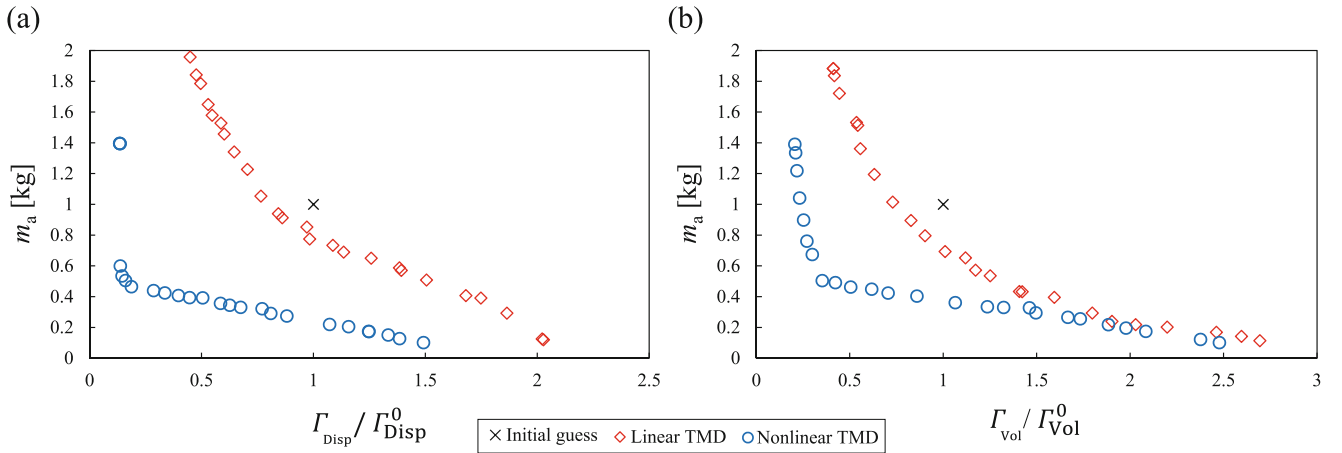


Fig. 4.9 Pareto fronts for the linear and nonlinear TMDs: (a) OS1; (b) OS2

Indeed, the Pareto sets achieved for OS1 and OS2 reveal that the optimization results are not affected by varying the reference exciting force amplitude (F_{ref}). This is in agreement with the GSA results shown in Fig. 4.4. Therefore, with the aid of the GSA, one can carry out the multiobjective optimization for a constant reference exciting force amplitude (F_{ref}) and expect that the obtained Pareto optimized results are valid for the case that the exciting force amplitude (F_{ref}) is also varies on the desired range. This can significantly reduce the computational efforts.

From the Pareto fronts shown in Fig. 4.9a, b it can be seen that the linear TMD can slightly reduce the vibrations in the HHIM. However, there are only few Pareto optimal points which simultaneously minimize both objective functions (i.e. lead to a lighter HHIM ($m_a < 1$) and lower vibrations in terms of Γ_{Disp} and Γ_{Vol} (i.e. $\Gamma_{\text{Disp}} / \Gamma_{\text{Disp}}^0 < 1$ and $\Gamma_{\text{Vol}} / \Gamma_{\text{Vol}}^0 < 1$).

In contrast, the Pareto fronts associated with the nonlinear TMD obtained for OS1 and OS2 not only reduce the vibrations more efficiently in comparison with to the linear TMD, but also give more possibilities for the Pareto optimal solutions which can simultaneously minimize the total weight and vibrations of the HHIM in terms of Γ_{Disp} and Γ_{Vol} (see, blue circles in Fig. 4.9).

The Pareto sets associated with the nonlinear TMD are shown in Fig. 4.10 for OS1 and OS2. It should be noted that the 25 Pareto set points are sorted in a descending order with respect to the auxiliary mass (m_a). Indeed, lower numbers denote a heavier HHIM but less vibrations and higher numbers correspond to a lighter machine but more vibrations. It should be noted that there is a mapping between the Pareto sets shown in Fig. 4.10 and the Pareto fronts shown in Fig. 4.9. As an example, the values of the design parameters m_a , k_a , a , and F_0 associated with number one in Fig. 4.10 denote the optimal characteristics of the nonlinear TMD minimizing vibrations of the HHIM (the point corresponding to $m_a = 1.4$ kg in Fig. 4.9).

Similar to the linear case, higher auxiliary mass (m_a) and stiffer auxiliary stiffness (k_a) lead to a better vibration absorber capacity in comparison with to the initial configuration. As long as the auxiliary mass (m_a) decreases the unpleasant vibration level increases. The minimum auxiliary mass required to reduce the vibrations with respect to the initial configuration is around $m_a \approx 0.4$ kg which is half of the value attained by the linear analysis.

It is interesting to note that to some extent the Pareto optimized solutions associated with Γ_{OS1} and Γ_{OS2} are following the same trend. In other words, the multiobjective optimization results are not noticeably affected by varying the reference force amplitude (F_{ref}). This is in agreement with the GSA results shown in Fig. 4.6 and the linear TMD analysis. Therefore, one can run the multiobjective optimization of the nonlinear TMD for the OS1 and expect to get the same Pareto optimized solutions for OS2. This can significantly reduce the computational burden of optimization. As an example, assume that the optimization with respect to Γ_{OS2} is carried out by varying the reference force amplitude (F_{ref}) at n_f different points. This means that the simulation time required to run optimization with respect to Γ_{OS2} are n_f times the simulations required to run the optimization with respect to Γ_{OS1} (which is accomplished for one single value of F_{ref}). Therefore, the computational efficiency of the optimization can be significantly improved (n_f times faster) by using the GSA results.

It is also interesting to note that the Pareto set characteristics which denote the case with minimum vibration level (Pareto set points number 1) represent the same optimal values of the design parameters for both operational scenarios OS1 and OS2.

The maximum RMS of displacements (x_1 , x_2 , and x_3) for a fixed reference force amplitude ($F_{\text{ref}} = 351$ N) at different exciting frequencies (f) are plotted in Figs. 4.11 (a-c) for the in service configuration and three optimal cases with minimum

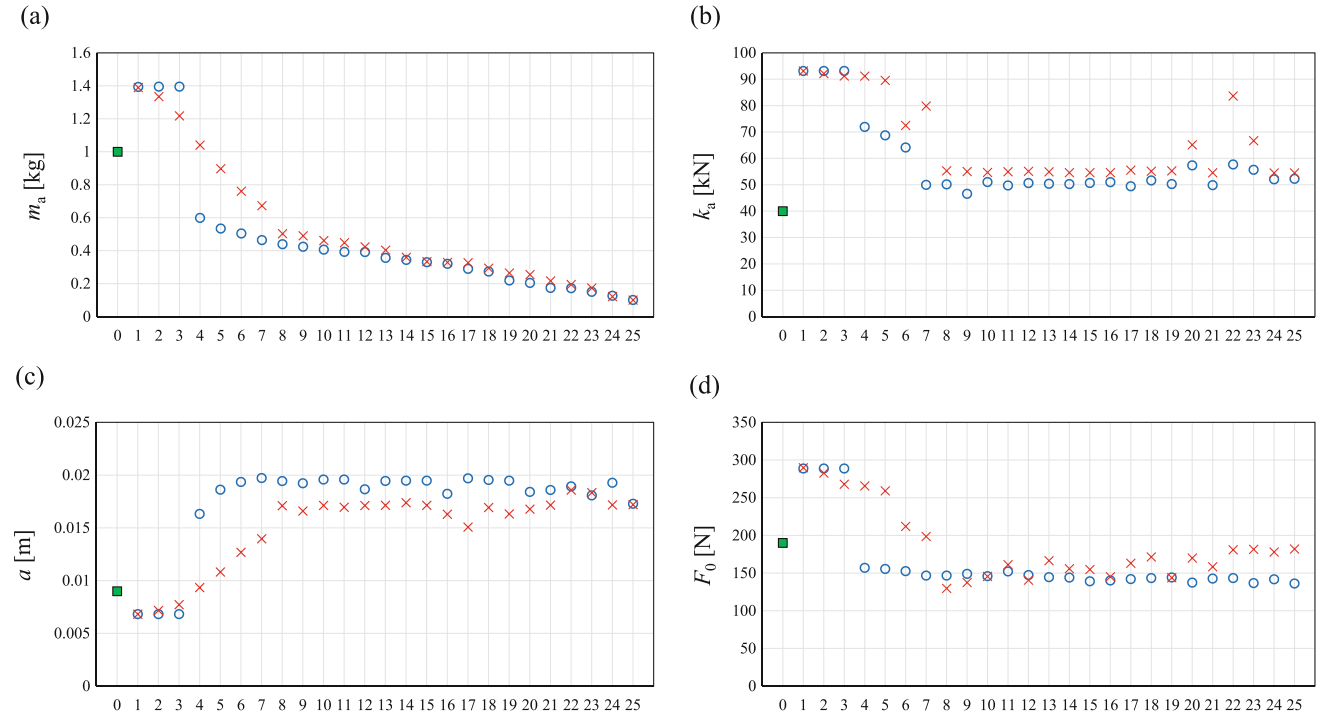


Fig. 4.10 Pareto sets for the nonlinear TMD: ■ initial guess; ○ OS1; × OS2

and maximum auxiliary masses ($m_a = 0.1$ kg and $m_a = 1.4$ kg) as well as an interstitial mass ($m_a = 0.5$ kg). These optimal cases represent the point number 1, 25, and 5 from the Pareto set shown in Figs. 4.10 for OS1, respectively. It should be noted that the vertical axes in Figs. 4.11a-c are in logarithmic scale. From Fig. 4.11c it can be seen that by using the Pareto optimized values of the design parameters corresponding to $m_a = 1.4$ kg minimum vibration level can be achieved. However, the total mass of the HHIM will be increased by 0.4 kg. By choosing $m_a = 0.5$ kg, makes it possible to simultaneously reduce the weight of the HHIM (by 0.5 kg) and vibrations in x_3 (See Fig. 4.11c). The weight of the HHIM can be reduced by maximum 0.9 kg (using $m_a = 0.1$ kg). However, this would increase the vibration level. Similar behavior is observed for maximum RMS of x_1 shown in Fig. 4.11a. The maximum RMS of the displacement of the auxiliary mass (x_2) is also shown in Fig. 4.11b.

The system vibration response corresponding to the in service and optimized design parameters are compared in Fig. 4.12 for the case that both the exciting force frequency and amplitude are varying on the prescribed design range. Here, the set which gives minimum vibration (point number one for OS2 in the Pareto set shown in Fig. 4.10) is chosen as the optimized case. The vibrations of the HHIM (maximum RMS of x_3) are significantly mitigated by using the Pareto optimized values of the design parameters compared to the in service case. It should be noted that for exciting frequencies around 24 Hz and reference force amplitudes close to 400 N the vibrations of the HHIM (maximum RMS of x_3) are increased using the optimized values of the design parameters compared to the in service case. This shows one of the limitations of the passive TMD technology.

4.6.3 Closed-Form Representation

In this section the nonlinear least squares method is utilized to develop closed-form formulas that express the relation between the optimal values of TMD design parameters (auxiliary stiffness (k_a), gap (a), and preload (F_0)) as functions of the auxiliary mass (m_a). Indeed, it is assumed that the optimal values of the auxiliary stiffness (k_a), gap (a), and preload (F_0) are expressed as a function of the auxiliary mass (m_a) through the following functional relationship:

$$f_i(m_a) \approx \frac{\alpha}{\beta + \delta(m_a)^\gamma}, \quad f_i = k_a, a, F_0. \quad (4.19)$$

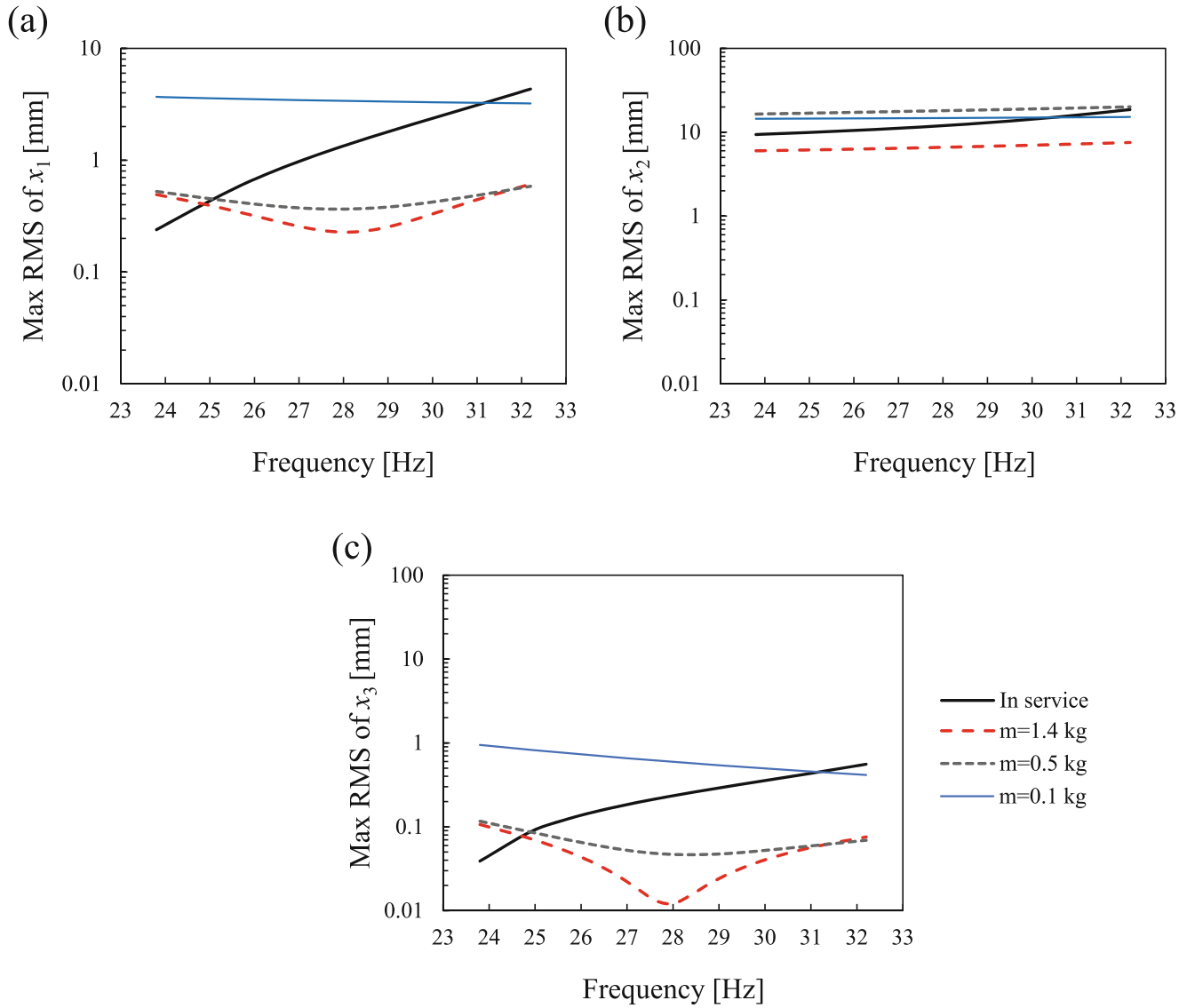


Fig. 4.11 The system vibration response with initial and some optimized cases

The variables α , β , δ , and γ have been determined by using the nonlinear least squares method based on the Pareto optimized solutions shown in Fig. 4.10, and given by Eq. (4.20):

$$\begin{aligned}
 k_a(m_a) &\approx \frac{40e3}{0.368 + 0.087(m_a)^{-1.761}}, \\
 a(m_a) &\approx \frac{0.009}{0.452 + 0.444(m_a)^{2.258}}, \\
 F_0(m_a) &\approx \frac{190}{0.227 + 0.532(m_a)^{-0.853}}.
 \end{aligned} \tag{4.20}$$

The closed-form formulas given by Eqs. (4.20) make it possible to approximate the optimal values of the design parameters of the TMD for given values of the auxiliary mass ($0.4 \text{ kg} \leq m_a \leq 1.4 \text{ kg}$). Functions $k_a(m_a)$, $a(m_a)$, and $F_0(m_a)$ are plotted in Fig. 4.13a–c and compared with the respective values from Pareto set shown in Fig. 4.10. It can be seen that there exist an appropriate correlation between the Pareto set data and the fitted functions.

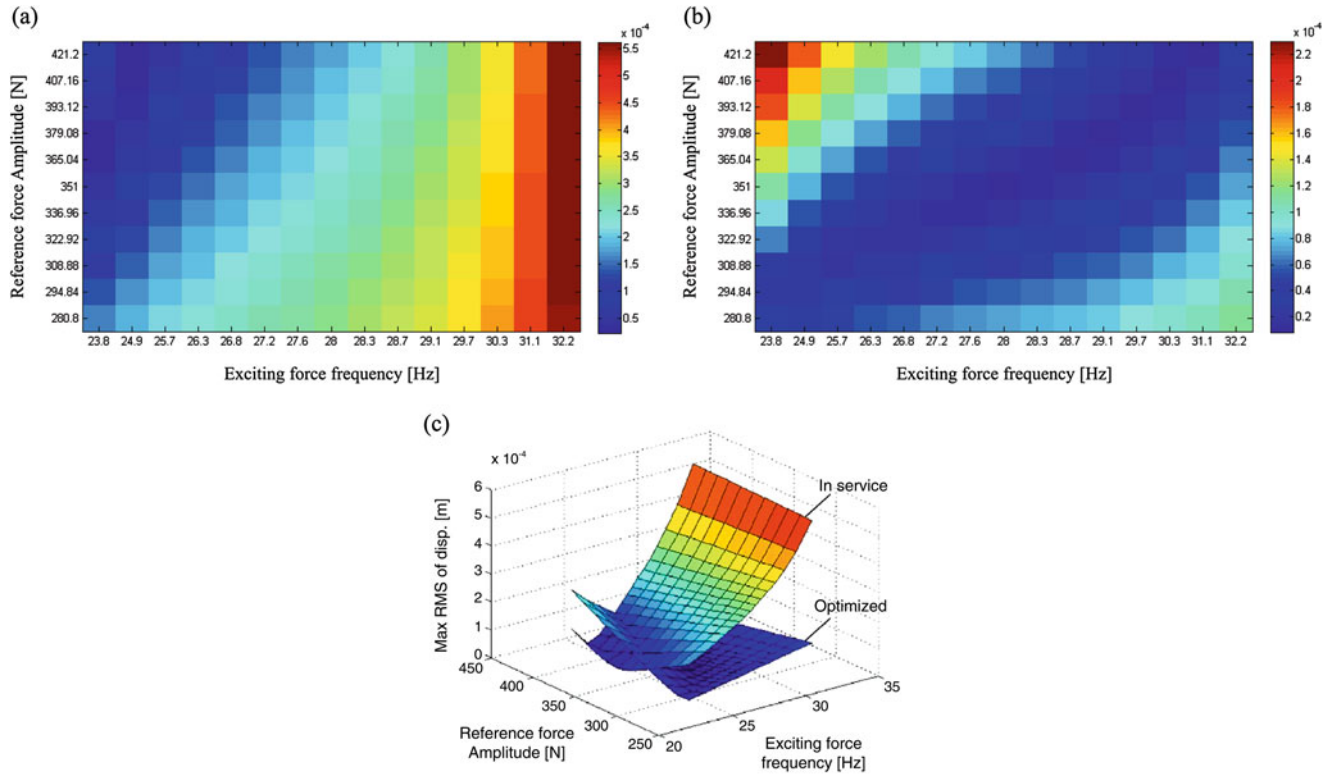


Fig. 4.12 The system vibration response: (a) In service; (b) optimized; (c) In service vs. optimized

In a similar manner, the nonlinear least squares method is utilized to develop a closed-form expression for the objective function Γ_{Vol} as a function of the auxiliary mass (m_a). It is given by Eq. (4.21).

$$f_{\Gamma_{\text{Vol}}}(m_a) / \Gamma_{\text{Vol}}^0 = -3.209 - 1.855(m_a)^{-0.149} + 0.987 \left(\frac{k_a}{40e3} \right)^{1.692} + 1.269 \left(\frac{a}{0.009} \right)^{1.393} + 0.32 \left(\frac{F_0}{190} \right)^{-4.795}. \quad (4.21)$$

Here, $k_a(m_a)$, $a(m_a)$, and $F_0(m_a)$ are evaluated using Eqs. (4.20).

The normalized function $f_{\Gamma_{\text{Vol}}}$ given by Eq. (4.21) is compared with simulation results and the Pareto front associated with OS2 (shown in Fig. 4.9b) in Fig. 4.14. The simulation results are achieved by varying the auxiliary mass at 13 equally distributed points in the range of $0.4 \text{ kg} \leq m_a \leq 1.4 \text{ kg}$. The corresponding values of the stiffness (k_a), gap (a), and preload (F_0) are then evaluated using Eqs. (4.20). For these values of the nonlinear TMD parameters the system vibration response is evaluated through direct simulation by using Eqs. (4.1, 4.2 and 4.3) and expressions (4.5 and 4.7) and is plotted in Fig. 4.14.

It can be seen that there is a good correlation between the Pareto front, fitted function (Eq. (4.21)), and simulation results. Therefore, for a desired value of the auxiliary mass ($0.4 \text{ kg} \leq m_a \leq 1.4 \text{ kg}$), using Eqs. (4.20, 4.21) makes it possible to approximate the corresponding optimal values of the auxiliary stiffness (k_a), gap (a), preload (F_0) as well as the system response (Γ_{Vol}) for the considered 3 DOF system and prescribed structural parameters without running simulations.

4.7 Conclusion

GSA and multidisciplinary design optimization of a linear and a nonlinear TMD have been considered to reduce the total weight and vibrations in a 3 DOF system which represents a HHIM. The M-DRM has been employed to carry out the GSA in an efficient manner and reduce the number of input variables for optimization. GA has been utilized to perform the multiobjective optimization. Using the least squares method and Pareto optimization the analytical expressions for the stiffness, gap, and spring preload as functions of the auxiliary mass of the nonlinear TMD have been obtained.

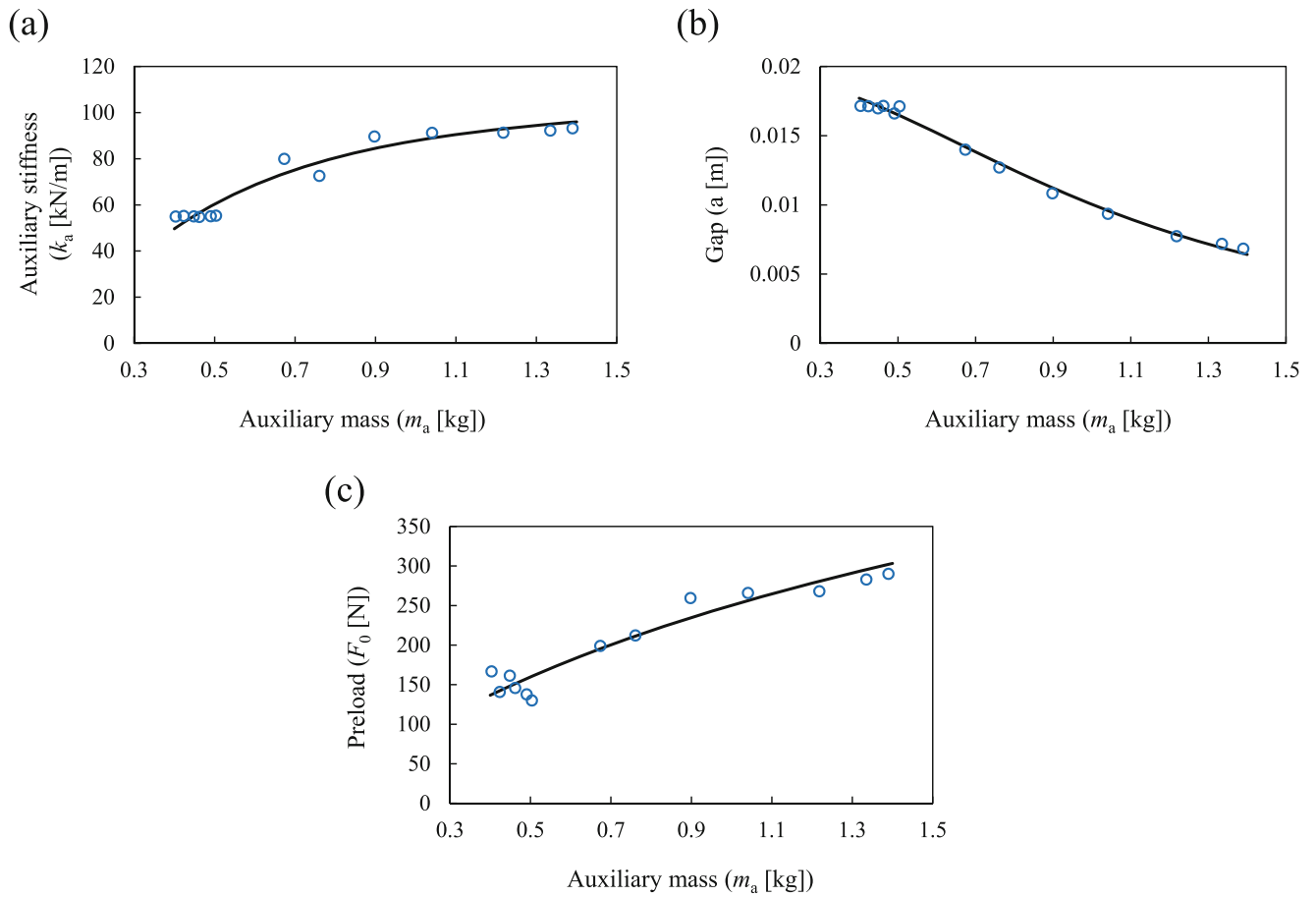


Fig. 4.13 Variation of optimal values of design parameters of the TMD with respect to auxiliary mass: (a) $k_a(m_a)$; (b) $a(m_a)$; (c) $F_0(m_a)$. Pareto optimized solutions (\circ); fitted functions (—)

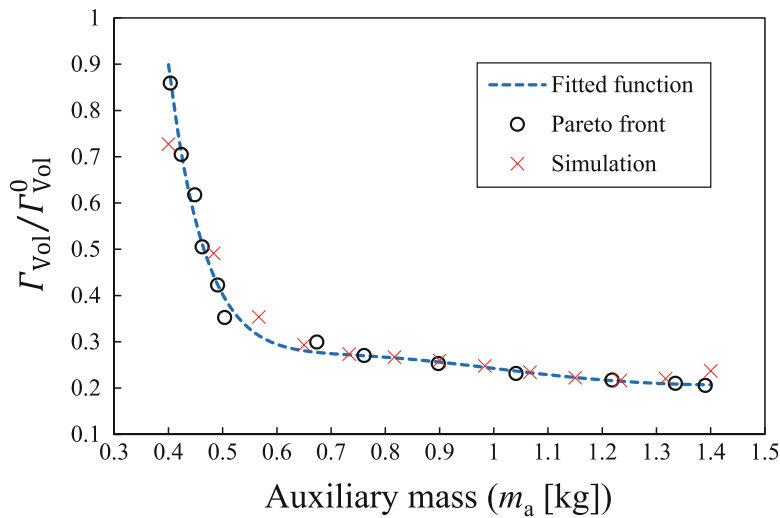


Fig. 4.14 Variation of $\Gamma_{Vol}/\Gamma_{Vol}^0$ against the auxiliary mass (m_a)

Finally, the following concluding remarks have been drawn:

- Linear model of the TMD has limitations in design of the HHIM and a nonlinear TMD model should be considered in practice. Indeed, the nonlinear TMD has more vibration absorption capacity rather than a linear one.
- The optimization results for the case that only the frequency of the exciting force was varying were close to those associated with the case that both frequency and amplitude of the exciting force were varying.
- The GSA results showed that the exciting force amplitude does not influence the system response as much as the TMD parameters. Therefore, instead of running simulations with different exciting force frequency and amplitude, one can merely shift the exciting frequency and get optimization results that are robust against exciting force amplitude. This can significantly reduce the computational effort of optimization.
- The Pareto optimized solutions provided several design possibilities to reduce the harsh vibrations and/or the total weight of the system.

Although the Pareto optimized solutions give the possibility to operate the HHIM with lower harsh amplitudes, in certain ranges of frequency and exciting force amplitude, the optimized results might worsen the condition in comparison with those corresponding to the HHIM with in-service structural data. This shows the limitation of the passive vibration control using TMD technology in application to HHIMs and further studies can be laid within robustness analysis of the optimization results achieved with respect to uncertainties in the design parameters. Active control of HHIMs can also be considered as an interesting focus for further analysis in this field.

Acknowledgments This work was financially supported by the Ekman family foundation and the Sweden's Innovation Agency (VINNOVA) through the project "Noll Vibrationsskador-steg 2" (Dnr: 2015-00352), which are gratefully acknowledged. The authors also would like to thank Hans Lindell and Snævar Leó Grétarsson, Swerea IVF AB, Mölndal, Sweden for interesting communication and fruitful discussions.

References

1. Yang, Y., Dai, W., Liu, Q.: Design and implementation of two-degree-of-freedom tuned mass damper in milling vibration mitigation. *J. Sound Vib.* **335**(2015), 78–88 (2015). <https://doi.org/10.1016/j.jsv.2014.09.032>
2. Li, S., Tang, J.: On vibration suppression and energy dissipation using tuned mass particle damper. *J. Vib. Acoust.* **139**(011008), 1–10 (2017). <https://doi.org/10.1115/1.4034777>
3. Dinh, V.-N., Basu, B.: Passive control of floating offshore wind turbine nacelle and spar vibrations by multiple tuned mass dampers. *Struct. Control. Health Monit.* **22**, 152–176 (2015). <https://doi.org/10.1002/stc.1666>
4. Mrabet, E., Guedri, M., Ichchou, M., Ghanmi, S.: New approaches in reliability based optimization of tuned mass damper in presence of uncertain bounded parameters. *J. Sound Vib.* **355**, 93–116 (2015). <https://doi.org/10.1016/j.jsv.2015.06.009>
5. Venanzi, I.: Robust optimal design of tuned mass dampers for tall buildings with uncertain parameters. *Struct. Multidiscip. Optim.* **51**, 239–250 (2015). <https://doi.org/10.1007/s00158-014-1129-4>
6. Lievens, K., Lombaert, G., Roeck, G.D., den Broeck, P.V.: Robust design of a TMD for the vibration serviceability of a footbridge. *Eng. Struct.* **123**, 408–418 (2016). <https://doi.org/10.1016/j.engstruct.2016.05.028>
7. Miguel, L.F.F., Lopez, R.H., Torii, A.J., Miguel, L.F.F., Beck, A.T.: Robust design optimization of TMDs in vehicle–bridge coupled vibration problems. *Eng. Struct.* **126**, 703–711 (2016). <https://doi.org/10.1016/j.engstruct.2016.08.033>
8. Tripathi, A., Grover, P., Kalmár-Nagy, T.: On optimal performance of nonlinear energy sinks in multiple-degree-of-freedom systems. *J. Sound Vib.* **388**, 272–297 (2017). <https://doi.org/10.1016/j.jsv.2016.10.025>
9. Marano, G.C., Quaranta, G., Greco, R.: Multi-objective optimization by genetic algorithm of structural systems subject to random vibrations. *Struct. Multidiscip. Optim.* **39**(4), 385–399 (2009). <https://doi.org/10.1007/s00158-008-0330-8>
10. Ribeiro, E.A., Pereira, J.T., Bavastri, C.A.: Passive vibration control in rotor dynamics: optimization of composed support using viscoelastic materials. *J. Sound Vib.* **351**, 43–56 (2015). <https://doi.org/10.1016/j.jsv.2015.04.007>
11. Mousavi Bideleh, S.M., Berbyuk, V., Persson, R.: Wear/comfort Pareto optimisation of bogie suspension. *Veh. Syst. Dyn.* **54**(8), 1053–1076 (2016). <https://doi.org/10.1080/00423114.2016.1180405>
12. Ok, S.-Y., Song, J., Park, K.-S.: Development of optimal design formula for bi-tuned mass dampers using multi-objective optimization. *J. Sound Vib.* **322**, 60–77 (2009). <https://doi.org/10.1016/j.jsv.2008.11.023>
13. Mohtat, A., Dehghan-Niri, E.: Generalized framework for robust design of tuned mass damper systems. *J. Sound Vib.* **330**, 902–922 (2011). <https://doi.org/10.1016/j.jsv.2010.09.007>
14. Greco, R., Marano, G.C., Fiore, A.: Performance–cost optimization of tuned mass damper under low-moderate seismic actions. *Struct. Des. Tall Special Build.* **25**, 1103–1122 (2016). <https://doi.org/10.1002/tal.1300>
15. Detroux, T., Habib, G., Masset, L., Kerschen, G.: Performance, robustness and sensitivity analysis of the nonlinear tuned vibration absorber. *Mech. Syst. Signal Process.* **60–61**, 799–809 (2015). <https://doi.org/10.1016/j.ymsp.2015.01.035>
16. Zhang, X., Pandey, M.D.: An effective approximation for variance-based global sensitivity analysis. *Reliab. Eng. Syst. Saf.* **121**, 164–174 (2014)
17. Mousavi Bideleh, S.M., Berbyuk, V.: Global sensitivity analysis of bogie dynamics with respect to suspension components. *Multibody Sys Dyn.* **37**(2), 145–174 (2016). <https://doi.org/10.1007/s11044-015-9497-0>

18. Mousavi-Bideleh, S.M., Berbyuk, V.: Multiobjective optimisation of bogie suspension to boost speed on curves. *Veh. Syst. Dyn.* **54**(1), 58–85 (2016). <https://doi.org/10.1080/00423114.2015.1114655>
19. Lindell, H., Berbyuk, V., Josefsson, M., and Grétarsson, S.L.: Nonlinear dynamic absorber to reduce vibration in hand-held impact machines. In *International Conference on Engineering Vibration*. Ljubljana, Slovenia, pp. 1530–1539 (2015)
20. Li, G., Rosenthal, C., Rabitz, H.: High dimensional model representations. *Chem. A Eur. J.* **105**, 7765–7777 (2001)
21. Sobol', I.M.: Global sensitivity indices for nonlinear mathematical models and their Monte Carlo estimates. *Math. Comput. Simul.* **55**, 271–280 (2001)
22. Sobol', I.M.: Theorems and examples on high dimensional model representation. *Reliab. Eng. Syst. Saf.* **79**, 187–193 (2003)
23. Mousavi Bideleh, S.M.: Robustness analysis of bogie suspension components Pareto optimized values. *Veh. Syst. Dyn.* **55**(8), 1189–1205 (2017). <https://doi.org/10.1080/00423114.2017.1305115>
24. Mousavi Bideleh, S.M., and Berbyuk, V.: Acomputer code for sensitivity analysis and multiobjective optimization: SAMO tutorial. Research report 2017:01, Chalmers University of Technology, Gothenurg, Sweden



Chapter 5

Inverse Methods for Characterization of Contact Areas in Mechanical Systems

Matthew Fronk, Kevin Eschen, Kyle Starkey, Robert J. Kuether, Adam Brink, Timothy Walsh, Wilkins Aquino, and Matthew Brake

Abstract In computational structural dynamics problems, the ability to calibrate numerical models to physical test data often depends on determining the correct constraints within a structure with mechanical interfaces. These interfaces are defined as the locations within a built-up assembly where two or more disjointed structures are connected. In reality, the normal and tangential forces arising from friction and contact, respectively, are the only means of transferring loads between structures. In linear structural dynamics, a typical modeling approach is to linearize the interface using springs and dampers to connect the disjoint structures, then tune the coefficients to obtain sufficient accuracy between numerically predicted and experimentally measured results. This work explores the use of a numerical inverse method to predict the area of the contact patch located within a bolted interface by defining multi-point constraints. The presented model updating procedure assigns contact definitions (fully stuck, slipping, or no contact) in a finite element model of a jointed structure as a function of contact pressure computed from a nonlinear static analysis. The contact definitions are adjusted until the computed modes agree with experimental test data. The methodology is demonstrated on a C-shape beam system with two bolted interfaces, and the calibrated model predicts modal frequencies with <3% total error summed across the first six elastic modes.

Keywords Modal analysis · Linearized contact · Multi-point constraints · Model updating · Mechanical interfaces

5.1 Introduction

Frictional joints are common in mechanical designs as a cost effective means of building up easy-to-manufacture substructures. However, the effect that frictional interfaces add to the mechanical response of the structure are complex and require advanced computational and experimental techniques to characterize. Nonlinear stiffness and damping are two salient examples of the complicated phenomena that arise due to joints in structures. Consequently, it is important to understand joint interactions at a fundamental level to more accurately account for them in models and thus better inform design making decisions. This study aims to update the contact conditions to identify the true contact area of the interface(s) in a linearized computational structural dynamics model of a jointed structure using low-level, linear test data. The calibration routine aims to match computational and experimental modal frequencies by updating contact definitions at the element level in the

M. Fronk
Department of Material Engineering, Georgia Institute of Technology, Atlanta, GA, USA

K. Eschen
Department of Mechanical Engineering, University of Minnesota, Twin Cities, Minneapolis, MN, USA

K. Starkey
Department of Mechanical Engineering, Purdue University, West Lafayette, IN, USA

R. J. Kuether (✉) · A. Brink · T. Walsh
Sandia National Laboratories, Albuquerque, NM, USA
e-mail: rjkueth@sandia.gov

W. Aquino
Department of Civil and Environmental Engineering, Duke University, Durham, NC, USA

M. Brake
William Marsh Rice University, Houston, TX, USA

finite element model as a function of the numerically computed contact pressure. The results of this analysis provide greater insight into the contact area that occurs at frictional interfaces of bolted connections and confidence in the method developed to calibrate numerical models to modal test data.

The calibration of computational models with experimental data, commonly known as model updating, has been well studied by the engineering community. Mottershead and Friswell provide an overview as it relates to vibration testing in [1]. Additionally, Ewins [2] discusses challenges to model updating, emphasizing the need to incorporate nonlinearities and the complexities introduced by joints. A common approach to matching modal test data to finite element models of jointed structures is to linearize the interface with springs, masses, and/or dampers and vary the parameters until an acceptable level of agreement is reached [3–6]. Other approaches of model updating with joints include geometric parameters [7] and solving a reduced order polynomial identified from both computational and modal data [8]. In a more recent study conducted by Adel et al. [9], the mechanical properties of a “doubly-connective layer” in a computational model of a lap joint were optimized to match modal test data. In experimental settings, direct measurements of pressure patches have included electrical measurements that capture time-dependent patches [10] and ultrasonic techniques [11]. Furthermore, many computational modeling techniques have been developed that capture *nonlinear* joint behavior [12–15], however this is beyond the scope of this work.

This paper presents a model updating scheme to determine the contact area at a linearized bolted interface joining two C-shaped beams. Experimentally measured modal frequencies are compared to those generated with a finite element (FE) model of the structure. The first step in the inverse method is to solve a nonlinear static preload analysis of the FE model with the appropriate torque/preload force on the bolt to obtain the contact pressure at the interface. A single parameter, namely the cut-off pressure, is then varied to determine the contact definitions governing each element in the interface. The cut-off pressure is a continuous variable that defines the following condition: elements with contact pressures above this value are considered stuck (i.e. welded together), and elements below this value can either slide or are unconstrained. With the updated contact definition for a given cut-off pressure, the modal frequencies are re-computed and compared to the experimentally measured modes using a least-squares error metric. An optimal solution is found once this objective function is minimized.

A brief outline of the paper is as follows: Sect. 5.2 details the model updating procedure. Section 5.3 overviews the system geometry, experimental data acquisition procedure, and modal characteristics of the beam system. Section 5.4 presents results of the static preload analysis that determines the contact pressure distribution on the interface, as well as the results from the model updating routine and a discussion on the accuracy. The conclusions from this research are presented in Sect. 5.5.

5.2 Single Parameter Inverse Method

5.2.1 Inputs and Outputs

This work proposes a single parameter inverse method as a model updating procedure to adjust the contact definitions of element faces at the interface of a jointed structure with the goal of finding modal solutions that best match experimentally-measured modes. The only parameter that is adjusted is the cut-off pressure associated with the contact pressures computed from a nonlinear static preload analysis. An inverse method has the objective of adjusting the unknown system parameters (i.e. contact definitions) to agree with known inputs and outputs. This objective is in contrast to forward problems, in which the output is determined for known system parameters and inputs.

The inverse problem has multiple inputs associated with the finite element model. The geometry of the structure is required to develop a finite element mesh, and the material properties, such as the density ρ and the modulus of elasticity E , are required to develop the discretized equations of motion. The normal contact pressure distribution is a model input that is computationally-obtained from a static preload analysis using a (presumably) known preload force from the tightened bolt. The single parameter inverse method uses normal contact pressure information to update the contact definition in the interface. As described in Sect. 5.4.1, commercial finite element solvers can be used to obtain normal contact force data on a single node, f_{node} . Consequently, these nodal forces can then be translated into element pressures, p_{elem} , by averaging the nodal pressures associated with each element face. In addition to the aforementioned inputs, the single parameter inverse method uses output data that is observable from both the experimental and computational system. This research relies on the modal solutions computed from the linearized finite element model, and the modes extracted from test data on the physical hardware.

5.2.2 Contact Definitions

Within the node-to-face constraints employed in this research, three linearized contact conditions are possible: stuck, sliding, and no contact. The no contact condition allows for deformation of the faces without restricting any degree of freedom. Under this condition, there are no normal forces or tractions transferred from one face onto another and interpenetration may occur. A level of constraint is added in the sliding contact condition, which restricts normal displacements on the master and slave node/face pair to be equal, but allows for tangential motion. This contact definition resembles a Coulomb friction definition with a friction coefficient $\mu = 0$. All degrees of freedom in the interface are constrained when using the stuck contact definition, not allowing for any relative motion between contacting node/face pair. A Coulomb friction model is employed during the nonlinear preload analysis to capture the appropriate contact pressures, but is not used for the linearized modal analysis.

5.2.3 Contact Area Optimization

The single parameter from which this inverse method derives its name from is the cut-off pressure, p_l , used to adjust the contact definitions along the interface. This free variable is used as the sole optimization parameter for the model updating procedure. The numerically calculated element pressures, p_{elem} , from the nonlinear static analysis are determined, and the contact definitions are enforced based on whether the pressures are above or below p_l . Two different updating schemes are described in the following paragraphs and compared later in Sect. 5.4.2.

The first implementation of the single parameter inverse method utilizes all three of the possible contact conditions: stuck, sliding, and no contact. Each element face with a pressure equal to numerical zero receives a no contact condition. The sliding contact condition is assigned to element face pressures that are below the cut-off pressure, p_l , but greater than numerical zero. Every element with pressures above or equal to p_l is rigidly tied using the stuck condition. These logic statements are described in Eqs. 5.1, 5.2, and 5.3.

$$p_{elem} \leq 0 \rightarrow \text{No Contact} \quad (5.1)$$

$$0 < p_{elem} < p_l \rightarrow \text{Sliding Contact} \quad (5.2)$$

$$p_{elem} \geq p_l \rightarrow \text{Stuck Contact} \quad (5.3)$$

The second implementation of the single parameter inverse method is similar to the first, but instead only permits the stuck and no contact definitions. These logic statements are described in Eqs. 5.4 and 5.5. Now the element faces with a contact pressure between zero and the cut-off pressure p_l are also assigned a no contact condition. Note that this contrasts that of the first implementation, which assigns sliding contact to elements within this range. The contact condition for elements with pressures above p_l are defined to be in stuck contact.

$$p_{elem} < p_l \rightarrow \text{No Contact} \quad (5.4)$$

$$p_{elem} \geq p_l \rightarrow \text{Stuck Contact} \quad (5.5)$$

Based on these contact definitions for a given inverse approach and value of p_l , the multi-point constraints within the finite element model end up modifying the discretized mass and stiffness matrices. An eigenanalysis is formulated for a given constrained system and solved using a commercial finite element solver. The eigenanalysis equation is described as,

$$(\mathbf{K} - \omega_{n,m}^2 \mathbf{M}) \boldsymbol{\phi}_m = \mathbf{0} \quad (5.6)$$

where \mathbf{K} and \mathbf{M} correspond to the constrained stiffness and mass matrices, respectively. The index m corresponds to the mode number associated with a computed modal frequency, $\omega_{n,m}$, and mode shape, $\boldsymbol{\phi}_m$. These equations are solved using Lanczos-method, a computationally efficient pre-defined method found in most commercial finite element solvers.

The optimal value of p_l is sought for either implementation of the single parameter inverse method, as shown later in Sect. 5.4.2. This is achieved by defining an objective function that is a measure of the error between the experimentally measured and numerically calculated modal frequencies. This error metric is defined as the scalar, $|e|$,

$$|e| = \sqrt{\sum_{m=1}^N \left(\frac{\omega_{n,m,exp} - \omega_{n,m}}{\omega_{n,m,exp}} \right)^2}, \quad (5.7)$$

where the number of the elastic modes, N , are defined by the experimentally-obtained modal frequency of a specific mode, $\omega_{n,m,exp}$, and the numerically-calculated frequency, $\omega_{n,m}$, as provided in Eq. 5.6. The minimization of this objective function yields a single cut-off pressure p_l at which the modal frequencies of the modeled system most closely match those of the experiment.

5.3 System Description

5.3.1 Experimental Set-Up

The system considered in this study consists of two identical C-shaped beams brought into contact through two bolted joints on each end. A schematic of the geometry is provided in Fig. 5.1. There are two general regions on each 508 mm long beam: the slender center portion with cross-sectional dimensions of 31.8×9.65 mm and the elevated surfaces on the ends of the beams with the cross-sectional dimensions of 31.8×12.7 mm. The beams are bolted together using $5/16''$ -24 bolts, nuts, and washers at each end of the beam assembly. The interfaces were machined to be nominally flat with a surface roughness average of $R_a = 8$. The R_a value corresponds to the average height deviations from the mean line along a given surface. Holes were machined through the slender, center portions of the beams to enable the attachment of fishing line and soft bungee cords to approximate free-free boundary conditions.

Experimental modes of the beam assembly were collected from low-level impact excitations to supply the reference data to the inverse method. To mimic free-free boundary conditions, two sets of fishing line looped into the beam through holes to an overhead fixture. Figure 5.2 displays a labeled experimental set-up, identifying the locations of the boundary conditions (i.e. low stiffness springs) and accelerometers. Four points were identified along the beam structure to place the accelerometers to capture the expected mode shapes. Furthermore, the beam was impulsively struck at approximately every 2.5 cm along the beam in a roving hammer test to fully capture the modal responses. The test yielded linear results with impacts at approximately 15 N in the z and y directions. These directions correspond to a Cartesian coordinate system in which x and y define perpendicular directions along the beam's height and length, respectively, and z defines the direction along the beam's thickness.

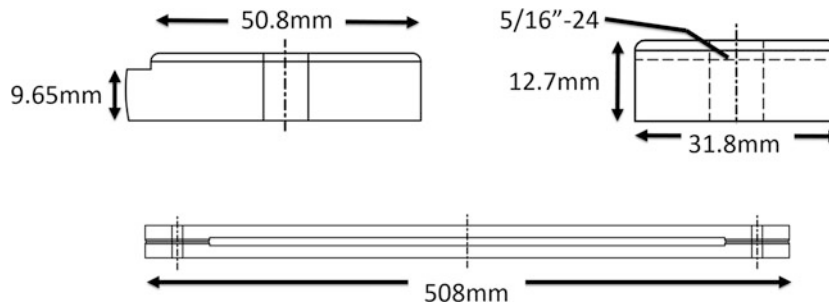


Fig. 5.1 Beam system drawing with important dimensions

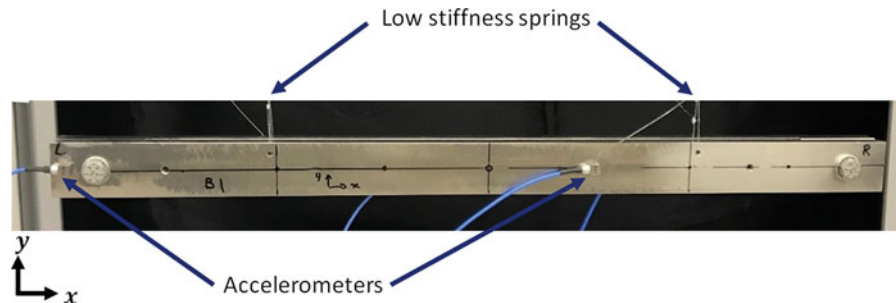


Fig. 5.2 Experimental set-up to collect measurements for model updating

Table 5.1 Comparison between test and analysis for the first six elastic modes of the C-shaped beam system

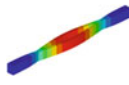

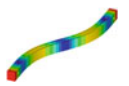

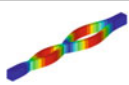
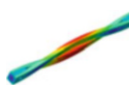
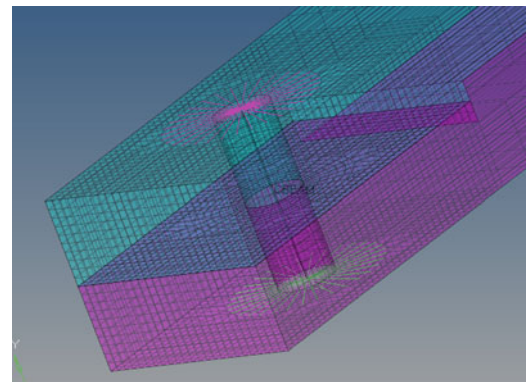
Mode number	FEA natural frequency [Hz]	Experimental natural frequency [Hz]	Mode shape
7	271	258	
8	338	331	
9	483	478	
10	571	567	
11	744	710	
12	892	855	

Fig. 5.3 FE modeling of washers and bolt

The accelerometer data collected in the experiments was used to estimate the frequency response functions (FRFs) from which the first six elastic vibration modes were fitted. There were a total of six rigid body modes present in the FRFs with modal frequencies < 10 Hz due to the low-stiffness boundary conditions that were not extracted or used throughout this research. The first six elastic modes occur within the 1000 Hz frequency bandwidth of interest. Table 5.1 shows the natural frequencies from the test data, as well as the mode shapes of the corresponding modes predicted by the FE model later in Sect. 5.3.2. The mode shapes from the computational model imposed fully stuck contact conditions at all elements on each of the flat interfaces. For each of the modes, the finite element model overpredicts the natural frequencies of interest due to the fact that the interface is overconstrained with all elements fully stuck. This data comparison serves as the upper boundary of the model predictions.

5.3.2 Finite Element Model

A finite element model of the C-shape beam system was developed for the inverse study consisting of approximately 47,500 8-noded hexahedral elements. The bolt, washer and nut subassembly was simplified with beam elements (25 across the bolt length) whose ends are rigidly spidered to the surface corresponding the area underneath the washers. It is assumed that there is no slip occurring at these interfaces. The beam elements running through the bolt holes add both the longitudinal and bending stiffness associated with the actual bolts. Rigid spiders branching out from the ends of the beam elements to the surrounding nodes in the beam structures model the contact interface of the washers. A view of the beam element and rigid spider assembly is pictured in Fig. 5.3. Both the models of the bolt and the C-shape beams use nominal material properties of structural steel with density 8000 kg/m^3 , modulus of elasticity 194 GPa, and Poisson's ratio 0.29.

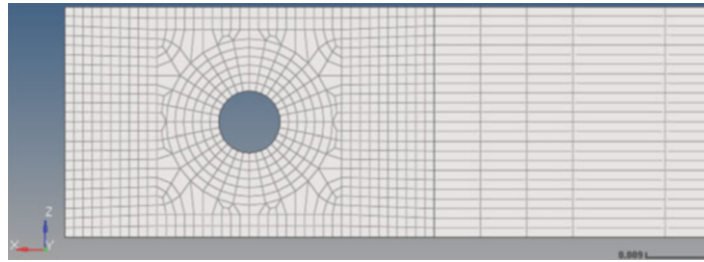


Fig. 5.4 Optimal mesh to balance resolution with computational expense

Table 5.2 Mesh sensitivity comparison of the first six elastic modal frequencies for bounding contact conditions

#-nodes	#-elements	Fully stuck	Hole-nodes stuck	7th mode [Hz]	8th mode [Hz]	9th mode [Hz]	10th mode [Hz]	11th mode [Hz]	12th mode [Hz]
7835	1152	–	X	178	332	501	514	515	594
31,798	5702	–	X	177	332	501	513	515	594
7835	1152	X	–	287	353	502	594	787	957
31,798	5702	X	–	287	353	502	594	788	957

Finite element discretizations of structures with local interface kinematics in structural dynamics applications often require detailed models with fine mesh resolution. The balance between the appropriate mesh size and computational expense is a major challenge in computational modeling and is vital to achieving accurate results for applications when a large number of analysis iterations are needed, such as inverse methods. The beam mesh density is chosen to obtain converged results while keeping the mesh as coarse as possible. A total of approximately 50,000 8-noded hexahedral elements are used for the most refined solution, which correlates to approximately 2,000 element faces on the contact surfaces shown in Fig. 5.4. The sensitivity of the computational modal analysis results for the first five elastic modes is summarized in Table 5.2. Two bounding contact conditions are presented in this table: a fully stuck interface and a predominantly no contact interface with stuck elements in a small annulus around the through hole. Mode shapes and natural frequencies under both bounding contact conditions do not vary appreciably as the number of nodes changes between 7,835 and 31,798. These results assure that the optimal mesh can be based purely on its resolution of local contact phenomena and the associated computational expense.

The normal mode calculations from the FE model for the two bounding contact conditions provides insight into the sensitivity of individual modes to interface contact definitions. For example, mode 10 is a bending deformation in the y -direction and does not appear to load the interface. This shape is especially insensitive (deviation below 1%) to the applied contact conditions. Due to this insensitivity, the 10th mode provides a basis for the material properties to be calibrated. A match between the experimentally-obtained and numerically-calculated modal frequency for the 10th mode occurs for a modulus of elasticity of 181 GPa. While the masses of the accelerometers used in the experimental set-up are small in comparison to the mass of the beams, they contribute to the system response depending on their position within the beam system set-up. In particular, the accelerometers positioned on the beam, as displayed in Fig. 5.2, have a nontrivial effect on the numerical solution for specific modes (approximately 5 Hz deviation in the 7th and 11th modes) and thus are modeled as point masses with mass $m = 0.02$ kg.

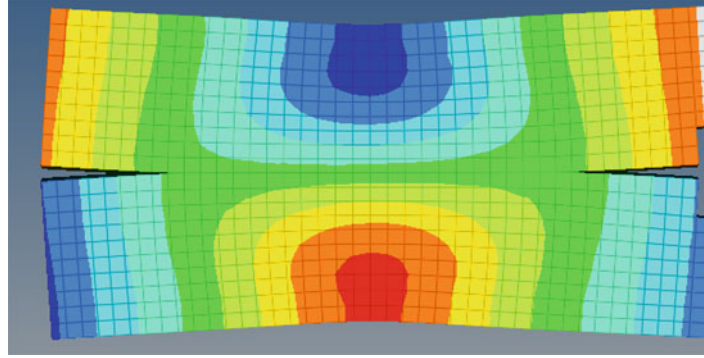
5.4 Results

5.4.1 Static Preload Analysis

The single parameter inverse method uses the computed pressure distribution at the interfaces from a nonlinear static preload analysis subject to a given bolt torque/preload force. These solutions are obtained using Altair's Optistruct implicit solver, which incrementally applies loads and iteratively solves equilibrium equations until certain convergence criteria are met (e.g. displacement, load, work). In the nonlinear static FE model, frictional contact between the beam surfaces is accounted for using Coulomb friction and the penalty method. A static friction coefficient of $\mu = 0.3$ governs the tangential forces between the metallic surfaces. The penalty stiffness at each element is set to the software's default value. Contact pressure results from simulations at various bolt torque levels reveal that the friction coefficient does not affect the pressure distribution shape (i.e. only the pressure magnitudes are scaled proportional to the bolt force). This observation is consistent with receding contact

Table 5.3 Bolt torque to axial pretension conversions

Exp. torque [N-m]	Motosh force [kN]
10.2	8.6
16.9	14.3
25.1	21.2

**Fig. 5.5** Deformed side view of the structure subjected to bolt pretension of 21.2 kN; colorbar corresponds to vertical displacements

theory for flat-on-flat surfaces with similar materials [16]. While the experimental setup employs low-stiffness supports to mimic free-free boundary conditions, the computational model does not enforce such restraints and uses purely free-free boundary conditions to ensure the bolt loads transfer directly into the interface. The inertial relief option is applied to the static simulation to prevent rigid body motion.

For the preload step, the finite element software applies bolt pretensions instead of torques. Since the experimental hardware measured the bolt load using a torque wrench, an appropriate constitutive relationship was used to map the specified torque level to a corresponding axial force. One well known relationship, known as the Motosh equation [17], relates torque to bolt force as,

$$T = F \left(\frac{P}{2\pi} + \frac{\mu_t r_t}{\cos(\beta)} + \mu_n r_n \right) \quad (5.8)$$

where T denotes the applied bolt torque, F is the axial force supplied by the bolt, P is the thread pitch, μ_t is the coefficient of friction between the nut and bolt threads, r_t is the effective contact radius of the threads, β is the half-angle of the threads, μ_n is the coefficient of friction between the face of the nut and the upper surface of the joint, and r_n denotes the effective radius of contact between the nut and joint surface. Results from applying Eq. 5.8 to torque values of 10.2, 16.9, and 25.1 N-m are presented in Table 5.3. These torque values correspond to the values at which the pressure film measurements were taken on the experimental hardware.

A side profile view of the deformations near one of the bolted joints resulting from the static preload analysis is presented in Fig. 5.5. Note that the flat interfaces are in contact near the bolt hole but bend away (or recede) from each other far away from it. The deformation has been amplified to reveal the characteristics of the deformation. Contact pressure profiles for the beam structure subjected to 21.2 kN of pretension are shown in Fig. 5.6, which displays contact pressure contours throughout the interface. The plot in Fig. 5.7 shows a line slice of the interface contact pressure along the horizontal centerline in Fig. 5.6. Notice that the contact pressure is highest around the bolt hole (region between the blue dashed lines in Fig. 5.7) and decreases in concentric rings outward from the bolt location.

To assess the validity of the static pressure simulations, the results are compared with digitized pressure film measurements taken in the actual beam hardware when the bolts were tightened to 25.1 N-m. Both low (range of 2.4–9.7 MPa) and medium (range of 9.7–49 MPa) scale pressure films were used and these results are shown in Fig. 5.8. Note that both pressure films exhibit saturation as evidenced by the red colored regions, indicating the measured pressure exceeds the films upper boundary of either 9.7 MPa or 49 MPa. Consequently, the low pressure film proves useful for reading pressures away from the bolt hole while the medium pressure film better captures the pressure values near the bolt hole.

Due to the uncertainty in the analytical relationship between axial pretension force and bolt torque, the bolt pretension values were calibrated in the FE model to match experimentally measured peak pressure values obtained from the pressure film measurements. The results from the medium pressure film in Fig. 5.8 are used since the peak pressure values are visible and better capture the maximum contact pressure that occurs around the bolt hole. The results of the calibration process are

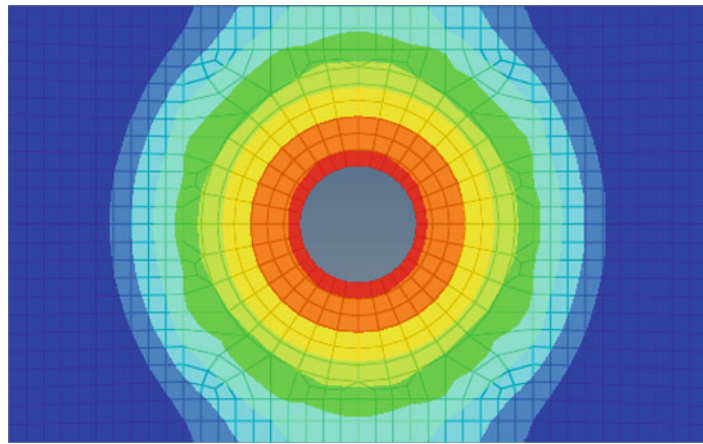


Fig. 5.6 Normal contact pressure profile in the FE beam subjected to bolt pretension of 21.2 kN

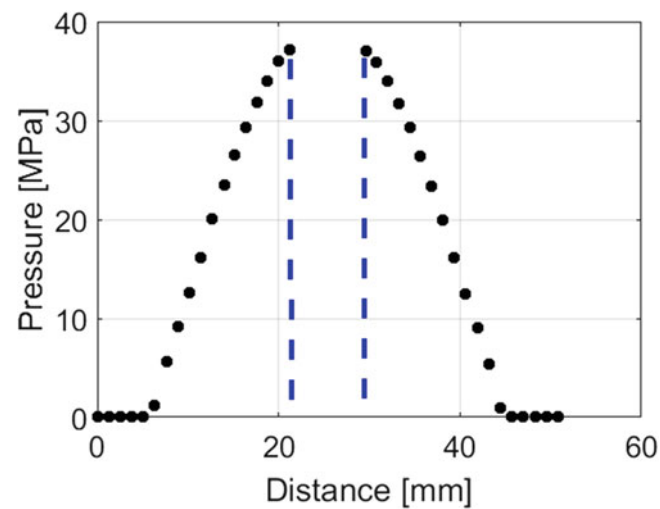


Fig. 5.7 Interface contact pressure along the horizontal centerline in a beam subjected to bolt pretension of 21.2 kN

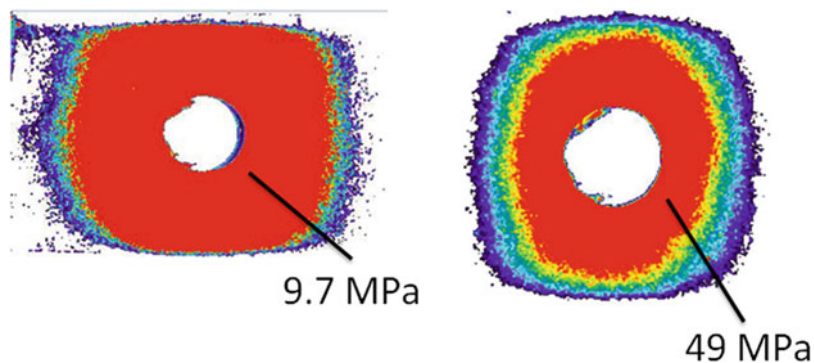


Fig. 5.8 Low (left) and medium (right) film measurements taken in the actual beam assembly

presented in Fig. 5.9. Note that the FE model achieves a peak pressure value of approximately 49 MPa when using a 28.0 kN pretension force. This agrees well with the peak pressure value measured by the medium pressure film measurement in Fig. 5.8, but requires a force that is 32% larger than the value predicted by the Motosh Equation in Eq. 5.8. It is important to note that there is considerable uncertainty associated with mapping a torque to an bolt pretension using closed form analytical solutions [18], thus highlighting the importance of measuring the contact pressures experimentally.

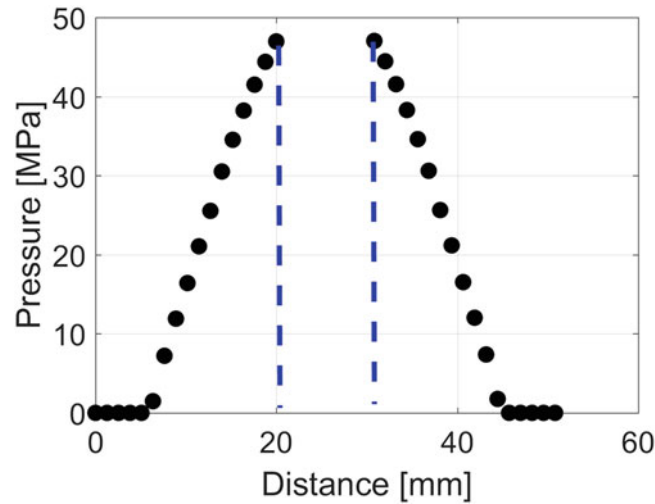


Fig. 5.9 Interface contact pressure along the horizontal centerline in a beam subjected to calibrated bolt pretension of 28.0 kN

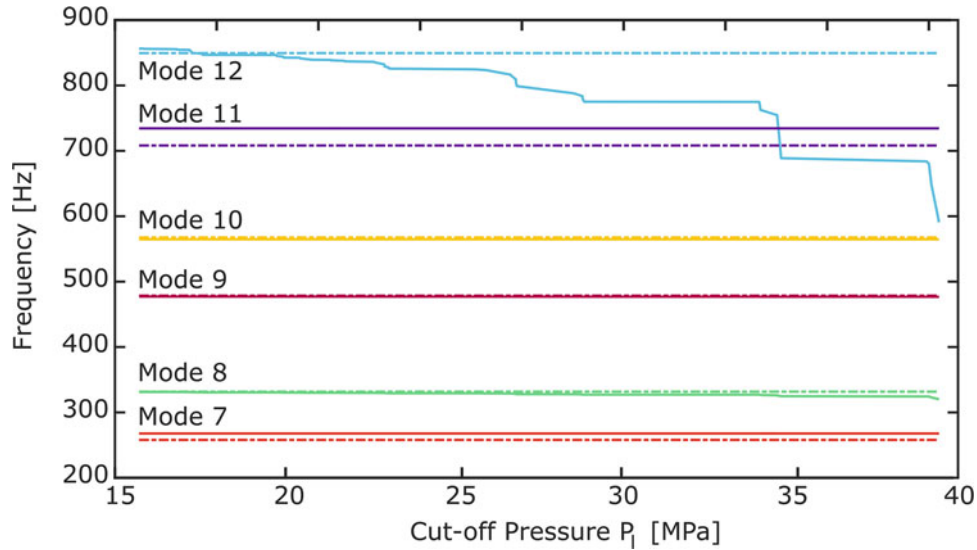


Fig. 5.10 Modal frequencies computed at various cut-off pressures using three contact conditions

5.4.2 Model Updating Results

This subsection compares the results for the two versions of the single parameter inverse method described in Sect. 5.2.3. Due to the discrete nature of the pressures predicted by static analysis at a finite number of element faces, a given value of p_l would produce a zero or discontinuous derivative. This means that there are only discrete changes in cut-off pressure values that would alter the contact definition at the interface. Standard gradient-based optimizers require a continuous parameter space with continuous derivatives and hence could not be used in this work. The results presented in this subsection are obtained by sampling the cut-off pressures at the discrete values obtained from all the interface elements in the static preload analysis.

The results from the first implementation are shown in Fig. 5.10, such that the sliding condition is utilized for pressure below the cut-off value but greater than zero. This plot displays the modal frequencies of modes 7 through 12, relating to the first six elastic modes, computed at discrete cut-off pressures, p_l . The dashed-lines correspond to the modal frequencies measured from experiment, and the solid lines correspond to the modes from the FE model. A given mode can be considered optimal when the solid line crosses the dashed experimental line. The first observation made from this plot is that modes 7, 8, 9, 10 and 11 show little sensitivity to the contact definition associated with p_l . Recall that modes 8 and 9 are bending modes in the xy -plane, as seen in Table 5.1. Notice that the interfaces do not bend when the beam deforms in the shapes of

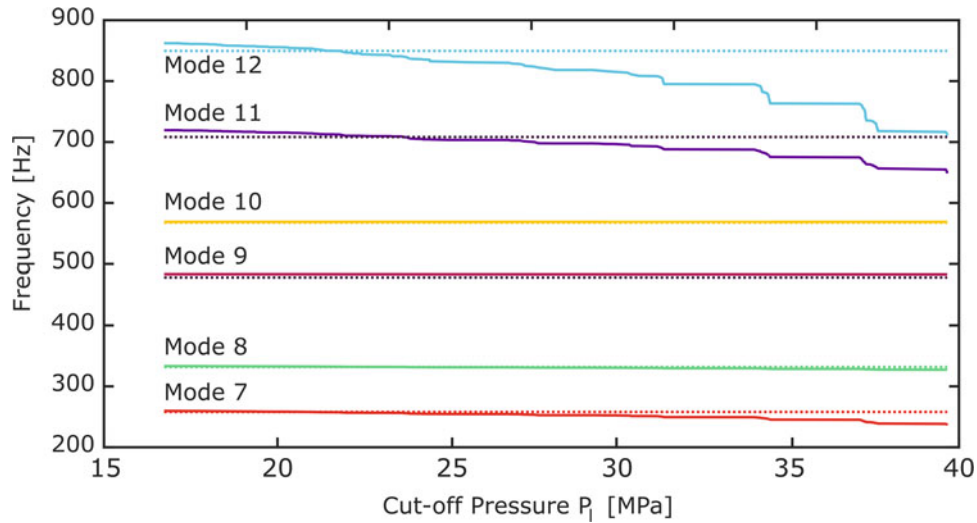


Fig. 5.11 Modal frequencies computed at various cut-off pressures using two contact conditions

these modes. As a result, the joint is not loaded significantly and is insensitive to changes in the contact conditions. Mode 10 is a similar bending mode in the xz -plane, which, similarly to modes 8 and 9, has minimal influence on the shear loads in the joint. Modes 7 and 11 are clapping modes in the xy -plane leading to an opening and closing of the contact surface. While the sliding contact definition can capture relative displacements tangential to the contact surface, it restricts relative displacements normal to the contact surface, resulting in an essentially stuck contact condition for these two clapping modes. In contrast, mode 12 is highly sensitive to its contact definition as the contact surface around the bolt experiences significant shearing for this mode and the sliding contact definition captures this motion well. This mode is considered optimal at a cut-off pressure of about 18 MPa. These results reveal that not all of the modes are sensitive to the change in contact condition, and there is still a significant amount of error observed in the modes of interest (i.e. modes 7 and 11 in particular).

The second implementation of the single parameter inverse method overcomes the limitations observed with the two clapping modes 7 and 11. Figure 5.11 displays the modal frequencies for the first six elastic modes for the second implementation for discrete values of cut-off pressure p_l . In this case, modes 8, 9, and 10 are still not sensitive to the contact definitions due to the reasons previously discussed. Mode 12 is still highly sensitive since the interface is allowed to rotate and shear more or less with changing cut-off pressures. This mode crosses the experimental line now at a higher cut-off pressure, around 23 MPa, compared to the previous case at 18 MPa. The biggest improvement from the second implementation was seen with the sensitivity of modes 7 and 11, which were the clapping modes in the xy -plane. Since the change in p_l now releases the tangential *and* normal constraints, the stiffness of the clapping modes is able to decrease with increasing p_l . Now modes 7 and 11 cross the experimental value at around 22 and 24 MPa, respectively. The change from sliding to no contact conditions now have all of the sensitive modes of interest cross at nearly the same pressure, suggesting a better solution is obtainable with the second approach.

The individual mode representations in Figs. 5.10 and 5.11 give insight into the ability of the inverse method to capture true contact area at the bolted joint interface. The frequency errors are quantified in Fig. 5.12 by evaluating the objective function in Eq. 5.7 at each cut-off pressure p_l . The three contact condition implementation is shown in blue while the two condition case is in green. The method using two contact conditions provides the optimal result with an error of $|e| < 3\%$ at a cut-off pressure of $p_l = 23$ MPa, and the contact area of this is shown in the subplot within Fig. 5.12. The method using three contact conditions achieves a minimal error of $|e| = 6.5\%$ at $p_l = 17$ MPa. The low error associated with the second implementation (i.e. two contact conditions) highlights the insight that can be gained from understanding how the mode shapes load the interface, and how to assign realistic contact definitions.

The objective function plot in Fig. 5.12 reveals the discrete nature of the single parameter p_l . The objective function is clearly discontinuous and would not work with gradient-based optimization algorithms. This problem was small enough that sampling the design space was completed in less than 24 h on a standard laptop computer. The sampling approach could be parallelized with high performance computing resources, but this was not necessary for this research. These results reveal a successful proof-of-concept that the linearized structural dynamics model can be calibrated to test data by simply adjusting the contact area in a bolted interface by systematically adjusting the cut-off pressure from the results obtained from a nonlinear static preload analysis.

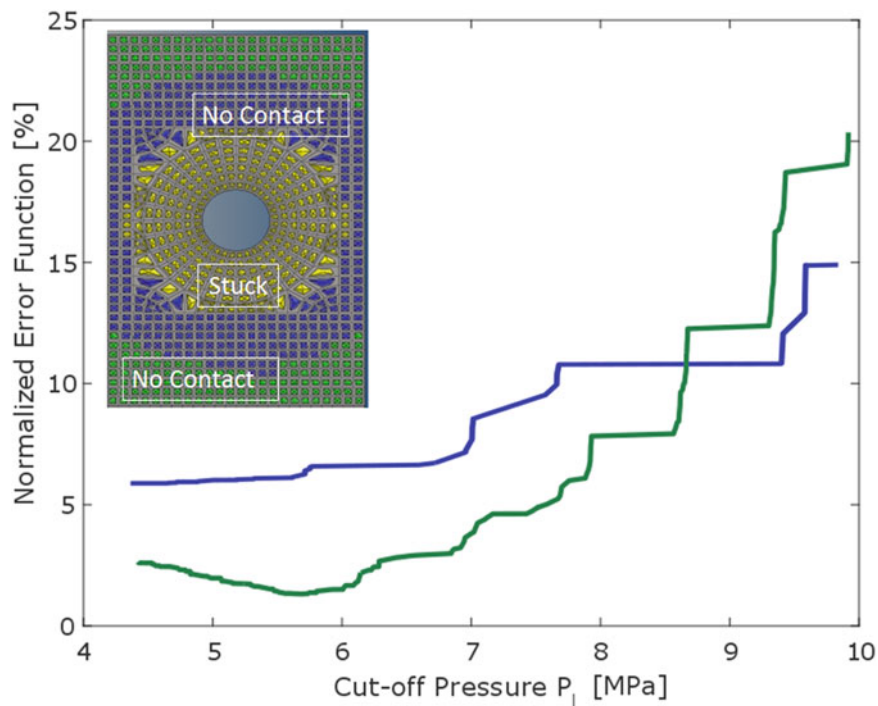


Fig. 5.12 Objective function evaluation for various cut-off pressures for both implementations of the single parameter inverse method: (blue) three contact conditions and (green) two contact conditions

5.5 Conclusions

A single parameter inverse method is developed in this research to update contact definitions in a linearized finite element model of a jointed structure to match with experimental modal data. A nominal finite element model of the structure is developed and a nonlinear static preload analysis is completed to estimate the normal contact pressures at the bolted interface. A single parameter, termed the cut-off pressure, is then used to systematically adjust the constraint conditions at the element faces in the interface. Three conditions are utilized in this study: no contact, sliding and stuck. The no contact condition does not enforce any constraints to the elements and hence allows for unrestricted motion in all degrees of freedom. The sliding condition enforces constraints to the displacements in the normal direction, but not in the tangential motion. The stuck condition restricts motion in all degrees of freedom relative to the node-face pair. The inverse method adjusts the contact constraint in the finite element model using only the value of the cut-off pressure variable and whether or not the predicted normal contact pressures are above or below.

Two implementations of the inverse method are studied. The first assigns no contact for elements with zero pressure, sliding for those less than the cut-off value but greater than zero, and stuck for those with pressures greater than the cut-off value. The second implementation is similar to the first, but instead eliminates the possibility of sliding contact for normal pressures less than the cut-off and enforcing no contact instead. For the C-shape beam system studied in this work, excellent agreement is obtained for the second implementation and the error summed across the first six elastic modes is $<3\%$. The second approach outperforms the first since there are two “clapping” modes that open and close the interface and need the ability to release the contact constraints in the normal direction. The single parameter inverse method combines model updating approaches, test data, and physical understanding of mode shapes to identify the appropriate contact area within a linearized structural dynamics model. Because of the good agreement obtained from a relatively simple structure, this approach could be used with confidence to explore higher-fidelity models of jointed structures.

Future studies could build on this work by including damping and frictional contact to account for other important physical phenomena in jointed structures with the objective of matching test data with high accuracy. Such a technique would provide greater insight into the physics occurring within frictional interfaces during vibration. In addition, a discrete optimization routine would benefit this approach in order to avoid evaluating the model for a large number of discrete cut-off pressure values and thus more quickly reach the minimum value of the objective function. The need for optimization routines in comparison to open-loop objective function evaluation becomes especially prevalent when increasing the mesh refinement, which can result in a single iteration runtime on the order of minutes or hours.

Acknowledgements This research was conducted at the 2017 Nonlinear Mechanics and Dynamics (NOMAD) Research Institute supported by Sandia National Laboratories. Sandia National Laboratories is a multimission laboratory managed and operated by National Technology and Engineering Solutions of Sandia, LLC., a wholly owned subsidiary of Honeywell International, Inc., for the U.S. Department of Energy's National Nuclear Security Administration under contract DE-NA-0003525. SAND2017-11517 C.

References

1. Mottershead, J., Friswell, M.: Model updating in structural dynamics: a survey. *J. Sound Vib.* **167**(2), 347–375 (1993)
2. Ewins, D.J.: Exciting vibrations: the role of testing in an era of supercomputers and uncertainties. *Meccanica* **51**(12), 3241–3258 (2016)
3. Nobari, A.S., Robb, D.A., Ewins, D.J.: Model updating and joint identification methods – applications, restrictions and overlap. *Int. J. Anal. Exp. Modal Anal.* **8**, 93–105 (1993)
4. Kim, T.R., Wu, S.M., Eman, K.F.: Identification of joint parameters for a taper joint. *J. Eng. Ind.* **111**(3), 282 (1989)
5. Ehmann, K.F., Ehmann, K.F., Wu, S.M.: Identification of joint structural parameters between substructures. *J. Manuf. Sci. Eng.* **113**(4), 419 (1991)
6. Mottershead, J.E., Weixun, S.: Correction of joint stiffnesses and constraints for finite element models in structural dynamics. *J. Appl. Mech. Trans. ASME* **60**(1), 117–122 (1993)
7. Mottershead, J., Friswell, M., Ng, G., Brandon, J.: Geometric parameters for finite element model updating of joints and constraint. *Mech. Syst. Sig. Process.* **10**(2), 171–182 (1996)
8. LI, W.: A new method for structural model updating and joint stiffness identification. *Mech. Syst. Sig. Process.* **16**(1), 155–167 (2002)
9. Adel, F., Shokrollahi, S., Jamal-Omidi, M., Ahmadian, H.: A model updating method for hybrid composite/aluminum bolted joints using modal test data. *J. Sound Vib.* **396**, 172–185 (2017)
10. Brake, M.R.W., Stark, J.G., Smith, S.A., Lancereau, D.P.T., Jerome, T.W., Dossogne, T.: In Situ Measurements of Contact Pressure for Jointed Interfaces During Dynamic Loading Experiments, pp. 133–141. Springer International Publishing, Cham (2017)
11. Marshall, M.B., Lewis, R., Dwyer-Joyce, R.S.: Characterisation of contact pressure distribution in bolted joints. *Strain* **42**(1), 31–43 (2006)
12. Segalman, D.J.: A four-parameter Iwan model for lap-type joints. *J. Appl. Mech.* **72**(5), 752 (2005)
13. Allen, M.S., Lacayo, R.M., Brake, M.R.W.: “Quasi-Static Modal Analysis Based on Implicit Condensation for Structures with Nonlinear Joints,” Proceedings of ISMA2016 - International Conference on Noise and Vibration Engineering. Leuven, Belgium (2016)
14. Sellgren, U., Olofsson, U.: Application of a constitutive model for micro-slip in finite element analysis. *Comput. Methods Appl. Mech. Eng.* **170**(1), 65–77 (1999)
15. Flicek, R.C., Ramesh, R., Hills, D.A.: A complete frictional contact: the transition from normal load to sliding. *Int. J. Eng. Sci.* **92**, 18–27 (2015)
16. Johnson, K.L.: *Contact Mechanics*. Cambridge University Press, Cambridge (1985)
17. Motosh, N.: Development of design charts for bolts preloaded up to the plastic range. *J. Eng. Ind.* **98**, 849 (1976)
18. Bickford, J.H.: *An Introduction to the Design and Behavior of Bolted Joints*. Marcel Dekker, New York (1995)



Chapter 6

Experimental Characterization of a New Benchmark Structure for Prediction of Damping Nonlinearity

Aabhas Singh, Matteo Scapolan, Yuta Saito, Matthew S. Allen, Daniel Roettgen, Ben Pacini, and Robert J. Kuether

Abstract Spacecraft, airplanes, automobiles, machines and civil structures are all constructed from multiple parts joined by bolts, rivets or other fasteners and these joints lead to large uncertainties in the structural stiffness, damping and can even introduce nonlinearity. Even with the best available simulation tools, it is still difficult to predict the effective stiffness and damping of bolted interfaces, and so these parameters are often assumed and updated after tests have been performed. Damping estimates are critical to limit the resonant vibration response of a structure and thus prevent failure. Even so, it remains poorly understood and available methods for modeling damping are inaccurate and computationally expensive. A new benchmark structure has been created that is designed so as to be predictable with current simulation tools. This paper presents a thorough experimental characterization of this new benchmark structure using the Hilbert transform method applied to modally filtered time data. The nonlinear frequency and damping of each mode is characterized for various levels of bolt preload and excitation amplitude. The interfaces of the bolted structure are also characterized in detail by measuring the contact pressure distribution using pressure sensitive film. The resulting data presents a set of well characterized tests that can be used to validate numerical methods that seek to predict the nonlinear behavior of bolted interfaces.

Keywords Modal testing · Modal analysis · Hilbert transform · Mechanical interfaces · Contact pressure characterization

6.1 Introduction

The finite element method has developed to the point that one can now create remarkably accurate and predictive models of parts even with complicated and intricate geometry. However, this is only true so long as they are constructed of a single piece of metal. Interfaces between parts of different materials or the same material lead to large uncertainties. Airplanes, automobiles, machines and civil structures are all constructed from multiple parts joined by bolts, rivets or other fasteners and these joints introduce large uncertainties in the structural stiffness, damping and nonlinearity. Even with the best available simulation tools, it is still difficult to predict the effective stiffness and damping of bolted interfaces, and so often these parameters are assumed and updated after tests have been performed. Damping is critical to limit the resonant response of a structure and thus prevent failure, and yet it remains poorly understood and available methods for modeling damping are inaccurate and computationally expensive.

In recent years, test methods have been developed that can accurately describe the nonlinear stiffness and damping of structures with joints, and these have been used to tune models to measurements up to moderately large amplitudes. Recent experimental works by Roettgen et al. [1], and Deaner et al. [2] show that the modes of a structure with joints can remain uncoupled. This characteristic has been used to test several structures to update the corresponding finite element

A. Singh · M. S. Allen (✉)

Department of Engineering Physics, University of Wisconsin-Madison, Madison, WI, USA
e-mail: singh36@wisc.edu; msallen@engr.wisc.edu

M. Scapolan

Politecnico di Torino, Turin, Italy
e-mail: matteo.scapolan@polito.it

Y. Saito

University of Illinois at Urbana-Champaign, Champaign, IL, USA
e-mail: ysaito2@illinois.edu

D. Roettgen · B. Pacini · R. J. Kuether

Sandia National Laboratories, Albuquerque, NM, USA
e-mail: droett@sandia.gov; brpacin@sandia.gov; rjkueth@sandia.gov



Fig. 6.1 The unbolted S4 beam

models to describe the nonlinear effects of the joints. Free response time histories have been used for this purpose to allow quick comparisons between these experimental data and simulations from models using some recently developed signal processing and analysis techniques. The amplitude dependent natural frequencies and damping ratios estimated with the Hilbert transform from experimental data, allowing the models to be calibrated using the analysis proposed by Allen et al. [3] and Festjens et al. [4]. The thesis by Lacayo [5] has successfully demonstrated this workflow using the Brake-Reuss (BRB) beam.

Previous work towards understanding the characteristics of the joint nonlinearity in the structural dynamic response has proved successful in correlating Iwan models to the nonlinear characteristics of the Brake – Reuss Beam. This benchmark structure has a square cross-section with a three-bolt lap joint at the center [5]. The work in this paper aims to characterize a beam with a simpler two – bolt joint assembly in an effort to create simpler interfaces to investigate the joints influence on the nonlinear stiffness and damping. This new benchmark structure, termed the “S4 Beam”, features two bolted interfaces at the ends of two c – shaped beams, designed to model the nonlinear effects of joint bending and shearing in bolted structures. The beam structure is depicted below in Fig. 6.1.

Prior to the characterization the joint, a comprehensive test sequence is developed to understand the effects of bolt torque level, excitation level, and joint interface curvature on the nonlinear dynamics of the structure. Similarly to the BRB, the Hilbert Transform is used on the free response data to detect the degree of nonlinearity [6]. In addition to the nonlinearity, the joint is characterized by measuring the pressure distribution along the surface of the interface through pressure film measurements taken at various torque levels.

6.2 Theoretical Background

Experimental modal analysis of a structure is used to identify the linear modal parameters (i.e. shapes, frequencies and damping) of a linear, time invariant system. However, if the system is nonlinear, then nonlinear techniques are needed to characterize the degree of nonlinearity for each mode of the system. In this research, the nonlinearity is characterized numerically using the Hilbert transform. Below is a summary of the Hilbert transform as described by Allen and Roettgen [1].

The Hilbert transform has been widely used for nonlinearity detection for single degree of freedom (SDOF) systems. However, given that the physical measurements ($\ddot{x}(t)$) from accelerometers commonly used in modal testing incorporate coupling when multiple modes are excited for a given input, the measurements are transformed into the modal domain ($\ddot{q}(t)$) using a modal filter to result in modal SDOF systems as described in Kerschen et al. [7] and as shown in Eq. 6.1.

$$\ddot{x}(t) = \Phi \ddot{q}(t) \rightarrow \ddot{q}(t) = \Phi^\dagger \ddot{x}(t) \quad (6.1)$$

If the modes can be sufficiently uncoupled, then the envelope of the modal signal for the r th mode can be described as a sum of the decaying harmonic function and its Hilbert transform as given by Eq. 6.2.

$$Q_r(t) = q_r(t) + i\tilde{q}_r(t) \quad (6.2)$$

where $\tilde{q}_r(t)$ is the Hilbert transform of the signal and $Q_r(t) = A(t) \exp(i\psi(t))$. $A(t)$ denotes the magnitude of the envelope as given by $A(t) = \sqrt{q_r(t)^2 + \tilde{q}_r(t)^2}$ and $\psi(t)$ represents the instantaneous phase of the modal response as given by $\psi(t) = \tan^{-1} \left(\frac{\tilde{q}_r(t)}{q_r(t)} \right)$ [8]. Equation 6.2 is depicted in terms of modal displacement amplitude, but can also be applied to modal velocity and acceleration amplitude as governed by

$$|q_r| = \frac{|\dot{q}_r|}{\omega_r} = \frac{|\ddot{q}_r|}{\omega_r^2} \quad (6.3)$$

The objective is to describe the nonlinear damping and stiffness as a function of peak velocity amplitude such that type of nonlinearity can be described with the increase in amplitude. As a result, the instantaneous damped natural frequency can be described as the time derivative of the instantaneous phase and the instantaneous damping can be calculated from the time derivative of the amplitude as shown below

$$\omega_{r \text{ damped}} = \frac{d\psi(t)}{dt} \quad (6.4)$$

$$-\omega_r \zeta_r = \frac{dA(t)}{dt} \quad (6.5)$$

where ω_r is the natural frequency as governed by $\omega_r = \omega_{r \text{ damped}} / \sqrt{1 - \zeta_r^2}$. However, given that experimental data yields discrete points, the data is fit with a spline with 50 points (knots). An in-depth discussion of the derivation of the Hilbert transform can be found in Feldman [9].

6.3 Experimental Methodology

The work presented in this paper was conducted on two C-shaped beams manufactured with Stainless Steel type ANSI 304. The two beams before and after assembly with two bolted connections at the ends are shown in Fig. 6.2.

Each beam is 20 inches long, with two 2" \times 1.25" contact surfaces. Each beam is 0.5" tall at the contact surface, and 0.38" elsewhere. All dimensions on the beam were manufactured with a 0.005" tolerance. Two different sets of beams were manufactured with variable surface conditions at the bolted interfaces: (1) convex interface with a center to edge drop of 0.005" to 0.008", and (2) flat interface as shown below. All contact surfaces were polished to a minimum surface finish of Ra = 8 (Fig. 6.3).

Prior to modal testing, four configurations of beams were assembled as indicated in Fig. 6.4. B1-B2 features an interface of two convex surfaces in contact. This contact was modified slightly by placing thin stainless-steel washers at the interface

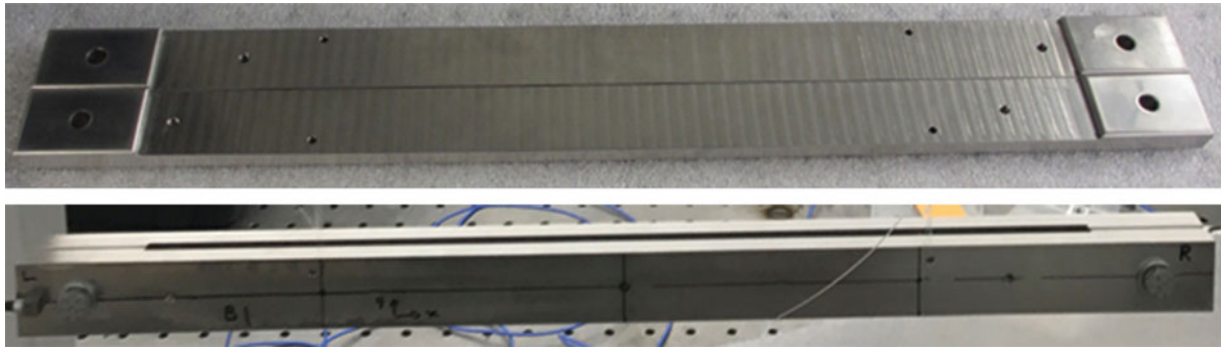


Fig. 6.2 Two separate beam halves of the S4 beam (top) and the assembled beam (bottom)

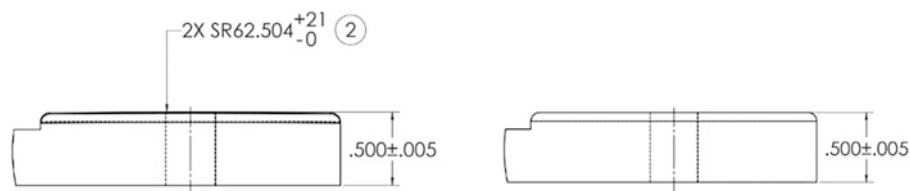


Fig. 6.3 Drawing of the convex (left) and flat (right) interfaces

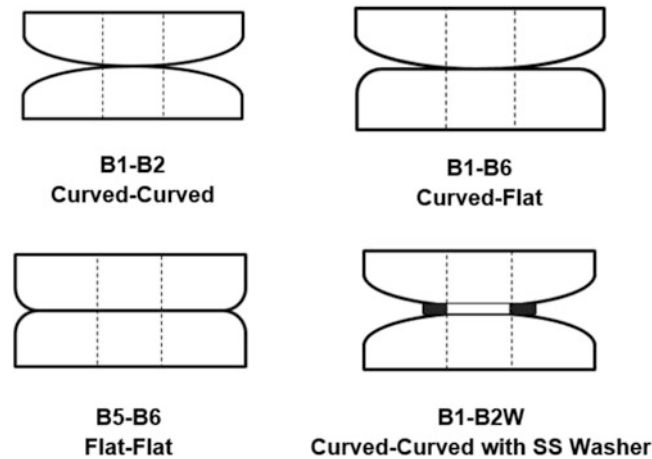


Fig. 6.4 Combinations of beams and their corresponding contact surfaces

for B1-B2W, in an effort to move the contact pressure distribution further away from the bolt holes. In B1-B6, the contact was such that a convex surface is mated with a flat surface. The flat-flat surface case is examined with B5-B6. All beams were assembled by $5/16''$ -24 bolts and nuts, and type – A washers.

6.3.1 Impact Hammer Testing

Modal testing of the S4 Beam was accomplished by hanging the assembly using bungee cords and fishing line to emulate “free–free” boundary conditions with as little impact on the dynamics of the system as possible. Discrete points along the beams were excited by an impact hammer to obtain the linear mode shapes (at low impact amplitudes) and nonlinear time histories (at higher amplitudes) for the nonlinear system parameter identification. The bolted beams were tested at three torque levels: 10.2 N-m, 16.9 N-m, and 25.1 N-m to evaluate the effect of preload, and four input forces 10 N, 100 N, 250 N, and 500 N to assess the effect of input force on the joint nonlinearity. The experiment was then repeated for the four combinations of beams.

Prior to commencing testing at all torque and impact levels, the optimal setup was found to minimize the cable damping, and hence the number of accelerometers necessary to capture the desired mode shapes. This optimization process was carried out by progressively increasing the number of accelerometers and checking experimental natural frequencies and modal damping. Small variations with respect to a setup with a minimum number of accelerometers indicated that the added sensors did not significantly influence the structure. Cables were taped to the beam, as it was found that it mitigated additional damping to the system in these conditions. In this phase, prior to nonlinear data collection, the interest was not in the mode shapes, but rather in the natural frequencies and damping ratios, so that the setup with a minimum number of sensors was used as a reference to evaluate structural effects (mass and damping) of the accelerometers on the beam.

The first six elastic mode shapes for B1-B2 are reported in Fig. 6.5 and were considered the target modes when defining the accelerometer placement.

Figure 6.6 depicts the optimal sensor setup for B1-B2, which was then replicated for the three other combinations.

Accelerometer locations were chosen to obtain completely observable modes in the bandwidth of interest. Input locations were similarly selected such that for each mode there was at least one point efficiently exciting the mode. As a result, the final setup consisted of ten accelerometers, with nine tri-axial and one uniaxial, for a total of 28 output channels. Additional optimization was done using a roving hammer test to evaluate the ideal input locations as depicted in Appendix A. To capture the first six elastic modes, the test bandwidth was limited to 800 Hz based on the preliminary modal simulation of the finite element model. The data acquisition was performed by Siemens LMS Test Lab and LMS SCADAS system.

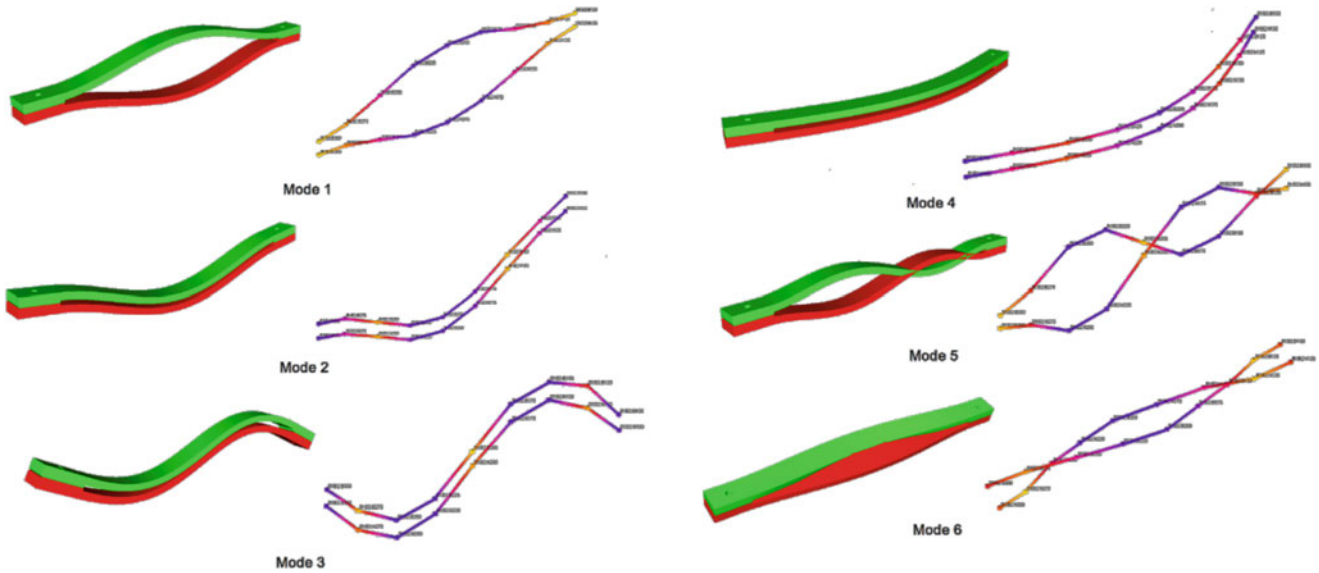


Fig. 6.5 Linear elastic mode shapes of the S4 beam

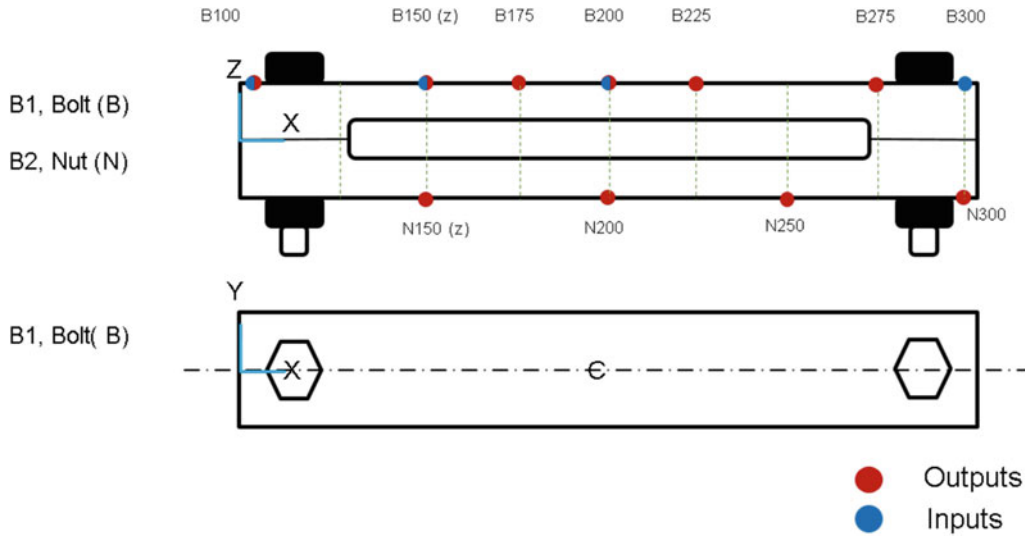


Fig. 6.6 Optimal test setup

Table 6.1 Film types and corresponding pressure ranges

Film type	Pressure range [MPa]
Low	2.41–9.65
Medium	9.65–48.95
High	48.95–127.55

6.3.2 Joint Profile Testing

In order to capture the change in the joint characteristics due to the change in torque, the two contact areas of the beams were characterized with normal contact pressure measurements using Fujifilm Prescale pressure films. Three film types were used to capture different pressure ranges for all torque levels as depicted in Table 6.1. The films were placed between the two contacting surfaces as the beams were fastened with two bolts up to the prescribed torque level. Following the preload, the beams were held together for 2 min before loosening the bolts and removing the pressure film. The experiment was repeated for all three torque levels and all beam sets.

6.4 Experimental Results

Three types of data were collected during the experiments: (1) joint pressure distributions, (2) frequency response functions (FRFs), and (3) time histories. The pressure film results were used to qualify the influence of the pre-stress on the joint interface due to the torque. The FRFs were used to determine the linear mode shapes and linear modal parameters, whereas the time histories were used to determine the nonlinear characteristics of the beam. For the subsequent discussion, beam sets B1-B2 and B5-B6 were mainly analyzed with respect to pressure distribution, torque level, and impact level.

6.4.1 Interface Characterization

The pressure film measurements of the three torque cases for different contact surface combinations are summarized below in Figs. 6.7, 6.8 and 6.9. The B1-B2 (convex-convex) case had a high concentration of pressure at the proximity of the through hole and showed small changes in pressure areas across the film due to the change in torque levels. As an intermediate between a spherical interface and a flat interface, the B1-B6 (convex-flat) case was similar to the previous case with a concentration of pressure near the hole, but with a larger contact area. In contrast, the B5-B6 (flat-flat) case showed a significant amount of pressure saturation with low to medium pressure readings across most of the film. This suggests that the B1-B2 (convex-convex) should have the smallest contact area, whereas B5-B6 (flat-flat) should have the largest. The pressure readings and contact area decreased for all contact surface combinations as the value of the preload torque was decreased on the joint. It is worth pointing out that the B5-B6 (flat-flat) showed the most dramatic reduction in pressure readings compared to the other cases.

To understand the correlation between the pressure readings across the joint and the structural response of the assembly, the change in the linear natural frequency with respect to varying torque levels was examined for the three contact surface combinations. Table 6.2 summarizes the linear natural frequency of the first six modes for the three contact surface combinations at varying torque levels.

Modes 2, 3, and 4 show similar linear natural frequency values for any torque level or contact surface combination, concluding that the stiffness of these modes is not affected by the joint. Since the ends of the beams deflect parallel to each other at the joints, the influence of the joint characteristics to the structural response of the assembly due to varying contact conditions is mitigated. However, Mode 2 is a possible exception to this rule, since bending in this shape induces a shear stress onto the bolted interfaces.

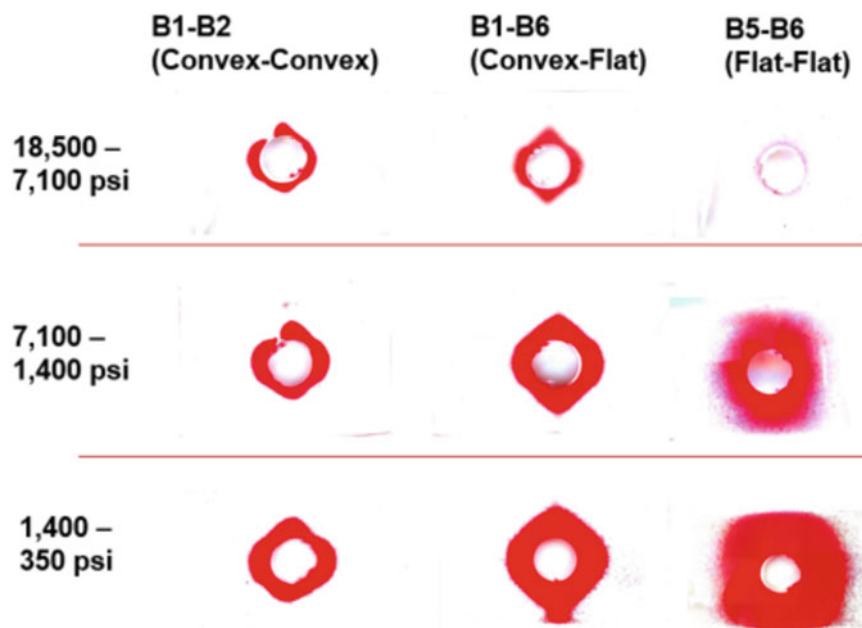


Fig. 6.7 Pressure film measurement at 25.1 N-m torque

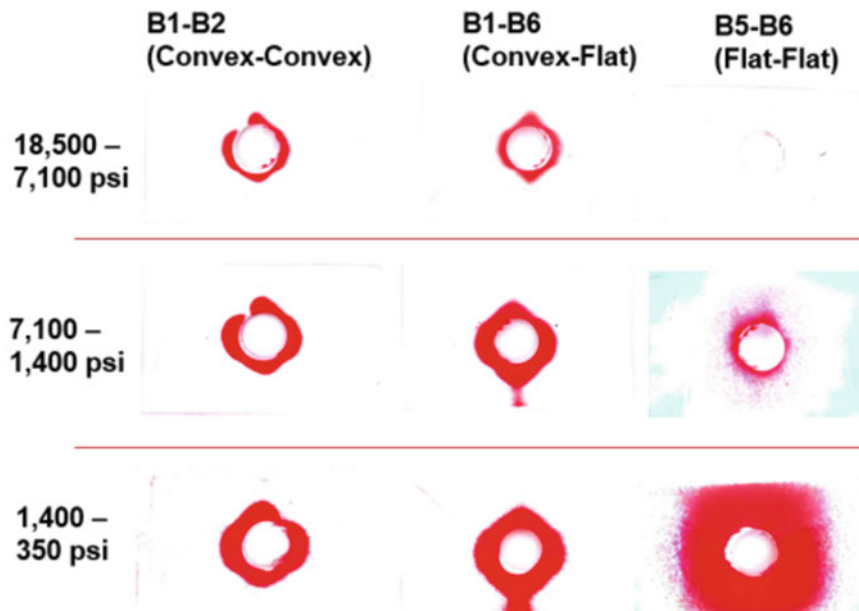


Fig. 6.8 Pressure film measurement at 16.9 N-m torque

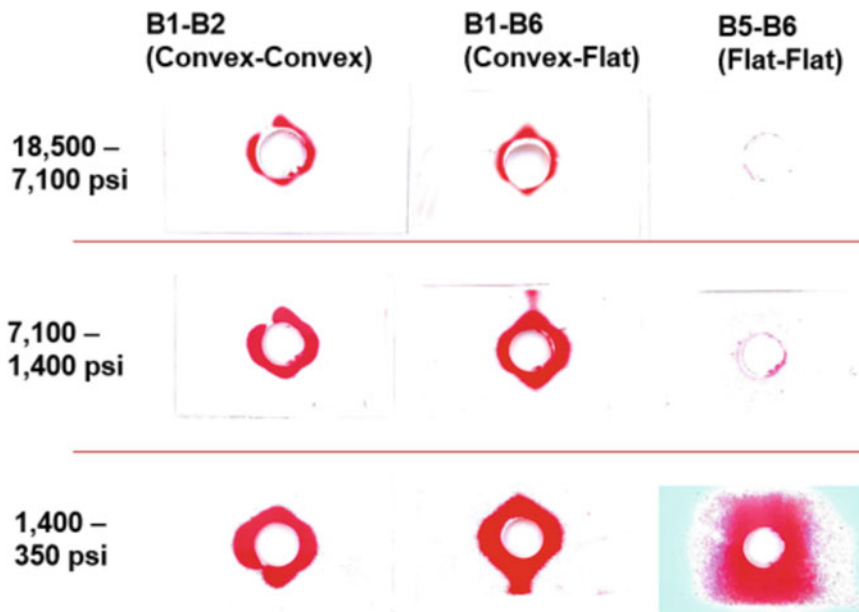


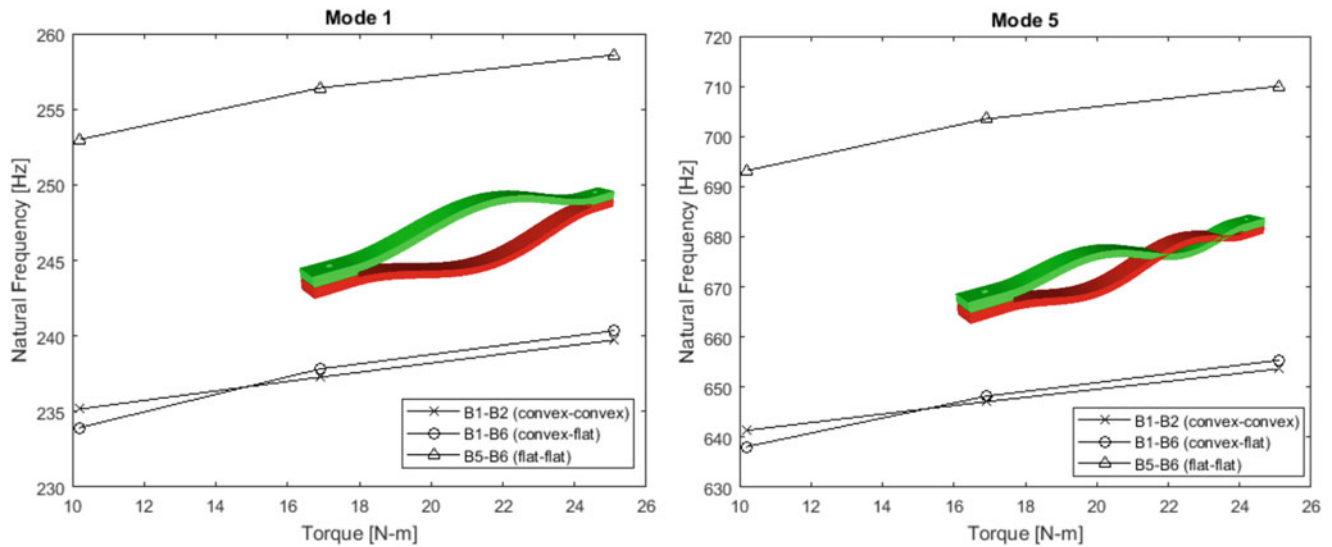
Fig. 6.9 Pressure film measurement at 10.2 N-m torque

In contrast, for the mode shapes with tensile loads or breathing of the joint, and with shearing of joints (Modes 1, 5, and 6), the structural response of the assembly demonstrated a strong correlation to the varying joint characteristics. Fig. 6.10 shows the plot of the natural frequencies of Modes 1 and 5 as the torque is varied. It seems reasonable that both of these modes show identical trends since they have tensile loads at the joints and exhibit joint breathing. In addition, for a constant torque level, Mode 6 for the flat – flat configuration (B5-B6) depicts a frequency shift of 150 Hz in comparison to B1-B2 as a result of the flat interface.

These observations follow the results of the pressure film measurements in Figs. 6.7, 6.8 and 6.9, where B5-B6 (flat-flat) case has a larger contact area at all torque levels compared to the other two cases. At 10.2 N-m torque, B1-B2 (convex-convex) case shows a similar contact area to the B1-B6 (convex- flat) case, but a higher pressure reading since the pressure is concentrated near the bolt, resulting in stiffer joint. As the torque is increased, the contact area of the B1-B6 (convex-flat) case exceeds the B1-B2 (convex-convex) case, and therefore a higher stiffness at these torque levels. It is also interesting to

Table 6.2 Linear natural frequencies (Hz) of the assembly vs bolt torque

Mode #	B1-B2 (convex-convex)			B1-B6 (convex-flat)			B5-B6 (flat-flat)			Mode description
	10.2 [N-m]	16.9 [N-m]	25.1 [N-m]	10.2 [N-m]	16.9 [N-m]	25.1 [N-m]	10.2 [N-m]	16.9 [N-m]	25.1 [N-m]	
1	235.2	237.3	239.7	233.9	237.8	240.3	253	256.4	258.6	1st out of phase bending – Z
2	327.8	328.5	329.1	326.4	327.3	327.8	330.3	331	331.8	1st in phase bending – Z
3	483.7	483.7	483.7	481.6	481.6	481.8	478.7	478.5	478.5	2nd in phase bending – Z
4	570.5	570.6	570.7	568.8	568.7	569.3	568	567.6	567.4	1st in phase bending – Y
5	641.4	647.1	653.6	638.1	648.2	655.4	693.2	703.5	710	2nd – Out of phase bending – Z
6	655.6	672.2	686.5	655	682.2	696.8	823.4	841.4	854.8	1st – Out of phase bending – Y

**Fig. 6.10** Linear natural frequency of modes 1 (left) and Mode 5 (right)

note that the natural frequency is measurably sensitive to the bolt torque even for B1-B2 and B1-B6, even though the contact pressure distributions shown previously suggested that the contact area changed very little for these structures.

Figure 6.11 shows the case of Mode 6, which involves rotational shearing at the joints. Mode 6 follows an almost identical trend to the previous comparison where the B5-B6 (flat-flat) case has a significantly higher natural frequency across the torque level compared to the other contact surface combinations and B1-B6 (convex-flat) has a higher natural frequency at 16.9 N-m and 25.1 N-m torque levels.

To evaluate the repeatability and accuracy of the linear analysis, the most linear case where the structure is assembled with the largest torque (25.1 Nm) and impacted at the lowest excitation level is examined. A larger torque should produce less slipping along the contact interface, therefore less friction and nonlinearity. The linear resonance frequencies for the two extreme configurations (convex–convex, flat–flat), are depicted below in Table 6.3 with the percent variation from the average value for the natural frequency. The variation in frequency was computed through multiple measurements to ensure that the beam had repeatable results within a single test setup.

Though the repeatability resulted in frequency disparities, all remained within 5% variance. Next, the Hilbert transform can be used on the decoupled modes to identify the nonlinearities in select modes.

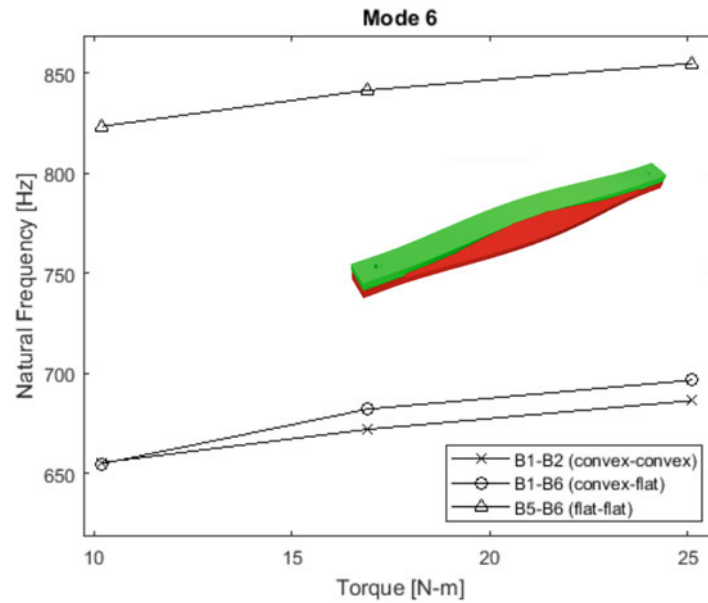


Fig. 6.11 Linear natural frequency of Mode 6

Table 6.3 Natural frequencies (Hz) and percent variation at a 25.1 Nm torque

Mode	B1-B2	B5-B6
1	239.1 (+1.92%)	258.0 (+1.98%)
2	328.6 (0.34%)	331.7 (+0.42%)
3	483.5 (−0.02%)	478.5 (−0.04%)
4	570.7 (+0.05%)	567.7 (−0.05%)
5	652.4 (+1.94%)	708.3 (+2.16%)
6	683.8 (+4.73%)	851.8 (+3.14%)

6.4.2 Nonlinearity Detection and Analysis

FRFs are used to qualitatively determine which modes exhibited nonlinearity. To do this, the FRFs were compared between each beam combination and between different torque levels and different force amplitudes. This comparison is only qualitative, since the amplitude-varying, and hence time varying modal properties are all convolved into a single FRF. In the following subsection, the time histories will be used to quantitatively identify the nonlinearities in those modes that exhibited significant nonlinearity. Within the first six linear elastic modes, three modes of interest were chosen based on the behavior of the joint as well as the degree of nonlinearity in response to a larger excitation. Figure 6.12 depicts the cumulative summation of all FRFs for the four levels of excitation at the middle torque level (16.9 Nm) for the B1-B2 (convex-convex) beam, and Fig. 6.13 shows the results for the B5-B6 (flat-flat) beam.

As evident by both beam configurations, mode six exhibits a large degree of damping nonlinearity as depicted by the widening of the peak and drop in amplitude. Therefore, it is a mode of interest to identify this damping nonlinearity using the Hilbert transform algorithm. To help explain why each mode does or does not exhibit significant nonlinearity, Table 6.4 describes the effect that each mode shape is expected to have on the joint.

The Hilbert transform analysis results for the fundamental mode of the system are presented in Appendix B. It exhibits the breathing of the joint which results in a weak stiffness nonlinearity, with no significant change in damping due to micro-slip. The results in Appendix B show erratic behavior of the damping, but it is important to note that the changes are small and are probably dominated by uncertainty in the Hilbert transform analysis.

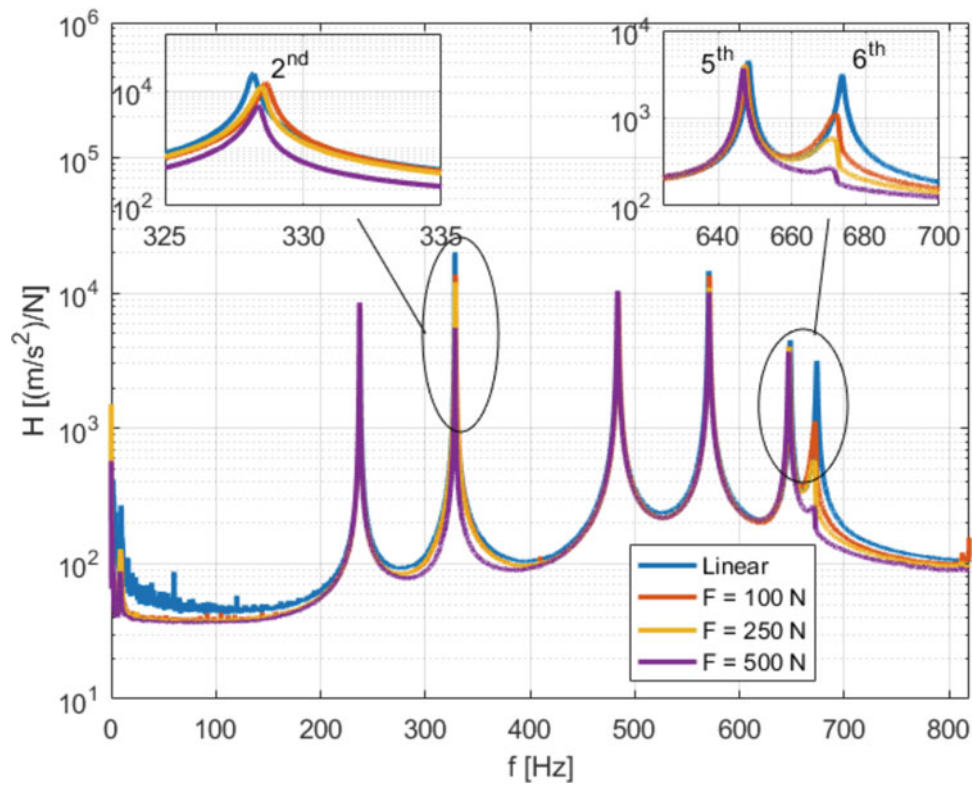


Fig. 6.12 Amplitude and force variation for B1-B2 for 16.9 Nm Torque

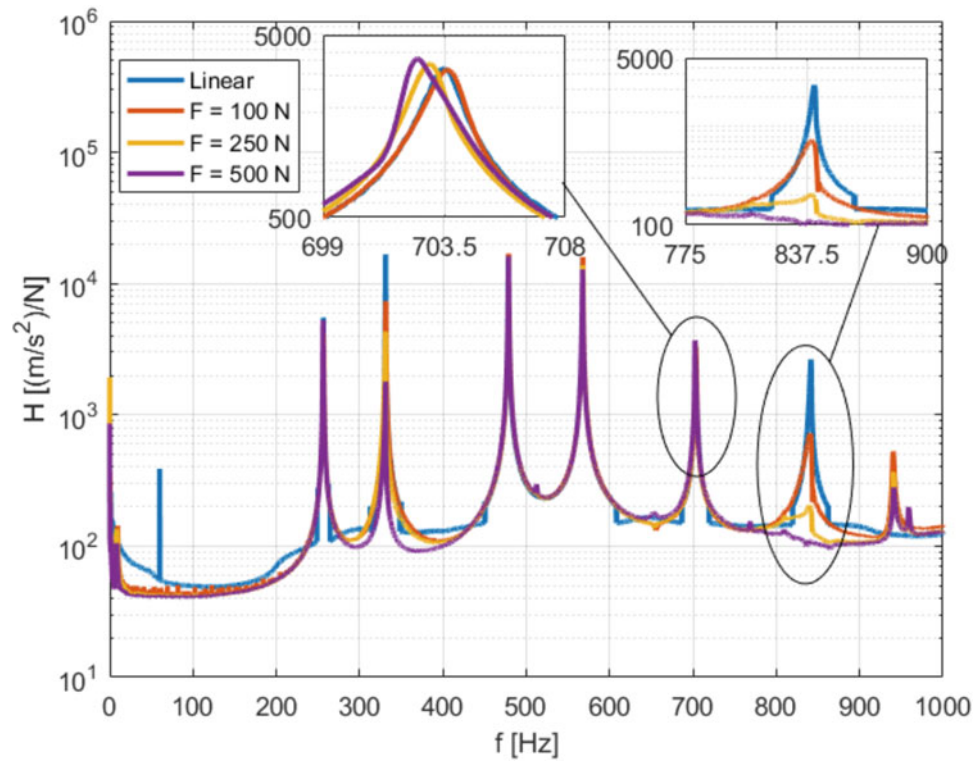
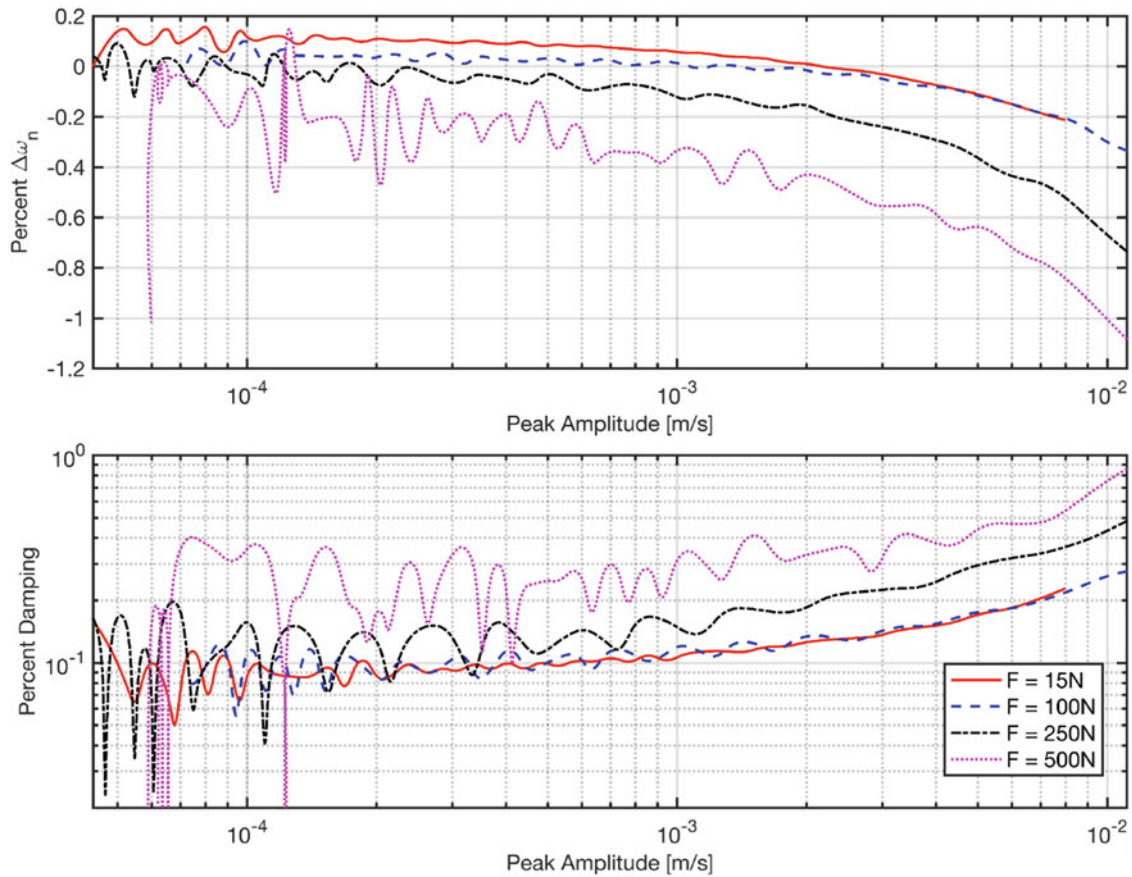


Fig. 6.13 Amplitude and force variation for B5-B6 for 16.9 Nm Torque

Table 6.4 Beam motion and joint behavior

Mode	Description	Joint Behavior
1	1 st out of phase bending - Z	Opening/closing of the joint
2	1 st in phase bending - Z	Shearing of the joint
3	2 nd in phase bending - Z	None
4	1 st in phase bending - Y	None
5	2 nd – out of phase bending - Z	Opening/closing of the joint
6	1 st – out of phase bending - Y	Rotational shearing of the joint

**Fig. 6.14** Natural frequency and damping versus amplitude for Mode 6 at 10.2 Nm torque for B1-B2 using B200Y as the drive point

Modes 2 and 6 are further analyzed in this section since both modes produce shearing at the joint and hence produce damping nonlinearity. Therefore, to evaluate the degree of nonlinearity of each mode with respect to the lowest torque, the Hilbert transform was used to find the damping and frequency variation as a function of peak velocity amplitude. The frequency variation is depicted as a percent change from the linear natural frequency. Prior to examining additional trends for torque, impact, and configuration of the beams, the results for mode six are depicted in detail in Figs. 6.14 and 6.15 for the two different configurations at the lowest torque. Given that multiple points can efficiently excite each mode, as detailed in Appendix A, these results are based on the analysis of the data at B200Y, the center of the beam. The horizontal axis in each of these plots is the peak amplitude, here defined as the amplitude at the point on the beam that has the largest motion for the mode of interest. In each response, the system is expected to behave linearly, although the measured signals become noisy at very low amplitudes leading to spurious oscillations in the measurements. At higher amplitudes the nonlinearity is evident.

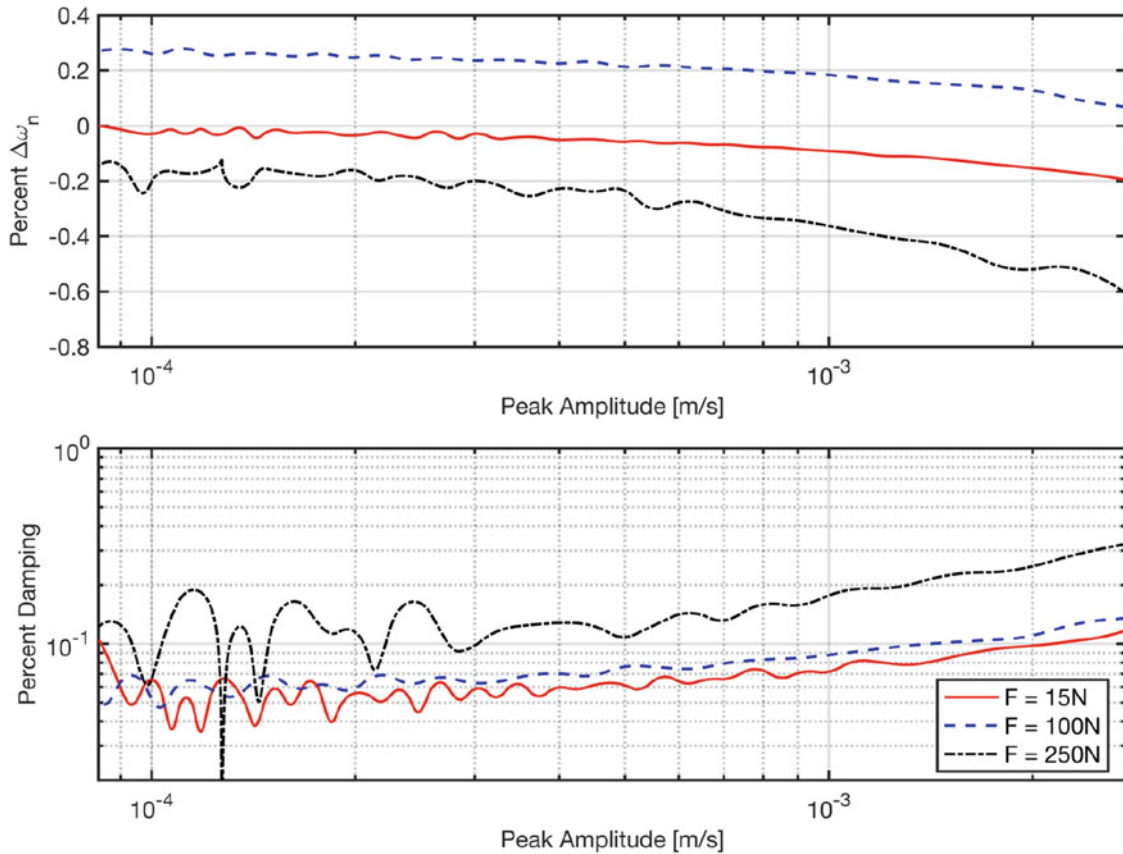


Fig. 6.15 Natural frequency and damping versus amplitude for Mode 6 at 10.2 Nm torque for B5-B6 using B200Y as the drive point

Table 6.5 Drive point used for each mode

Mode	Drive point	Description
2	B100 – Z	Left end of beam
	B200 – Z	Center of beam
	B300 – Z	Right end of beam
6	B100 – Y	Left end of beam
	B200 – Y	Center of beam

The results show that B5-B6 did not always return to the same linear natural frequency when larger forces were applied. This suggests that some change has occurred at the interface due to the vibration, and potentially calls the measurements into question. This is surprising because the joints were “broken in” prior to the tests by tapping the beam many times with a rubber mallet. No result is shown for mode six at an impulse of 500 N for B5-B6. This is because the mode became so heavily damped that Hilbert transform analysis was no longer possible. The smoothness of the damping versus amplitude curves at low force levels suggests that the nonlinearity is weak and the joints are in a state of micro-slip. However, at greater excitation levels the modal behavior does not follow the same trend, suggesting either that macro-slip has occurred or that this mode has become coupled to other modes in the structure. The remainder of the analysis presented below shows only those cases that seem to be dominated by micro-slip, because only those cases have the weak modal coupling necessary for the Hilbert transform analysis to be valid.

The following four figures examine modes two and six for both configurations of beams at various drive points. A single drive point is capable of exciting multiple modes, which can then induce additional modal coupling. However, the results in [5] suggest that the curve with the lowest damping should be a good estimate for the damping due to that mode alone. Table 6.5 gives the drive points used for each mode in this analysis (Figs. 6.16, 6.17, 6.18 and 6.19).

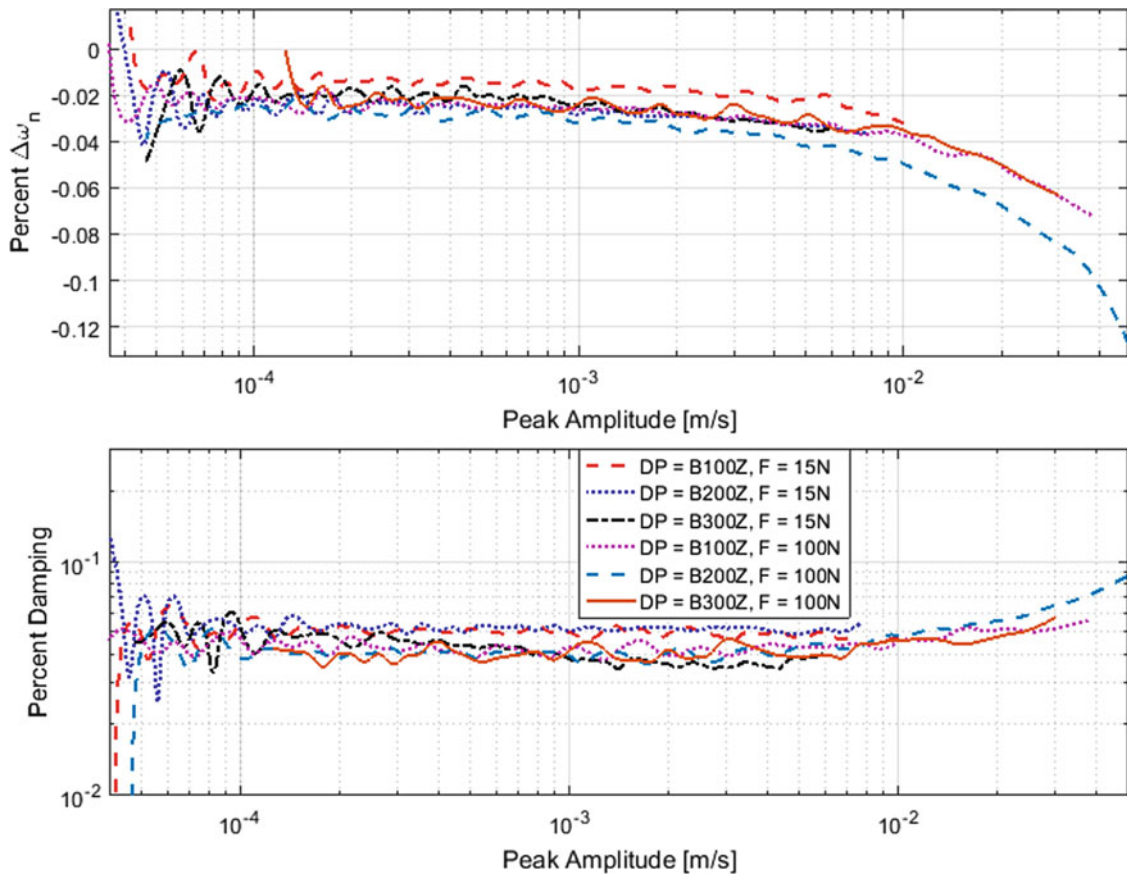


Fig. 6.16 Natural Frequency and damping versus amplitude for Mode 2 at 10.2 Nm torque for B1-B2

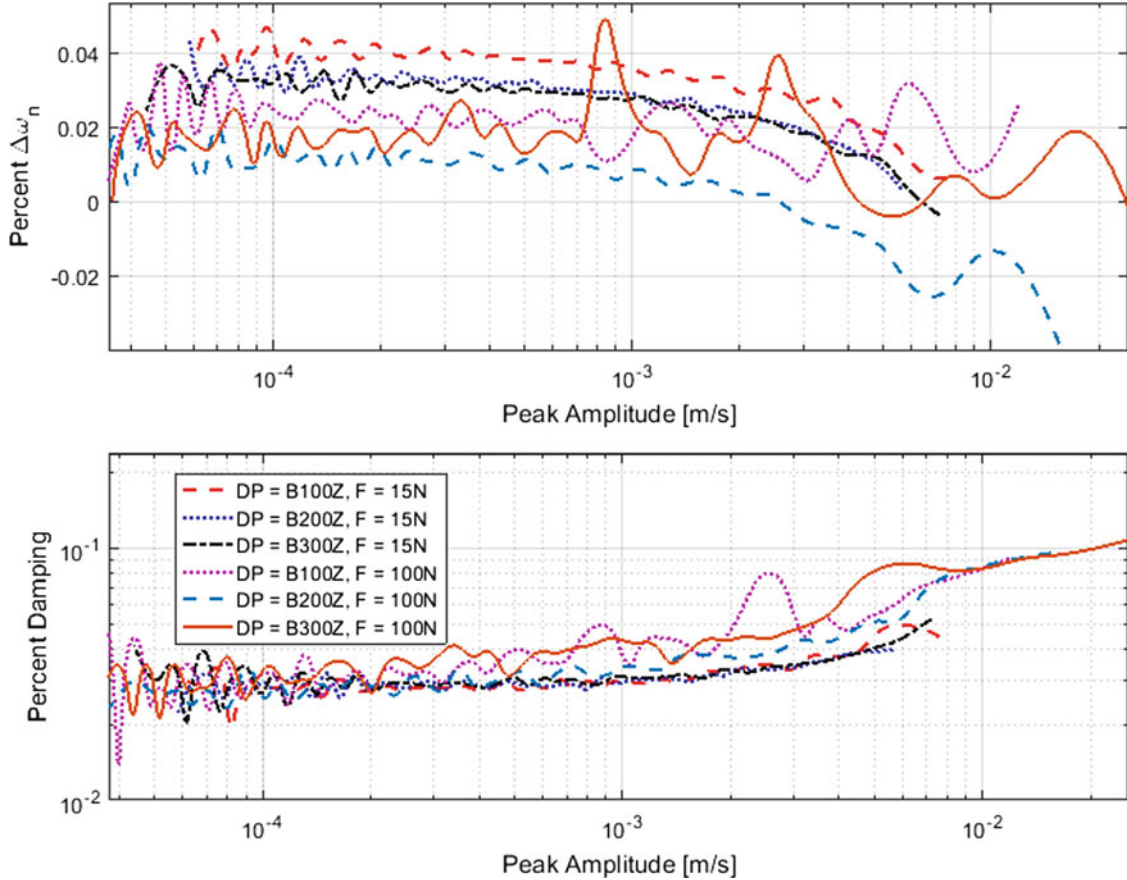


Fig. 6.17 Nat. Freq. and Damping versus amplitude for Mode 2 at 10.2 Nm torque for B5-B6

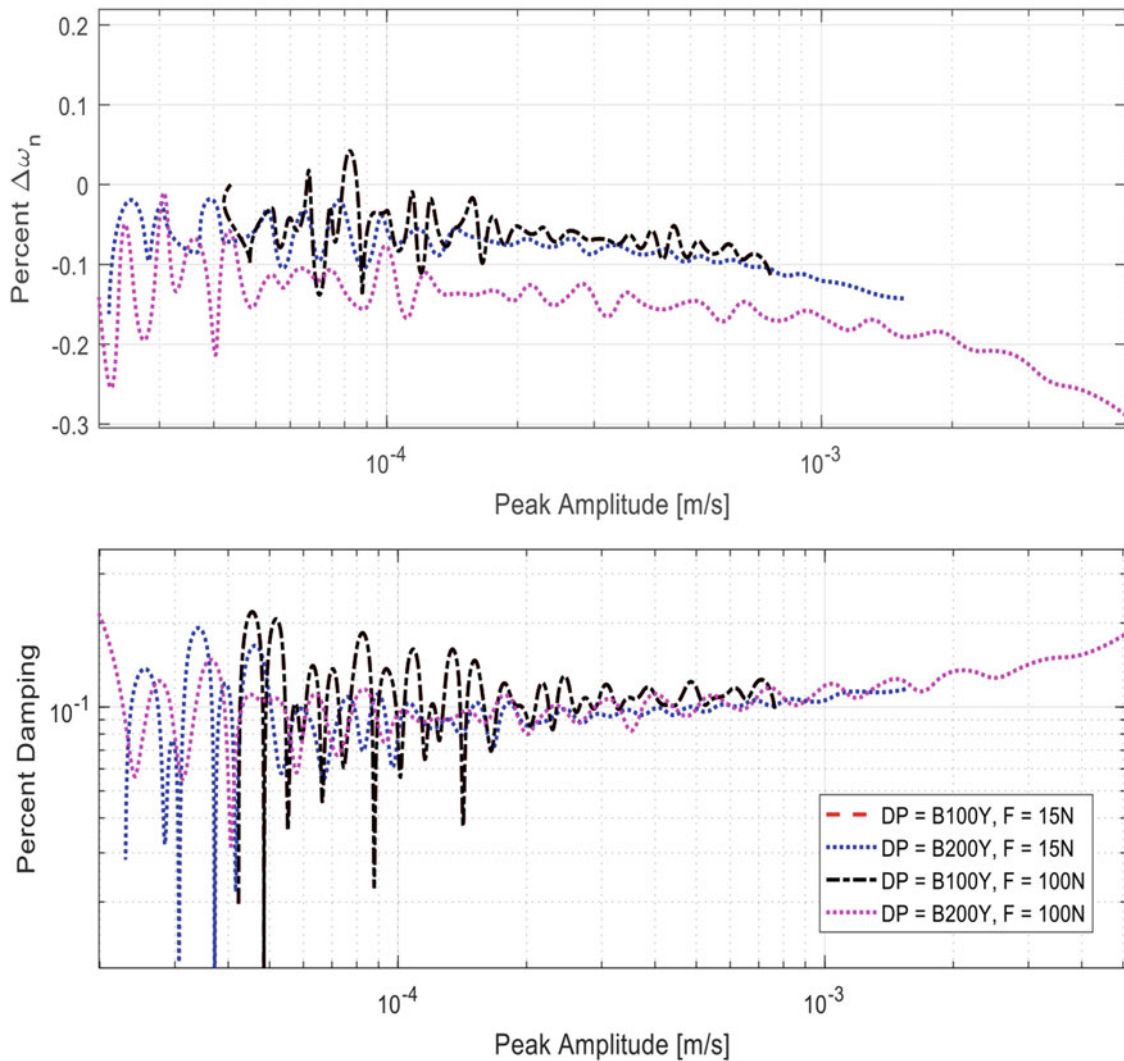


Fig. 6.18 Nat. Freq. and Damping versus amplitude for Mode 6 at 10.2 Nm torque for B1-B2

Neglecting the scatter in the data at low amplitudes, the different drive points produced relatively similar trends. For modeling purposes, the results of the center drive point, B200-Z and B200-Y should be used for both modes for both configurations. The other drive points either do not excite the beam well or introduce additional modal coupling. To understand the percent variation of the damping and frequency, Table 6.6 depicts the maximum deviation for the two modes of interest.

In both cases for mode six, the percent damping of the mode increased extensively, depicting a large damping nonlinearity for the mode with much smaller stiffness nonlinearity. In addition, the force varying Hilbert transform curves for mode six for the largest torque (25.1 Nm) are also shown below (Figs. 6.20 and 6.21).

Even at the largest torque with the stiffest joint, mode six exhibits large stiffness and damping nonlinearities. At 500 N, mode six seems to exhibit macro-slip as seen by the erratic deviating trend from the other impulse levels, and so that data should be used appropriately.

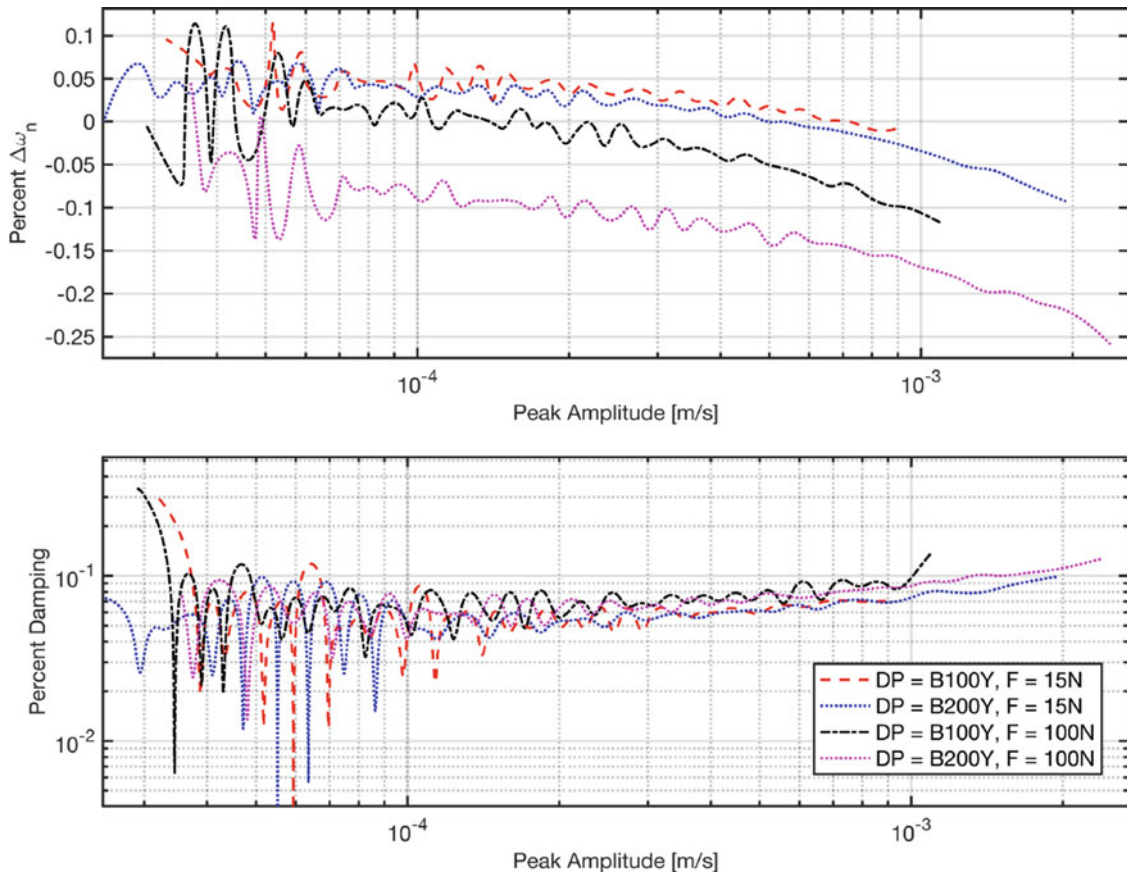


Fig. 6.19 Nat. Freq. and Damping versus amplitude for Mode 6 at 10.2 Nm torque for B5-B6

Table 6.6 Maximum deviation as a function of amplitude for 10.2 Nm torque

Beam	Mode	Max frequency change	Max damping change	Type of nonlinearity
B1-B2	2	-0.14%	148%	Damping NL
	6	-0.33%	582%	Damping NL
B5-B6	2	-0.08%	95%	Damping NL
	6	-0.26%	316%	Damping NL

Note that the shift for B5-B6 is in response to a 250 N excitation, rather than a 500 N excitation as with B1-B2, given that the mode was not able to be modally filtered due to the significant nonlinearity

In an effort to classify the linearity of the four configurations, the variance of frequency and damping for each beam set was analyzed at an intermediate force (100 N) and both the lowest and highest torque to lightly excite the nonlinearity. Fig. 4.16 depicts the results of this comparison (Figs. 6.22 and 6.23).

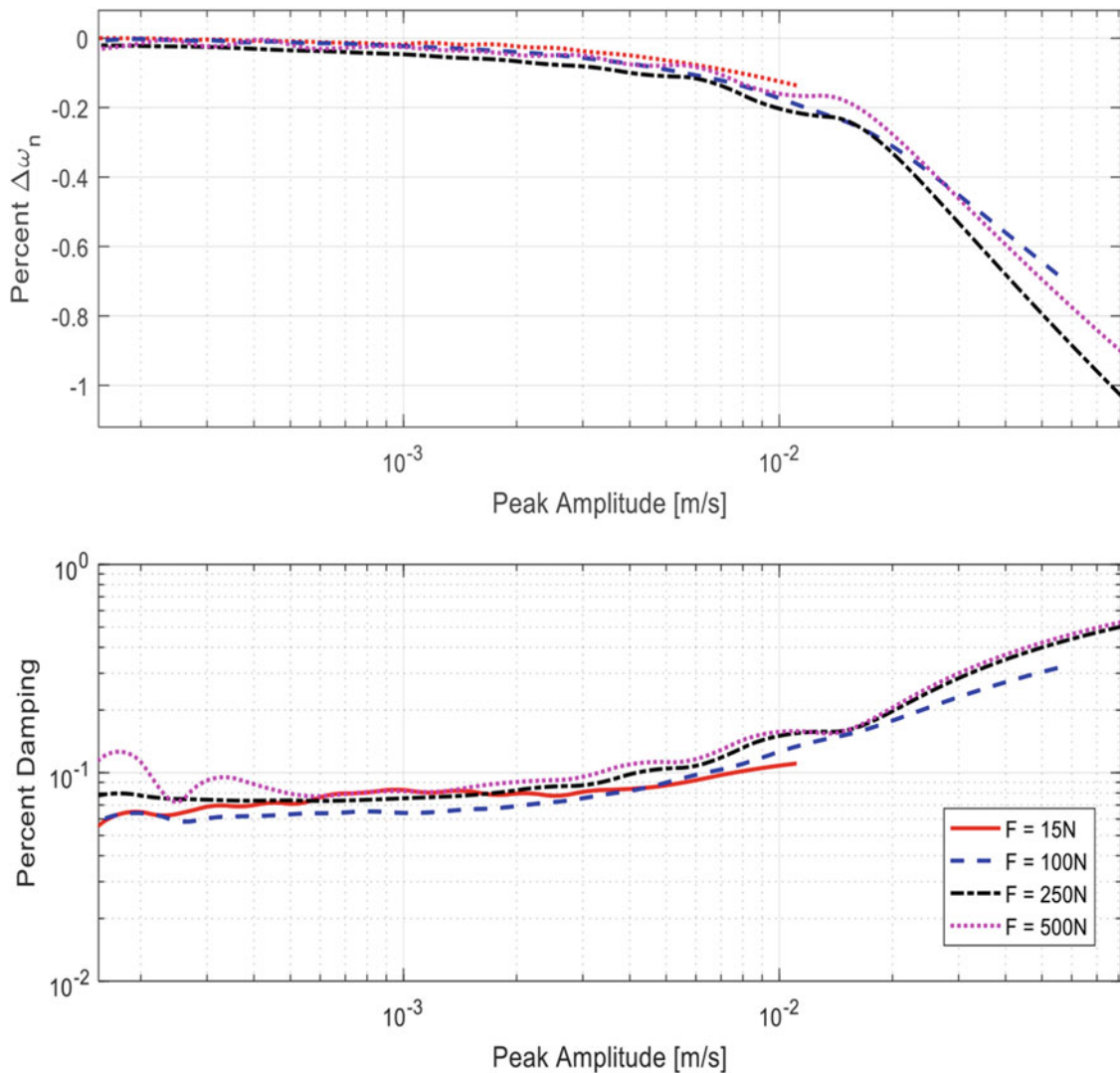


Fig. 6.20 Nat. freq. and damping versus amplitude for Mode 6 at 25.1 Nm torque for B1-B2

Between the four beam sets, the convex beam set and the convex – flat set are classified in the same “family” due to similar modal frequencies, whereas the other two sets are in the same “family” of beams. The washer configuration and flat–flat configuration had similar resonant frequencies, whereas the convex–flat and convex beams had similar resonances. In terms of damping for the lowest torque, the beams can be classified from relatively linear to significantly nonlinear based on the damping variance as given: (1) convex–convex with washer (B1-B2W), (2) convex–convex (B1-B2), (3) convex–flat (B1-B6), and (4) flat–flat (B5-B6). However, at the higher torque, the beams show variable trends with respect damping, yielding it difficult to classify the beams. Even though the slip is restricted at the higher torque, the pressure in the contact surface increases, requiring the same energy dissipation as with lower torque; therefore, additional torque does little to impact the nonlinearity in the joint.

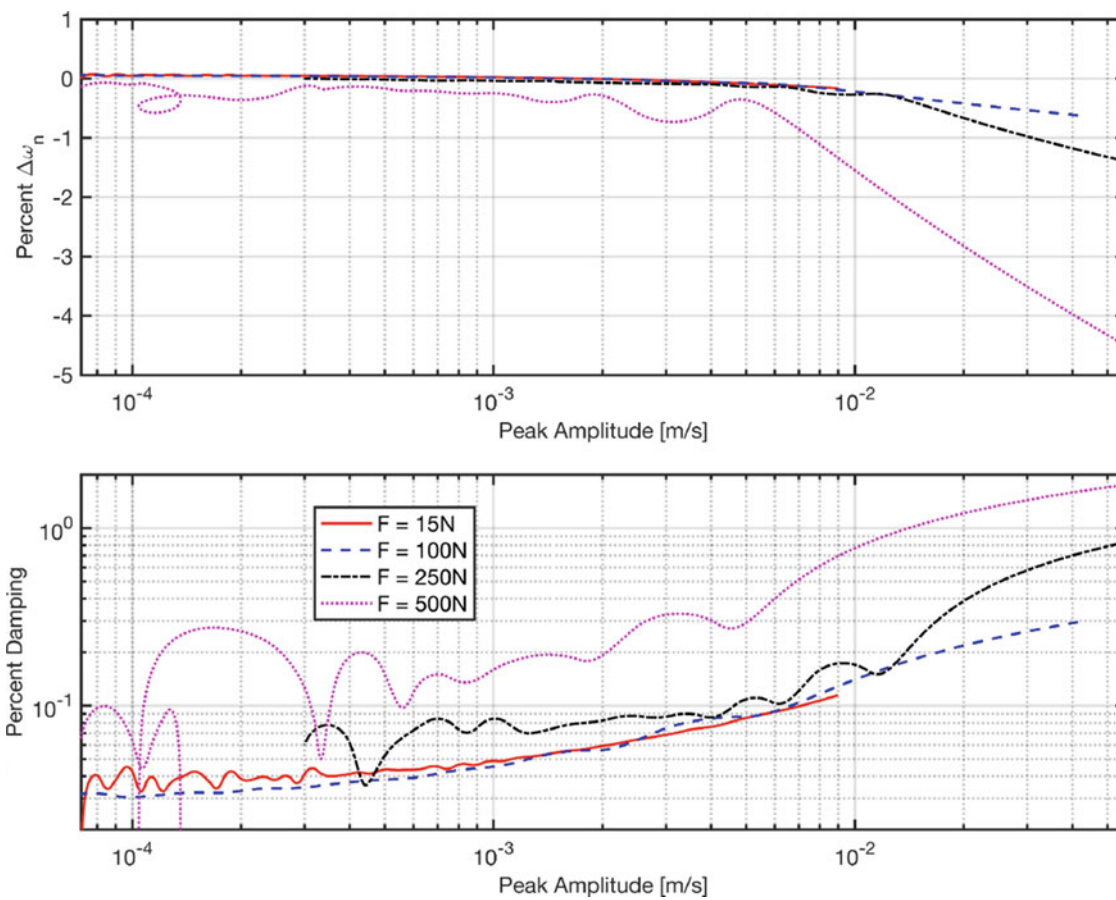


Fig. 6.21 Nat. freq. and damping versus amplitude for Mode 6 at 25.1 Nm torque for B5-B6

6.5 Conclusion

This work sought to characterize a new benchmark structure and to provide a rich data set against which simulations may be compared when seeking to predict damping nonlinearities. The S4 beam, consisting of two C beams bolted together at the ends, was tested and the first six elastic modes, all below 800 Hz were characterized both linearly and nonlinearly. The pressure distributions were characterized and qualitatively correlated to variations in the linear natural frequencies and in the nonlinearity observed. As in other studies, those modes that exhibited shearing of the joint yielded as the strongest nonlinearity with respect to damping. In general, none of the modes showed large stiffness nonlinearities even though the damping of some modes changed by a factor of five or more.

Between the four configurations of beams, the beams that had flat interfaces depicted the largest damping nonlinearity with a 316% increase in damping for the second largest impact excitation level, the highest that could be reliably characterized. On the other hand, the curved beams with a washer depicted the least damping nonlinearity.

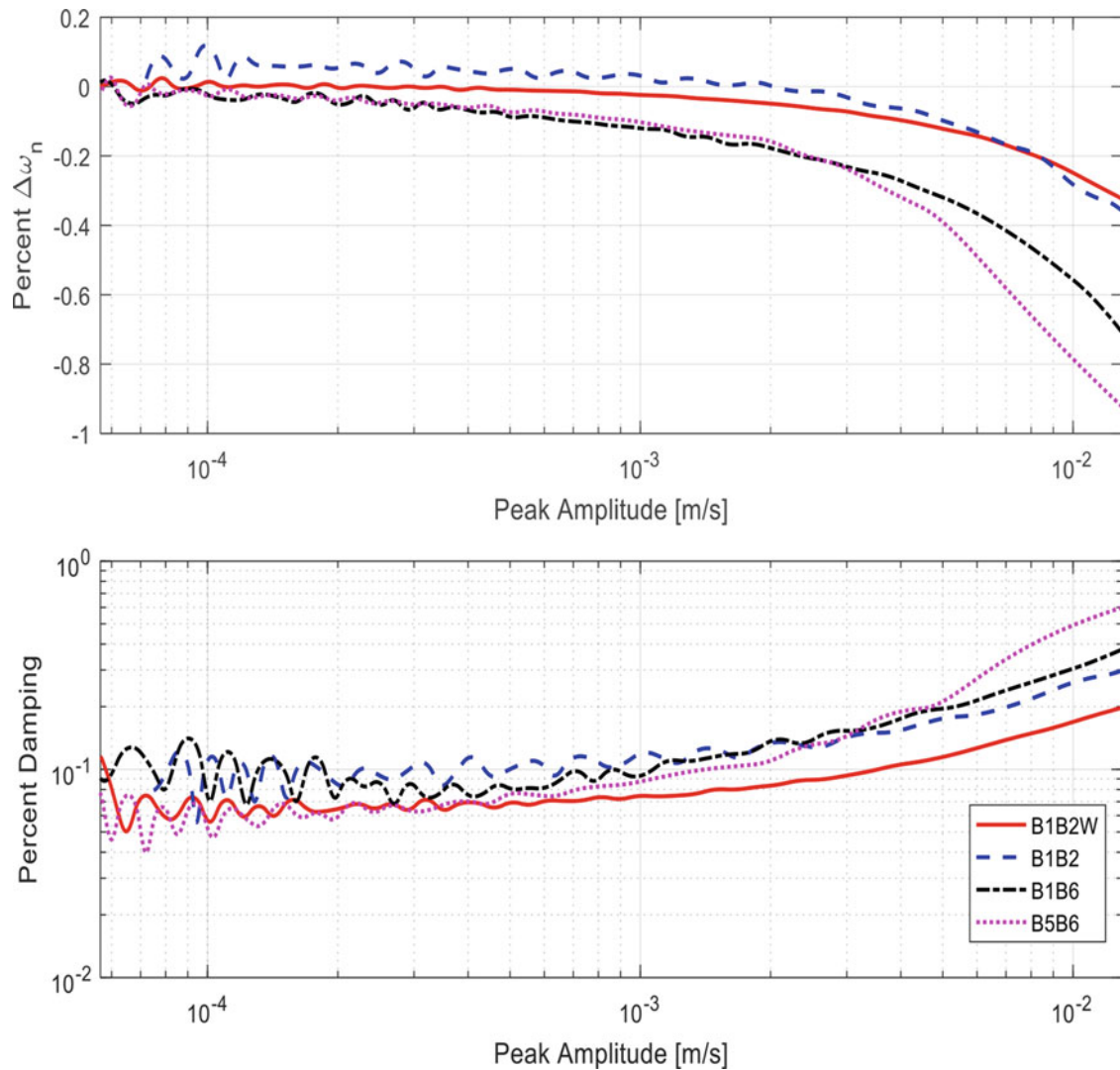


Fig. 6.22 Comparison of frequency and damping across the different beam combinations for an intermediate force level and the lowest torque

Although the testing was judged successful, throughout the process of nonlinear model identification, some lessons were learned that could improve the results in future testing. Most importantly, the sample rate chosen was barely adequate, and while the LMS system was not able to take longer time records in FFT mode, throughput mode should have been used so that the modal hammer impacts could be captured more accurately and then it might have been possible to use alternate identification methods such as the Restoring Force Surface Method as an additional method to characterize the joint [7]. Furthermore, a shaker or automatic hammer could provide additional accuracy when compared to a modal hammer. Lastly, it was sometimes noted that if the modal filtered response was not a SDOF system with a single mode, the results of the Hilbert transform for frequency and damping were erratic, impeding the proper fit of the data. Perhaps the modal filter used for this system could have been improved by testing at even lower levels than was used here (i.e. perhaps using higher sensitivity sensors) to extract the mode shapes more accurately.

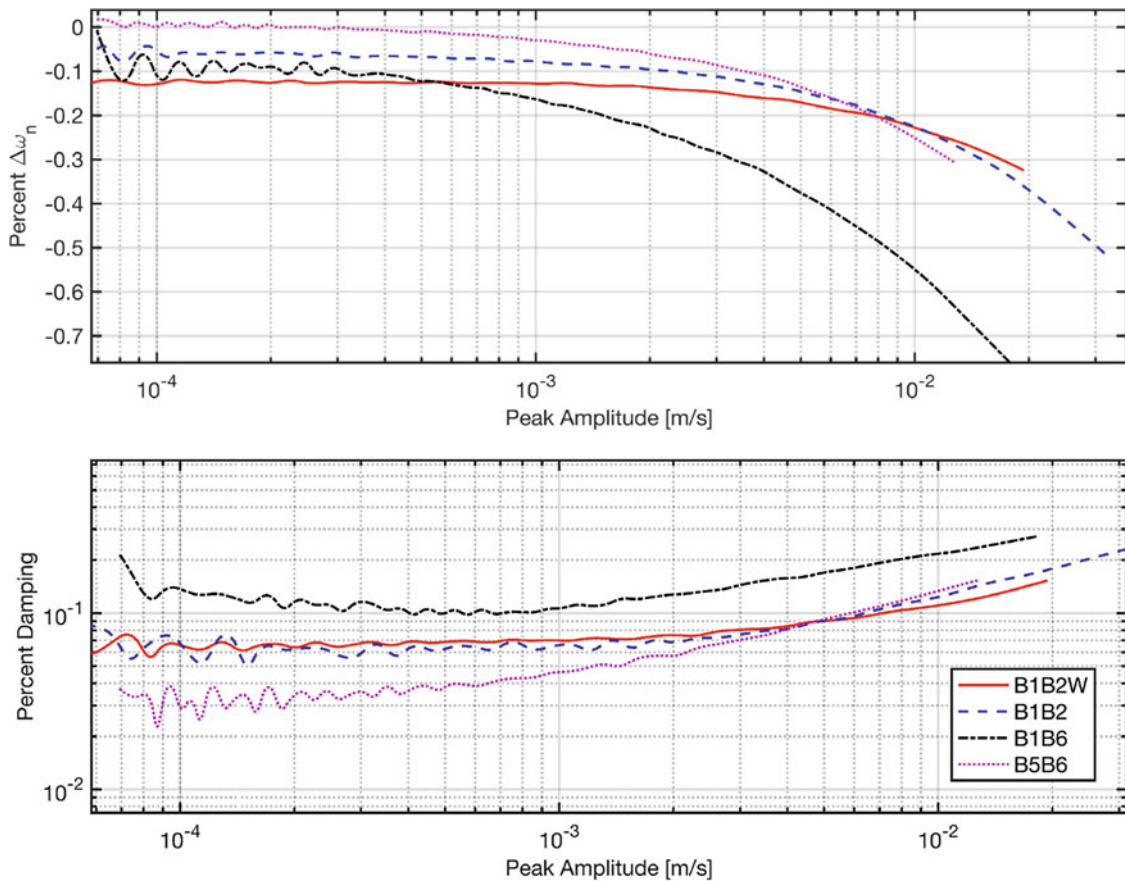


Fig. 6.23 Comparison of frequency and damping across the different beam combinations for an intermediate force level and the highest torque

In any event, this beam provides a significant data set that can now be used to validate numerical predictions of damping. Given that the beam exhibits modes with all degrees of damping nonlinearities, the beam should provide a good test case for numerical methods.

Acknowledgements This research was conducted at the 2017 Nonlinear Mechanics and Dynamics (NOMAD) Research Institute supported by Sandia National Laboratories. Sandia National Laboratories is a multi-mission laboratory managed and operated by National Technology and Engineering Solutions of Sandia, LLC., a wholly owned subsidiary of Honeywell International, Inc., for the U.S. Department of Energy's National Nuclear Security Administration under contract DE-NA-0003525.

Appendix A

Test Setup

For modal data acquisition, two beams were bolted together and a set of points was identified along the two beams, naming B the beam with the bolt and N the beam with the nut. Points were numbered from 100 to 300, 100 as the extremity close to the origin and 300 the other end of the beams. A point every 25 units is defined, for both beams. Table 6.7 reports the coordinate of each point.

Optimal Input Location

To define the location of each accelerometer and to select the input point, Table 6.8 was constructed using the amplitude of the linear mode shapes as a basis from the roving hammer test, with the modes of interest highlighted. It reports the amplitude of motion of each mode at each of the point, using a 0–3 scale with 0 not affecting the mode, and 3 having the largest effect.

The table allowed to easily identify, from a qualitative point of view, modal nodes and to define inputs and outputs suitable to excite and collect information about all the first 6 modes (additional modes 7 to 10 reported).

Table 6.7 Testing points names and locations

Name	x [m]	y [m]	z [m]	Name	x [m]	y [m]	z [m]
B100	0.0125	0.0000	0.0111	N100	0.0125	0.0000	−0.0111
B125	0.0635	0.0000	0.0111	N125	0.0635	0.0000	−0.0111
B150	0.1270	0.0000	0.0111	N150	0.1270	0.0000	−0.0111
B175	0.1905	0.0000	0.0111	N175	0.1905	0.0000	−0.0111
B200	0.2540	0.0000	0.0111	N200	0.2540	0.0000	−0.0111
B225	0.3175	0.0000	0.0111	N225	0.3175	0.0000	−0.0111
B250	0.3810	0.0000	0.0111	N250	0.3810	0.0000	−0.0111
B275	0.4445	0.0000	0.0111	N275	0.4445	0.0000	−0.0111
B300	0.4955	0.0000	0.0111	N300	0.4955	0.0000	−0.0111

Table 6.8 Points amplitude scale for each mode

Mode	B100	N100	B125	N125	B150	N150	B175	N175	B200
1	0	0	0	0	1	1	2	2	3
2	3	3	2	2	0	0	2	2	3
3	3	3	0	0	3	3	3	3	0
4	3	3	1	1	0	0	2	2	3
5	0	0	1	1	3	3	3	3	0
6	1	1	0	0	1	1	2	2	3
7	1	1	2	2	3	3	2	2	0
8	0	0	2	2	3	3	0	0	3
9	2	2	0	0	0	3	0	0	3
10	3	3	3	3	0	0	3	3	0
Mode	N200	B225	N225	B250	N250	B275	N275	B300	N300
1	3	2	2	1	1	0	0	0	0
2	3	2	2	0	0	2	2	3	3
3	0	3	3	3	3	0	0	3	3
4	3	2	2	0	0	1	1	3	3
5	0	3	3	3	3	1	1	0	0
6	3	2	2	1	1	0	0	1	1
7	0	2	2	3	3	2	2	1	1
8	3	0	0	3	3	2	2	0	0
9	3	0	0	3	3	0	0	2	2
10	0	3	3	0	0	3	3	3	3

Appendix B

Mode 1 Results

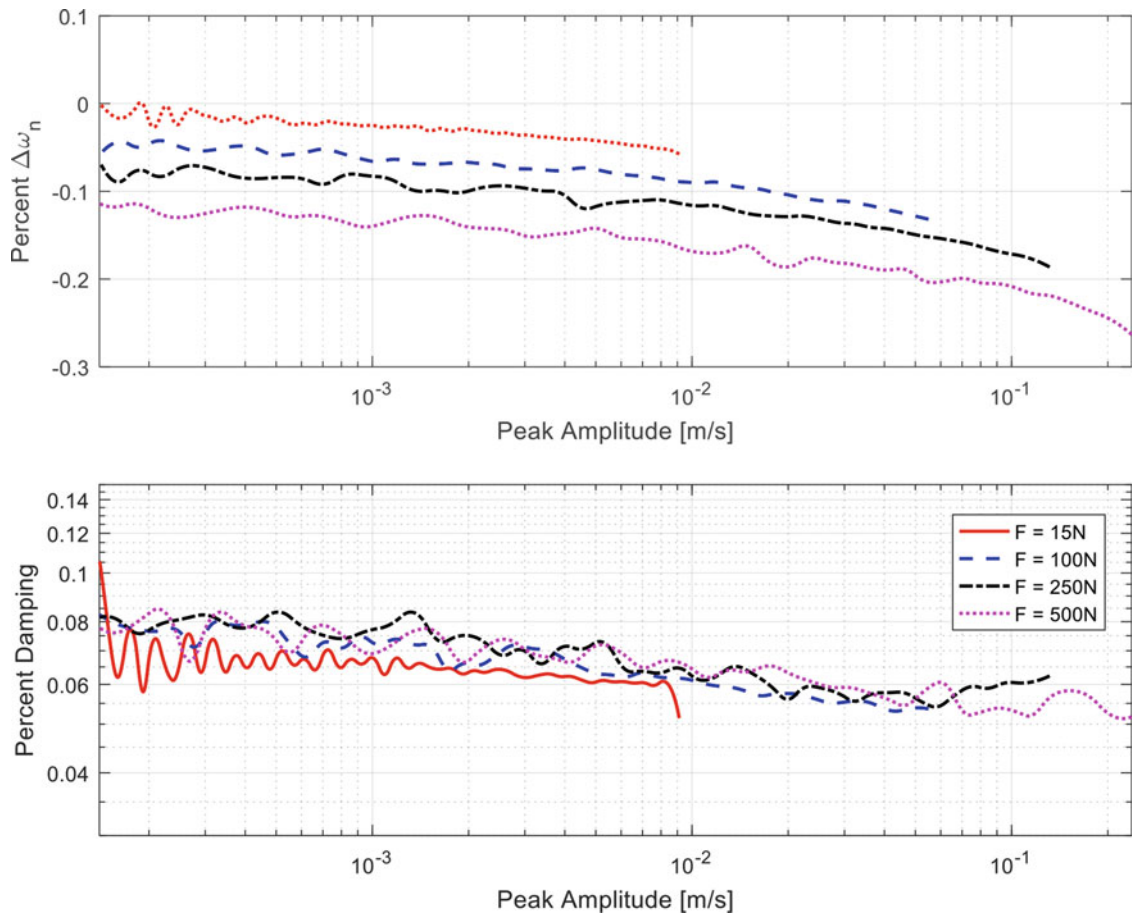


Fig. 6.24 Mode 1 at 10.2 Nm torque for B1-B2

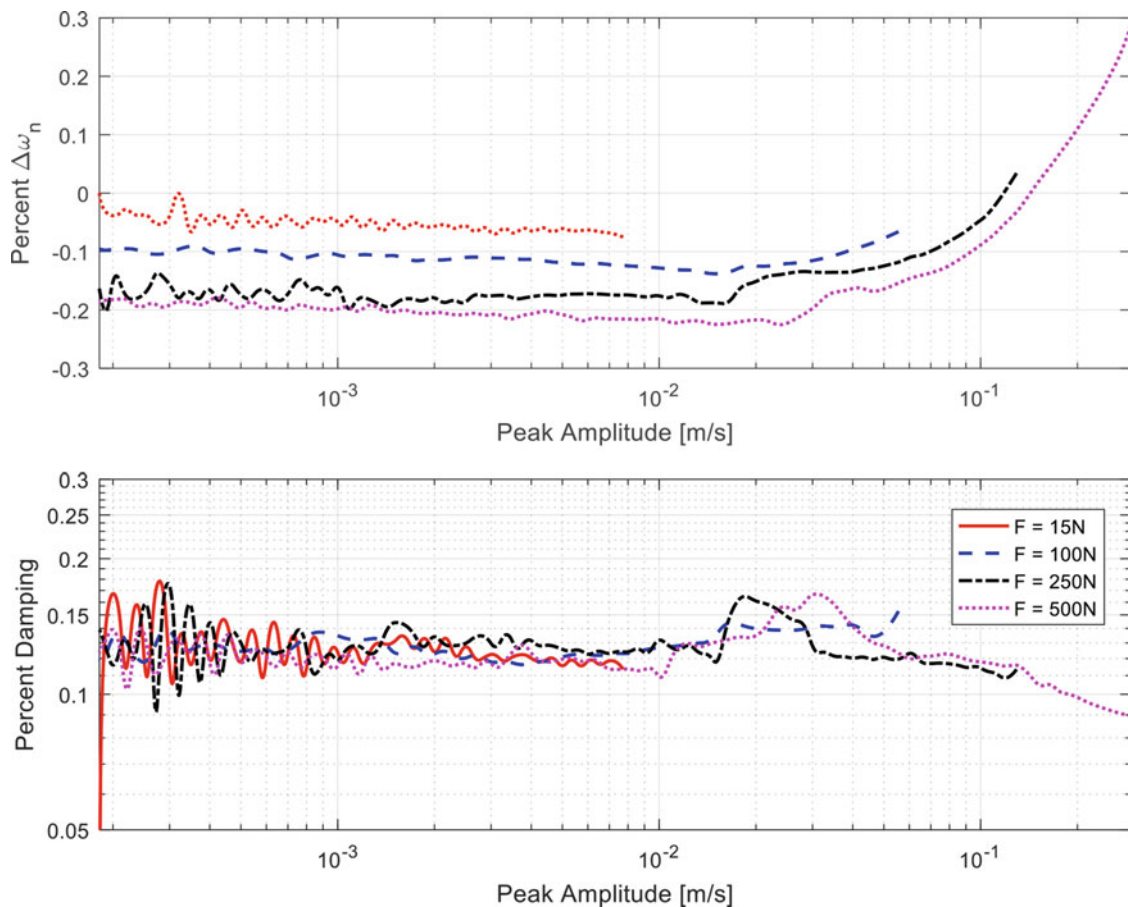


Fig. 6.25 Mode 1 at 10.2 Nm torque for B5-B6

References

1. Roettgen, D.R., Allen, M.S.: Nonlinear characterization of a bolted, industrial structure using a modal framework. *Mech. Syst. Signal Process* (2016)
2. Deaner, B.J., Allen, M.S., Starr, M.J., Segalman, D.J., Sumali, H.: Application of viscous and iwan modal damping models to experimental measurements from bolted structures. *ASME J Vib Acoust.* **137**, 12 (2015)
3. Allen, M.S., Lacayo, R., Brake, M.R.W.: Quasi-static Modal Analysis based on Implicit Condensation for Structures with Nonlinear Joints. In ISMA. Leuven, Belgium (2016)
4. Festjens, H., Chevallier, G., Dion, J.-L.: A numerical tool for the design of assembled structures under dynamic loads. *Int J Mech Sci.* **75**, 170–177 (2013)
5. Bonney, M.S., Robertson, B.A., Schempp, F., Mignolet, M., Brake, M.R.: Experimental Determination of Frictional Interface Models. In *Dynamics of Coupled Structures – Proceedings of the 34th IMAC*, New York, (2016)
6. Dossogne, T.: Experimental Assessment of the Influence of Interface Geometries on Structural Dynamic Response In: Allen M., Mayes R., Rixen D. (eds) *Dynamics of Coupled Structures*, in *Conference Proceedings of the Society for Experimental Mechanics Series* (2017)
7. Kerschen, G., Worden, K., Vakakis, A.F., Govindal, J.-C.: Past, present and future of nonlinear system identification in structural dynamics. *Mech. Syst. Signal Process.* **20**, 505–592 (2006)
8. Lacayo, R.M., Deaner, B.J., Allen, M.S.: A numerical study on the limitations of modal Iwan models for impulsive excitations. *J Sound Vib.* **390**, 118–140 (2017)
9. Feldman, M.: Non-linear system vibration analysis using Hilbert transform–I. Free vibration analysis method ‘Freevib’. *Mech. Syst. Signal Process.* **8**(2), 119–128 (1994)



Chapter 7

Nonlinear System Identification for Joints Including Modal Interactions

Alexander H. Haslam, Gaurav Chauda, Nalik Kenia, Esther S. Rufat-Meix, Matthew S. Allen, Robert M. Lacayo, Malte Krack, and Matthew R. W. Brake

Abstract Even with the best available simulation tools, it is still not possible to predict the effective stiffness and damping of bolted interfaces. Hence, it is currently necessary to identify models for these non-linear structures experimentally. One approach is to assume that the modes are decoupled and to fit a non-linear model to match the response for each mode in isolation. This modal approach has found to be suitable for systems with very weak non-linearities. However, it has been observed that in many assembled structures, the multiple modes of jointed structures can interact non-linearly and become coupled. This work focuses on the micro-slip regime where the coupling is weak, and investigates ways to extend existing approaches to this more general case. Two methods are proposed: (i) generating multi-modal maps of instantaneous natural frequency and damping as a function of the modal amplitudes; (ii) fitting polynomial models including coupling terms between the modes using the Restoring Force Surface Method. The proposed techniques were tested against data from a simulated 2DOF non-linear system representative of a simple jointed structure with a discrete non-linearity. This analysis was then extended to the particular case of a 3DOF system where only 2 modes are coupled by a non-linearity. It was found that both approaches were able to capture the modal coupling to a suitable accuracy for smooth non-linearities, although the modal-map approach generally performed slightly better than the Restoring Force Surface Method. However, both approaches had considerably higher errors when the non-linearity was discontinuous. This work suggests that both approaches warrant further investigation.

Keywords Non-linear dynamics · Jointed structures · Modal coupling · Restoring force · Backbone curve

Nomenclature

χ, β	Parameters of Segalman's Iwan element
ϵ_m	Error metric
Φ	Modal transformation matrix
\mathbf{c}	Vector of polynomial coefficients to fit the restoring force
\mathbf{f}_e	Excitation force

A. H. Haslam (✉)
Imperial College London, London, UK
e-mail: a.haslam16@imperial.ac.uk; ahh316@ic.ac.uk

G. Chauda
Michigan State University, East Lansing, MI, USA

N. Kenia
Arizona State University, Tempe, AZ, USA

E. S. Rufat-Meix
ISAE-SUPAERO, Toulouse, France

M. S. Allen
Department of Engineering Physics, University of Wisconsin-Madison, Madison, WI, USA

R. M. Lacayo · M. Krack
Universität Stuttgart, Stuttgart, Germany

M. R. W. Brake
William Marsh Rice University, Houston, TX, USA

M, C, K	Mass, damping and stiffness matrices
P	Vector of polynomial terms to fit the restoring force
U	Vector of restoring forces
$\omega_{d,j}$	Instantaneous damped natural frequency
$\omega_{n,0}$	Natural frequency of the underlying linear system
$\omega_{n,j}$	Instantaneous natural frequency
σ_j	Instantaneous decay constant
τ_j	Instantaneous phase
$\theta(t)$	Instantaneous phase from Hilbert transform
ζ_j	Instantaneous damping ratio
A_j	Instantaneous amplitude of dominant component
B_j	Instantaneous amplitude of cross-component
c	Damping coefficient of a viscous damper
$d(t)$	Log of instantaneous amplitude from Hilbert transform
F_j	Instantaneous amplitude of dominant component arising from non-linearities
F_S	Sliding force of Iwan element
G_j	Instantaneous amplitude of cross-component arising from non-linearities
k	Spring stiffness
K_T	Tangent stiffness of Iwan element
m	Mass
$Q(t)$	Analytic Hilbert transform signal
$q_j, \dot{q}_j, \ddot{q}_j$	Modal displacement, velocity, acceleration
$x_j, \dot{x}_j, \ddot{x}_j$	Physical displacement, velocity, acceleration
DOF	Degree of Freedom
EMA	Experimental Modal Analysis
HBM	Harmonic Balance Method
MDOF	Multiple Degree of Freedom
MMM	Multi-modal Maps
NNM	Non-linear Normal Modes
ODE	Ordinary Differential Equation
RFS	Restoring Force Surface
RMS	Root Mean Square
SDOF	Single Degree of Freedom

7.1 Introduction

Most structures are assembled from parts that are jointed by fasteners. In most applications of interest, the bolts are well tightened so the bolted surfaces do not slip completely, therefore they do not exhibit macro-slip. Instead, the joint remains intact but the surface at the edge of the contact slips introducing hysteresis into the system and greatly increasing the damping. This phenomenon is called micro-slip, and is thought to be the source of much of the damping in built up structures. This allows the modes of the linearised system to be modelled as independent SDOF systems as is shown in Fig. 7.1a. This helps to explain why modal analysis has been successful on aircraft, rockets and other structures where non-linearities are known to exist.

Some recent works have shown experimentally that the linearised modes of a structure with joints remain uncoupled, even when the non-linear effects of micro-slip start to become significant [1, 2]. This has allowed each mode to be modelled as a non-linear SDOF system, as depicted in Fig. 7.1b. These are often termed “modal” models [3]. This mitigates the need to use fully non-linear techniques to analyse such systems, and instead models can be identified for each mode using techniques such as the Restoring Force Surface Method [4]. Another approach is to use the FREEVIB method [5] which attempts to express the modal properties as a function of amplitude to create a “backbone” curve. These approaches were recently applied to a simple bolted structure, and their relative merits were compared [6].

Unfortunately, several structures have been shown to exhibit some degree of modal coupling at higher amplitudes. Much effort has been put into investigating the highly non-linear behaviour in the macro-slip regime, and it has been shown that this leads to coupling between the linearised modes [7, 8]. Modelling such behaviour would require a fully non-linear treatment

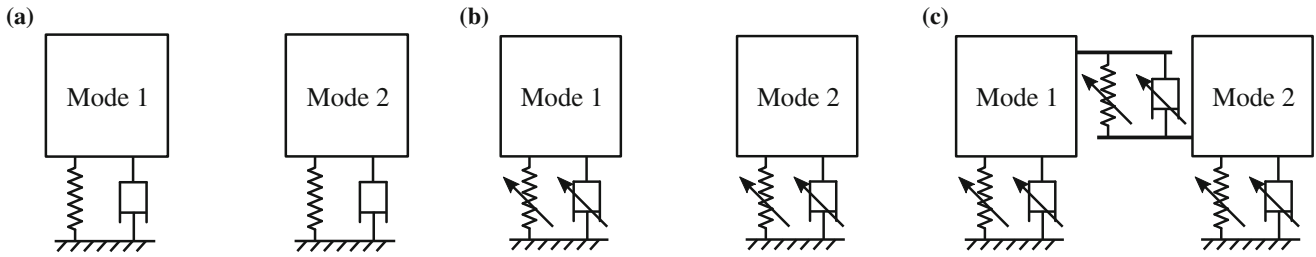


Fig. 7.1 Visualisation of the different modes of an MDOF system for different levels of non-linearity. (a) Linear modes. (b) Non-linear modes. (c) Non-linear modes with non-linear coupling

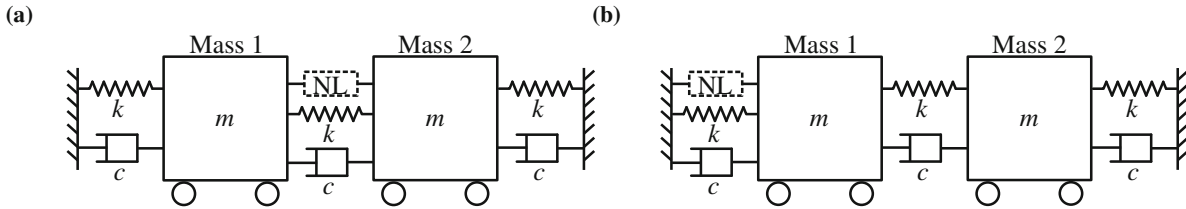


Fig. 7.2 Schematic of the 2DOF system. (a) Symmetric arrangement. (b) Asymmetric arrangement

such as Non-linear Normal Modes (NNM) [4]. At intermediate amplitudes, when the joint remains in the micro-slip regime, it has been shown that some degree of modal coupling still arises [3], but it is much weaker than in the macro-slip case. The behaviour in this regime can be visualised in Fig. 7.1c, where there are some springs and dampers coupling the SDOF systems of each mode. This paper will attempt to extend existing modal modelling approaches to include the effects of modal coupling, thus retaining some of their simplicity.

This project will focus on two different approaches:

1. Extend the concept of the backbone curve into multiple dimensions to create a Multi-Modal Map (MMM). Rather than expressing the frequency and damping as a function of the modal amplitude ($\omega_{n,j}, \zeta_j = f(A_j)$), these properties become function of two modal amplitudes ($\omega_{n,j}, \zeta_j = f(A_1, A_2)$). A polynomial or spline will be used to approximate this function.
2. Extend the Restoring Force Surface (RFS) method by including additional “cross” terms between the different modes. Normally a model of the form $\ddot{q}_j = f(q_j, \dot{q}_j)$ is sought for each mode. The proposed approach is to assume the more complex form $\ddot{q}_j = f(q_1, \dot{q}_1, q_2, \dot{q}_2)$, so that each modal acceleration is now a function of two modal displacements. This parametric model can then theoretically be used to simulate the response to arbitrary excitations.

7.2 Systems of Interest

7.2.1 2DOF System

This paper will initially focus on the 2DOF system shown in Fig. 7.2. This system has three identical linear springs and dampers, and two identical masses. This underlying linear system will have one in-phase mode where the two masses move together and the middle spring does not deflect; and another out-of-phase mode where the two masses move by equal amounts but in opposite directions. This means that the modal coupling can be controlled, depending on which spring the non-linearity is in parallel with:

- **Central spring:** Only the out-of-phase mode will engage the non-linearity to become non-linear, leaving the in-phase mode to be linear. There will therefore also be no modal coupling. This will be referred to as the symmetric arrangement.
- **Left spring:** Both modes will engage the non-linear element, so the modes will be coupled. This will be referred to as the asymmetric arrangement.

The baseline parameters are shown in Table 7.1. The damping coefficient was chosen so that the damping ratio was approximately 1%.

Table 7.1 Parameters of the underlying linear 2DOF system

Parameter	Value	Units
m	2	kg
k	800	N m^{-1}
c	0.8	N s m^{-1}

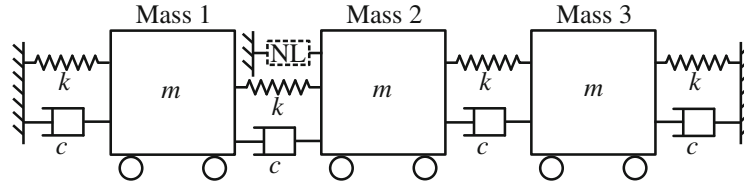


Fig. 7.3 Schematic of the 3DOF system with two coupled modes

7.2.2 3DOF System

Later on, the focus will turn to the 3DOF system shown in Fig. 7.3. The masses, springs and dampers are again identical, and the same parameters are used as for the 2DOF system, as shown in Table 7.1. This system will have one mode in which the central mass remains stationary and the other two masses move in opposite directions. The other two modes will engage the central mass.

The non-linear element is connected between the central mass and ground, so the system is symmetrical. The mode where the central mass does not move will not engage this non-linearity, so this mode will remain linear. However, the other two modes will however become non-linear and will be coupled. Since only two of the three modes will be coupled, this allows the system to be analysed using the same techniques as the 2DOF system.

7.2.3 Equations of Motion

The equations of motion of either system can be written in the form below, where the non-linearities are grouped in the term \mathbf{f}_{nl} . These were integrated numerically in MATLAB using `ode45`.

$$\mathbf{M}\ddot{\mathbf{x}} + \mathbf{C}\dot{\mathbf{x}} + \mathbf{K}\mathbf{x} + \mathbf{f}_{nl}(\mathbf{x}, \dot{\mathbf{x}}) = \mathbf{f}_e \quad (7.1)$$

7.2.4 Modal Transformation

Modal analysis was performed on each system assuming negligible damping, thereby yielding the Φ matrix where each column corresponds to one of the mode shapes of the system. For an experimental system, it is assumed that Experimental Modal Analysis (EMA) had already been applied to identify the mode shapes of the underlying linear system. This matrix was used to transfer from physical coordinates \mathbf{x} to modal coordinates \mathbf{q} as shown in Eq. 7.2.

$$\mathbf{q} = \Phi^{-1}\mathbf{x} = \Phi^T\mathbf{M}\mathbf{x} \quad (7.2)$$

7.2.5 Non-linear Elements

Three types of non-linearity were considered, as shown below. In each case, the non-linear parameters were chosen so that the system was weakly non-linear; this was defined as the region where natural frequency and damping ratio varied by 1–3% of their values for the underlying linear system. This is representative of jointed structures in the micro-slip regime.

- **Cubic spring term:** This is the simplest form of symmetric non-linearity.
- **Jenkins element:** This consists of a spring in series with a slider. This is the simplest model which introduces frictional energy dissipation.

- **Iwan element:** This consists of infinitely many Jenkins elements in series, where the distribution of the slider strengths was set according to Segalman [9]. This is commonly used to model jointed structures.

7.2.6 Generating Test Data

The response of the system to multiple hammer tests was simulated, with different proportions of the applied impulse going to each mass in each case. This allows variable amounts of each mode to be excited. For a physical system, this may be difficult to achieve, but this was not deemed a concern for this project.

The accelerations of each mass were projected into modal accelerations using the Φ matrix. However, it was assumed that like in a physical system, it was not possible to measure the displacements and velocities. Instead, these were regenerated from the acceleration signals by the following procedure:

1. Integrate the acceleration using `cumtrapz` in MATLAB, to compute the velocity.
2. Find the positive and negative peaks in the velocity, by finding the zero crossings in the acceleration.
3. Find the envelopes of the peaks and troughs. The average of these two signals gives the drift of the velocity.
4. Subtract this drift from the velocity signal.
5. Go back to step 1, but start with the velocity signal rather than the acceleration, in order to compute the displacement.

This procedure was repeated for all modal accelerations.

7.3 Methods of Capturing the Modal Coupling

7.3.1 Multi-modal Maps (MMM)

The softening and stiffening behaviour of SDOF non-linear systems is often visualised by plotting the variation of the natural frequency with amplitude to create what is known as the “backbone curve”, which can be expressed mathematically as $\omega_n = f(A)$. A similar relation can also be extracted for the damping. This can be extended to MDOF systems where the modes are uncoupled by computing a separate backbone curve for each mode.

It is proposed that this approach can be extended to the case of light modal coupling, by allowing the natural frequency and damping to vary with more than one modal amplitude. This is expressed mathematically in Eqs. 7.3 and 7.4 for the case that two modes are coupled.

$$\omega_{n,j} = f_{\omega}(A_1, A_2) \quad (7.3)$$

$$\zeta_j = f_{\zeta}(A_1, A_2) \quad (7.4)$$

The approach can be split into the following stages, and will be discussed further in the following sections.

1. Band-pass filter each modal acceleration and apply the Hilbert transform to extract the instantaneous frequency, damping ratio and amplitude of each mode from a set of hammer tests. This is described in Sect. 7.3.1.1.
2. Fit a polynomial or spline surface to this data. This is described in Sect. 7.3.1.2.
3. Simulate the impulse response using the modal maps using an averaging method described in Sect. 7.3.1.3.

7.3.1.1 Signal Processing

The first stage is to band-pass filter each modal coordinate, so that each mode only contains components at its respective natural frequency. This is because the Hilbert transform requires mono-component data. A second order Butterworth filter was created using `butter`, and was applied to the data using `filtfilt` thereby avoiding phase distortion. The next stage was to take the Hilbert transform of the modal displacement to generate the following analytic signal:

$$Q(t) = q(t) + iH(q(t)) \quad (7.5)$$

The magnitude of this signal yields the instantaneous amplitude $A(t) = |Q(t)|$. The following derived parameters will also be useful later on:

$$d(t) = \log |Q(t)|$$

$$\theta(t) = \angle Q(t)$$

Splines were fit to each of these signals in MATLAB using `spar2`, which could then be analytically differentiated using `fnder`, thereby avoiding noisy numerical differentiation. It can be shown that the original signal can be regenerated from these signals [6]:

$$q(t) = e^{d(t)+i\theta(t)} \quad (7.6)$$

Using this information, the following relations for the instantaneous damped natural frequency ω_d and decay constant σ can be found [5]:

$$\omega_d(t) \approx \dot{\theta}(t) \quad (7.7)$$

$$\sigma(t) \approx -\left(\dot{d}(t) + \frac{\ddot{\theta}(t)}{2\dot{\theta}(t)}\right) \quad (7.8)$$

The natural frequency and damping ratio are then defined as [6]:

$$\omega_n(t) \triangleq \sqrt{\omega_d(t)^2 + \sigma(t)^2} \quad (7.9)$$

$$\zeta(t) \triangleq \frac{\sigma(t)}{\omega_n(t)} \quad (7.10)$$

7.3.1.2 Fitting the Map to the Data

Once the modal amplitudes, frequencies and damping ratios are known, it is possible to plot this information on a set of 3D axes. The amplitudes of the coupled modes A_j are on the x and y axes, and one of the natural frequencies or damping ratios is plotted on the z -axis. An example of this is shown in Fig. 7.4 for the 2DOF system with an asymmetric cubic spring non-linearity. Each of the different coloured lines corresponds to a different hammer test, where each span different ranges of A_1 and A_2 .

The next stage is to fit a surface to this data from all of the hammer tests. Two different approaches were used in this project:

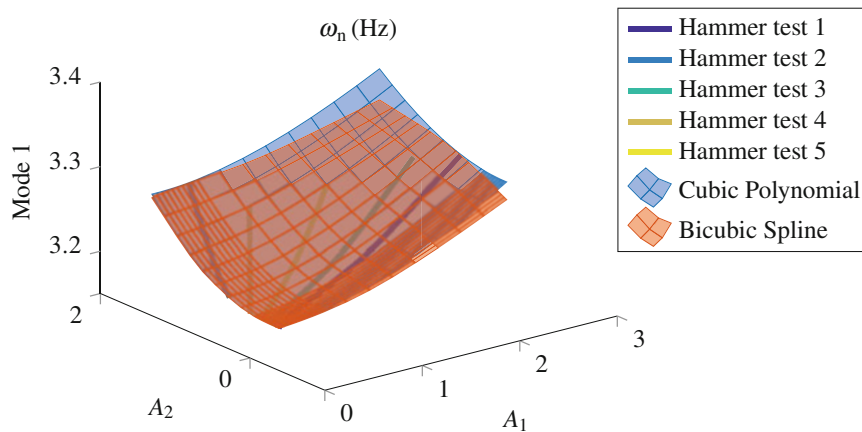


Fig. 7.4 Example multi-modal map of the 1st natural frequency for the 2DOF system with an asymmetric cubic spring non-linearity

- **Polynomial:** Fit a quadratic or cubic polynomial in A_1 and A_2 , including cross terms between A_1 and A_2 . These coefficients were optimised by solving a linear least squares problem using the backslash operator in MATLAB. In the example in Fig. 7.4, cubic terms were required for a good fit.
- **Spline:** Fit a biquadratic or bicubic spline surface to the data using `spap2`. The slight complication here is that this function requires gridded data, so the data was first regularised using `gridfit` [10]. The smoothness parameter of the regulariser was set to a low value (0.1), so that the gridded data passed to the MATLAB spline toolbox would match the original data closely. This ensures that the results are comparable to the polynomial fit which does not require a regulariser. The number of knots used for the spline fit was found to have a significant effect on the quality of the fit to the data, but 5 was the lowest value which gave consistently good results.

7.3.1.3 Averaging Method to Simulate the Time Response

The final stage is to use the map to predict the impulse response. Under free decay, the equation of motion for each modal coordinate can be written as:

$$\ddot{q} + 2\zeta\omega_n\dot{q} + \omega_n^2q = 0 \quad (7.11)$$

where ω_n and ζ can be found from Eqs. 7.3 and 7.4 respectively, but the arguments have been dropped for brevity. The response is assumed to be of the following form:

$$q(t) = A(t)e^{i\tau(t)} \quad (7.12)$$

which can be differentiated to give:

$$\dot{q}(t) = \left(\frac{\dot{A}(t)}{A(t)} + i\dot{\tau}(t) \right) A(t)e^{i\tau(t)} \quad (7.13)$$

It is now assumed that the frequency varies slowly so that terms involving $\ddot{\tau}(t)$ can be neglected. This means the acceleration can be approximated as:

$$\ddot{q}(t) \approx \left(\frac{\ddot{A}(t)}{A(t)} + 2\frac{\dot{A}(t)}{A(t)}i\dot{\tau}(t) - \dot{\tau}(t)^2 \right) A(t)e^{i\tau(t)} \quad (7.14)$$

Once Eqs. 7.12, 7.13 and 7.14 are substituted into Eq. 7.11, and the real and imaginary parts are equated, the following ODEs can be derived:

$$\frac{\dot{A}(t)}{A(t)} = -\omega_n\zeta \quad (7.15)$$

$$\dot{\tau}(t)^2 - \frac{\ddot{A}(t)}{A(t)} = \omega_n^2(1 - 2\zeta^2) \quad (7.16)$$

Equation 7.15 now directly gives an ODE for the instantaneous amplitude A . At this point it is assumed that ω_n and ζ will vary slowly in time. This means that the instantaneous values can be replaced with their local ‘‘average’’ values [11], so can effectively be treated as constants. This allows Eq. 7.15 to be differentiated to give:

$$\frac{\ddot{A}(t)}{A(t)} = \omega_n^2\zeta^2$$

which can then be substituted into Eq. 7.16 to yield the following ODE for the phase τ :

$$\dot{\tau}(t) = \omega_n\sqrt{1 - \zeta^2} \quad (7.17)$$

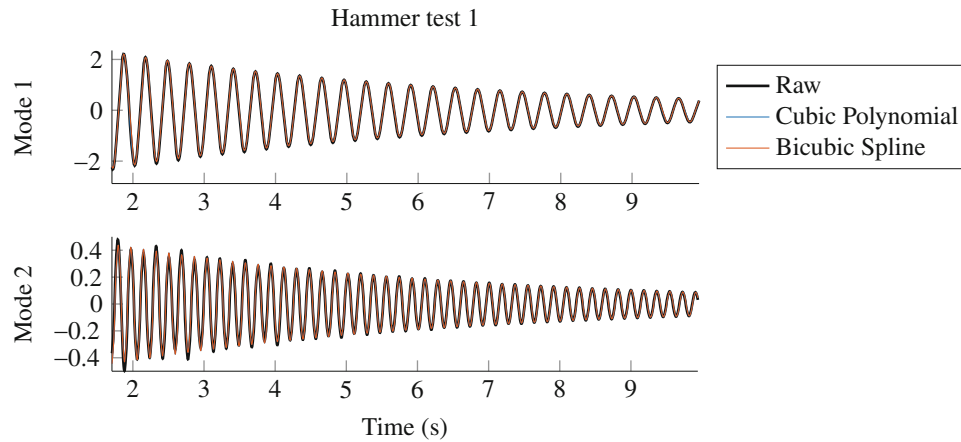


Fig. 7.5 Example of the simulated time response of the first mode from the multi-modal map for the 2DOF system with an asymmetric cubic spring non-linearity

At each integration step, the instantaneous values of ω and ζ at the current modal amplitudes must be computed using the multi-modal maps; the ODEs in Eqs. 7.15 and 7.17 can then be integrated forwards. This process was implemented in MATLAB using `ode45`.

This approach was used to simulate the response to each of the hammer tests which were used to generate the multi-modal map. The initial conditions were set to the amplitudes and phases just after the hammer strike; the amplitude was taken from the Hilbert transform, and the initial phase was estimated from $\tau(0) \approx \arctan \frac{-\dot{q}(0)}{\omega_n q(0)}$ where it was assumed the response is instantaneously sinusoidal. If the fit to the multi-modal map is good, it would be expected that the time domain response should match the original data well. An example is shown in Fig. 7.5 above for the same system as the modal map in Fig. 7.4. The response from the modal maps clearly matches the raw data well, apart from the initial part of the decay in mode 2 where there is clearly a secondary frequency component from the other mode which this approach cannot capture.

7.3.1.4 Computation of the Restoring Force

To allow comparison with the RFS method discussed later in Sect. 7.3.2, it was deemed useful to also compute the modal forces based on the modal maps. Equation 7.11 can be rearranged to give:

$$\ddot{q} = -2\zeta\omega_n\dot{q} - \omega_n^2q \quad (7.18)$$

To find the instantaneous frequency and damping from the modal map in each hammer test, the instantaneous amplitudes from the Hilbert transform can be substituted into Eq. 7.18. The recorded modal velocities \dot{q}_j and displacements q_j can then be substituted into Eq. 7.18 to yield the modal forces.

7.3.2 Restoring Force Surface (RFS)

The restoring force surface approach is one of the most common methods of model identification of SDOF non-linear systems. Typically the approach begins by applying an impulse to the system, and then recording the free decay. In this case, since there are no external forces on the system after the initial strike, it is possible to write $\ddot{q} = f(\dot{q}, q)$. The idea is to assume some functional form for $f(\cdot)$ and optimise the coefficients so as to match the experimental data. This can be plotted in 3D allowing easy visualisation, where the displacement q , velocity \dot{q} and restoring force \ddot{q} are on each axis. Thus fitting $f(\cdot)$ to the data can equivalently be thought of as fitting a Restoring Force Surface.

In the case of a MDOF system with no modal coupling, this approach can easily be extended by merely treating each mode as an independent SDOF system. However, as the non-linearities become more significant, the linear modes are no longer orthogonal so they become coupled. The approach presented here is to add more inputs to the function $f(\cdot)$ so that $\ddot{q}_j = f(q_1, \dot{q}_1, q_2, \dot{q}_2)$.

Table 7.2 Different polynomial forms used for the RFS method

Order	Coupling	Mathematical form
Linear	Uncoupled	$k_1 q_1$
Quadratic	Uncoupled	$k_1 q_1 + k_2 q_1 q_1 $
	Coupled	$k_1 q_1 + k_2 q_1 q_1 + k_3 q_1 q_2 + k_4 q_1 q_2 + k_5 q_2 q_2 $
Cubic	Uncoupled	$k_1 q_1 + k_2 q_1 q_1 + k_6 q_1^3$
	Coupled	$k_1 q_1 + k_2 q_1 q_1 + k_3 q_1 q_2 + k_4 q_1 q_2 + k_5 q_2 q_2 + k_6 q_1^3 + k_7 q_1^2 q_2 + k_8 q_1 q_2^2 + k_9 q_2^3$

7.3.2.1 Forms of the Model Used

In this work, it was assumed that for each mode, the restoring force was the sum of an elastic term purely dependent on displacement, and a damping term purely dependent on velocity, which was the approach taken in [6]. This is shown in Eq. 7.19.

$$\ddot{q}_j = F_j^k(q_1, q_2, |q_1|, |q_2|) + F_j^c(\dot{q}_1, \dot{q}_2, |\dot{q}_1|, |\dot{q}_2|) \quad (7.19)$$

A quasi-polynomial representation from [6] was used to represent each of these forces. This means an absolute $|\cdot|$ was introduced into certain terms to ensure that the resulting stiffness and damping forces remain symmetric. Various orders of polynomial were considered as shown in Table 7.2. For simplicity, only the polynomial coefficients for the stiffness have been shown, but the same forms were used for the damping. Note that there is no linear coupling term, since this would mean the modes are no longer orthogonal even in the linear regime.

Equation 7.19 can be rewritten in the following matrix form:

$$\mathbf{U} = \mathbf{P}\mathbf{c} \quad (7.20)$$

where the vector \mathbf{U} contains the values of the restoring force \ddot{q}_j and the matrix \mathbf{P} is assembled from each of the polynomial terms shown in Table 7.2. The vector \mathbf{c} is comprised of the stiffness and damping coefficients shown below, which are the unknowns:

$$\mathbf{c} = [k_1 \ k_2 \ \cdots \ k_9 \ c_1 \ c_2 \ \cdots \ c_9] \quad (7.21)$$

7.3.2.2 Data Conditioning and Model Fitting

The accuracy of the resulting RFS model fit to the data is highly susceptible to noise as well as higher harmonic frequencies. To mitigate this, it is desirable to fit the data predominantly around the natural frequency of the mode of interest. This means the data has to be conditioned. The initial response directly after the impulse will have very high frequency components, as well as components at the frequency of the coupled mode, so only the data after the fifth peak will be retained. Additionally, the data after the point where the amplitude drops below one 500th of the initial amplitude was discarded, where the data was observed to become noisy.

The fitting of the data then takes place in the frequency domain, using the procedure from [6]. The Fast Fourier Transform is applied to both the assembled matrix \mathbf{P} and the restoring force matrix \mathbf{U} using `fft` in MATLAB. This will yield complex matrices $\hat{\mathbf{U}}$ and $\hat{\mathbf{P}}$, which will each have the same size as \mathbf{U} and \mathbf{P} respectively. Each row will correspond to a different frequency; the frequencies will range from zero to the sampling frequency, although the second half of the rows corresponding to frequencies above the Nyquist frequency will merely be complex conjugates of the first half. Therefore, the second half of these matrices was discarded. The data was truncated to frequencies below the sixth harmonic of the linearised natural frequency of the mode of interest, which covered the frequencies of both the coupled modes. Before the coefficients can be identified, the complex matrices need to be split into their real and imaginary parts which can then be concatenated as shown below:

$$\hat{\mathbf{U}}^* = \begin{bmatrix} \Re(\hat{\mathbf{U}}) \\ \Im(\hat{\mathbf{U}}) \end{bmatrix} \quad (7.22)$$

$$\hat{\mathbf{P}}^* = \begin{bmatrix} \Re(\hat{\mathbf{P}}) \\ \Im(\hat{\mathbf{P}}) \end{bmatrix} \quad (7.23)$$

Both the $\hat{\mathbf{U}}^*$ and $\hat{\mathbf{P}}^*$ matrices have many more rows than columns, resulting in an over-constrained problem. Therefore the coefficients were fit to the data by minimizing the least-squares error, which can be achieved by multiplying both sides of the equation by the pseudo-inverse of $\hat{\mathbf{P}}^*$. This was implemented using the backlash operator in MATLAB.

Even after truncation it is important that the behaviour near the natural frequencies is well-captured. This can be achieved by weighting particular rows of the matrices $\hat{\mathbf{U}}^*$ and $\hat{\mathbf{P}}^*$ more highly. The weighting for frequencies within 5% of the linear natural frequency $\omega_{n,0}$ of each mode were weighted to 25, whereas the weighting was 1 for all other frequencies.

7.3.2.3 Parameter Reduction

As RFS is a non-parametric least-squares based method, it tends to over-fit the data. Therefore, some of the terms in the polynomial might not have much effect. These terms cannot be eliminated merely on the magnitude of their coefficient. Instead, the following parameter reduction technique was employed:

- Set one of the coefficients to zero.
- Recompute the error in the frequency domain.
- If the change in error is lower than a specified tolerance, the term is removed.
- Go back to the first step, but remove a different term.

Once the optimal value for the coefficient vector \mathbf{c}^* has been found, the restoring force can be computed from Eq. 7.19.

7.3.2.4 Combining Multiple Data Sets

The RFS method described so far has only used data from a single hammer test to identify the coefficients of the model. However, if the method is applied to each hammer test individually, a slightly different parameter set will be obtained each time. Also, each parameter set will not necessarily generalise well to other hammer tests, even though it might have a low error for the particular case that it was fit to, which is known as over-fitting.

In order to work around this, the data was fit to the data from multiple hammer tests simultaneously. The \mathbf{U}^* and \mathbf{P}^* matrices were determined for each hammer test using the data conditioning described previously, and then concatenated together as shown in Eqs. 7.24 and 7.25. This larger problem can then be solved in the same way as before. The resulting error may be higher than fitting to each test individually, but it allows a unified parameter set to be obtained which should generalise well.

$$\hat{\mathbf{U}}_{comb}^* = \begin{bmatrix} \hat{\mathbf{U}}_1^* \\ \hat{\mathbf{U}}_2^* \\ \vdots \\ \hat{\mathbf{U}}_N^* \end{bmatrix} \quad (7.24)$$

$$\hat{\mathbf{P}}_{comb}^* = \begin{bmatrix} \hat{\mathbf{P}}_1^* \\ \hat{\mathbf{P}}_2^* \\ \vdots \\ \hat{\mathbf{P}}_N^* \end{bmatrix} \quad (7.25)$$

7.3.2.5 Time Integration

The system can now be expressed as a set of ODEs. These can easily be numerically integrated using `ode45` in MATLAB. The initial conditions were taken as the displacement and velocity after the fifth peak of each hammer test.

7.3.2.6 Numerical Computation of Instantaneous Natural Frequency and Damping

It is desirable to be able to compare the modal maps derived from the Hilbert transform, to those from the model identified by RFS. It is of course possible to simply apply the same Hilbert transform-based analysis from Sect. 7.3.1.1 to the time response of the RFS model; however, this process is slow and sometimes requires manual tuning of the fitting parameters to obtain clean results. It would be preferable to be able to compute model map directly from the RFS model.

The approach used here is based on the Harmonic Balance method and Chapter 4 of [12] which discusses how describing functions can be used to analyse transient signals. It is first assumed that the equations of motion have an underlying linear system, with a relatively weak non-linear term:

$$m_1 \ddot{q}_1 + c_1 \dot{q}_1 + k_1 q_1 + f_1(q_1, q_2, \dot{q}_1, \dot{q}_2) = 0 \quad (7.26)$$

$$m_2 \ddot{q}_2 + c_2 \dot{q}_2 + k_2 q_2 + f_2(q_1, q_2, \dot{q}_1, \dot{q}_2) = 0 \quad (7.27)$$

where all of the non-linear terms are collected into the functions $f_1()$ and $f_2()$. To apply this method to RFS, it was therefore necessary to separate the linear coefficients from those associated with the non-linear terms. It is then assumed that the response is harmonic with exponential decay and has components at both $\omega_{d,1}$ and $\omega_{d,2}$. This can be expressed in a multi-dimensional time domain (or hypertime) as follows [13]:

$$q_1(t_1, t_2) = A_1 e^{s_1 t_1} + B_1 e^{s_2 t_2} \quad (7.28)$$

$$q_2(t_1, t_2) = B_2 e^{s_1 t_1} + A_2 e^{s_2 t_2} \quad (7.29)$$

where $s_j = -\sigma_j + i\omega_{d,j}$. Note that the amplitudes of the dominant components A_j are to be specified, whilst the cross-components B_j are unknown and must be solved for; these may turn out to be complex, which indicates a phase offset. If it is assumed that the damping and natural frequency vary slowly in time, known as the quasi-static assumption [12], then the following differentiation rule applies:

$$\frac{\partial}{\partial t_j} (e^{s_j t_j}) \approx s_j e^{s_j t_j} \quad (7.30)$$

Once these expressions are substituted into the equations of motion Eqs. 7.26 and 7.27, the coefficients of $e^{s_j t_j}$ can be equated to yield the following four equations:

$$(m_1 s_1^2 + c_1 s_1 + k_1)A_1 + F_1 = 0 \quad (7.31)$$

$$(m_1 s_2^2 + c_1 s_2 + k_1)B_1 + G_1 = 0 \quad (7.32)$$

$$(m_2 s_1^2 + c_2 s_1 + k_2)B_2 + G_2 = 0 \quad (7.33)$$

$$(m_2 s_2^2 + c_2 s_2 + k_2)A_2 + F_2 = 0 \quad (7.34)$$

where F_j and G_j are the amplitudes from the non-linear terms, which are unknown. These equations are complex, so both the real and imaginary parts must sum to zero. Again invoking the quasi-static assumption, it can be assumed that the response is approximately locally periodic with frequencies $\omega_{d,j}$. This allows us to evaluate the effect of the non-linearity over one cycle in the time domain, which is equivalent to computing the describing function of the non-linear terms. If there is some energy dissipation, then F_j, G_j will turn out to be complex. This process is shown in Eq. 7.35.

$$A_j, B_j \xrightarrow{\text{IFFT}} f_j(q_1, q_2, \dot{q}_1, \dot{q}_2) \xrightarrow{\text{FFT}} F_j, G_j. \quad (7.35)$$

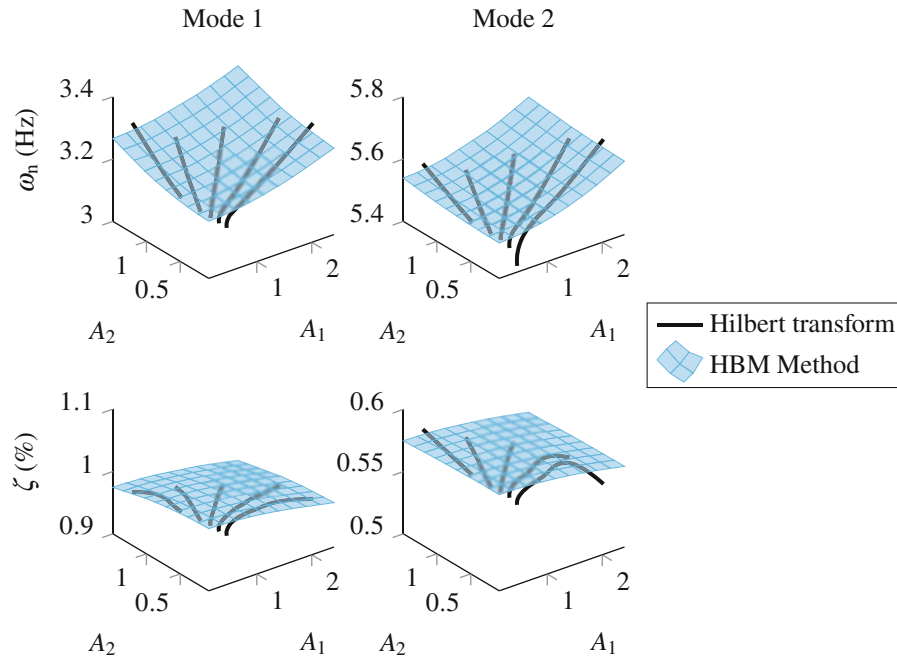


Fig. 7.6 Multi-modal maps for a system with a cubic spring non-linearity: comparison between Hilbert transform & HBM-based method

In this case, the FFT and IFFT will be 2D operations which can be executed efficiently in MATLAB with `fft2` and `ifft2`. An optimiser can now be used to find the values of σ_j , $\omega_{d,j}$, $\Re(B_j)$ and $\Im(B_j)$ which solve Eqs. 7.31, 7.32, 7.33, and 7.34. Once the values of σ_j and $\omega_{d,j}$ are known, the natural frequency and damping ratio can be extracted using Eqs. 7.9 and 7.10. This problem can be solved over a grid of different A_1 - A_2 values, to generate multi-modal maps for the natural frequencies and damping ratios.

In order to validate the approach, it was applied to the case of an asymmetric system with a cubic spring non-linearity. However, instead of using $f_1(\cdot)$ and $f_2(\cdot)$ derived from RFS, these functions were derived analytically from the model. It would be expected that the maps derived by simulating the free decay by time integration and applying the Hilbert transform would match those derived from the HBM-based method. The results are plotted in Fig. 7.6, and it can be seen that the natural frequencies agree very well. However, the damping ratio does not agree so well, which may be partly because the HBM-based method is approximate, but errors may also be introduced when a spline is fit to the Hilbert transform in the signal post-processing.

Once the natural frequency and damping maps have been computed, they can be used to compute the instantaneous frequency and damping during each hammer test. This can be achieved by interpolating into this gridded data with the amplitudes from each hammer test, found from the Hilbert transform. This was implemented in MATLAB using the `interp2` function.

7.3.3 Error Metrics

In order to quantitatively assess the accuracy of the two approaches, three different types of error metrics were computed. These were computed for each hammer test, and the average can then be taken. These metrics can be calculated for each mode.

7.3.3.1 Natural Frequency and Damping

The natural frequency and damping ratio can be extracted from the data using the process in Sect. 7.3.1.1, which can be denoted by ω_{hilb} and ζ_{hilb} . The multi-modal maps derived from MMM can then be evaluated at the same amplitudes. For RFS, the map can be computed using the approach from Sect. 7.3.2.6, and then this map can be interpolated at the relevant values. These frequencies and damping ratios will be denoted by ω_{map} and ζ_{map} . The relative error in each map can then be computed from Eqs. 7.36 and 7.37. This is also the error in the fitting process from the MMM.

$$\epsilon_{\omega} = \sqrt{\left\langle \frac{(\omega_{map} - \omega_{hilb})^2}{\omega_{hilb}^2} \right\rangle} \quad (7.36)$$

$$\epsilon_{\zeta} = \sqrt{\left\langle \frac{(\zeta_{map} - \zeta_{hilb})^2}{\zeta_{hilb}^2} \right\rangle} \quad (7.37)$$

7.3.3.2 Time Response

The time response can be computed from the MMM using the averaging technique in Sect. 7.3.1.3, or by simple time integration in the case of RFS. A similar RMS relative error metric was then computed to quantify the error in the time response:

$$\epsilon_{time} = \sqrt{\left\langle \frac{(q_{sim} - q_{data})^2}{A_q^2} \right\rangle} \quad (7.38)$$

where q_{sim} is the simulated modal response computed from MMM or RFS, and q_{data} is the modal response from the raw data. The variable A_q is an approximate measure of the local envelope given by:

$$A_q^2 \approx q_{data}^2 + \frac{\dot{q}_{data}^2}{\omega_{n,0}^2} \quad (7.39)$$

where $\omega_{n,0}$ is the natural frequency of the underlying linear system. This scaling factor was used instead of the amplitude from the Hilbert transform, so as to be as independent as possible of the signal processing.

7.3.3.3 Restoring Force

By definition, RFS generates a model which directly yields the restoring force. This can also be computed from MMM using the approach in Sect. 7.3.1.4. The following error metric was then computed, which is particularly relevant to RFS as it is the residual from the fitting process:

$$\epsilon_{\ddot{q}} = \sqrt{\left\langle \frac{(\ddot{q}_{rf} - \ddot{q}_{data})^2}{(\omega_{n,0}^2 A_q)^2} \right\rangle} \quad (7.40)$$

where \ddot{q}_{rf} is the restoring force from the MMM or RFS model. Similar to the time response error metric, an approximate expression for the instantaneous amplitude of the restoring force has been introduced in the denominator as a scaling factor.

7.4 Results

7.4.1 Results for a 2DOF System

7.4.1.1 Cubic Spring Non-linearity

An extra cubic term with a coefficient of 100 N m^{-3} was added to either the central or left hand spring, to create symmetric and asymmetric arrangements respectively. The variation of the natural frequency and damping ratio with amplitude has been plotted in Fig. 7.7, and the error metrics in Fig. 7.8.

Symmetric System

As expected, in the symmetric arrangement shown in Fig. 7.7a, the modal properties of the first mode do not vary with amplitude, and those of the second mode only depend on the second modal amplitude. Both the quadratic polynomial and cubic spline modal maps from MMM fit the data well, but the spline fit is slightly closer at higher amplitudes. This is reflected in the map error metrics in Fig. 7.8a. However, this has not led to a reduced time response error; the two MMMs perform equally well in terms of the time response error. The errors in the modal maps are lower for MMM than RFS, perhaps because this method is directly fitting these modal properties.

With the RFS method, the error in the restoring force is lower for the linear first mode than for the second mode as would be expected since it is linear. For the non-linear second mode, the error is very comparable when fitting to a single test or the combined data. Since RFS directly tries to match the restoring force, the errors are slightly lower than those from the MMM method. The modal maps from RFS in Fig. 7.7a agree well with the data, but are not quite as accurate as those from MMM. For the linear first mode, both single and combined RFS appear to be over-fitting, as the error in the time response is much higher than from MMM; this agrees with the small natural frequency offset as high amplitudes in Fig. 7.7a.

Asymmetric System

For the asymmetric case in Fig. 7.7b, both sets of modal properties vary with both modal amplitudes. Again, both modal maps from MMM appear to fit the natural frequencies well. However, the spline fit appears to be over-fitting the damping ratio as the surface is quite bumpy, and despite the fact that the spline fit has lower residuals for the maps, this has not led to lower errors in the time response in Fig. 7.8b. One potential explanation for this dichotomy is that some of the features

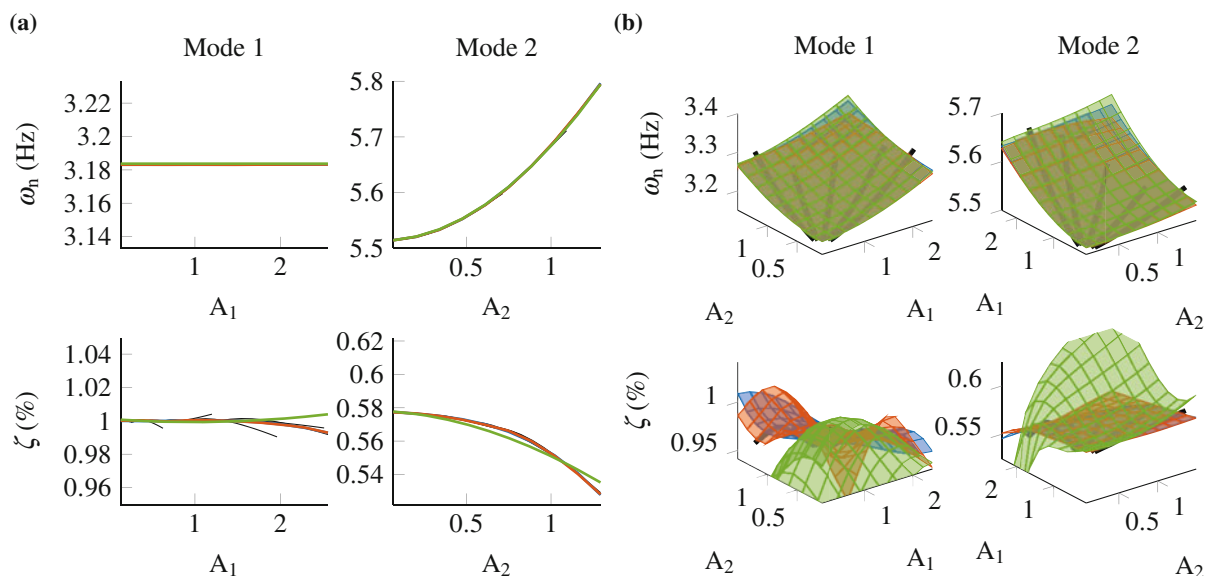


Fig. 7.7 Multi-modal maps for the 2DOF system with a cubic spring non-linearity: MMM – polynomial (—), MMM – spline (—), RFS – combined (—). (a) Symmetric system. (b) Asymmetric system

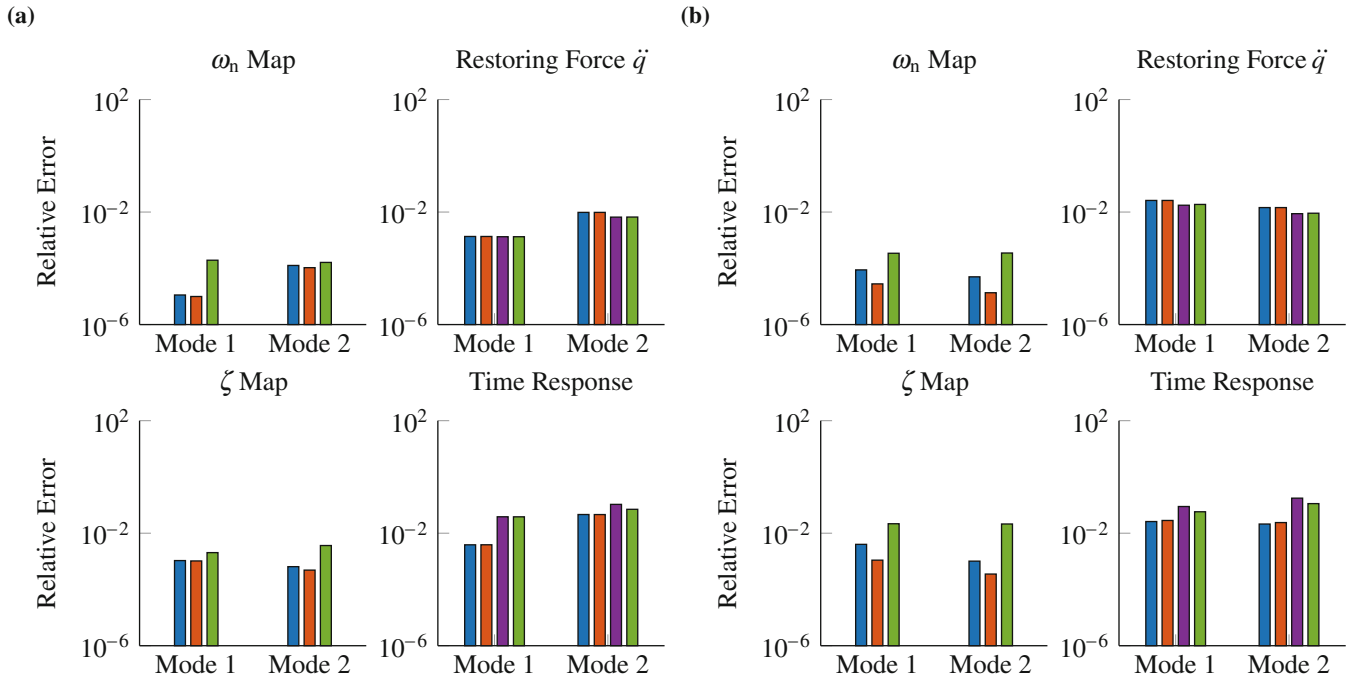


Fig. 7.8 Error analysis for the 2DOF system with a cubic spring non-linearity: MMM – polynomial (■), MMM – spline (■), RFS – single (■), RFS – combined (■). (a) Symmetric system. (b) Asymmetric system

present in the modal map from the data are artefacts of data-processing. Despite this, MMM still has much lower errors in the time response than RFS, and for mode 2 they are comparable to the symmetric case.

The error in the restoring force from RFS has increased for the first mode compared to the symmetric case, because it is now non-linear. The errors in the modal maps are now considerably higher, particularly for the damping, and this can be seen visually in Fig. 7.7b. This suggests RFS has struggled to capture modal coupling correctly, in particular the damping effects, which are weaker than the stiffness effects. The combined RFS yields better results than single RFS for both modes, indicating it is preventing over-fitting.

7.4.1.2 Jenkins Element

The Jenkins element consists of a spring attached to a slider, and is one of the simplest dissipative models. It is also the basis of the Iwan element which will be discussed later in Sect. 7.4.1.3. As with the cubic non-linearity, a single Jenkins element was introduced in both symmetric and asymmetric arrangements. The spring stiffness within the Jenkins element was set to 100 N m^{-1} and the sliders strength to 30 N. The modal maps are plotted in Fig. 7.9 and the errors in Fig. 7.10.

Symmetric System

As expected, the modal map for mode 2 shown in Fig. 7.9 looks quite different from the cubic spring case. This is because the Jenkins element is a non-smooth non-linearity and there is a sharp drop in frequency and rise in damping ratio at $A_2 \approx 0.5$ when the slider unsticks. This kink is captured well by MMM method using a spline fit, but the polynomial deviates far from the data at high amplitudes. RFS captures the natural frequency relatively well, but the damping ratio deviates considerably. The multi-modal map errors in Fig. 7.10 are therefore slightly higher for RFS than MMM with a spline fit. All of the error metrics are higher than for the cubic polynomial, because the non-smooth nature is much harder to fit. This suggests that the forms of model assumed by both approaches are deficient in complexity. When the raw time response was examined, it was found the amplitude was generally over-predicted once the Jenkins element starts to stick, and a slight phase lead was also introduced. In terms of the time response, the MMM spline fit and combined RFS have very similar errors.

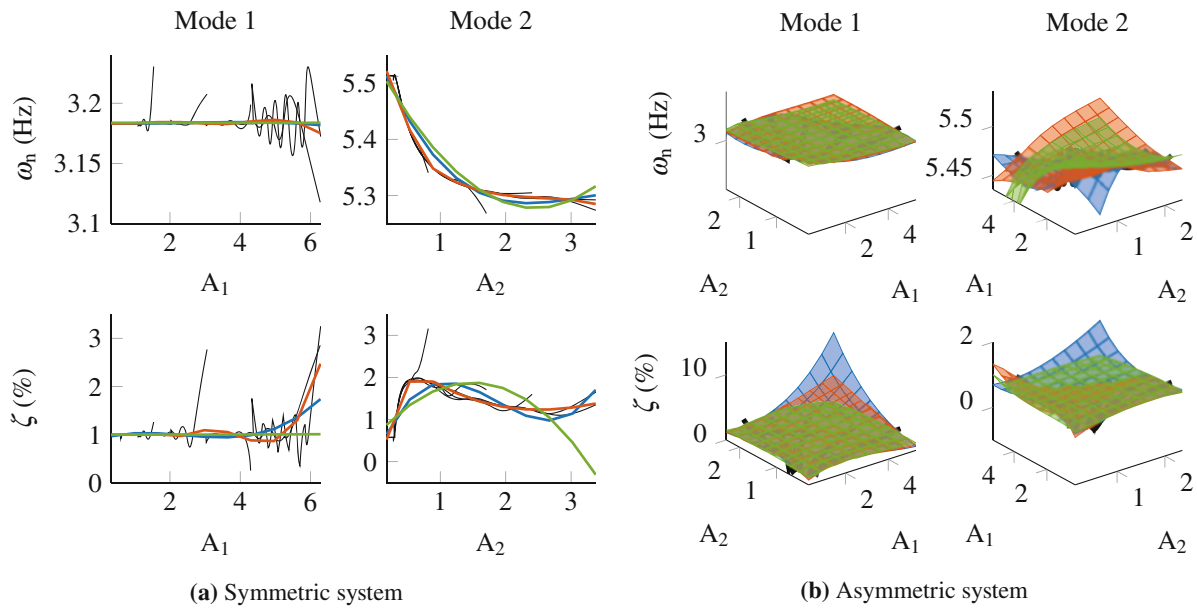


Fig. 7.9 Multi-modal maps for the 2DOF system with a Jenkins element: MMM – polynomial (—), MMM – spline (—), RFS – combined (—). (a) Symmetric system. (b) Asymmetric system

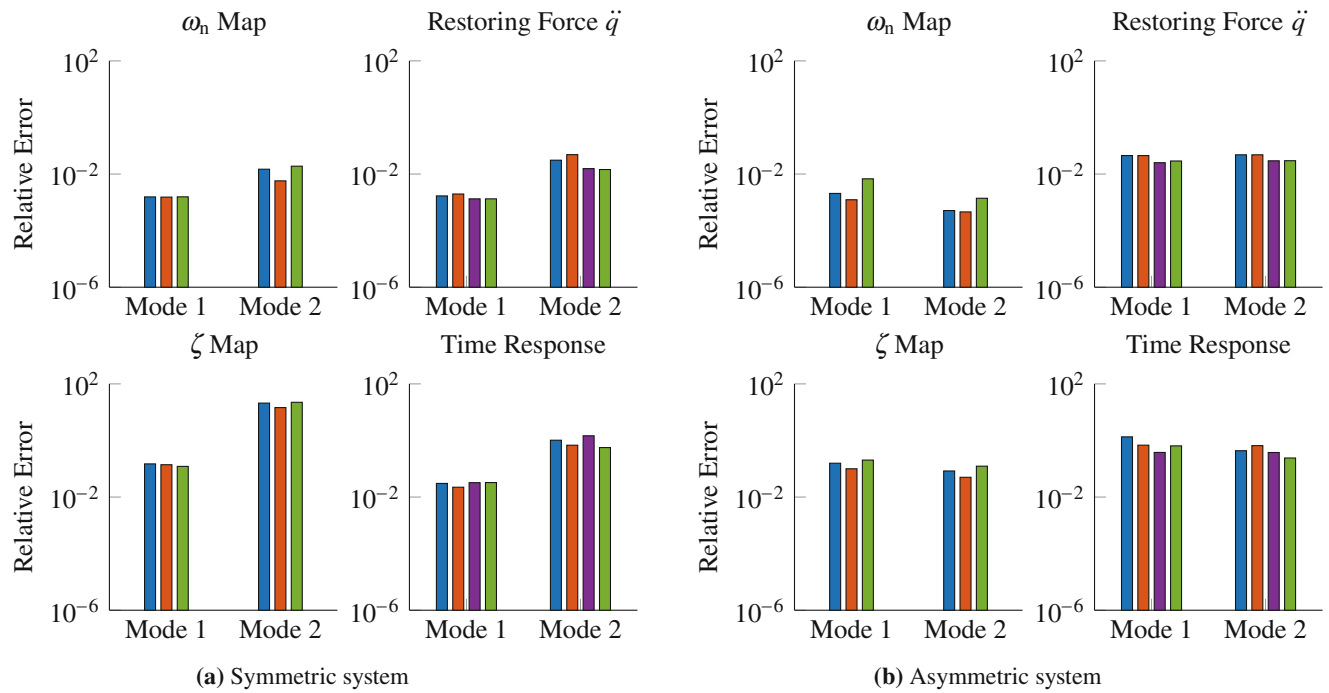


Fig. 7.10 Error analysis for the 2DOF system with a Jenkins element: MMM – polynomial (■), MMM – spline (■), zRFS – single (■), RFS – combined (■). (a) Symmetric system. (b) Asymmetric system

Asymmetric System

For the asymmetric case, the modal maps in Fig. 7.9b show that the second natural frequency is captured badly by both approaches. The mode 1 damping ratio from the MMM polynomial also overshoots the data considerably, whereas the spline fit is closer to the data. The multi-modal map errors in Fig. 7.10b are therefore generally higher for both approaches, when compared to the symmetric case. The only exception is the damping ratio for mode 2 which now has a lower error than

in the symmetric case, indicating the problem is now better conditioned. Surprisingly, the restoring force errors shown in Fig. 7.10a have not risen so considerably compared to the cubic element. However, the error in the time response from both approaches have risen. Combined RFS now has the lowest error in the time response, indicating that this approach may be more robust to non-smooth non-linearities.

7.4.1.3 Iwan Element

It was shown in the previous section that both methods struggled to model systems with a Jenkins element, and the errors were much higher in Fig. 7.10 when compared to those for the cubic non-linearity in Fig. 7.8. The poor quality of the fit to the data from the Jenkins model was not deemed such a concern, as it was known to exhibit a discontinuity that would challenge these methods, and was analysed as an intermediary step before moving over to the Iwan element, which will now be discussed.

Segelman’s four parameter Iwan element [9] is commonly used to model the non-linear behaviour of bolted joints in the microslip regime, and was therefore a good test of whether the proposed methods would apply to real jointed structures. The Iwan element is essentially a set of multiple Jenkins elements with varying slider strengths up to a maximum of F_S . This results in a smooth transition towards macro-slip. For this project, the Iwan parameters were chosen carefully in such a way that the system remained in the micro-slip regime when the joint is lightly non-linear and are tabulated in Table 7.3. The assumption that the modal coupling is light may otherwise break down if the joint enters the highly non-linear macro-slip regime. The results are plotted in Figs. 7.11 and 7.12.

Table 7.3 Parameters of the Iwan element

Parameter	Value	Units
K_T	500	N m^{-1}
F_S	100	N
χ	5	–
β	5	–

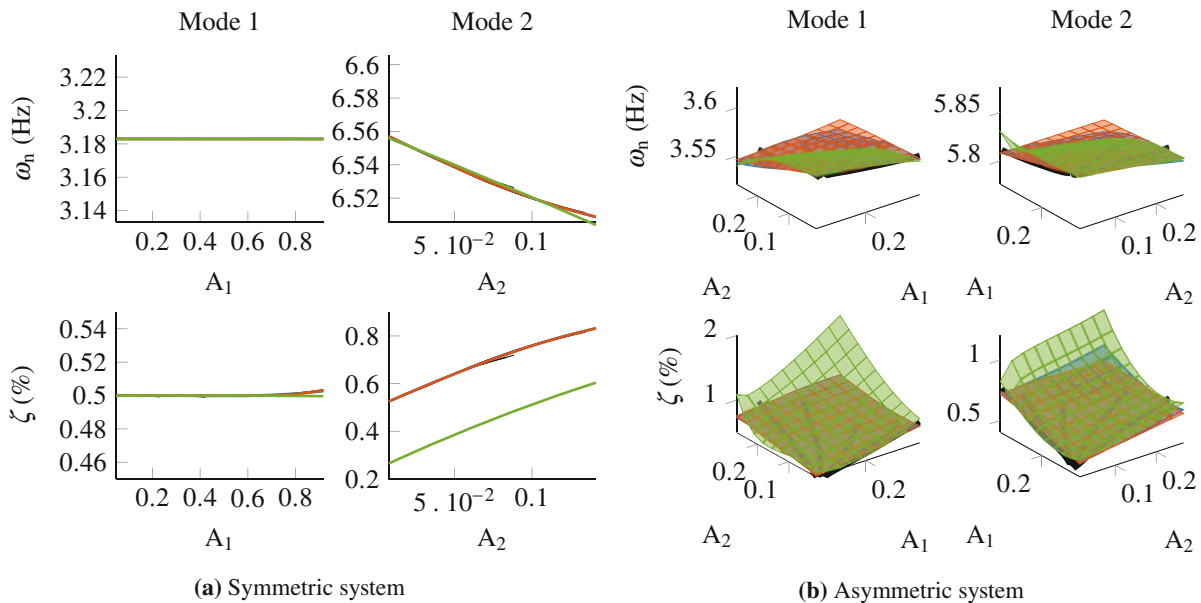


Fig. 7.11 Multi-modal maps for the 2DOF system with an Iwan element: MMM – polynomial (—), MMM – spline (—), RFS – combined (—). (a) Symmetric system. (b) Asymmetric system

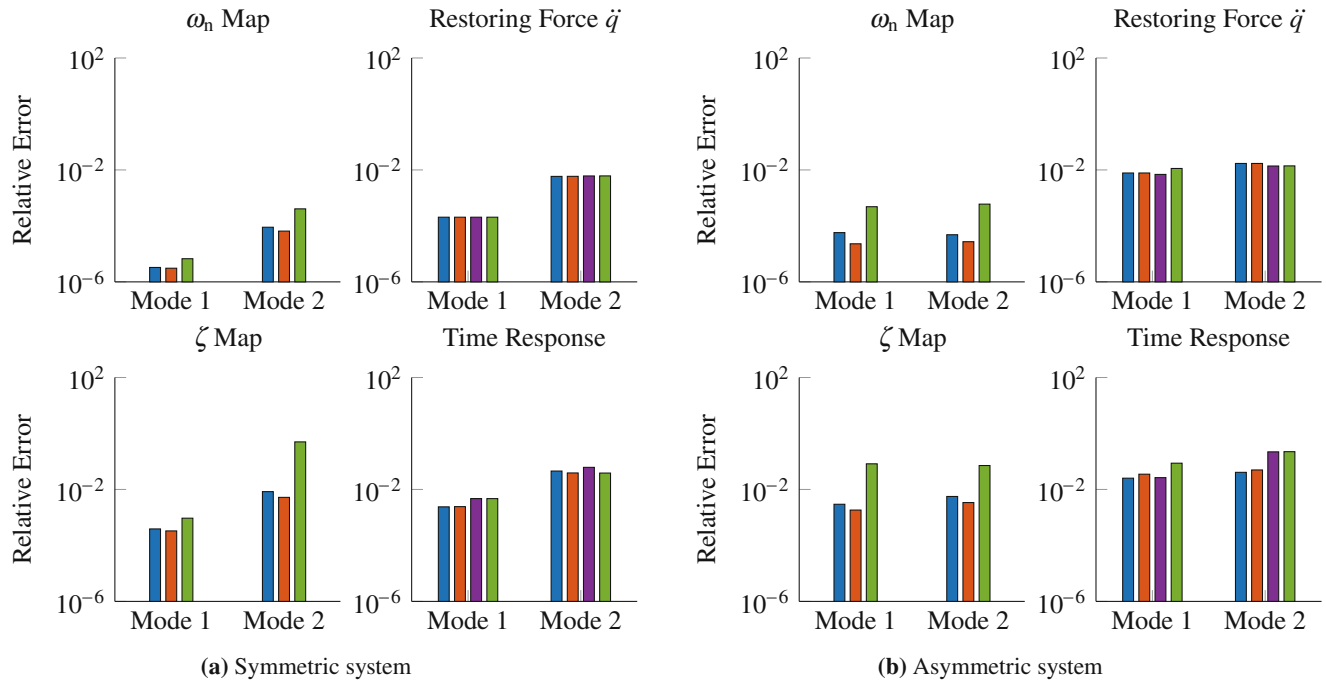


Fig. 7.12 Error analysis for the 2DOF system with an Iwan element: MMM – polynomial (blue), MMM – spline (orange), RFS – single (purple), RFS – combined (green). (a) Symmetric system. (b) Asymmetric system

Symmetric System

The smoothness of the Iwan joint compared to the Jenkins element is instantly apparent from Fig. 7.11. For the symmetric case in Fig. 7.11a, both of the MMM methods are able to fit the smoother transition towards micro-slip much more easily. This has resulted in errors in Fig. 7.12a which are very comparable to the errors from the cubic non-linearity shown in Fig. 7.8a. The spline fit still appears to perform better compared to the cubic map, when comparing the error in the modal-maps, but the time response errors are very close. The results from the RFS method display similar trends to the cubic non-linearity, and the combined RFS method again has a lower error in the time domain than single RFS. Surprisingly, the offset in the damping ratio in Fig. 7.11a appears to have had minimal effect.

Asymmetric System

For the asymmetric case shown in Fig. 7.12b, the errors are again very comparable to the results from the cubic non-linearity in Fig. 7.8b. However, the errors are slightly larger for the more non-linear second mode. The polynomial fit MMM has a slightly lower time response than the spline fit, despite the fact that it has lower multi-modal map errors, suggesting the spline is over-fitting slightly. The MMM method has the lower errors in the time response, and additionally has a lower error in the restoring force than the RFS method, suggesting RFS has struggled to capture the coupling for this type of non-linearity.

7.4.2 Results for a Symmetric 3DOF System

The focus now moved onto the 3DOF system in Fig. 7.3. For this system, modes 1 & 3 are non-linearly coupled, whilst mode 2 remains linear. This specially chosen 3DOF system serves as an intermediary step to being able to capture modal coupling of more than 2 modes in the future.

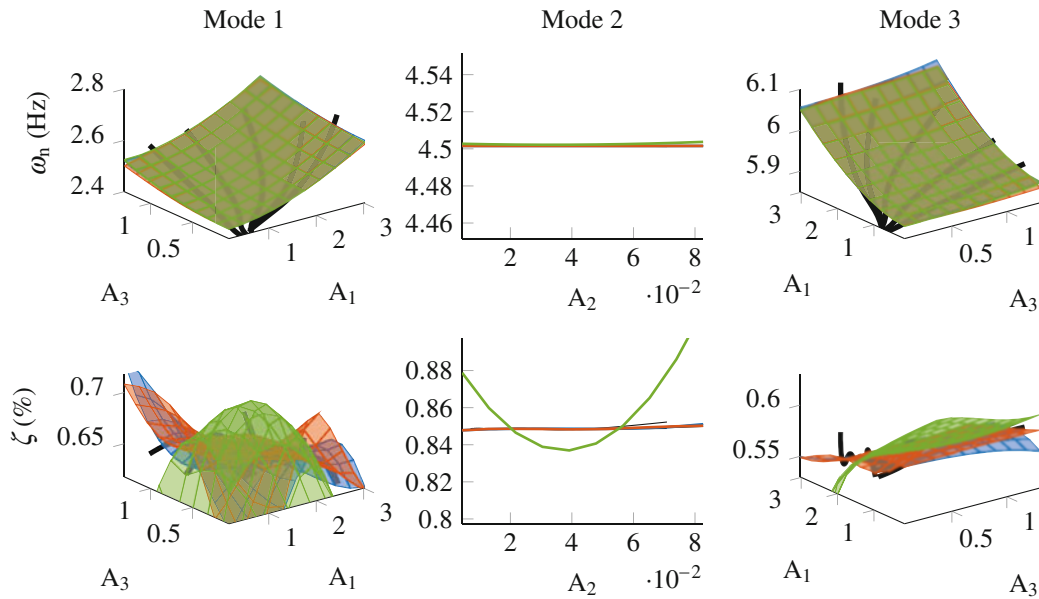


Fig. 7.13 Multi-modal maps for the symmetric 3DOF system with a cubic spring non-linearity: MMM – polynomial (—), MMM – spline (—), RFS – combined (—)

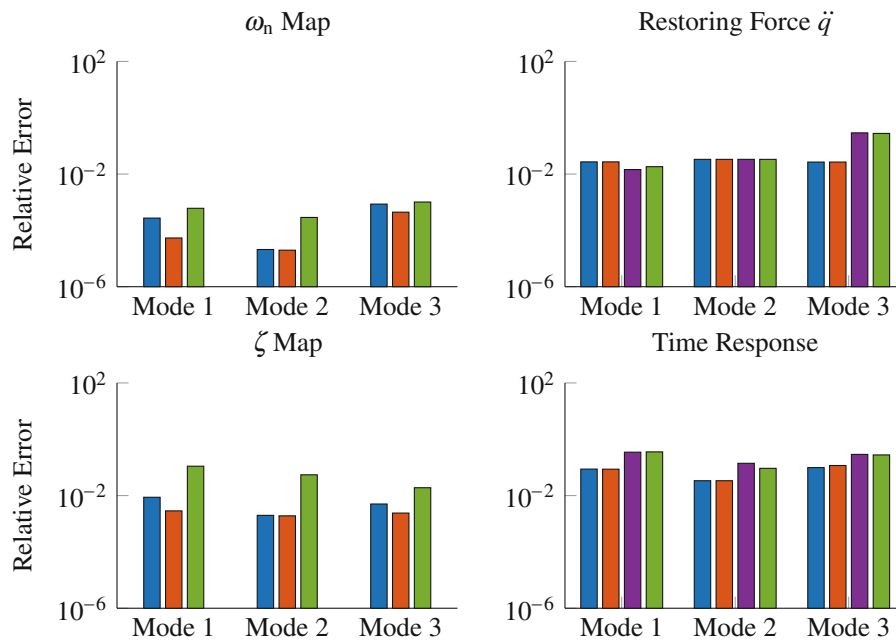


Fig. 7.14 Error analysis for the symmetric 3DOF system with a cubic spring non-linearity: MMM – polynomial (■), MMM – spline (■), RFS – single (■), RFS – combined (■)

7.4.2.1 Cubic Spring Non-linearity

The system was first simulated with the same cubic spring non-linearity from the 2DOF system. The modal maps are shown in Fig. 7.13 and the errors in Fig. 7.14. It can be seen from the modal maps in Fig. 7.13 that as expected, mode 2 is linear with constant modal properties, whilst modes 1 & 3 are coupled. The natural frequencies maps from both approaches match the experimental data very well. However, as was found with the 2DOF system, the damping from RFS displays much worse agreement with the data than the MMM method. This is also reflected in the error metrics in Fig. 7.14. As before, the error in the restoring forces are lower from the RFS method. When it comes to the time response, MMM has a slightly lower error

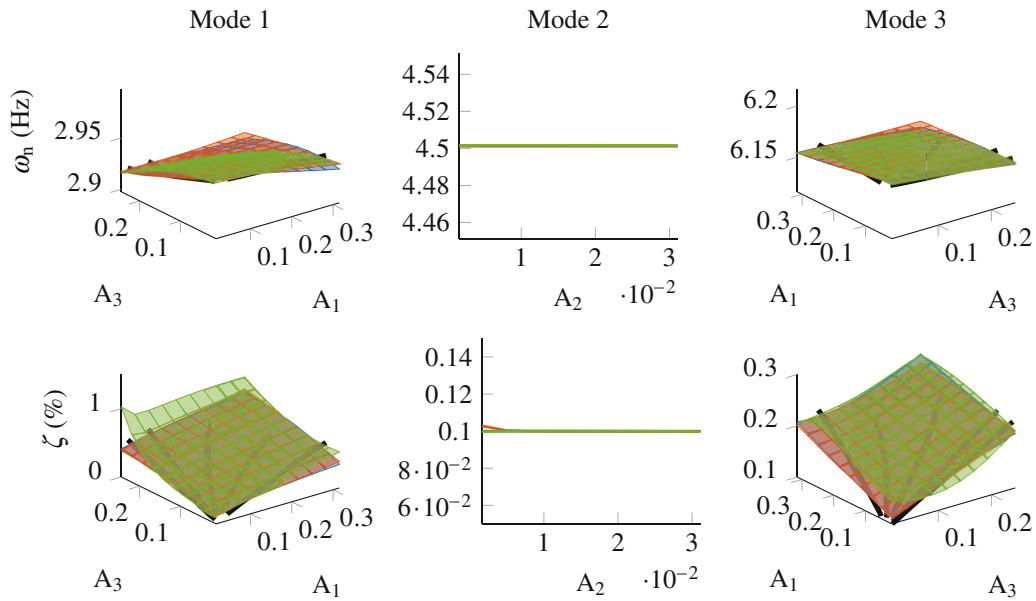


Fig. 7.15 Multi-modal maps for the symmetric 3DOF system with an Iwan element: MMM – polynomial (—), MMM – spline (—), RFS – combined (—)

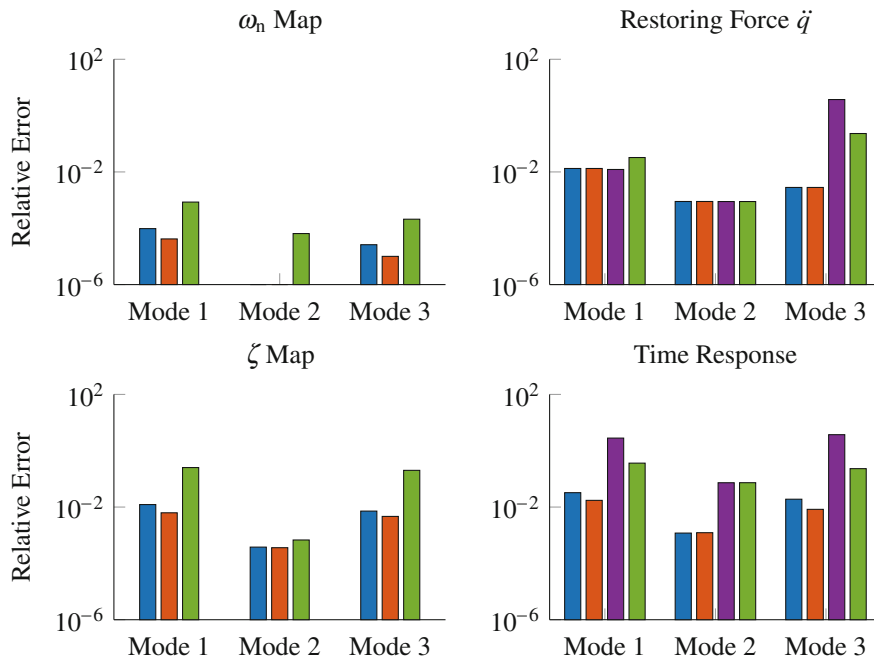


Fig. 7.16 Error analysis for the symmetric 3DOF system with an Iwan element: MMM – polynomial (—), MMM – spline (—), RFS – single (—), RFS – Combined (—)

than RFS, but both approaches appear to have captured the coupling reasonably well. Within each method, the spline and polynomial variants of MMM, and the single and combined variants of RFS perform equally well.

7.4.2.2 Iwan Element

The non-linearity was now replaced with an Iwan element, with the same parameters as Table 7.3. The modal maps are shown in Fig. 7.15 and the errors in Fig. 7.16. The modal maps in Fig. 7.15 show a very similar trend to the 2DOF system with an Iwan element Fig. 7.11; the data is matched reasonably well by both approaches, but the RFS surface is slightly offset. The

spline fit is now able to better approximate the surface than the polynomial within the MMM method. The restoring force error in Fig. 7.16 now show MMM and RFS to be equally well performing for the first two modes, and MMM performs better for mode 3. Similar trends were also found for the asymmetric 2DOF system. When it comes to the error in the time response, the MMM method is now significantly better than the RFS method. The spline MMM method has a slightly lower error than the polynomial which is consistent with the reduced error in the modal properties. The opposite was observed for the asymmetric 2DOF system. The combined RFS variant now has a much lower time response and restoring force error than the single variant, indicating that using more data is preventing over-fitting.

7.5 Conclusions

1. It was demonstrated that the concept of backbone curves can be extended to the case where there is modal coupling by adding an extra dimension, thereby creating a multi-modal map. This provided a good fit to the instantaneous frequency and damping. This works well for smooth non-linearities, but the relative error is higher when there is a discontinuous non-linearity. This approach warrants further investigation.
2. An averaging-based method for using the multi-modal maps to compute the time domain response was presented and the resulting time histories were found to match the original data well.
3. The RFS method can be extended to the case with modal coupling by including terms involving both modes in the functional form. This was found to generally match the natural frequency very well, but the damping was more difficult. The error in the predicted time response was generally higher than from the modal map approach, but it was slightly more robust when the non-linearity was non-smooth so still warrants further investigation.
4. A Harmonic Balance-based approach for computing the multi-modal maps directly from coupled modal models was presented. The results were found to match those computed from time integration and applying the Hilbert transform. This can be a useful visualisation tool for verifying models identified from RFS or otherwise.
5. The methods need to be extended to the case where more than 2 modes are coupled. This will make the modal maps more difficult to visualise. In doing so, it may be helpful to devise a means to identify which modes are coupled so attention can be paid to the appropriate pairs or sets of modes.
6. It may be interesting to investigate different functional forms for both the modal-map and restoring force based approaches. This may allow systems with discontinuities to be better captured.

References

1. Roettgen, D.R., Allen, M.S.: Nonlinear characterization of a bolted, industrial structure using a modal framework. *Mech. Syst. Signal Process.* **84**(Part B), 152–170 (2017). Recent advances in nonlinear system identification
2. Deane, B.J., Allen, M.S., Starr, M.J., Segalman, D.J., Sumali, H.: Application of viscous and Iwan modal damping models to experimental measurements from bolted structures. *J. Vib. Acoust.* **137**, 021012–021012–12 (2015)
3. Lacayo, R.M., Deane, B.J., Allen, M.S.: A numerical study on the limitations of modal Iwan models for impulsive excitations. *J. Sound Vib.* **390**, 118–140 (2017)
4. Kerschen, G., Worden, K., Vakakis, A.F., Golinval, J.-C.: Past, present and future of nonlinear system identification in structural dynamics. *Mech. Syst. Signal Process.* **20**(3), 505–592 (2006)
5. Feldman, M.: Non-linear system vibration analysis using Hilbert transform–I. Free vibration analysis method ‘Freevib’. *Mech. Syst. Signal Process.* **8**, 119–127 (1994)
6. Mayes, R.L., Pacini, B.R., Roettgen, D.R.: A Modal Model to Simulate Typical Structural Dynamic Nonlinearity, pp. 57–76, Springer, Cham (2016)
7. Do, N., Ferri, A.A.: Energy transfer and dissipation in a three-degree-of-freedom system with stiction friction. *ASME Appl. Mech. Div. Pub.* **256**, 195–204 (2005)
8. Festjens, H., Chevallier, G., Dion, J.: Nonlinear model order reduction of jointed structures for dynamic analysis. *J. Sound Vib.* **333**(7), 2100–2113 (2014)
9. Segalman, D.J.: A four-parameter Iwan model for lap-type joints. *J. Appl. Mech.* **72**(5), 752–760 (2005)
10. D’Errico, J.: Surface fitting using gridfit. <http://uk.mathworks.com/matlabcentral/fileexchange/8998-surface-fitting-using-gridfit> [Online; Accessed: 22 July 2017]
11. Bogoliubov, N.N., Mitropolski, Y.A.: *Asymptotic Methods in the Theory of Non-linear Oscillations*. International Monographs on Advanced Mathematics and Physics, 1st edn. Gordon and Breach, New York (1961)
12. Gelb, A., Vander Velde, W.: *Multiple-Input Describing Functions and Nonlinear System Design*. McGraw-Hill Electronic Sciences Series. McGraw-Hill, New York (1968)
13. Guskov, M., Thouvez, F.: Harmonic balance-based approach for quasi-periodic motions and stability analysis. *J. Vib. Acoust.* **134**, 031003 (2012)

Chapter 8

Performance of Nonlinear Modal Model in Predicting Complex Bilinear Stiffness



Benjamin R. Pacini, Wil A. Holzmann, and Randall L. Mayes

Abstract Several recent studies (Mayes, R.L., Pacini, B.R., Roettgen, D.R.: A modal model to simulate typical structural dynamics nonlinearity. In: Proceedings of the 34th International Modal Analysis Conference. Orlando, FL, (2016); Pacini, B.R., Mayes, R.L., Owens, B.C., Schultz, R.: Nonlinear finite element model updating, part I: experimental techniques and nonlinear modal model parameter extraction. In: Proceedings of the 35th international modal analysis conference, Garden Grove, CA, (2017)) have investigated predicting nonlinear structural vibration responses using modified modal models. In such models, a nonlinear element is added in parallel to the traditional linear spring and damping elements. This assumes that the mode shapes do not change with amplitude and there are no interactions between modal degrees of freedom. Previous studies have predominantly applied this method to idealistic structures. In this work, the nonlinear modal modeling technique is applied to a more realistic industrial aerospace structure which exhibits complex bilinear behavior. Linear natural frequencies, damping values, and mode shapes are first extracted from low level shaker testing. Subsequently, the structure is excited using high level tailored shaker inputs. The resulting response data are modally filtered and used to empirically derive the nonlinear elements which, together with their linear counterparts, comprise the nonlinear modal model. This model is then used in both modal and physical domain simulations. Comparisons to measured data are made and the performance of the nonlinear modal model to predict this complex bilinear behavior is discussed.

Keywords Nonlinear System Identification · Nonlinear Simulation · Bilinear Stiffness · Modal Model · Restoring Force Surface

Nomenclature

c	Damping coefficient
\mathbf{c}	Vector of nonlinear coefficients
f	Frequency in cycles/sec
$f_{d,nl}$	Nonlinear damping force
f_q	Modal excitation force
\mathbf{f}_{qrfs}	Vector of nonlinear restoring forces, time domain
\mathbf{F}_{qrfs}	Vector of nonlinear restoring forces, frequency domain
$f_{rfs,nl}$	Nonlinear restoring force
$f_{s,nl}$	Nonlinear stiffness force
\mathbf{H}	Frequency response function matrix
j	Imaginary number variable

Sandia National Laboratories is a multimission laboratory managed and operated by National Technology and Engineering Solutions of Sandia, LLC., a wholly owned subsidiary of Honeywell International, Inc., for the U.S. Department of Energy, National Nuclear Security Administration under contract DE-NA-0003525.

Notice: This manuscript has been authored by National Technology and Engineering Solutions of Sandia, LLC. under Contract No. DE-NA0003525 with the U.S. Department of Energy/National Nuclear Security Administration. The United States Government retains and the publisher, by accepting the article for publication, acknowledges that the United States Government retains a non-exclusive, paid-up, irrevocable, world-wide license to publish or reproduce the published form of this manuscript, or allow others to do so, for United States Government purposes.

B. R. Pacini (✉) · W. A. Holzmann · R. L. Mayes
Structural Dynamics Department, Sandia National Laboratories, Albuquerque, NM, USA
e-mail: brpacin@sandia.gov; waholzm@sandia.gov; rlmayes@sandia.gov

k	Stiffness coefficient
\mathbf{p}	Matrix of modal responses, time domain
\mathbf{P}	Matrix of modal responses, frequency domain
q	Modal degree of freedom
t	Time
x	Physical displacement degree of freedom
ζ	Modal damping ratio
ω	Frequency in radians per second
φ_{dp}	Drive point mode shape value
$\overline{\Psi}$	Modal filter vector
$+$	Moore-Penrose pseudo-inverse of a matrix

8.1 Introduction and Motivation

Nonlinear models are becoming increasingly popular in the field of structural dynamics. Two main methods to capture nonlinearities are: local physical modeling and pseudo-modal modeling. The former relies on a description of each source of nonlinearity and are typically computationally expensive because of the tiny scales required to model the local physics. Experimentally identifying each model parameter associated with each nonlinear source can be prohibitively difficult especially for complicated structures with many interfaces of varying types (e.g. bolted joints combined with continuous press-fit type contact) and materials with complex behavior. On the other hand, the pseudo-modal modeling approach captures nonlinearity on a mode-by-mode basis. For each modal degree of freedom (DOF), the many complex sources of nonlinear response can be modeled using a single nonlinear spring and single nonlinear damper in parallel with their corresponding linear elements. This method is computationally inexpensive and recent studies have demonstrated its successful implementation on mildly complicated structures where nonlinear model parameters were experimentally identified [1, 2]. The pseudo-modal method assumes that mode shapes do not change nor do modes interact, and works best for structures whose responses are weakly nonlinear in stiffness (modal frequency change of a few percent) but can be severely nonlinear in damping (hundreds of percent change in damping ratio).

This work demonstrates the performance of the pseudo-modal approach in characterizing the nonlinear properties of a joint of interest within a test article. The test article and fixture were designed to generate the assembled fundamental bending and axial modes in order to study the nonlinear characteristics of a critical joint. The study is on-going and only information regarding the first bending mode is presented here. Testing showed this mode exhibits complex bilinear behavior in the joint of interest, certain aspects of which the pseudo-modal model approach was unable to capture.

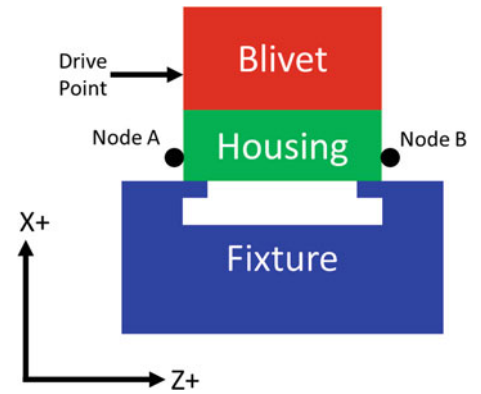
The methodology used for this work follows that of [2], which used the pseudo-modal model to characterize the nonlinearities of a mildly complex structure via the Restoring Force Surface (RFS) technique. The approach begins with a standard modal test where low input forces are utilized to minimize the nonlinear response in order to obtain linear springs and dampers for each mode. Nonlinear elements for the first bending mode are then connected in parallel with their linear counterparts to the associated modal mass. The parameters for these nonlinear elements are identified from an experiment which used a windowed sinusoid to excite only the first bending mode of the structure to a large response amplitude. The data from this experiment is transformed to a single modal single degree of freedom (SDOF) response via modal filtering. The nonlinear elements are then realized by fitting low order polynomials for stiffness and damping as a function of modal response amplitude.

The test article, linear modal testing and the high-level excitation used for nonlinear parameter extraction are discussed in Sect. 8.2. The modal filtering approach utilized is described in Sect. 8.3. Section 8.4 presents the nonlinear parameter identification technique and the validation of extracted nonlinear parameters. The nonlinear mode of interest is combined with the remaining elastic and rigid body modes to predict the physical domain responses in Sect. 8.5. Observations are discussed in Sect. 8.6 followed by conclusions in Sect. 8.7.

8.2 Experiments

8.2.1 Test Hardware Description

The test article for this work consisted of three main components: a fixture representing the next level assembly, thin-walled housing, and a solid metal object, referred to herein as a blivet. The blivet was welded to the top of the thin-walled housing.

Fig. 8.1 Illustration of test article**Table 8.1** Linear modal analysis results^a

Mode	Description	Frequency (Hz)	Damping (%)
7	1st bend of assembly in Z	680.7	0.088
8	1st bend of assembly in Y	1011.3	0.065
9	Inner wall bending	1267.8	0.039
10	Axial mode	1293.3	0.058

^aRigid body modes not shown

This assembly was bolted to a flange built into the fixture to complete the test article, see Fig. 8.1 for a representation of the cross-section. Note that the flange upon which the housing was mounted was designed to exactly match the geometry of this interface seen in the next level assembly. This provides identical interface physics of the joint. The thin-walled housing (an actual aerospace component) had an asymmetric footprint with respect to the mounting bolts. The entire assembly was instrumented to adequately observe modes below 1600 Hz; measurements from nodes A and B are selected and shown in Sect. 8.5 when comparing simulation results with measured data in the physical domain.

8.2.2 Linear Modal Test

This section describes the modal testing conducted on the test article using low excitation forces to minimize the nonlinear response and extract the linear modal model. Low level burst random input with a modal shaker was used to excite the structure. Modal analysis was performed with the Synthesize Modes and Correlate (SMAC) algorithm [3]. Extracted natural frequencies and damping values for each mode are given in Table 8.1.

To judge the adequacy of the modal fit, frequency response functions (FRFs) were synthesized using the extracted modal parameters. A Complex Mode Indicator Function (CMIF) computed from the synthesized FRFs was compared against that calculated from the experimental FRFs, see Fig. 8.2.

8.2.3 High Level Shaker Testing

The first bending mode of the assembly in the Z direction (mode 7) from Table 8.1 is the subject of the nonlinear study for this work. Achieving a pure SDOF response is critical for the pseudo-modal modeling approach. Additionally, nonlinear influences are typically greater at larger response amplitudes. Therefore, the windowed sinusoidal modal shaker input described in [2] is utilized to excite the test article to the highest response amplitudes achievable. The signal is a sine wave at a target frequency that was windowed by a Blackman-Harris window [4]. Note that in [2] a triangular window was used, however the Blackman-Harris window results in much smaller side-lobes. The spectrum of this signal has a main lobe centered at the target frequency (selected as the natural frequency of the target mode) whose width is inversely proportional to the rise time of the window in the time domain (see Fig. 8.3). This approach excites the test article by focusing as much energy as possible near the resonance of interest.

Note that due to the very small damping of the target mode, a large force dropout at the mode's natural frequency occurred. Therefore, the correction procedure detailed in [2] was implemented. This involves running an initial experiment with the shaker input voltage defined by the windowed sinusoid as mentioned above. The transfer function between the resulting measured force and shaker voltage is calculated and used in conjunction with a desired force spectrum to create a corrected

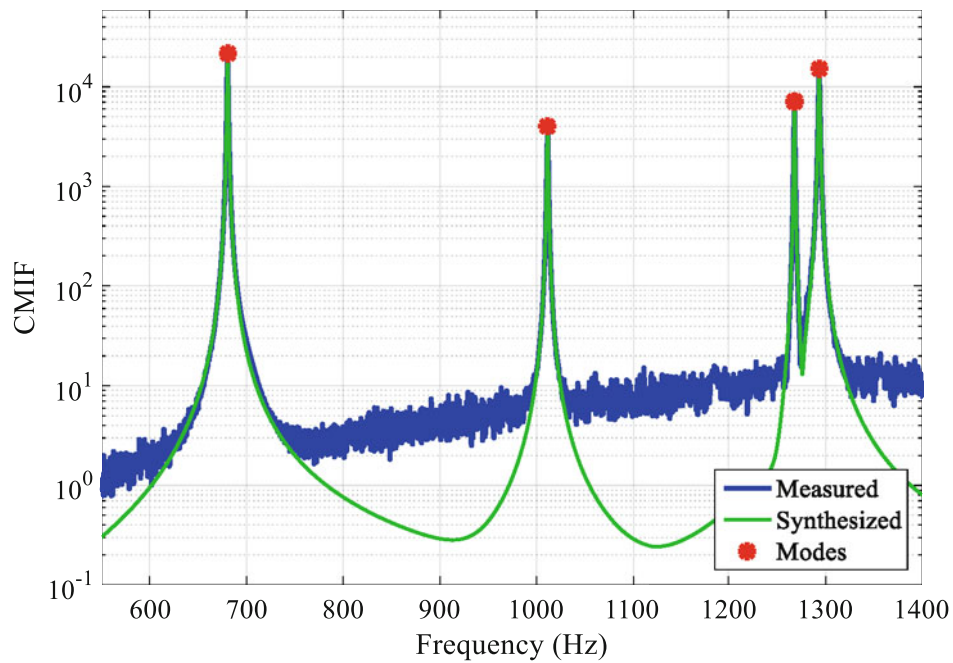


Fig. 8.2 Measured vs synthesized CMIF for linear modal test

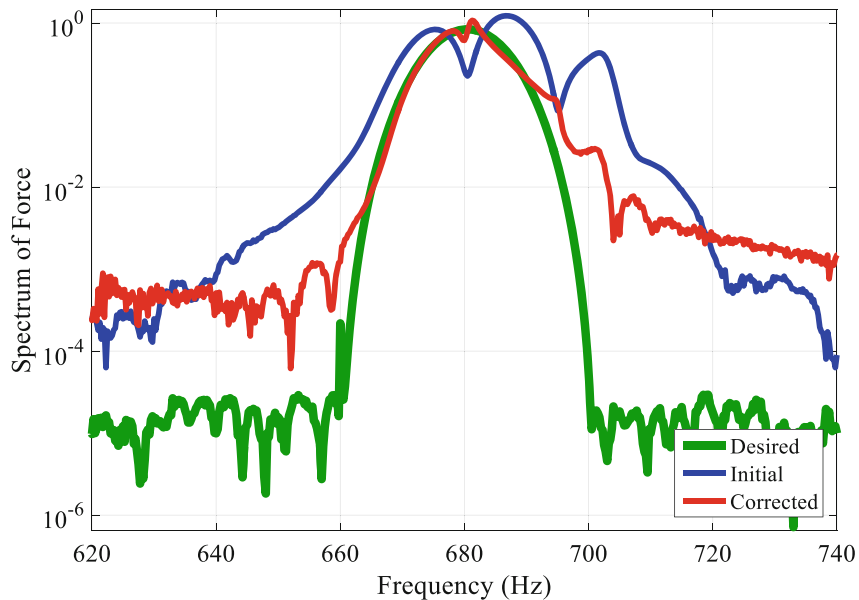


Fig. 8.3 Force input signals for nonlinear testing

voltage signal. A second experiment is then conducted with this corrected shaker input voltage signal which produces an improved force spectrum that has a reduced dropout at resonance. Figure 8.3 compares the force signals resulting from the initial and corrected shaker input signals. Note that even after the correction there is still a slight force dropout, however this is acceptable since the main goal of this process is to maximize the force applied at resonance. Thus, a perfect match to the desired force profile is not necessary. The data measured during the second experiment were modally filtered (see Sect. 8.3) and the resulting SDOF response was used to extract the nonlinear parameters for the bending mode of interest (see Sect. 8.4).

Note that the bandwidth of interest was below 1600 Hz, but data were collected to 6400 Hz to achieve high time resolution of the nonlinear response. However, since the instrumentation was selected to only observe modes below 1600 Hz, the data measured during the high-level shaker tests were first low-pass filtered to 1800 Hz prior to modal filtering and nonlinear model parameter fitting.

8.3 Modal Filtering

A critical step in the development of a nonlinear pseudo-modal model is the extraction of a single mode's response from measured data. This is accomplished using a modal filter. Previous work [1] evaluated several different types of modal filters and, of the options explored, found the modal filter embedded in the SMAC algorithm [5] to generally perform better than others at isolating target modes. Thus, the SMAC modal filter was used in this work. For brevity, only a brief derivation of the SMAC modal filter is given here, see [1] for further details.

A modal filter is a vector of weights, $\bar{\Psi}$, which transforms measurements in physical space to the modal domain as in the following:

$$\bar{\Psi}^T \bar{\mathbf{x}} = q_i \quad (8.1)$$

where $\bar{\mathbf{x}}$ is a column vector containing measured responses and q_i is the response of mode i . In the SMAC modal filter, (8.1) is divided by the excitation force and transformed into the frequency domain to produce FRFs. $\bar{\Psi}$ can then be solved as shown in (8.2)

$$\bar{\Psi} = \mathbf{H}_x^T + \bar{\mathbf{H}}_{qi} \quad (8.2)$$

where \mathbf{H}_x is a matrix of measured FRFs with columns for every frequency line and rows for every measured response DOF and $\bar{\mathbf{H}}_{qi}$ is an analytically calculated modal SDOF FRF of the following form

$$\bar{\mathbf{H}}_{qi}(\omega) = \frac{\varphi_{dp,i}}{\omega_{ni}^2 - \omega^2 + j2\zeta_i\omega_{ni}\omega} \quad (8.3)$$

where ω_{ni} , ζ_i , and $\varphi_{dp,i}$ are the natural frequency, damping ratio, and drive point shape value, respectively, for the i^{th} mode. For this work, the ω_{ni} , ζ_i , and $\varphi_{dp,i}$ values for the modal filter were those extracted during the linear modal test described in the Sect. 8.2.2.

8.4 Nonlinear Model Form and Extraction of Nonlinear Parameters

The nonlinear modeling method follows closely to that applied in [2] which used the Restoring Force Surface (RFS) with cubic polynomials for both stiffness and damping. However, for this work, restoring force plots will be used to determine the model form. A brief description of this method is given here. RFS is based on Newton's Second Law, shown in Eq. (8.4) in the modal domain for a SDOF system.

$$\ddot{q}(t) + c_0\dot{q}(t) + f_{d,nl}(\dot{q}(t)) + k_0q(t) + f_{s,nl}(q(t)) = f_q(t) \quad (8.4)$$

where $f_{d,nl}$ and $f_{s,nl}$ are the nonlinear damping and stiffness forces, respectively, and c_0 and k_0 are the linear damping and stiffness coefficients that are known from the linear modal testing. In order to determine the form of the nonlinear model, the nonlinear restoring force is calculated by rearranging (8.4) to

$$f_{rfs,nl}(q(t), \dot{q}(t)) = f_q(t) - \ddot{q}(t) - c_0\dot{q}(t) - k_0q(t) \quad (8.5)$$

Plotting $f_{rfs,nl}$ versus q will give the form of the stiffness nonlinearity and likewise for damping if $f_{rfs,nl}$ is plotted versus \dot{q} . Figure 8.4 shows these two plots which indicate that the nonlinear forms are dominated by a quadratic term. Note that these figures were created by only keeping the data at the peak values of q and \dot{q} , respectively, otherwise these plots would resemble spirals from which it is much more difficult to deduce the nonlinear model form. These figures represent a starting point for choosing model form. It is desired to have the lowest polynomial order possible while still obtaining accurate simulation results. For this work, quadratic and cubic damping and stiffness were originally chosen; see Fig. 8.4 for fits of these polynomials to the measured nonlinear restoring force. The cubic fit provides only a marginal improvement over the quadratic fit.

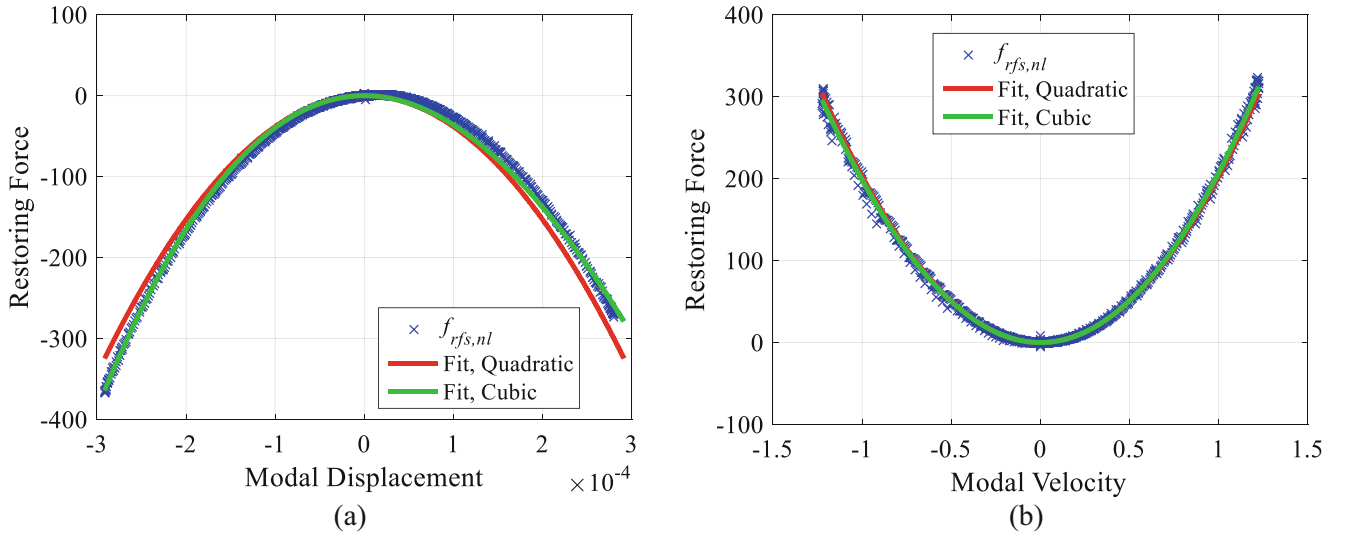


Fig. 8.4 Nonlinear restoring force plots for (a) stiffness and (b) damping

While Fig. 8.4 provides an initial starting point to determine the nonlinear model form, the following process was used to compute the final nonlinear model parameters. With an assumed nonlinear model form, Eq. (8.5) can be further parsed to isolate the nonlinear coefficients to solve for them in a least-squares sense. As an example, if cubic damping and stiffness are assumed to be the nonlinear model forms, Eq. (8.5) becomes

$$\mathbf{p}\mathbf{c} = \mathbf{f}_{\text{qrf}s} \quad (8.6)$$

where

$$\mathbf{p} = \begin{bmatrix} \dot{q}\dot{q}|_{t=t_0} & \dot{q}^3|_{t=t_0} & q\dot{q}|_{t=t_0} & q^3|_{t=t_0} \\ \dot{q}\dot{q}|_{t=t_1} & \dot{q}^3|_{t=t_1} & q\dot{q}|_{t=t_1} & q^3|_{t=t_1} \\ \vdots & \vdots & \vdots & \vdots \\ \dot{q}\dot{q}|_{t=t_n} & \dot{q}^3|_{t=t_n} & q\dot{q}|_{t=t_n} & q^3|_{t=t_n} \end{bmatrix} \quad (8.7)$$

$$\mathbf{c} = \begin{bmatrix} c_1 \\ c_2 \\ k_1 \\ k_2 \end{bmatrix} \quad (8.8)$$

$$\mathbf{f}_{\text{qrf}s} = \begin{bmatrix} f_q - \ddot{q} - c_0\dot{q} - k_0q|_{t=t_0} \\ f_q - \ddot{q} - c_0\dot{q} - k_0q|_{t=t_1} \\ \vdots \\ f_q - \ddot{q} - c_0\dot{q} - k_0q|_{t=t_n} \end{bmatrix} \quad (8.9)$$

Each row of \mathbf{p} and $\mathbf{f}_{\text{qrf}s}$ correspond to a single time sample of the measured time history. Additionally, experience has shown that (8.6) gives better results when solved in the frequency domain. This involves taking the one-sided FFT of each of the columns of \mathbf{p} and $\mathbf{f}_{\text{qrf}s}$, denoted here as \mathbf{P} and $\mathbf{F}_{\text{qrf}s}$, respectively. To ensure that real coefficients are obtained, the real and imaginary parts of \mathbf{P} and $\mathbf{F}_{\text{qrf}s}$ are stacked, so (8.6) becomes

$$\begin{bmatrix} \text{real}(\mathbf{P}) \\ \text{imag}(\mathbf{P}) \end{bmatrix} \mathbf{c} = \begin{bmatrix} \text{real}(\mathbf{F}_{\text{qrf}s}) \\ \text{imag}(\mathbf{F}_{\text{qrf}s}) \end{bmatrix} \quad (8.10)$$

The nonlinear coefficients in \mathbf{c} are then solved for by pre-multiplying both sides of (8.10) by the pseudo inverse of the stacked \mathbf{P} :

$$\mathbf{c} = \begin{bmatrix} \text{real}(\mathbf{P}) \\ \text{imag}(\mathbf{P}) \end{bmatrix}^+ \begin{bmatrix} \text{real}(\mathbf{F}_{\text{qrfs}}) \\ \text{imag}(\mathbf{F}_{\text{qrfs}}) \end{bmatrix} \quad (8.11)$$

Note that the stacked \mathbf{P} are poorly scaled for inversion, so it is recommended that the columns be rescaled. In this work, each column was scaled by its RMS prior to computing the pseudo inverse. The coefficients must subsequently be divided by the root-mean-square (RMS) of the corresponding columns of the stacked \mathbf{P} in order to get the true coefficients. Equation (8.11) was solved for the target bending mode assuming many different nonlinear model forms. Each resulting nonlinear model was subsequently used to simulate the modal response to the measured modal input force. The final model form chosen was that which compared best to the measured modal response. While Fig. 8.4 indicates that cubic stiffness and damping appear to fit the measured $f_{rfs,nl}$ the best, it was determined through this series of simulations that quadratic stiffness and cubic damping resulted in a simulated modal response that matched the measured modal response the best and were thus selected as the final model form. The final extracted nonlinear parameters are: $k_I = -3.83\text{E}9$, $c_I = 206$, and $c_2 = 5$. Figures 8.5 and 8.6 shows the linear and nonlinear simulation responses overlaid with the measured data.

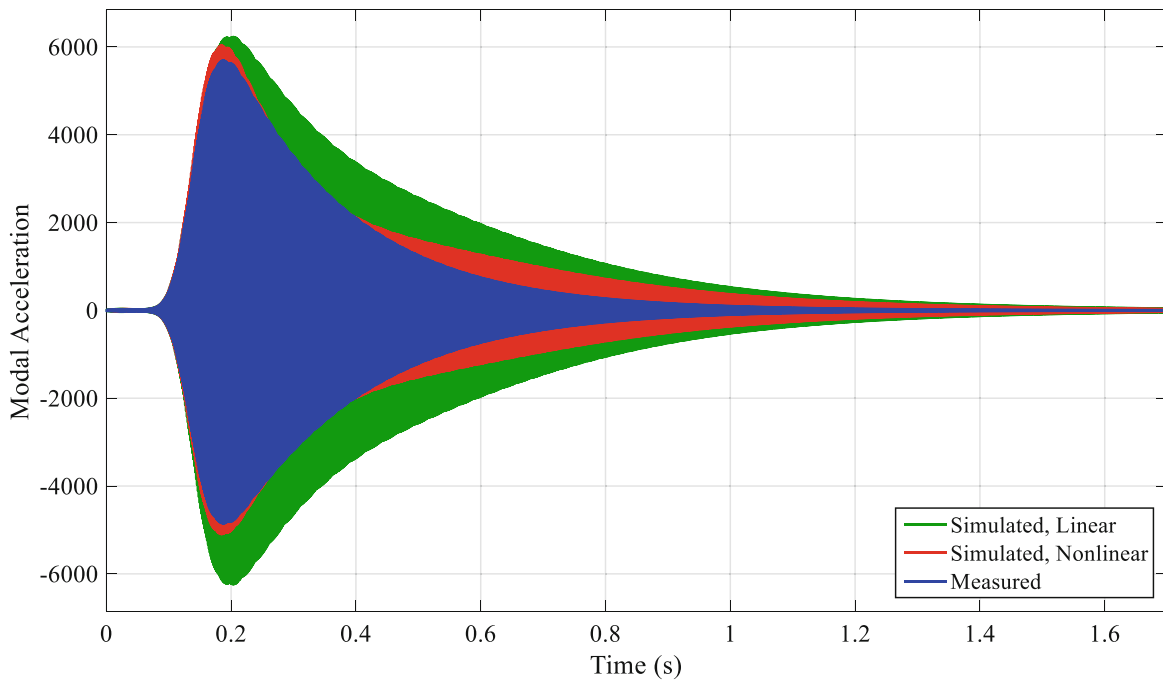
The nonlinear model appears to better match the damping of the measured data, especially after the peak response at approximately 0.2 s. Also Fig. 8.6 shows that the nonlinear model does capture the second harmonic whereas the linear does not. However, the frequency of the nonlinear model does not appear to be an appreciable improvement over that of the linear model, see Fig. 8.5b, c. Closer inspection of the measured time response of Fig. 8.5a shows that the measured amplitude of the positive oscillation is noticeably larger than that of the negative oscillation. The nonlinear model is able to replicate this trend as well. In the next section, the linear and nonlinear models of this mode will be used in conjunction with the rigid body modes and modal models of modes 8, 9 and 10 to calculate the response of the structure in the physical domain.

8.5 Comparison to Physical Domain Data

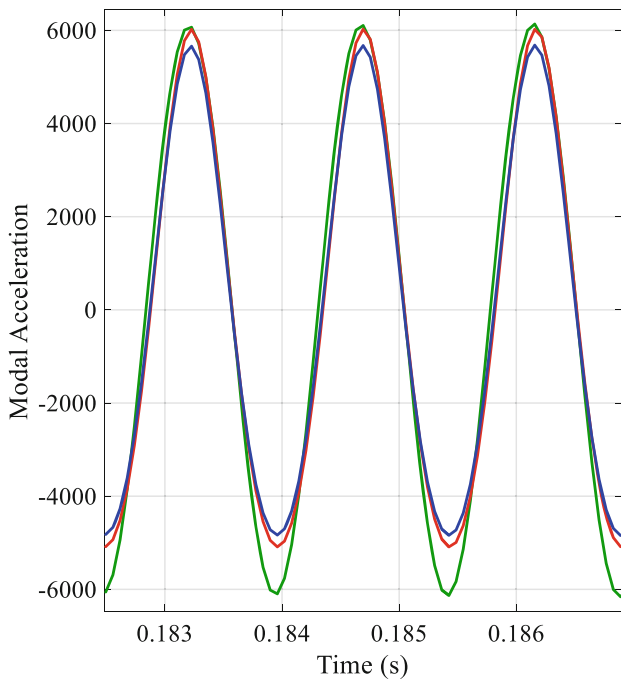
Comparing the measured modal frequency with that of the linear model from Figs. 8.5 and 8.6 indicates almost no stiffness nonlinearity of the test article. However, the measured time histories in the physical domain show significant nonlinear response, see Fig. 8.7. These are X-direction measurements from accelerometers located on opposite sides of the housing (nodes A and B, respectively from Fig. 8.1) and show a significant bilinear response; the period of one half cycle of oscillation is much shorter than that of the other half cycle. Note also that the response amplitude of the stiffer oscillation (shorter half period) is much larger than that of the softer oscillation (longer half period). Additionally, the stiff portion of the oscillation for node A is during the soft oscillation for node B and vice versa. The shape of the first bending mode shows the housing-blivet assembly rocking on the fixture where one side of the bottom face of the housing (e.g. node A) contacts the fixture while the other side (e.g. node B) separates. This could approximately be replicated by two physical nonlinear springs, one in the joint very near node A and one in the joint very near node B. Both springs are bilinear, much stiffer in compression than tension. Thus, considering Fig. 8.7 along with the mode shape, the stiff oscillation for a given node corresponds to when that side of the housing is in contact with the fixture and the soft oscillation occurs as that side of the housing separates from the fixture. Note that accelerations are shown and that displacement is 180° out of phase, so a positive acceleration corresponds to a negative displacement.

The half periods of the positive and negative oscillations for nodes A and B were used to compute the corresponding frequencies of each half oscillation. These are plotted in Fig. 8.8 along with the frequency associated with each complete oscillation. This figure shows that, although the frequencies associated with the positive and negative half-cycle oscillations are varying significantly, the frequency over one full cycle does not change appreciably. The significance of this will be discussed in Sect. 8.6.

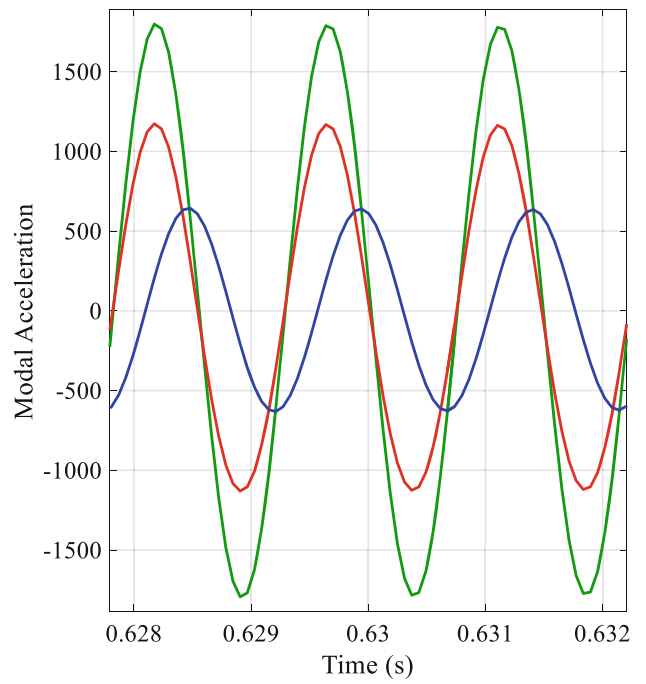
A pseudo-modal model was constructed with all ten modes (six rigid body modes, one nonlinear mode, and three linear) and a simulation was run using the high-level shaker input from Sect. 8.2.3. The responses of each mode were then transformed into the physical domain using the linear mode shape matrix. Figures 8.9, 8.10, 8.11 show the comparison between the results of this nonlinear simulation, linear model results, and the measured acceleration data for the drive point and nodes A and B, respectively. These figures show that the pseudo-modal model was not able to sufficiently capture the details of the physical response of the structure for each measured DOF. Figure 8.9 looks reasonable with some amplitude



(a)



(b)



(c)

Fig. 8.5 Mode 7 linear and nonlinear simulation results compared to measured response, time domain

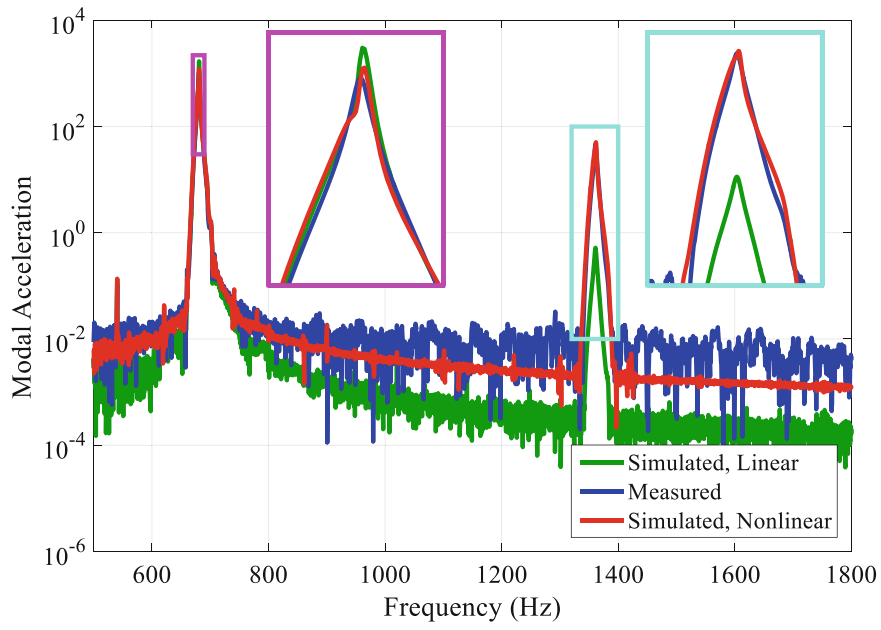


Fig. 8.6 Mode 7 linear and nonlinear simulation results compared to measured response, frequency domain

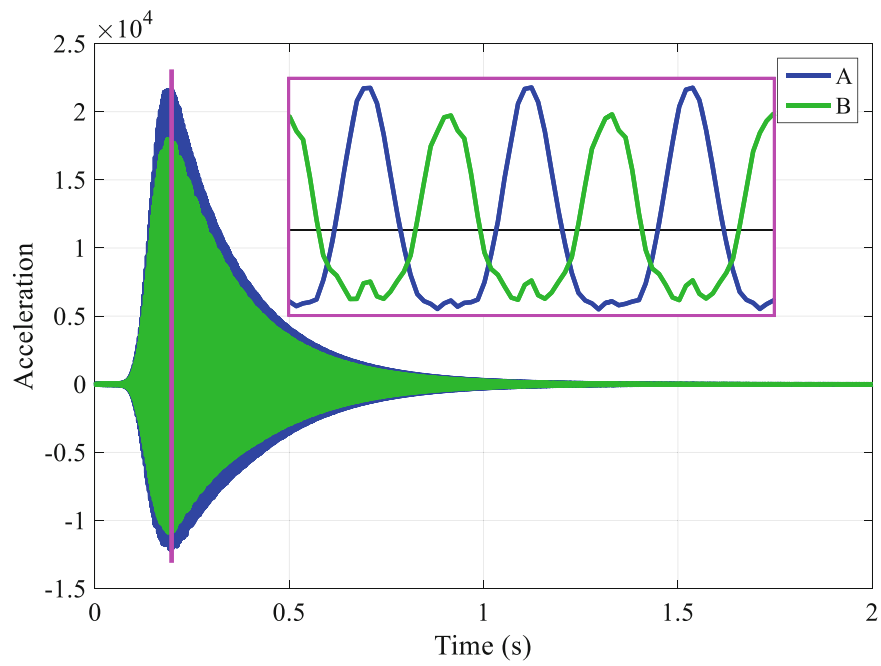


Fig. 8.7 Measured X-direction times responses of nodes A and B, zero ordinate indicated in zoomed plot

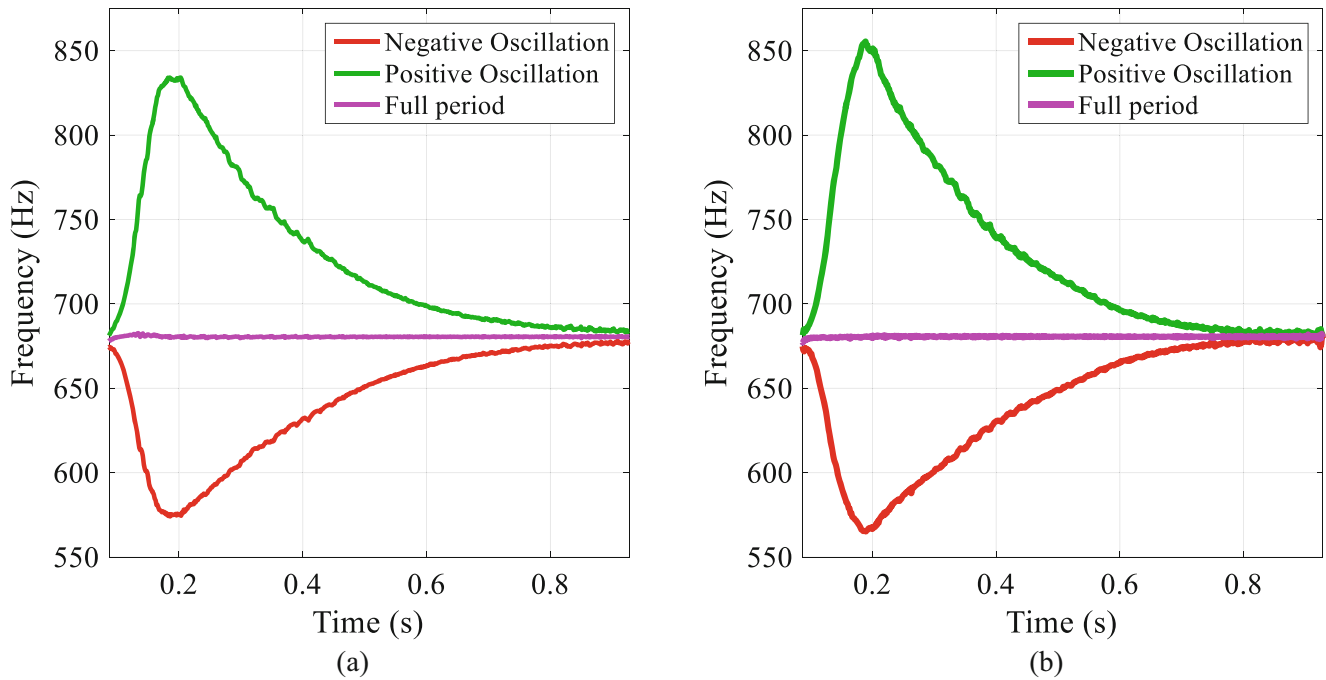


Fig. 8.8 Frequencies associated with half periods of positive and negative oscillations and full cycles for (a) node A and (b) node B

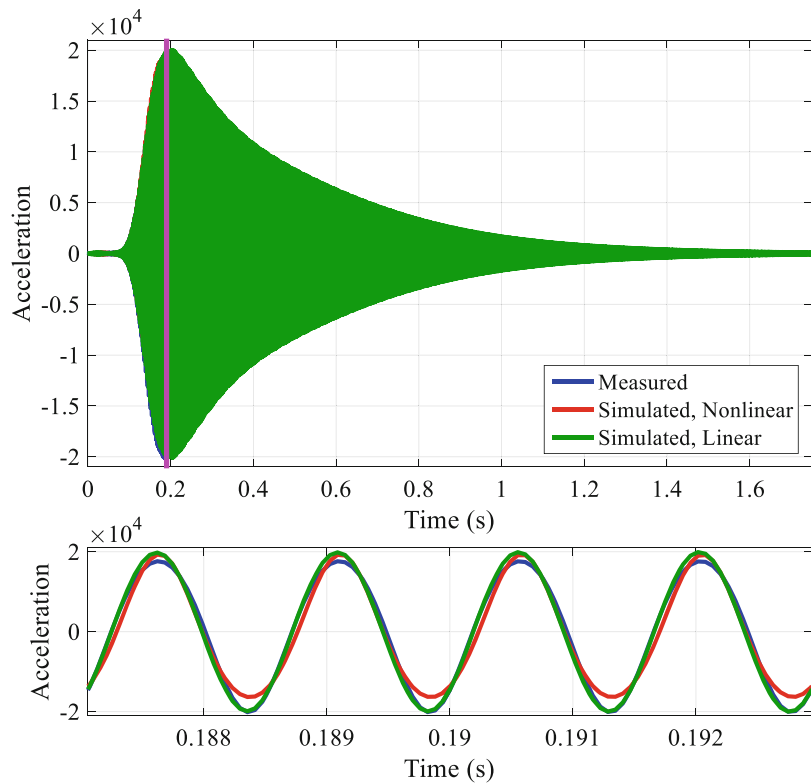


Fig. 8.9 Comparison of nonlinear and linear simulation results with measured data, drive point

differences. Figure 8.10 shows that positive oscillations of the measured data correspond to the stiff portion of the locally bilinear spring closest to this DOF, but the nonlinear model shows the opposite: the negative oscillation is associated with the stiff portion of the bilinearity. Figure 8.11 shows that the nonlinear model appears to have more closely matched the amplitude, but not the distortion in the amplitude on the negative half cycle.

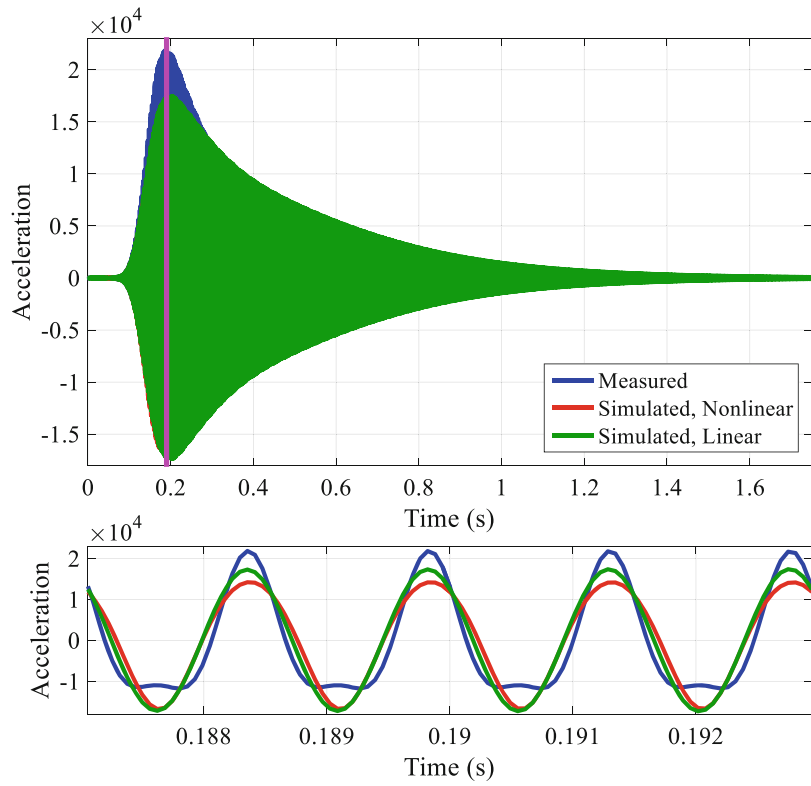


Fig. 8.10 Comparison of nonlinear and linear simulation results with measured data, node A X-direction

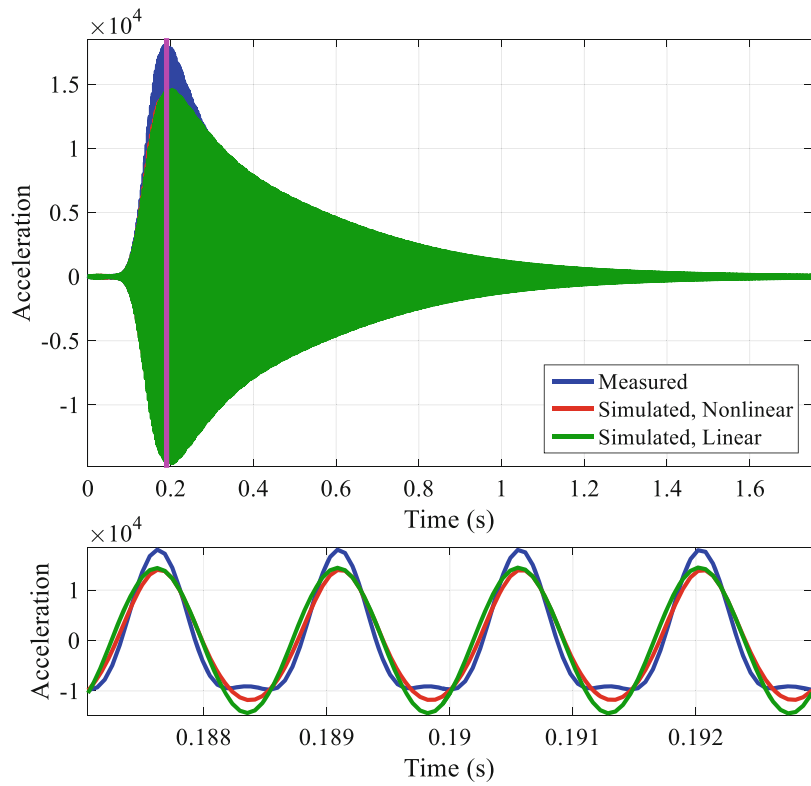


Fig. 8.11 Comparison of nonlinear and linear simulation results with measured data, node B X-direction

8.6 Discussion

It appears that when the modal filter was applied to the measured data, the frequency associated with the overall period of one cycle (680 Hz) was maintained, but the large disparities in stiffnesses associated with the positive and negative oscillations were not. Since the period of one cycle in the measured data does not significantly change (Fig. 8.8), the stiffness nonlinearity appeared to be slight in the modally filtered data. Because the modal filter operates on a real modes assumption, the measured modally filtered data would not be able to reflect the bilinear phasing where one part of the structure is in the stiff portion of the bilinear oscillation while another is in its soft portion. Moreover, a single modal nonlinear spring cannot represent the details of the physical response of two physical bilinear springs acting nearly 180 degrees out of phase with each other. It should be noted, a pseudo-modal model with bilinear stiffness was created, but the resulting response did not match the measured data well and as such was not used in this work. The poor performance of the bilinear model is attributed to the modal filter eliminating the majority of the bilinear stiffness seen in the measured data.

The modal filtered data did reflect some of the asymmetry in amplitude between the negative and positive oscillations. The resulting nonlinear model captured this behavior primarily with nonlinear damping terms instead of stiffness. This is believed to be an inappropriate assignment of nonlinearity; while there is most likely damping nonlinearity, the majority of the amplitude difference between positive and negative oscillations is believed to be due to their corresponding stiffness disparities [6].

8.7 Conclusions

A pseudo-modal model was created to study the nonlinear characteristics of a critical joint within a test article. Using previously developed methods, the restoring force surface technique was used to create amplitude dependent stiffness and damping polynomials. While the simulated modal response using this nonlinear model matched the modally filtered measured data, it was unable to capture the detailed distortions and one-sided amplitudes in the measurements in the physical domain near localized physical nonlinearities. At any given moment in time, some portions of the structure will be in the stiff region of the bilinearity while others are in the soft region. The modal filter appeared to keep the overall period of oscillation (which remained constant) and the asymmetry about the origin in peak response amplitude, but was unable to maintain this phasing in the bilinearity. Thus, the nonlinear model extracted from this modally filtered data had a relatively weak stiffness term and a large quadratic damping term which created the asymmetry in response amplitude.

There are many types of nonlinearity, and one must consider whether an assumed nonlinear model form can meet the objectives of the analysis. For example, the nonlinear pseudo-modal model identified here may be adequate to provide frequency-domain, qualification acceleration random environment specifications since they usually include some conservatism. It even captures response of the harmonics of the mode. However if local physical response with distortions were needed, one might need a more complex nonlinear modeling approach. At the least, this analysis has provided insight to a nonlinear effect that we have never observed in experimental data before.

References

1. Mayes, R.L., Pacini, B.R., Roettgen, D.R.: A modal model to simulate typical structural dynamics nonlinearity. In: Proceedings of the 34th International Modal Analysis Conference. Orlando, FL (2016)
2. Pacini, B.R., Mayes, R.L., Owens, B.C., Schultz, R.: Nonlinear finite element model updating, part I: experimental techniques and nonlinear modal model parameter extraction. In: Proceedings of the 35th international modal analysis conference, Garden Grove, CA (2017)
3. Hensley, D.P., Mayes, R.L.: Extending SMAC to multiple references. In: Proceedings of the 24th international modal analysis conference, (2006)
4. Harris, F.J.: On the use of windows for harmonic analysis with the discrete fourier transform. *Proc. IEEE*. **66**(1), 51–83 (1978)
5. Mayes, R.L., Johansen, D.D.: A modal parameter extraction algorithm using best-fit reciprocal vectors. In: Proceedings of the 16th International modal analysis conference, Santa Barbara, CA (1998)
6. Feldman, M.: Hilbert transform applications in mechanical vibration, pp. 241–244. Wiley, Chichester (2011)

Chapter 9

Low Order Nonlinear Dynamic Modelling of Fuel Supply Pipes



Alberto Sanchez and Christoph W. Schwingshackl

Abstract In industrial applications the vibration analysis mostly focuses on the main components, while accessories, such as pumps, electronics or pipe work are often neglected. This can lead to failures in these support systems, which can lead to performance reduction, shut down, or in the worst case catastrophe failure of the application due to secondary effects. One such accessory system is the fuel manifold of an aero engine, which delivers the kerosene to the fuel injectors. Previous experimental work has highlighted a strong nonlinear dynamic response of this setup, making an accurate prediction during the design process very challenging. In this study, a low order nonlinear modelling approach for fuel supply pipes, based on linear finite element and implicit nonlinear element analysis, is presented and its advantages and limitations are discussed.

Keywords Nonlinear model · Pipe modelling · Low order · Fuel supply · Accessories

9.1 Introduction

The modelling of the linear dynamic response of pipes is well established in the literature [1–3] but several experimental investigations demonstrated a strong underlying nonlinear dynamic behaviour [4, 5], which is regularly ignored during the analysis.

A fuel supply pipe assembly is typically formed of a pipe with several clips which are attached to some kind of support. Previous experimental results have shown [4] that the clips thereby are the main source of nonlinearity, which needs to be included in a model for an accurate response prediction. One potential approach is therefore an implicit nonlinear modelling technique, which condenses a complex nonlinear dynamic behaviour onto a simplified element and which can be found in multiple applications such as under platform dampers [6], or flanged joints [7, 8]. The alternative is an explicit modelling approach where a large amount of dedicated elements are used to replicate the physical behaviour of the component accurately in order to capture its nonlinear dynamic response. Explicit modelling has been successfully applied to engineering assemblies such as bladed disks [9] or bolted assemblies [10] where it has been proven to be accurate but computationally highly expensive.

Due to the potentially large number of nonlinearities in a fuel manifold assembly, an implicit, reduced order modelling approach will be considered in this study with the aim of obtaining a realistic prediction of the nonlinear dynamic behaviour of a fuel supply pipe assembly at an early design stage.

9.1.1 A Short Summary of the Experimental Evaluation

A set of experiments were conducted in [4] to identify the dynamic behaviour of a pipe assembly, and localise potential sources of nonlinearity. Only a very short summary of these results will be presented here to provide the necessary background for the modelling approach, but for more information on the experimental behaviour the readers is referred to the above reference.

A. Sanchez (✉) · C. W. Schwingshackl
Imperial College London, London, UK
e-mail: a.sanchez-pinilla@imperial.ac.uk

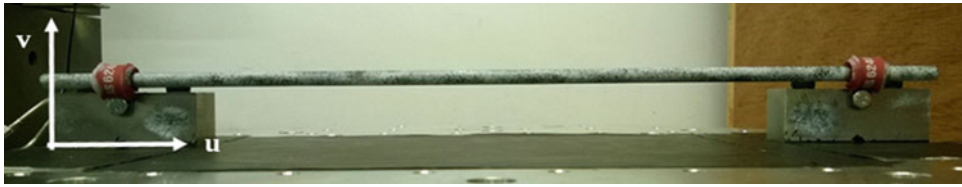


Fig. 9.1 Experiment set up (HADES)

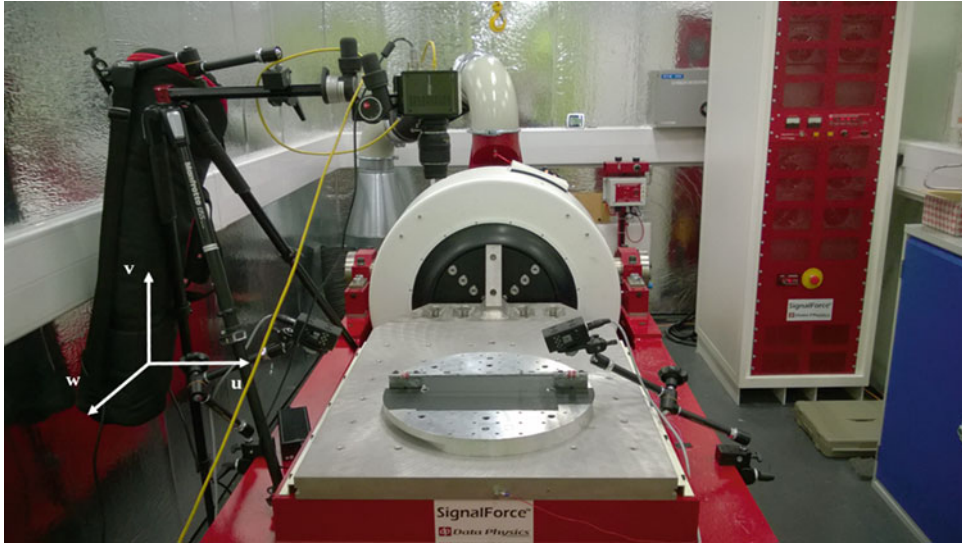


Fig. 9.2 Experiment set up (HADES)

9.1.1.1 Test Set Up

A 500 mm straight pipe was used for the tests, which was attached towards both ends via two clips to a rigid base (see Fig. 9.1), which in turn was bolted onto the slip table of the High Amplitude Dynamic Excitation System (HADES) which consists of a Data Physics Signal Force GW-V3544 shaker in Fig. 9.2.

Two different tests were conducted to extract obtain an understanding of the dynamic behaviour of the system and to provide the required data for the extraction of the relevant model parameters.

The 1st test performed was a roving hammer test (HT) along the pipe in the horizontal and vertical direction, with accelerometers mounted in both directions slightly off centre. The obtained low level excitation data was used to extract the baseline mode shapes, the background modal damping and the linear stiffness coefficients to provide reliable data for the updating of the underlying linear model of the assembly.

The 2nd test was performed using HADES, where the frequency response function of the pipe/clip assembly was obtained via a sine sweep in the horizontal direction (w in Fig. 9.2). For each sweep the base excitation was kept constant, and the assembly was tested at different levels of amplitude between 0.5 and 5 g (See Fig. 9.3). The aim of this test was to observe the evolution of the nonlinear behaviour introduced by the clips as the excitation levels increase, and hence being able to adjust the nonlinear stiffness and dashpot values accordingly in the model. Figure 9.3 shows a strong increase in damping with a small drop in resonance frequency of the system at higher amplitudes, indicating an amplitude dependent damping and stiffness behaviour. Based on some of the problems reported in the literature [4] for the validation tests of the nonlinear model the accelerometers were replaced with a Scanning Laser Doppler Vibrometer (SLDV) leading to a significantly improved repeatability of the tests. More details about all the conducted experiments and a thorough discussion of the results can be found in [4].

A thorough evaluation of the test data in [4] indicated, that the pipe itself behaved linearly, since it was far away from reaching geometric nonlinearity, whereas the clips were identified as the main source of nonlinearity, leading to the response in Fig. 9.3.

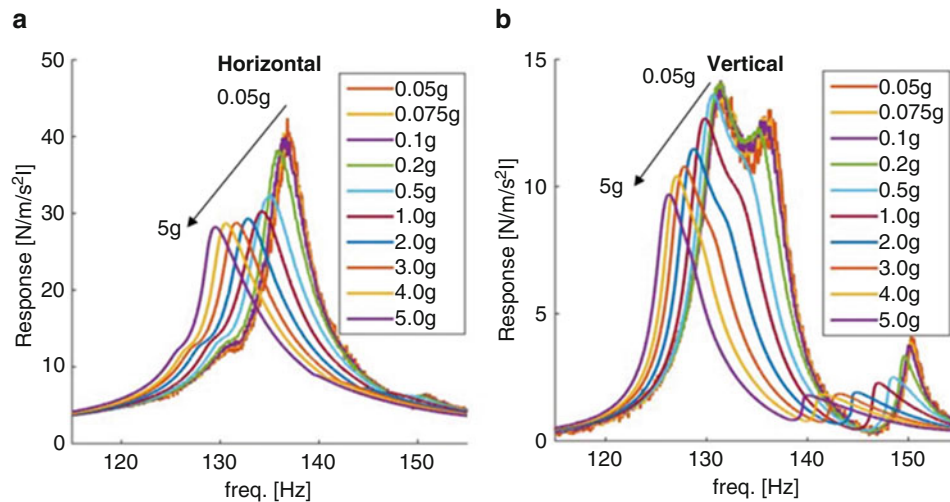


Fig. 9.3 Nonlinear evolution of the 1st bending mode [4]

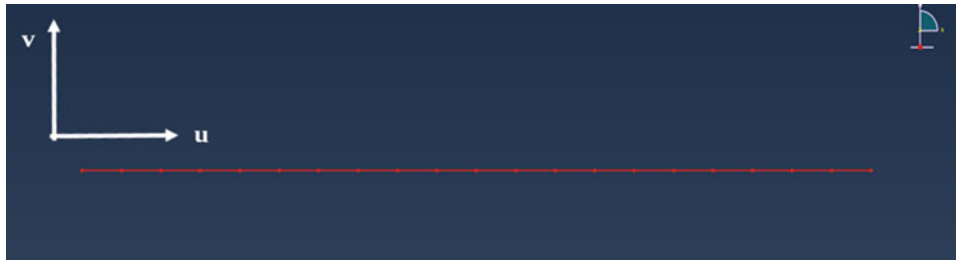


Fig. 9.4 FE pipe representation

9.1.2 Basic Implicit Nonlinear Dynamic Pipe Model

Based on the experimental findings of the basic pipe assembly from Fig. 9.1, the linear pipe and the nonlinear clip behaviour must be included in the model to predict the nonlinear dynamic response.

9.1.2.1 Pipe Modelling

Typically, the length-to-diameter and thickness-to-diameter ratio in a fuel supply pipe are quite large and main frequencies of interest are often below 1000 Hz. This allows the use of Euler Bernoulli beam elements, instead of Timoshenko elements, or a full three dimensional solid model, leading to a very streamlined model of the pipe. For the proposed analysis Euler Bernoulli beam elements were used in Abaqus to model a 500 mm stainless steel pipe with an 8 mm diameter and a wall thickness of 0.6 mm that was used in the experimental part. In order to obtain a geometrically convenient and even element distribution, 50 elements were used. The eigenvalues in free-free condition were computed and compared against a fine meshed 3D brick quadratic model, resulting in an error of less than 1% for all the modes below 1000 Hz (Fig. 9.4).

9.1.2.2 Clip Modelling

The modelling of the clip represented a significantly bigger challenge, since it needed to introduce the observed nonlinear dynamic behaviour [4] of the system without the inclusion of a full physical model. Given the geometry of the clip, a series of linear and nonlinear springs and dashpots seemed to be the obvious choice for the mode. Initially, all 6 Degrees Of Freedom (DOF) were considered for the clip model (3 directions and 3 rotating planes) where all springs and dashpots were represented as elements with a linear and a nonlinear part. For the nonlinear part, a cubic spring.

$$F_{nls} = kx^3 \quad (9.1)$$

and a cubic damper element

$$F_{nld} = c\dot{x}^3 \quad (9.2)$$

were used for each direction to represent the observed softening and increase in damping at higher amplitudes.

9.1.2.3 Nonlinear Dynamic Analysis

The nonlinear dynamic response of the straight pipe with two clips was computed with the help of Imperial College's in house Multi Harmonic Balance solver FORSE [11]. The Euler-Bernoulli beam model of the pipe was created with the commercial FE code Abaqus and its stiffness and mass matrices were extracted as the linear input into FORSE. The six nonlinear elements, making up the implicit clip model, were added directly in FORSE, where the chosen connection points of the beam (at 40 mm from both tips) were linked to ground via the nonlinear spring and damper elements. The excitation force was applied at the geometric centre of the pipe. The frequency range studied was from 0 to 800 Hz, as it is the range of interest for operative fuel supply pipes. Hence, all modes below 800 Hz were studied. In the analysis, the number of harmonics used were determined by performing a quick convergence study. As a result, the optimum number of harmonics was found to be 3.

After assembling the two main components of the fuel supply pipe, the nonlinear model was ready to be updated to ensure an accurate linear base-line model and the identification of the nonlinear input parameters required for the clip model.

9.1.3 Model Updating

A two stage model updating process was used to find a reliable representation of the pipe assembly. Initially, model verification was used to identify which of the 6 springs and dampers of each clip were actually contributing to the linear and nonlinear dynamic response of the system, in order to reduce the element size and minimise the required input parameters. For the identified necessary DOFs, a parameter search was then conducted in a second stage to identify the inputs that lead to the best matching of the measured and computed response.

9.1.3.1 Model Verification

The influence of every DOF on the dynamic response of the system was assessed via a parameter study to determine which DOFs are dominating and which ones can be neglected in the model to ensure that the final model can capture all the features of the pipe model correctly.

Linear Verification

Firstly, the clip stiffness parameters were approximated manually by using an iterative trial and error approach until the resonance frequencies laid close to the experimental ones, making these values somehow reasonable. This initial parameters were the following in N/mm:

$$K_u = 1e4; K_\theta = 30; K_v = 300; K_w = 200; K_\phi = 40; K_\psi = 0.$$

Then, each stiffness was increased individually by 10% from its best fitting value and its impact on the first six resonance frequencies observed (see Table 9.1).

The results in Table 9.1 indicate:

- K_ψ , the stiffness along the central axis of the pipe, had very little influence on the response calculation. This stiffness represents the rotation around the pipe axis which is very unlikely to alter the frequency response of investigated bending modes of the pipe.

Table 9.1 Resonance frequency variation (%) due to individual stiffness increase

Modes	%10 K_u	%10 K_θ	%10 K_v	%10 K_w	%10 K_ϕ	%10 K_ψ
1	0	0.529	0	0	0	0
2	0	0	0	0.073	1.605	0
3	0	0.141	0.164	0	0	0
4	0	0	0	0.221	0.597	0
5	0	0.065	0.355	0	0	0
6	0	0	0	0.672	0.245	0

Table 9.2 Stiffness parameters initial and optimised values

K (DOF)	Initial values (N/mm)	Optimised values (N/mm)
K_u	10,000	500
K_v	300	200
K_θ	30	27.5
K_w	200	100
K_ϕ	40	40

- K_θ , K_ϕ , K_v and K_w did have an important influence on the resonance frequency of the bending modes of the pipe since they cause displacements in v and w , and consequently also lead to a rotation around w and v . Hence, a change in one of these stiffness strongly influences the frequency response of the system.
- K_u had a mild influence due to its high value (almost fixed condition) required to match the experimental data.
- The added mass of the clip, m_c , physically is significantly smaller than the pipe and it was therefore ignored in the model.

Based on the above evaluation it can be concluded that 5 DOF/node are required to fully characterise the linear clip element. Individual linear dampers were not used. Instead, modal damping obtained from experimental data (see Sect. 9.1) was introduced as an input in FORSE.

Nonlinear Verification

Similarly to the linear verification process, the influence of every nonlinear DOF was studied. In this case, the stiffness values were modified in the nonlinear model for every DOF individually to determine which frequencies and modes were affected by which nonlinear stiffness.

As a result it was concluded that K_θ controls the frequency shift in the vertical bending modes, whereas K_ϕ controls the frequency shift in the horizontal bending modes, whereas the translational DOFs did not have a significant impact on the nonlinear response. This sensitivity could be attributed to the strong rotational components around θ and ϕ (see Fig. 9.1) during the first bending modes.

Based on these findings it was decided to model the nonlinear clip behaviour with two nonlinear springs in θ and ϕ angles. A similar study was conducted for the damping element, which led to the identification of the same two DOFs as the driving nonlinear DOFs, and therefore two nonlinear dashpots were also added in the θ and ϕ direction.

9.1.3.2 Optimisation and Validation

Once the most influential DOF were identified, the linear and nonlinear stiffness values were optimised in such a way that the analytic resonance frequencies and mode shapes match as closely as possible with the experimental ones.

Initially, the linear stiffness parameters were selected and varied manually until a good agreement was achieved. As it was shown in the linear verification section, there were only 4 parameters that controlled the resonance frequencies. Besides, some parameters had no influence on the horizontal modes whereas others had no influence on the vertical ones. All this made the optimisation quite a simple exercise, and no complex optimisation routines were required (Table 9.2).

The tuning of the nonlinear parameters was significantly more complex due to the increased objectives, since the response amplitude ($m/s^2/m/s^2$) and frequency (Hz) at 5 different excitation levels (1, 5, 25, 75, 125 m/s^2) had to be matched for six modes, leading to a total of 60 target values. A total of 8 coefficients, two nonlinear springs and two nonlinear dashpots in two directions, had to be optimised to find a best fit. A manual optimisation was quickly dismissed as a viable option to identify the correct parameters and an automated optimisation was therefore implemented.

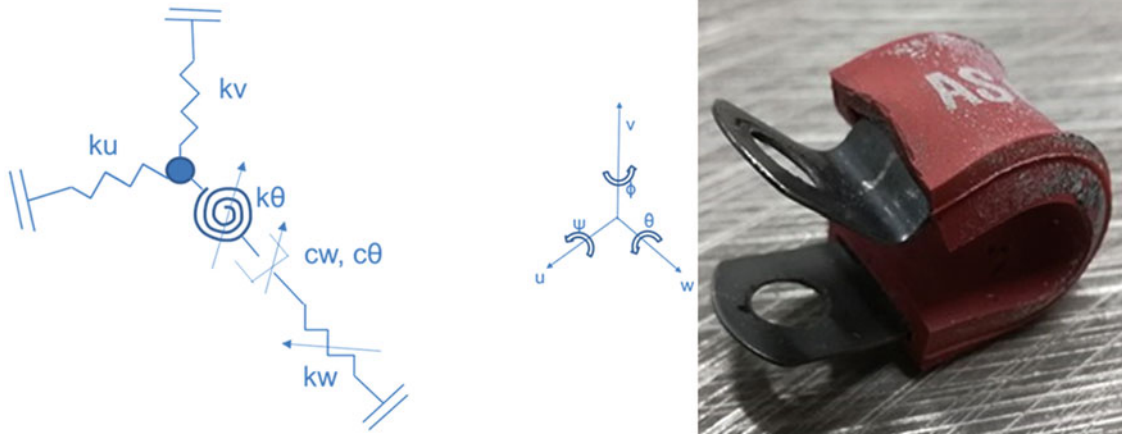


Fig. 9.5 Clip explicit model and real clip

The optimisation algorithm for the identification of the nonlinear clip model was developed in Matlab and a Genetic Algorithm (GA) was used due to its robustness and multi-objective optimisation capabilities [12]. This optimisation routine consists of a series of input parameters that includes objectives (parameters to optimise), initial parameters (initial value of those parameters) and relative weight of the objectives (importance of every parameter to optimise). In this particular case, amplitude objective weights were considered more relaxed (0.8) than frequency objectives (1), as a large error in frequency prediction was considered more critical than the same error for the amplitude.

Based on the input parameters, the algorithm generated five FORSE input files in each optimisation loop, for the five chosen excitation amplitudes. The five nonlinear FRFs were then computed in FORSE, which calculated the “multiharmonic forced response of nonlinear (and linear, as a particular case) mechanical systems which are subjected to periodic excitation” [11]. The resulting FRFs were imported into Matlab and their values used as the new input to the objective function. The GA gave each iteration a certain score depending on how good the results were compared to the objective, and kept iterating looking for the best scores until the problem finally converged.

It is essential during the optimisation to select the correct boundary conditions for the optimisation and to check the successful continuation in FORSE. Under certain conditions the continuation may fail and a modification of the continuation parameters will be required to ensure the accurate computation of the FRFs. For all these reasons, the target of the optimisation was reduced to the 1st bending mode, as otherwise it was not possible to achieve convergence.

After running the optimisation for the first mode, the following nonlinear values were obtained $Fnl_s = -1e7x^3$ and $Fnl_d = 0.03x^3$ (Fig. 9.5).

9.1.3.3 Summary

Once the model validation process was in place, the most appropriate linear and nonlinear parameters were identified, leading to the results presented in the next section.

9.1.4 Results

The model obtained in the previous section was then validated against experimental measurements conducted in HADES with regards to its capability to capture the dynamic response of the system accurately. The considered frequency range included the first four experimental bending modes up to 550 Hz. The reason for this frequency cut off was the immediate appearance of a travelling wave afterwards, whose identification and effects were thoroughly explained in [4].

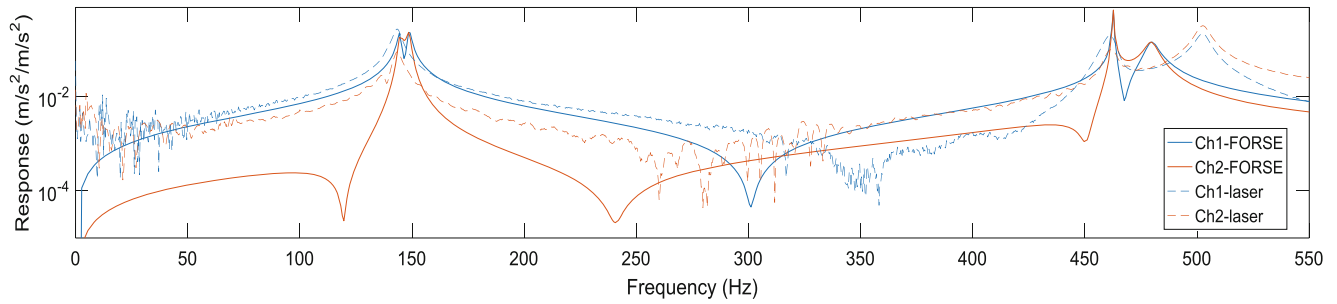


Fig. 9.6 Linear model validation

Table 9.3 Nonlinear validation

Amplitude level (m/s ²)	Frequency FORSE (Hz)	Frequency test (Hz)	Error (%)	Amplitude FORSE (m/s ²)	Amplitude test (m/s ²)	Error (%)
1.00	57.47	56.07	2.50	11.13	10.83	2.77
5.00	57.39	52.46	9.40	56.82	43.25	31.38
25.00	55.91	48.11	16.21	177.00	173.30	2.14
75.00	52.59	45.62	15.28	295.40	395.10	25.23
125.00	49.56	45.02	10.08	330.10	566.60	41.74

9.1.4.1 Linear Validation

An initial low excitation level test at 0.1 g was carried out to obtain the linear response of the system in Fig. 9.6. The first two modes around 150 Hz were captured quite well, where the strong modal interaction experienced in the real test was present. On the other hand, the damping on the third mode was slightly off target, while the frequency match was good. Also, the fourth mode frequency and amplitude predictions were way off the experimental values. All these mismatches observed in modes 3 and 4 can be explained by the appearance of the before mentioned travelling wave. Besides, the mounting and dismounting of the assembly proved to induce a good amount of variability in the system [4], impacting the experimental validation process.

9.1.4.2 Nonlinear Validation

Due to its multi-objective nature, a good agreement between the nonlinear model and the experimental data was significantly harder to achieve. A particular issue thereby was the very poor repeatability observed in the experiments, which could partly be improved by using SLDVs instead of accelerometers [4], but was mainly attributed to alignment tightening issues of the clips, which was very difficult to control. Nevertheless, an attempt was made to predict the amplitude dependence of the pipe with regards to the first bending mode. The results in Table 9.3 show a reasonable good agreement between the resonance frequencies, where the softening of the beam was captured. Also errors of up to 15% were observed for certain amplitude levels, indicating that additional features in the clip were activated at these high levels, which were not correctly captured with the proposed simplified implicit model. A much bigger error was observed for the amplitudes, where the provided damping in the model led to up to 40% over prediction.

9.1.5 Discussion

The creation of a reduced order model able to capture the nonlinear dynamic behaviour of a pipe assembly, represented a significant challenge since the level of complexity in terms of interaction between the pipes and the rubber clip, and the clip with its foundation introduces a multitude of unknown contact conditions. This highlights to the need of a multitude of input parameters for the presented implicit model, which in turn leads to a significant challenge in determining the correct parameters. Due to this complexity, the presented results should be considered as a significant improvement over traditional linear modelling, since the main nonlinear trends were captured correctly. However, there is still plenty of room for improvements regarding absolute accuracy in capturing the full dynamic behaviour of the pipe assembly.

9.1.6 Conclusion

An implicit modelling approach was presented to capture the nonlinear dynamic behaviour of a real fuel supply pipe assembly. The approach was based on a combination of linear pipe, and nonlinear spring and damper elements, taking advantage of experimental data and parameter optimisation to identify the element input parameters.

The complex nonlinear behaviour of the pipe, observed during experimentation, presented a significant challenge to the modelling approach. Linear and nonlinear model updating eventually led to a reasonable agreement for the linear model, and a nonlinear model that was able to replicate the correct trends of the amplitude dependence.

References

1. Horr, A.M., Safi, M.: Full dynamic analysis of offshore platform structures using exact timoshenko pipe element. *J. Offshore Mech. Arct. Eng.* **125**(3), 168 (2003)
2. Laithier, B.E., Paidousis, M.P., Luu, T.P.: Dynamics of finite-length tubular beams conveying fluid. *J. Sound Vib.* **106**, 311–331 (1986)
3. Tannous, M., Cartraud, P., Dureisseix, D., Torkhani, M.: A beam to 3D model switch in transient dynamic analysis. *Finite Elem. Anal. Des.* **91**, 95–107 (2014)
4. Sanchez, A., Schwingshackl, C., Grolet, A.: Influence of nonlinear dynamics in the analysis of rotating machinery accessories. In: *Vibrations in rotating machinery*. VIRM, Manchester (UK) (2016)
5. Schwingshackl, C.W., Joannin, C., Pesaresi, L., Green, J.S., Hoffmann, N.: Test method development for nonlinear damping extraction of dovetail joints, in dynamics of coupled structures, Volume 1: Proceedings of the 32nd IMAC, A conference and exposition on structural dynamics, Allen, M., Mayes, R., Rixen, D. (eds.) pp. 229–237. Springer International Publishing, Cham (2014)
6. Schwingshackl, C.W., Petrov, E.P., Ewins, D.J.: Effects of contact interface parameters on vibration of turbine bladed disks with underplatform dampers. *J. Eng. Gas Turbines Power.* **134**(3), 32507 (2012)
7. Joshi, D., Mahadevan, P., Marathe, A., Chatterjee, A.: Unimportance of geometric nonlinearity in analysis of flanged joints with metal-to-metal contact. *Int. J. Press. Vessel. Pip.* **84**(7), 405–411 (2007)
8. Schwingshackl, C.W., Petrov, E.P.: Modelling of flange joints for the nonlinear dynamic analysis of gas turbine engine casings. *ASME.* **134**, 1–11 (2012)
9. Petrov, E.P., Ewins, D.J.: Generic friction models for time-domain vibration analysis of bladed disks. *J. Turbomach.* **126**(1), 184 (2004)
10. Rashquinha, I.A., Hess, D.P.: Modelling nonlinear dynamics of bolted assemblies, *Appl. Math. Modell.* Elsevier. **97**, 801–809 (1997)
11. Petrov, E.P., Ewins, D.J.: State-of-the-art dynamic analysis for non-linear gas turbine structures. *Proc. Inst. Mech. Eng. Part G J. Aerosp. Eng.* **218**(3), 199–211 (2004)
12. Holland, J.H., Reitman, J.S.: Cognitive systems based on adaptive algorithms. *SIGART Bull.* **63**, 49 (1977)

Chapter 10

System Identification to Estimate the Nonlinear Modes of a Gong



Daniel Piombino, Matthew S. Allen, David Ehrhardt, Tim Bebernis, and Joseph J. Hollkamp

Abstract Nonlinear Normal Modes (NNMs) have proven useful in a few recent works as a basis for comparing nonlinear models during model updating. In prior works the authors have used force appropriation to measure NNMs, but this is time consuming, generally requiring hand tuning of both the frequency in question and the strength of its harmonics. This paper explores the use of system identification, using a small set of broadband response data, to estimate a model from which the NNMs can be extracted. The Frequency Domain Restoring Force Surface (RFS) method will be used to perform identification, in which the nonlinearity of the system is assumed to be a polynomial function of the modal displacements, and a least squares problem is formed to solve for the nonlinear coefficients. Existing NNM calculation approaches can then be applied to the experimentally determined model in order to calculate the NNMs of the system. This approach is evaluated by applying it to full-field measurements from a traditional Gong, obtained using Stereo 3D Digital Image Correlation (3D-DIC). The results obtained using system identification are validated with measurements of the NNMs obtained using force appropriation and a scanning laser vibrometer.

Keywords Reduced order modeling · Implicit condensation · Vibration musical instrument · Model updating

10.1 Introduction

In extreme environments, the skin panels of high speed vehicles can experience large fluctuating pressures [1], so that geometric nonlinearity can become important, causing dramatic shifts in the resonance frequencies or even causing emergent behavior such as jump phenomena, superharmonic resonance or changes in the deformation pattern [2] and hence the stresses that the panel experiences. For constrained structures such as a pinned-pinned beam, geometric nonlinearity typically becomes important as the vibration amplitude approaches the panel thickness. Prior works [3–5], have shown that linear models are unable to provide reliable predictions in this regime, and so nonlinear models must be considered to obtain reasonable estimates of the vehicle's life. In many cases geometric nonlinearity is actually beneficial, since it may cause the resonance to de-tune itself or distribute the stress in the panel more evenly than the linear modes; hence, if reliable models of these structures could be created then it might be possible to exploit nonlinearity to create significantly lighter structures.

While modeling methods for these types of structures have advanced considerably in the past decade or two [1, 4, 6], far fewer works have explored model updating strategies or even how to comprehensively compare simulation results with measurements. This is important, as our experience with linear aerospace structures has taught us that Finite Element Models (FEMs) are almost never predictive; except for the simplest structures, some level of model tuning or model updating is always needed. In many cases significant effort is needed to update the FEM to bring it into agreement with measurements.

In [2, 7], Ehrhardt, Allen and Bebernis proposed to update finite element models for geometrically nonlinear structures by comparing their Nonlinear Normal Mode (NNM) backbone curves derived from both the FEM and measurements. The NNMs used here follow the modified Rosenberg [8] definition, and are simply periodic solutions to the undamped, nonlinear equation of motion [9, 10]. In [2, 7], the NNMs of the FEM were computed using a reduced order model, as described in [6]. The NNMs were extracted from test using force appropriation, as proposed by Peeters et al. [11, 12], and the methodology was further developed in [13].

D. Piombino · M. S. Allen (✉)

Department of Engineering Physics, University of Wisconsin-Madison, Madison, WI, USA
e-mail: piombino@wisc.edu; msallen@engr.wisc.edu

D. Ehrhardt · T. Bebernis · J. J. Hollkamp

Air Force Research Laboratory, Dayton, OH, USA

e-mail: david.ehrhardt.1.ctr@us.af.mil; timothy.bebernis@us.af.mil; joseph.hollkamp@us.af.mil

While previous works have shown that it is possible to measure NNMs using force appropriation, this poses a few challenges. First, a sinusoidal input must be applied, which typically precludes the use of most non-contact excitation devices. Furthermore, recent works (not yet published), have often found that multiple, synchronized shakers may be needed to adequately isolate the NNMs of more complicated structures. Second, even when force appropriation is possible, it is still quite time consuming. As an alternative, Noel et al. [14] proposed to use a two tiered approach in which a pseudo-random broadband input is first applied and a system identification algorithm is used to fit a model to the structure. The NNMs can then be derived from the identified model once the damping forces have been eliminated.

This work explores this paradigm in more detail, with several variations to what was done by Noel et al. [14]. First, whereas Noel et al. utilized a frequency domain nonlinear subspace algorithm, this work employs a far simpler method, the frequency domain Restoring Force Surface method (RFS). Second, the system treated by Noel et al. had discrete nonlinearities that could be described in terms of displacements of a few points on the structure. The structures studied here have distributed, geometric nonlinearities, and so the identification is performed in the modal domain, where the model is assumed to contain stiffness terms that are quadratic and cubic functions of the displacements of the modal displacements, which are found by applying a modal filter based on the vibration modes of the underlying linear system. To the best of the authors knowledge, the first work to employ a similar system identification approach was that of Spottswood et al. [15, 16], although they used the Nonlinear Identification through Feedback of the Output (NIFO) algorithm, which is described in the review [17].

The paper is organized as follows. Section 10.2 outlines the approach used. In Sect. 10.3 the proposed techniques are applied to a circular Gong, a musical instrument whose unique sound comes about due to geometric nonlinearity [18–20]. The conclusions are then presented in Sect. 10.4.

10.2 Theoretical Development

Geometric nonlinearity can be accurately captured by finite element models, which describe the system with a conservative equation of motion of the following form,

$$\mathbf{M}\ddot{\mathbf{x}} + \mathbf{K}\mathbf{x} + \mathbf{f}^{nl}(\mathbf{x}) = \mathbf{f}^{ex}(t) \quad (10.1)$$

where \mathbf{M} , and \mathbf{K} are the $N \times N$ linear mass and stiffness matrices, $\mathbf{f}^{nl}(\mathbf{x})$ are the nonlinear forces due to geometric nonlinearity and $\mathbf{f}^{ex}(t)$ represents the applied forces. The nonlinear normal modes of this system are the solutions $\mathbf{x}(t)$ to the equation of motion above when $\mathbf{f}^{ex}(t) = 0$, and are denoted $\mathbf{x}^{NNM}(t)$.

$$\mathbf{M}\ddot{\mathbf{x}}_{NNM} + \mathbf{K}\mathbf{x}_{NNM} + \mathbf{f}^{nl}(\mathbf{x}_{NNM}) = 0 \quad (10.2)$$

The NNMs of a system such as this can be computed using the method in [21], which is expensive but operates on the FEM directly, or by reducing the model and applying the algorithm by Peeters [22], a harmonic balance approach (see [23] for an excellent implementation and a through review of prior literature). See the references cited here and also [6] for further details.

The actual test hardware can be assumed to obey a similar governing equation, but realistic structures exhibit energy dissipation, which must also be considered. In the absence of additional information, this work assumes that either a modal damping or a linear viscous damping model is appropriate.

$$\mathbf{M}\ddot{\mathbf{x}} + \mathbf{C}\dot{\mathbf{x}} + \mathbf{K}\mathbf{x} + \mathbf{f}^{nl}(\mathbf{x}) = \mathbf{f}^{ex}(t) \quad (10.3)$$

Force appropriation methods [11, 12] seek to find a force, $\mathbf{f}^{ex}(t)$, that approximately cancels the damping forces in the structure. For example, if the applied force is a pure sinusoid at frequency ω_1 (including higher harmonics) $\mathbf{f}^{ex}(t) = \sum_k \mathbf{a}_k \sin(k\omega_1 t)$ and the displacement, $\mathbf{x}(t)$, is a pure cosine (also including higher harmonics) $\mathbf{x}(t) = \sum_k \mathbf{b}_k \cos(k\omega_1 t)$, and if the nonlinearities are purely polynomial functions of the displacements (e.g. x_1^2 , x_1^3 , $x_1 x_2^2$, etc. . . .) then because the sine and cosine functions are orthogonal, the equation of motion can be separated into the two equations below.

$$\mathbf{M} \sum_k -k^2 \omega_1^2 \mathbf{b}_k \cos(k\omega_1 t) + \mathbf{K} \sum_k \mathbf{b}_k \cos(k\omega_1 t) + \mathbf{f}^{nl} \left(\sum_k \mathbf{b}_k \cos(k\omega_1 t) \right) = 0 \quad (10.4)$$

$$\mathbf{C} \sum_k -k\omega_1 \mathbf{a}_k \sin(k\omega_1 t) = \sum_k \mathbf{a}_k \sin(k\omega_1 t) \quad (10.5)$$

The top equation is simply a variant of Eq. (10.2), the equation that is solved to obtain the NNMs of the system. Equation (10.5) can be used to determine the force that must be applied so that the response of the system will be equivalent to an NNM. In general, Eq. (10.5) defines a force that must be applied at every point on a structure, which is clearly not feasible. Fortunately, various works have shown that one can obtain a very good approximation to the NNM so long as Eq. (10.5) is satisfied in an average sense, or more specifically, if the power input over one cycle of vibration equals the power dissipated by damping [24, 25].

10.2.1 System Identification Methods

As mentioned earlier, the force appropriation method requires that one apply a carefully tuned sinusoidal force, which typically requires a contact exciter such as a shaker, and it can be time consuming to adjust the forcing so that Eqs. (10.4 and 10.5) are satisfied. Furthermore, recent experiences have shown that for many structures it may be very difficult to adequately isolate the modes of interest using only one shaker, and applying multiple shakers complicates the method considerably. The alternative is to apply an arbitrary input and use system identification to identify a model for the system, and then to extract the NNMs from the identified model in order to understand it and to compare it with the FEM.

This work uses the frequency domain restoring force surface method, following the same procedure outlined in [26]. In summary, the method assumes that the system is describable by a modal model with nonlinear coupling terms between the modes. Specifically, if we apply the modal transformation $\mathbf{x}(t) = \Phi_m \mathbf{q}(t)$ to Eq. (10.1), where the basis vectors Φ_m are the linearized modes or solutions to $(\mathbf{K} - \omega_r^2 \mathbf{M})\varphi_r = 0$, then one obtains the following,

$$\ddot{q}_r + \omega_r^2 q_r + \theta_r(q_1, q_2, \dots, q_m) = \varphi_r^T \mathbf{f}(t) \quad (10.6)$$

Where the nonlinear term $\theta_r(\mathbf{q}) = \varphi_r^T \mathbf{f}_{NL}(\Phi_m \mathbf{q})$ can be assumed to have the following polynomial form.

$$\theta_r(q_1, q_2, \dots, q_m) = \sum_{i=1}^m \sum_{j=i}^m B_r^{ij} q_i q_j + \sum_{i=1}^m \sum_{j=i}^m \sum_{k=j}^m A_r^{ijk} q_i q_j q_k \quad (10.7)$$

A modal filter is applied based on the measured linear modes to estimate the modal displacements (from DIC data), i.e.

$$\mathbf{q}(t) = \Phi_m^\dagger \mathbf{x}(t) \quad (10.8)$$

Then each of terms on the right hand side of Eq. (10.7) can be determined from the time histories $q_j(t)$. The modal velocity and acceleration are determined by differentiating $q_j(t)$, and then all of the signals are transferred to the frequency domain to obtain a least squares problem as shown below, where the FFTs of the signals are represented with capital letters, e.g. $Q_j(\omega) = FFT(q_j(t))$, $Q_j^v(\omega) = FFT(\dot{q}_j(t))$, $Q_j^a(\omega) = FFT(\ddot{q}_j(t))$, $Q^{112}(\omega) = FFT(q_1(t)^2 q_2(t))$, etc. . . .

$$Q_r^a(\omega) + 2\zeta_r \omega_r Q_r^v(\omega) + \omega_r^2 Q_r(\omega) + A_r^{111} Q^{111}(\omega) + A_r^{112} Q^{112}(\omega) + \dots = \varphi_r^T \mathbf{F}(\omega) \quad (10.9)$$

$$\begin{bmatrix} Q_r^v(\omega_1) & Q_r(\omega_1) & Q^{111}(\omega_1) & Q^{112}(\omega_1) & \dots \\ Q_r^v(\omega_2) & Q_r(\omega_2) & Q^{111}(\omega_2) & Q^{112}(\omega_2) & \dots \\ \vdots & \vdots & \vdots & \vdots & \ddots \end{bmatrix} \begin{bmatrix} 2\zeta_r \omega_r \\ \omega_r^2 \\ A_r^{111} \\ A_r^{112} \\ \vdots \end{bmatrix} = \begin{bmatrix} \varphi_r^T \mathbf{F}(\omega_1) - Q_r^a(\omega_1) \\ \varphi_r^T \mathbf{F}(\omega_2) - Q_r^a(\omega_2) \\ \vdots \end{bmatrix} \quad (10.10)$$

The frequencies where significant excitation can be seen are included in the least squares problem, which is solved to obtain a model for the nonlinear system. Then the damping terms can be eliminated and the modes of the model found using the NNM computation algorithm in [22].

It is important to assure that the matrix on the left in Eq. (10.10) is well conditioned so that a unique solution can be obtained. To address this, initially models were only fit to a single mode in isolation, i.e. neglecting any modal coupling terms such as A_r^{112} , and then terms were added to the nonlinear model one at a time, and were only retained if they improved the fit to the measurements noticeably. This made it possible to minimize the number of unknowns in the curve fit while including any terms that were found to be important.

10.3 Experimental Application

The proposed approach was applied to the system depicted in Fig.10.1, which consists of a small gong suspended from a metal frame by a rope.

Two Photron cameras were used to capture images of the gong at a rate of 2000 frames/s while a National Instruments PXI-Chassis recorded the response of two Polytec fiberoptic LDVs and a load cell at 5000 samples per second. The load cell was attached to the gong on the outer rim, and to a small electrodynamic shaker, which was used to excite the system.

10.3.1 Linear System Identification

A low amplitude pseudo-random input, band limited from 100 to 900 Hz was first applied to the system, and the response recorded for 22 s. The spectra of the signals were then calculated using a Hanning window with a blocksize of 4.096 s, which resulted in 9 averages at a 50% overlap. The H_1 estimator [27] was then used to calculate the displacement frequency response matrix of the system with respect to the measured force exerted by the shaker. The Frequency Response Functions (FRFs) obtained are shown in Fig. 10.2. The x- and y- direction DIC measurements were always at least an order of magnitude smaller than those in z (out-of-plane) and they were quite noisy, so they were ignored.

The Algorithm of Mode Isolation [28] was used to fit 17 modes to the DIC data and obtain their natural frequencies, damping ratios, and mode shapes. The frequencies and damping ratios of the identified modes can be found in Table 10.1. The corresponding mode shapes are shown in Fig. 10.3.

It is important that the set of modes be independent on the coordinate set if we are to obtain accurate system identification results. To evaluate this, the Modal Assurance Criterion (MAC) [29] of the mode shapes was computed and is shown in Fig. 10.4. This reveals two pairs of modes that are indistinguishable on the measurement set, but fortunately neither is one of the modes that is expected to exhibit the most nonlinearity. After eliminating those modes, the linear FRFs were modally filtered to test the ability of these shapes to uncouple the modes of the system. The resulting modal FRFs are shown in Fig. 10.5, and show that the remaining modes are capable of adequately uncoupling the system for frequencies below 700 Hz.

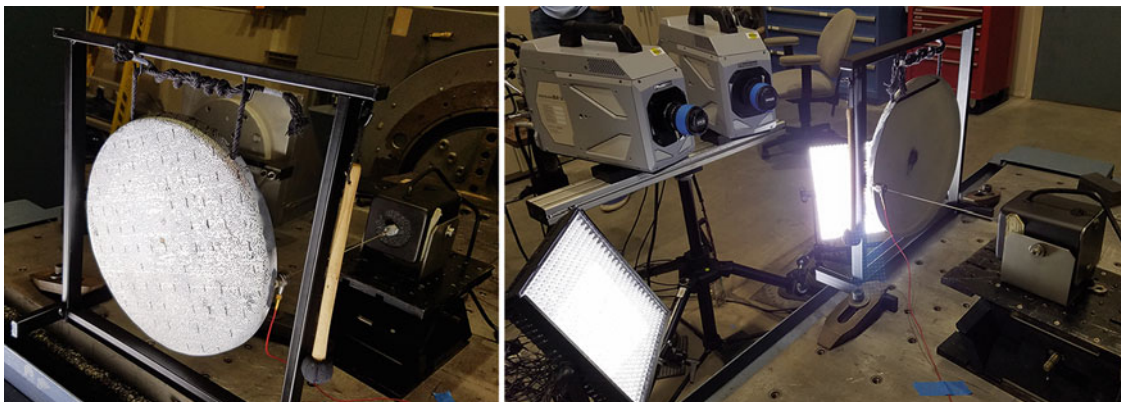


Fig. 10.1 Photographs of setups used for DIC tests for system identification. (a) Front view of gong. (b) Photograph showing shaker setup, lighting and DIC system. Two LDVs were also used, which are part of the hardware seen behind the leftmost DIC camera

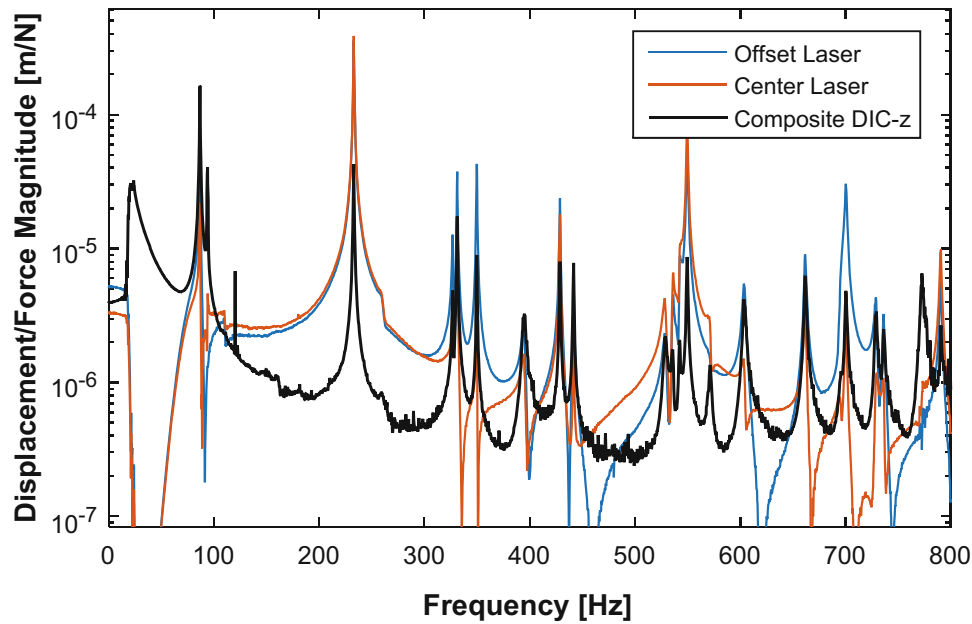


Fig. 10.2 Low-amplitude (linear) Displacement/Force FRFs measured on the Gong using two LDVs and the DIC measurements. The DIC measurements consisted of 388 points distributed over the surface of the plate, and the composite or average of all of the out-of-plane DIC FRFs, is shown

Table 10.1 Linear modal parameters identified from the low-amplitude DIC measurements

Mode number	Natural frequency [Hz]	Percent damping
1	86.63	0.25%
2	93.72	0.20%
3	232.74	0.11%
4	326.75	0.12%
5	331.01	0.09%
6	349.72	0.03%
7	394.58	0.19%
8	428.71	0.06%
9	441.60	0.06%
10	528.60	0.23%
11	535.80	0.16%
12	542.40	0.10%
13	549.60	0.06%
14	571.45	0.16%
15	603.92	0.10%
16	661.87	0.07%
17	700.55	0.05%
18	86.63	0.25%
19	93.72	0.20%

10.3.2 Force Appropriation

The experimental setup used to perform force appropriation was similar to that used for DIC, but employed a larger shaker and a more secure means of attaching the load cell to the gong. This testing was performed in a different lab, where the DIC system was not available, so instead Polytec PSV-400 M scanning laser vibrometer was used to capture the response of the gong. The experimental setup is shown in Fig. 10.6. The velocity of the center of the plate was monitored using the LDV along with the force measured by the load cell, and the procedure described in [13] was used to manually adjust the

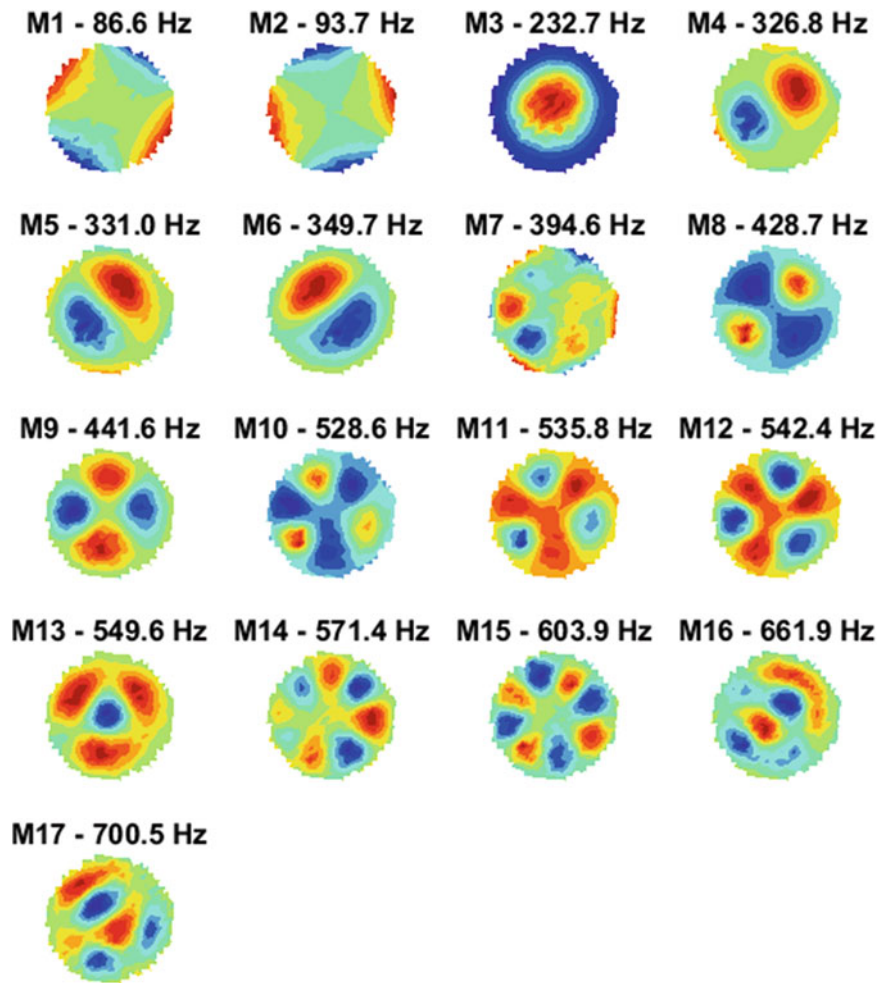


Fig. 10.3 Mode shapes identified by AMI from the DIC measurements

frequency and amplitude of the input signal until the force and velocity were in phase, as evidenced by a Lissajous figure, indicating that the system was vibrating near an NNM. Then the step-scanning feature in the Polytec software was used to capture the vibration of the plate over several cycles, at a grid of 121 points.

The NNMs of the 230 Hz and 550 Hz modes of the system were measured in this manner. The recorded natural frequency at each excitation level was plotted against the RMS velocity of the center of the gong, and can be seen in Figs. 10.7 and 10.8. The modes of a circular plate are typically labeled (d,c) according to the number of node lines parallel to a diameter and those that follow the circumference, respectively. If the outer edge of the gong is considered to be fixed, then these two modes of interest would be the (0,0) and (0,1) modes, respectively and they shall be referred to as such for the remainder of the work. The first two modes of the gong, shown in Fig. 10.3 would be the (2,0) modes, and so forth.

The first NNM shows only hardening behavior over the range of amplitudes tested, exhibiting about a 0.7% frequency shift. This is a small nonlinearity, but the shift in the frequency was certainly noticeable in the force appropriation process; the Lissajous figure would change visibly due to changes in the drive frequency of only 0.01 Hz. The second NNM shows both softening and hardening, with the frequency decreasing in the softening region by 0.03%, followed by a 0.1% increase in the frequency.

10.3.3 Nonlinear System Identification

A swept sine from 225 to 245 Hz with a 1 Hz/s sweep rate, resulting in an RMS amplitude of 13.8 N was then applied in order to nonlinearly excite the system near the (0,0) mode and data was recorded over 34 s, encompassing a sweep up from

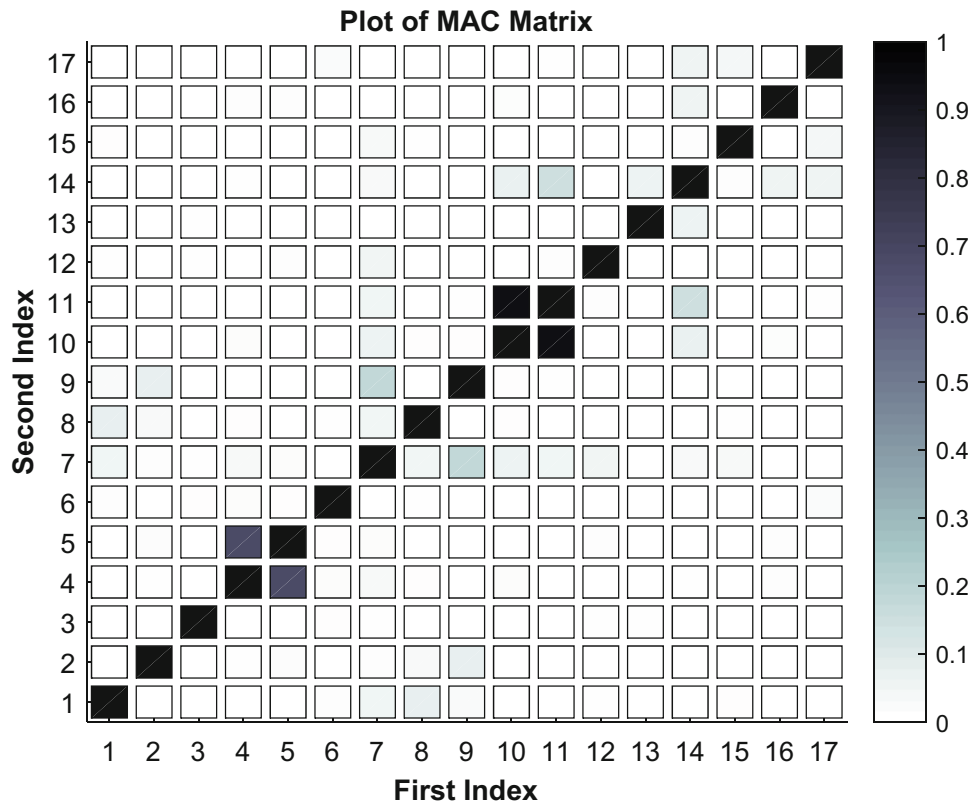


Fig. 10.4 Auto-MAC between mode shapes identified by AMI from the DIC measurements. This reveals which modes are linearly dependent on the measurement set

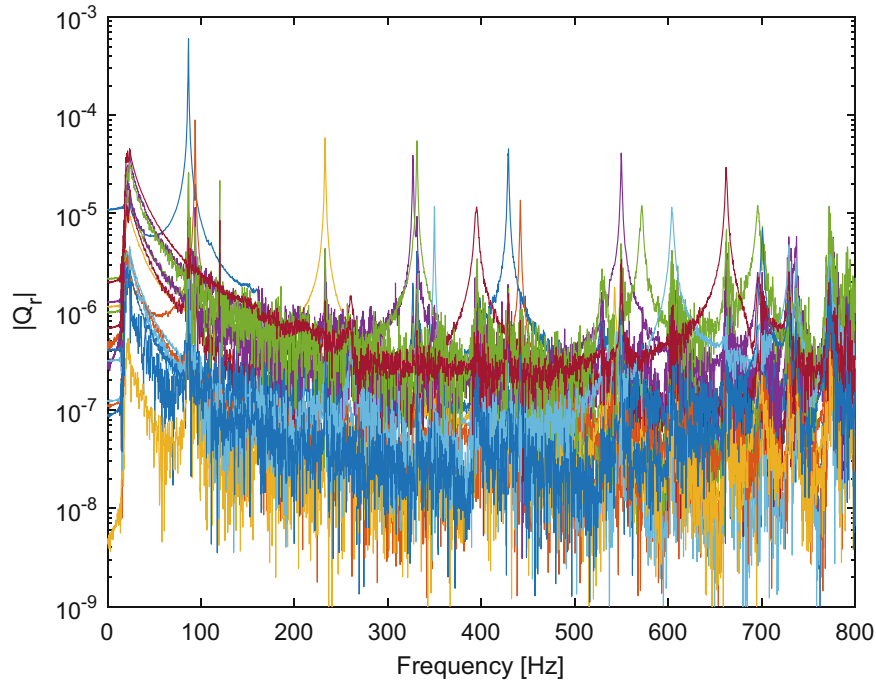


Fig. 10.5 Linear FRFs, modally filtered to isolate each mode

225 to 245 Hz, followed immediately by a sweep down from 245 to 231 Hz. The mode shapes obtained in Sect. 10.3.1 were used to determine the modal response of the system which was converted to the frequency domain via an FFT.

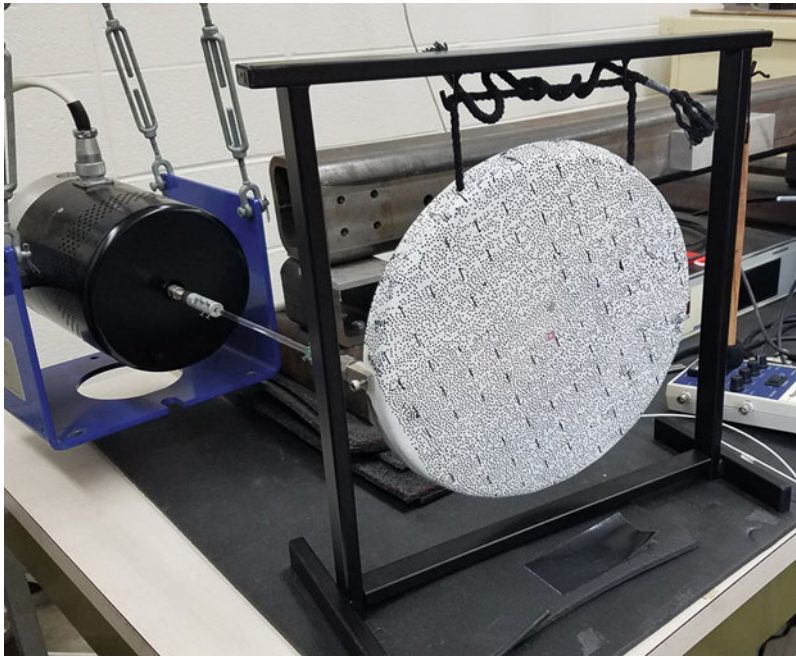


Fig. 10.6 Photograph of test setup used to perform force appropriation to estimate the NNMs of the Gong

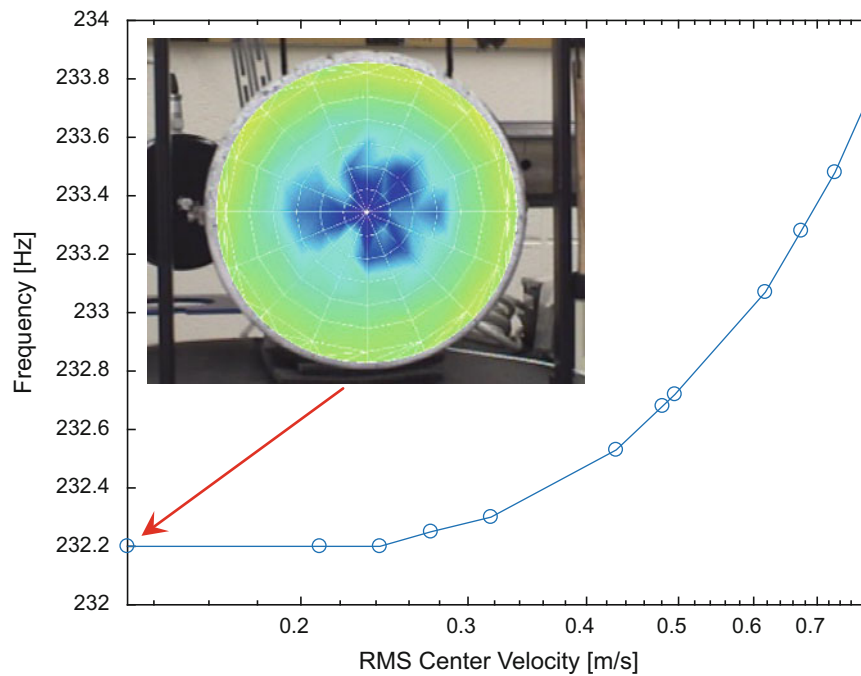


Fig. 10.7 NNM frequency vs center point RMS velocity for the (0,0) of the gong, measured using force appropriation

Before fitting the response data to a nonlinear model, the frequency response of the (0,0) mode was compared to the response predicted by the linear FRF due to the measured forcing, which can be seen in Fig. 10.9. Similar plots for the (0,1) mode can be seen in Fig. 10.10. For the (0,0) mode, which is directly excited by the forcing, there is a clear over-prediction of the response by the linear model at the resonance frequency. In the measured response the system does not achieve as large of an amplitude at the linear natural frequency since the effective resonance shifts due to nonlinearity.

Although the input signal was a swept sine ranging from 225 to 245 Hz, nonlinearity in the system causes the force to be non-negligible at some other frequencies, and this causes the response predicted with the linear FRF to show some motion

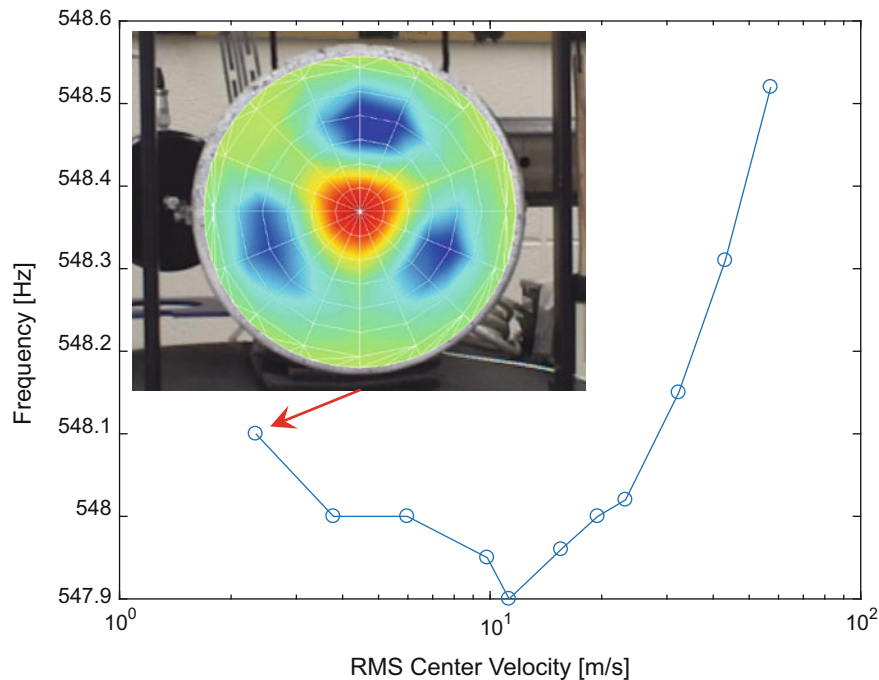


Fig. 10.8 NNM frequency vs center point RMS velocity for the (0,1) mode of the gong, measured using force appropriation

at higher frequencies. However, the measured data show that the (0,0) mode is excited more significantly in these higher frequency bands. Similarly, the response of the (0,1) mode can be seen to differ significantly from the linear FRF prediction, showing that the system is exhibiting significant nonlinearity, and that any nonlinear model for this system should be one which significantly affects the response in the aforementioned frequency bands.

As described in Sect. 10.2.1, it was assumed that the nonlinearities in the system could be adequately modeled by quadratic and cubic functions of the modal displacements. In an initial effort, only the measurements in the frequency range that was excited (i.e. 225–245 Hz) were used in the identification. However, this produced a model that was inaccurate at the harmonics of the forcing and so four frequency bands of interest were identified in the figures above, specifically those which showed significant response in Figs. 10.9 and 10.10 and these were used to define the input data for RFS. The measurements from these four frequency bands were used to populate Eq. (10.10), and the least squares equation was solved for the nonlinear stiffness terms. Considering nonlinearity in all 13 modes, with coefficients up to cubic and considering all possible nonlinear coupling terms, there were over 600 terms to identify. Initially, numerical ill-conditioning was a challenge, yet after scaling each signal by its RMS value, it was possible to obtain a reliable fit to the measurements.

To evaluate the accuracy of the model found through nonlinear system identification, the restoring force of the system was constructed using the identified parameters, along with the measured displacement, velocity, etc. . . . The sum of these measured terms multiplied by their respective polynomial terms reproduces the left hand side in Eq. (10.10), and this was compared with the measured right hand side to see how well the identified parameters reconstruct the response. Figure 10.11 contains plots of the restoring force reconstructed for the (0,0) mode compared to the measured restoring force. It also contains the same reconstruction obtained using only the linear terms, which were identified from the linear FRFs and are identical to those used to reconstruct the FRFs used to compute the linear response in Figs. 10.9 and 10.10. It is interesting to note that the linear RFS prediction matches the measurements quite well, even though the true linear response to the measured forcing in Figs. 10.9 and 10.10 showed significant error. This stems from the fact that only the forcing is available as an input when using the FRFs to compute the response (i.e. in Figs. 10.9 and 10.10), whereas the RFS method uses the measured acceleration, velocity and displacement as well and these implicitly contain the effect of the nonlinearity. This seems to be a deficiency of the RFS method and deserves further investigation.

Setting that issue aside, one can use the responses in Fig. 10.11 to evaluate the accuracy of the identified nonlinear model. In order to more easily do this, the error between the measured restoring force and that reproduced by the nonlinear model was computed and is shown in Fig. 10.12. In this figure one can see that the nonlinear model reduces the error near significantly near the first two frequency bands, while leaving it roughly the same at the two higher frequency bands. The same plots for the (0,1) mode can be seen in Figs. 10.13 and 10.14.

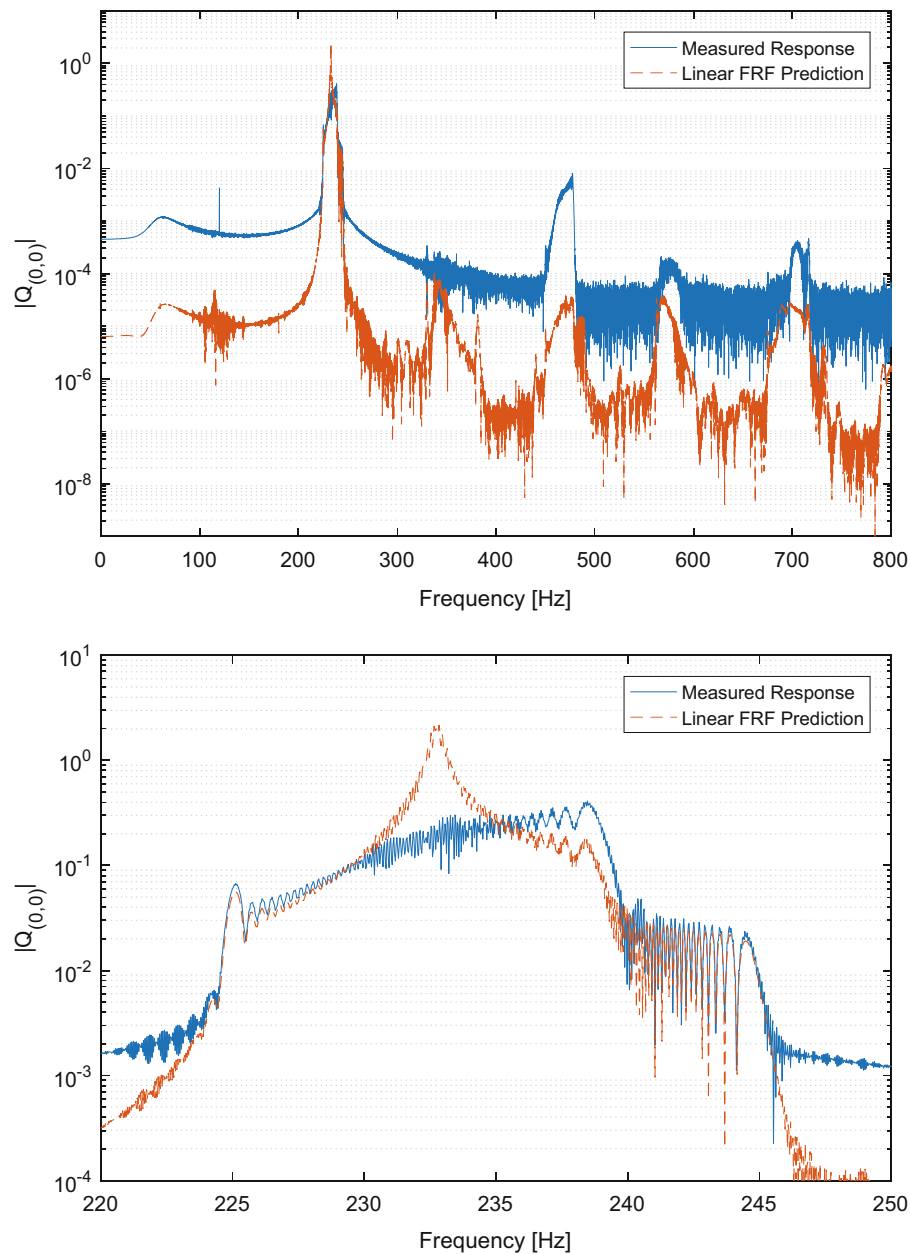


Fig. 10.9 Measured frequency response of (0,0) mode compared to linear FRF prediction. (top) across the entire frequency range of interest, (bottom) across the excited frequency band

It can be gathered from the figures above that the nonlinear model is capable of fitting the restoring force of the two modes of interest to a reasonable degree of accuracy across the entire frequency range. Specifically, when compared to a purely linear model, the error in the (0,0) mode restoring force can be seen to decrease by as much as roughly two orders of magnitude near the excited frequency band, and one order of magnitude near the 2nd harmonic of the excited frequency band. In the 3rd and 4th frequency bands, however, no noticeable improvement in error can be seen. The error in the restoring force for the (0,1) mode decreases by similar amounts. Based on this comparison, the identified nonlinear model was considered to be an accurate fit to the dynamics of the system.

The linear and nonlinear stiffness terms for the system were then used in a continuation method, as described in Sect. 10.2, to solve for the NNMs of the two modes of interest. The NNMs of the nonlinear model were compared to the NNMs of the system measured with the force appropriation method from Sect. 10.3.2, and this comparison can be seen in Figs. 10.15 and 10.16. As with Figs. 10.7 and 10.8, the NNM frequencies were plotted against the RMS of the center point velocity.

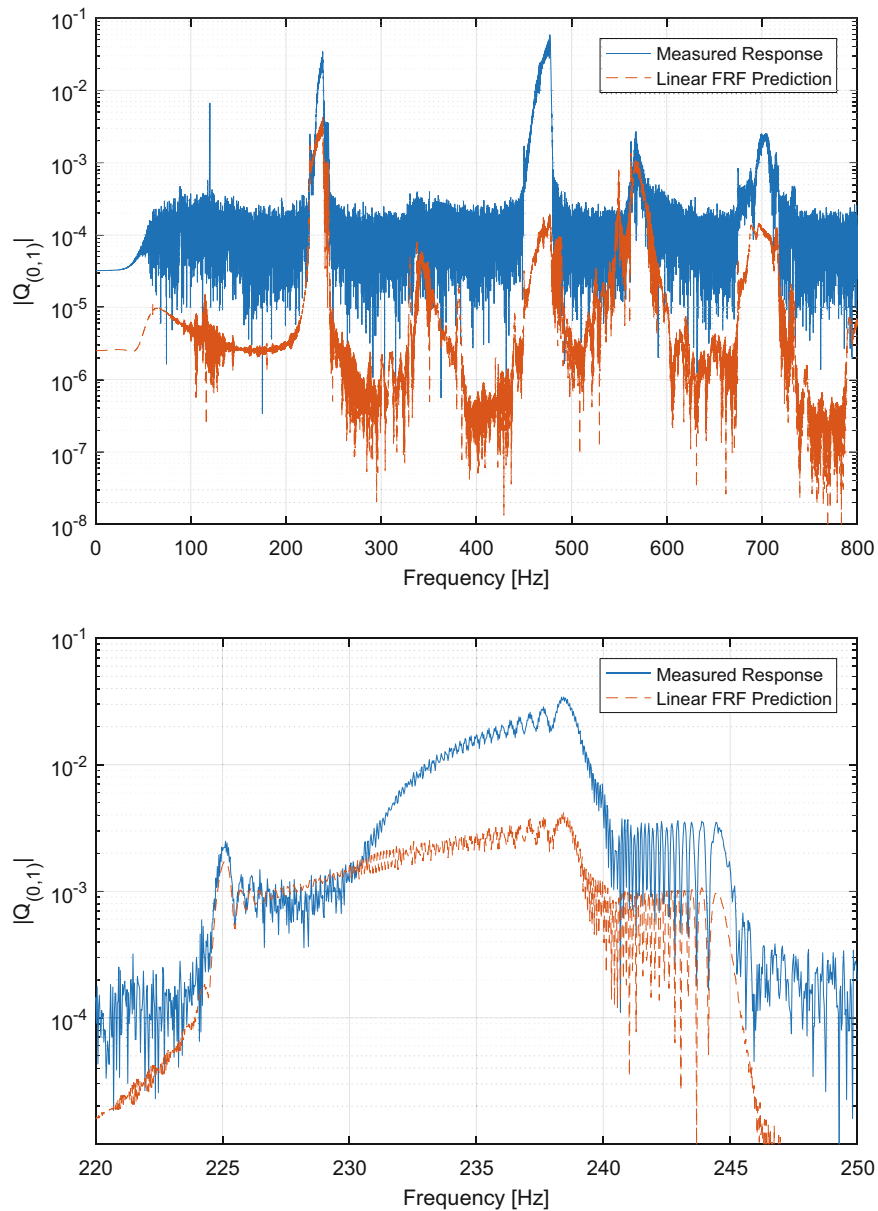


Fig. 10.10 Measured frequency response of (0,1) mode compared to linear FRF prediction. (top) across the entire frequency range of interest, (bottom) across the excited frequency band

It can be seen in Figs. 10.15 and 10.16 that the identified model is not capable of predicting the NNMs of either mode of interest. Both predicted NNMs can be seen to experience nonlinear behavior at a lower excitation level than the corresponding NNMs measured via force appropriation. Additionally, the nonlinear behavior predicted for each mode differs greatly from the measured phenomena. However, what is even more problematic is that it was discovered that these NNMs were far from unique. In other words, a slight change to the procedure used to identify the modes would change both the quality of the curve fit and the NNMs significantly. To illustrate this, the identification was repeated including the nonlinear terms for only modes 3 and 13, but accounting for linear stiffness and damping of modes 1 through 17 when performing the fit. This was thought to be reasonable since modes 3 and 13 dominate the response, however the resulting model was visibly inferior to the model presented above in terms of the residual error in the least squares problem. In any event, the NNMs of this model were computed, and were found to be dramatically different from those presented earlier, as shown in Figs. 10.15 and 10.16.

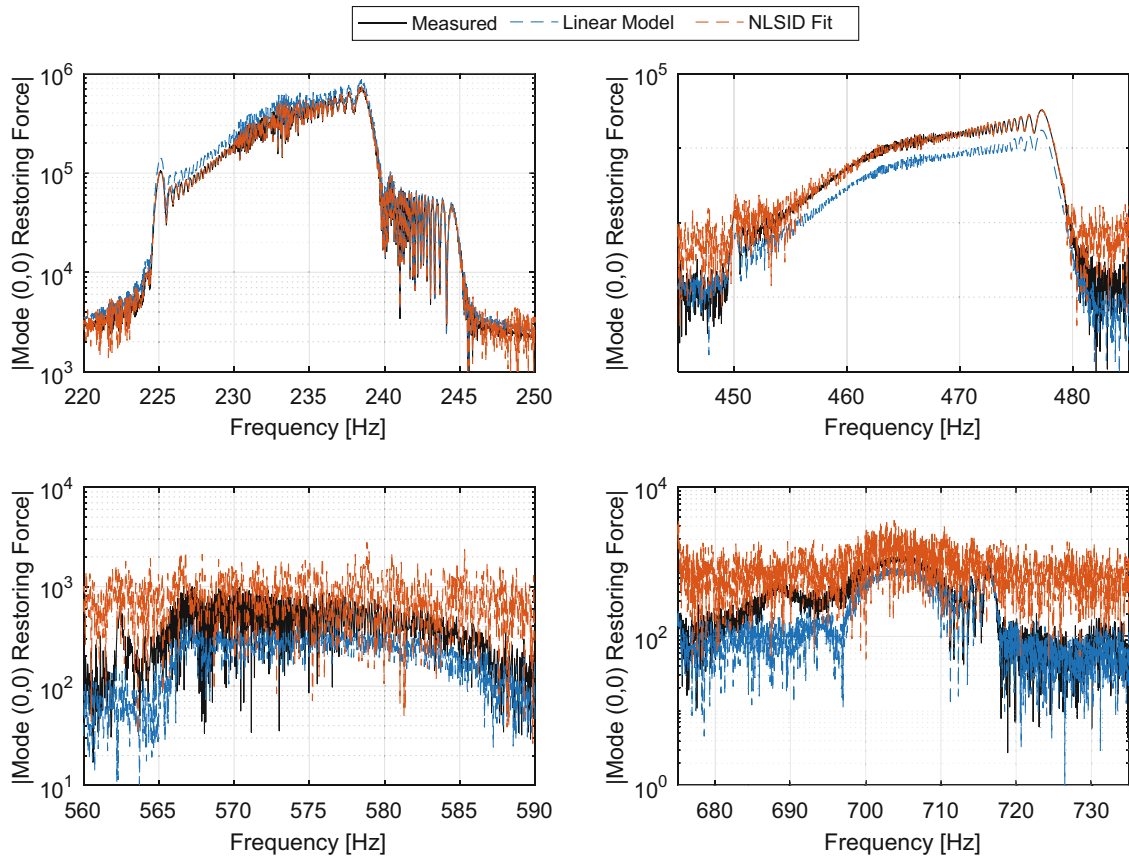


Fig. 10.11 Comparison of the mode (0,0) reconstructed restoring force to the measured restoring force

10.4 Conclusions

This paper explored the use of system identification in order to determine a nonlinear model which can be used to estimate the NNMs of a system, through the use of a case study on a circular gong. To this end, a low amplitude, random input force was first applied to the system, and the linear modes of the system were found and used to convert the response of the nonlinear (i.e. excited at high amplitude) system to modal coordinates. Then those histories were used to fit a model consisting of nonlinearities that are polynomial functions of the modal displacements. The resulting model satisfied the governing equations of the RFS method quite well at the frequencies where the response was significant, but only after including all of the identified linear modes in the model with every possible cross term. It was surprisingly challenging to obtain a model that produced a low residual error in Eq. (10.10); models with only a few modes showed significantly larger errors.

Once the best possible system identification model had been obtained, a numerical continuation algorithm was then used to approximate the NNMs of the two modes of interest of the system based on the identified nonlinear stiffness terms. To evaluate the accuracy of the NNMs of the identified model, the force appropriation method was used as in [13] to directly measure the NNM of each mode of interest. It was found that the NNMs predicted by the identified nonlinear model differed greatly from the measured NNMs of the system. The NNMs obtained by system identification varied greatly as the system identification procedure was varied, and so the authors had little confidence in those estimates. In contrast, while the force appropriation method is somewhat slow, as the system was driven with increasing amplitude near each resonance one could tell with high confidence that the NNM had been well approximated based on the phase of the laser velocity and the response. It seemed that even very small frequency shifts of less than 1%, could be measured confidently. Hence, the preliminary conclusion of this work is that force appropriation is preferable to nonlinear system identification when seeking to characterize a geometrically nonlinear system such as this gong. It seems that further research is needed to improve the RFS method before it can be used to confidently compute the response of a system such as this.

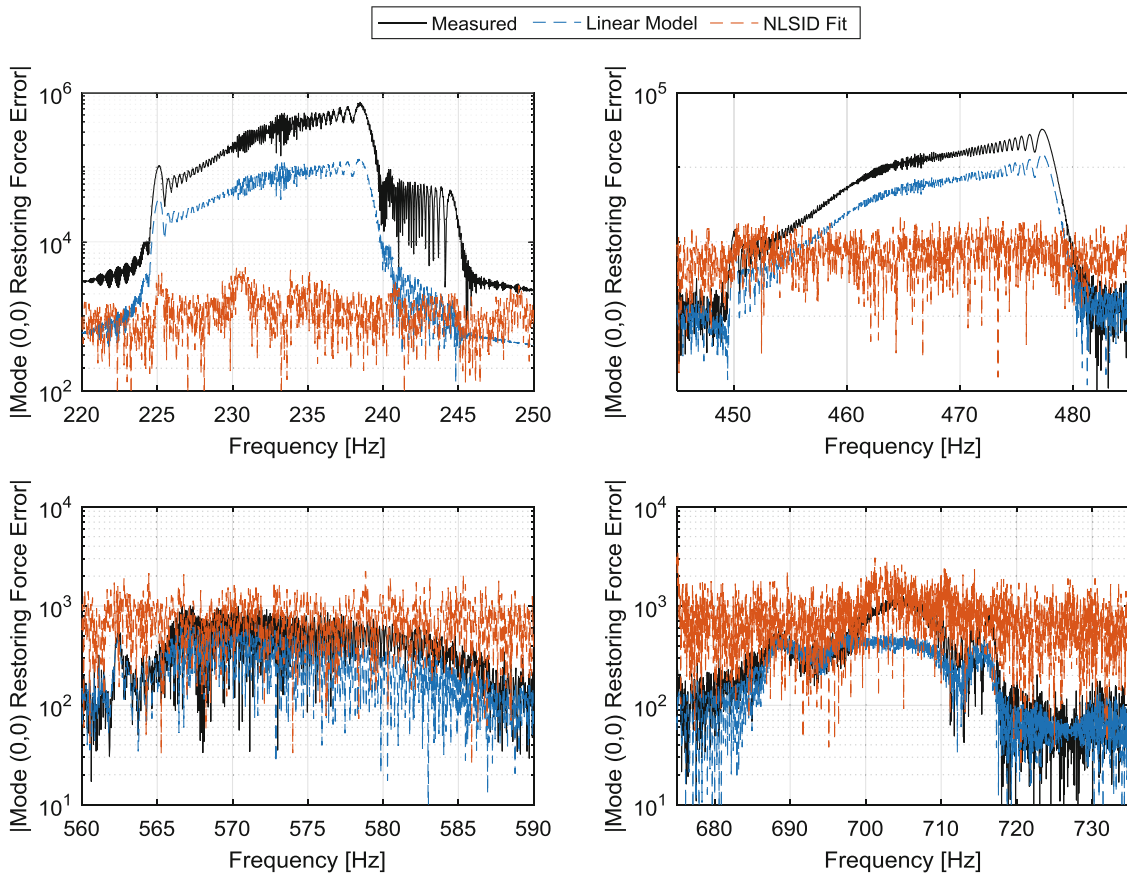


Fig. 10.12 Error in the mode (0,0) reconstructed restoring force compared to the measured restoring force

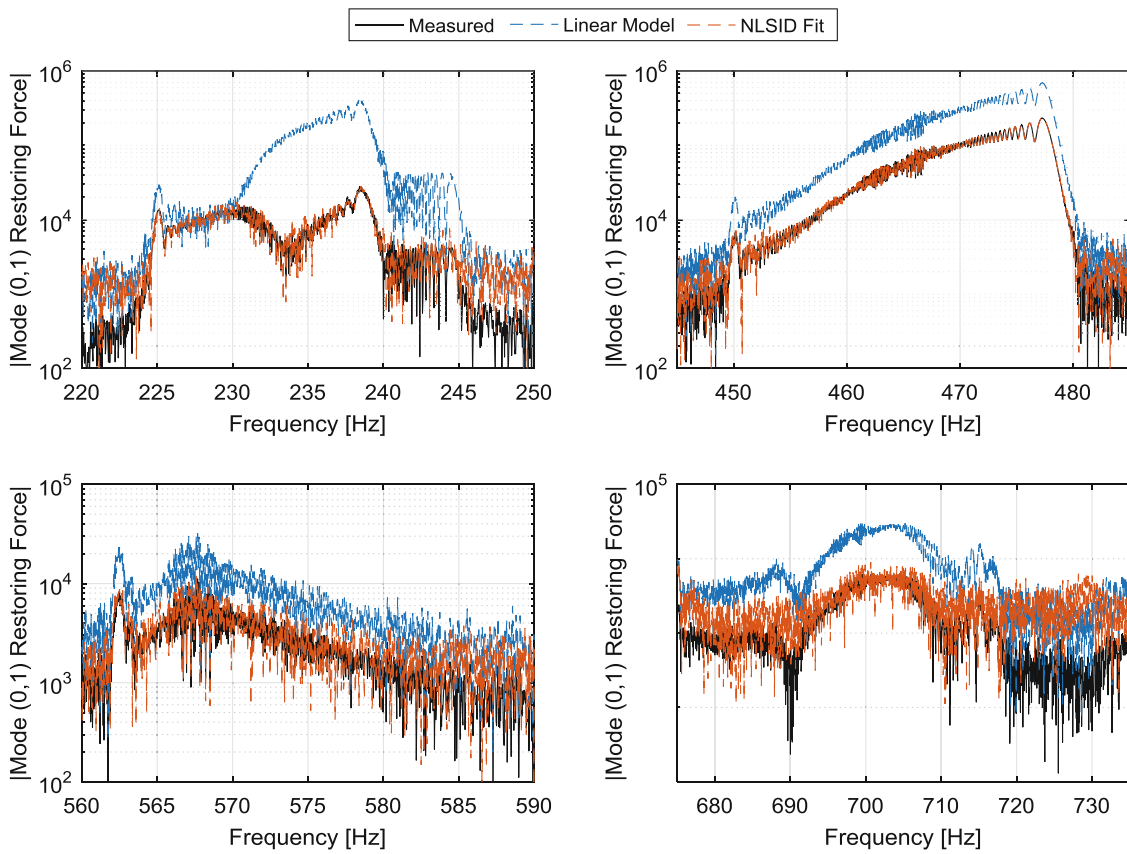


Fig. 10.13 Comparison of the mode (0,1) reconstructed restoring force to the measured restoring force

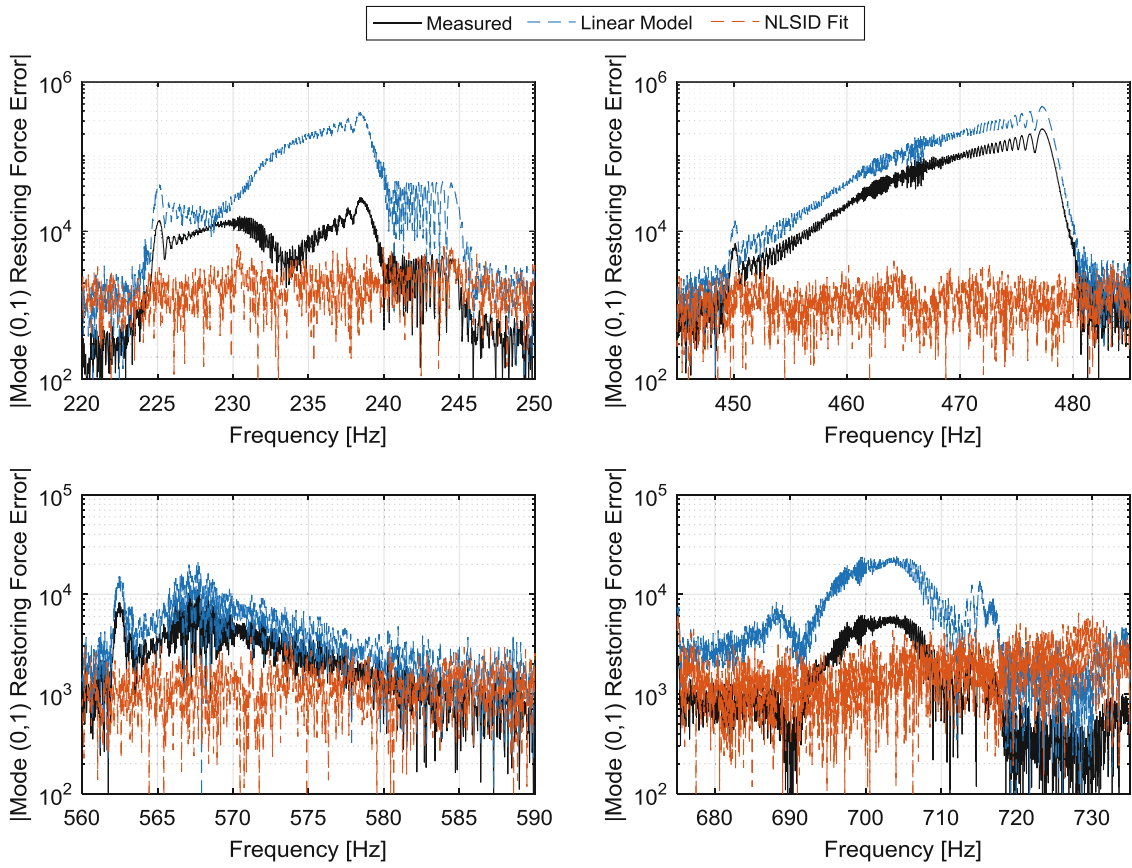


Fig. 10.14 Error in the mode (0,1) reconstructed restoring force compared to the measured restoring force

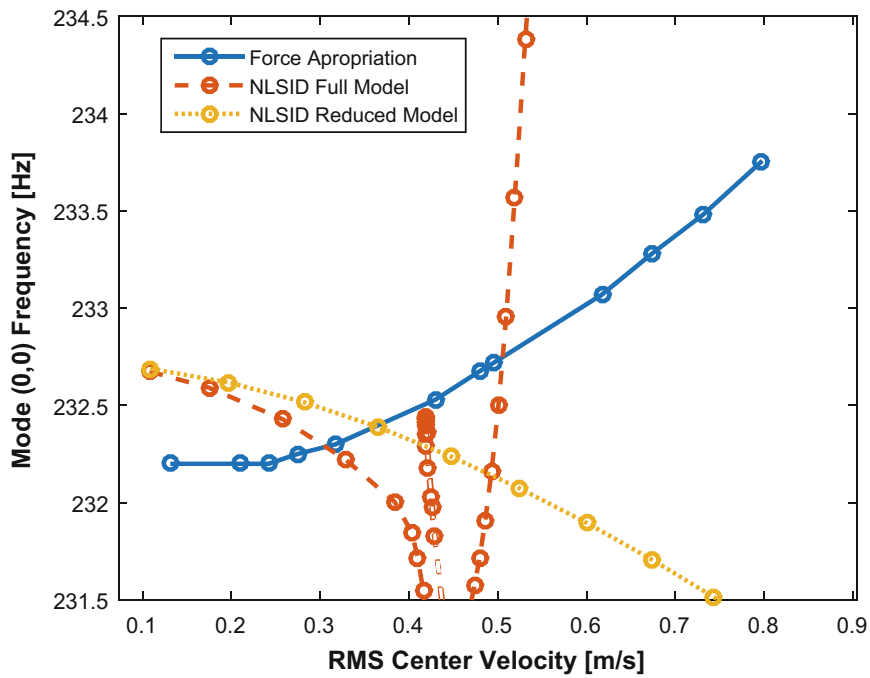


Fig. 10.15 NNM of the (0,0) mode based on Identified (NLSID) model, compared to the NNM measured using force appropriation

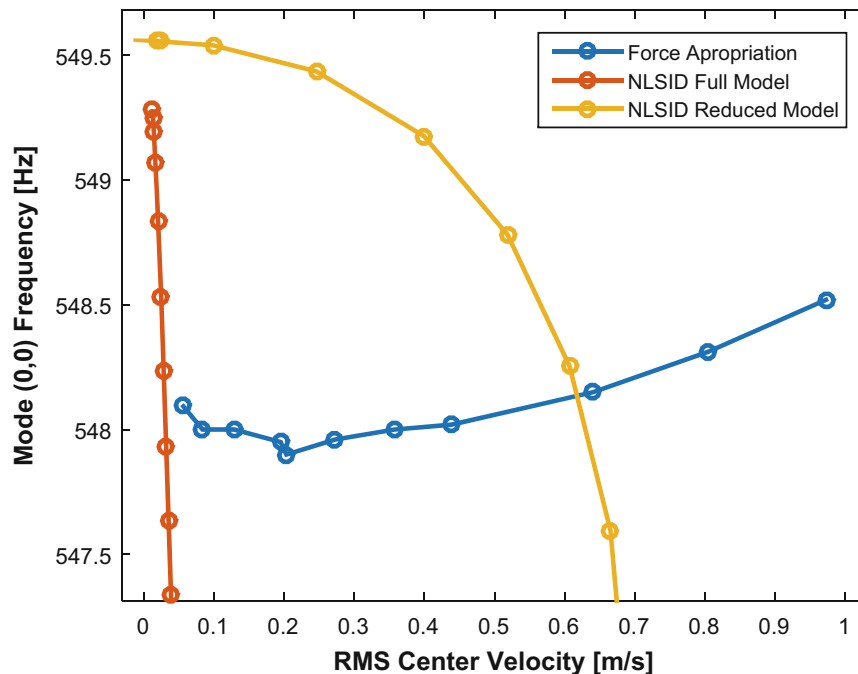


Fig. 10.16 NNM of the (0,1) mode based on Identified (NLSID) model, compared to the NNM measured using force appropriation

Acknowledgements This work was supported by the Air Force Office of Scientific Research, Award # FA9550-17-1-0009, under the Multi-Scale Structural Mechanics and Prognosis program managed by Dr. Jaimie Tiley. The authors also wish to thank Mike Spottswood other collaborators in the Structural Sciences Center at the Air Force Research Laboratory for their support and for many helpful discussions.

References

- Mignolet, M.P., Przekop, A., Rizzi, S.A., Spottswood, S.M.: A review of indirect/non-intrusive reduced order modeling of nonlinear geometric structures. *J. Sound Vib.* **332**, 2437–2460 (2013)
- Ehrhardt, D.A., Allen, M.S., Bebernis, T., Neild, S.A.: Finite element model calibration of a nonlinear perforated plate. *J. Sound Vib.* **392**, 280–294 (2017)
- Gordon, R.W., Hollkamp, J.J.: Reduced-order models for acoustic response prediction, Air Force Research Laboratory, AFRL-RB-WP-TR-2011-3040, Dayton, OH (2011)
- Hollkamp, J.J., Gordon, R.W.: Reduced-order models for nonlinear response prediction: implicit condensation and expansion. *J. Sound Vib.* **318**, 1139–1153 (2008)
- Hollkamp, J.J., Gordon, R.W., Spottswood, S.M.: Nonlinear modal models for sonic fatigue response prediction: a comparison of methods. *J. Sound Vib.* **284**, 1145–1163 (2005)
- Kuether, R.J., Deaner, B., Allen, M.S., Hollkamp, J.J.: Evaluation of geometrically nonlinear reduced order models with nonlinear normal modes. *AIAA J.* **53**, 3273–3285 (2015)
- Ehrhardt, D.A., Kuether, R.J., Allen, M.S.: Nonlinear normal modes in finite element model validation of geometrically nonlinear flat and curved beams, Scitech 2015, 56th AIAA Structures, Structural Dynamics and Materials Conference, Kissimmee, Florida (2015)
- Rosenberg, R.M.: Normal modes of nonlinear dual-mode systems. *J. Appl. Mech.* **27**, 263–268 (1960)
- Kerschen, G., Peeters, M., Golinval, J.C., Vakakis, A.F.: Nonlinear normal modes. Part I. A useful framework for the structural dynamicist. *Mech. Syst. Signal Process.* **23**, 170–194 (2009)
- Vakakis, A.F.: Non-linear normal modes (NNMs) and their applications in vibration theory: an overview. *Mech. Syst. Signal Process.* **11**, 3–22 (1997)
- Peeters, M., Kerschen, G., Golinval, J.C.: Dynamic testing of nonlinear vibrating structures using nonlinear normal modes. *J. Sound Vib.* **330**, 486–509 (2011)
- Peeters, M., Kerschen, G., Golinval, J.C.: Modal testing of nonlinear vibrating structures based on nonlinear normal modes: experimental demonstration. *Mech. Syst. Signal Process.* **25**, 1227–1247 (2011)
- Ehrhardt, D.A., Allen, M.S.: Measurement of nonlinear normal modes using multi-harmonic stepped force appropriation and free decay. *Mech. Syst. Signal Process.* **76**, 612–633 (2016)
- Noël, J.-P., Renson, L., Grappasonni, C., Kerschen, G.: Identification of nonlinear normal modes of engineering structures under broadband forcing. *Mech. Syst. Signal Process.* **74**, 95–110 (2016)

15. Spottswood, S.M., Allemang, R.J.: Identification of nonlinear parameters for reduced order models. *J. Sound Vib.* **295**, 226–245 (2006)
16. Spottswood, S.M., Allemang, R.J.: On the investigation of some parameter identification and experimental modal filtering issues for nonlinear reduced order models. *Exp. Mech.* **47**, 511–521 (2007)
17. Kerschen, G., Worden, K., Vakakis, A.F., Golinval, J.-C.: Past, present and future of nonlinear system identification in structural dynamics. *Mech. Syst. Signal Process.* **20**, 505–592 (2006)
18. Ducceschi, M., Touze, C.: Modal approach for nonlinear vibrations of damped impacted plates: application to sound synthesis of gongs and cymbals. *J. Sound Vib.* **344**, 313–331 (2015)
19. Chaigne, A., Touze, C., Thomas, O.: Nonlinear vibrations and chaos in gongs and cymbals. *Acoust. Sci. Technol.* **26**, 403–409 (2005)
20. Spelman, G.M., Langley, R.S.: *Statistical Energy Analysis of Nonlinear Vibrating Systems*. ISMA, Leuven (2014)
21. Kuether, R.J., Allen, M.S.: A numerical approach to directly compute nonlinear normal modes of geometrically nonlinear finite element models. *Mech. Syst. Signal Process.* **46**, 1–15 (2014)
22. Peeters, M., Viguie, R., Serandour, G., Kerschen, G., Golinval, J.C.: Nonlinear normal modes, Part II: toward a practical computation using numerical continuation techniques. *Mech. Syst. Signal Process.* **23**, 195–216 (2009)
23. Detroux, T., Renson, L., Masset, L., Kerschen, G.: The harmonic balance method for bifurcation analysis of large-scale nonlinear mechanical systems. *Comput. Methods Appl. Mech. Eng.* **296**, 18–38 (2015)
24. Kuether, R.J., Renson, L., Detroux, T., Grappasonni, C., Kerschen, G., Allen, M.S.: Nonlinear normal modes, modal interactions and isolated resonance curves. *J. Sound Vib.* **351**, 299–310 (2015)
25. Hill, T.L., Cammarano, A., Neild, S.A., Wagg, D.J.: Interpreting the forced responses of a two-degree-of-freedom nonlinear oscillator using backbone curves. *J. Sound Vib.* **349**, 276–288 (2015)
26. Mayes, R.L., Pacini, B.R., Roettgen, D.R.: A modal model to simulate typical structural dynamic nonlinearity, 34th International Modal Analysis Conference (IMAC XXXIV), Orlando, FL (2016)
27. Bendat, J.S., Piersol, A.G.: *Engineering Applications of Correlation and Spectral Analysis*. Wiley, New York (1980)
28. Allen, M.S., Ginsberg, J.H.: A global, Single-Input-Multi-Output (SIMO) implementation of the algorithm of mode isolation and applications to analytical and experimental data. *Mech. Syst. Signal Process.* **20**, 1090–1111 (2006)
29. Rades, M., Ewins, D.J.: MIFs and MACs in modal analysis, 20th International Modal Analysis Conference (IMAC-20), Los Angeles, CA (2002)



Chapter 11

An Enhanced Static Reduction Algorithm for Predictive Modeling of Bolted Joints

Iman Zare, Matthew S. Allen, and Emily Jewell

Abstract Bolted joints in assembled structures are responsible for much of the structure's damping and gives rise to nonlinear behavior. While a bolted joint can presumably be modeled in commercial FE codes, even quasi-static analysis is extremely expensive due to the level of detail required to capture micro-slip. This work explores the application of a new static reduction method to reduce the computation costs associated with analyzing built-up structure. This novel method applies a Gauss-Seidel algorithm to a model that has been statically reduced to retain only the DOF at the contact interface. To validate the approach, a simple contact problem was first considered that examined contact between a deformable block and a rigid surface. Coulomb friction was used at the interface and the results were verified by examining the load dependence of contact area and model nonlinearities. Subsequently, a contact problem between two deformable bodies in 2D was considered which modeled two beams in a sandwich configuration. In all cases it was found the static reduction method's resulted in dramatic computational savings while providing good accuracy as compared to simulations in commercial finite element software.

Keywords Component Mode Synthesis · Hurty/Craig-Bampton · Boundary Conditions · Residual Flexibility · Residual Stiffness

11.1 Introduction

Bolted joints in assembled structures are responsible for much of the structure's damping and gives rise to nonlinear behavior. While a bolted joint can presumably be modeled in commercial FE codes, even quasi-static analysis is extremely expensive due to the level of detail required to capture micro-slip. This work explores the application of a new static reduction method to reduce the computation costs associated with analyzing built-up structure. This novel method applies a Gauss-Seidel algorithm to a model that has been statically reduced to retain only the DOF at the contact interface. To validate the approach, a simple contact problem was first considered that examined contact between a deformable block and a rigid surface. Coulomb friction was used at the interface and the results were verified by examining the load dependence of contact area and model nonlinearities. Subsequently, a contact problem between two deformable bodies in 2D was considered which modeled two beams in a sandwich configuration. In all cases it was found the static reduction method's resulted in dramatic computational savings while providing good accuracy as compared to simulations in commercial finite element software.

While most studies to date have presumed that a nonlinear transient analysis must be used to correctly account for friction in the interfaces between structures, Festjens et al. [1] recently proposed a model reduction technique in which a single quasi-static loading is applied to the structure and they showed how this can be used to predict the dynamic response for oscillations up to some maximum displacement. Their method spatially decomposes a structure into a linear domain away from the joint and a nonlinear domain near the joint. Then the inertial term in the joint domain is neglected and the joint is assumed to behave quasi-statically. Lacayo and Allen [2] later presented a variant on this method, known as Quasi-Static Modal Analysis, and applied it to structures where the joints were modeled as discrete Iwan elements. They that Quasi-Static Modal Analysis produces very accurate estimates of nonlinear behavior of the joint, especially the amplitude-dependent modal damping and natural frequency when the response is dominated by a single mode. In essence, Quasi-Static Modal Analysis (QSMA) is an extension of modal analysis to structures with weakly nonlinear joints in that one can estimate the amplitude dependent natural frequency and damping of a structure using a few nonlinear static simulations. The modes are assumed to remain uncoupled and any changes in the mode shapes are neglected.

I. Zare · M. S. Allen (✉) · E. Jewell
Department of Engineering Physics, University of Wisconsin-Madison, Madison, WI, USA
e-mail: msallen@engr.wisc.edu

This advancement prompted Jewell et al. [3] to apply this technique to detailed finite element models that included nonlinear contact between the bolted interfaces using a commercial software package. While their results showed that such an analysis is feasible, they struggled to obtain accurate results and noted that, once the structure had been meshed with adequate fidelity to capture micro-slip, the computational cost was very significant even to perform a single static analysis. This work explores a more computationally efficient alternative that follows the work of Ahn and Barber [4, 5]. Specifically, static reduction is used to eliminate all of the DOF except those at the contact interface, and then a Gauss-Seidel algorithm is used to solve the nonlinear contact problem in Matlab. A variant on the Gauss-Seidel algorithm has been developed, based on the Block-Gauss Seidel approach and will be elaborated in the presentation, that seems to improve the computational efficiency and the resulting algorithm is evaluated by comparing it with the commercial software package, Abaqus[®].

11.2 Sample Results

The proposed algorithm was tested by applying it to the structure shown in Fig. 11.1, which represents a very simple structure with a bolted joint. The normal load, P , represents the clamping load from a bolt and the lateral load, Q , provides a loading to the structure that induces micro-slip.

A finite element model was created of this structure, with 300 nodes along the contact interface. Then the stiffness matrices for the top and bottom blocks was exported to Matlab and statically reduced using the approach in [5]. The proposed algorithm was then to find the contact forces at the interface, and they were compared to a solution of the full order FEM in Abaqus. The results were indistinguishable, and so only the result from the proposed algorithm is shown. The difference between the solutions, expressed as a percentage by dividing it by the largest force over the contact surface, was computed and is shown below. There are small differences at the edges of the contact, presumably due to a slightly different number of nodes being in contact in the two solutions, but the forces are within 1% of each other (Fig. 11.2).

While this simple model could be solved very quickly in Abaqus, the solution above took only 30 s, the proposed algorithm was even faster, solving in uncompiled code in less than 0.15 s. This difference is expected to be very important when going to three-dimensional models, where solve times have been in excess of 24 h even for relatively simple models [3]. Furthermore, commercial contact algorithms are known to favor robustness over accuracy, which perhaps explains the challenges encountered in [3] in obtaining physically reasonable results using a commercial code. In the future this algorithm will be used to compare predictions of the stiffness and damping of joints to experimental measurements.

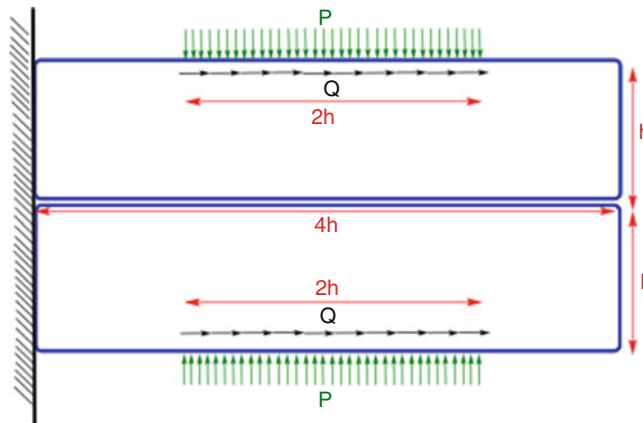


Fig. 11.1 Beam structure with a clamping load representing a bolted joint and a shear load which exercises the joint

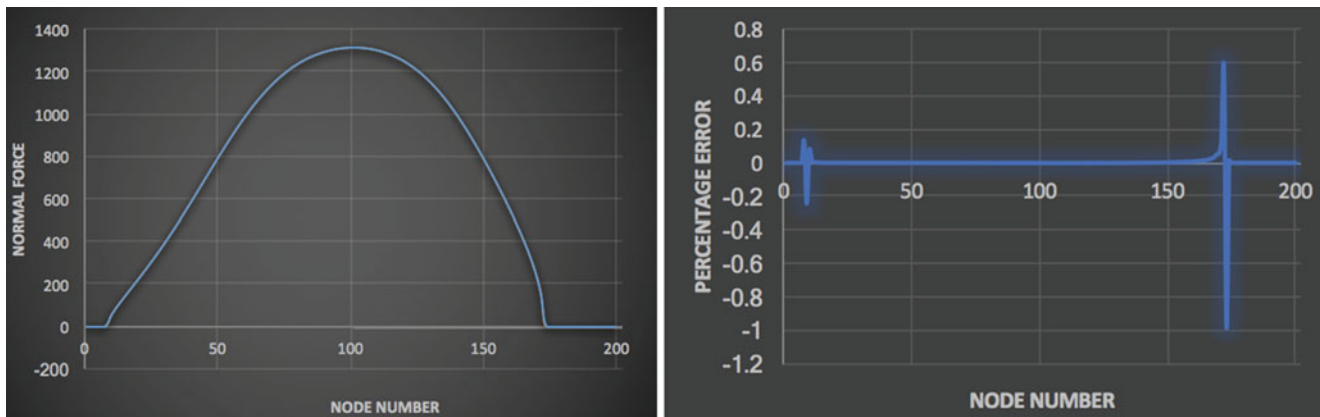


Fig. 11.2 (left) Normal force at the contact of the beams as computed by the proposed algorithm. The result from Abaqus was visually indistinguishable. (right) Percent error in the result computed by the proposed algorithm, taking the result from Abaqus as the truth model

Acknowledgements This material is based in part upon work supported by the National Science Foundation under Grant Number CMMI-1561810. Any opinions, findings, and conclusions or recommendations expressed in this material are those of the author(s) and do not necessarily reflect the views of the National Science Foundation.

References

1. Festjens, H., Chevallier, G., Dion, J.-L.: A numerical tool for the design of assembled structures under dynamic loads. *Int. J. Mech. Sci.* **75**, 170–177 (2013)
2. R. M. Lacayo and M. S. Allen, Updating structural models containing nonlinear iwan joints using quasi-static modal analysis. *Mech. Syst. Signal Process.* **2017** (2017)
3. Jewell, E., Allen, M.S., Lacayo, R.: Predicting damping of a cantilever beam with a bolted joint using quasi-static modal analysis, Proceedings of the ASME 2017 International Design Engineering Technical Conference & 13th International Conference on Multibody Systems, Nonlinear Dynamics, and Control IDETC/ MSNDC 2017, Cleveland, OH, USA (2017)
4. Ahn, Y.J., Barber, J.R.: Response of frictional receding contact problems to cyclic loading. *Int. J. Mech. Sci.* **50**, 1519–1525 (2008)
5. Flicek, R.C., Hills, D.A., Barber, J.R., Dini, D.: Determination of the shakedown limit for large, discrete frictional systems. *Eur. J. Mech. A. Solids.* **49**, 242–250 (2015)



Chapter 12

Time-varying Spectral Submanifolds: Analytic Calculation of Backbone Curves and Forced Response

Thomas Breunung and George Haller

Abstract To understand and analyze the behavior of realistic nonlinear structures it is desirable to reduce the dimensionality of the system, as well as simplify the equation of motion. Reduction to Spectral submanifolds (SSMs) has recently been shown to provide such a dimension reduction, yielding exact and unique reduced-order models for nonlinear unforced mechanical vibrations. Here we extend these results to periodically or quasiperiodically forced mechanical systems, obtaining analytic expressions for forced responses and backbone curves on modal (i.e. two-dimensional) time-dependent SSMs. We demonstrate our analytical formulae on numerical examples and compare them to results obtained from alternative methods.

Keywords Backbone curves · Forced-damped vibrations · Nonlinear vibrations · Reduced order models · Spectral submanifolds

The dynamic behavior of realistic nonlinear structures is governed by complex dynamic evolution equations of a high number of degrees of freedom. To understand and analyze such behavior, it is desirable to reduce the dimensionality and simplify the equations of motion. Traditionally, these two tasks have been dealt with separately. The goal of this work is to construct a reduction of a forced, dissipative nonlinear mechanical system to a lower-dimensional invariant manifold and simplify the dynamics on this manifold at the same time.

Various concepts of modal decomposition have been proposed in the literature for nonlinear mechanical systems (see e.g. Kerschen et al. [1]). These approaches invariably seek invariant subspaces or manifolds to achieve a dimensional reduction. Since this is a challenging and generally unsolved problem by itself, the reduced dynamics, which govern the evolution of the system on some approximation to an envisioned invariant manifold, are usually not simple, and hence give no immediate insight into the nonlinear behavior. For example, Jiang et al. [2] and Gabale and Sinha [3] integrate the reduced dynamics numerically, and hence do not obtain a symbolic representation or general statements about the forced response.

In order to simplify equations of motion, analytical methods have been widely used for low-dimensional examples. For instance, Jezequel and Lamarque [4] and Neild and Wagg [5] indicate the usability of the method of normal forms to simplify the equations of motion for higher-dimensional systems. However, since the method applies a series of smooth transformations to all state variables, the dimensionality of the system is not reduced in the process.

Perhaps the most broadly sought features of nonlinear mechanical systems are their backbone curves, i.e., graphs depicting the maximal response amplitudes under different forcing frequencies and amplitudes. For simplicity, such backbone curves are often calculated for the conservative limit of the unforced system (see e.g., Neild and Wagg [5] and Peeters et al. [6]). The hope is that these results carry over to the original system for low values of damping and forcing. In practice, however, one does not know in advance if this expectation is justified for the damping and forcing values under consideration.

As detailed by Haller and Ponsioen [7], the abstract invariant manifold results of Cabré et al. [8] provide an efficient method to reduce an autonomous (i.e., unforced) mechanical system to low-dimensional invariant manifolds that serve as nonlinear extensions of modal subspaces. The smoothest nonlinear continuation of such a modal subspace is called a spectral submanifold (SSM) Haller and Ponsioen [7]. As observed by Haller and Ponsioen [7], the existence and uniqueness of an SSM for the non-autonomous (i.e., forced) system follows from the results of Haro and de la Llave [9].

To the best of our knowledge, the full power of the results of Cabré et al. [8] and Haro and de la Llave [9] have not yet been exploited for mechanical systems. Here we show that these results enable the explicit continuation of backbone curves without costly numerical experimentation. To this end, we consider oscillations around an arbitrary equilibrium of the system. Via the parametrization method, we reduce the system to a two-dimensional SSM and give strict conditions for

T. Breunung (✉) · G. Haller
Institute for Mechanical Systems, ETH Zürich, Zürich, Switzerland
e-mail: brethoma@ethz.ch

the validity of such a reduction. We then continue with a given autonomous parameterization of the SSM and the reduced dynamics under the addition of small forcing terms. For near-resonant forcing, we eliminate the small denominators arising in the parameterization of the SSM. We give an explicit parameterization of the non-autonomous SSM and the reduced dynamics. Through a judicious choice of the parameterization, we simplify the reduced dynamics significantly, such that we can solve for forced-periodic responses analytically.

Having derived condensed formulas for the forced response, we solve for the forcing frequency at which the response amplitude is maximal. Such amplitude-frequency pairs form a one dimensional curve (i.e. the backbone curve) as the forcing amplitude is varied as a parameter. Furthermore, we can analytically compute stability regions of the forced response.

We show the application of our SSM-based analytic results on forced responses and backbone curves in numerical examples. On these examples, we compare our results with an approach from Neild and Wagg [5], with a normal-form type method from Touzé and Amabili [11] and with direct numerical continuation.

References

1. Kerschen, G., Peeters, M., Golinval, J.C., Vakakis, A.: Nonlinear normal modes, Part I: a useful framework for the structural dynamicist. *Mech. Syst. Signal Process.* **23**, 170–194 (2009)
2. Jiang, D., Pierre, C., Shaw, S.: Nonlinear normal modes for vibratory systems under harmonic excitation. *J. Sound Vib.* **288**, 791–812 (2005)
3. Gabale, A., Sinha, S.: Model reduction of nonlinear systems with external periodic excitations via construction of invariant manifolds. *J. Sound Vib.* **330**, 2596–2607 (2011)
4. Jezequel, L., Lamarque, C.H.: Analysis of non-linear dynamical systems by the normal form theory. *J. Sound Vib.* **149**(3), 429–459 (1991)
5. Neild, S., Wagg, D.: Applying the method of normal forms to second-order nonlinear vibration problems. *Philos. Trans. R. Soc. A Math. Phys. Eng. Sci.* **467**, 1141–1163 (2015)
6. Peeters, M., Kerschen, G., Golinval, J.-C.: Dynamic testing of nonlinear vibrating structures using nonlinear normal modes. *J. Sound Vib.* **330**(3), 486–509 (2011)
7. Haller, G., Ponsioen, S.: Nonlinear normal modes and spectral submanifolds: existence, uniqueness and use in model reduction. *Nonlinear Dyn.* **86**(3), 1493–1534 (2016)
8. Cabré, X., Fontich, E., de la Llave, R.: The parameterization method for invariant manifolds i: manifolds associated to non-resonant subspaces. *Univ. Indiana Math. J.* **52**, 283–328 (2003)
9. Haro, A., de la Llave, R.: A parameterization method for the computation of invariant tori and their whiskers in quasi-periodic maps: rigorous results. *J. Differ. Equ.* **228**(2), 530–579 (2006)
10. Szalai, R., Ehrhardt, D., Haller, G.: Nonlinear model identification and spectral submanifolds for multi-degree-of-freedom mechanical vibrations. *Proc. R. Soc. A.* **473**, (2017)
11. Touzé, C., Amabili, M.: Nonlinear normal modes for damped geometrically nonlinear systems: application to reduced-order modelling of harmonically forced structures. *J. Sound Vib.* **298**(4), 958–981 (2006)

Chapter 13

Operational Modal Analysis Based Stress Estimation in Friction Systems



Marius Tarpø, Tobias Friis, Bruna Nabuco, Sandro Amador, Evangelos Katsanos, and Rune Brincker

Abstract It is possible to estimate the strain response of a structure in unmeasured points by the use of operational modal analysis and modal expansion. Both techniques are based on the assumption that the system is linear. However, this is not always the case since nonlinear elements often violate this assumption. In this paper, the precision of estimating the strain response of a nonlinear system is investigated using the operational response of numerical simulations. Local nonlinearities are introduced by adding friction to the test specimen and this paper finds that this approach of strain estimation can still predict the strains with high precision.

Keywords Operational modal analysis · Strain estimation · Modal expansion · Structural health monitoring · Non-linear dynamics

13.1 Introduction

Fluctuating forces continuously influence offshore structures and it causes the structures to fatigue over time. Eventually, this load history leads to failure of the structure. In the design process of offshore structures, we account for the fatigue by a designed lifetime, which is based on approximations of this load history. However, the actual lifetime of the structure in operation is unknown and there is a significantly potential profit if we determine the remaining lifetime. Vibration based Structural Health Monitoring might provide a better access to the actual integrity than the design process could. Unfortunately, several issues complicate the monitoring of offshore structures [1, 2]. The environment is hostile and the structures are abstruse. The seawater corrodes and damages underwater sensors, which makes subsea monitoring difficult. Non-linear connectors between platforms can make the system response non-linear. The structural properties change over time and the structural response can become non-stationary due to temporary operational forces.

We are able to estimate the full-field dynamic strain response of a linear structure in unmeasured points above sea level. Here, we use operational modal analysis to identify the modal parameters and we expand the measured response to the strain response of the entire structure. Different methods exist for the full-field strain estimation where the *Modal Expansion* [3–7] and the *Kalman filter* [7–9] are among the most used techniques.

However, the mentioned techniques are based on linear systems whereas many actual structures have some amount of non-linearities. Various types of non-linearities introduce potential errors in the operational modal analysis based strain estimation. Zhang et al. checked the effect of non-linearities on operational modal analysis and they found output-only identification techniques can extract the modal parameter of non-linear systems [10]. In their tests the mode shapes and natural frequencies had low variance and bias whereas the damping ratios had a higher variance and bias.

In this paper, we will use operational modal analysis and the modal expansion so we can estimate the strain response of a simulated system where we add friction in order to introduce non-linearity to the system. This paper is a part of an ongoing project regarding non-linearities in operational modal analysis and strain estimation [11, 12]. We are able to estimate the strain response in a non-linear friction system with high precision. In this test, the frequency domain decomposition and the modal expansion are unaffected by the local non-linearities caused by the friction.

M. Tarpø
Aarhus University, Aarhus, Denmark
e-mail: martar@eng.au.dk

T. Friis (✉) · B. Nabuco · S. Amador · E. Katsanos · R. Brincker
Technical University of Denmark, Kongens Lyngby, Denmark
e-mail: brunan@byg.dtu.dk; sdio@byg.dtu.dk; vakat@byg.dtu.dk; runeb@byg.dtu.dk

13.2 Theory

13.2.1 Operational Modal Analysis and the Frequency Domain Decomposition

Operational Modal Analysis is an experimental technique that only use the system response for modal identification. We assume that the system is linear and time invariant and the excitation of the system has a high level of white Gaussian noise characteristics [13]. For this paper, we will use the *Frequency Domain Decomposition* as identification technique [14]. The spectral density matrix is defined as [13]

$$\mathbf{G}_{yy}(\omega) = \mathcal{F} \left(\mathbb{E} [\mathbf{y}(t)\mathbf{y}^T(t + \tau)] \right) \quad (13.1)$$

where \mathcal{F} denotes the Fourier transformation, \mathbb{E} is the expectation operator, $\mathbf{y}(t) \in \mathbb{R}^{N \times 1}$ is the system response and N denotes the number degrees-of-freedom. The *Modal Decomposition* states that the response of the linear system, $\mathbf{y}(t)$, is a linear combination of the mode shape, $\mathbf{B} \in \mathbb{R}^{N \times M}$, and the modal coordinates, $\mathbf{q}(t) \in \mathbb{R}^{M \times 1}$. Here M is the number of modes.

$$\mathbf{y}(t) = \mathbf{B}\mathbf{q}(t) \quad (13.2)$$

This is also called a linear transformation. We insert the modal decomposition into the spectral density matrix.

$$\mathbf{G}_{yy}(\omega) = \mathbf{B}\mathbf{G}_{qq}(\omega)\mathbf{B}^H \quad (13.3)$$

where $\mathbf{G}_{qq}(\omega) \in \mathbb{R}^{M \times M}$ is the spectral density matrix of the modal coordinates, $\mathbf{q}(t)$. Next, we perform a singular value decomposition of the spectral density matrix.

$$\mathbf{G}_{yy}(\omega) = \mathbf{U}(\omega)\mathbf{S}(\omega)\mathbf{U}(\omega)^H \quad (13.4)$$

We see a similarity between Eqs. (13.3) and (13.4). The Frequency Domain Decomposition is based on the approximation that the singular vectors are analogous to the mode shapes and the singular values are similar to the spectral density matrix for the modal coordinates. However the technique is a approximation [13]. For one thing, we assume that the modal coordinates are uncorrelated, which is only the case for a linear system.

13.2.2 Strain Estimation

In this section, we will show how to estimate the strain response in any point of a structure using the Modal Expansion technique. We want to expand the experimental mode shapes so we create a linear relationship between the modal matrices using the *Local Corresponding principle* [15].

$$\hat{\mathbf{A}} = \mathbf{B}_a\mathbf{P} \quad (13.5)$$

where \mathbf{A} is the experimental modal matrix, $\hat{\mathbf{A}}$ is the smoothen experimental modal matrix, \mathbf{B}_a is a reduced modal matrix from a highly correlated finite element model and \mathbf{P} is the transformation matrix. We expand the experimental modal matrix by replacing the reduced finite element modal matrix with the full modal matrix, \mathbf{B} .

$$\hat{\mathbf{A}}_{full} = \mathbf{B}\mathbf{P} \quad (13.6)$$

where $\hat{\mathbf{A}}_{full}$ is the expanded experimental modal matrix. Next, we want to find the response of the entire structure so we estimate the modal coordinates from Eq. (13.2).

$$\hat{\mathbf{q}}(t) = \mathbf{A}^+\mathbf{y}(t) \quad (13.7)$$

The modal coordinates for the strain response and displacement are the same [16]. Therefore, we estimate the strain response if we use the estimated modal coordinates, the finite element model and the transformation matrix, \mathbf{P} .

$$\hat{\boldsymbol{\varepsilon}}(t) = \mathbf{B}_\varepsilon \mathbf{P} \hat{\mathbf{q}}(t) \quad (13.8)$$

where \mathbf{B}_ε is the full strain modal matrix from the finite element model and $\hat{\boldsymbol{\varepsilon}}(t)$ is the predicted strain response of the structure.

13.2.3 Quality Measurements

We use the Time Response Assurance Criterion (*TRAC*) [6] and Frequency Response Assurance Criterion (*FRAC*) [5] as quality measurements of the strain prediction.

$$TRAC_i = \frac{(\boldsymbol{\varepsilon}_i(t)^T \hat{\boldsymbol{\varepsilon}}_i(t))^2}{(\boldsymbol{\varepsilon}_i(t)^T \boldsymbol{\varepsilon}_i(t)) (\hat{\boldsymbol{\varepsilon}}_i(t)^T \hat{\boldsymbol{\varepsilon}}_i(t))} \quad (13.9)$$

$$FRAC_i = \frac{(\boldsymbol{\varepsilon}_i(f)^H \hat{\boldsymbol{\varepsilon}}_i(f))^2}{(\boldsymbol{\varepsilon}_i(f)^H \boldsymbol{\varepsilon}_i(f)) (\hat{\boldsymbol{\varepsilon}}_i(f)^H \hat{\boldsymbol{\varepsilon}}_i(f))} \quad (13.10)$$

where $\boldsymbol{\varepsilon}_i(f)$ is the Fourier transformation of the signal $\boldsymbol{\varepsilon}_i(t)$. Both *TRAC* and *FRAC* compare general shapes and tendencies in the data, however, neither of them take amplitude differences into account.

13.3 Case Study

We simulate the response of a structure to test the precision of strain prediction in the present of friction. First we estimate the strain response in the linear case, then we add friction to the system and estimate the strain response again. For the rest of the paper, we will refer to the system with and without friction as the linear and non-linear case.

13.3.1 Numerical Simulation Case

For the numerical simulation case, we chose to employ a finite element model of a scale model of the unmanned offshore platform Valdemar. The real structure is a tripod oil platform and it is located in the Danish part of the North Sea. The scaling of the scale model is 1:50 and it is made of polymethyl methacrylate, see Fig. 13.1.

The finite element model includes 5083 elements of beam and shell type. We modelled all of the tubing parts of the structure by linear beam elements based on the Timoshenko beam theory with six degrees-of-freedom at each node. Similarly, the shell elements for the deck on the topsite are rectangular four node elements and they are based on Mindlin-Reissner shell theory with six degrees-of-freedom at each node. The full model has been reduced using the System Equivalent Reduction and Expansion Process (SEREP) by O'Callahan to 22 degrees-of-freedom [17]. This resembles seven measurement point on the real structure, see Fig. 13.2, and 15 additional degrees-of-freedom that enables us to calculate the strains in the vertical direction in two points, see Fig. 13.3. The strain response resembles two "virtual strain gauges" as on a real structure and we will use them as reference for the strain estimation. The reduced model contains five physical modes.

It is desirable for the simulation case to have a situation that resembles a realistic case with measurements of a real structure. With this in mind, we created two different versions of the finite element model. The first model is the finite element model as described without any changes and we change the second model by adding five small masses intentionally placed. The idea is that the first model will constitute an updated model, which matches reasonably well with the tested structure, and the second model is the "real" structure.

We apply two types of damping to the reduced model: (i) linear proportional damping and (ii) friction damping. For the linear damping term, we construct a damping matrix directly from the desired damping ratios of 1% for each mode. For the second damping term, we add friction by attaching a special element to the sixth degree-of-freedom, see Fig. 13.1.

Fig. 13.1 Finite element model and the position of friction

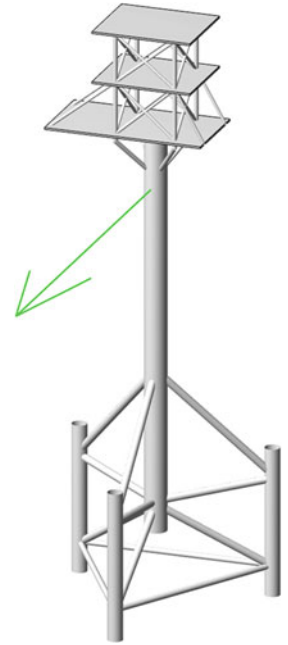
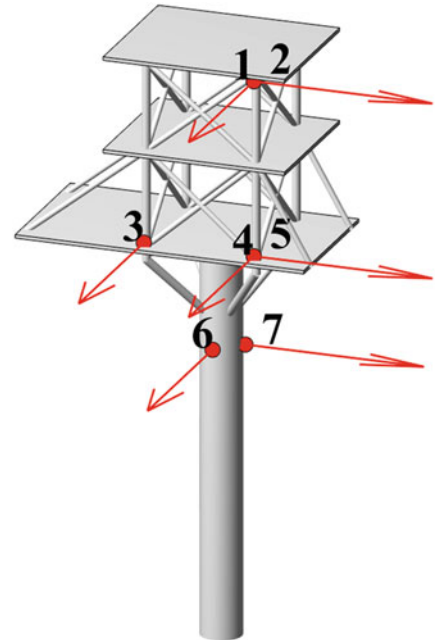


Fig. 13.2 Position of virtual displacement sensors



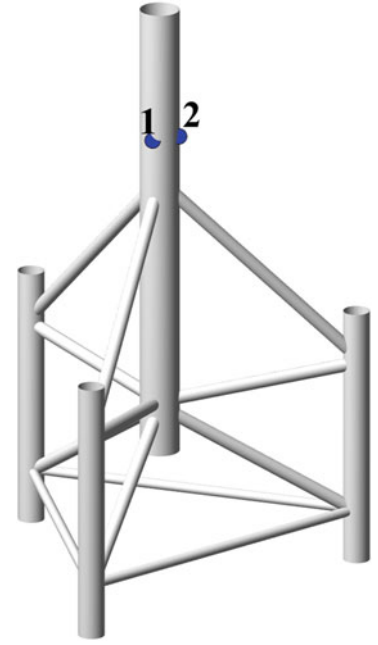
This element is basically a bilinear spring where the stiffness of the second part is zero. In this way, stiffness will be added to the structure at lower amplitudes of oscillation, but when the force in the element exceeds the slip force, i.e. when the second part of the bilinear spring is reached, purely friction is applied by a constant force.

When we formulate the system of second-order differential equations, the traditional equation of motion of the linear system is left unchanged with the inertia term, viscous damping term, stiffness term and load term. The non-linear friction force is simply implemented through an additional term, $\mathbf{D} \mathbf{f}_d(\mathbf{y}(t))$. Thus, the system of equations becomes:

$$\mathbf{M}\ddot{\mathbf{y}}(t) + \mathbf{C}\dot{\mathbf{y}}(t) + \mathbf{K}\mathbf{y}(t) + \mathbf{D}\mathbf{f}_d(\mathbf{y}(t)) = \mathbf{x}(t) \quad (13.11)$$

where $\mathbf{M} \in \mathbb{R}^{N \times N}$, $\mathbf{C} \in \mathbb{R}^{N \times N}$ and $\mathbf{K} \in \mathbb{R}^{N \times N}$ are the system matrices of the linear system, $\mathbf{D} \in \mathbb{R}^{N \times Q}$ is the damper placement matrix, $\mathbf{f}_d(\mathbf{y}(t)) \in \mathbb{R}^{Q \times 1}$ is the nonlinear (bilinear) force from the friction element and $\mathbf{x}(t) \in \mathbb{R}^{N \times 1}$ is the

Fig. 13.3 Position of virtual strain gauges



external load. N denotes the number degrees-of-freedom and Q denotes the number of dampers. In the present case study, the system is subjected to uncorrelated white Gaussian noise in the seven degrees-of-freedom, see Fig. 13.2.

We use the algorithm by Lu et al. to simulate the non-linear response of the friction damped system [18]. The algorithm utilises a rewriting version of Eq. (13.11) in the following state space format.

$$\dot{\mathbf{z}}(t) = \mathbf{A}_c \mathbf{z}(t) + \mathbf{D}_c \mathbf{f}_d(t) + \mathbf{E}_c \mathbf{x}(t) \quad (13.12)$$

where $\mathbf{z}(t)$ represents the vector of state variables, \mathbf{A}_c is the system matrix and \mathbf{D}_c & \mathbf{E}_c are the counterparts of the damper placement matrix \mathbf{D} and the excitation. These parts are defined as

$$\mathbf{z}(t) = \begin{bmatrix} \dot{\mathbf{y}}(t) \\ \mathbf{y}(t) \end{bmatrix} \in \mathbb{R}^{2N \times 1}, \quad \mathbf{A}_c = \begin{bmatrix} -\mathbf{M}^{-1} \mathbf{C} & -\mathbf{M}^{-1} \mathbf{K} \\ \mathbf{I} & \mathbf{0} \end{bmatrix} \in \mathbb{R}^{2N \times 2N} \quad (13.13)$$

$$\mathbf{D}_c = \begin{bmatrix} \mathbf{M}^{-1} \mathbf{D} \\ \mathbf{0} \end{bmatrix} \in \mathbb{R}^{2N \times Q}, \quad \mathbf{E}_c = \begin{bmatrix} \mathbf{M}^{-1} \\ \mathbf{0} \end{bmatrix} \in \mathbb{R}^{2N \times N} \quad (13.14)$$

The solution of Eq. (13.12) is formulated in discrete time by assuming that the variation is linear, of the damper force and external force between time-steps. The non-linear damper force is calculated by iterating the non-linear force from the attached friction element within each time-step. For a full description of the algorithm and the iterative procedure see [18].

In order to illustratively quantify the non-linearity of simulation case, we employ two different approaches. In the first approach, we apply an impulse force to the numerical model at the first and second degree-of-freedom and obtain the maximum displacement of the modal coordinates. We repeat the process while varying the size of the impulse force and achieve a relation between the force and the maximum modal coordinates, see Fig. 13.4. From these results, the second and fifth mode display an evident non-linear relationship between force and modal coordinate. The position of the damping force affects the modes where it directly hinders movement of the mode shapes. For the second approach, we assess the distribution of the modal coordinate of the second mode, which is one of the effected modes, with and without applying the friction element, see Figs. 13.5 and 13.6. This difference relates directly to the behaviour of a friction damped system. The response will stay longer at a smaller intensity, when the friction element is adding stiffness, and damping is lower at higher amplitudes resulting in more outliers.

Figure 13.7 presents the modal coordinates for the linear and non-linear case and Figs. 13.8 and 13.9 show the singular values of the spectral density matrix of the response in the seven degrees-of-freedom in the linear and non-linear case. From the mentioned results, the response of mode 2 and 5 are markedly reduced, while the response of the remaining three modes is only slightly effected. By adding friction, the energy and the width of the peak change for the second and fifth mode in the spectral density matrices.

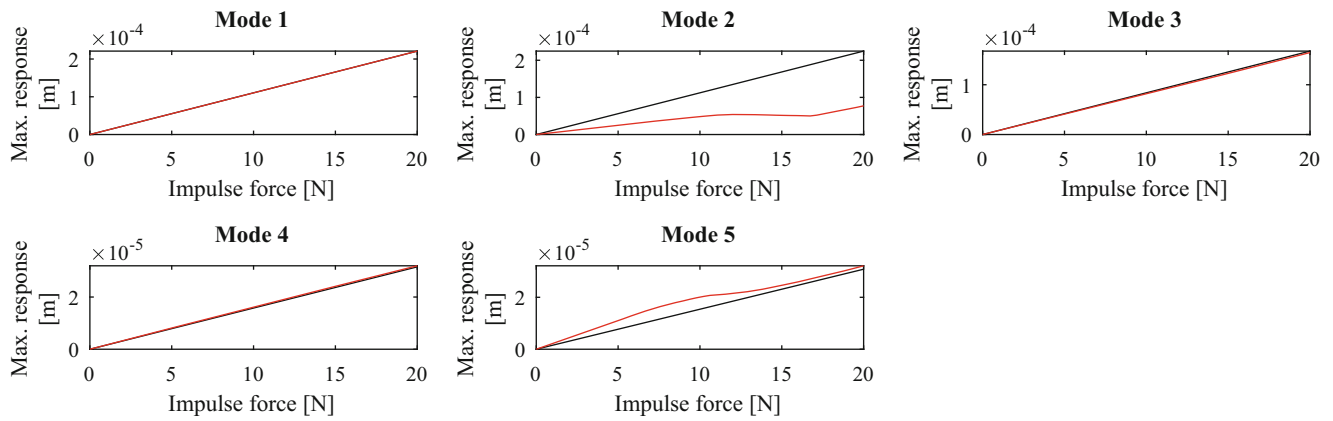


Fig. 13.4 Relationship between applied impulse load and the corresponding maximum modal coordinate, the black line is the linear case and the red line is the non-linear case

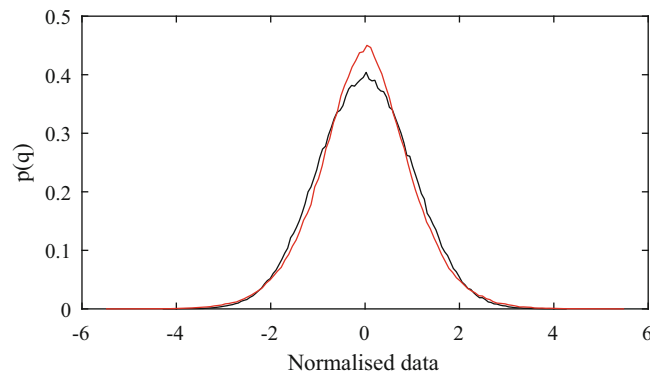


Fig. 13.5 Probability density for the normalised modal coordinate for mode 2 with zero mean and a variance of one simulation with a duration of 30-min, the black line is the linear case and the red line is the non-linear case

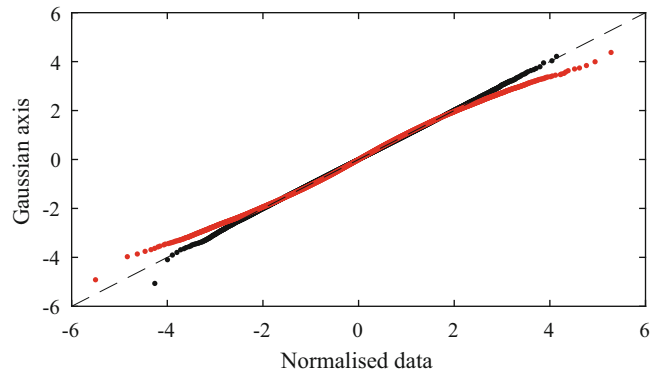


Fig. 13.6 QQ (quantile-quantile) plot for the normalised modal coordinate for mode 2 with zero mean and a variance of one simulation with a duration of 30-min, the black line is the linear case and the red line is the non-linear case

13.3.2 Results of Operational Modal Analysis and Strain Estimation

The mode shapes and natural frequencies are found using the Frequency Domain Decomposition for both the linear and non-linear scenario [14]. The spectral density matrices are plotted with the identified modes in Figs. 13.8 and 13.9. The experimental mode shapes have high correlation with the finite element model and the non-linearities have little effect on the relationship, see Figs. 13.10 and 13.11. The identified mode shape are almost identical in both the linear and non-linear scenario as seen in Fig. 13.12.

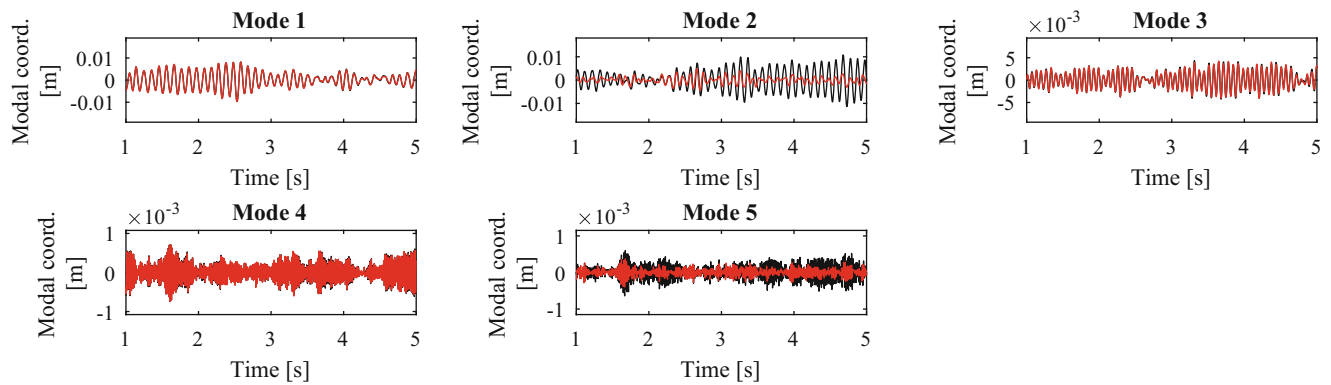


Fig. 13.7 Change in modal coordinates, the black line is the linear case and the red line is the non-linear case

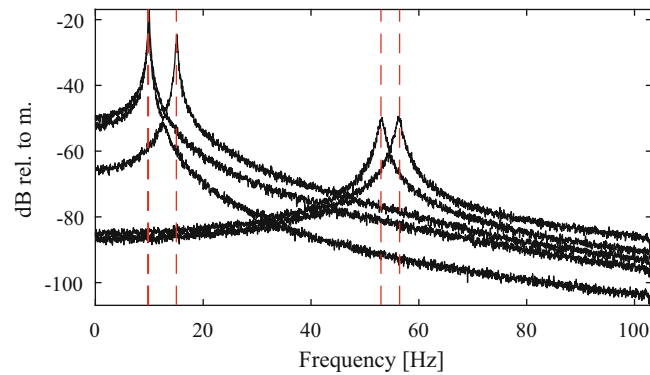


Fig. 13.8 Singular values of the spectral density matrix and marking of the identified modes, linear case

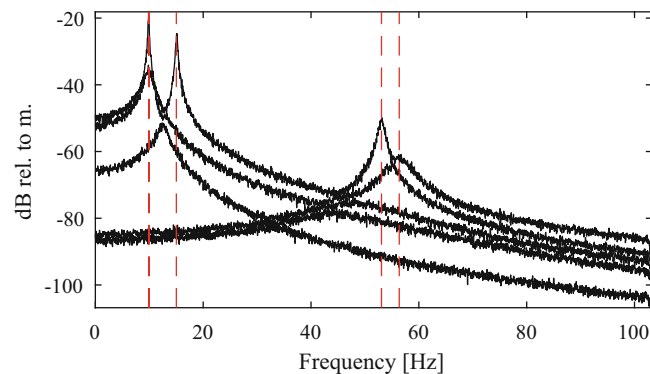


Fig. 13.9 Singular values of the spectral density matrix and marking of the identified modes, non-linear case

We estimate the strain response in the points where we have a reference strain response, which we call “virtual strain gauges”, see Fig. 13.3. The estimated and reference strain responses are plotted on Figs. 13.13 and 13.14 and their corresponding spectral densities are illustrated on Figs. 13.15 and 13.16. The quality measurements show high correlation between the estimated and the reference strain response for both linear and non-linear, see Table 13.1. In the non-linear case, we see a slight decrease in the quality measurements for the first virtual strain gauge. However, this decrease is on the third significant figure.

Fig. 13.10 MAC value for experimental and finite element mode shapes, linear scenario

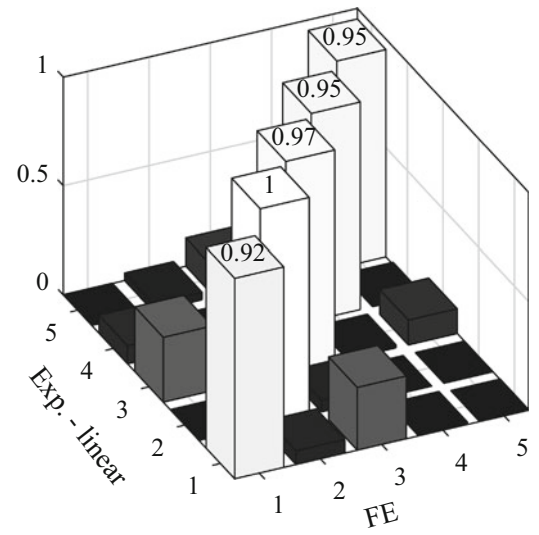


Fig. 13.11 MAC value for experimental and finite element mode shapes, non-linear scenario

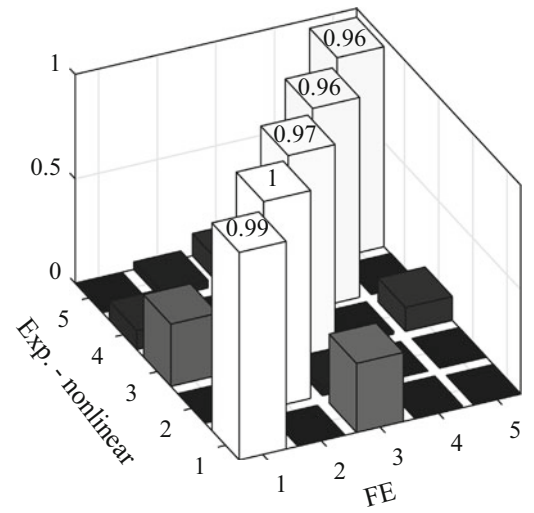
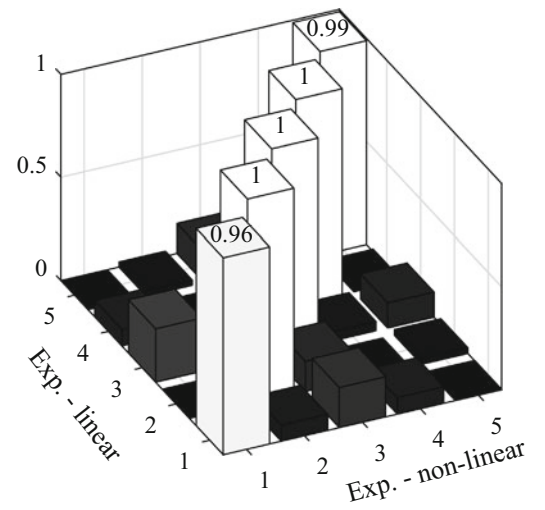


Fig. 13.12 MAC value for experimental mode shapes



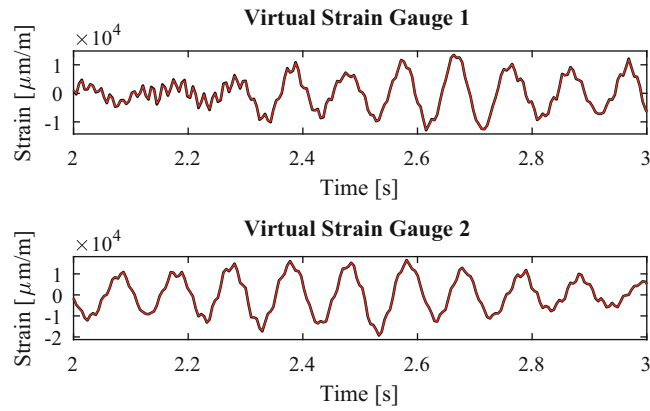


Fig. 13.13 Linear case, estimated and measured strain response, the red line is the estimated and the black line is the measured response

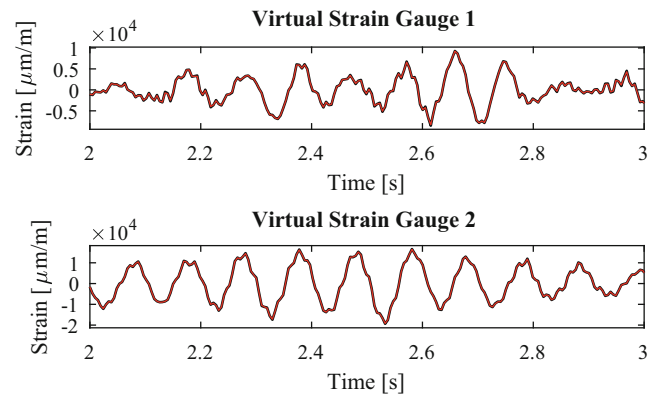


Fig. 13.14 Non-linear case, estimated and measured strain response, the red line is the estimated and the black line is the measured response

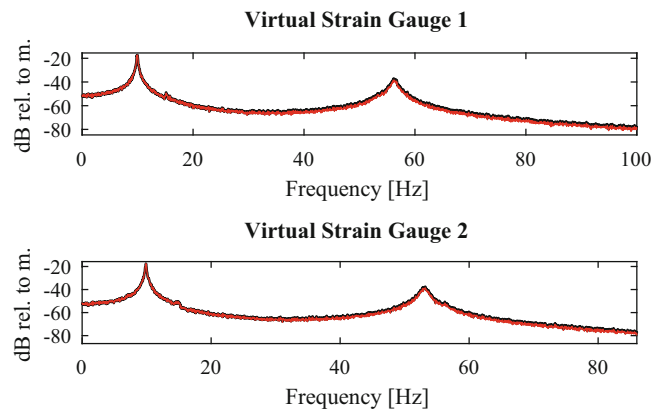


Fig. 13.15 Linear case, auto spectral density of strain response, the red line is the estimated and the black line is the measured response

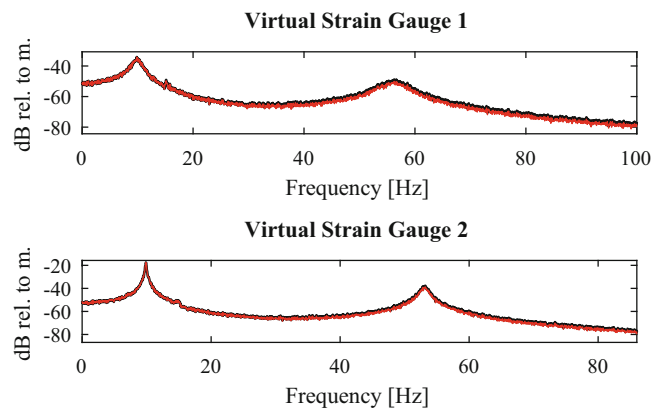


Fig. 13.16 Non-linear case, auto spectral density of strain response, the red line is the estimated and the black line is the measured response

Table 13.1 Quality measurements

	Linear case		Non-linear case	
	Virtual strain gauge 1	Virtual strain gauge 2	Virtual strain gauge 1	Virtual strain gauge 2
<i>TRAC</i>	0.9993	0.9994	0.9984	0.9995
<i>FRAC</i>	0.9993	0.9994	0.9984	0.9995

13.4 Conclusion

We have shown that the simulated system acts non-linear and we are able to identify mode shapes in this friction system. In this test, we observed a distinct change of the system response when we add friction. The position of friction affects specific modes and the corresponding modal coordinates become non-linear and non-Gaussian distributed. Furthermore, the energy of these modes decreases in the spectral density plot. However, the non-linearities of the friction have a limited effect on the mode shapes and operational modal analysis can still extract the mode shapes.

Furthermore, we are able to estimate the strain response of the friction system using Modal Expansion. We would expect a high correlation for the linear case because we have a simulation where everything is nearly perfect and there is only a little numerical noise in the simulation. The estimation of strain response has a similar correlation for the non-linear case.

Even though, Operational Modal Analysis and the Modal Expansion are based on a linear system then the work of this paper indicates that these techniques are still valid for systems with non-linearities caused by friction. This needs to be tested further in future research.

Acknowledgements The authors acknowledge the funding received from Centre for Oil and Gas – DTU/Danish Hydrocarbon Research and Technology Centre (DHRTC).

References

- Farrar, C.R., Worden, K.: Structural Health Monitoring: A Machine Learning Perspective. Wiley, Chichester (2013). ISBN:9781118443118
- Loland, O., Dodds, C.J.: Experiences in developing and operating integrity monitoring systems in the North Sea. Proc. Offshore Technol. Conf. **2**, 313–320 (1976)
- Tarpø, M., Nabuco, B., Skafte, A., Kristoffersen, J., Vestermark, J., Amador, S., Brincker, R.: Operational modal analysis based prediction of actual stress in an offshore structural model. Procedia Eng. **199**, 2262–2267 (2017). X International Conference on Structural Dynamics EURO DYN 2017
- Skafte, A., Kristoffersen, J., Vestermark, J., Tygesen, U.T., Brincker, R.: Experimental study of strain prediction on wave induced structures using modal decomposition and quasi static ritz vectors. Eng. Struct. **136**, 261–276 (2017)
- Iliopoulos, A., Shirzadeh, R., Weijtjens, W., Guillaume, P., Hemelrijck, D.V., Devriendt, C.: A modal decomposition and expansion approach for prediction of dynamic responses on a monopile offshore wind turbine using a limited number of vibration sensors. Mech. Syst. Signal Process. **68–69**, 84–104 (2016)
- Avitabile, P., Pingle, P.: Prediction of full field dynamic strain from limited sets of measured data. Shock Vib. **19**(5), 765–785 (2012)

7. Maes, K., Iliopoulos, A., Weijtjens, W., Devriendt, C., Lombaert, G.: Dynamic strain estimation for fatigue assessment of an offshore monopile wind turbine using filtering and modal expansion algorithms. *Mech. Syst. Signal Process.* **76–77**, 592–611 (2016)
8. Ren, P., Zhou, Z.: Strain response estimation for fatigue monitoring of an offshore truss structure. *Pac. Sci. Revi* **16**(1), 29–35 (2014)
9. Papadimitriou, C., Fritzen, C.P., Kraemer, P., Ntotsios, E.: Fatigue predictions in entire body of metallic structures from a limited number of vibration sensors using kalman filtering. *Struct. Control Health Monit.* **18**(5), 554–573 (2011)
10. Zhang, E., Pintelon, R., Guillaume, P.: Modal identification using OMA techniques: nonlinearity effect. *Shock Vib.* **2015**, 1–12 (2015)
11. Friis, T., Katsanos, E., Amador, S., Brincker, R.: Damping estimation of friction systems in random vibrations. In: *Proceedings of the 36th International Modal Analysis Conference* (2018)
12. Orfanos, A., Friis, T., Katsanos, E., Amador, S., Brincker, R.: Effect of friction-induced nonlinearity on OMA-identified dynamic characteristics of offshore platform models. In: *Proceedings of the 36th International Modal Analysis Conference* (2018)
13. Brincker, R., Ventura, C.: *Introduction to Operational Modal Analysis*. Wiley, Chichester (2015). ISBN:9781119963158
14. Brincker, R., Zhang, L.M., Andersen, P.: Modal identification of output-only systems using frequency domain decomposition. *Smart Mater. Struct.* **10**(3), 441–445 (2001)
15. Brincker, R., Skaftø, A., López-Aenlle, M., Sestieri, A., D’Ambrogio, W., Canteli, A.: A local correspondence principle for mode shapes in structural dynamics. *Mech. Syst. Signal Process.* **45**(1), 91–104 (2013)
16. Debaò, L., Hongcheng, Z., Bo, W.: The principle and techniques of experimental strain modal analysis. In: *Proceedings of 7th IMAC*, pp. 1285–1289 (1989)
17. O’Callahan, J.: System equivalent reduction and expansion process. In: *Proceedings of the 7th International Modal Analysis Conference*. Society of Experimental Mechanics, Bethel, pp. 29–37 (1989)
18. Lu, L.-Y., Chung, L.-L., Wu, L.-Y., Lin, G.-L.: Dynamic analysis of structures with friction devices using discrete-time state-space formulation. *Comput. Struct.* **84**(15–16), 1049–1071 (2006)

Chapter 14

Damping Estimation of Friction Systems in Random Vibrations



Tobias Friis, Evangelos Katsanos, Sandro Amador, and Rune Brincker

Abstract Friction is one of the most efficient and economical mechanisms to reduce vibrations in structural mechanics. However, the estimation of the equivalent linear damping of the friction damped systems in experimental modal analysis and operational modal analysis can be adversely affected by several assumptions regarding the definition of the linear damping and the identification methods or may be lacking a meaningful interpretation of the damping. Along these lines, this project focuses on assessing the potential to estimate efficiently the equivalent linear damping of friction systems in random vibrations with the use of one novel method and two existing ones, modified, though, appropriately. Results of numerical simulations using the three procedures enabled their preliminary comparative assessment in terms of the related damping estimation potential. Indications from the current study showed that two of the methods estimate efficiently the equivalent linear damping, however, the equivalent linear damping seems to depend on the definition of the equivalence. Nonetheless, it seems that the variation of the equivalent linear damping estimates based on the three aforementioned methods becomes less significant when compared to their actual influence on the linear response.

Keywords Friction damping · Random vibrations · Equivalent linear damping · Nonlinear simulation · Modal decomposition

14.1 Introduction

When dealing with structural dynamics, linear damping is usually a rough and oversimplified approximation to describe sufficiently the dynamic performance of the real structures exposed to time varying excitations. In principles, the structural systems experience damping forces due to either the hysteretic behavior (e.g. internal friction in materials), yielding of the structural members or even the soil-structure interaction. An additional source of damping is related to the various friction mechanisms that are commonly developed between sliding parts, the latter is, for example, the case of the external friction dampers. The aforementioned damping mechanisms typically introduce nonlinearities that, in turn, are in contradiction with the linear calculations commonly adopted for the structural performance and the assumption about the equivalent linear damping. Along these lines, the current extended abstract focuses on the estimation of equivalent linear damping of friction systems exposed to random vibrations. Especially, three methods, founded on different fundamental assumptions, are presented herein in order to provide meaningful interpretation of the equivalent linear damping of friction systems. Using these methods, the equivalent linear damping can be estimated allowing for their comparative evaluation.

14.2 Methodology

Three different methods are currently employed for estimating the equivalent linear damping based on the nonlinear response of a frictionally damped systems subjected to random vibrations. Especially, the fundamental assumptions of the first method, being a novel one, are based on physics and statistics while it is formulated on the basis of modal components and modal decomposition of the response in the time domain by using the pseudo inverse of the mode shape matrix [1]. The equivalent linear damping is estimated by balancing the intensity of the response with the transfer of the spectral density of the excitation. By doing so, the method has one particular advantage being that the nonlinear and the equivalent linear

T. Friis (✉) · E. Katsanos · S. Amador · R. Brincker
Technical University of Denmark, Kongens Lyngby, Denmark
e-mail: vakat@byg.dtu.dk; sdio@byg.dtu.dk; runeb@byg.dtu.dk

response respectively will share identical intensity (i.e. variance). This particular relation is established through the fact that the expected value of the response squared, $E[y^2]$, being identical to the variance, σ_y^2 , for a zero mean process, can be calculated by the integrated product of the squared absolute frequency response function, $|H(\omega)|^2$, and the spectral input of the excitation, $S_x(\omega)$, [2, 3]:

$$E[y^2] = \sigma_y^2 = \int_{-\infty}^{\infty} |H(\omega)|^2 S_x(\omega) d\omega \quad \text{where} \quad H(\omega) = \frac{1}{-m\omega^2 + ic\omega + k} \quad (14.1)$$

where m , c and k are the mass, the dashpot coefficient and the stiffness of the system and ω is the angular frequency.

Likewise to the first method, the second one, proposed originally by Iourtchenko and Dimentberg [4], was modified herein to account for the uncorrelated modal components, widely adopted to describe a given system. More specifically, this method is based on stochastic averaging of the response in terms of displacement, $y(t)$, and velocity, $\dot{y}(t)$, introducing slowly varying amplitude, A , and phase, φ , with the use of the following transformation [5].

$$y(t) = A \cos(\omega t + \varphi), \quad \dot{y}(t) = -\omega A \sin(\omega t + \varphi) \quad (14.2)$$

where t is the time. In other words, this method deals with the estimation of probability densities from the response amplitudes, i.e. the peaks of the response, and a damping model is fitted to the established probability densities. Therefore, it is reasonable to claim that the estimation of the equivalent linear damping is based on statistics. Furthermore, the respective technique for estimating equivalent damping enables its evaluation directly targeting a specific magnitude of the response of the respective system (i.e., the estimate could be based on amplitudes below or above a certain limit).

Regarding the third method adopted by the current study, the so-called energy-dissipation method [6–8] was modified herein in order to provide an estimation of equivalent linear damping instead of friction forces and dashpot coefficients as this is the case in the original formulation. The basic idea of this method, founded entirely on physics, is that the energy of all non-damping terms in the nonlinear equation of motion is calculated and then the estimation of system's damping is based on the amount of the dissipated energy:

$$W_d = W_e - W_i \quad (14.3)$$

where W_d is the dissipated energy, W_e is the external energy and W_i is the internal energy. The latter two energy contributions constitute the energy associated with the non-damping terms. The main advantage of this method stems from the fact that the equivalence is directly related to the dissipated energy. This means that the amount of energy dissipated in the nonlinear model and in the equivalent linear model is identical.

14.3 Application

A numerical model of a simple T-shaped structure was created to provide the testbed for employing the aforementioned methods and comparatively evaluating the corresponding estimates of equivalent linear damping. Thus, a finite element model of the structure was created by using three dimensional (3D) beam elements and the system equivalent reduction and expansion process, proposed by O'Callahan [9], was used to reduce the degrees of freedom of the structural system from 156 (initially) to 10. Subsequently, two types of damping were applied: (i) linear proportional damping and (ii) friction damping. The latter was introduced by attaching a friction element to the top of the structure in connection with a spring. Employing the described friction system, 100 Monte Carlo nonlinear simulations were carried out while randomly generated white noise excitation was applied in each of the ten degrees-of-freedom of the T-shaped structure, ensuring uncorrelated random vibrations of all modes. It is notable that numerical simulations were performed herein by using the algorithm proposed by Lu et al. [10]. The latter is based on a discrete-time state-space formulation, in which the system forces are iterated within each time step in order to have the correct force of the nonlinear friction element. Finally, the nonlinear numerical simulations results were used to apply the three aforementioned methods enabling their comparative evaluation in terms of equivalent linear damping estimates.

14.4 Conclusions

One novel method and two modified methods, dedicated to estimating equivalent linear damping of friction systems in random vibrations, are presented and comparatively assessed within the present project. Preliminary results indicate that the three methods, briefly described above, provide reliable estimates for a generic estimation of equivalent linear damping, while the second method may be used for estimating equivalent linear damping targeted a specific magnitude of the response and for assessment of the nonlinear behaviour of the damping. Moreover, initial indications, emerged from the current study, show that the equivalent linear damping depends on the definition of the damping equivalence. However, it seems that the variation of the equivalent linear damping estimates based on the three aforementioned methods becomes less significant when compared to their actual influence on the linear response.

Acknowledgements The authors acknowledge the funding received from Centre for Oil and Gas – DTU/Danish Hydrocarbon Research and Technology Centre (DHRTC).

References

1. Brincker, R., Ventura, C.: *Introduction to Operational Modal Analysis*. Wiley, New York (2015)
2. Newland, D.E.: *An Introduction to Random Vibrations, Spectral and Wavelet Analysis*. Longman Scientific & Technical, Harlow (1993)
3. Clough, R.W., Penzien, J.: *Dynamics of Structures*. Computers & Structures Inc., Berkeley (1995)
4. Iourtchenko, D.V., Dimentberg, M.F.: In-service identification of non-linear damping from measured random vibration. *J. Sound Vib.* **255**(3), 549–554 (2002)
5. Roberts, J.B., Spanos, P.D.: Stochastic averaging: an approximate method of solving random vibration problems. *Int. J. Non-Linear Mech.* **21**(2), 111–134 (1986)
6. Liang, J.-W., Feeny, B.F.: Balancing energy to estimate damping parameters in forced oscillators. *J. Sound Vib.* **295**(3), 988–998 (2006)
7. Liang, J.-W.: Damping estimation via energy-dissipation method. *J. Sound Vib.* **307**, 349–364 (2007)
8. Feeny, B.F.: Estimating damping parameters in multi-degree-of-freedom vibration systems by balancing energy. *J. Vib. Acoust. Trans. ASME* **131**(4), 410051–410057 (2009)
9. O’Callahan, J.: System equivalent reduction and expansion process. In: *Proceedings of the 7th International Modal analysis conference* (1989)
10. Lu, L.-Y., Chung, L.-L., Wu, L.-Y., Lin, G.-L.: Dynamic analysis of structures with friction devices using discrete-time state-space formulation. *Comput. Struct.* **84**(15–16), 1049–1071 (2006)



Chapter 15

System Identification of Jointed Structures: Nonlinear Modal Testing Vs. State-Space Model Identification

Maren Scheel, Gleb Kleyman, Ali Tatar, Matthew R. W. Brake, Simon Peter, Jean-Philippe Noël, Matthew S. Allen, and Malte Krack

Abstract Two approaches for experimental identification of the nonlinear dynamical characteristics of jointed structures are investigated, (a) Nonlinear Modal Testing, (b) State-Space Model Identification. Both require only minimal a priori knowledge of the specimen. For method (a), the definition of nonlinear modes as periodic motions is used, in its generalized formulation recently proposed for nonconservative systems. The theoretically required negative damping compensating the frictional dissipation is experimentally realized by properly controlled excitation. This permits the extraction of modal frequencies, damping ratios and vibrational deflection shapes as a function of the vibration level. For method (b), a state-space model with multivariate polynomial nonlinear terms is identified from the vibration response to a properly designed excitation signal. Both methods are applied to a structure with bolted joints. The quality of the extracted modal and state-space models, respectively, is assessed by comparing model-based predictions of the forced vibration response to reference measurements.

Keywords Nonlinear system identification · Nonlinear modes · Force appropriation · Brake-Reuss beam · Jointed structures

15.1 Introduction

Assembled structures often feature nonlinear contact interactions [1] which can significantly influence the dynamical behavior and lead to a dependence of vibration features on the vibration level. It is the present state of knowledge that vibrations of jointed structures cannot be modeled from first principles. Instead, empirical models have to be used, which rely heavily on experimental parameter identification and validation. An important experimental task is the extraction of dynamic models from measurements, i.e., system identification. In the past, numerous methods for nonlinear system identification have been developed [2], however, most of them are not applicable to systems with nonlinear damping as in the case of hysteretic dry friction in joints.

In this contribution, two promising approaches for nonlinear system identification of jointed structures are considered. The first is a nonlinear modal testing approach referred to as enforced phase resonance (EPR) testing. It is based on the extended

M. Scheel (✉) · M. Krack
Institute of Aircraft Propulsion Systems, University of Stuttgart, Stuttgart, Germany
e-mail: krack@ila.uni-stuttgart.de

G. Kleyman
Institute of Dynamics and Vibration Research, Leibniz Universität Hannover, Hannover, Germany

A. Tatar
Department of Mechanical Engineering, Imperial College London, London, UK

M. R. W. Brake
William Marsh Rice University, Houston, TX, USA

S. Peter
Institute for Nonlinear Mechanics, University of Stuttgart, Stuttgart, Germany

J. -P. Noël
Space Structures and Systems Laboratory, Department of Aerospace and Mechanical Engineering, University of Liège, Liège, Belgium

M. S. Allen
Department of Engineering Physics, University of Wisconsin-Madison, Madison, WI, USA

periodic motion concept [3], a nonlinear mode definition explicitly applicable to nonlinearly damped systems. The second approach is an input-output identification technique, namely the polynomial nonlinear state-space (PNLSS) method, which has been recently applied to a numerical model of a single degree of freedom oscillator with a hysteretic nonlinearity [4].

15.2 Theoretical Background of the Identification Methods

15.2.1 EPR Testing

A nonlinear mode is commonly defined as a family of periodic motions of an autonomous system. Motions of damped autonomous systems decay with time. An extended periodic motion concept for nonlinear modes was therefore proposed in [3], where the periodic motions are enforced by suitably appropriated negative damping. It has been shown that this definition of nonlinear modes leads to an accurate representation of the forced response near resonances, for a wide range of test cases including jointed structures.

In the present work, a practical realization of the extended periodic motion concept is used [5]. Consider the following vibration system,

$$\mathbf{M}\ddot{\mathbf{q}} + \mathbf{K}\mathbf{q} + \mathbf{g}(\mathbf{q}, \dot{\mathbf{q}}) = \mathbf{f}^{\text{ex}}. \quad (15.1)$$

Here, the system is described by generalized coordinates \mathbf{q} , the symmetric mass and stiffness matrices \mathbf{M} and \mathbf{K} , respectively, and a vector \mathbf{g} which may contain linear and nonlinear restoring and damping forces. The idea of EPR testing is to replace the aforementioned negative damping, proposed in the extended periodic motion concept, by a periodic external forcing \mathbf{f}^{ex} in phase resonance with the vibration response. The 90° phase lag between forcing and displacement response is enforced using a phase-locked loop controller. Then, the response is measured as the forcing amplitude increases, effectively tracking the system's backbone curve directly. From the measurements, amplitude dependent modal frequencies can be directly extracted. Based on a linear modal analysis, deflection shapes are mass-normalized and a modal amplitude is computed. Using power considerations, the modal damping ratio can be obtained.

15.2.2 PNLSS Identification

The purpose of the PNLSS identification [4] is to estimate a nonlinear state-space model in the form

$$\begin{cases} \mathbf{x}(t+1) = \mathbf{A}\mathbf{x}(t) + \mathbf{B}\mathbf{u}(t) + \mathbf{E}\mathbf{e}(\mathbf{x}, \mathbf{u}) \\ \mathbf{y}(t) = \mathbf{C}\mathbf{x}(t) + \mathbf{D}\mathbf{u}(t) + \mathbf{F}\mathbf{f}(\mathbf{x}, \mathbf{u}) \end{cases} \quad (15.2)$$

Herein, \mathbf{y} are the output states, in our case accelerations, \mathbf{u} are input states, in our case excitation forces, and \mathbf{x} are internal states. Nonlinearities are assumed in the form of multivariate polynomial $\mathbf{e}(\mathbf{x}, \mathbf{u})$ and $\mathbf{f}(\mathbf{x}, \mathbf{u})$. The unknown coefficient matrices (\mathbf{A} , \mathbf{B} , \mathbf{C} , \mathbf{D}), \mathbf{E} and \mathbf{F} are determined by an optimization algorithm with the objective to minimize the deviation between the measured and simulated response. A broadband, multisine excitation with random phase is generated as excitation signal. It is applied in a periodic sequence of blocks to avoid transients.

15.3 Experimental Study

The comparison of the two approaches is performed by means of the Brake-Reuss beam [6], a benchmark structure for the investigation of jointed structures, featuring an interface with three bolts. The beam is hung from two strands of fishing line for the experiments and excited around the first mode with a shaker, coupled by a stinger. The models are identified independently based on different measurements. For EPR testing, the system is excited using the phase-locked loop controller implemented on a dSPACE MicroLabBox with increasing forcing level. The random phase multisine excitation signal used for PNLSS identification covers a frequency bandwidth from 75 to 225 Hz, and the amplitude is varied during the experiments. The LMS SCADAS Mobile system is utilized as a signal generator, and the force is measured by an impedance head while the response is recorded using four accelerometers distributed over the beam.

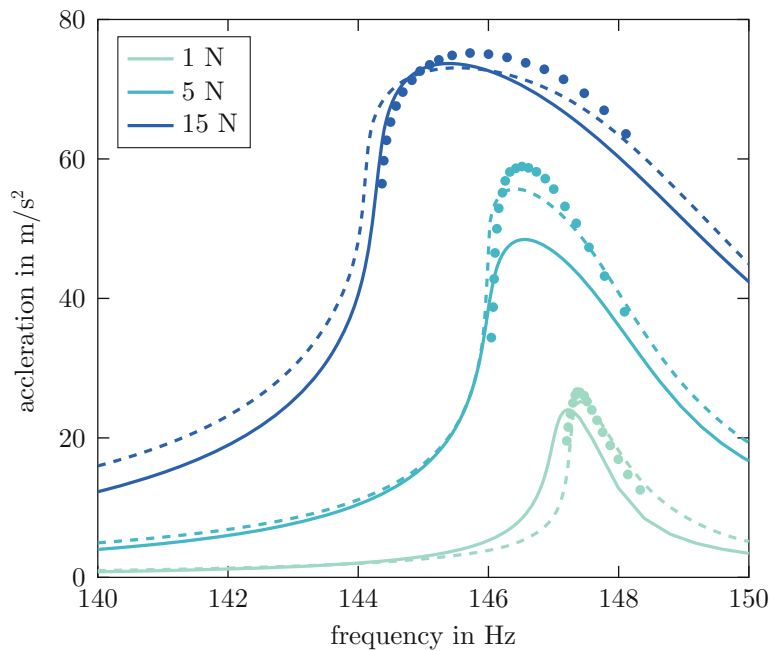


Fig. 15.1 Measured (*dots*) and synthesized frequency responses (*EPR dashed line, PNLSS solid line*) for three different forcing levels

From the identified models, the frequency responses are synthesized using a constant forcing amplitude. Additionally, forced responses around the first mode are measured for validation purposes at the same excitation levels. The results can be seen in Fig. 15.1 for one exemplary setup. At low and high excitation level, the forced response is synthesized with moderate accuracy. Yet, at medium forcing level, both methods underestimate the amplitude significantly. Furthermore, both models predict slightly lower resonance frequencies, where the PNLSS model shows larger deviations to the comparison measurements especially for the lowest excitation level.

This work will be presented in more detail at the conference, in which the choice of input signals as well as the achieved model quality are discussed. Moreover, the variability of the measurements, caused by changes in the interface, is addressed. Finally, the methods are compared more thoroughly regarding the prediction capabilities for different forcing scenarios, including steady-state vibrations and fast sine sweeps.

15.4 Conclusion

Both EPR testing and PLNSS identification can be used to extract dynamic models of jointed structures. The model quality is deemed satisfactory in the considered range near the first resonance, giving the high measurement variability encountered for the considered benchmark system. Further work, involving more reproducible benchmarks, is required to explore and better understand the limitations of the methods for experimental characterization of jointed structures.

References

1. Brake, M.R.W.: *The Mechanics of Jointed Structures*. Springer, Cham (2018)
2. Noël, J.-P., Kerschen, G.: Nonlinear system identification in structural dynamics: 10 more years of progress. *Mech. Syst. Signal Process.* **83**, 2–35 (2017)
3. Krack, M.: Nonlinear modal analysis of nonconservative systems: extension of the periodic motion concept. *Comput. Struct.* **154**, 59–71 (2015)
4. Noël, J.-P., Esfahani, A., Kerschen, G., Schoukens, J.: A nonlinear state-space approach to hysteresis identification. *Mech. Syst. Signal Process.* **84**, 171–1847 (2017)
5. Scheel, M., Peter, S., Leine, R.I., Krack, M.: A phase resonance approach for modal testing of structures with nonlinear dissipation. *J. Sound Vib.* (2018) (submitted)
6. Brake, M.R.W., Reuss, P., Segalman, D.J., Gaul, L.: Variability and repeatability of jointed structures with frictional interfaces. In: Allen, M. (ed.) *Dynamics of Coupled Structures*, vol. 1, pp. 245–252. Springer, Cham (2014)

Chapter 16

Effect of Boundary Conditions on Finite Element Submodeling



Michael W. Sracic and William J. Elke

Abstract When a built-up structure such as a turbine or compressor is modeled with finite elements, a submodeling procedure can be used to assess critical features such as holes, fillets, or contact interfaces. To employ the method, one builds and solves a coarse-mesh finite element model of the whole structure. Then, a fine-mesh finite element submodel of the critical feature is built and solved by using boundary conditions that were estimated from the global model solution. This procedure reduces computational expense, but the predicted results from the submodel can be inaccurate if the global model produces inaccurate boundary conditions for the submodel. While a number of studies have considered the best methods to extract boundary conditions, little work has been done to assess how the submodel boundary location affects the results. This paper presents a case study to assess how the submodel boundary location affects the predicted results of the submodel. Specifically, a cantilever beam with stress concentration hole was analyzed. Numerous global models and submodels were generated and solved with the submodeling method. The maximum stress at the hole was reviewed as a metric. The results suggest that the location of the submodel boundary has a strong influence on the maximum stress predicted by the submodel. In particular, submodels with boundaries placed very close to the edge of the hole underpredicted the global model converged stress by up to 20%. The error in the submodels decreased as the submodel boundary was placed farther from the hole. The error also decreased as the mesh of the initial global model is refined. The results provided could inform analysts who employ this method in applications but do not investigate convergence of the global model or optimize the location of the submodel boundary.

Keywords Finite Element Submodeling · Boundary Interpolation · Error Convergence

16.1 Introduction

Analysts can effectively model large, built-up structures with the finite element method when a submodeling routine is employed to reduce the computational burden. The critical features in a structure that define the operational life or maintenance schedule of a structure tend to be localized to small regions within a large assembly. Submodeling refers to the approach where one creates a global finite element model of the large structure as well as a submodel of the local region of interest. By enforcing a coarse mesh with a limited number of elements on the global model, the size and computational cost of the global model is controlled. The local submodel, however, is created with a very fine mesh that is capable of estimating accurate finite element analysis results in the region of interest. These two models are required to establish the submodeling procedure, which entails first solving the global model and using the result of the global model to establish the boundary conditions to apply to the submodel. The submodel is subsequently solved and then refined to the desired level of accuracy. Figure 16.1 shows a basic flowchart of this procedure.

Submodeling is well established in research and has been effectively applied in numerous industrial finite element modeling applications. Since the technique requires the modeler to obtain boundary conditions from one model that are then applied to another model, studies employ one of two possible techniques: the application of boundary conditions as displacements or the application of boundary conditions as tractions. For example, Zienkiewicz and Zhu developed an efficient technique to recover the stress tractions on element boundaries [1, 2]. This procedure has been used effectively to produce traction boundary conditions from a global model to apply to a submodel. For example, Kitamura et al. have explored and enhanced the method for large deformation problems [3] and then applied the method effectively to the analysis of a

M. W. Sracic (✉) · W. J. Elke
Milwaukee School of Engineering, Milwaukee, WI, USA
e-mail: sracic@msoe.edu

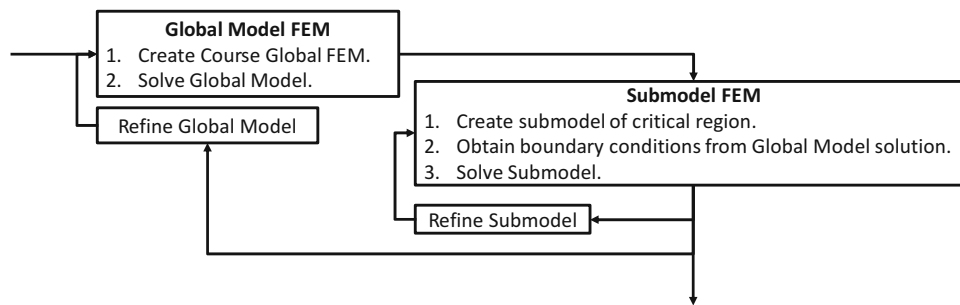


Fig. 16.1 Basic analysis flow for finite element submodeling

large ship structure [4]. In both of these works, the stresses of interest produced with the submodels had less than a few percent error as compared to the stresses from a reference global model.

Displacements can be used instead of stress tractions as the boundary conditions for the submodel. There are numerous implementations of this method in the literature [5–10]. A few pertinent studies are described here. For example, Cormier et al. [11] investigated using finite element shape functions versus cubic splines to interpolate the boundary conditions from the global model to the submodel at the boundary of the submodel. They found the procedure can be quite effective for models with stress concentrations and nonlinear contact interfaces, and they suggest that displacements may be preferable to stress tractions because the discretization error converges more rapidly with displacements. The procedure from [11] was applied in two-dimensional [12] and three-dimensional analysis [13] of dovetail attachments of gas turbine engine rotors. The fine mesh provided by the submodeling procedure allowed the authors to more accurately characterize the peak contact stresses and the gradients of those stresses in the dovetail interface, while a coarse global model might have mischaracterize those quantities. A few studies have effectively used the submodeling approach to study crack propagation in fracture mechanics [14, 15], where very fine meshes are needed to predict crack mechanics.

The main goal of any submodeling technique is to alleviate the computational burden of finely meshing a global, whole-structure model, but the method adds sources of additional error to the finite element method. For example, when either displacements or loads are applied at the submodel boundaries, those conditions must be estimated from the global model solution at the boundary of the submodel. Any deficiencies that exist in the global model will be propagated to the submodel through errors in the estimates for the boundary conditions. This is especially problematic if the boundary of the submodel is established in an area of the global model that has high stress gradients, which will always tend to be the case if the analyst places the boundaries near a critical feature. In fact, in [11] the authors show that the boundary errors must be precisely controlled, often using successive refinements on the global model at the submodel boundary, in order to produce converged displacement and stress results from a submodel at the location of interest. Using this procedure, the computational cost would approach the cost associated with adequately refining the global model at the location of interest, which would void the benefit of the submodeling approach. In industrial applications, analysts will typically employ iterative submodel mesh refinements to ensure their model provides converged results, but they may be less likely to also iterate on the global model to achieve convergence at the location of the submodel boundary.

The problem with the submodeling approach that most studies do not address is that an analyst must first choose how close to place the submodel boundary to the location of interest in the global model. Most locations of interest in a structural finite element analysis include features such as holes, fillets, or contact interfaces where the stress tends to concentrate, leading to contours of large stress gradients. For a given global model coarseness, the estimated submodel boundary conditions might be improved by simply moving the submodel location farther from the stress concentration of interest. This idea is well established by Saint-Venant's Principle [16, 17], which argues that different but statically equivalent loads produce equivalent stress fields at a distance from where the loads are applied. To the best of the authors' knowledge there are no studies that consider the convergence of the submodeling procedure as the location of the submodel boundary changes.

This work seeks to study the effect that the submodel boundary location on the convergence of the submodel solution. First, the theory used to interpolate displacements from the global model solution onto the submodel boundary is briefly reviewed. Traction boundary conditions are not considered in this work. Following this development, a case study is presented that includes a tip-loaded cantilever beam with a hole near its fixed support. An algorithm is presented to generate submodels of the hole with boundaries that are located at increasing distances from the edge of the hole. The concentrated stress at the hole is tracked and assessed for accuracy versus a converged global model solution. This case study is used to generate and discuss the results. Finally, some conclusions are presented.

16.2 Theoretical Development

A finite element model solution generates displacement values at the nodal degrees of freedom, but those nodal displacements can be used to estimate displacement or stress solutions at locations in the model besides the nodes. This premise is needed for submodeling, because the desired boundary of a submodel likely will not contain nodes at the same locations as the related global model. Figure 16.2 illustrates an example where a global model of four elements is shown, and a submodel boundary is sketched in the upper right corner of the global model. The submodel and the global model only share Node 1, while the remaining nodes on the boundary of the submodel must be estimated from the global model elements, which contain the space where the submodel boundary nodes are defined.

This study considers only the application of displacements at boundary conditions. In particular, the geometric locations X_S of the boundary nodes of a submodel, d_S , are a subset of the geometric coordinate space X'_G . The coordinate space X'_G is circumscribed by the boundaries of the elements in the vector e'_G , which is a subset of the total global model element set, e_G .

$$X_S \subset X'_G \quad (16.1)$$

$$e'_G \subset e_G \quad (16.2)$$

In Eq. 16.1, X_S is a matrix of xyz-coordinates for each node in the submodel boundary node vector, d_S (e.g., the filled nodes shown in Fig. 16.2b) and X'_G is the xyz-coordinate space of the elements in e'_G (e.g., Element 1 shown in Fig. 16.2a). Using the submodeling analysis procedure, the global model must be solved,

$$K_G d_G = f_G \quad (16.3)$$

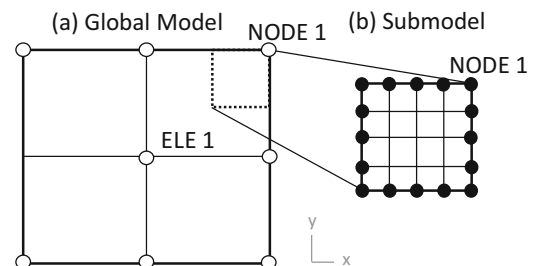
where d_G is a column vector of nodal displacement solution values, K_G is the global model stiffness matrix, and f_G is a column vector of the loads that are applied to the global model nodes. Once d_G is determined, one of several methods can be used to estimate d_S , which is a column vector of boundary condition displacements for the refined submodel. The most convenient approach is to use the shape functions that define the elements in e'_G . Such shape functions are already used in commercial finite element packages for element generation and results post-processing, and some commercial packages such as ANSYS [18] and Abaqus [19] already providing submodeling commands which use the shape functions. Other researchers have instead suggested that cubic splines should be used to estimate d_S so that derivatives of displacements (i.e., strain and stress computations) are ensured to be continuous [11]. In this work, the shape functions of the elements will be used to estimate the displacements, and the models use primarily bi-linear quadrilaterals.

In general, the displacement field of an element in the global model is computed using a function made from a linear combination of products of shape functions and the global model degree of freedom solution.

$$u_j = \sum_{i=1}^{Nele} N_i(X) d_{G,i}^j \quad (16.4)$$

In Eq. 16.4, u_j is the estimated x-directional displacement field for the j^{th} element in the global model. $Nele$ is the number of degrees-of-freedom for the j^{th} element. $N_i(X)$ is the shape function for the i^{th} degree-of-freedom evaluated at any xyz-coordinates X within the element. Finally, $d_{G,i}^j$ is the global model degree-of-freedom solution for the i^{th} degree-of-freedom from the j^{th} element.

Fig. 16.2 Schematic of (a) global and (b) submodel finite element models



Once the nodal coordinates of the boundary nodes of a submodel, X_S , are known, they can be used to estimate any displacement within and including the boundaries of the elements in e'_G according to Eq. 16.5,

$$d_{s,k} = \sum_{i=1}^{Nele} N_i(X_{s,k}) d'_{G,i} \quad (16.5)$$

where $d_{s,k}$ is the k^{th} degree-of-freedom in the boundary node vector d_S and is desired at the xyz-coordinate $X_{s,k}$. Once all boundary node degrees-of-freedom have been estimated, they can be applied to the submodel as Step 2 in Fig. 16.1 and the submodel can be solved.

For this work, the submodel boundary node displacements are estimated from global models that are not converged in order to assess how the location of the submodel boundary affects the submodel solution. In particular, an algorithm was developed to move the submodel boundary location and solve the resulting submodels in an automated fashion. The next section describes a case study to explore this algorithm and to establish the convergence of a given analysis with respect to submodel boundary location.

16.3 Case Study

A cantilever beam with a stress concentration hole was used as a case study for this paper. The length of the beam is 100 inches, the width of the beam is 5 inches, and the thickness of the beam is 0.125 inches. The diameter of the hole is 2.5 inches, and the hole is located 25 inches from the left end of the beam. A schematic of the structure is shown in Fig. 16.3.

The beam was modeled as steel with an elastic modulus of $E = 30,000$ ksi and a Poisson's Ratio of $\nu = 0.3$. The geometry of the beam was modeled as surface body, and plane stress elements were used to generate the finite element model. The mesh was generated with mostly 4-node (bi-linear) quadrilateral elements and a few 3-node (linear) triangle elements. An example global model mesh with 0.5 inch element edge lengths is shown in Fig. 16.4.

The nodes on the left end of the model were fixed to zero in all degrees of freedom. The out of plane displacements were fixed to zero. A 100 lb. load was applied downwards at the free end. Under these conditions, the cantilever beam model was solved and is denoted as the global model for the rest of this paper.

Once the global model was solved, submodels were created according to the scheme shown in Fig. 16.1. The primary goal of the case study is to assess how the location of the boundary of the submodel affects the accuracy of the submodel solution, so numerous submodels were produced. In order to eliminate the effects of different meshes, each submodel mesh was controlled using a meshing algorithm. First, the element edge length for all submodels was chosen. Then, the nodes and elements of the first submodel were placed in controlled positions. Each subsequent submodel was then built using the preceding submodel mesh as a starting point, but a single row of elements was added to all the previous edges in order extend the boundary of the new submodel away from the hole by the distance of one element edge length.

The first submodel boundary was located approximately one element edge length from the edge of the hole. The submodel boundary progression is illustrated in Fig. 16.5. The example shown depicts the global model mesh with element edge lengths of 0.5 inches. The dashed lines depict each submodel boundary, which for this example also have element edge lengths of 0.5 inches. Note that Submodels 1 and 2 would cut an entire square submodel from the global model beam, whereas Submodels 3–10 would only cut through vertical sections of the beam, leaving the top and bottom free-edges of the beam unaffected between the vertical boundaries.

After each submodel mesh was created, the locations of nodes on the submodel boundary surfaces that would cut through the global model were used to estimate displacements from global model solution at those locations. This procedure was done according to Eqs. 16.1, 16.2, 16.3, 16.4, and 16.5. In this work, ANSYS was used generate the models. The ANSYS command "NWRITE" was used to generate boundary cut node files, and the ANSYS command "CBDOF" was used to



Fig. 16.3 Schematic of cantilever beam with a tip load



Fig. 16.4 Example global model of the beam (0.5 inch element edge lengths)

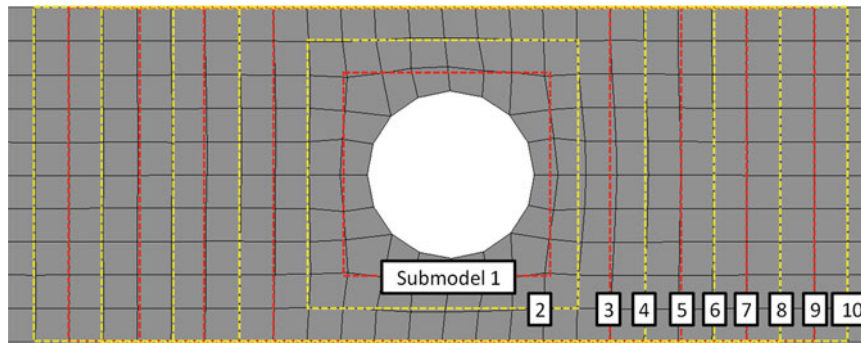


Fig. 16.5 Submodel sequence example for element edge size of 0.5 inch

Table 16.1 Model element edge lengths in inches

Global, [in]	Submodels, [in]	
0.5	0.05	0.025
0.25	0.05	0.025
0.05	0.05	0.025

estimate the submodel boundary displacements from the global model displacement solution. Finally, the global model material properties were provided to each submodel and they were solved. The following section provides the results of this case study.

16.4 Results

The algorithm described in the previous section was executed on the cantilever beam with a stress concentration hole. Several combinations of global model and submodel element sizes were explored, including global model element sizes of 0.5, 0.25, and 0.05 inch edge lengths and submodel element sizes of 0.05 and 0.025 inch edge lengths. These combinations are shown in Table 16.1.

For each global and submodel solution, the normal stress in the x-direction at the top-center of the hole, which is denoted $\sigma_{x,h}$, was determined. For example, Fig. 16.6 shows the stress contour plot for the entire cantilever beam, and the inset plot shows the stress near the hole. The stress concentrates near the top and bottom of the hole as expected, and the maximum x-direction normal stress for the global model with 0.5 inch element edge lengths is 12.41 ksi. The stress at the top center of the hole was used as a metric for all models to assess convergence versus the location of the boundary of a submodel.

Figure 16.7 shows a plot of $\sigma_{x,h}$ for each submodel versus the dimensionless parameter d/D , which is denoted the “boundary location ratio”, where d is the distance between the submodel boundary and the edge of the hole and D is the diameter of the hole. Submodel results were computed for d/D ranging from zero to one. The results points are organized according to global and submodel element sizes. Submodel stress values that are obtained using a global model element edge size of 0.5 inches, 0.25 inches, and 0.05 inches are plotted with circles, squares, and triangles, respectively. Additionally, the markers are open for stresses predicted with a submodel with 0.05 inch element edge lengths versus a filled marker for stresses from submodels with 0.025 inch edge lengths. Finally, a convergence study was performed on the global model until the stresses from subsequently refined models differed by less than 0.5%. The converged stress at the top center of the hole was estimated as 15.89 ksi using a global model element edge size of 0.025 inches and is plotted in Fig. 16.7 as a solid line.

One can see from Fig. 16.7 that the stress concentration magnitude at the top center of the hole depends on how far from the hole edge the submodel boundary is placed. Submodels that have boundary location ratios smaller than 0.05 may underpredict or overpredict the converged stress, depending on the mesh character and density of the submodel. Submodels with boundary location ratios between 0.1 and 0.5 all tend to underpredict the converged stress. The results are grouped according to which global model is used to estimate the submodel boundary displacements, and there appears to be no discernable difference in results when the submodels are refined from 0.05 to 0.025 inch element edge lengths.

The submodels that are derived from global models with 0.5 inch element edges (i.e., the circles in Fig. 16.7) predict a maximum stress near 12.5 ksi when the submodel boundary location ratio is about 0.01, and the predicted stress increases to approximately 15.6 ksi as the boundary location ratio approaches one. The trend between these values is not monotonic; the

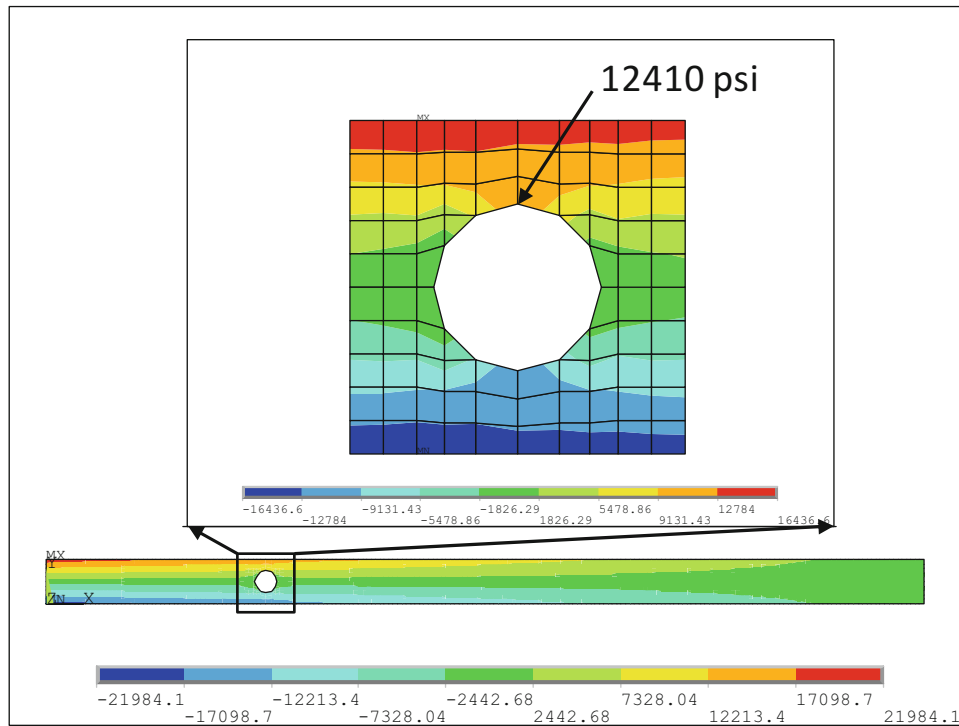


Fig. 16.6 Global model x-direction normal stress contours for element edge size 0.5 inches (inset of stress near the hole)

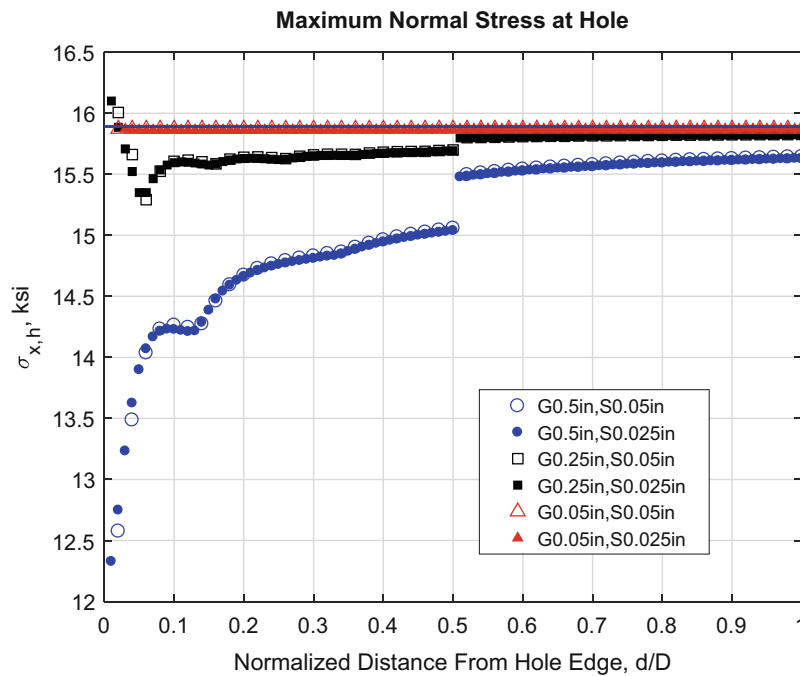


Fig. 16.7 Submodel maximum concentrated x-direction stress

early changes in stress are steep and the stress even decreases for submodels with boundary location ratios near 0.1, before increasing again. Submodels that are derived from a global model with 0.25 inch element edges (i.e., the squares in Fig. 16.7) predict a maximum stress near 16 ksi for the first submodel. As these submodels boundaries are cut farther from the hole, the stress dips to near 15.25 ksi and then slowly increases to a maximum predicted stress near 15.8 ksi. All the submodels derived from a global model with 0.05 inch element edges(i.e., the triangles in Fig. 16.7) predict a maximum stress near

15.85 ksi. Finally, note that the stresses plotted with circles and squares both experience a discontinuous jump increase in stress when the submodel boundary location ratio reaches 0.5.

The jump between data points at a boundary location ratio of 0.5 inches occurs when the submodel boundary reaches the top and bottom surface of the beam (e.g., Submodel 3 in Fig. 16.5). Every submodel prior to reaching this interface has four edges that are interior to the beam's free surfaces. The displacements on all four of these edges were estimated from a global model that is coarser than the submodels and therefore has different stiffness than the submodels. The displacements are generally under-estimated in this case because the global model was too stiff. Every submodel placed with a boundary location ratio greater than 0.5 had only two vertical interfaces where displacements were estimated from the global model. In this configuration, top and bottom free surfaces of the beam were free to displace, as the loading required. In particular, the Poisson effect was over-constrained for models with displacement constraints on the top and bottom edges, so when these surfaces were left free to displace, the stress exhibited a jump increase.

The general character of the change in stress versus the boundary location ratio is determined by the specific makeup of elements in the global model. For example, the meshing algorithm did not include checks or iterations to remove any degraded elements such as three-node triangles, which have different shape functions than the four-node quadrilaterals that make up most of the mesh. It is believed that the general differences from one global mesh to the next will affect the local slope of the change in submodel stress in Fig. 16.7. These factors depend on the case study rather than the submodeling method in general, so they were not investigated in detail for this study.

16.5 Conclusion

In this work, a submodeling routine was presented in which a global coarse finite element model is solved and used to estimate boundary conditions to apply to a refined submodel. The submodel must be located interior to the geometric space of the global model. Usually, the method is employed to determine accurate displacements and stresses of small features in structures such as holes, fillets, or contact interfaces.

In this paper, a cantilever beam with a stress concentration hole was analyzed using the submodeling method. In particular, the submodeling routine was employed to determine how the location of the submodel boundary with respect to edge of the hole affects the predicted maximum concentrated stress at the hole. To accomplish this, the authors designed an algorithm that generated numerous submodel meshes. Each new submodel was generated to have the same mesh as the preceding submodel with a single new row of elements on its exterior, which placed the new submodel boundary farther away from the edge of the hole. Global models were solved for a few element sizes and submodels were generated for all global model sizes at two different refinements. The global model was also refined to determine a converged global mesh.

All the submodels were used to determine the maximum concentrated stress of the hole in the beam. The predicted stresses were plotted versus the submodel boundary location. The stress was generally underpredicted when the submodel boundary was located within a distance equal to one hole-radius from the edge of the hole. When the submodel boundary was move from near the hole to farther from the hole, the submodel predicted a max concentrated stress closer to the global model converged stress. When submodels were generated with boundary conditions from a coarse global model, all the derived submodels underpredicted the global model converged stress more than if the submodels were derived from a more refined global model. Finally, the submodels that were derived from the most refined global model predicted the same max concentrated stress at the hole independent of the submodel boundary location.

Based on the results shown, two conclusions seem apparent. First, if a global model is not converged, the location of a submodel boundary with respect to a stress concentration has a great impact on the major results predicted by that submodel. In this case, the Saint-Venant's Principle seems to be a valid general guiding rule, meaning that the submodel should be placed a minimum distance away from the feature of interest, where that distance is about equal to the feature's defining dimension or more appropriately the minimum cross section dimension where the feature is located. Second, if the original global model is appropriately converged, then it does not appear to matter how close to the feature the boundary of the submodel is placed. This is not helpful in general, because the purpose of employing the submodeling technique is to avoid the expense of refining the global model until it is converged.

In practice, engineers tend to place submodel boundaries at convenient geometric locations, and less emphasis is put on choosing the distance of the submodel boundary from the feature of interest. Unless the appropriate distance is placed between the submodel boundary and the feature of interest, the analyst must verify that the global model mesh is sufficiently converged in the area of the submodel boundary. Under these conditions, the submodel procedure can be trusted to produce useful results at the feature of interest.

References

1. Zienkiewicz, O.C., Zhu, J.Z.: The superconvergent patch recovery and a posteriori error estimates. Part 1: the recovery technique. *Int. J. Numer. Methods Eng.* **33**, 1331–1364 (1992)
2. Zienkiewicz, O.C., Zhu, J.Z.: The superconvergent patch recovery and a posteriori error estimates. Part 2: error estimates and adaptivity. *Int. J. Numer. Methods Eng.* **33**, 1365–1382 (1992)
3. Kitamura, M., Gu, H., Nobukawa, H.: A study of applying the Superconvergent Patch Recovery (SPR) method to large deformation problem. *J. Soc. Nav. Arch. Jpn.* **187**, 201–208 (2000)
4. Kitamura, M., Ohtsubo, H., Akiyama, A., Bandoh, H.: Submodeling analysis of ship structure with superconvergent patch recovery method. *Int. J. Offshore Polar Eng.* **13**, 216–222 (2003)
5. Hirai, I., Wang, B.P., Pilkey, W.D.: An effective zooming method for finite element analysis. *Int. J. Numer. Methods Eng.* **20**, 1671–1683 (1984)
6. Kondo, M., Sinclair, G.B.: A simple substructuring procedure for finite element analysis of stress concentrations. *Commun. Appl. Numer. Methods.* **1**, 215–218 (1985)
7. Mao, K.M., Sun, C.T.: A refined global-local finite element analysis method. *Int. J. Numer. Methods Eng.* **32**, 29–43 (1991)
8. Whitcomb, J.D.: Iterative global/local finite element analysis. *Comput. Struct.* **40**, 1027–1031 (1991)
9. Whitcomb, J.D., Woo, K.: Application of iterative global/local finite element analysis, Part 1: linear analysis. *Commun. Numer. Methods Eng.* **9**, 745–756 (1993)
10. Whitcomb, J.D., Woo, K.: Application of iterative global/local finite element analysis, Part 2: geometrically non-linear analysis. *Commun. Numer. Methods Eng.* **9**, 757–766 (1993)
11. Cormier, N.G., Smallwood, B.S., Sinclair, G.B., Meda, G.: Aggressive submodelling of stress concentrations. *Int. J. Numer. Methods Eng.* **46**, 889–909 (1999)
12. Sinclair, G.B., Cormier, N.G., Griffin, J.H., Meda, G.: Contact stresses in dovetail attachments: finite element modeling. *J. Eng. Gas Turbines Power.* **124**, 182–189 (2002)
13. Beisheim, J.R., Sinclair, G.B.: On the three-dimensional finite element analysis of dovetail attachments. *J. Turbomach.* **125**, 372–379 (2003)
14. Marenic, E., Skozrit, I., Tonkovic, Z.: On the calculation of stress intensity factors and J-integrals using the submodeling technique. *J. Press. Vessel. Technol.* **132**, 041203.1–041203.12 (2010)
15. Arai, K., Yodo, K., Okada, H., Yamada, T., Kawai, H., Yoshimura, S.: Ultra-large scale fracture mechanics analysis using a parallel finite element method with submodel technique. *Finite Elem. Anal. Des.* **105**, 44–55 (2015)
16. Saint-Venant, A.J.C.B.: Memoire Sur La Torsion Des Prismes. *Mem. Divers Savants.* **14**, 233–560 (1855)
17. von Mises, R.: On Saint-Venant's principle. *Bull. AMS.* **51**, 555–562 (1945)
18. ANSYS, Inc.: Ch. 4: Submodeling. In: ANSYS Advance Analysis Techniques. http://www.ansys.stuba.sk/html/guide_55/g-adv/GADV4.htm
19. Dassault Systemes: 10.2: Submodeling. In: Abaqus User's Manual. <http://abaqusdoc.ucalgary.ca/v6.9/books/usb/default.htm?startat=pt04ch10s02aus53.html>

Chapter 17

On Euler Buckling and Snap-Through



Richard Wiebe, Mihaela Nistor, and Ilinca Stanciulescu

Abstract Bistable structures have seen significant attention in recent years for their potential uses in switching and energy harvesting. The behavior of these structures, however, is very sensitive to boundary conditions and initial geometry making their calibration for various applications a difficult task. Additionally, obtaining the force-deformation behavior of these highly (geometrically) nonlinear structures often requires computationally expensive continuation methods. This paper presents a very simple closed-form method which estimates several important characteristics of classical snap-through curves of transversely loaded beams. The estimation is based on a relationship between classic Euler buckling of beams under axial load and the snap-through of post-buckled and curved beams and arches under transverse loading that has recently been investigated by the authors.

Keywords Bistable structures · Stability · Buckling · Snap-through · Continuation

17.1 Introduction

This work is related to the load-deformation response of post-buckled beams under transverse load as shown in Fig. 17.1. The analysis of systems of this type has long captured the interests of researchers, and recently methods to exploit their unique characteristics have increased the interest in this topic, for example in energy harvesting using bistable systems [1]. Systems of this nature (beams that are bistable either via buckling, or being initially curved) have been studied extensively, and the discussion of the many studies is beyond the scope of this presentation. Some examples of analytical, computational, and experimental research efforts on bistable systems may be found in [2–4], along with papers cited therein.

This work is based on a recent publication by the authors [5] on a relationship between Euler-buckling and snap-through buckling. That research was motivated by the fact that, as can be seen in Fig. 17.1, the zero-transverse load crossings (ZTLCs) appear unchanged by different load configurations (the beam parameters are $L = 305$ mm, $I = 0.139$ mm⁴, $A = 0.322$ mm², $E = 207$ GPa). The results are, at the moment, limited to initially flat, post-buckled beams. Initially curved or otherwise non-symmetric (e.g. through imperfections) beams are a topic of further study.

17.2 Computational Exploration of the Relationship Between Euler Buckling and Snap-Through

Figure 17.2 shows post-buckled beams with three different levels of rise. The different rise levels were obtained by the continuation-based solution of the force-deformation curves (a projection of the equilibrium configuration and full-field snap-shots are shown) were obtained using a co-rotational model from [6, 7]. Of note is the fact that the ZTLCs appear to consistently coincide with the Euler buckling mode shapes and axial loads, and that this trend continues for deeper arches. The hypothesis is that deeper arches allow for larger axial loads, and thus allow the beam to access higher buckling

R. Wiebe (✉)

Department of Civil & Environmental Engineering, University of Washington, Seattle, WA, USA
e-mail: rwiebe@uw.edu

M. Nistor · I. Stanciulescu

Department of Civil & Environmental Engineering, Rice University, Houston, TX, USA

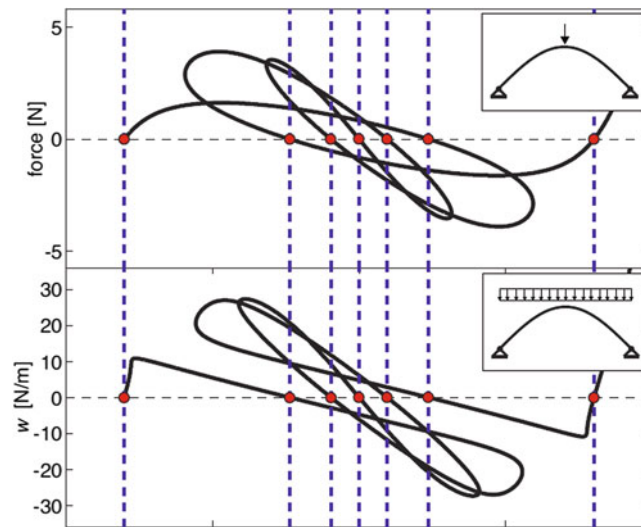


Fig. 17.1 Pinned end, post-buckled beams under two types of transverse loading [5]

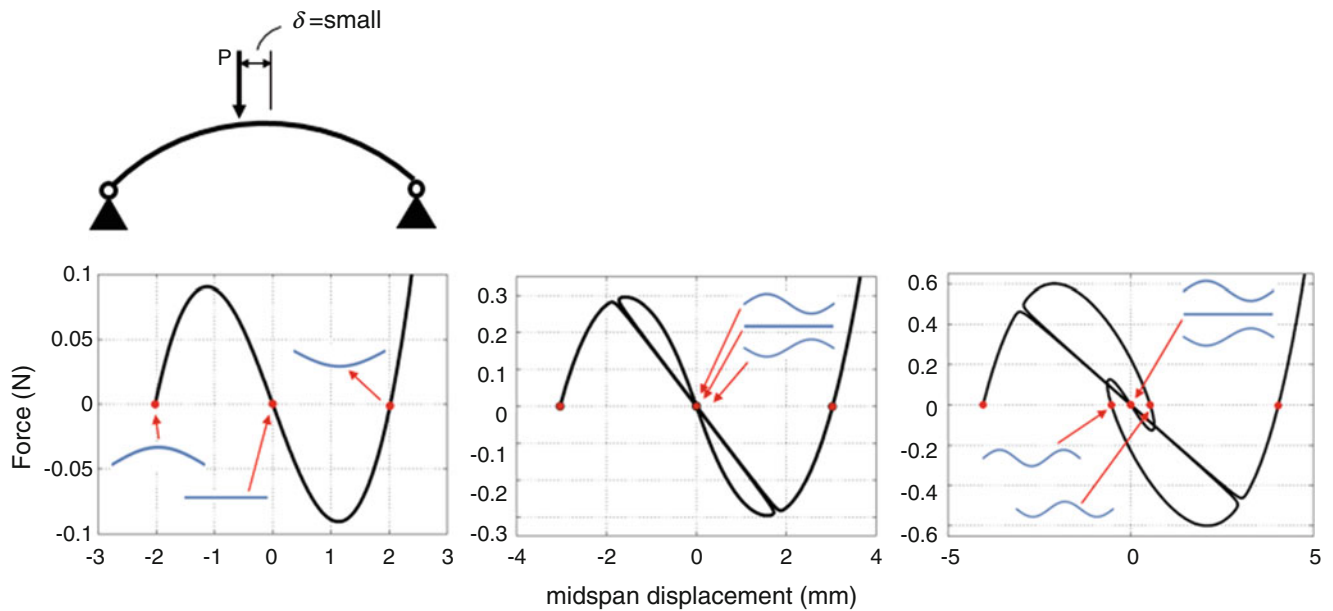


Fig. 17.2 Euler buckling and snap-through of post-buckled pinned beams

modes. Additionally, it was hypothesized that the maximum possible axial load, which will occur when the buckled beam is ‘squashed’ to a flat configuration between the supports, will provide an indication of the maximum number of ZTLCs, and hence maximum number of ‘loops’ in the force-deformation curve. It is inherently assumed that at the ZTLCs, the beam slopes are sufficiently such that the Euler-Bernoulli assumptions are valid, and that the beam configuration represents a classical Euler buckling condition. The work in [5] showed that this hypotheses were remarkably accurate, and that the ‘squash’ load provided an excellent indicator of the number of ZTLCs in a force deformation curve based only on the initial geometry that requires no continuation methods to obtain.

17.3 A Simple Approximation to Predict Force-Deformation Characteristics

The hypothesis discussed in the prior section can be described mathematically by the equation:

$$\frac{n_c^2 \pi^2 EI}{L^2} = P_{squash}, \quad (17.1)$$

which compares the classical n^{th} Euler buckling load which compares the maximum possible axial load with the maximum possible axial ‘squash’ load in the beam. This maximum possible load is based on the assumption of constant axial strain, and can be geometrically understood through the schematic in Fig. 17.3. The determination of the squash load in terms of the buckled geometry can be estimated by using the assumption that the post-buckled axial load remains equal to the first Euler-buckling load, i.e.,

$$P_{squash} = (P_1 + \varepsilon) + \frac{AE}{L} \Delta L \approx P_1 + \frac{AE}{L} \Delta L, \quad (17.2)$$

where the final term represents the *additional load* beyond the first Euler buckling load, P_1 , caused by flattening the beam between the supports. As shown in the Fig. 17.3, this assumption begins to lose accuracy for larger levels of rise as the classical pitchfork begins to turn upward (carry more load) for larger geometric nonlinearity. Depending on the constitutive law of the material, it could be argued that engineering strain should be used as opposed to true strain, i.e., that the denominator should be the initial length of the beam, L_0 , as opposed to the current length, L , however, this distinction results in a higher-order effect than the other calculations that follow. The length change can be obtained using an arc-length integral as follows

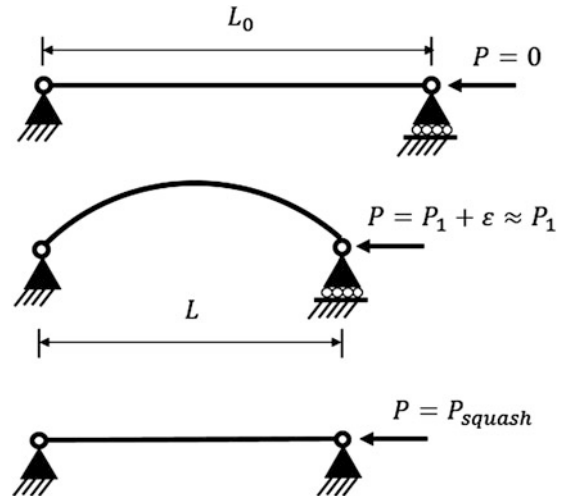
$$\Delta L = \int_0^L \sqrt{1 + (y')^2} dx - L \approx \int_0^L \left(1 + \frac{1}{2} y'^2\right) dx - L = \int_0^L \frac{1}{2} y'^2 dx. \quad (17.3)$$

Using the first Euler buckling mode shape of $y(x) = \alpha \sin \pi x/L$ as the assumed solution form, and combining Eqs. (17.2) and (17.3) yields

$$P_{squash} = P_1 + \frac{AE}{L} \Delta L = \frac{\pi^2 EI}{L^2} + \frac{AE}{L} \left(\frac{\pi^2}{4L} \alpha^2\right) = \frac{\pi^2 EI}{L^2} + \frac{\pi^2 AE}{4L^2} \alpha^2 \quad (17.4)$$

Finally, combining Eqs. (17.1) and (17.4) yields an expression for the critical buckling mode number n_c as a function of the buckled rise, α , or vice-versa as shown below.

Fig. 17.3 Illustration of approximation used to develop analytical expressions. P_1 is the first Euler buckling load



$$n_c = \sqrt{1 + \frac{A}{4I}\alpha^2}, \quad (17.5)$$

$$\alpha_c = \sqrt{\frac{4I}{A}(n^2 - 1)}, \quad (17.6)$$

where in the latter expression α_c is the rise needed to allow the formation of n buckling modes. In Eq. (17.5), the n_c value is a real number, whereas the highest accessible buckling mode is the largest integer smaller than n_c . These equations offer a very simple estimation of the necessary rise level needed to achieve a desired nonlinear response. For example, if one desires to observe bifurcation buckling, which engages asymmetric snap-through (which is represented by the second Euler buckling load at its ZTLCs), one can select $n = 2$. Crucially, however, these equations predict the onset of a new bifurcation, but not necessarily when the bifurcation will practically affect the response. In the case of bifurcation vs. limit point buckling, the bifurcation buckling initially occurs after the limit point as rise is gradually increased.

The accuracy of Eq. (17.6) has been investigated via a comparison with the co-rotational ‘truth’ model for the beam parameters discussed earlier. The exact onset of the second and third modes occur at 2.27 mm and 3.70 mm of rise respectively, while these are predicted to occur at 2.28 mm and 3.72 mm respectively. These results are remarkably accurate using only simple geometric arguments.

17.4 Conclusions

The presented analysis and equations offer a simple method to predict the characteristics of the nonlinear, snap-through type, force-deformation response of buckled beams. The method only applies to pinned-end beams, however, the extension to clamped beams would be a simple analysis exercise. The results are also specific to a particular beam, however, the accuracy nominally holds for beams of a wide range of rise/span ratios and a wide range of cross-sections. Additionally, the method only applies to initial flat beams that obtain their bistability through axial buckling. Extensions to curved beams and beams with imperfections are a part of ongoing work by the authors.

References

1. Hame, R.L., Wang, K.W.: A review of the recent research on vibration energy harvesting via bistable systems. *Smart Mater. Struct.* **22**(2), 023001 (Online) (2013)
2. Plaut, R.H.: Buckling of shallow arches with supports that stiffen when compressed. *J. Eng. Mech.* **116**(4), 973–976 (1990)
3. Stanciulescu, I., Mitchell, T., Chandra, Y., Eason, T.G., Spottswood, S.M.: A lower bound on snap-through instability of curved beams under thermomechanical loads. *Int. J. Non Linear Mech.* **47**(5), 561–575 (2012)
4. Murphy, K.D., Virgin, L.N., Rizzi, S.A.: Experimental snap-through boundaries for acoustically excited, thermally buckled plates. *Exp. Mech.* **36**(4), 312–317 (1996)
5. Nistor, M., Wiebe, R., Stanciulescu, I.: Relationship between Euler buckling and unstable equilibria of buckled beams. *Int. J. Non Linear Mech.* **95**(1), 151–161 (2017)
6. Battini, J.M.: Co-rotational beam elements in instability problems. PhD Thesis, KTH Royal Institute of Technology, Stockholm (2002)
7. Wiebe, R.: Nonlinear dynamics of discrete and continuous mechanical systems with snap-through instabilities. PhD Thesis, Duke University, Durham NC (2012)

Chapter 18

Solitons in Cyclic and Symmetric Structures



Filipe Fontanela, Aurelien Grolet, Loic Salles, and Norbert Hoffmann

Abstract This research focuses on localised states arising from modulationally unstable plane waves in non-conservative cyclic and symmetric structures. The main application is on vibrations of bladed-disks of aircraft engines experiencing non-linear effects, such as large displacements, friction dissipation, and/or complex fluid-structure interactions. The investigation is based on a minimal model composed of a chain of linearly damped Duffing oscillators under external travelling wave excitation. The computed results are based on two strategies: (1) a Non-Linear Schrödinger Equation (NLSE) approximation; and (2) the periodic and quasi-periodic Harmonic Balance Methods (HBM). In both cases, the results show that unstable plane waves may self-modulate, leading to stable and unstable single and multiple solitons configurations.

Keywords Localised vibrations · Solitons · Cyclic structures · Non-linear Schrödinger equation · Harmonic balance methods

18.1 Introduction

Localisation of vibrations is a very important topic in rotating machines, such as bladed-disks of aircraft engines, due to high cycle fatigue. In the linear regime, localised vibrations arise in ideally periodic structures due to inherent inhomogeneities resulting e.g. from the manufacturing processes or wear. However, in real applications, when structures e.g. experience large deformations induced by strong excitations, their behaviours deviate from the linear regime due to non-linearities. It is well-known that, in the non-linear regime, energy localisation may arise even in perfect period structures due to bifurcations.

This research focuses on the non-linear dynamics of cyclic and symmetric structures excited by travelling waves. This excitation is very common in turbomachinery applications since it can be generated due to unbalances or aerodynamic excitations. The findings are based on two different strategies: (1) a non-conservative NLSE approximation; and (2) a fully numeric periodic and quasi-period HBM approach. The results show that stable solitons may emerge from unstable homogeneous solutions, leading to localised vibrations which move along the structure preserving their shapes.

18.2 Physical System

The physical system under investigation consists of N_s unitary masses, cyclically connected to each other by linear springs ω_c^2 , and attached to the ground by linear springs ω_0^2 , viscous dampers γ^2 , and cubic springs ξ . The displacement for the n th degree of freedom u_n is written as

$$\ddot{u}_n + \gamma^2 \dot{u}_n + \omega_0^2 u_n - \omega_c^2 (u_{n-1} + u_{n+1} - 2u_n) + \xi u_n^3 = f_n, \quad (18.1)$$

F. Fontanela (✉) · L. Salles
Imperial College London, London, UK
e-mail: ff515@ic.ac.uk; ffontanela@gmail.com

A. Grolet
Arts et Métiers ParisTech, Lille, France

N. Hoffmann
Imperial College London, London, UK

Hamburg University of Technology, Hamburg, Germany

where f_n represents the external excitation. For the following analysis, it is assumed that f_n has a travelling wave form such as

$$f_n(t) = F_0 \exp \{i[k(n-1)a - \omega_f t]\} + \text{c.c.} \quad (18.2)$$

where F_0 is the force amplitude, k is the corresponding wave number, $a = 2\pi/N_s$ is the lattice parameter, ω_f is the external frequency, i is the imaginary unit, and c.c. states the complex-conjugate of the first expression. It should be noted that, due to the cyclic symmetry ($f_1 = f_{N_s+1}$), k can only assume integer numbers.

18.3 Solution Approach

In this section, the two proposed solution approaches are presented. Firstly, the requirements to derive a non-conservative NLSE is introduced, and its limitations are discussed. Finally, a periodic and quasi-periodic HBM is proposed to compute homogeneous solutions and localised states emerging from unstable plane waves, respectively.

18.3.1 Non-conservative NLSE

In the weakly non-linear regime the displacement u_n is assumed to have the form

$$u_n(t) = \epsilon \Psi(X, T) \exp \{i[k(n-1)a - \omega_k t]\} + \text{c.c.}, \quad (18.3)$$

where $\Psi(X, T)$ is an envelope function which modulates the travelling wave response, $\omega_k = \sqrt{\omega_0^2 + 4\omega_c^2 \sin^2(\frac{ka}{2})}$ is the linear natural frequency, and ϵ is a small parameter. In Eq. (18.3), X and T are continuous variables such as $X = \epsilon x = \epsilon(n-1)a$ and $T = \epsilon t$. After plugging Eq. (18.3) into Eq. (18.1), it is possible to obtain

$$i \frac{\partial \Psi}{\partial \tau} + P \frac{\partial^2 \Psi}{\partial \eta^2} + Q |\Psi|^2 \Psi = -i\Gamma \Psi - h \exp\{i\delta_\omega \tau\}, \quad (18.4)$$

where $\tau = \epsilon T$, while $\eta = X - c_g t$ is a frame moving with the group velocity $c_g = \frac{d\omega_k}{dk}$. In Eq. (18.4), the parameter $P = \frac{1}{2} \frac{d^2 \omega_k}{dk^2}$ accounts for the dispersion, $Q = -\frac{3\xi}{2\omega_k}$ is the non-linear term, $\Gamma = \frac{\gamma^2}{2}$ models the linear damping effect, $h = \frac{F_0}{2\omega_k}$ is the external force, and $\delta_\omega = \omega_k - \omega_f$ is a detuning parameter. The approach is based on a multiscale approximation and the continuous limit [1–3]. In practical terms, Eq. (18.4) is valid when: (1) the solution Ψ varies slowly in space and time compared to a and $2\pi/\omega_f$; (2) the detuning parameter δ_ω is small and the system is close to the resonance; and (3) the system weakly forced and weakly damped. Finally, the carrier wave is assumed to vibrate with ω_f such as $\Psi(\eta, \tau) = \psi(\eta, \tau) \exp\{i\delta_\omega \tau\}$, leading Eq. (18.4) to an autonomous system.

18.3.2 Quasi-periodic HBM

In the quasi-periodic HBM approach, the solution u_n is expanded in a truncated Fourier series such as

$$u_n(t) = \sum_{-k_2}^{k_2} \sum_{-k_1}^{k_2} A_{k_2 k_1} \cos(k_2 \omega_2 t + k_1 \omega_1 t) + B_{k_2 k_1} \sin(k_2 \omega_2 t + k_1 \omega_1 t), \quad (18.5)$$

where k_1 and k_2 are the numbers of retained harmonics, $A_{k_2 k_1}$ and $B_{k_2 k_1}$ are the corresponding amplitudes, while ω_1 and ω_2 are the two incommensurable frequencies. It is important to notice that if $k_1 = 0$ or $k_2 = 0$ Eq. (18.5) recovers the standard periodic HBM. The values of $A_{k_2 k_1}$ and $B_{k_2 k_1}$ are obtained by plugging Eq. (18.5) into Eq. (18.1), followed by a Galerkin projection, in order to represent the response in Fourier space such as

$$[L] \{Z\} + \{f_{nl}\} - \{g\} = \{0\}. \quad (18.6)$$

In Eq. (18.6), $\{Z\}$ is the vector containing the Fourier coefficients $A_{k_1 k_2}$ and $B_{k_1 k_2}$, $[L]$ is a matrix representing the linear dynamics, while the vectors $\{f_{nl}\}$ and $\{g\}$ are the projections of the non-linear and the external forces into the Fourier space, respectively (see [4] for a more detailed discussion). The projection from time domain to Fourier space is calculated using a two-dimensional FFT algorithm, where the two frequencies ω_1 and ω_2 are sampled using a hyper-time approach [4]. Finally, one should note that this paper is interested in quasi-periodic oscillations arising from Neimark-Sacker bifurcations (see Sect. 18.4). Therefore, the frequency ω_2 is an unknown in Eq. (18.6), and an additional equation representing a phase condition is added to compute the value of ω_2 (see [5] for a more detailed discussion).

18.4 Numerical Results

The system described by Eq. (18.1) is solved assuming $N_s = 36$, $\gamma^2 = 0.01 \text{ kg} \cdot \text{s}^{-1}$, $\omega_0^2 = 1.0 \text{ kg} \cdot \text{s}^{-2}$, $\omega_c^2 = 1.0 \text{ kg} \cdot \text{s}^{-2}$, $\xi = 0.10 \text{ kg} \cdot \text{m}^{-2} \cdot \text{s}^{-2}$. The external force f_n is assumed to vibrate with amplitude $F_0 \sim 0.0225 \text{ N}$ and wave number $k = 16 \text{ m}^{-1}$.

In order to solve the previous example with the NLSE approach, standing solutions ($\frac{\partial \psi}{\partial \tau} = 0$) resulting from the autonomous system discussed in Sect. 18.3.1 is solved with the continuation code AUTO [6]. Figure 18.1 shows the maximum displacement of u as a function of ω_f . In Panel (a) of Fig. 18.1 solid lines indicate stable solutions, while dashed lines identify unstable ones (see [7] for the stability analysis of ψ). Panel (b) of Fig. 18.1 shows the envelope function ψ for four different points identified in Panel (a): P1, P2, P3 show solutions for the branch detaching around $\omega_f \sim 2.2125 \text{ rad/s}$, corresponding to solitons with one hump; and P4 identifies a solution with two humps corresponding to the branch detaching at $\omega_f \sim 2.2160 \text{ rad/s}$.

The HBM approach is also applied to the same example using an arc-length continuation [4]. Solutions are shown in Panel (a) of Fig. 18.1 with dotted blue lines. For the plane wave branch Eq. (18.5) is solved assuming $k_2 = 0$ and $k_1 = 3$, while the solitons branches are calculated assuming $k_2 = 5$ and $k_1 = 1$. Initial conditions from S1 are used to solve Eq. (18.1) with a time-marching algorithm. Figure 18.2 shows the results from the quasi-periodic HBM approach compared to the numerical integration of Eq. (18.1). The results show great agreement.

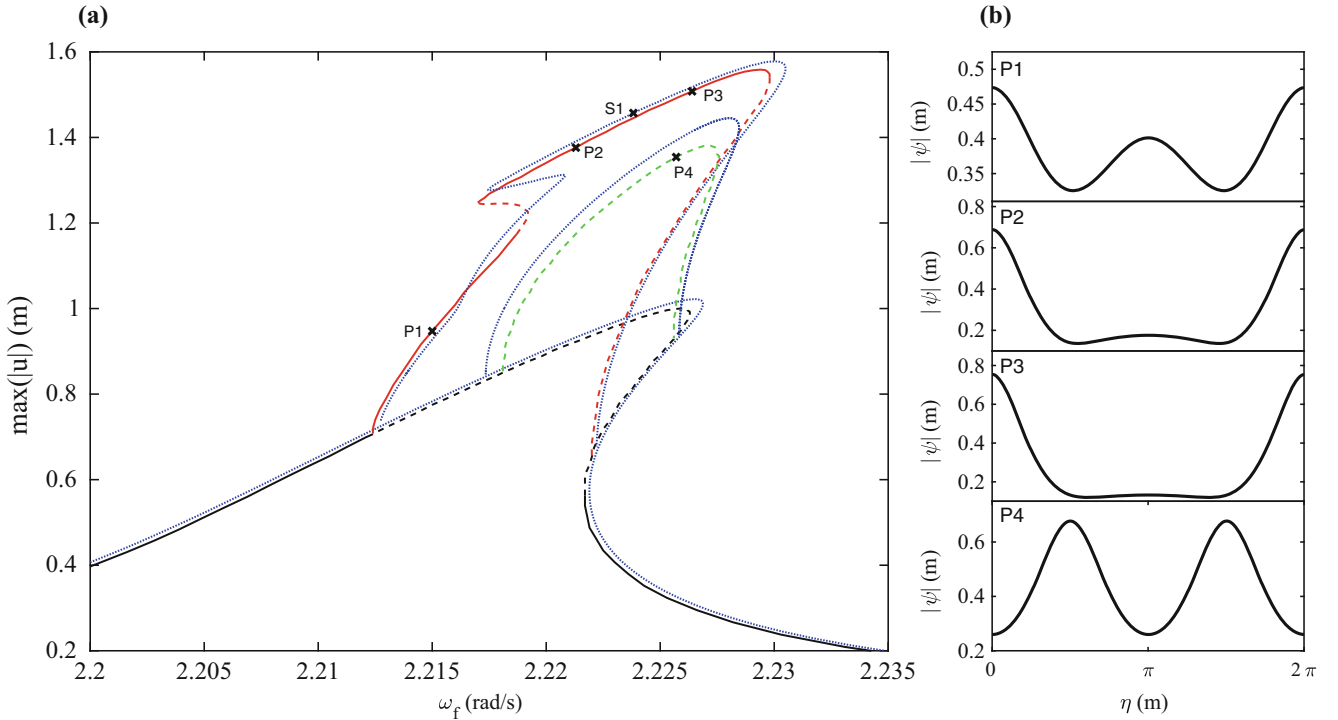


Fig. 18.1 Panel (a) shows the bifurcation diagram computed with the NLSE and the HBM approaches. For the NLSE, solid lines show stable solutions while dashed lines identify unstable ones. Blue dotted lines show results obtained from the HBM approach. Panel (b) shows the envelope functions calculated with the NLSE

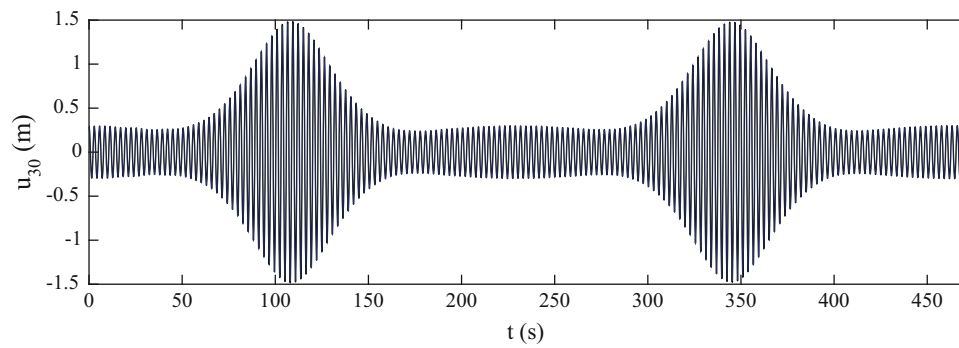


Fig. 18.2 Time evolution of u_{30} calculated with the quasi-periodic HBM (blue) and with a time-marching algorithm (black)

References

1. Remoissenet, M.: *Waves Called Solitons: Concepts and Experiments*. Advanced Texts in Physics. Springer, Berlin (1994)
2. Grolet, A., Hoffmann, N., Thouverez, F., Schwingshackl, C.: Travelling and standing envelope solitons in discrete non-linear cyclic structures. *Mech. Syst. Signal Process.* **81**(15), 1–13 (2016)
3. Fontanela, F., Grolet, A., Salles, L., Chabchoub, A., Hoffmann, N.: Dark solitons, modulation instability and breathers in a chain of weakly nonlinear oscillators with cyclic symmetry. *J. Sound Vib.* **413**, 467–481 (2017)
4. Guskov, M., Thouverez, F.: Harmonic balance-based approach for quasi-periodic motions and stability analysis. *J. Vib. Acoust.* **134**(3), 031003 (2012)
5. Guillot, L., Vigué, P., Vergez, C., Cochelin, B.: Continuation of quasi-periodic solutions with two-frequency harmonic balance method. *J. Sound Vib.* **394**, 434–450 (2017)
6. Doedel, E.J., Champneys, A.R., Fairgrieve, T.F., Kuznetsov, Y.A., Oldeman, B., Paffenroth, R., Sandstede, B., Wang, X., Zhang, C.: *AUTO-07P: Continuation and Bifurcation Software for Ordinary Differential Equations*. Concordia University, Montreal, Canada (2007)
7. Barashenkov, I., Smirnov, Y.: Existence and stability chart for the AC-driven, damped nonlinear Schrödinger solitons. *Phys. Rev. E* **54**(5), 5707–5725 (1996)



Chapter 19

Experimental and Numerical Nonlinear Modal Analysis of a Beam with Impact: Part I – Numerical Investigation

F. Schreyer, S. Peter, and R. I. Leine

Abstract In this contribution we describe a method for numerical nonlinear modal analysis of a beam with impact. To model the nonsmooth contact law efficiently a novel approach which combines the shooting and the harmonic balance method is proposed. This approach allows for the solution of contact problems without penalty parameters or restitution coefficients. Due to the conservative nature of this contact law, the method is particularly suitable for the calculation of nonlinear modes of undamped systems. The results are compared to experimentally extracted nonlinear modes obtained in Part II of this study.

Keywords Nonlinear modes · Harmonic balance method · Contact · Nonsmooth systems · Finite element method

19.1 Introduction

Several numerical methods exist to predict the periodic behavior of oscillating structures, e.g., the finite difference method, the shooting method and the harmonic balance method. However, if nonsmooth mechanical systems are considered, then most methods have their difficulties to deal with the set-valued force laws used to describe hard unilateral constraints and Coulomb-type friction.

This contribution proposes a novel approach which combines the shooting and the harmonic balance method in order to handle nonsmooth structural dynamical problems efficiently. The method, which is referred to as the Massless Mixed Shooting-Harmonic Balance Method (MMS-HBM), yields a combined frequency time domain formulation of the equation of motion. For the analysis of finite element models with local unilateral constraints the standard MS-HBM proposed in [1] is augmented by a massless boundary at the contact surface [2].

The numerical method is demonstrated on the example of a laboratory benchmark system consisting of a beam structure with impact at the tip. The calculated nonlinear modes are validated against experimental results obtained with an automated phase resonance approach as described in Part II [3].

19.2 Numerical Procedure and Benchmark Structure

In this contribution nonlinear modes are defined as the periodic solutions of autonomous conservative dynamical systems. Hence, for the numerical benchmark system depicted in Fig. 19.1 the definition yields the problem to find the periodic solution of

$$\mathbf{M}\ddot{\mathbf{q}}(t) + \mathbf{K}\mathbf{q}(t) + \mathbf{w}\lambda = 0, \quad (19.1)$$

where \mathbf{M} and \mathbf{K} are obtained by a Finite Element discretization of the beam. Following [2] the mass of the contact node, here the node of the tip of the beam, is neglected. To prevent strong changes of the system characteristics the element length is

F. Schreyer (✉) · S. Peter · R. I. Leine
Institute for Nonlinear Mechanics, University of Stuttgart, Stuttgart, Germany
e-mail: schreyer@inn.uni-stuttgart.de; peter@inn.uni-stuttgart.de; leine@inn.uni-stuttgart.de

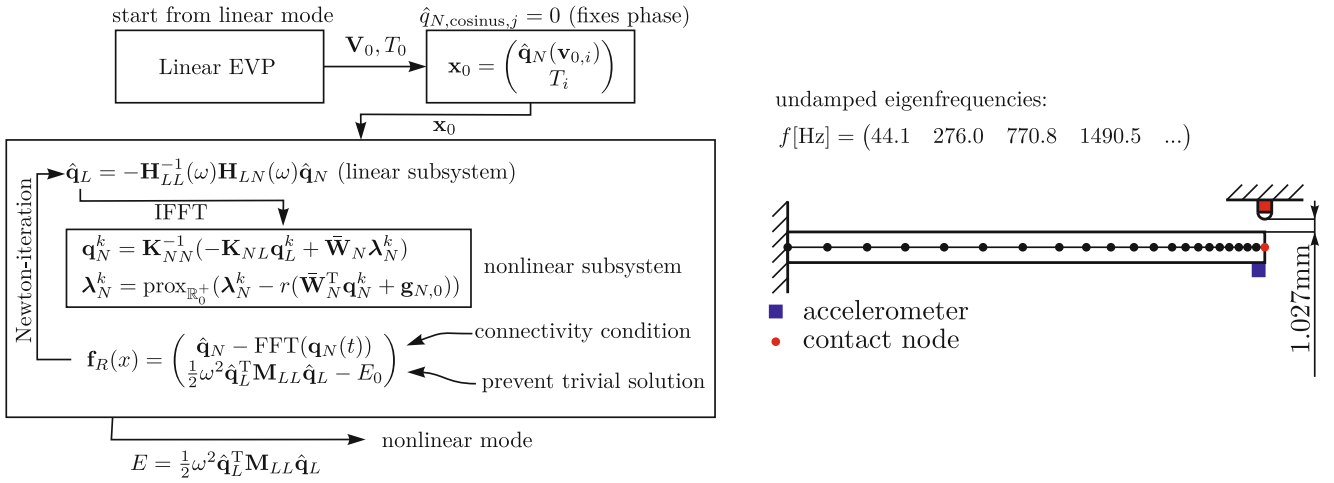


Fig. 19.1 Left: Numerical scheme for the calculation of nonlinear modes. Right: Analyzed finite element model of the beam with impact

refined towards the contact node, which makes a complicated redistribution of the mass unnecessary. The massless approach makes it possible to avoid impulsive contact forces. The set-valued signorini contact law can be described using the inequality complementarity condition

$$0 \leq \mathbf{w}^T \mathbf{q} + g_{N,0} \perp \lambda \geq 0. \quad (19.2)$$

This equation can be rewritten with the proximal point function as an implicit nonlinear equation [4].

We use the Harmonic Balance Method to obtain periodic solutions of Eq. (19.1) which is numerically robust and efficient for large systems with many DOF. However, the harmonic ansatz functions cannot fulfill the non-penetration condition (19.2) directly. Therefore, we divide the system into a linear and a nonlinear subsystem. The linear subsystem is described in frequency domain and the nonlinear subsystem results in a static equation with inequality condition expressed as a proximal point function. The calculation scheme is depicted in Fig. 19.1. The system can be completely described by the vector of unknowns \mathbf{x} which consists of the Fourier coefficients of the nonlinear subsystem and the oscillation period. To find a solution of the problem we use a Newton-type solver which must therefore only iterate in the nonlinear DOF, which are generally only a few compared to the numerous linear DOF. The benchmark system features two nonlinear DOF: the angle and displacement at the contact node, respectively. Additionally, the Jacobian matrix can be calculated semi-analytically, which makes the method also suitable for systems with more nonlinear DOF. The autonomous problem demands a phase anchor which can be considered by setting one Fourier coefficient to zero. Using a prediction-correction path following technique the branch of a nonlinear modes is calculated starting from the linear eigenfrequency with a low energy level of the analyzed mode.

19.3 Numerical Results

The previously explained numerical method is applied to the beam structure with impact and compared against experimental results. Exemplary, the first nonlinear mode is considered. Experimentally, the phase-locked loop (PLL) based nonlinear modal analysis method as described in [3] is applied to the test structure. For the interpretation of the results it is important to note that only the linear parameters of the numerical model, namely the Young's modulus and the density of the material are identified to fit the measured linear eigenfrequencies. Due to the adopted massless approach, no additional contact parameter such as a restitution coefficient or stiffness is employed. Figure 19.2 shows a comparison of numerical results for two different numerical models with a discretization with 8 and 21 Timoshenko beam elements, i.e., 9 and 22 nodes, respectively. It can be observed that both models yield very similar results. Furthermore, the influence of the number of harmonics considered in the Harmonic Balance calculation is investigated. The results in Fig. 19.2 show that even for comparatively low amplitudes the fundamental harmonic calculation (H1) deviates from the calculations with three (H3) and five (H5) harmonics. An interesting difference between the calculation with three and five harmonics can be observed for higher

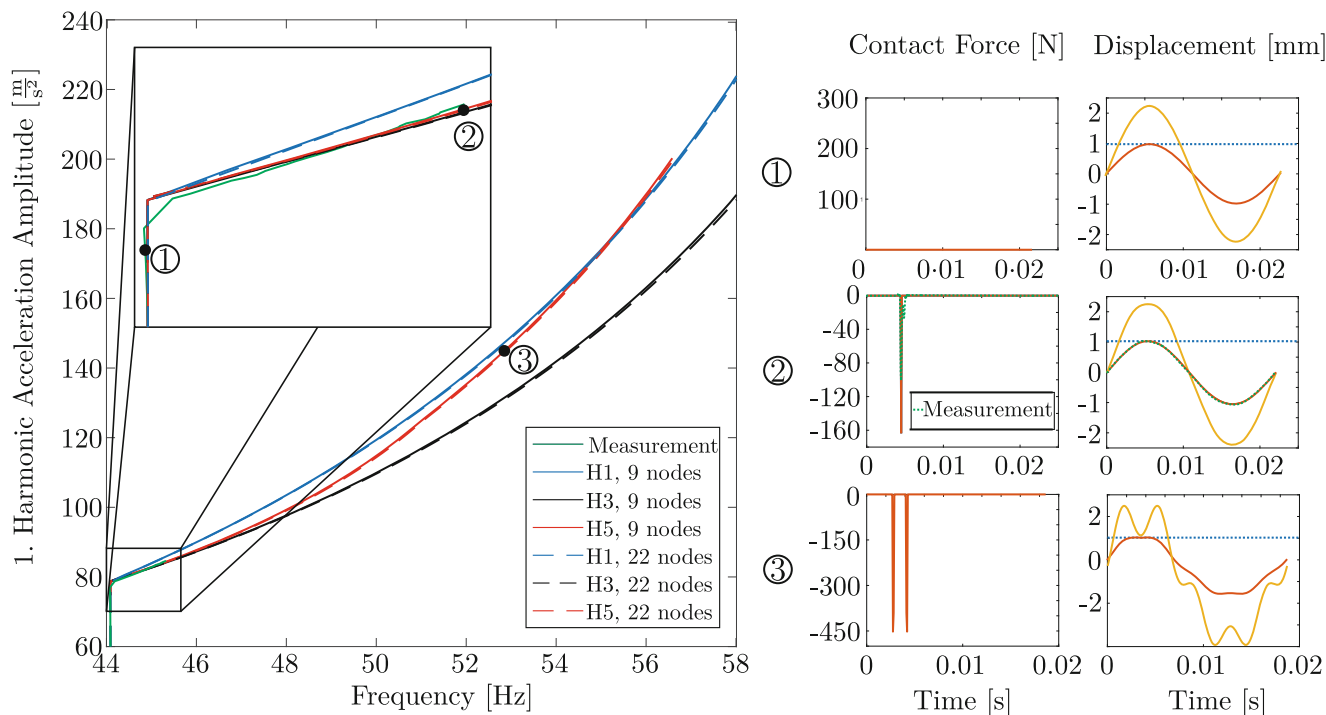


Fig. 19.2 Left: Numerical and experimental backbone curve for the beam tip. Right: Comparison of contact force and displacement for marked points

amplitudes, as the frequency approaches an integer fraction of the second modal frequency (276 Hz), i.e., the system is operated close to a 5:1 internal resonance. The time signal of the displacement and angle of point 3 on the backbone curve already shows a considerable contribution of the fifth harmonic.

An interesting characteristic of the numerical method proposed here is that internal resonances can be analyzed, but similarly to conventional Harmonic Balance approaches, the filtering property is retained. This filtering characteristic, which is not available in pure time domain methods, such as the shooting method, can considerably save computational time. This is particularly interesting when the global behavior of the backbone curve of complex systems with many modal interactions is of interest or in cases where modal interactions do not affect the behavior of the damped system.

Compared to the experimental results measured in Part II a good agreement with the simulations with three and five harmonics can be observed. The experimental curve shows a slightly softer characteristic, i.e., a slightly lower frequency. This can also be observed for the contact force at the second point, which is experimentally slightly lower. An explanation of this difference could be the compliance of the contact element which is neglected in the numerical model and regarded as rigid. However, the displacement at the tip node shows very good agreement. In the experiment the amplitude range for which the nonlinear mode can be extracted is limited due to the high contact forces and accelerations caused by the hard contact.

19.4 Conclusion

This contribution shows that nonlinear modes of systems with unilateral constraints can be calculated with a novel mixed frequency time domain approach which allows to consider nonsmooth contact forces. This approach allows for the solution of contact problems without penalty parameters or restitution coefficients. Due to the conservative nature of the contact law, the method is particularly suitable for the calculation of nonlinear modes, defined as periodic solutions of a conservative autonomous system. The numerical results show a good agreement with the experimental results obtained in Part II of the study. The harmonic ansatz functions which are used to approximate the dynamics of the linear subsystem lead to a numerically efficient method. The filtering characteristic of the harmonic ansatz is essential to calculate nonlinear modes of large finite element systems using a feasible numerical effort.

Further research will be focused on more complex finite element systems and the detailed study of internal resonance phenomena.

References

1. Schreyer, F., Leine, R.I.: A mixed shooting – harmonic balance method for unilaterally constrained mechanical systems. *Arch. Mech. Eng.* **LXIII**(2), 297–313 (2016)
2. Schreyer, F., Leine, R.I.: Mixed shooting-HBM: a periodic solution solver for unilaterally constrained systems. In: *Proceedings of the IMSD, Montréal* (2016)
3. Peter, S., Schreyer, F., Leine, R.I.: Experimental and numerical nonlinear modal analysis of a beam with impact: Part II – experimental investigation. In: *Proceedings of the 36th IMAC, a Conference and Exposition on Structural Dynamics* (2018, to be published)
4. Leine, R.I., Nijmeijer, H.: *Dynamics and Bifurcations of Nonsmooth Mechanical Systems*, vol. 18. Springer, Berlin (2004)



Chapter 20

Experimental and Numerical Nonlinear Modal Analysis of a Beam with Impact: Part II – Experimental Investigation

S. Peter, F. Schreyer, and R. I. Leine

Abstract Methods for nonlinear experimental modal analysis, such as nonlinear phase resonance testing, are currently limited to smooth nonlinearities. However, the modeling of systems with contact interactions, being relevant in many industrial applications, often leads to models with strong nonsmooth nonlinearities. This contribution investigates the capability of nonlinear phase resonance testing to analyze systems with nonsmooth nonlinearities. Therefore, a series of automated steady-state measurements with phase controlled excitation is used. The experimental investigation is complemented with the numerical results obtained in Part I of this study.

Keywords Nonlinear modes · Nonlinear phase resonance testing · Contact interactions · Nonsmooth systems · Nonlinear system identification

20.1 Introduction

In many industrial applications contact interactions significantly influence the dynamic behavior, leading to models with nonsmooth nonlinearities. However, the identification and modeling of these nonsmooth nonlinearities, such as impacts and unilateral constraints, is still a difficult endeavor. For instance, impacts lead to local impulsive forces which are difficult to measure directly in the contact interface and require high experimental effort due to the short duration of the contact phase.

Therefore, this contribution proposes a method to capture the global behavior of structures subjected to impacts in the framework of nonlinear modes. The concept of nonlinear modes is widely applied for the theoretical and numerical analysis of nonlinear structures, while its application to the experimental identification of nonlinear structures is still in its infancy. The commonly used manual force appropriation lacks robustness for strong nonlinearities and the time-frequency analysis of the free-decay, with which it is often combined, limits the resolution of the extracted backbone curves. Therefore, this method seems to be infeasible for the experimental extraction of amplitude dependent nonlinear modal characteristics of nonsmooth systems. A recent method for nonlinear experimental modal analysis [1], which uses a series of steady-state measurements with phase controlled excitation provides a more robust experimental procedure and can be exploited for the analysis of nonsmooth systems. The robustness and accuracy of this method for systems with strong nonsmooth nonlinearities is investigated based on a benchmark beam structure with impact and compared to numerical simulations performed with the method proposed in Part I of this study [2].

20.2 Experimental Procedure and Benchmark Structure

The method for the experimental extraction of nonlinear modes is based on the phase resonance method proposed by Peeters [3]. Thus, the method aims at extracting periodic motions which can be described by the conservative nonlinear equation of motion

$$\mathbf{M}\ddot{\mathbf{q}}(t) + \mathbf{K}\mathbf{q}(t) + \mathbf{f}^{\text{nl}}(\mathbf{q}(t)) = \mathbf{0}. \quad (20.1)$$

S. Peter (✉) · F. Schreyer · R. I. Leine
Institute for Nonlinear Mechanics, University of Stuttgart, Stuttgart, Germany
e-mail: peter@inm.uni-stuttgart.de; schreyer@inm.uni-stuttgart.de; leine@inm.uni-stuttgart.de

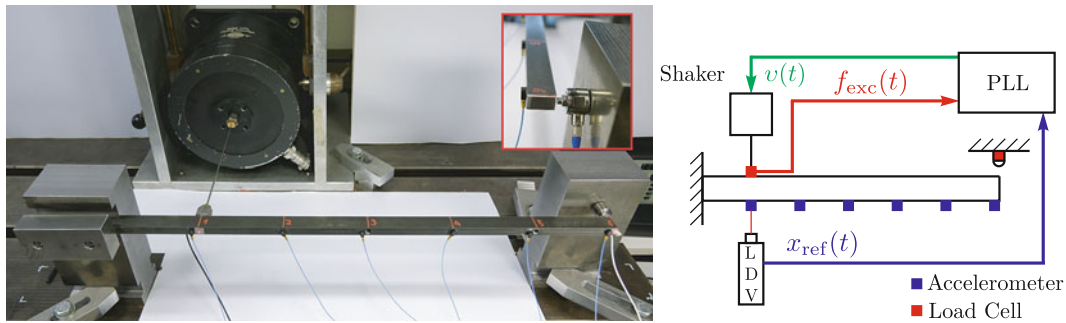


Fig. 20.1 Photo and schematic sketch of the experimental setup

In contrast, the real structure is damped and has to be excited to enforce a periodic motion. In theory, this can be accomplished by a spatially distributed force vector which is shifted in phase by 90° with respect to all harmonics of the displacement for all points of the structure. In practice, for weakly damped systems with smooth nonlinearities, often a single point single harmonic excitation force with the aforementioned phase lag gives satisfactory results, i.e., is capable of isolating the nonlinear mode. This simple approximation is retained for the case of severe nonsmooth nonlinearities and it is shown for the benchmark example that the nonlinear modes can be isolated in this case with a reasonable accuracy. To control the phase of the fundamental harmonic force a phase-locked loop (PLL) controller as proposed in [1] is used. The PLL generates a harmonic voltage signal with a frequency which is controlled such that the phase lag between the fundamental harmonic of the force and the displacement is 90° . The PLL provides a simple control concept with a high robustness in the case of strong nonlinear distortions, that are to be expected due to nonsmooth nonlinearities.

The benchmark structure used in this study consists of a steel beam subjected to a rigid stop at one end. The stop is realized by a steel contact element mounted on a load cell to measure the impact force. A photo of the test rig is shown in Fig. 20.1. The structure is excited by an electrodynamic shaker in the first bending mode, the excitation force is measured with a load cell and the response with six accelerometers. The excitation level is increased incrementally from a low level, where the gap between stop and beam remains open, i.e., the structure behaves linear, up to a high level where the beam is in contact with the impact element. For the PLL controller the excitation force and the displacement at the excitation position are used as reference signals. For the measurement of the displacement a laser doppler vibrometer (LDV) with a displacement decoder is applied. The use of the displacement signal as reference provides, compared to the acceleration, the advantage that the displacement is less distorted by higher harmonics. Therefore, it is found that the control based on the displacement signal provides a higher robustness in the strongly nonlinear regime. A schematic sketch in Fig. 20.1 summarizes the experimental procedure.

20.3 Experimental Results

The PLL based nonlinear modal analysis method as described above is applied to the test structure shown in Fig. 20.1. Furthermore, a numerical model of the test structure which consists of 21 beam elements subjected to a hard contact at the tip is used to calculate the nonlinear modes numerically with the method described in Part I (see [2]). In contrast to the experimental results, for which an approximate force appropriation is used, the numerical results are obtained by directly solving Eq. (20.1) describing the motion of the conservative system. Exemplary, the experimental and numerical results for the backbone curve for the point at the beam tip, i.e., the contact point, are shown in Fig. 20.2. It can be seen that in the measured amplitude range both curves agree very well for a numerical calculation with five harmonics as described in detail in Part I [2]. There is a small difference of both backbone curves suggesting the contact in the experiment is slightly softer compared to the numerical calculation. This difference may be caused by the fact that in the numerical simulation the contact is regarded as perfectly rigid, whereas in reality the contact element has some compliance. However, it is emphasized that the numerical results are obtained without the need for the identification of any impact parameters or any calibration of the nonlinear numerical model. Solely, the linear parameters of the beam have been identified to match the linear eigenfrequencies. The agreement of the simulations and the measurements also indicate that the isolation of the nonlinear mode is possible to a satisfying accuracy even with the rough approximation of a single harmonic single point force controlled with the PLL. A more detailed comparison of the displacement at the beam tip shows an almost perfect agreement

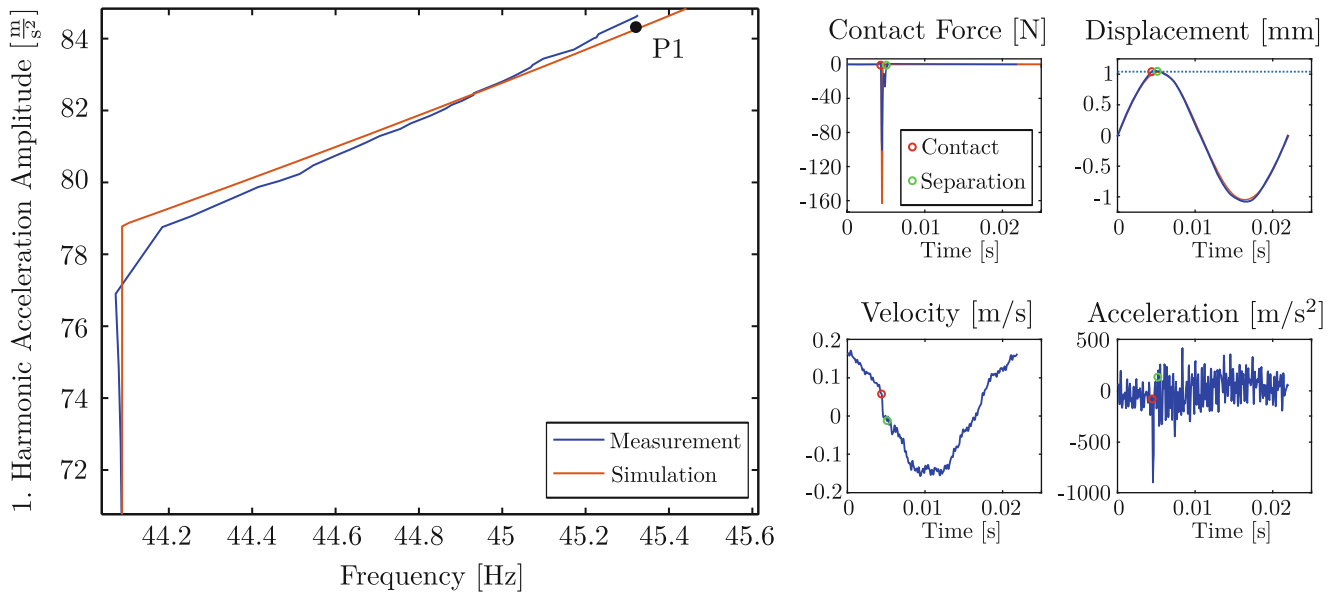


Fig. 2.2 Left: Experimental and numerical backbone curve for the beam tip. Right: Comparison of contact force and displacement (top) and measured velocity and acceleration (bottom) for point P1

of simulation and experiment. However, there is some deviation in the contact force. Firstly, the maximum contact force in the simulation significantly exceeds the contact force in the experiment. Secondly, the contact duration is longer in the experiment and a small second peak can be seen. This peak suggests that there is a local high frequency vibration in the contact area.

This local high frequency vibration can also be observed in the velocity and acceleration signals measured at the beam tip. The velocity and acceleration signals illustrate the significantly nonlinear behavior of the beam. Particularly, the acceleration signal reveals strong high frequency content caused by the impact. The impulsive character of the very hard steel-to-steel contact manifests itself in the acceleration signal as a high peak of almost 1000 m/s^2 at the contact instant. Furthermore, a sudden jump in velocity can be observed due to the impact.

20.4 Conclusion

This contribution shows that recent steady state measurement methods can open the door towards the experimental analysis of nonlinear modes of nonsmooth systems. The experimental approach relies on a PLL controlled excitation force. The PLL controller proves to be robust even in the case of a severe impact nonlinearity. For the studied benchmark test the isolated nonlinear modes are in good agreement with the theoretical nonlinear modes calculated with the method proposed in Part I of this study. It is noted that this is the case even though only a single point force with phase control of the fundamental harmonic is applied, which can be seen as a rather rough approximation. The simplicity and robustness make the method appealing for the analysis of the complicated dynamics of impacting structures. Future work aims at investigating the generality of the proposed method for different test cases.

References

- Peter, S., Leine, R.I.: Excitation power quantities in phase resonance testing of nonlinear systems with phase-locked-loop excitation. *Mech. Syst. Signal Process.* **96**, 139–158 (2017)
- Schreyer, F., Peter, S., Leine, R.I.: Experimental and numerical nonlinear modal analysis of a beam with impact: Part I – numerical investigation. In: *Proceedings of the 36th IMAC, a Conference and Exposition on Structural Dynamics* (2018)
- Peeters, M., Kerschen, G., Golinval, J.C.: Dynamic testing of nonlinear vibrating structures using nonlinear normal modes. *J. Sound Vib.* **330**, 486–509 (2011)

Chapter 21

The Effect of Non-Flat Interfaces On System Dynamics



I. Lawal, S. Shah, M. Gonzalez-Madrid, T. Hu, C. W. Schwingshackl, and M. R. W. Brake

Abstract Manufactured surfaces are never completely flat due to a variety of reasons including: variability in manufacturing operations, material behavior and achievable geometric tolerances. The curvature of surfaces is a local geometric effect that affects part-to-part variability of jointed surfaces. Joints with different interface geometries behave in unpredictable ways (Brake (2018) *The Mechanics of Jointed Structure: Recent Research and Open Challenges for Developing Predictive Models for Structural Dynamics*. Sandia National Laboratories, William Marsh Rice University. Springer, Cham). Among the factors that drive the uncertainty in joint performance are frictional micro and macro sliding events, surface tribology effects, residual stress from manufacturing and assembly, loss of bolt pre-load, changes in contact area and the resulting pressure field variation around the joint. The goal of this research is to identify key variables that account for the measured uncertainty in the dynamics of jointed structures, which may have local regions of conformal and non-conformal contact due to variability inherent in the manufacturing process. Using the standard benchmark system of the Brake-Reuß beam (BRB), recommendations are made for which design parameters require higher tolerances than others to minimize variability in a cost-effective manner. Conformal beams with strong and weak curvature are studied as well as non-conformal (flat vs. curved) beams. Experimental and numerical approaches model and validate the physical behavior of beams to understand primary causes of non-linearity in joints with different interface geometries.

Keywords Joint · Interface · Nonlinear · Curvature · Variability

21.1 Introduction

Structural dynamics of the Brake-Reuß beam (BRB) with flat interfaces have been extensively studied both experimentally and numerically. Schwingshackl [2] has shown with numerical studies that the baseline BRB behaves nonlinearly and is sensitive to input excitation level, assembly stiffness, and interface curvature. The current project explores the effect interface curvature has on the variability of the structural dynamics of the BRB. A total of seven BRBs with conformal interfaces of different curvatures are modeled using SolidWorks (v2017, Dassault Systèmes, Johnston, RI) and simulated using Abaqus (v6.14, Dassault Systèmes, Johnston, RI) to provide insight into cause of nonlinearity. Figure 21.1 shows the standard BRB with typically machined flat joint interface.

Conformal beams are similar to the standard BRB in that they have complete contact at the interface. Non-conformal beams consist of one flat beam and one curved beam. In the non-conformal case, two configurations exist. An edge gap (EG) configuration where the flat beam is joined to an inward curved beam. And the center gap (CG) configuration where the flat

I. Lawal · M. R. W. Brake (✉)
William Marsh Rice University, Department of Mechanical Engineering, Houston, TX, USA
e-mail: brake@rice.edu

S. Shah
Arizona State University, School for Engineering of Matter, Transport & Energy, Phoenix, AZ, USA

M. Gonzalez-Madrid
ISAE SUPAERO, Department of Aerospace Engineering, Toulouse, France

T. Hu
Duke University, Department of Mechanical Engineering & Materials Science, Durham, NC, USA

C. W. Schwingshackl
Imperial College London, Department of Mechanical Engineering, London, UK

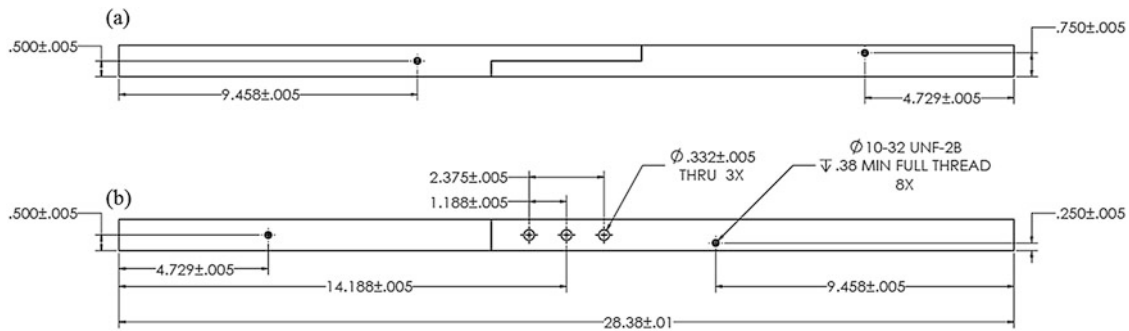


Fig. 21.1 Standard 316 stainless steel Brake-Reuß beam (BRB): (a) Side view showing interface. (b) Top view showing lap joints

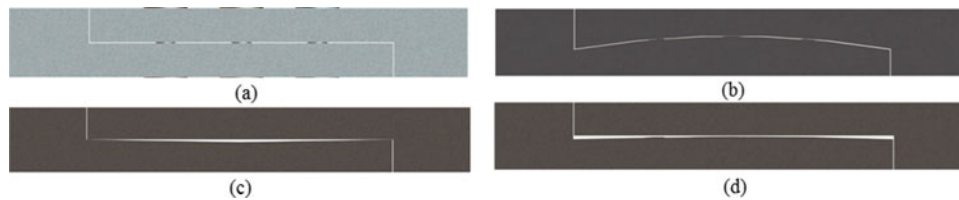


Fig. 21.2 Interface geometries: (a) Flat interface (b) Conformal (Curved-Curved) (c) Center-gap interface (d) Edge-gap interface

beam in joined to an outward curved beam. During assembly three lap joints are tightened by a torque wrench to “squeeze” the upper and lower beams together. Each joint assembly consists of 1 bolt, 1 nut, and 2 washers.

A parametric study for each of the tested configuration was performed in Abaqus to explore effects of bolt preload, interface curvature, and responding direction on system dynamics. For simplicity and computational efficiency, fully threaded bolt surface is simplified to a smooth cylindrical surface, and all fillets and patterns on the bolt and nut are removed.

The paper organization proceeds first with a description of experimental and numerical procedures, followed with discussion of results from both methods. An assessment of how well the numerical model matched the experimental trends will be discussed with consideration for the limitations in quasi-static modelling of dynamic systems. One key objective of the study was to develop a better intuition about how curvature at the joint affects non-linearity in a structure. This will be addressed in the conclusion.

21.2 Experimental Setup

Experimental investigation was focused on assessing the influence of non-flat surfaces on system dynamics. The dynamic response of different combinations was investigated via impact hammer testing. Experiments were performed to determine which of the dynamic parameters (resonance frequency and damping were most influenced by the variations in the interface geometry.

21.2.1 Test Specimens

Seven BRBs are modeled in SolidWorks, using the original SolidWorks model file for the baseline BRB. The interface curvature height were modified by changing the peak distance in vertical direction at the midline of the joint interface. To identify interfaces, two numbers are combined to represent the curvature heights at the interface, i.e. “0–0” means, in side view of the interfaces, the upper and lower interfaces have curvature heights of $0 \mu m$ and $0 \mu m$, respectively. Representative curved interfaces are shown in Fig. 21.2.

The beams were manufactured using wire electrical discharge machining. BRB with interface curvature varying from $0 \mu m$ to $5000 \mu m$ and grouped into three major categories: Baseline (Flat-Flat), Conformal (Curved-Curved) and Non-Conformal (Flat-Curved). Non-conformal beams are interface combinations in which the flat surface of the Baseline model is matched with either the concave or convex interface of the curved beams, forming gaps either at the center of the interface (center gap) or at ends of the interface (edge-gap). For the conformal cases, BRB with Flat interface ($0 \mu m$), BRB with

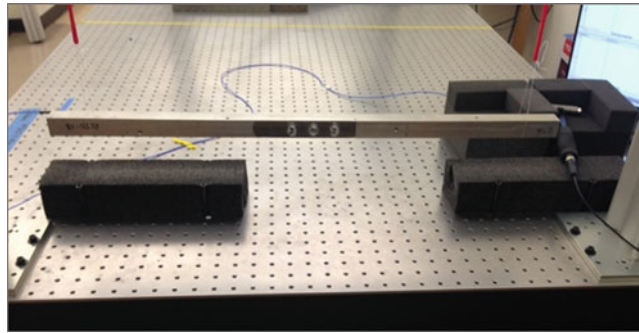


Fig. 21.3 Experimental test setup for impact hammer testing

50 μm and 5000 μm were studied. For the non-conformal cases, the flat (0 μm) were joined with the 50 μm and 250 μm BRBs.

21.2.2 Physical Setup and Data Acquisition

To ensure consistency with experimental procedure, BRB assemblies were carried out in the method outlined by Dossogne, Tilan, et al. [3]. Beam halves were joined with three lap joints each with a stainless steel 5/16//24 bolt and two washers. To ensure consistency in beam assembly, a constant gap is maintained using a standard business card along one edge of the two beam halves. The beams were suspended using bungee cord to simulate a free-free boundary condition. The impact testing experimental setup is shown in Fig. 21.3. BRB response was acquired using a single PCB Piezo electronics 3-axis accelerometer (Model 356A03) mounted in the direction opposite to the impact force. Impact hammer used for the excitation was a PCB Piezo electronics Impact Hammer, (PCB 086C03). Signal processing and data acquisition was carried out using an 8-channel Siemens LMS Data Acquisition system using the Siemens Spectral module to collect transient ring-down response of the BRB. The dynamic response of different beam combinations was sampled at 4096 Hz with a spectral resolution of 0.25 Hz for a time period of 4 s. Signal processing techniques were applied to process the time response signal obtained using LMS Data acquisition. Time response was captured by the accelerometer in the direction of the impact force.

Frequency response function (FRF) from the time response data was processed in Matlab where damping and natural frequency were extracted for the 1st mode using a band pass filter. Figure 21.4 shows results from the filtered signal using Hilbert transformation and spline interpolation technique. Natural frequency of the system and damping ratio when extracted for different amplitudes of impact force overtime gave an understanding of the non-linear behavior of the systems.

21.2.3 Parametric Study

As a part of the investigation, four parameters were varied at high and low levels to understand their impact on joint non-linear behavior. Interface curvature, Excitation Force, Bolt Load and Beam Orientation were varied. In addition to these parameters, it was found that joint reassembly contributes to the non-linear behavior at the joint interface [2]. The impact of joint reassembly was studied by having three re-assemblies for each test level. For the excitation force the two levels were 100 N and 600 N with an allowable range of 10%. Bolt loads at 5.4 N.m and 19.6 N.m were used. Finally, impact hammer testing was carried out with two different beam orientations. As depicted in Fig. 21.5, when the impact force is in the same direction as the bolt heads, the direction is defined as “Bending”. When impact force is across the joint interface or along the length of the interface bolts, the direction is defined as “Longitudinal”.

For each test condition, there are 3 re-sets and during each re-set, 5 ringdown data or samples collected, making for a total of 15 samples per test condition where a test condition is based on the four parameters: Beam Configuration Excitation Level, Bolt Torque and Orientation. A spline interpolation was performed in Matlab to resolve the data for each test condition from 15 trends to a resultant trend.

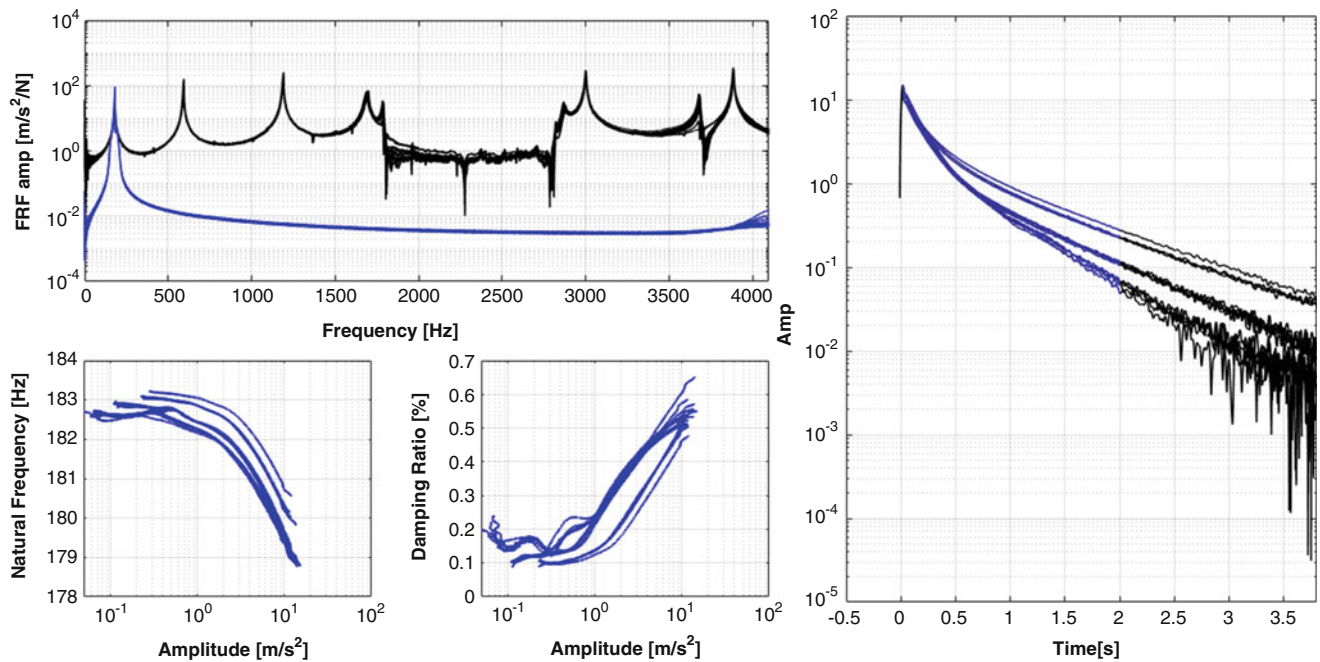


Fig. 21.4 Sample postprocessing results showing (a) frequency response function and modally filtered response, (b) amplitude dependent natural frequency, (c) amplitude dependent damping ratio, and (d) envelope of decay of transient ringdown

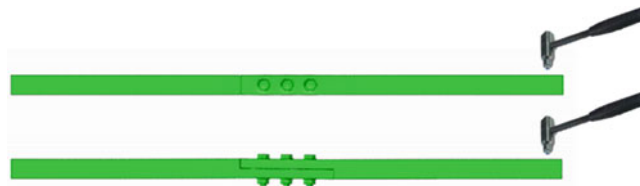


Fig. 21.5 Hammer tests in two different orientations exciting different bending modes. (a) “Longitudinal” modes and (b) “Bending” modes

21.3 Numerical Setup

The next sections of the study detail numerical setup in Abaqus and include the modeling criteria developed to represent experimental test conditions so that reasonable insights can be gained from the numerical model.

21.3.1 Model Development

To account for the quasi-static modeling of a dynamic system, ‘ABAQUS Implicit’ solver was employed to simulate friction and sliding contact at the joint interface. Linear hexahedral elements (C3D8R), and an 8-node linear brick with reduced integration (C3D8RH^(S)), was used to mesh the beams. Tetrahedral element of type “C3D10”, a 10-node quadratic tetrahedron, was used to mesh the joint assembly. Models were meshed (Fig. 21.6) with extensive attention to (a) create sharp edges and corners for hex mesh, (b) ensure that nodes in the upper interface match exactly, or stay within a negligible adjustment range with, the nodes in the lower interface, (c) keep relative consistency in models with different interface curvature heights [4].

Material properties and contact behavior are critical to calibrating system response. Even though no significant amount of effort was made to tune the model to behave the exact same way as observed in experiments, physically reasonable values or estimations were used whenever possible. Both beam and joint assembly were considered to be linear isotropic, homogeneous stainless steel AISI 304 with density $8 \times 10^{-6} \text{ kg/m}^3$, Young’s modulus 200 GPa, and Poisson’s ratio 0.29.

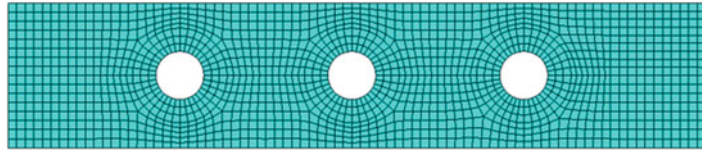


Fig. 21.6 Surface view with grid lines showing the mesh at the contact interface of flat BRB. Curved interfaces use the same algorithm to generate meshes

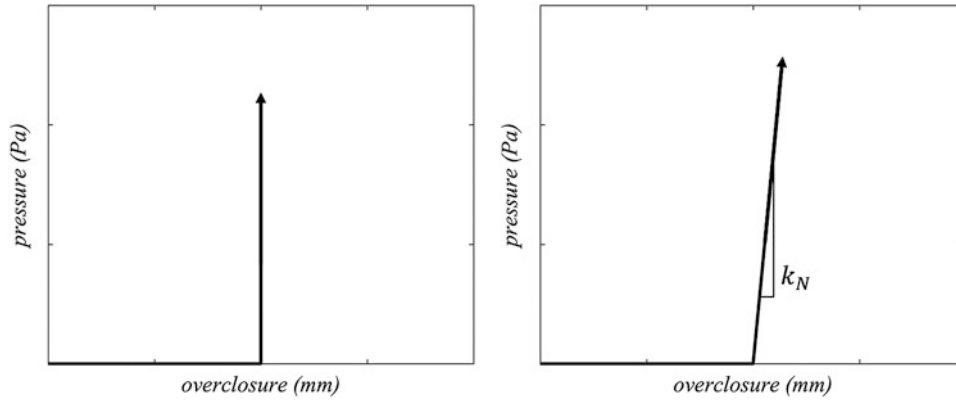


Fig. 21.7 Constitutive relationship of (a) an ideal hard contact, and (b) a numerical softened contact using normal stiffness k_N

In Abaqus, normal behavior defines a contact pressure-overclosure relationship that governs the motion of the surfaces in contact. An ideal “hard” contact (Fig. 21.7a) yields zero penetration and can produce any finite positive contact pressure. However, the ideal contact model results in numerical hassle due to the discontinuity of contact pressure right before and after contact, where contact displacement is zero. To avoid the numerical difficulty and approach the ideal case of contact, we implemented a “softened” contact relationship, in which the contact pressure is a linear function of the clearance between the surfaces (Fig. 21.7b). Overclosure, the negative of clearance, was used to keep a positive sign convention. The contact stiffness was gradually increased and tested until no significant change was observed between trials, which concluded a contact normal stiffness $k_N = 1 \times 10^7 \text{ MPa}$. A direct method was used to strictly enforce the given pressure-overclosure behavior for each constraint, without approximation or use of augmentation iterations.

Coulomb friction was used to model the tangential behavior of the contact surfaces. An empirical friction coefficient [1, 2] of 0.6 was used throughout the analysis. In Abaqus, Coulomb friction model is formulated by a penalty method based on contact pressure and elastic slip. It assumes that no relative motion occurs if the frictional shear stress τ is less than the critical stress τ_{crit} which is linearly proportional to the contact pressure p ,

$$\tau_{crit} = \mu p \quad (21.1)$$

where μ is friction coefficient. The condition of no relative motion was approximated by stiff elastic behavior, and the tangential stiffness (Fig. 21.8) was chosen such that the elastic slip limit caused by shear stress below threshold was bounded by a user-specified elastic slip limit γ_{crit} , $3 \times 10^{-7} \text{ mm}$.

$$k_T = \frac{\tau_{crit}}{\gamma_{crit}} = \frac{\mu p}{\gamma_{crit}} \quad (21.2)$$

Therefore, depending on the contact pressure between the surfaces, the tangential stiffness floats around $2 \times 10^6 \text{ MPa}$ during the analysis.

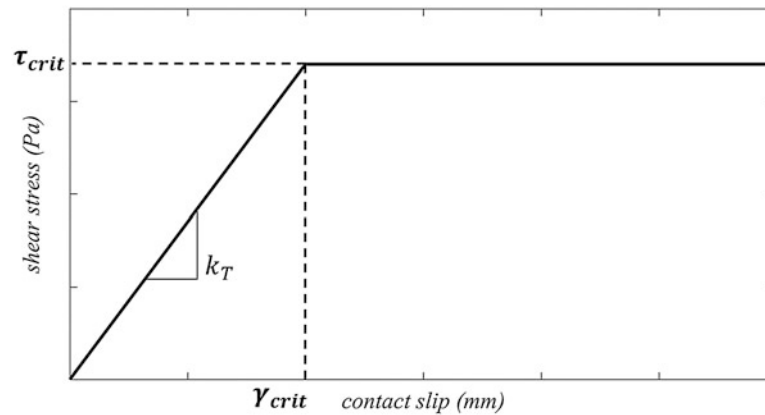


Fig. 21.8 Relationship between shear stress and contact slip (relative displacement between contacting nodes). When shear stress is less than the critical stress, contact nodes can undergo “elastic” slip, where shear stress is linearly proportional to slip with a slope k_T . When shear stress is about to exceed the critical stress, or equivalently the slip exceeds the critical elastic slip limit, friction appears in the opposite direction of slip

21.3.2 Quasi-Static Analysis

A quasi-static analysis in Abaqus allows simulation of a dynamic system based on fixed, incremental time-steps that are akin to taking “snap-shots” of a dynamic system. To study the mechanics between contact surfaces, a quasi-static analysis was performed to simulate the BRB behavior, with a focus at the contact interface, under an arbitrary bending shape following the first mode shape. A combination of pin and roller support boundary conditions, together with a periodic tip displacement, are used to simulate two cycles of bending.

A pin support was defined at 168.1 mm away from the left tip, which constrains all translational degrees of freedom (DOF). A roller support was defined at 168.1 mm away from the right tip, which constrained DOF in y- and z- directions. In experiment, bolts were tightened using a torque wrench with scales. In Abaqus, an equivalent bolt preload was calculated and defined in each joint using the following equation:

$$F = \frac{\tau}{kD} \quad (21.3)$$

where F is the bolt preload, τ is the bolt torque, k is the torque coefficient, and D is the nominal diameter of the bolt. For example, a stainless steel 5/16" bolt with applied torque 20 Nm has an equivalent bolt preload of 12.5 kN. Displacement at tips ranged from 0.001 mm to 0.1 mm to generate a reasonably smooth log-scaled curve, with a periodic amplitude $\sin(2\pi t)$. The angular frequency was selected such that the BRB completes exactly one cycle of bending per second. This ensures that the quasi-static analysis which ignores inertial effect does not introduce frequency that would give incorrect simulation results [6].

Simulation proceeded by first defining a Static, General step in Abaqus to settle the contact. Pin-roller boundary condition and all bolt preloads were present. Bolt preload magnitude was ramped to prevent convergence issue. At the end of this step, the nodal contact pressure, CPRESS, and nodal contact gap, COPEN were written into the output database. The static step to form interface contact was followed by a quasi-static step to represent the first mode bending. A sinusoidal tip displacement was introduced and an arbitrary displacement amplitude was applied at tips (Fig. 21.9).

In the next step, an amplitude sweep was performed by simulating a series of cases with discrete amplitude increment: 0.001, 0.005, 0.01, 0.02, 0.04, 0.05, 0.08, 0.1 mm. In addition to CPRESS and COPEN, energy dissipation due to friction in the whole model, ALLFD, was requested every 0.02 s in the output so that each cycle was divided into 50 evenly spaced time intervals. Nodal contact shear force, CSHEARF, Nodal contact slip, CSLIP1 & CSLIP2, were also requested and exported to MATLAB to compute nodal energy dissipation.

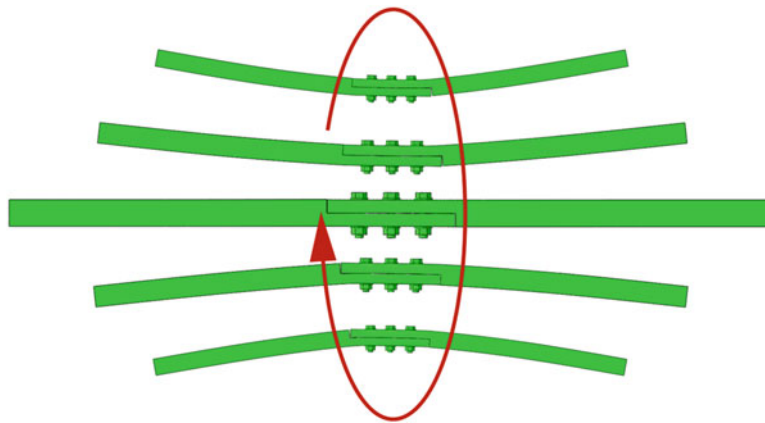


Fig. 21.9 Schematic diagram showing one cycle of first mode bending

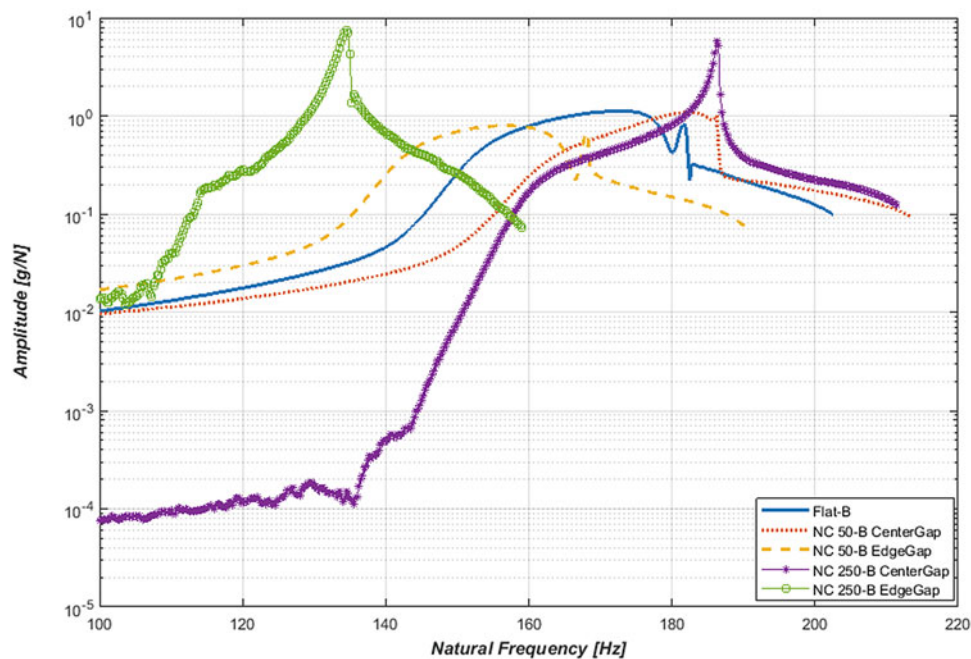


Fig. 21.10 Non-conformal cases ($50\mu\text{m}$ and $250\mu\text{m}$) with flat beam in Bending Direction at 600 N excitation and 5 N.m Bolt Torque

21.4 Results

The results section describes finding from experimental and numerical results. Experiment results show how dynamic behavior captured in the natural frequency of the beams were affected by the parameters.

21.4.1 Experimental Results

The frequency Response Function (FRF) in the bending direction for the flat interface BRB “0–0” and the two non-conformal cases are shown in Fig. 21.10. The FRF shows that the natural frequency of the non-conformal $250\mu\text{m}$ EG and $250\mu\text{m}$ CG bracket the rest of the beams at 134.5 Hz and 186.3 Hz respectively. The non-conformal $50\mu\text{m}$ EG and CG case form the next bracket at 156.0 Hz and 182.0 Hz respectively. The natural frequency for the flat interface is located in the middle at 172.5 Hz.

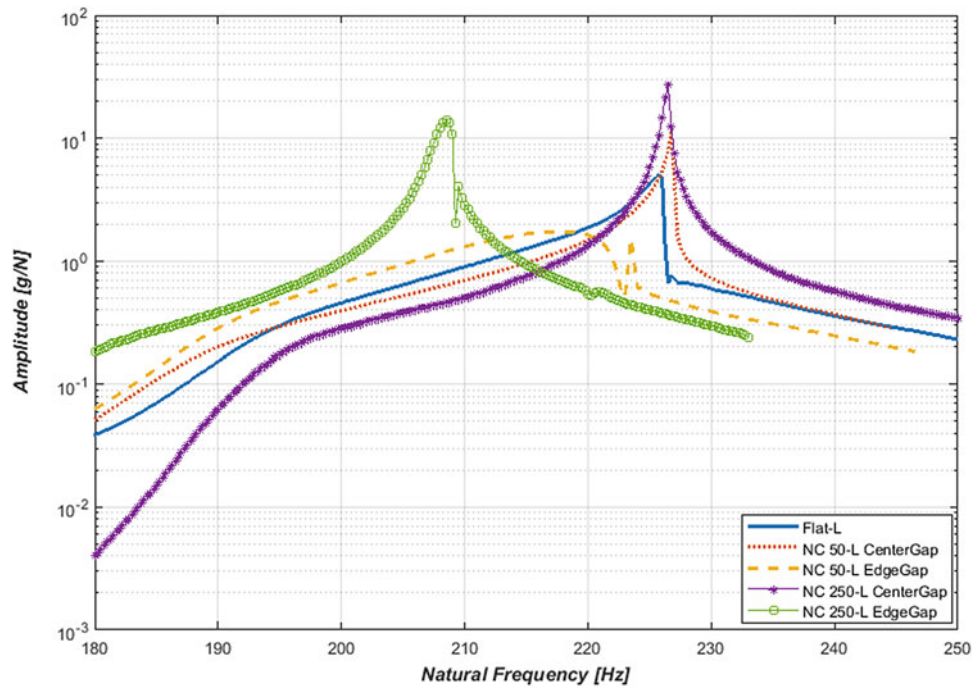


Fig. 21.11 Non-conformal cases ($50\mu\text{m}$ and $250\mu\text{m}$) with flat beam in Longitudinal Direction at 600 N excitation and 5 N.m Bolt Torque

Features of non-linear behavior that can be identified is the low amplitude and broad FRF peaks found in the flat and $50\mu\text{m}$ cases. This indicates more damping in the structure compared to the much higher amplitude and narrower FRF peaks observed in the $250\mu\text{m}$ cases. However each of the curves except for perhaps the $250\mu\text{m}$ CG show a change in natural frequency during transient ring-down data collection. This is observed as a jump towards the right of the curves. We also observe an asymmetric skew of the FRF for all the beams.

The FRF for the same set of beams in the longitudinal direction is shown in Fig. 21.11. The same trend is observed with the $250\mu\text{m}$ cases bracketing the other beams. The beams tend to be much stiffer in the longitudinal direction than in the bending direction. The non-conformal $250\mu\text{m}$ EG and $250\mu\text{m}$ CG in the longitudinal direction are 226.5 Hz and 208.5 Hz respectively.

The effect of Bolt Torque and Excitation Level on the natural frequency for non-flat beams is shown in Fig. 21.12(a) and 21.12(b) respectively. In all cases, a lower torque level and high excitation force provides a softening in the non-linear behavior of the BRB. The $50\mu\text{m}$ CG has the highest frequency while the $50\mu\text{m}$ EG beam has the lowest frequency. The $50\mu\text{m}$ conformal beam has a higher frequency than the $5000\mu\text{m}$ conformal beam.

21.4.2 Numerical Results and Validation

Comparisons between the numerical and experimental results can be made from comparing the damping behavior. The quasi-static analysis is able to show the trend in modal damping of the different beam configurations.

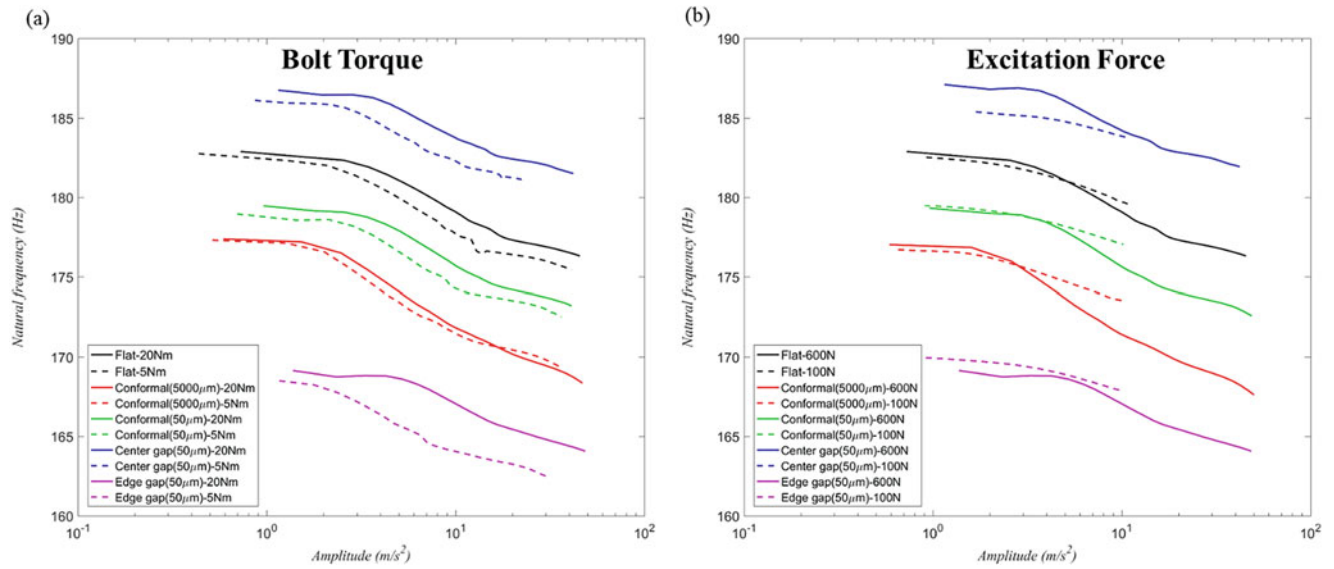


Fig. 21.12 Experimental curves of natural frequency vs. amplitude for five different interface curvatures. (a) Effect of Bolt preload/torque at two levels of bolt preload, 20 Nm and 5 Nm. (b) Effect of excitation force tested at two levels, 100 N and 600 N

With each numerical setup, Abaqus outputs accumulated energy dissipation due to friction. The energy dissipation can be related to measured damping ratio using the following equation as derived in M. Allen, et al [7]:

$$\xi = \frac{D}{2\pi mV^2} \quad (21.4)$$

where D represents frictional dissipation per cycle, m is the effective mass of the mode, and V is the mean velocity of all nodes at the interface.

The effects of bolt torque or preload on damping ratio for the flat BRB is shown in Fig. 21.13. Damping from the experimental data shows good agreement with the damping ratio obtained from the numerical energy dissipation model. The higher bolt preload of 20 N.m has the lowest damping values at a given amplitude in both cases.

The impact of curvature height on damping is observed in Fig. 21.14, where damping ratios for different interface curvatures are shown. The experimental and numerical results for the conformal 5000 μm configuration has the largest damping ratio at a given amplitude. The damping for the remaining beam tend to be much closer together with the 50 μm CG configuration having the lowest damping.

Given that the system is sensitive to parameter variations, numerical efforts were planned to be qualitative instead of quantitative. The limitation of the commercial software package meant that inertial effects and material damping were not included, and a less than ideal frictional model was used. Given all the assumptions and limitations, the numerical model tends to be less damped than the actual system observed experimentally.

21.5 Conclusions

The objective of this study was to gain a better understanding of the nonlinear behavior of a joint with curved interfaces. The results from both experimental and numerical computations show good agreement. The influence Bolt Torque, Excitation Force and Beam Orientation have on different interface geometries has been documented and presented in this study.

It is evident that at lower bolt preloads, the interfaces are loosely coupled resulting in higher dissipation of energy and a softening of the assembly. This observation has been captured by both numerical and experimental results. It is also clear from experimental results that higher excitation force results in a decrease in natural frequency, a softening in the BRB. Comparisons of beams with different interfaces show that the conformal beams have more energy dissipation than the flat beam configuration and thus have a higher damping ratio.

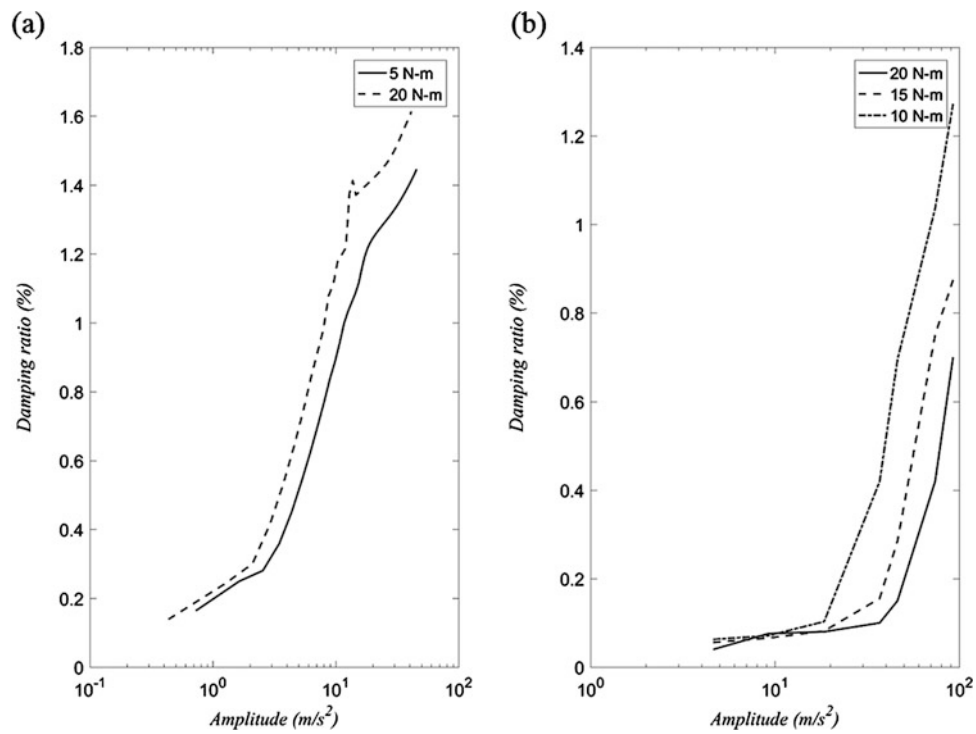


Fig. 21.13 Curves of Damping ratio vs. amplitude at different levels of bolt preload measured (a) from experiments and (b) from numerical simulations showing the effect of bolt preload

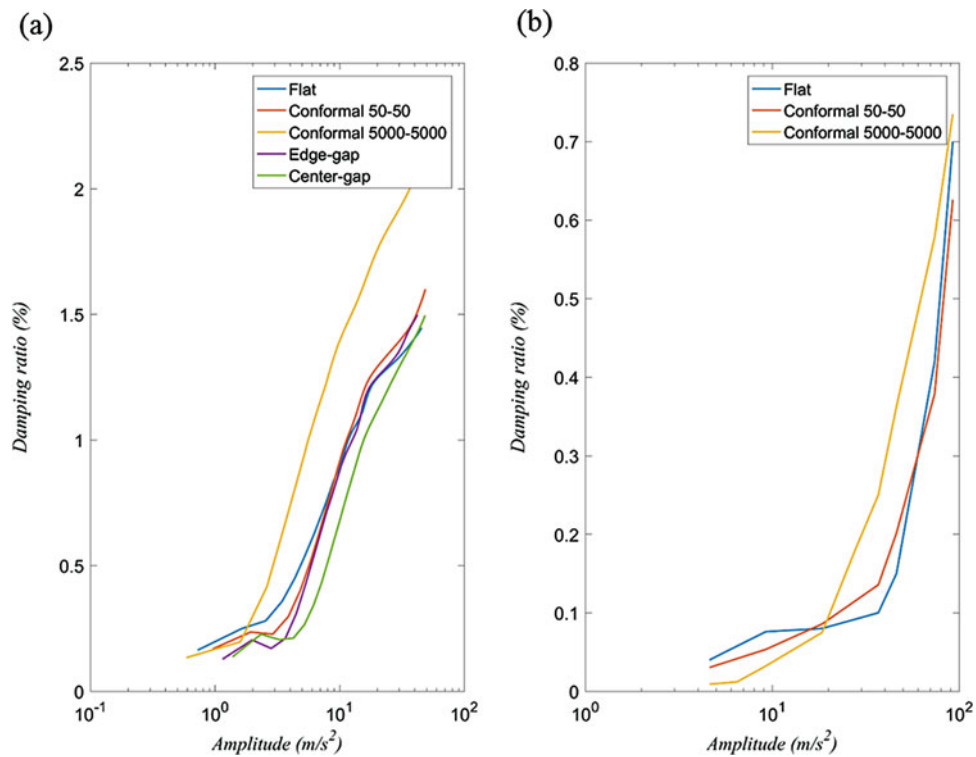


Fig. 21.14 Curves of Damping ratio vs. amplitude for different interface curvature heights measured (a) from experiments and (b) from numerical simulations showing the effect of curved interface

It is well documented that energy dissipation at the lap joint comes from micro-slip events generated towards the edge of the joint, away from the bolts [1, 2]. There also appears to be an impact (or “clapping”) occurring at the interface which would account for the extreme softening in the EG configurations. In contrast, the CG configurations tend to be much stiffer because of the higher pressure exerted at the edges of the lap joint, reducing micro-slip and creating a stiffer joint assembly.

By comparing responses of different beam orientations, it is observed that, irrespective of the interface geometry, the nonlinearity in the response is observed more clearly in the bending direction than in the longitudinal direction. It can be inferred that beams are stiffer in the longitudinal direction, and subsequently micro-slip at the interface in the longitudinal direction is less than in the bending direction.

Although the numerical model was not tuned to match the experimental observations identically and assumptions were made to simplify the model, reducing computational cost, the trends observed in the damping ratio from experimental results are still in good agreement with the trends observed from numerical computations.

Acknowledgement This work was developed during the 6-week 2017 ND-CSI (Nonlinear Dynamics of Coupled Structures and Interfaces) summer research program hosted at the William Marsh Rice University, Mechanical Engineering Department.

References

1. Brake, M.R.W. (ed.): *The Mechanics of Jointed Structure: Recent Research and Open Challenges for Developing Predictive Models for Structural Dynamics*. Sandia National Laboratories, William Marsh Rice University. Springer, Cham (2018)
2. Schwingshackl, C.W.: Identification reassembly uncertainties for a basic lap joint. In: *Dynamics of Coupled Structures*, vol. 4, pp. 53–61. Springer, Cham (2017)
3. Dossogne, T., Jerome, T.W., Lancereau, D.P.T., Smith, S.A., Brake, M.R.W., Pacini, B.R., Reuss, P., Schwingshackl, C.W.: Experimental assessment of the influence of interface geometries on structural dynamic response. In: *Dynamics of Coupled Structures*, vol. 4, pp. 255–261. Springer, Cham (2017)
4. Bonney, M.S., Robertson, B.A., Schempp, F., Mignolet, M., Brake, M.R.: Experimental determination of frictional interface models, in IMAC XXXIV A Conference and Exposition on Structural Dynamics, (Orlando, FL), February 2016
5. Sracic, M.W., Allen, M.S., Sumali, H.: Identifying the Modal Properties of Nonlinear Structures Using Measured Free Response Time Histories from a Scanning Laser Doppler Vibrometer, pp. 269–286. Springer, New York (2012)
6. Schwingshackl, C.W., Di Maio, D.D., Sever, I.I., Green, J.S.: Modeling and validation of the nonlinear dynamic behavior of bolted flange joints. *ASME. J. Eng. Gas Turbines Power.* **135**(12), 122504–122504-8 (2013). <https://doi.org/10.1115/1.4025076>
7. Roettgen, D.R., Allen, M.S.: Nonlinear characterization of a bolted, industrial structure using a modal framework. *Mech. Syst. Signal Process.* **84**, 152–170 (2017)

Chapter 22

Investigating Modal Contributions Using a Galerkin Model



A. J. Elliott, A. Cammarano, and S. A. Neild

Abstract The ability to accurately model the behaviour of a mechanical structure using a fraction of the original number of degrees of freedom is pursued throughout the study of dynamics and, in recent years, this has been key in the study of nonlinear systems. One of the first ways in which this was implemented was through the Galerkin method, and it has been continually used since its original derivation due to the fact that it does not require the use of any commercial finite element packages. In fact, the modeshapes of the system have been previously calculated analytically and the linear natural frequencies calculated numerically, leading to large reductions in the amount of time needed to develop the model.

This paper considers the modal reduction of a Galerkin clamped-clamped beam model, first deriving the equations of motion and introducing analytical terms for orthogonality, then comparing the behaviour it predicts with that from commercial finite element software for a range of forcing frequencies and amplitudes. Finally, the model can be used to derive the backbone curves of the system.

Keywords Nonlinear dynamics · Galerkin method · Reduced-order model · Finite element · Backbone curves

22.1 Introduction

The demand for lightweight, flexible materials for mechanical structures is becoming increasingly ubiquitous across the field of engineering. While the benefits of these are undoubtedly abundant, the introduction of such materials brings with it a shift away from the traditional linear dynamical techniques and necessitates the consideration of nonlinear dynamics. These are inherently more complicated, as the nonlinear terms that are introduced to the equations of motion ordinarily mean that approximation methods must be used to determine the behaviour of the system, a process which can often be prohibitively time-consuming. Further, for continuous systems, it is first necessary to discretise the system and generate a finite element model (FEM), the construction of which can have substantial ramifications for the overall accuracy of the model. Given these issues, it is desirable to develop methods which are able to obtain the same or similar accuracy of results, but with a much smaller computation cost.

Reduced-order models (ROMs) have long been offered as a solution to this problem; an in-depth review of recent developments in this area can be found in [1]. In this paper, a more classical approach is taken by considering a Galerkin model of a clamped-clamped beam [2, 3]. This method seeks to calculate the dynamical behaviour of a discretised continuous system by representing it in terms of a subset of its linear modeshapes. This is done by making the assumption that, at any time t , the displacement of the beam can be described by a weighted, linear sum of these modeshapes. It is, therefore, at the users discretion as to the size of this subset and, hence, the accuracy of the model.

Galerkin models have been used for a wide variety of applications (for example, see [4–6]) and offer an easily-implementable ROM which does not require the use of commercial FEM software. As such, it is useful to have an understanding of the level of model reduction which can be applied whilst still guaranteeing that a high level of accuracy is maintained. To investigate this, a Galerkin model for the aforementioned beam will be created, with an emphasis being put on the newly-derived analytical orthogonality terms. Then, a variational study into the number of modes retained in the model

A. J. Elliott (✉) · A. Cammarano
School of Engineering, University of Glasgow, Glasgow, UK
e-mail: A.Elliott.1@research.gla.ac.uk

S. A. Neild
Department of Mechanical Engineering, University of Bristol, Bristol, UK

will be conducted, investigating the behaviour both close to and away from the linear natural frequencies of the system. Finally, the backbone curves for this system will be derived using the Galerkin model. An explanation of the significance of these curves is given in [7].

22.2 Galerkin Model Development

The system under consideration is shown in Fig. 22.1, where x and z define the physical coordinate system, s is the position along the beam, w is the transverse displacement of the beam, and ℓ is the beam length. The beam has cross-sectional area \hat{A} , Young's modulus E , and density ρ .

As the transverse displacement of the beam, w , is increased the length of the beam also increases to length L . Further, in doing so, a tension force is generated and its calculation is an important step in deriving the Galerkin model.

For a small length of beam,

$$\Delta s \approx \sqrt{\Delta x^2 + \Delta w^2} \rightsquigarrow \frac{\partial s}{\partial x} = \sqrt{1 + \left(\frac{\partial w}{\partial x}\right)^2}. \quad (22.1)$$

Using this, the extended beam length, L , is given by

$$L = \int_0^\ell \sqrt{1 + \left(\frac{\partial w}{\partial x}\right)^2} dx. \quad (22.2)$$

By assuming that the transverse displacement is small when compared with the length of the beam, Eq. (22.2) can be approximated by

$$L \approx \int_0^\ell 1 + \frac{1}{2} \left(\frac{\partial w}{\partial x}\right)^2 dx = \ell + \frac{1}{2} \int_0^\ell \left(\frac{\partial w}{\partial x}\right)^2 dx. \quad (22.3)$$

Thus, the change in length can be written as

$$L - \ell = \frac{1}{2} \int_0^\ell \left(\frac{\partial w}{\partial x}\right)^2 dx. \quad (22.4)$$

This can now be used to calculate the tension force, as follows:

$$T = E\hat{A} \frac{(L - \ell)}{\ell} = \frac{E\hat{A}}{2\ell} \int_0^\ell \left(\frac{\partial w}{\partial x}\right)^2 dx. \quad (22.5)$$

Recalling that the equation of motion for a transverse beam deflection is written as

$$\frac{\partial^2 M}{\partial x^2} = F_z - P \frac{\partial^2 w}{\partial x^2} - \frac{\partial Q}{\partial x}, \quad (22.6)$$

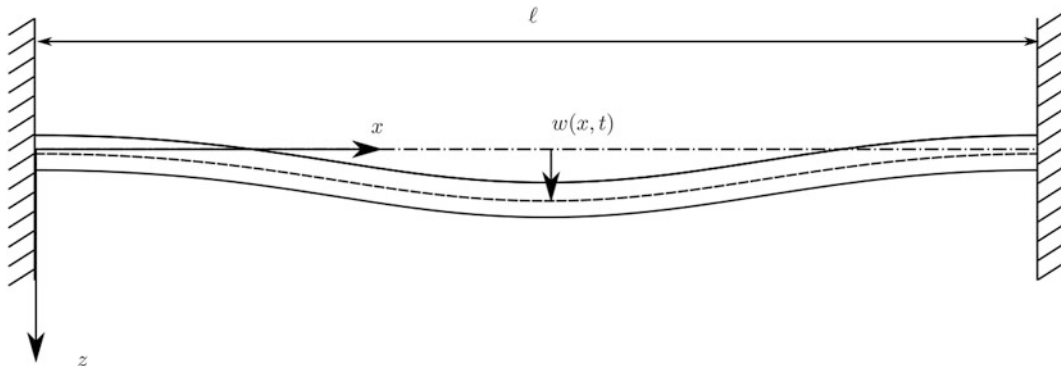


Fig. 22.1 A diagram of a clamped-clamped beam. The physical coordinates x, z are defined; it is assumed that the beam only deflects in this plane

and noting that, for small deflections, the compressive loading at the boundaries can be approximated by $P = -T$, the equation of motion for the pinned-pinned beam can be written as

$$\frac{\partial^2 M}{\partial x^2} = F_z + T \frac{\partial^2 w}{\partial x^2}. \quad (22.7)$$

Note that, here, the rotational inertia terms have been ignored by setting $Q = 0$. The term F_z represents a force per unit length including both internal loading and inertial effects in the z -axis, as well as the external loading force at the midpoint of the beam. This term is, therefore, given by

$$F_z = -\rho \hat{A} \frac{\partial s}{\partial x} \frac{\partial^2 w}{\partial t^2} + F(t) \delta \left(x - \frac{\ell}{2} \right), \quad (22.8)$$

where F is a time-dependent load and $\delta(x)$ is the Dirac delta function. Implementing Eqs. (22.5) and (22.8) in Eq. (22.7), and using the small-deflection approximation and bending moment relationship, $M = \frac{\partial^2 w}{\partial x^2}$, the equation of motion may be written as

$$EI \frac{\partial^4 w}{\partial x^4} - \frac{E\hat{A}}{2\ell} \int_0^\ell \left(\frac{\partial w}{\partial x} \right)^2 dx \left(\frac{\partial^2 w}{\partial x^2} \right) + \rho \hat{A} \frac{\partial^2 w}{\partial t^2} = F \delta \left(x - \frac{\ell}{2} \right). \quad (22.9)$$

It is now possible to apply the Galerkin decomposition, which makes the assumption that the transverse displacement can be approximated as follows:

$$w(x, t) = \sum_{j=1}^{\infty} \phi_j(x) q_j(t), \quad (22.10)$$

where ϕ_j and q_j denote the j th modeshape and modal displacement, respectively. Applying this decomposition in Eq. (22.9) results in the following equation.

$$EI \sum_{j=1}^{\infty} \frac{d^4 \phi_j}{dx^4} q_j - \frac{E\hat{A}}{2\ell} \sum_{k=1}^{\infty} \int_0^\ell \left(\frac{d\phi_k}{dx} \right)^2 dx \left(\frac{d^2 \phi_j}{dx^2} \right) q_j q_k^2 + \rho \hat{A} \phi_j \ddot{q}_j = F \delta \left(x - \frac{\ell}{2} \right). \quad (22.11)$$

Now, it is necessary to multiply Eq. (22.11) by an arbitrary modeshape, ϕ_n , and integrate across the length of the beam. Thus, the system can be written as

$$\begin{aligned} EI \sum_{j=1}^{\infty} \int_0^\ell \frac{d^4 \phi_j}{dx^4} \phi_n dx q_j - \frac{E\hat{A}}{2\ell} \sum_{j=1}^{\infty} \int_0^\ell \left[\sum_{k=1}^{\infty} \left(\int_0^\ell \left(\frac{d\phi_k}{dx} \right)^2 dx q_k^2 \right) \left(\frac{d^2 \phi_j}{dx^2} \right) q_j \phi_n \right] dx + \rho \hat{A} \int_0^\ell \phi_j \phi_n dx \ddot{q}_j \\ = F \int_0^\ell \delta \left(x - \frac{\ell}{2} \right) \phi_n dx. \end{aligned} \quad (22.12)$$

This equation can be separated into an infinite system of equations by applying the orthogonality conditions of the modes; these are as follows:

$$\begin{aligned} \int_0^\ell \phi_n \phi_j dx &= \begin{cases} \ell, & \text{if } n = j, \\ 0, & \text{otherwise,} \end{cases} \\ \int_0^\ell \phi_n \frac{d^2 \phi_j}{dx^2} dx &= \begin{cases} \alpha_{2,j}, & \text{if } n = j, \\ 0, & \text{otherwise,} \end{cases} \\ \int_0^\ell \phi_n \frac{d^4 \phi_j}{dx^4} dx &= \begin{cases} \alpha_{4,j}, & \text{if } n = j, \\ 0, & \text{otherwise,} \end{cases} \end{aligned} \quad (22.13)$$

where $\alpha_{i,j}$ are constants. Further, it can be noted that

$$\int_0^\ell \phi_n \delta \left(x - \frac{\ell}{2} \right) dx = \phi_n \left(\frac{\ell}{2} \right), \quad (22.14)$$

and it is useful to use the following notation:

$$\beta_k = \int_0^\ell \left(\frac{d\phi_k}{dx} \right)^2 dx. \quad (22.15)$$

Implementing these conditions in Eq. (22.12) and simplifying results in the j th modal equation being given by

$$\ddot{q}_j + \frac{EI\alpha_{4,j}}{\rho\hat{A}\ell} q_j + \frac{E\alpha_{2,j}}{2\rho\ell^2} \sum_{k=1}^N \beta_k q_k^2 q_j = \frac{F}{\rho\hat{A}\ell} \phi_j \left(\frac{\ell}{2} \right). \quad (22.16)$$

In the Galerkin method, the modes for the clamped-clamped case take the form [2, 3]

$$\phi_j = \cosh \left(\frac{\lambda_j x}{\ell} \right) - \cos \left(\frac{\lambda_j x}{\ell} \right) - \sigma_j \left(\sinh \left(\frac{\lambda_j x}{\ell} \right) - \sin \left(\frac{\lambda_j x}{\ell} \right) \right), \quad (22.17)$$

where λ_j and σ_j are numerically-calculated, dimensionless parameters which correspond to the boundary conditions and can be found in [2, 3], as can a full derivation of the expression in Eq. (22.17).

By utilising this expression for the modeshape, the constant coefficients in Eqs. (22.13) and (22.15) can be written as follows:

$$\begin{aligned} \alpha_{2,j} &= \frac{\lambda_j}{4\ell} (4\sigma_j(\sin^2(\lambda_j) - \lambda_j\sigma_j) + (\sigma_j^2 - 1) \sin(2\lambda_j) + (\sigma_j^2 + 1) \sinh(2\lambda_j) - 4\sigma_j \sinh^2(\lambda_j)), \\ \alpha_{4,j} &= \frac{\lambda_j^4}{\ell^3} + \frac{\lambda_j^3}{4\ell^3} ((\sigma_j^2 - 1)(4 \cos(\lambda_j) \sinh(\lambda_j) - \sin(2\lambda_j)) + (\sigma_j^2 + 1)(\sinh(2\lambda_j) - 4 \cosh(\lambda_j) \sin(\lambda_j)) \\ &\quad + \sigma_j(2 \cos(2\lambda_j) + 8 \sin(\lambda_j) \sinh(\lambda_j) - 2 \cosh(2\lambda_j)), \\ \beta_k &= \frac{\lambda_k}{4\ell} (4\lambda_k\sigma_k^2 + (\sigma_k^2 - 1)(\sin(2\lambda_k) - 4 \cosh(\lambda_k) \sin(\lambda_k)) + (\sigma_k^2 + 1)(\sinh(2\lambda_k) - 4 \cos(\lambda_k) \sinh(\lambda_k)) \\ &\quad - 4\sigma_k(\cos(\lambda_k) - \cosh(\lambda_k))^2). \end{aligned} \quad (22.18)$$

Using the constants defined in Eq. (22.18) in Eq. (22.16), it is possible to reducing the number of modes retained in the model and investigate the effects that this has on the accuracy achieved.

22.3 Model Reduction

To allow the effects of modal reduction in the beam model to be investigated, the system will be forced periodically and the time histories will be considered. As such, the forcing term in Eq. (22.16) is set as

$$F = F_0 \sin(\Omega t), \quad (22.19)$$

where F_0 and Ω denote the magnitude of the force and the forcing frequency, respectively; in varying the values of these variables over reasonable ranges, it is possible to explore the accuracy of the reduced-order models. Initially, Ω will be set at 200 rad/s, which is specifically chosen to be away from any of the linear natural frequencies, which can be investigated later in the paper; an arbitrary force of $F_0 = 500$ N will be used. Seven cases are considered, with each of these including the first n modes, where $n = 1, 2, 3, 4, 5, 10, 20$. The time histories from these cases are shown in Fig. 22.2, along with the time history from the Abaqus model.

As expected, Fig. 22.2 shows a clear convergence to the Abaqus time history as the number of modes included in the model is increased. In particular, when the number of modes included in the model is equal to the number of elements in the Abaqus model, i.e., 20, there is a strong agreement between the two time series. From initial inspection, these time histories suggest that a model including just 3 modes would give an accurate depiction of the full model. From this point forward, only the 1-, 5-, 10-, and 20-mode cases will be considered.

22.3.1 Frequency Investigation

It is now possible to investigate the behaviour at frequencies close to the linear natural frequencies of the system. This will initially be done by setting Ω equal to the natural frequency defined by the Galerkin method. The time histories for this forcing are given in Fig. 22.3.

The time histories shown in Fig. 22.3 show much less variation as the number of modes is increased when compared with Fig. 22.2. In particular, the prominence of $\omega_{n,1}$ in the response is well-captured for all of the cases considered. In spite of this, the convergence of the graphs when the number of modes is increased is still present, albeit in a less pronounced way and with very little difference between the 5-, 10-, and 20-mode cases.

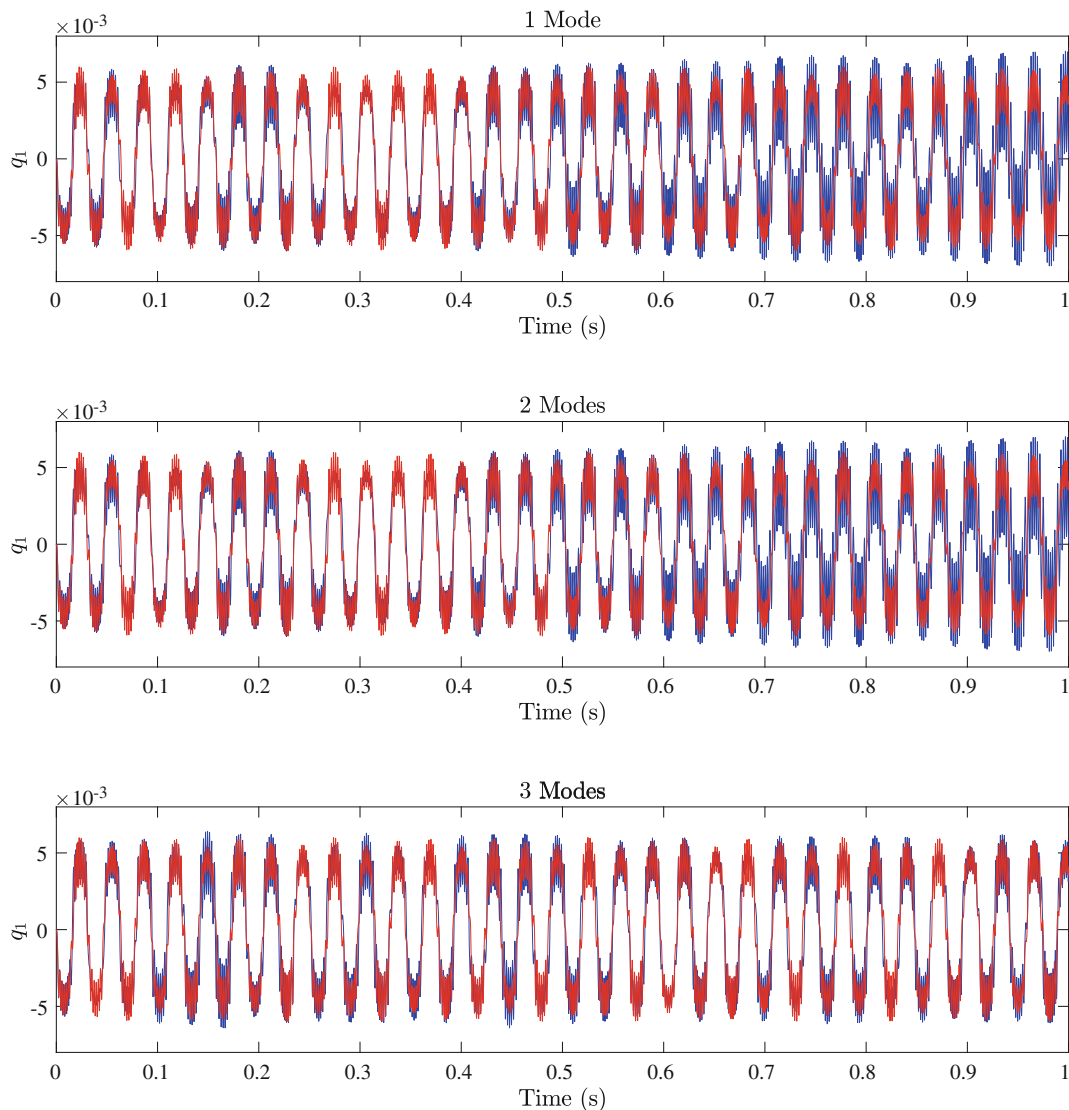


Fig. 22.2 Time histories with $\Omega = 200$ rad/s and $F_0 = 500$ N; blue: Galerkin model, red: Abaqus model

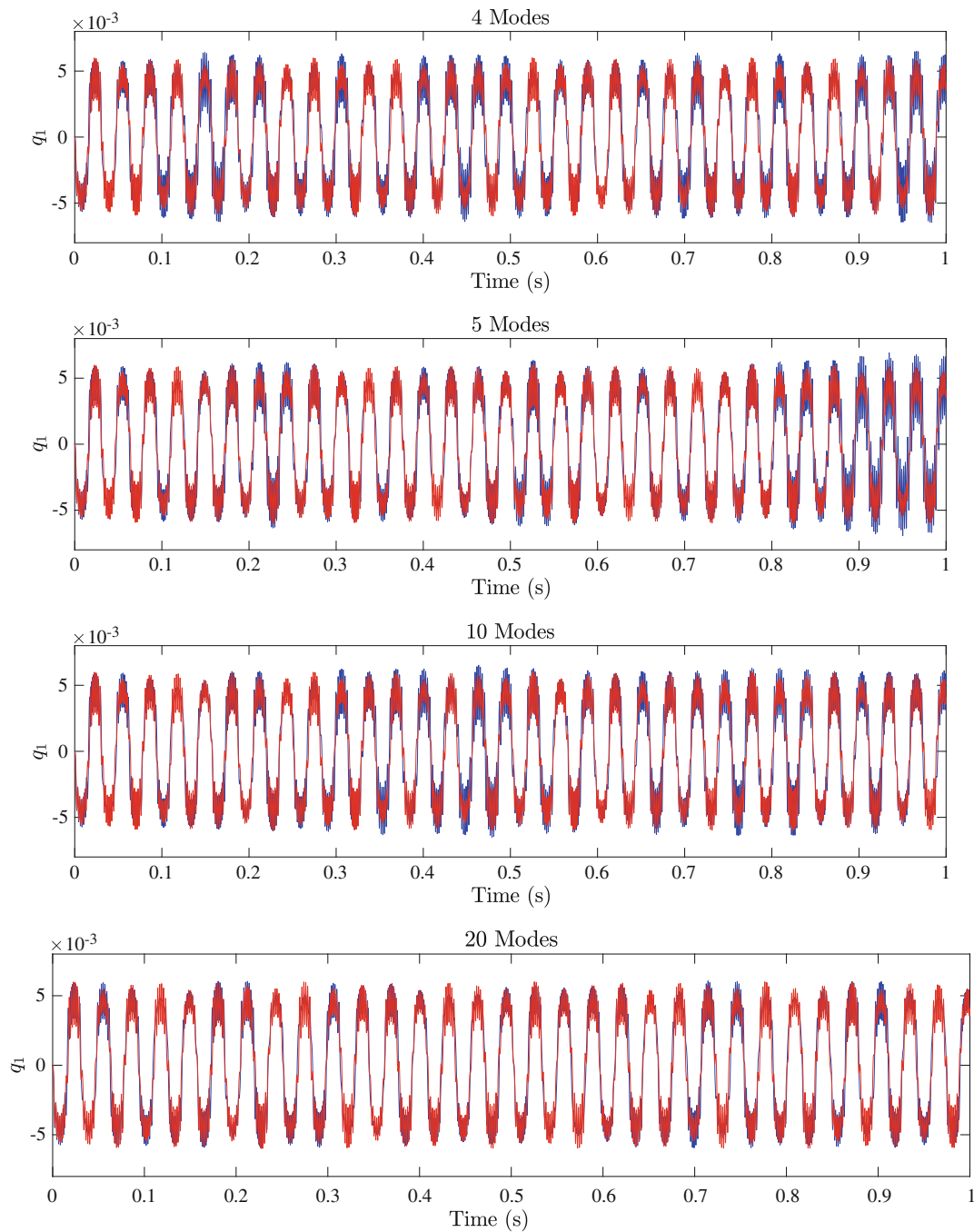


Fig. 22.2 (continued)

To investigate this behaviour, another forcing frequency will be considered, namely $\Omega = 90\% \times \omega_{n,1}$ rad/s; this case will allow the contribution of $\times \omega_{n,1}$ to be assessed when the forcing frequency approaches it. As one might expect, the behaviour shown in Fig. 22.4 is somewhere between that in Figs. 22.2 and 22.3. The convergence in amplitude is clearer than in Fig. 22.3, though certainly not to the extent shown in Fig. 22.2; this becomes more apparent when the full 1 s time history is considered, but these are not shown here for reasons of brevity. In addition, the model begins to overestimate the influence of higher-order modes. This overestimation seems to be a characteristic of the Galerkin model itself, rather than the forcing frequency.

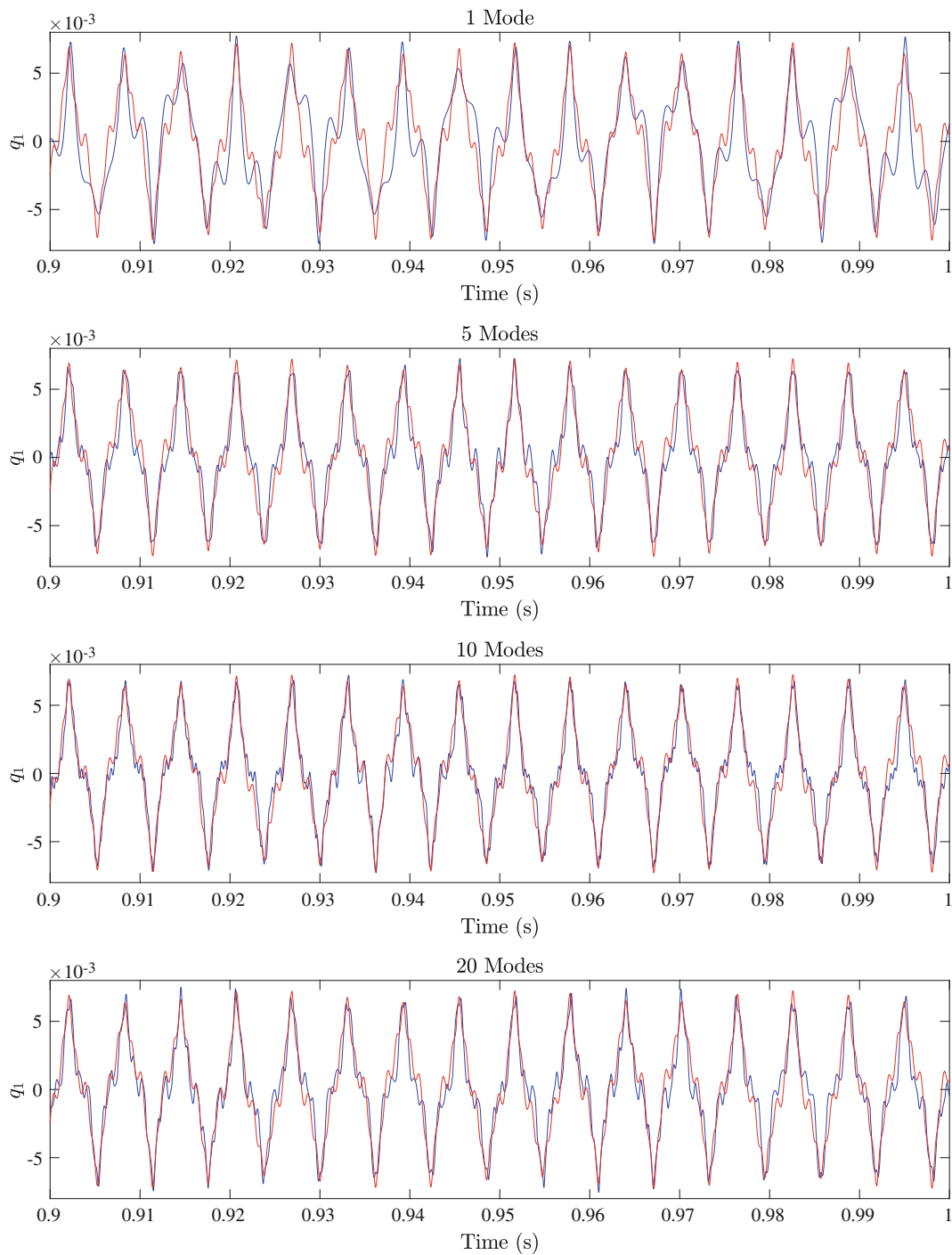


Fig. 22.3 Time histories with $\Omega = \omega_{n,1}$ rad/s and $F_0 = 500$ N; blue: Galerkin model, red: Abaqus model

Were only Fig. 22.3 or Fig. 22.4 considered for validating the Galerkin model, one might reasonably assume that any of the time histories shown give a reasonable approximation to the system. This highlights the importance of considering forcing cases away from the linear natural frequencies.

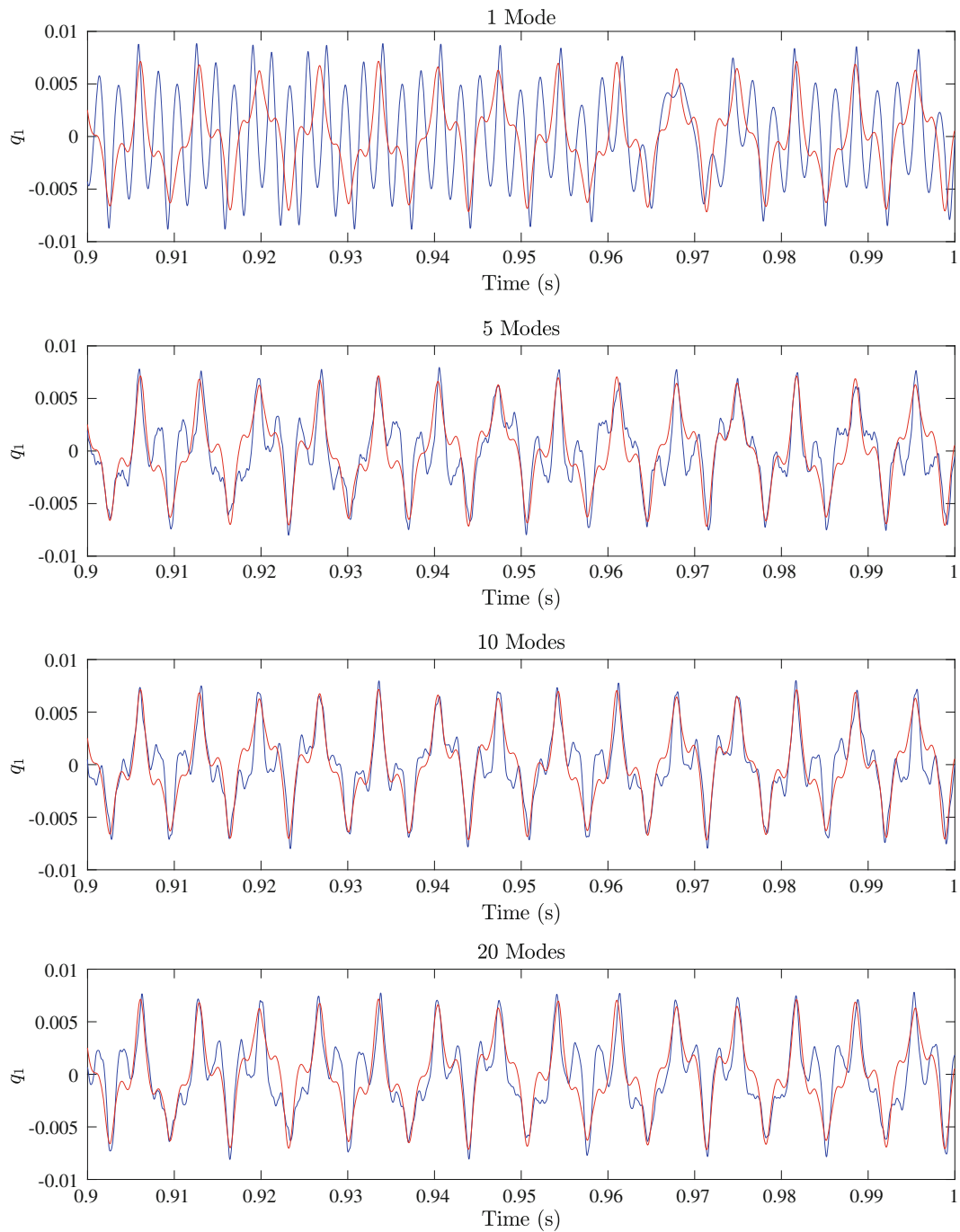


Fig. 22.4 Time histories with $\Omega = 90\% \times \omega_{n,1}$ rad/s and $F_0 = 500$ N; blue: Galerkin model, red: Abaqus model

22.3.2 Amplitude Investigation

As well as assessing the accuracy of the Galerkin model at different frequencies, it is also beneficial to consider the variation in response as the forcing amplitude is varied. In doing this, it is possible to obtain an approximate region of validity for frequency-amplitude relationships, such as backbone curves, which are derived from the model. To do this, two forcing scenarios will be investigated: one close to the linear regime, and one closer to the upper limits of elastic region. These cases will be defined by forces of $F_0 = 100$ N and $F_0 = 1000$ N, respectively; the number of modes considered will be 10 for all cases.

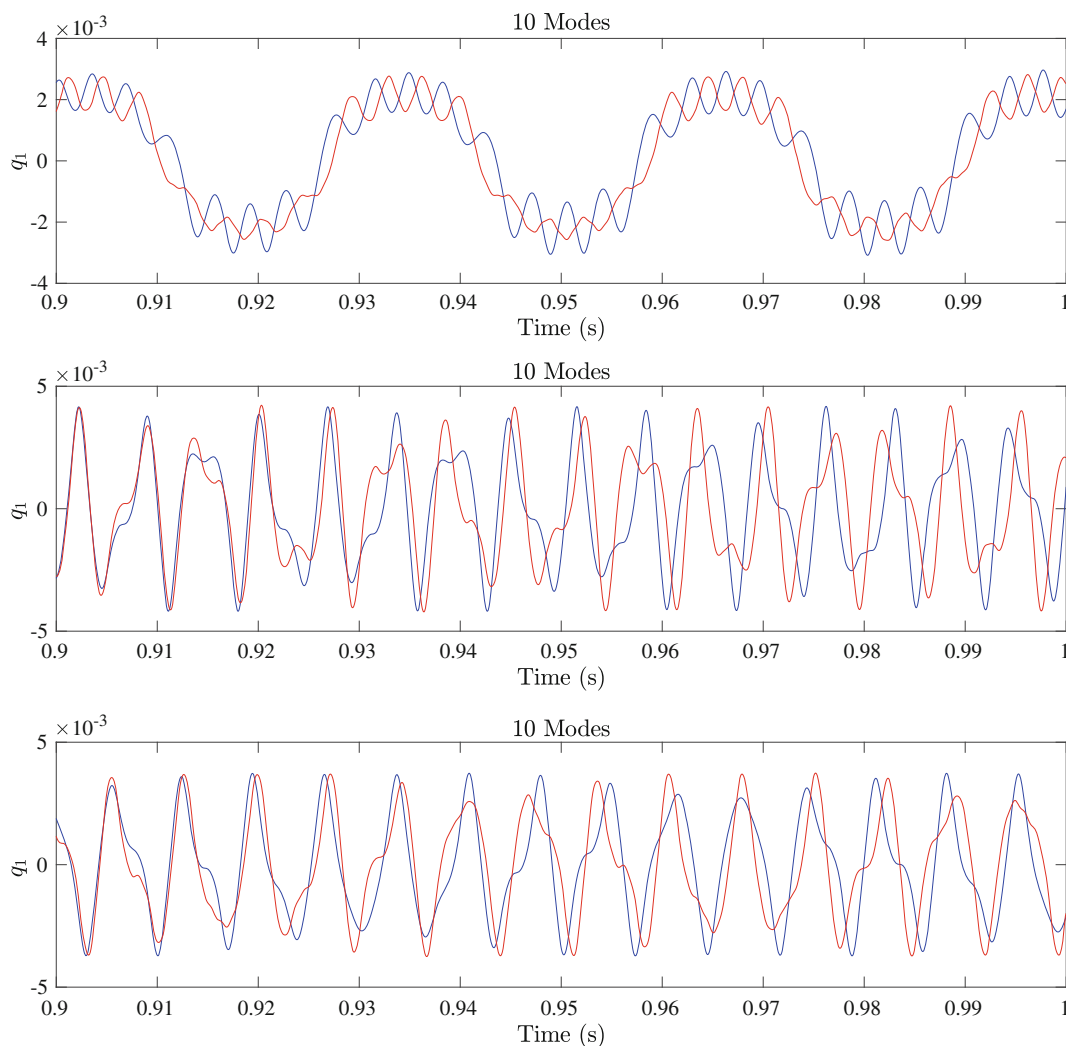


Fig. 22.5 Time histories with $F_0 = 100$ N for the cases $\Omega = 200$ rad/s, $\Omega = \omega_{n,1}$ rad/s, and $\Omega = 90\% \times \omega_{n,1}$ rad/s, respectively; blue: Galerkin model, red: Abaqus model

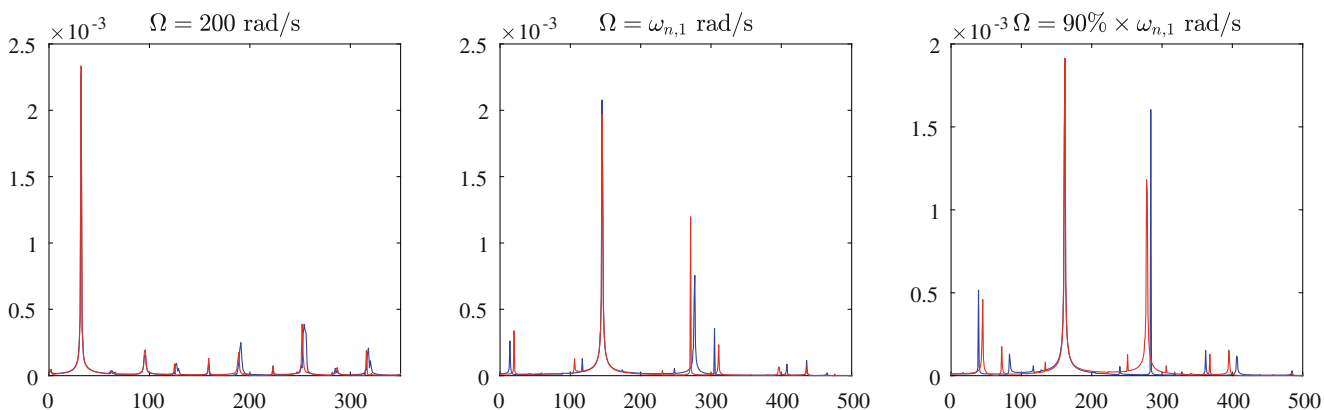


Fig. 22.6 Frequency contributions for the time histories in Fig. 22.5; blue: Galerkin model, red: Abaqus model

Figures 22.5 and 22.7 offer an interesting insight into the accuracy of the Galerkin model. In both the higher and lower forced cases, the approximation given is reasonable, although there are drawbacks for each of the forcing frequencies. In Fig. 22.5, when $\Omega = 200$, the representation of amplitude is good, but the apparent phase of the response is a clear issue.

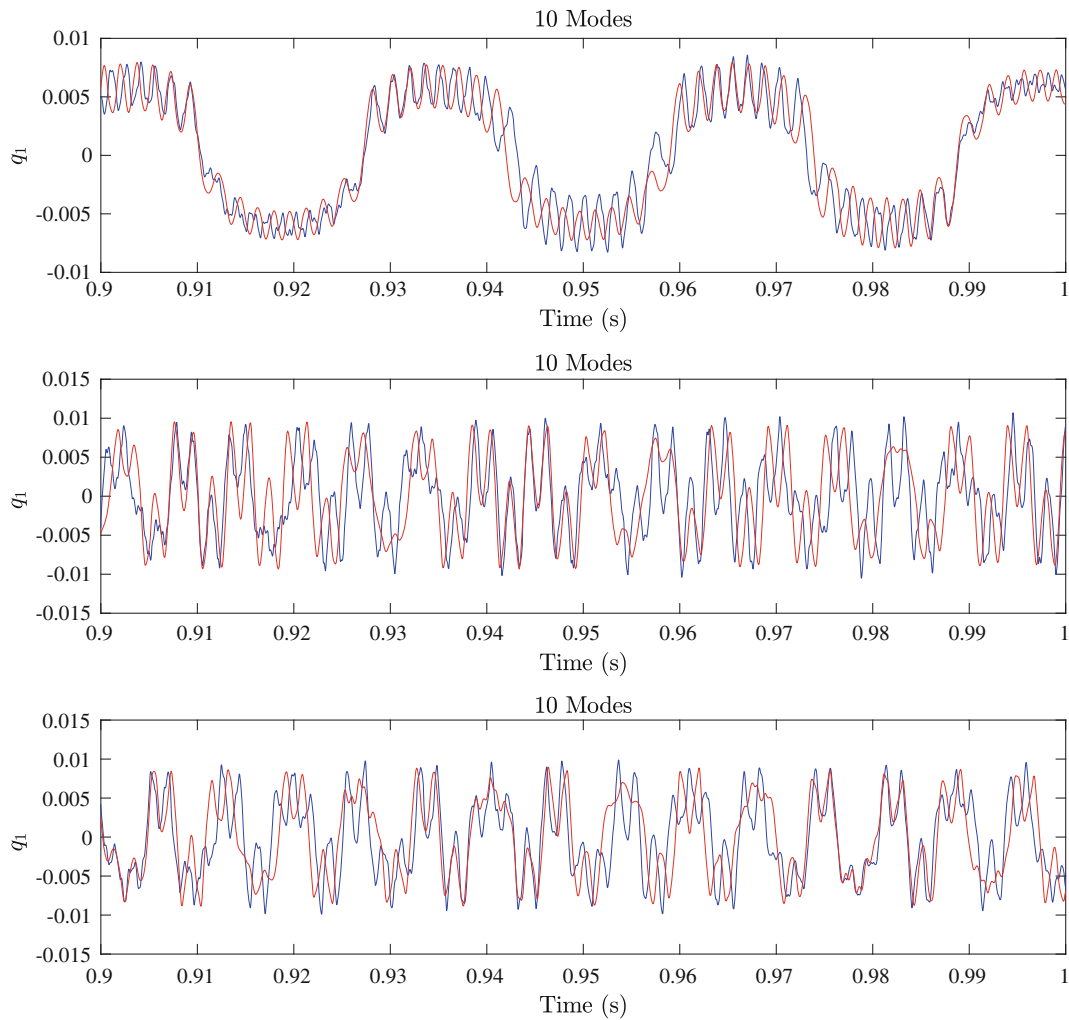


Fig. 22.7 Time histories with $F_0 = 1000$ N for the cases $\Omega = 200$ rad/s, $\Omega = \omega_{n,1}$ rad/s, and $\Omega = 90\% \times \omega_{n,1}$ rad/s, respectively; blue: Galerkin model, red: Abaqus model

From considering Fig. 22.6, it can be seen that this is, in fact, an issue of frequency calculation for the harmonic contributions. The frequency in the two cases close the linear natural frequency appears more accurately captured, though there are again differences in the contribution of higher modes, especially when $\Omega = 90\% \times \omega_{n,1}$ rad/s. Interestingly, in Fig. 22.7, the Galerkin model arguably appears to be most accurate when the forcing frequency is away from the linear natural frequencies. This information is particularly pertinent for the case of finding backbone curves, which act entirely at the natural frequencies of the system. The reason for this is once again explained by the presence of higher-order modal contributions, which are exacerbated at higher forces, as can be seen when comparing the frequency contributions in Fig. 22.8.

22.3.3 Backbone Curve

As the backbone curves can offer a great deal of information about a mechanical structure [7], it is sensible to investigate these for Galerkin models. The curves have been generated for this system using the Auto 07p continuation software [8], doing so for the mode cases considered in Fig. 22.2. Interestingly, the difference between the curves was negligible for all cases, suggesting that, to calculate the i th backbone curve (that is, the backbone curve that originates at $\omega_{n,i}$), only the i th Galerkin equation is necessary. Backbone curves in which only one mode is present have been previously seen instance, for instance in [4]. An investigation into this behaviour for further models is beyond the scope of this study, but will be pursued in future work.

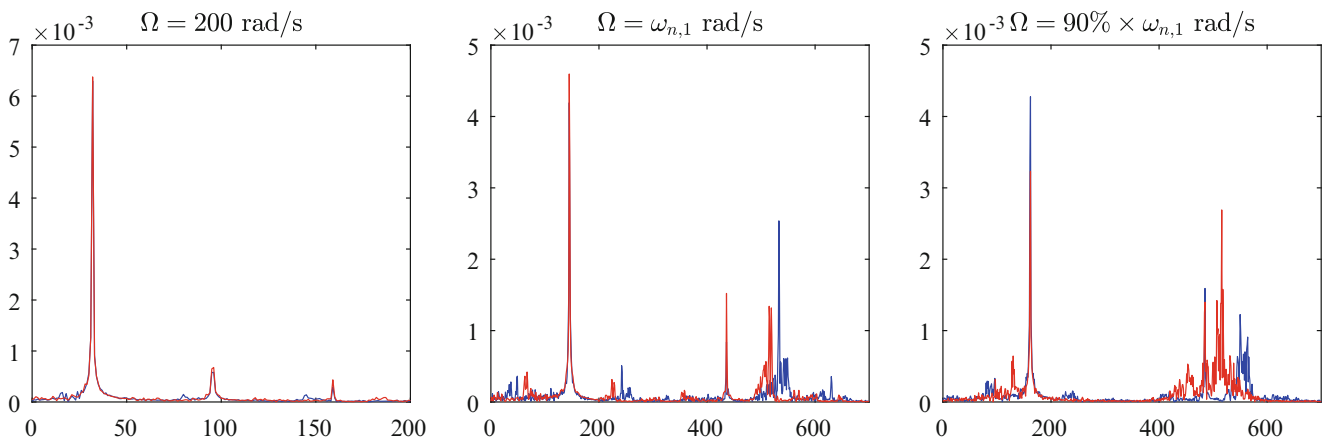


Fig. 22.8 Frequency contributions for the time histories in Fig. 22.7; blue: Galerkin model, red: Abaqus model

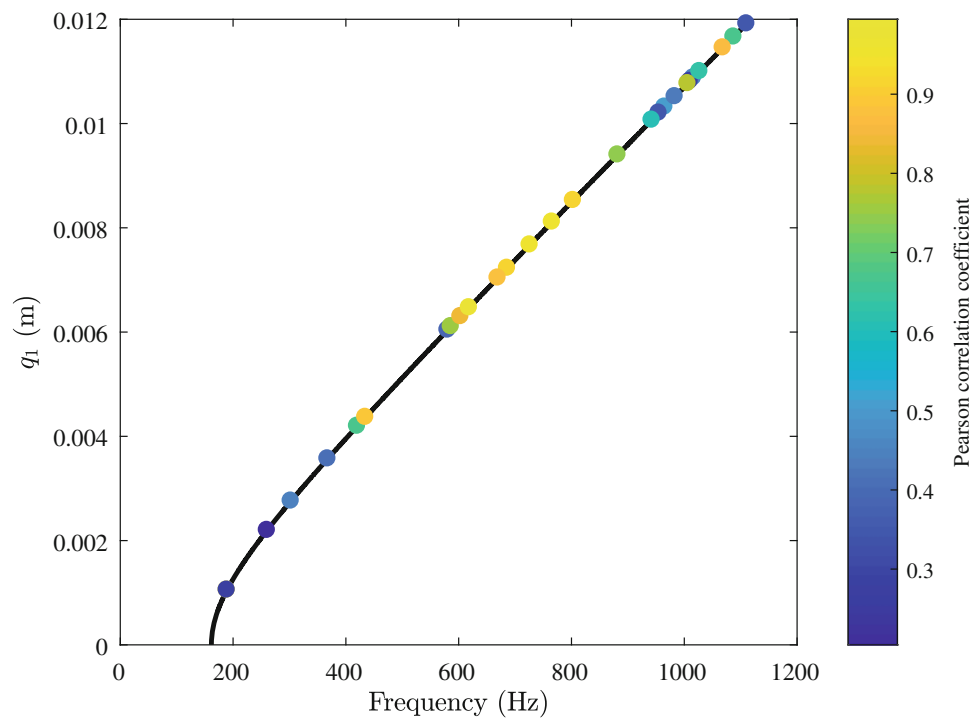


Fig. 22.9 First backbone curve for the clamped-clamped beam. The coloured circles denote the Pearson correlation coefficient between the Abaqus and Galerkin time histories at this amplitude

The first backbone curve for this system is shown in Fig. 22.9. As this paper has investigated the accuracy of the time histories across a range of amplitudes and frequencies, it is possible to display this information along the backbone curve. To assess this accuracy, the Pearson correlation coefficient has been used for the Abaqus and Galerkin time histories, calculated using the `corr` function in Matlab. While this measure is by no means a perfect representation, it does give some further insight into the Galerkin model. In Fig. 22.9, the first 5 modes have been included in the model and the forcing frequency has been maintained at $\Omega = \omega_{n,1}$.

Interestingly, at first inspection, the lower amplitude responses appear to be less accurate than those at higher amplitudes. In reality, this is caused by the fact that, for lower-amplitude responses, minor differences between calculated linear frequencies can lead to the apparent issues with phase which were shown in Figs. 22.5 and 22.7. Taking this into account, the accuracy of the Galerkin case forced at $\Omega = \omega_{n,1}$ decreases as the backbone curve deviates from this value, as would be expected.

22.4 Conclusion

In this paper, a Galerkin model for a clamped-clamped beam has been developed and an investigation into the accuracy ROMs based on this decomposition has been undertaken. In the mathematical development of the model, analytical terms for the orthogonality terms, which are necessary to develop accurate time histories, have been developed.

Following this, consideration has been given to the accuracy of these time histories when compared with those obtained using commercial FEM software. An initial examination of time histories at a forcing frequency away from the natural frequencies of the underlying system showed a quick convergence to the Abaqus results, with reasonable time series being produced using as few as three modes. Even better convergence was seen when the linear natural frequency was used as the forcing frequency, with the one-mode case producing relatively accurate results when one mode dominates the response. However, even minor deviations from this resulted in significantly less accurate results. It was further found that, at lower amplitudes, minor differences in the calculation of the linear natural frequencies were exaggerated in the system responses, to the extent that the system appeared to move in and out of phase. Despite this, the behaviour was well-captured in terms of amplitude.

Finally, it was possible to numerically continue the backbone curves of the system. An interesting result was that the backbone curves did not vary with the number of modes included in the Galerkin model; this suggests that, for the beam considered in this case, only one mode is necessary to calculate the curve. This phenomenon will be investigated for other systems in future studies.

References

1. Mignolet, M.P., Przekop, A., Rizzi, S.A., Spottswood, S.M.: A review of indirect/non-intrusive reduced order modeling of nonlinear geometric structures. *J. Sound Vib.* **332**, 2437–2460 (2013)
2. Timoshenko, S.P., Young, D.H., Weaver, W.: *Vibration Problems in Engineering*. Wiley, New York (1974)
3. Blevins, R.D.: *Formulas for Natural Frequency and Mode Shape*. Van Nostrand Reinhold Company, New York (1979)
4. Wagg, D., Neild, S.: *Nonlinear Vibration with Control: For Flexible and Adaptive Structures*, 2nd edn. Springer, Cham (2015)
5. Rao, J.S., Carnegie, W.: Solution of the equations of motion of coupled-bending bending torsion vibrations of turbine blades by the method of ritz-galerkin. *Int. J. Mech. Sci.* **12**(10), 875–882 (1970)
6. Bhashyam, G.R., Prathap, G.: Galerkin finite element method for non-linear beam vibrations. *J. Sound Vib.* **72**, 191–203 (1980)
7. Hill, T.L., Cammarano, A., Neild, S.A., Barton, D.A.W.: Identifying the significance of nonlinear normal modes. *Int. J. Mech. Sci.* **473**(2199), 20160789 (2017)
8. Doedel, E.J., Champneys, A.R., Fairgrieve, T.F., Kuznetsov, Y.A., Dercole, F., Oldeman, B.E., Paffenroth, R.C., Sandstede, B., Wang, X.J., Zhang, C.: *Auto-07p: Continuation and Bifurcation Software for Ordinary Differential Equations*. Concordia University, Montreal (2008). <http://cmvl.cs.concordia.ca>



Chapter 23

Acoustic Excitation of a Flanged Joint

Trevor W. Jerome, Micah R. Shepherd, and Stephen A. Hambric

Abstract Bolts, screws, rivets, and pins can significantly complicate the prediction of damping, stiffness, and resonance frequencies of built-up systems. Because the interaction of interfacial joints is not well understood, current predictive models incorporating fastened joints often require over-designing for safety. To better understand the behavior of fastened joints, several experiments have been performed on a built-up structure with two rectangular 1/4" plates fastened together by two screws on a 1/2" thick flange. The structure was excited via acoustic excitation, and acceleration was measured at multiple locations on the flange and plate during and after ensonifying. While the energy input to the system may be lower for acoustic excitations than other direct contact methods, the results in this paper show that ensonifying the structure has two important advantages over traditional impact hammer and shaker methods. First, resonances of the structure can be excited and analyzed individually in both steady state and free-decay conditions, which is an advantage over impact excitation. Second, the excitation method is non-intrusive and does not change the system properties, which is an advantage over shaker excitation. The proposed method is shown to be an effective way to excite structures for both steady-state and decay measurements.

Keywords Joint dynamics · Flange · Acoustic excitation · Damping · Fasteners

23.1 Introduction

The nonlinear vibration behavior of bolted joints introduces difficulty in system design. Current models to predict damping from bolted joints are either inaccurate or computationally inefficient [1, 2]. Well-documented heuristic investigation of systems with bolted or screwed joints has been sparse, but careful consideration of these types of energy loss in the context of experimental analysis may lead to better understanding of fastened joint dynamics. The presented work highlights methods used in measuring this nonlinear behavior, including the efforts made to minimize corrupting influences from boundary conditions and drive systems. In a previous study, the authors investigated the amplitude-dependent nature of the ring-down damping in a system via impact modal testing [3]. Using acoustical excitation of a test system, both steady-state hysteresis and ringdown decay can be measured.

In this paper, an experiment to characterize the dynamics of a flanged joint will be described. The testbed includes two aluminum plates which are fastened together at a flange. The bending and torsional modes of the system are first described in terms of their behavior at the interface. Next, commonly-used excitation methods for modal analysis will be compared and contrasted, with an emphasis on acoustic excitation. Finally, the benefits of using acoustic excitation for both decay and steady-state measurements are presented for examining the dynamics of both bending and torsion modes.

T. W. Jerome (✉) · M. R. Shepherd · S. A. Hambric

Graduate Program in Acoustics/Applied Research Laboratory, The Pennsylvania State University, State College, PA, USA
e-mail: mrs30@psu.edu; sah19@arl.psu.edu

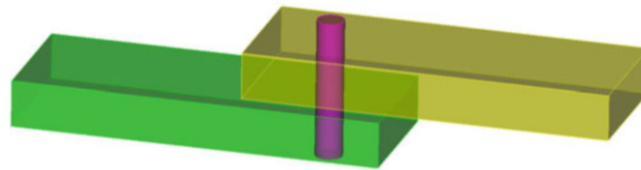


Fig. 23.1 Simple lap joint

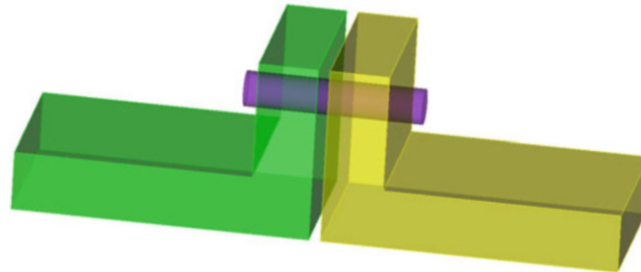


Fig. 23.2 Simple flange joint

23.2 Fastened Joints Discussion

23.2.1 *Lap Joints and Flange Joints*

Two popular configurations for bolted connections are lap joints and flange joints, shown in Figs. 23.1 and 23.2. In many geometries, lap joints are designed such that fasteners are inserted normal to the surfaces being connected. In simple geometries, the surfaces in contact (faying surfaces) are parallel to the structure surfaces. This configuration is beneficial because it simply requires that the specimen main body be pierced with screws or rivets, or drilled beforehand. The structure is preloaded normal to its main surfaces, and primarily sees high tangential or shear load at the faying surface. Design precautions must be taken to prevent shear structural tear-out of softer materials, and bolt shear stress in relatively stronger materials. This type of connection has been and continues to be an active research area.

Flange joints require extra material attached normal to the surfaces being connected. Fasteners are inserted parallel to the connecting surface, and the faying surfaces are perpendicular to the structure surfaces in the cases of simple geometries. This joint type is preloaded parallel to its main surfaces. It primarily sees high normal load, exerting longitudinal forces on the fastener and at the contact surface. The limits of this design require consideration of flange strength in softer materials, and longitudinal (tensile) strength of the fastener. Flange joints have been studied less than lap joints, but are still important to understand since they are used in many high-value applications. Additionally, there seems to be significant phenomenological overlap in the nature of both flanged and lap joints. While a flange joint is investigated in this work, it is anticipated that the principles learned will be at least partially applicable to lap joints.

23.2.2 *Mode Types and Damping*

Both lap joints and flange joints undergo different categories of modal response at the faying surfaces. One mode type (A) primarily involves forces that are parallel to the fastener, causing forces in the direction of normal separation and compression of the joint. Lap joints exhibit this type of excitation when the structure experiences flexure normal to the fasteners. In flange joints, this type manifests itself as modes that pry the structure at the flange. The other main type (B) primarily involves forces that are tangential to the faying surfaces, which cause relative shear. Forces of type (B) can be subdivided into those that are uniform for an entire surface, or torquing surfaces that rotate one of the sub-structures relative to the other about the axis of the fastener centerline.

Experimental hardware used in this study, described in detail later, responds to impact hammer excitation near a corner with the frequency response function shown in Fig. 23.3. This transfer function was obtained under high-torque conditions, and averaging the response of eight accelerometers for a total of seventy-five hammer excitations at a corner of the structure

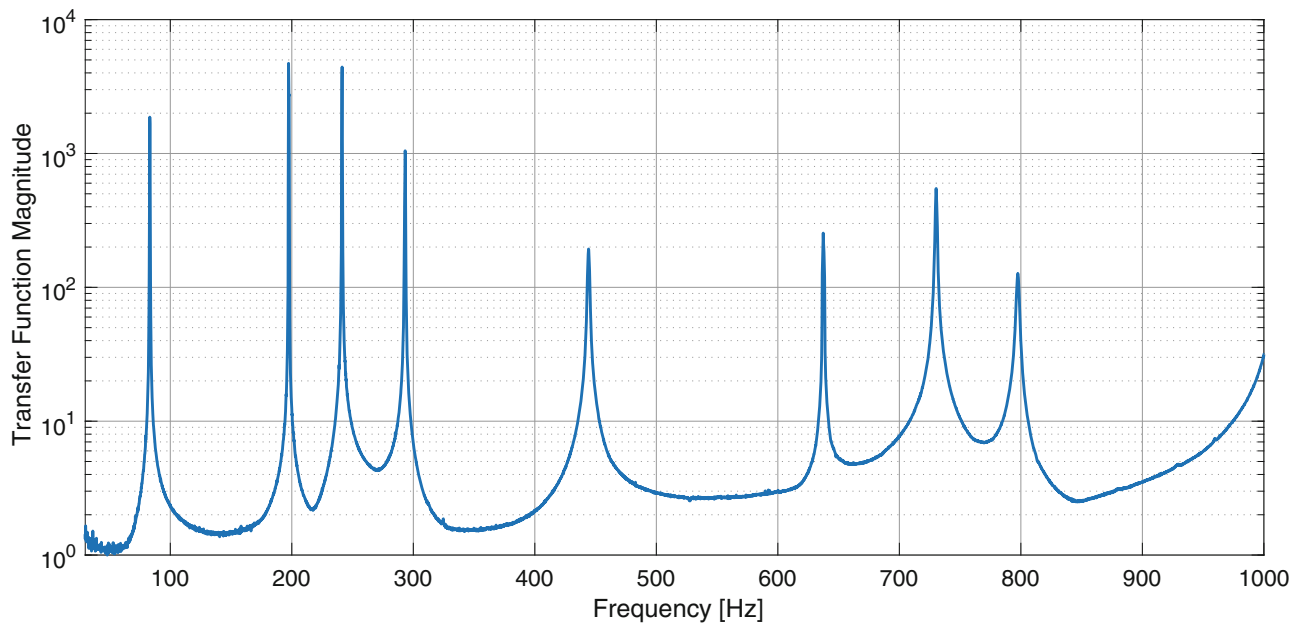


Fig. 23.3 Averaged frequency response function over 75 hammer impacts and 8 accelerometers, spread out across the assembled structure. The hit point on the assembled structure for each impact was near a corner far from the flanged joint interface

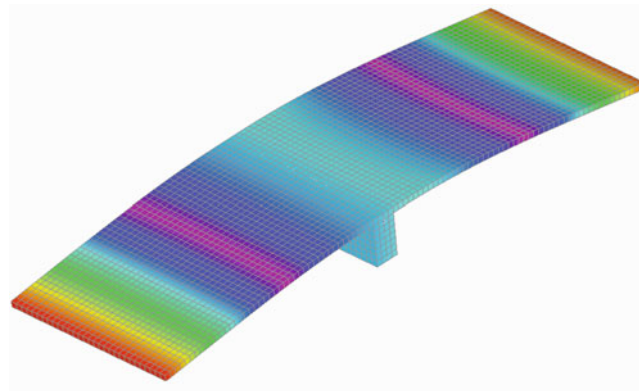


Fig. 23.4 First bending mode shape calculated from finite element model of the structure. For this mode, material stress causes joint prying due to global bending, type (A) motion. Contours show displacement magnitude, with maximum displacement in red, and minimum in purple

far from the joint. The first resonance is at 83 Hz, and corresponds to the first bending mode of the structure. The second resonance is at 197 Hz, and corresponds to the first torsional mode of the structure. See Figs. 23.4 and 23.5 for examples of these effects in a finite element model of the test structure with motion types (A) and (B), respectively. Nodal lines are in bright purple, and relatively large displacements are in red. Sketches of the joint dynamics with exaggerated amplitudes are shown in Figs. 23.6 and 23.7.

It is postulated in this work that energy loss due to a fastened joint for all modes of structural vibration could be described in terms of type (A) or type (B) modal behavior, or a superposition of these two. These two mode types can be more easily distinguished with low-order modes, which have relatively large stresses and displacements at the joint.

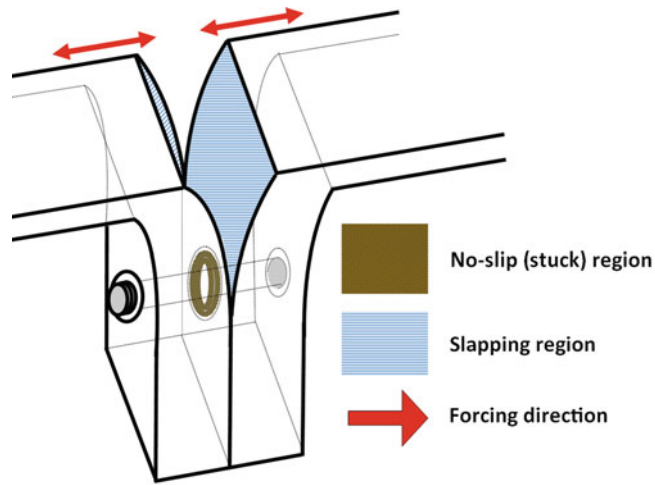


Fig. 23.5 Sketch of forces parallel to fasteners, type (A). The slapping region, or region of repeated impact, is highlighted in blue

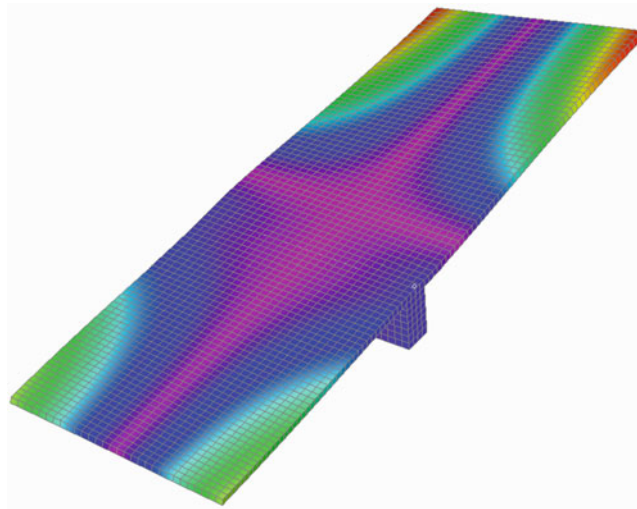


Fig. 23.6 First torsional mode shape calculated from finite element model of the structure. For this mode, the faying surface experiences high shear stress at the flange due to global torsion, type (B) motion. Contours show displacement magnitude, with maximum displacement in red, and minimum in purple

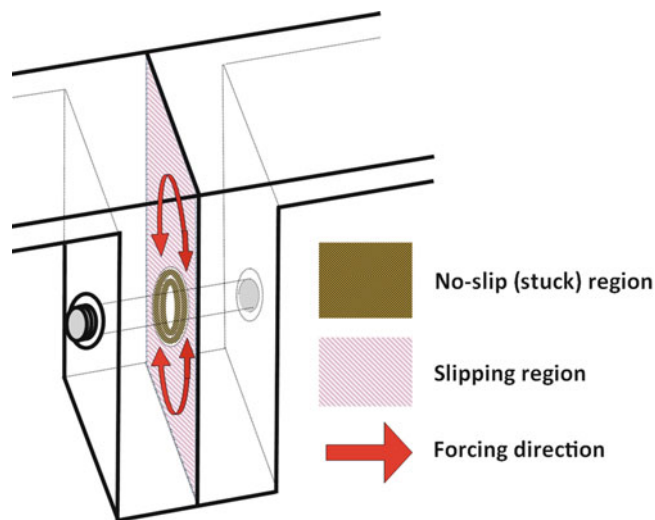


Fig. 23.7 Sketch of forces tangential to the faying surfaces, type (B). Faying surface area not in the stuck region is subject to slipping, highlighted in pink

23.2.3 *Methods of Excitation*

The two most common types of excitation methods for experimental modal analysis are impact (hammer) and shaker excitation. Another option, which is less utilized, is acoustic excitation or sonification. There are significant benefits and drawbacks to each method. Impact excitation is performed by simply striking a modal hammer at a specific location on the structure. Harder hammer hits introduce more force and cause larger vibration of the specimen. Too forceful of a hit may damage the structure, but a variety of hammer tips can be used to mitigate damage by spreading the impact time over a larger window. The trade-off is that with a softer hammer tip, the longer impact duration leads to a small excitation bandwidth. The benefit of impact testing is that it does not add mass or damping to the structure during the measurement period, and that it has a relatively good energy input efficiency. A drawback of impact testing is that modal filtering is more difficult. Careful placement of the impact location as well as post-processing steps such as bandpass filtering have the potential to help considerably with this issue, but can be cumbersome or impractical. In addition, impact testing does not allow for steady-state investigations, and sweeping across a resonance frequency cannot be done to investigate jumps in frequency response or other nonlinear phenomena.

Electrodynamic shakers are used widely in experimental modal analysis, often with a controlled acceleration level. Specimens under test can be attached directly to the mounting platform of the shaker; however, this procedure often couples the dynamic behavior of the specimen and the shaker. A long rod (stinger) can be used to decouple the shaker, but in many cases, the shaker still adds mass and damping to the system, especially when small or lightly-damped specimens are being tested. Slight misalignment of the shaker-structure assembly can also send transverse loads that force the structure off-axis from the intended direction. Another drawback of using shakers is the inability to perform true decay measurements. To do so would require complete and near-instantaneous decoupling of the actuator from the system. Moreover, such an abrupt decoupling would introduce a discontinuity in the input signal in addition to the modal energy already present in the system from the shaker, which would introduce broadband excitation into the structure. On the other hand, shakers are beneficial for their broad range of input possibilities, including the capability to provide steady-state excitation using relatively high efficiency of transferring energy into the system. These options include the capability of exciting a single frequency, a narrow- or broad-band range of frequency content, or stepping or sweeping across multiple frequencies.

Acoustic excitation can be performed using an amplified loudspeaker driver to excite a test structure. Excitation from the acoustic far field, when the speaker is a far enough distance away to provide plane-wave energy, can be used to drive the system at resonance. The acoustic near field provides energy content that can be useful as well, although not in plane-wave form. This type of excitation can be used to provide steady state or complex frequency content, as with a shaker, but without the drawback of coupling to the system. Alternatively, the method can also be used to get true decay measurements, as with a hammer, by cutting off signal after having reached a steady state and measuring the decay. For these types of measurements, preliminary investigations indicate that the driving frequency need not be the exact frequency of resonance to drive the resonance of the system after shutoff, but can be within several hertz. The main drawbacks to this method are that there is poor energy input efficiency, loudspeakers often introduce an amount of harmonic distortion (either directly or through an amplifier) which can excite the structure to some degree, and the magnitude of excitation is difficult to quantify when the ensounded specimen is in the acoustic near-field. Despite these challenges, the method of acoustic excitation is used in the present study to analyze a flanged structure with a fastened joint.

23.2.4 *Boundary Conditions*

Several methods are commonly applied to simulate free boundary conditions. One method is to place the structure on bubble wrap, taking advantage of the compliance of the trapped air pockets in contact with a large portion of the specimen surface area. Another includes suspending the structure using string-like material, such as fishing line or surgical tubing. This requires careful placement of the supports where there is relatively little structural displacement for the frequency range of interest. Guidance in the literature on methods for applying boundary conditions that approximate free vibration, while minimizing the resulting added energy loss, is sparse. The small nonlinear behavior to be measured from fastened joints requires a very good approximation of loss-free boundaries. Detailed description of the boundary conditions used in this study are outlined in Sect. 23.3.3.

23.3 Experimental Setup

23.3.1 Hardware

Two 6061 aluminum plates, shown in Fig. 23.8, are 0.25 in. (0.64 cm) thick and screw together with a flange surface. The flange surfaces are 2 in. (5.08 cm) high, and match the 7.5-in. (19.1 cm) width of the plates. The larger plate, left, is 13 in. (33.0 cm) long, and the smaller plate, right, is 11 in. (27.9 cm) long. Two commercially available 3/8–16 socket head cap screws and washers are used in the fastened joint. The fasteners are made of PH17-4 stainless steel (SS) in condition A. The longer plate has 3/8" clearance holes, and the shorter has tapped holes containing 3/8–16 SS Heli-Coil® thread inserts (PN 3585-6CN-W-562). The two centers of the fastener holes are 3.0 in. (7.6 cm) apart. All washer and fastener surfaces in contact with the structure are coated with Molykote P37 marine grade anti-seize paste.

23.3.2 Torquing

Despite careful procedures and the use of a precision torque wrench, contact pressure can be only approximately inferred from torquing values using the relationship of torque being the product of pressure, bolt diameter, and a “nut factor.” Nut factors are cataloged approximate dimensionless values in tables, and are related to friction coefficients of the fastener and structural materials under dry or lubricated conditions. Moreover, they account for torsion, bending, plastic deformation of threads, and all other possible contributions in the relation [4]. Using previously measured nut factors allows for a rough estimate of the pressure at the faying surfaces and some consistency in testing, but necessitates wider spread of experimental torquing values. Since aluminum is a relatively soft metal, slight changes to preload in highly torqued surfaces may not significantly change the system. Therefore, in order to highlight the nonlinear response in the joint, the plates were torqued to three different values for the present study: 23.0 pound-feet (lbf · ft), 11.5 lbf · ft, and lightly hand-tight.

23.3.3 Boundary Conditions

Several methods were used to support the structure in preliminary tests (see Figs. 23.9, 23.10, 23.11, 23.12 and 23.13). Previous attempts included supporting the structure in a cradle configuration with rubber surgical tubing (configuration A, Fig. 23.9) or fishing line (configuration B, Figs. 23.10 and 23.11). One boundary support method using glued fishing line provided the lowest modal loss factors compared to several other attempted methods. Figure 23.14 shows the difference

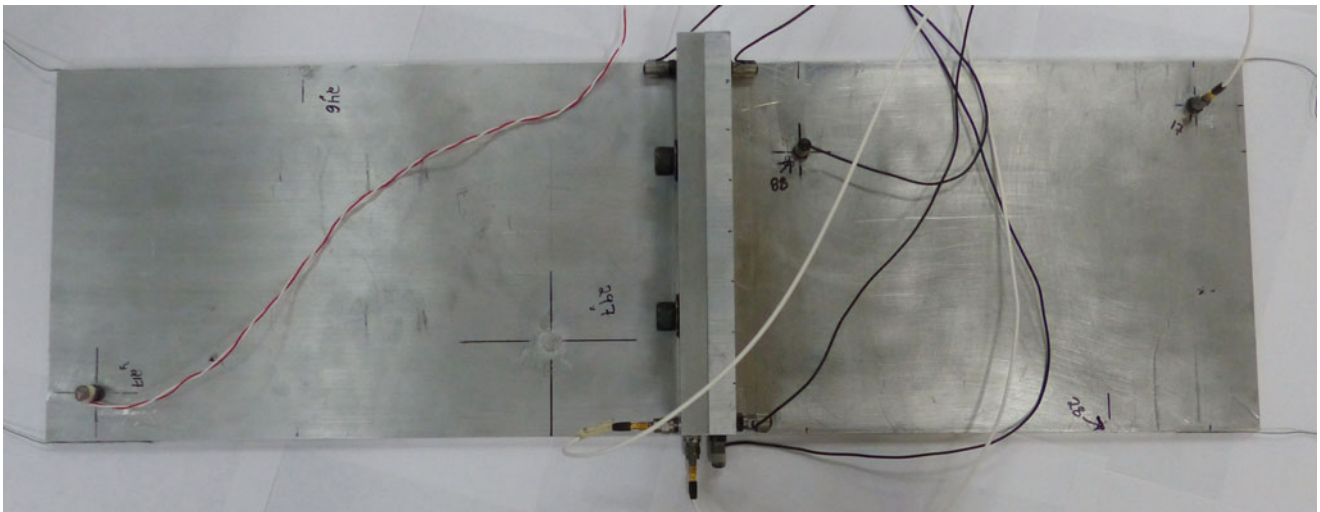


Fig. 23.8 Experimental plates with flange joint

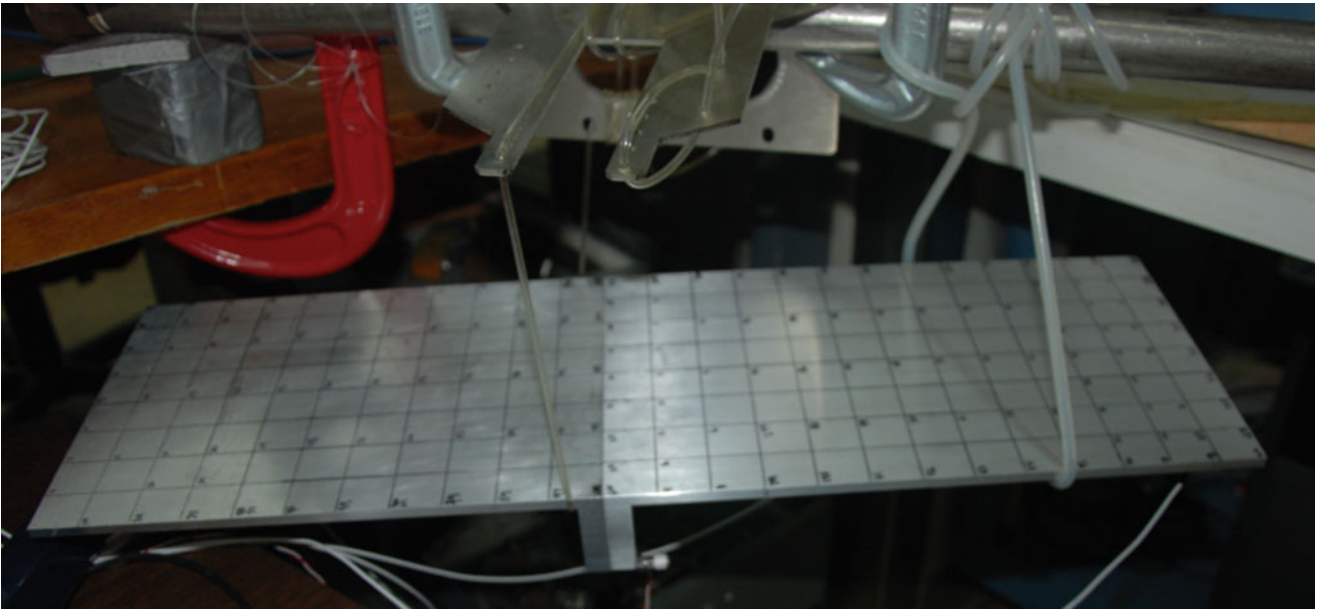


Fig. 23.9 Cradle of plates with surgical tubing (config. A)

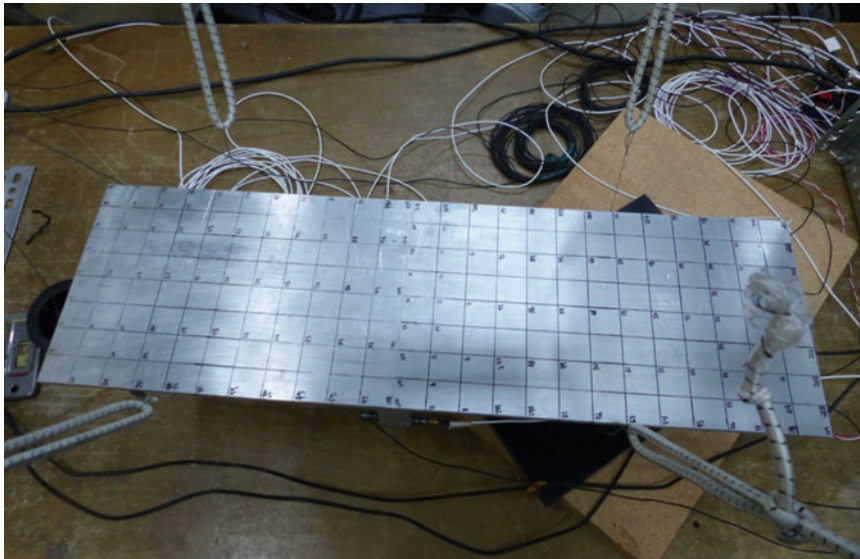


Fig. 23.10 Cradle of plates with fishing line (config. B)

between loss factors for some of the configuration types for the first five modes of a single plate. Suspension via glued fishing line was chosen as the approach for this study since it resulted in the lowest added damping.

To simulate free edges, the assembled plates were connected to fishing line using Loctite[®] 403 alkoxyethyl adhesive. Fishing line provides an inelastic connection between the structure and sections of surgical rubber tubing, which support the hanging plates from the crossbeam of a T-slotted framing support Fig. 23.12. The torsional, longitudinal, and swinging modes of the support are at least an order of magnitude below the first mode of the structure, and are easily filtered out of the measurement results.

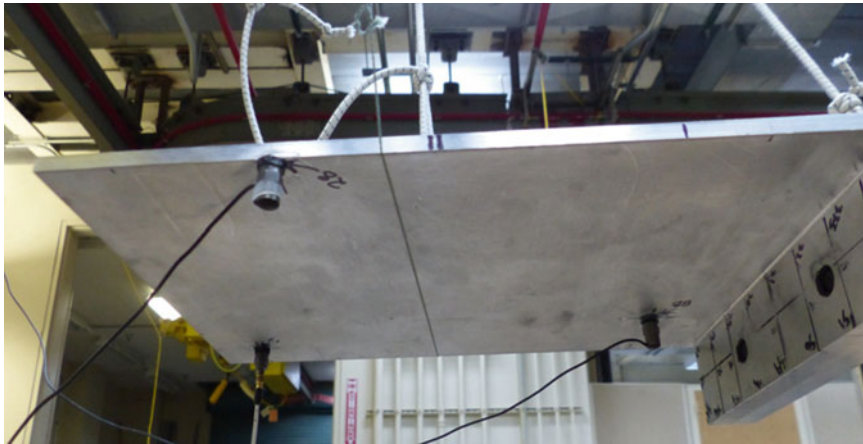


Fig. 23.11 Cradle of plates with fishing line, underside view (config. B)

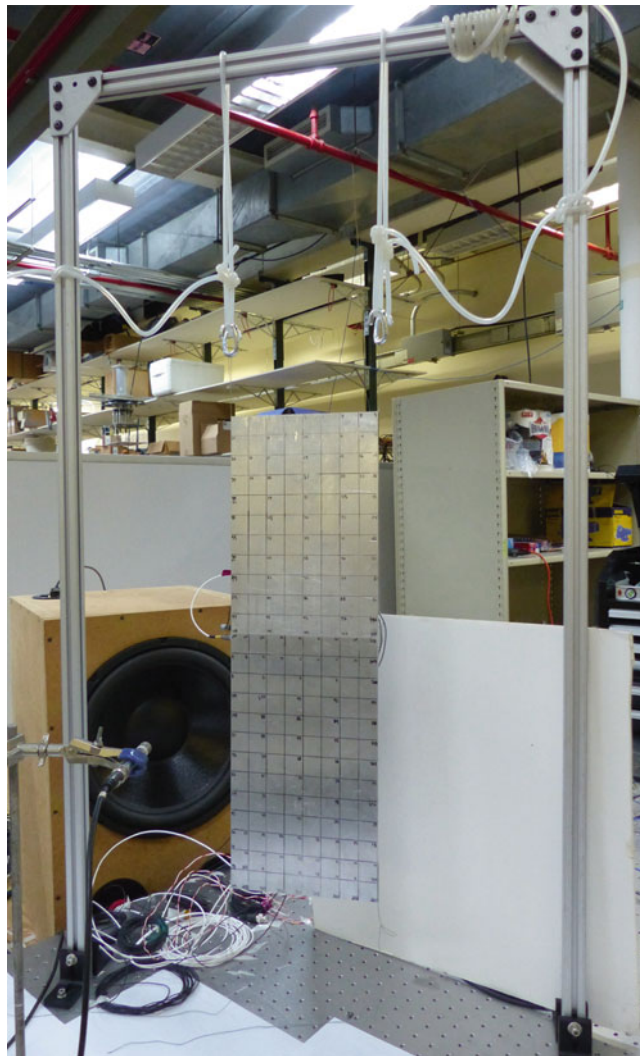


Fig. 23.12 Vertical suspension with glued fishing line at the two top corners (config. C)



Fig. 23.13 Glued fishing line at the upper corners of the vertically-suspended plates (config. C)

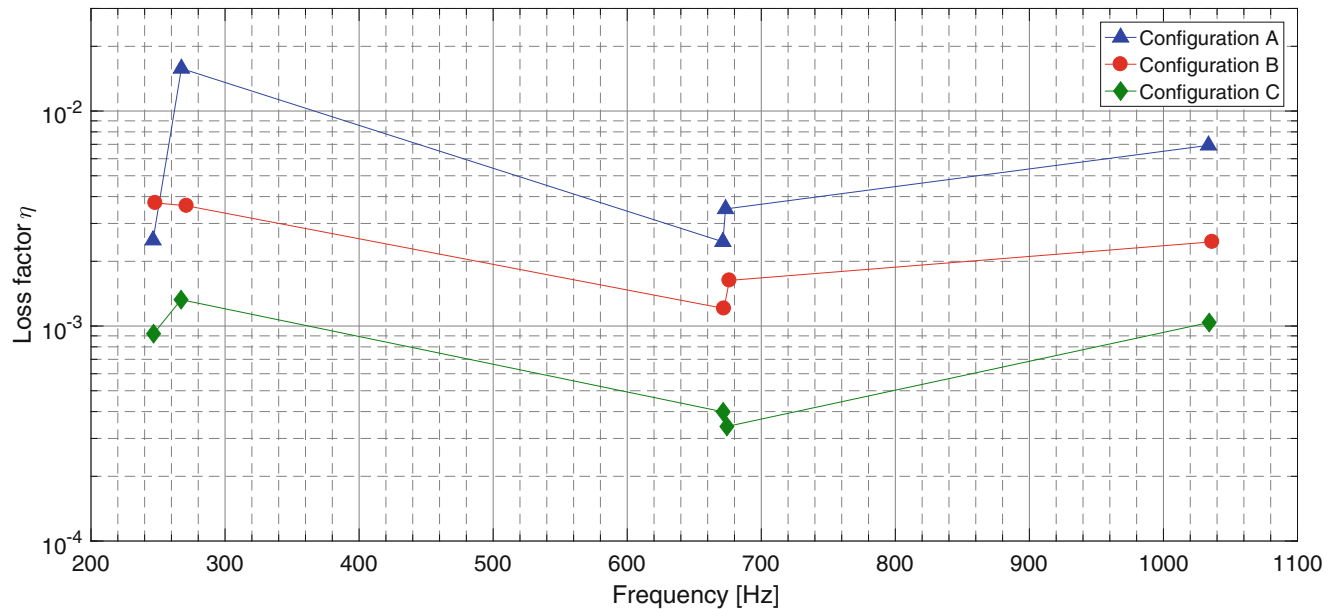


Fig. 23.14 Loss factors for the first five modes of a single plate under different boundary condition configurations

23.3.4 Setup Procedures

The final form of the experimental apparatus is shown in Figs. 23.12 and 23.13. Fishing line glued to the specimen at its upper corners is shown in Fig. 23.12. The fishing line connects to a surgical cord via a steel chain repair link. Two pairs of loops of surgical tubing on either side of the support beam are twisted once and then connected to the repair link. Accelerometers are secured using Loctite[®] 403 alkoxyethyl adhesive to various locations on the structure, both near to and far from the flange interface. The two plates are fastened before being hung, lying flat on the optical table shown at the bottom of Fig. 23.12. After coating all surface areas of the fastener and under the washers, both fasteners are torqued to 70% of the target value. Once partial torquing is complete, they are both tightened to the full target torque value. This procedure is standard practice for torquing when using a torque wrench, and allows better consistency in the preload value.

The assembled test structure is suspended near a boxed 12-in speaker driver. This driver provides good energy output with low harmonic distortion at frequencies below 500 Hz, which covers the first four structural vibration modes. A quick frequency sweep for any given torque level reveals the resonance frequencies of the system in the current configuration. With that information, single-frequency resonance excitation or sweeps of finer frequency resolution and longer time intervals are performed to investigate each mode individually.

23.4 Results

23.4.1 Damping

Acoustic excitation was used to induce free decay conditions for the first two resonances of the system with a fastened joint. Conditions for this test included torquing the fasteners to 23 lbf·ft and exciting the system for about 10 s. Accelerometer signal acquisition began at least one second before the acoustic signal was terminated, and continued until the accelerometer signal approached the noise floor. A sample of this decay is shown in Fig. 23.15. This signal was trimmed and processed using previously developed methods to extract time-dependent damping [3].

A clip of the time series for the first two modal excitations are shown in Figs. 23.16 and 23.17. The blue curve is the signal from an accelerometer mounted on the flange of the long plate, and the red curve is the signal from an accelerometer mounted near the far corner of the same long plate. Both accelerometers are on the same half of the structure as split along its long axis, which is the bottom half of the structure in Fig. 23.8.

Figure 23.16 shows the two accelerometers in phase, where the outside edge and the inside of the flange of the long plate are both either bending inward together or away from each other (see Fig. 23.4). In Fig. 23.17, the twisting motion of one corner is 180° out of phase with the flange corner on the same long side of the structure (see Fig. 23.5).

Damping curves for the first bending mode of this system in its configuration with very high torque are relatively constant in time. In Fig. 23.18, loss factor for the first bending mode is about 3.4×10^{-3} . For the first torsional mode in Fig. 23.19, loss factor is about 1.3×10^{-3} . These data show loss factors that are at or above the values obtained from initial boundary condition comparison data in Fig. 23.14. Loss factors in this section are greater than or equal to the corresponding modes of those in Fig. 23.14. For the fastened system, significant additional damping of some of the modes is expected due to friction losses at the interface.

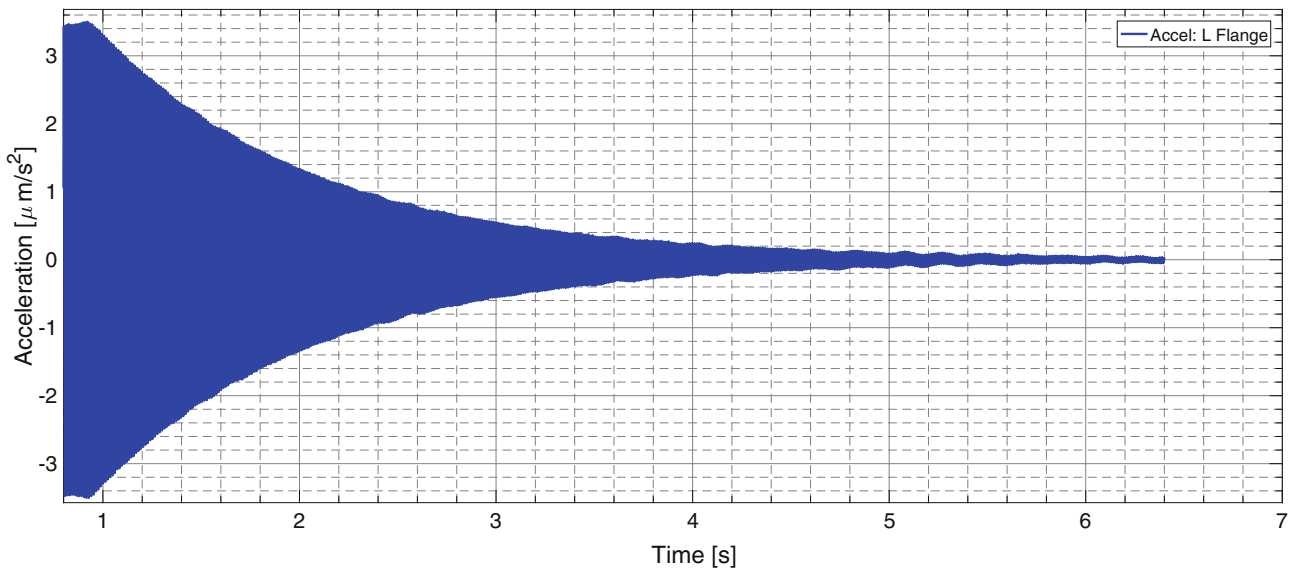


Fig. 23.15 Decay time series after exciting the first bending mode

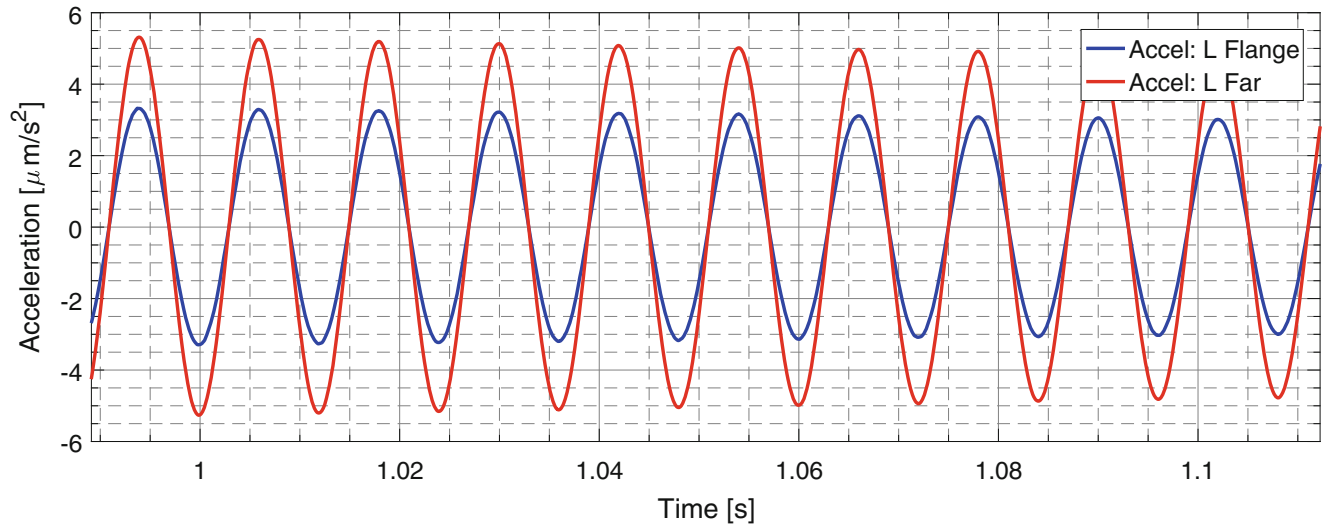


Fig. 23.16 Decay time series clip after exciting the first bending mode

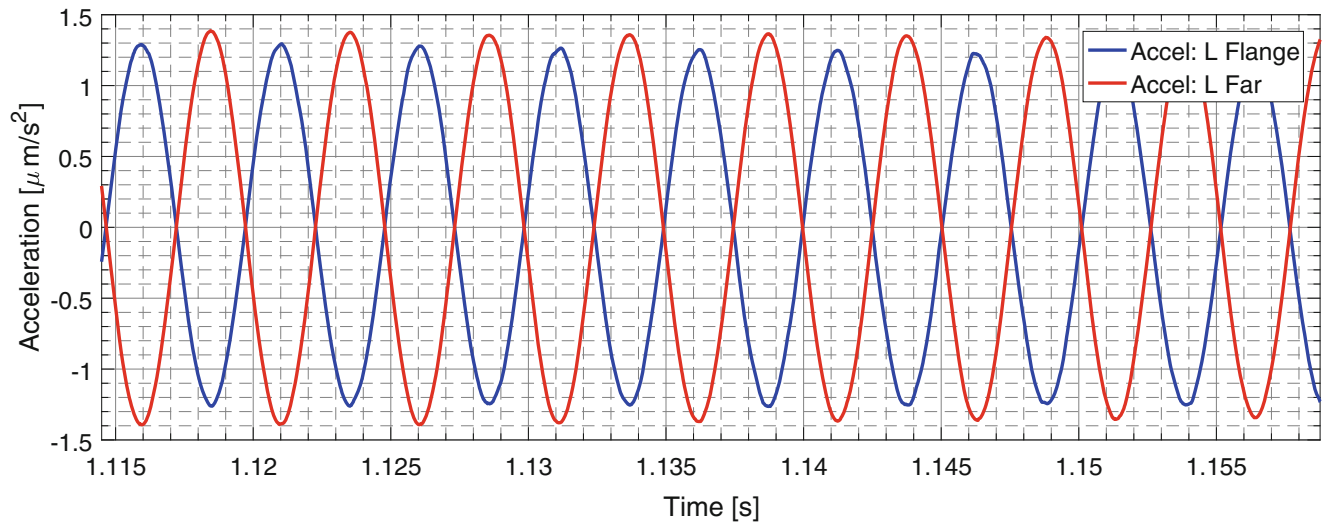


Fig. 23.17 Decay time series clip after exciting the first torsional mode

23.4.2 Steady-State

Acoustic excitation was also used to induce steady-state conditions for the first two resonances of the system. Conditions for this test included torquing the fasteners to either 11.5 lbf·ft (tightly torqued) or barely hand-tight (loosely torqued). The signal input to the loudspeaker amplifier $x(t)$ and the output signal measured with the accelerometer $y(t)$ can be compared for analysis. The signals in the time domain are converted to linear spectra in the frequency domain, $X(f)$ and $Y(f)$, respectively, using a Fast Fourier Transform (fft), where, for acquired signals with temporal resolution dt ,

$$X(f) = \text{fft}[x(t)] \cdot dt \quad (23.1)$$

$$Y(f) = \text{fft}[y(t)] \cdot dt. \quad (23.2)$$

In this case, only a single time record for each case was used. Since no averaging was performed, transfer functions $H(f)$ from the input and output signals can be computed using the ratio of the cross-spectrum (input to output) to the the input auto-spectrum:

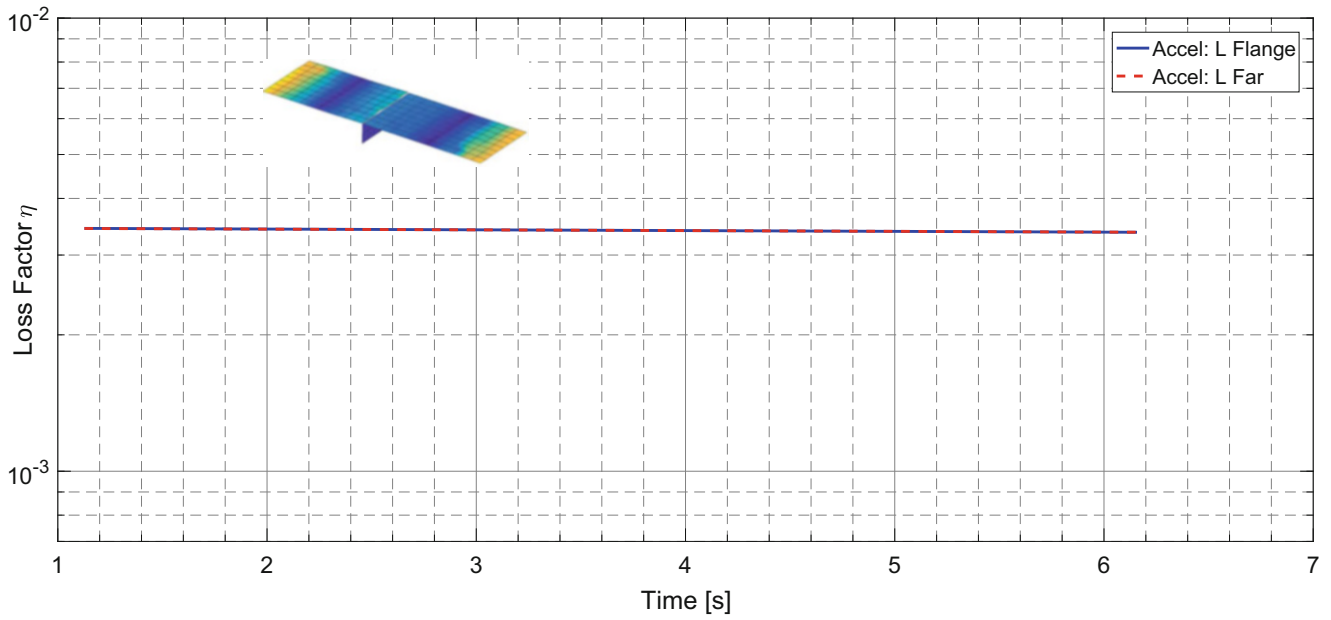


Fig. 23.18 Damping of the first bending mode

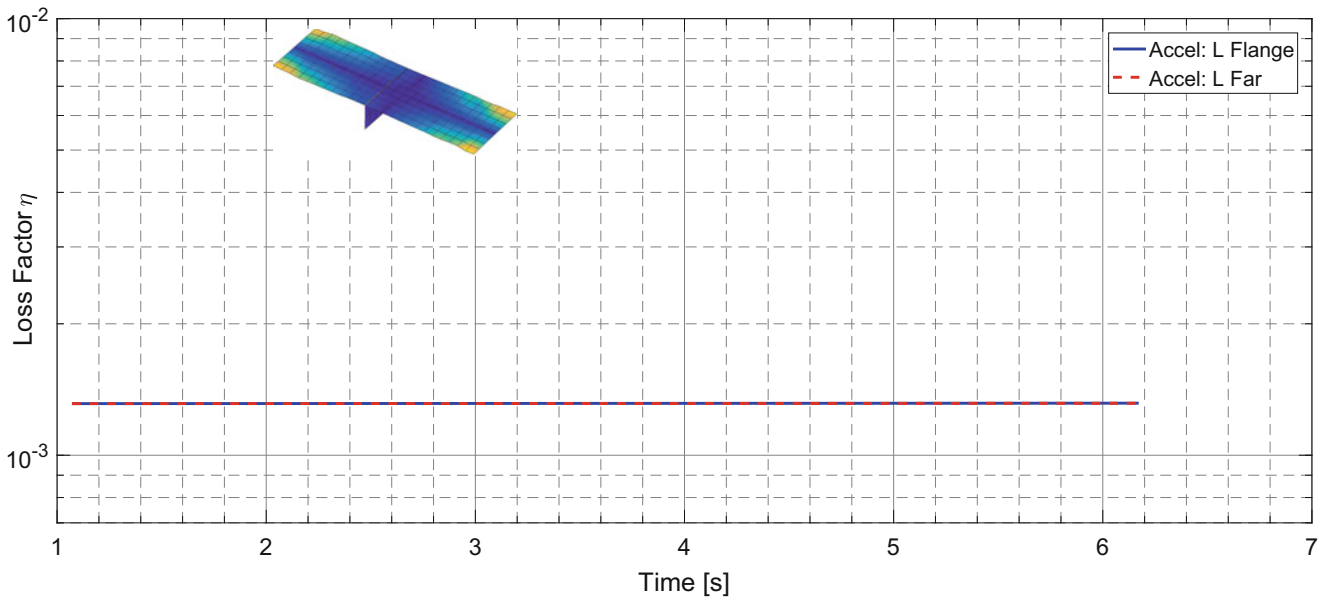


Fig. 23.19 Damping of the first torsional mode

$$H(f) = \frac{G_{XY}(f)}{G_{XX}(f)} \quad (23.3)$$

where, for acquired signals with period T , cross spectra are defined as

$$G_{XY}(f) = \frac{2}{T} X(f)^* \cdot Y(f) \quad (23.4)$$

$$G_{XX}(f) = \frac{2}{T} X(f)^* \cdot X(f) \quad (23.5)$$

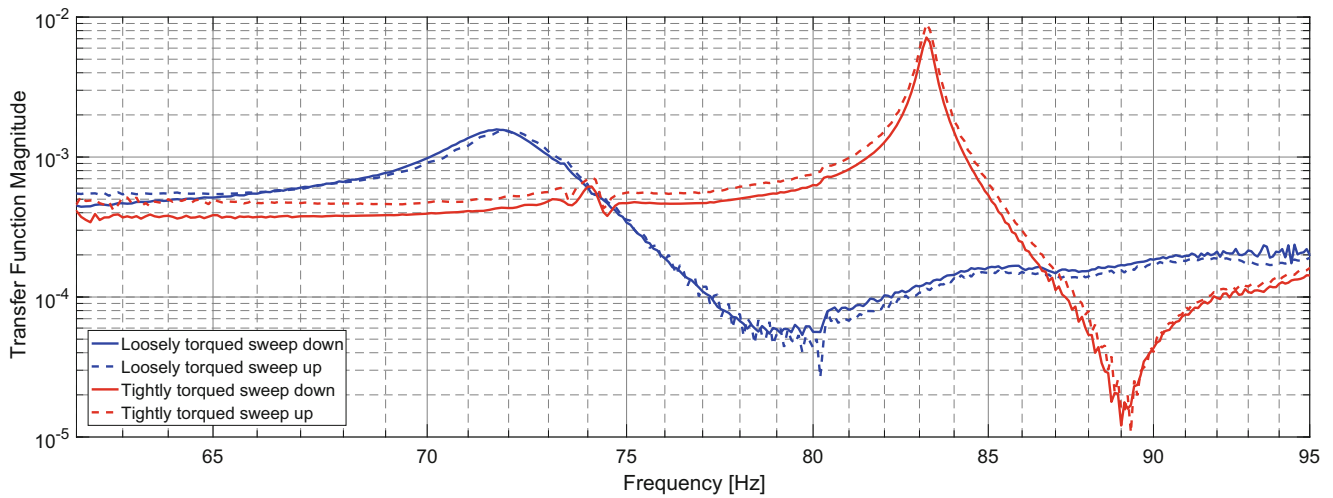


Fig. 23.20 First bending mode transfer function using quick frequency sweeps up and down, comparing loosely and tightly torqued configurations

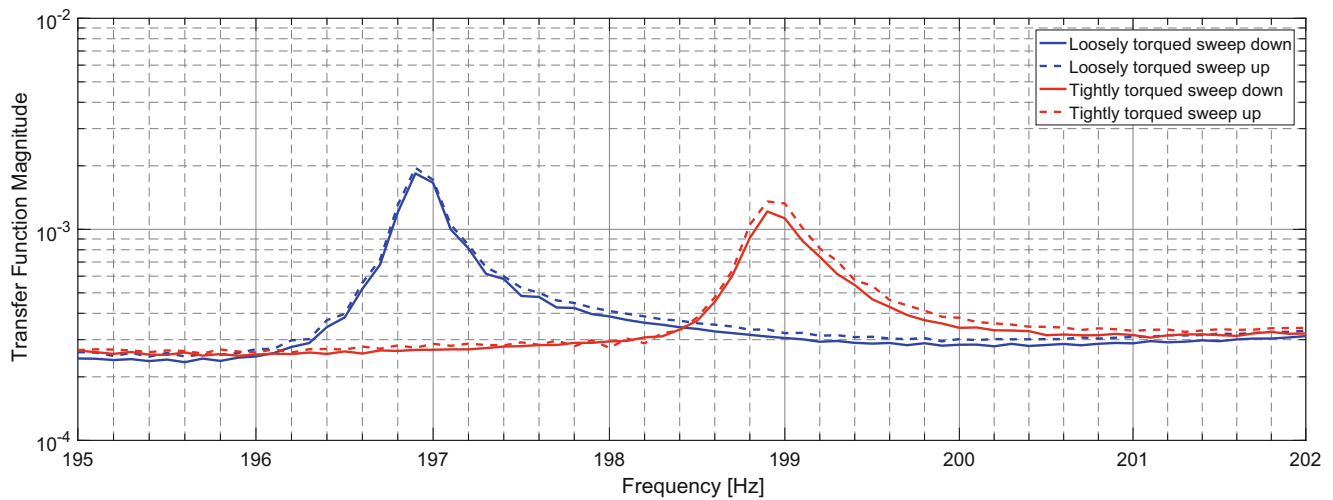


Fig. 23.21 First torsional mode transfer function using quick frequency sweeps up and down, comparing loosely and tightly torqued configurations

and where $*$ denotes the complex conjugate. Transfer function magnitudes for both torquing conditions are shown in Fig. 23.20 for the first bending mode and Fig. 23.21 for the first torsional mode. Each plot shows a curve for a fast sweep of decreasing or increasing frequency, where a softening effect of system resonance is seen for the loosely torqued condition compared to the tightly torqued condition.

23.5 Conclusion

Two general mode types have been discussed in this study, which could be used to form a basis for fastened joint dynamic behavior. One type (A) deals with forces normal to the faying surfaces, the other (B) involves forces tangential to the faying surfaces.

Different configurations to approximate free boundary conditions have been investigated for metal plates with a flange. The method of gluing fishing line to the specimen yielded lower overall modal damping than a cradle configuration of both fishing line and surgical tubing.

A method of acoustic excitation has been used to measure both damping from decaying vibration and hysteresis from steady-state excitation. Benefits of this method include no added mass or damping to the system, being able to measure steady-state and decay response, and manual modal filtering. Despite the drawbacks of poor energy input efficiency and harmonic distortion, preliminary efforts to investigate nonlinear damping are promising. This experimental method may be used in future work to formulate a design model for energy loss in fastened joints.

Acknowledgements The authors thank Eric Myer for his assistance in the design and procurement of the test hardware, and Tom Gabrielson for providing acoustic generation equipment. The authors also thank NAVSEA for sponsoring this work.

References

1. Segalman, D.J., Gregory, D.L., Starr, M.J., Resor, B.R., Jew, M.D., Lauffer, J.P., Ames, N.M.: Handbook on dynamics of jointed structures. Technical report, Sandia National Laboratories (2009)
2. Kuether, R.J., Brake, M.R.W.: Instantaneous frequency and damping from transient ring-down data. In: Allen, M., Mayes, R., Rixen, D. (eds.) Conference Proceedings of the Society for Experimental Mechanics Series CPSEMS, vol 4, pp 253–263. Springer (2016)
3. Jerome, T.W., Hambric, S.A., Shepherd, M.R.: Vibration amplitude and fastener torque dependence of damping in a jointed structure. In: Proceedings of the ASME 2017 International Design & Engineering Technical Conferences, Number DETC2016-60247, Cleveland, Aug 2017
4. Bickford, J.: An Introduction to the Design and Behavior of Bolted Joints, Revised and Expanded, vol. 97. CRC Press, Boca Raton (1995)



Chapter 24

In Situ Measurements of Interfacial Contact Pressure During Impact Hammer Tests

B. Seeger, P. Butaud, M. V. Baloglu, F. Du, M. R. W. Brake, and C. W. Schwingshackl

Abstract Understanding the nonlinear dynamical contact interactions within joints is crucial for understanding and predicting the dynamics of assembled structures. In spite of this, most experimental investigations focused on the global vibration behavior, since the local interactions at the interface cannot be observed with standard techniques. In the present work, an advance contact pressure measurement system is used in a unique way to analyze, in situ, the interfacial contact pressures and the contact area inside a bolted lap joint connecting two beams (Brake-Reuß beam). An important feature of the measurement system is that it is designed for frequency ranges including the typical vibration frequency of the Brake-Reuß beam's first eigenmode, and thus permits measurement under dynamic excitation. The dynamics of the contact pressures were investigated with different bolt torque levels and with different excitation levels. The experiments found that significant variations of the contact state occurred and that the contact pressure measurement system could adequately resolve this effect. The influence of the measurement system itself on the global vibration response of the Brake-Reuß beam was shown to be tolerable.

Keywords Assembly · Lapjoint · Nonlinear · Experimental · Pressure sensor

24.1 Introduction

Bolted joints are indispensable in most machines and mechanical devices. The interface characteristics of bolted joints, such as contact area and contact pressure distribution, greatly affect the dynamic characteristics of machines. Therefore, understanding the dynamical contact interactions that lead to a nonlinear dynamic response of a bolted lap joint is of great importance when it comes to the correct prediction of the dynamics of an assembled structure. However, it is very difficult to observe such behavior experimentally.

Until now, there are several techniques for contact area and contact pressure distribution measurements. Most of the actual techniques are static measurement methods, for example engineer's blue [1], optics [2, 3], ultrasound [4–8] and pressure film measurements [9–12]. The widely used engineer's blue technique is convenient for contact area measurements, however it is not very accurate and cannot be used for contact pressure measurement. The optical technique is accurate but a large microscope and a camera are necessary and one contact surface should be transparent. The ultrasonic technique is noninvasive and has almost exclusively been used for static contact pressure measurements of bolt joints [4, 5]. The authors are only aware

B. Seeger (✉)
Institute of Aircraft Propulsion Systems, University of Stuttgart, Stuttgart, Germany
e-mail: benjamin.seeger@ila.uni-stuttgart.de

P. Butaud
Department of Applied Mechanics, FEMTO-ST Institute, CNRS/UFC/ENSMM/UTBM, Université Bourgogne Franche-Comté, Besançon, France

M. V. Baloglu
Friedrich-Alexander University Erlangen-Nürnberg, Erlangen, Germany

F. Du
School of Astronautics, Northwestern Polytechnical University, Xi'an, People's Republic of China

M. R. W. Brake
William Marsh Rice University, Houston, TX, USA

C. W. Schwingshackl
Imperial College London, Department of Mechanical Engineering, London, UK

of one work using ultrasound for dynamic contact pressure measurements [8]. Under dynamic loading, a focused ultrasonic transducer as used in this work is only able to scan finite points, i.e., not a whole contact interface at once (thus only four discrete spots at the interface were measured in [8]).

Recently, Tekscan Inc. developed a digital pressure film using piezoresistive strips, suited for measurements of the dynamic contact pressure distribution and contact area by inserting the pressure film into the contact interface. In addition, it has a number of advantages, such as real-time monitoring capability, re-usability of the sensor and a direct computer interface. The signal acquisition system is capable of a sampling frequency up to 730 Hz.

In this paper, that Tekscan pressure sensor is used to measure, in situ, the dynamic contact area and contact pressure internal to a jointed interface during a transient response due to hammer excitation. A standard Brake-Reuß beam, consistent of two beams connected via a three bolt lap joint, is studied. Since the frequency range of the sensor includes the typical vibration frequency of the Brake-Reuß beam's first eigenmode, this sensor seems to be a promising tool for research on the nonlinear dynamic response of bolted joints. This paper is organized as follows: in Sect. 24.2, the experimental setup is described, the impact of the sensor sheet on the global response of the BRB is discussed in Sect. 24.3 and the recorded real time measurements of the contact pressure and area in the interface are presented in Sects. 24.4 and 24.5.

24.2 Experimental Setup

24.2.1 Impact Test Setup

To study the evolution of the contact pressure in the interface of a jointed system, the benchmark system of the Brake-Reuß Beam (BRB) is used [13]. The BRB structure consists of two stainless steel beams, each with a cross section of 25.4×25.4 mm, connected via a three bolt lap joint, as seen in Figs. 24.1 and 24.3a. The material of both beams is 304 stainless steel alloy and three 50 mm M8 bolts are used. Each bolt is tightened using a torque wrench. Four different torque levels (5, 10, 15 and 20 Nm) are applied to study the influence of the torque on the dynamically changing contact conditions in the interface. In order to obtain a better repeatability regarding the initial interface conditions, the bolts are tightened following the procedure established in [14]: first, 70% of the final torque is applied to each bolt, the center bolt being tightened first before the outer two bolts. Then the final torque is applied following the same order.

The experimental setup, shown in Fig. 24.3a, includes the beam, two bungee cords, two PCB 356A01 Triaxial ICP Accelerometers (“acc1” and “acc2”), a PCB 086D05 ICP Impact Hammer, a LMS 16 Channel Spectral Analyzer and a Tekscan shell sensor (described in Sect. 24.2.2).

Following the setup described in [15, 16], the BRB beam is suspended 50 mm from each end with fishing lines connected to bungee cords in order to approximate free-free boundary conditions. The system is excited using an impact hammer at three different impact force levels: 60, 300 and 600 N. The point of impact is located 240 mm away of the end beam (grey circle on Fig. 24.1). For each excitation level and torque level, the measurements are repeated five times. The results presented in Sect. 24.3 are the average of each set of five hits.

For the comparison of the BRB's response in terms of natural frequencies and damping with and without the sensor inserted in the interface, as presented in Sect. 24.3.1, two three-axis accelerometers are used (blue squares in Fig. 24.1). For the vibration data associated with the interface pressure measurements presented in Sects. 24.3.2 and 24.5, respectively, only one PCB 352A21 mono-axial accelerometer (“accZ” in Fig. 24.1) is used. This is due to the fact that, in contrast

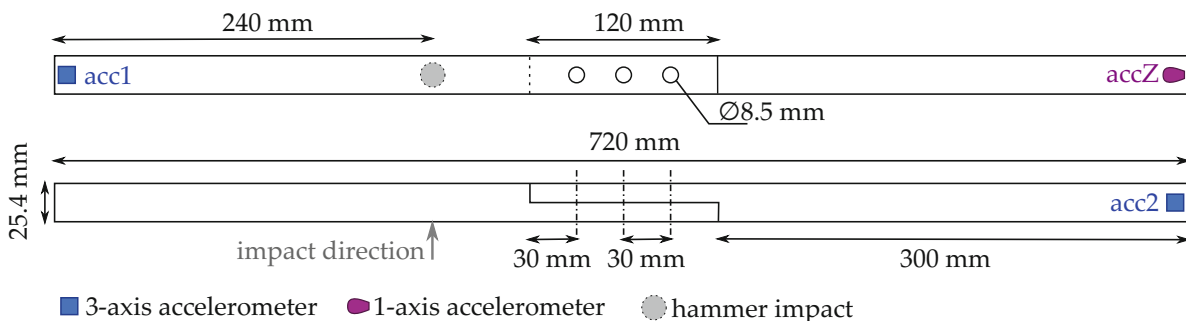


Fig. 24.1 Profile and side view drawings of the Brake-Reuß beam with the positions of the measurement and excitation systems

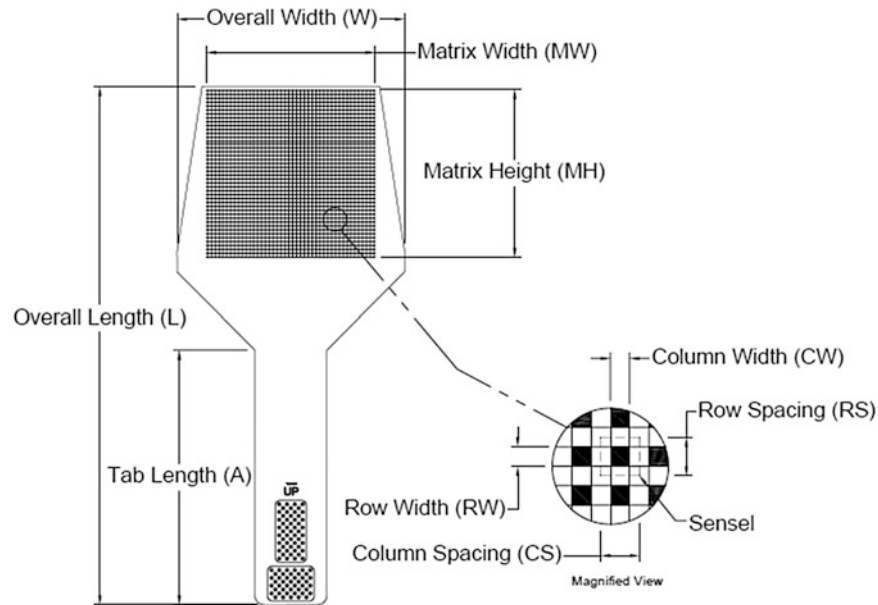


Fig. 24.2 Tekscan pressure mapping sensor 5101 [17]

to the mono-axial accelerometer, the three-axis accelerometers induced noise in the sensor sheet of the Tekscan system (see Sect. 24.2.2). It is most likely that the higher power demand of the three-axis accelerometers (compared to the mono-axial one), in combination with the beam being made of steel and with the blinding of the Tekscan sensor sheet being insufficient in the interface pressure measurements setup detailed in the subsequent section, caused electrical interferences that compromised the sensor sheet.

24.2.2 Interface Pressure Measurements Setup

The thin-film based Tekscan system consists of a matrix of semi-conductive ink coating that creates a pressure dependent electrical resistance at intersection points called sensels or sensor pixels. The sensor matrix is encased in a polymeric material (specifically mylar). A schematic drawing of the Tekscan 5101 sensor sheet used in this study, extracted from its data sheet provided by Tekscan Inc. [17], is shown in Fig. 24.2. The sensor has an 109.22×109.22 mm matrix (MW \times MH) consisting of 1936 sensels with a respective area of 6.4516 mm² (CS \times RS).

At 3450 MPa, the pressure saturation of the sensor is reached. A sampling frequency of 650 Hz, which is about four times the natural frequency of the BRB's first mode, was used to obtain the data presented in Sects. 24.4 and 24.5.

The sensor sheet is placed inside the interface of the BRB and connected to the I-scan 7.60 software and the electrical power supply by a paddle, as shown in the Fig. 24.3a. In order to be able to place the sensor sheet inside the lapjoint, three holes were required, made with a $\varnothing 8$ mm punch. At the edges of these holes, the semi-conductive ink coating inside the sensor sheet is not covered anymore by the polymeric material. It was found that it severely compromises the sensor data if the ink coating and the metal bolts come into electrical contact. To prevent this, each bolt at the interface is taped to separate the edges of the sensor holes from the metal bolts. With the holes punched in the sensor, data is still able to be collected; however, portions of several rows and columns are lost. Figure 24.3b illustrates the lost data (in red) when the sensor is placed at 45 to the longitudinal axis of the beam. The pattern of the lost data results from the sensor's specific matrix architecture. The 45 orientation is chosen to keep the maximum amount of information between the bolts and outside of the bolts, where the most interesting phenomena are assumed to happen.

The sensitivity of the Tekscan sensor can be adjust from one to 41, according to the pressure band of interest. The data obtained from the Tekscan sensor is dimensionless and given in "raw sum". The raw sum values of the sensor pixels represent the contact pressures relative to each other, i.e., not the absolute pressures at the pixels. A calibration using the area and applied force is required to obtain a scalar factor which converts the raw sum values into absolute pressure data. Since this paper is mainly concerned in monitoring the relative variation of pressure across the interface during a vibration cycle, and absolute values are not so much of relevance, the calibration process is not part of this paper.

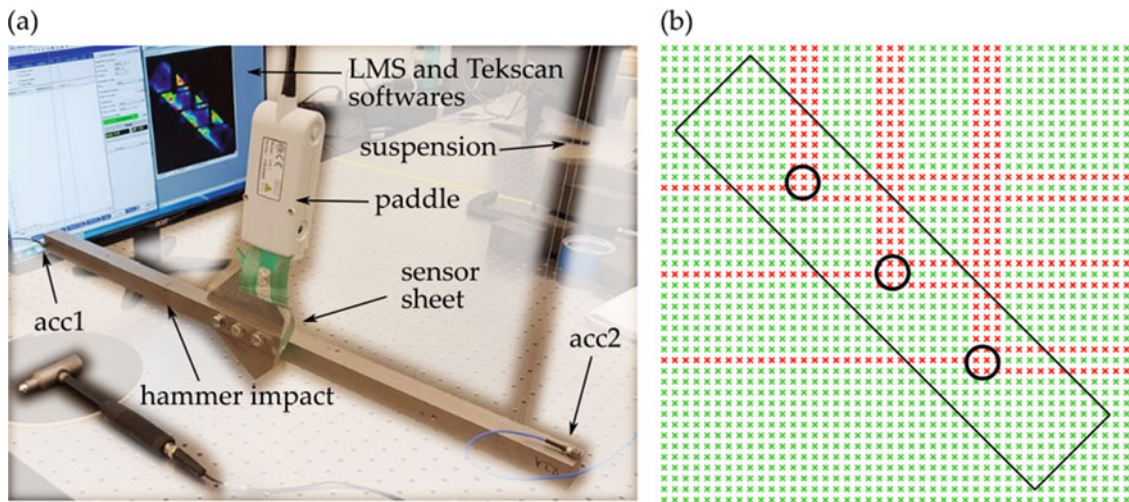


Fig. 24.3 (a) Typical experimental setup of the BRB with the Tekscan sensor sheet. (b) Illustration of the sensels, with active sensels marked green, inactive sensels marked red and the contour of the beam interface drawn in black

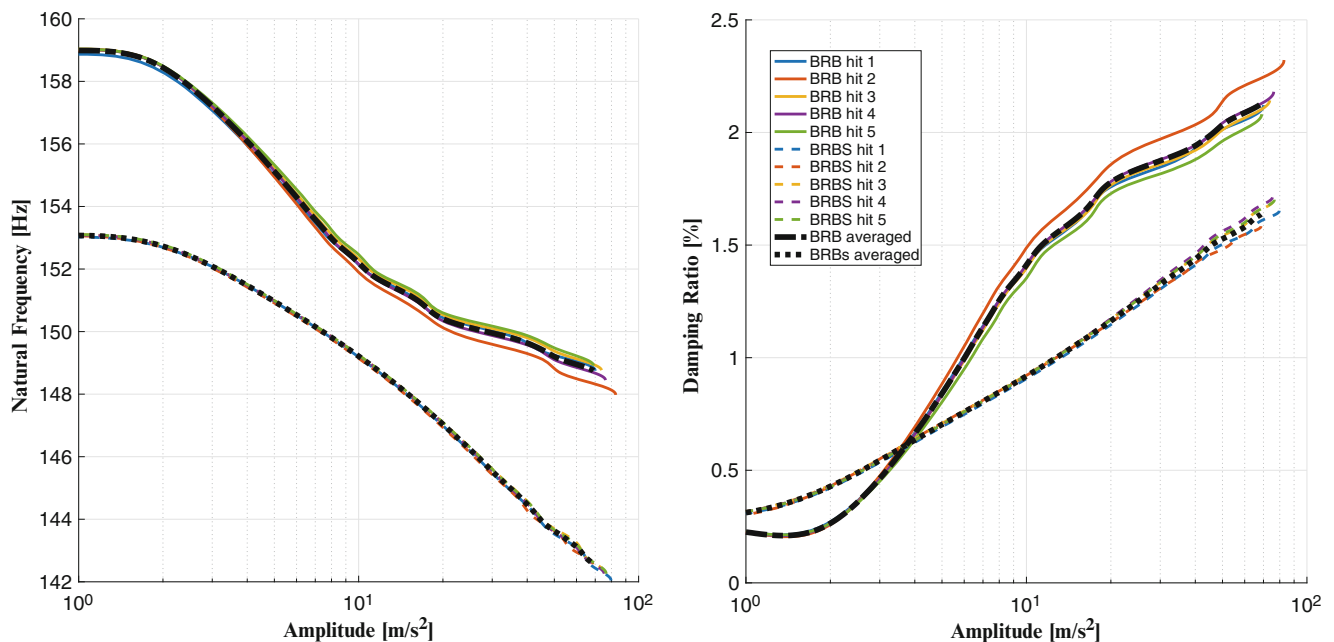


Fig. 24.4 Average of five hits for a high (600 N) impact force with a 5 Nm bolt torque, BRB and BRBS

24.3 Influence of the Interface Measurement System on the Global Response

In this section, the influence of inserting the sensor sheet in the interface of the Break-Reuß beam is studied. Inserting the polyester enveloped sensor introduces additional damping and flexibility to the interface, thus the quality of the measurements after changing the usual BRB interface has to be assessed. In the following, the BRB with the Tekscan sensor sheet placed in the interface is called BRBS (Brake-Reuß Beam with Sensor). Additionally, the variation of the nonlinear response with respect to changes of the bolt torque level and the impact force level for the BRBS are shown. Similar experiments with the focus on different interface geometries were performed in [14]. The here considered quantities, acquired from transient free decay time domain data with the help of the Hilbert transform outlined in [18] and [19], are the natural frequency and the damping ratio with respect to the amplitude. All values presented in the subsequent sections are the average of five hits, while every single measurement showed a very little deviation from its mean value. Figure 24.4 shows a representative example for the deviation of the five hits to their calculated average, both for the BRB and the BRBS at a 5 Nm bolt torque level and a high (600 N) impact force.

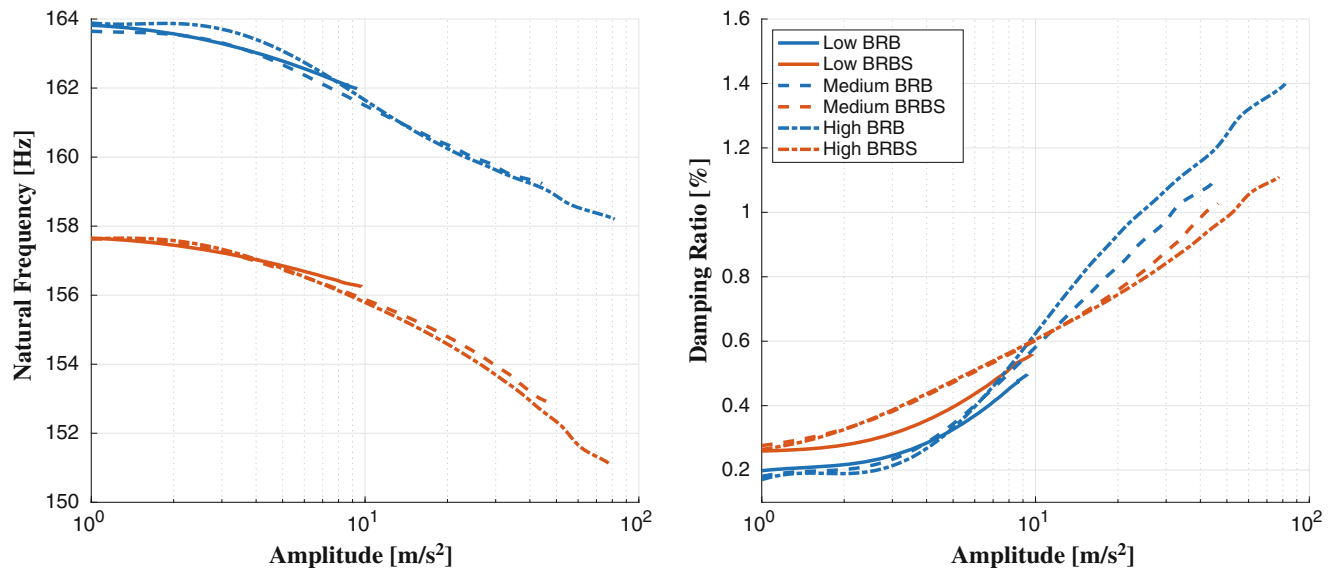


Fig. 24.5 Comparison of the BRB and the BRBS for a low (60 N), medium (300 N) and high (600 N) impact force with a 20 Nm bolt torque

24.3.1 Comparison Between BRB and BRBS

First, the natural frequencies and the damping of the BRB and the BRBS are compared for a constant bolt torque of 20 Nm and three different impact force levels, starting at the low (60 N), exciting with the medium (300 N) and ending at the high (600 N) impact force level. The results, which are used to estimate the error caused by the sensor sheet, are shown in Fig. 24.5.

The natural frequency, which seems to be independent from the excitation level in contrast to the amplitude, is shifted by an almost constant factor for every amplitude and is lower for the configuration with the sensor sheet. This expected softening behavior results from the polymeric casing material of the Tekscan sensor, which is weaker than the steel of the BRB. The damping ratio, by contrast, exhibits a slightly different behavior between the two systems. For the BRB, the measured damping ratios are not coincident for each excitation level (i.e., for higher excitation amplitudes, the damping ratio curves exhibit an increase above the previously measured levels). For the BRBS, however, the measured damping ratios for the medium and high excitation levels are coincident, that is, the measured curves overlap.

The ramifications of this result are that the dissipation mechanism between the two systems is slightly different. While for the BRB, the lack of coincidence in measurements could indicate evidence of modal coupling due to interfacial friction, the absence of these traits in the BRBS measurements indicate that more of the dissipation is coming from the polymeric film that constitutes the Tekscan sensor.

The damping ratio of the BRBS does not seem to be dependent on the amplitude as much as it is the case for the BRB. While for low amplitudes the damping ratio of the BRB is smaller than for the BRBS, the contrary is the case for higher amplitudes. One possible explanation is the polymeric material of the sensor sheet. At low amplitudes, the visco-elastic damping of the sensor sheet leads to higher damping of the BRBS compared to the BRB with its fully stuck interface. At high amplitudes, the interface of the BRB is sliding and dissipates more energy than the BRBS, which is still dominated by the visco-elastic damping. Nevertheless, these values stay in the same regime such that there is a justified hope to use the results of the BRBS for understanding the nonlinear dynamical contact interactions by keeping in mind that the natural frequency and the damping ratio are slightly affected in the above described way.

24.3.2 Variation of Bolt Torque and Impact Force for the BRBS

After the justification that the Break-Reuß beam with a sensor sheet placed at the interface can still produce representative results, four different bolt torque levels, namely 5, 10, 15 and 20 Nm, for the BRBS and a 600 N impact excitation are compared in Fig. 24.6.

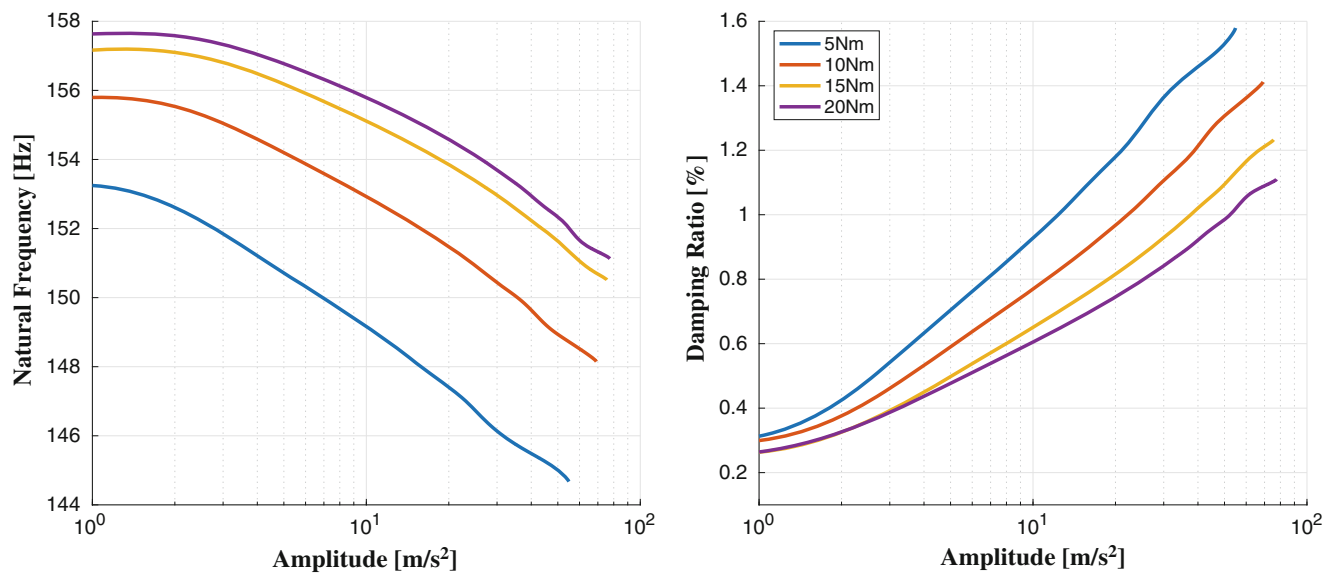


Fig. 24.6 Comparison of different bolt torque levels for the BRBS and a high (600 N) impact force

It can be recognized that the applied torque has a noticeable influence on the natural frequency as well as the damping ratio. The natural frequencies of the four bolt torque levels are clearly distinguishable. The increasing preload leads to more stiffness in the interface and therefore to higher natural frequencies. The slope of the decrease of the natural frequencies at higher amplitudes is almost identical for all four bolt torque levels. Contrary to the natural frequency, the damping ratio becomes smaller with increasing bolt torque, since the increasing preload reduces the permissible relative motion in the interface and therefore the energy dissipation. Additionally, the slope of the damping ratio at higher amplitudes flattens with increasing bolt torque. The relative shift between the natural frequencies as well as between the damping ratios gets smaller the higher the preload gets. On the one hand, this indicates a saturation of the joint (the same effect could be observed for the nominal BRB in [15]). On the other hand, this also indicates that especially for the 5 Nm case a strong softening of the system takes place and indicates additional frictional contact.

In the following, the two extreme cases at 5 and 20 Nm bolt torque level are examined more closely. For these two bolt torque levels, the influence of the excitation force level on the natural frequency and damping ratio for the BRBS is further studied. Analogously to Sect. 24.3.1, the BRBS is first excited at the low (60 N), then at the medium (300 N) and finally at the high (600 N) impact force level. The associated interface measurements of the first hit of each set of five hits are presented in Sect. 24.5. Even though Sect. 24.3.1 indicates that for 20 Nm torque the force level does not heavily affect the calculated parameters, Sect. 24.3.2 suggests that in combination with a lower torque this observation might not hold anymore. The results of this arrangement with three force levels and two torques are shown in Fig. 24.7.

For the 5 Nm bolt torque level, a significant difference between the frequency-vs-amplitude curves of the respective excitation level can be seen. The same difference is observable looking at the damping-vs-amplitude curves. This curve splitting depending on the excitation level strongly indicates several nonlinear phenomena. First, the energy dissipation and softening is due to the presence of microslip between the two surfaces (as opposed to macroslip, which would require relative motion between the two bodies). Second, that the curves for different amplitudes do not overlap is indicative of modal coupling. As more energy is put into the system, the nonlinearity of the interface excites multiple higher modes. Thus, as the excitation level is increased, more modes are contributing to the measured “mode 1” response. These results are further explored in Sect. 24.5.

The results of Sects. 24.3.1 and 24.3.2 show that the sensor sheet in the interface induces a frequency shift, but the relative change of the BRB’s natural frequencies with respect to the bolt torque level can still be assessed. The damping ratios of the BRBS stay in the same regime as the damping ratios of the nominal BRB. However, it is assumed that the dominating damping mechanism in case of the BRBS is different from the dominating damping mechanism of the BRB (cf. Sect. 24.3.1), thus one has to be cautious when comparing the damping ratios.

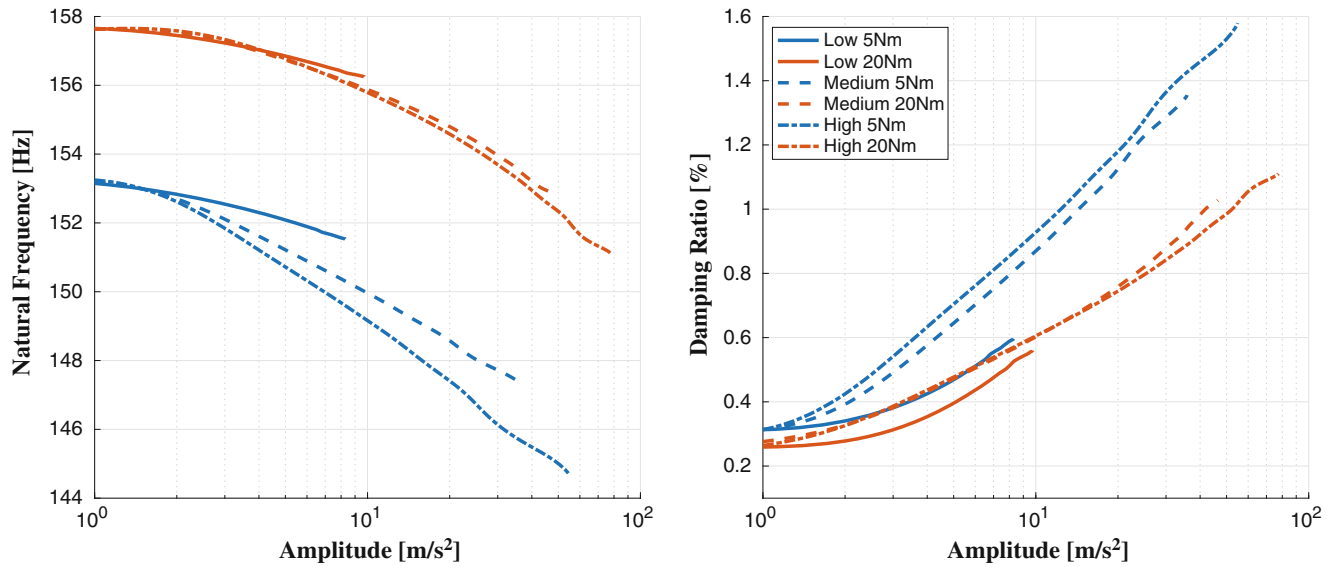


Fig. 24.7 Comparison of the natural frequency and damping ratio for low (60 N), medium (300 N) and high (600 N) impact force with 5 and 20Nm bolt torque

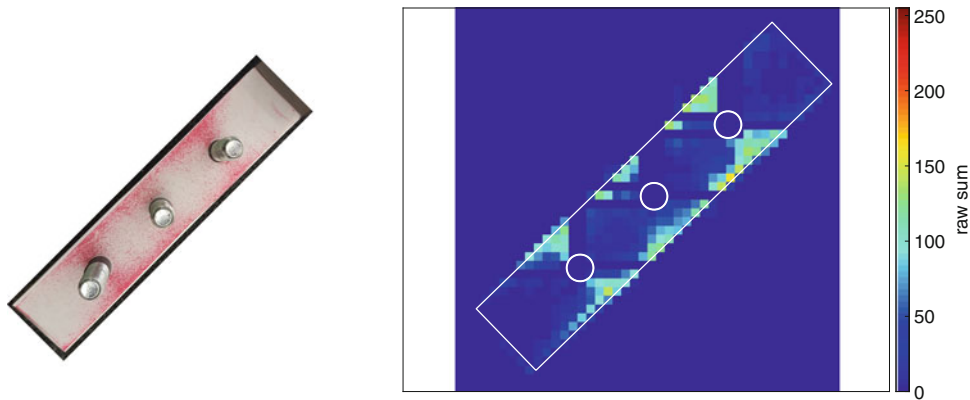


Fig. 24.8 Pressure field at 5 Nm with (left) Fujifilm and (right) Tekscan sensor

24.4 Validation of the Interface Measurement System

After investigating the influence of the sensor sheet on the global response, now the capabilities of the Tekscan system itself are assessed.

The static loading of the interface is done simply by tightening the beam's three bolts. Two different bolt torque levels are applied, namely 5 and 20 Nm. First, the pressure distribution inside the interface is measured with a Fujifilm pressure measurement film, then the Tekscan sensor sheet is used. The sensitivity chosen for the Tekscan sensor sheet (sensitivity = 6, cf. Sect. 24.2.2) and the pressure range of the Fujifilm pressure measurement film (medium) are the same for both bolt torque levels. Figure 24.8 shows the interface pressure distribution at 5 Nm, the pressure distribution at 20 Nm is shown in Fig. 24.9. In the Tekscan sensor output, the contour of the beam interface is displayed in white.

The difference in distribution and magnitude of the interfacial contact pressure at 5 and 20 Nm (shown in Fig. 24.9) is clearly visible in the output of the Tekscan sensor sheet.¹ At 5 Nm bolt torque level (Fig. 24.8), the contact pressure in the areas between the bolt holes and in the areas outside of the bolt holes towards the short edges of the interface is close to

¹Note that the static pressure film *appears* saturated, whereas the electronic pressure film shows clear gradients in the measured contact pressure. While these gradients may be evident in a digital analysis of the static pressure film, that information is inaccessible without a significant amount of work.

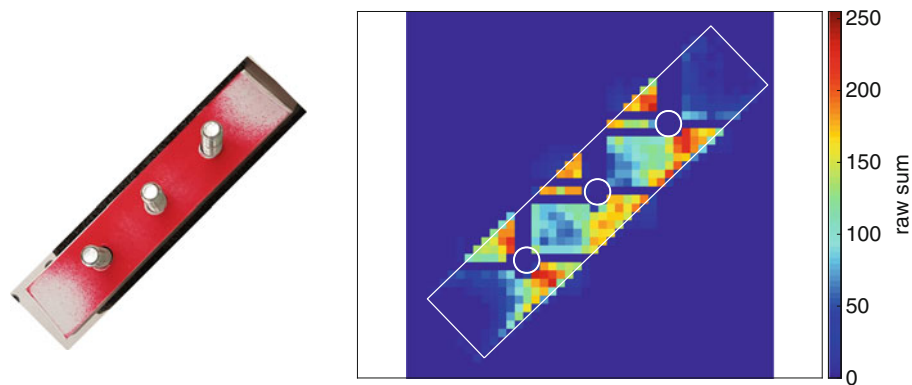


Fig. 24.9 Pressure field at 20 Nm with (left) Fujifilm and (right) Tekscan sensor

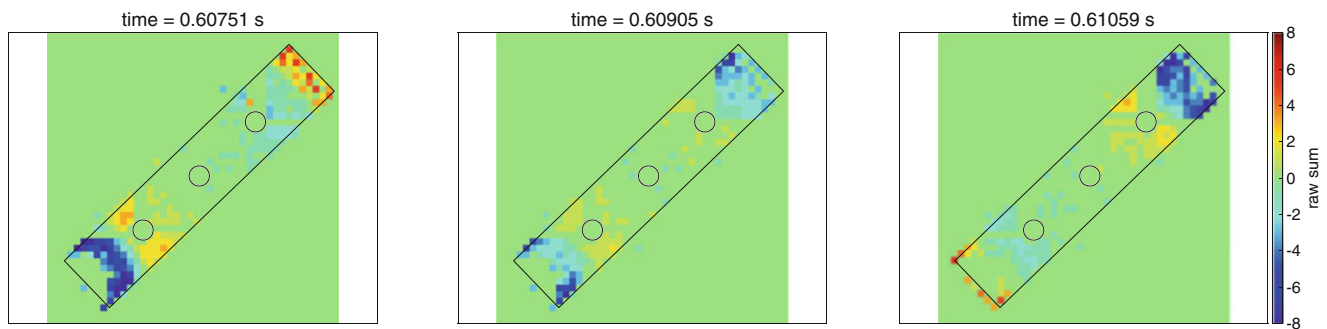


Fig. 24.10 Evolution of the dynamic contact pressure at 20 Nm bolt torque and medium excitation level

zero. The contact pressure is concentrated along the long edges of the interface, mainly in the vicinity of the bolt holes. At 20 Nm bolt torque level (Fig. 24.9), a higher contact pressure is measured in the area between the bolt holes, while the contact pressure in the areas outside of the bolt holes towards the short edges of the interface is still close to zero. Analogously to the 5 Nm case, most of the contact pressure is focused in the vicinity of the bolt holes and towards the long edges of the interface, but now the contact pressure is significantly higher. This distribution of the interfacial contact pressure (both, at 5 and 20 Nm) shows that the interface of the BRB used for the experiments is not flat, but exhibits a curvature orthogonal to the longitudinal axis of the interface. The results of the Tekscan sensor are consistent with the image on the Fujifilm pressure measurement film. Although some information is lost due to the necessary bolt holes (cf. Sect. 24.2.2), the pressure distribution between the bolt holes and outside the bolt holes is still well represented in the Tekscan setup.

In order to assess the capabilities of the Tekscan system with respect to dynamic loading, hammer impact tests were conducted with the sensor sheet placed inside the interface as shown in Fig. 24.3. As previously mentioned in Sect. 24.2, the sampling rate of the Tekscan system was 650 Hz. In the current section, the output of the sensor sheet under dynamic loading is only briefly illustrated, while the results of the dynamic interface measurements are presented and discussed in Sect. 24.5.

In Fig. 24.10, three consecutive frames of Tekscan sensor sheet output at medium excitation level (300 N) and 20 Nm bolt torque level are shown. The left frame was recorded 0.03076 s after the hammer impact at $t = 0.57675$ s. This time shift (with respect to the hammer impact) of the frames shown in Fig. 24.10 is chosen in order to be able to illustrate the change of the dynamic contact pressure mainly by means of the first mode.² For a better visibility of the dynamic portion of the contact pressure, the static pressure distribution as seen in Fig. 24.9(right) is subtracted from the original sensor sheet output data which consists of static and dynamic portions of the contact pressure.

²Immediately after the hammer impact, the sensor sheet output consists of a superposition of the dynamic contact pressures generated by all participating modes in the frequency band excited by the impact (unfortunately, no low-pass filter could be applied on the output signal of the sensor sheet). Assuming a similar modal damping for all modes, the higher modes decay faster than the lower modes due to their higher vibration frequencies. Thus it seems reasonable that some time after the impact, the first mode is dominating the response and most of the dynamic contact pressure is generated by that first mode.

Comparing the three frames in Fig. 24.10, one can clearly see the change of the pressure distribution in the area outside of the bolt holes towards the short edges of the interface. There, an unloading is followed by an increase in pressure. Additionally, one can observe a change of the contact pressure directly inside the pressure cones of the bolts. This demonstrates the Tekscan system's ability of capturing the evolution of the interfacial contact pressure under dynamic loading.

24.5 Dynamic Interface Measurements

In this section, the results of the interface measurements taken during the impact hammer tests associated with Fig. 24.7 are presented. While the results shown in Fig. 24.7 are the average of five hits in the respective configuration, the results of the interface measurements presented in this section are the results at the first hit of each set of five hits. Measurements were taken at 5 and 20 Nm bolt torque level, each level first excited at the low (60 N), then at the medium (300 N) and finally at the high (600 N) impact force level.

In Fig. 24.11, the normalized contact area over time is shown for both bolt torque levels. The contact area is calculated by summing up the number of sensor pixels with a raw sum greater than zero for each measurement frame, yielding one scalar value per frame. The normalization is with respect to the contact area of a measurement frame prior to the hammer impact, i.e., the contact area under static loading. Comparing the left hand (5 Nm) and right hand (20 Nm) side of Fig. 24.11, one can observe that especially during the first 0.1 s after the impact, the relative loss of contact area at medium and high excitation is significantly higher for the 5 Nm bolt torque level than for 20 Nm. This corresponds to the frequency shift in Fig. 24.7, since the less pre-stressed interface at 5 Nm allows more motion in normal direction than at 20 Nm, i.e., softening the system by additional separation.

All output signals of the normalized contact area in Fig. 24.11 show the same overall behavior: the signal drops after the hammer impact, followed by an oscillation back towards the initial value of one. It has to be noted that at in Fig. 24.11, the normalized contact area for the 20 Nm case does not go back to one again. Considering the (positive) slope of the output signal towards the end, the most probable explanation is that the signal acquisition time is insufficient for the 20 Nm case and the responses at the respective excitation levels have not fully decayed.

The relative change of the contact pressure is shown in Fig. 24.12. The normalized raw sum of each measurement frame is the sum of the raw sum values of all sensor pixels (cf. Sect. 24.2.2), normalized with respect to the sum of the raw sum values under static loading, analogously to the normalized contact area. The same measurement frame was used for the normalization of the raw sum and for the normalization of the corresponding contact area. Taking a look at Fig. 24.12, we see that the relative loss of the contact pressure under medium and high excitation is significantly higher for the 5 Nm bolt torque level than for 20 Nm.

The output signals of the normalized raw sum values for the 20 Nm case (right hand side Fig. 24.12) show the same behavior as the normalized contact areas: the signal drops after the hammer impact, followed by an oscillation back towards the initial value of one. Contrary to that, the normalized raw sum values for the three excitation levels with 5 Nm bolt torque clearly exhibit a difference at the end of the respective measurements. At a low excitation level, the normalized raw sum equals one again. After the impact at the medium excitation, the normalized raw sum does not reach again the initial value of one (here, the slope of the output signal is zero towards the end, implying a fully decayed response). Keeping in mind the order of the excitation levels (low, medium, high), this strongly indicates a different contact state in the interface after

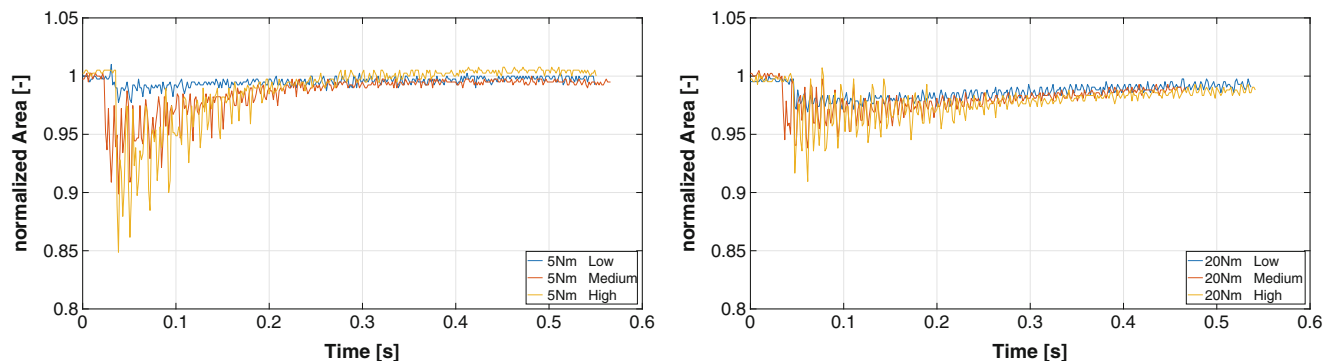


Fig. 24.11 Normalized contact area over time at (left) 5 Nm and (right) 20 Nm bolt torque level for low, medium and high excitation

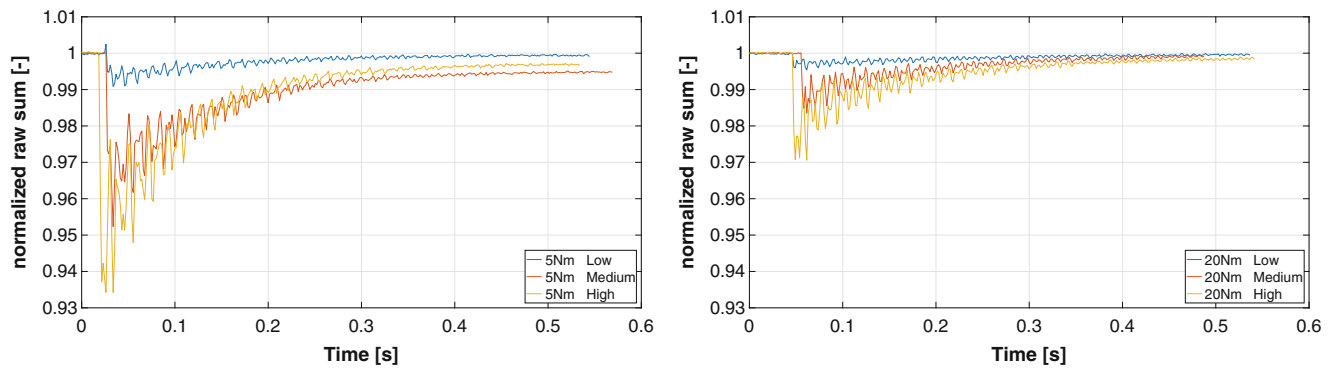


Fig. 24.12 Normalized raw sum over time at (left) 5 Nm and (right) 20 Nm bolt torque level for low, medium and high excitation

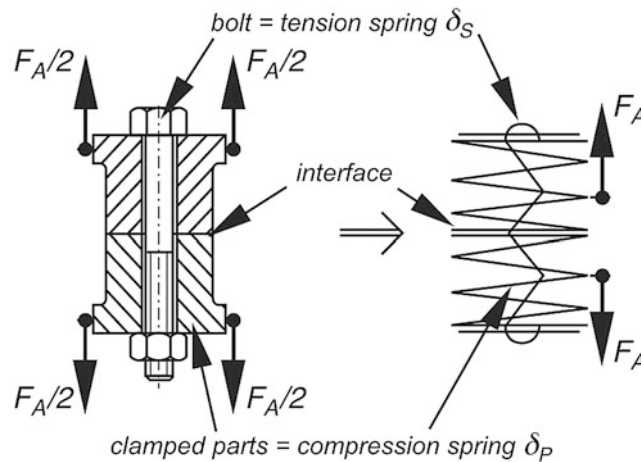


Fig. 24.13 Conversion of a clamped joint into the spring model [20]

the impact, i.e., that microslip occurred due to the impact. The same holds for the normalized raw sum before and after the impact at high excitation level. This observation corresponds to the splitting of the frequency-vs-amplitude curves at 5 Nm bolt torque level in Fig. 24.7.

An interesting observation at both bolt torque levels is the simultaneous drop of the contact area (Fig. 24.11) and the corresponding contact pressure (Fig. 24.12) which, at a first glance, seems somewhat counter-intuitive. Under the assumption of a constant bolt load, one would expect the contact pressure to increase when the contact area gets smaller and vice versa. A possible explanation can be given by using the perspective that the bolts and the beams can be represented as two springs in parallel [20]. The representation of the bolts as tension springs and the beams as compression springs is illustrated in Fig. 24.13.

In the static case, the bolt torque generates an axial force in the bolts and a corresponding reaction force in the beams. Because of the bolts' compliance δ_S and due to the axial force, the bolts elongate. The corresponding reaction force compresses the beams due to the beams' compliance δ_P . This induces a tensile stress in the bolts and a compression stress in the beams, the latter giving us the static contact pressure distribution measured in the interface (e.g., Fig. 24.9). Now we consider a stress wave propagating through the lap joint due to the hammer impact. This stress wave induces an additional axial force F_A acting on the clamped joint, as depicted in Fig. 24.13. Due to F_A and because of the axial compliance δ_S , the bolts additionally elongate, yielding a displacement u_{ax} and an additional tensile stress in the bolts. Because both "springs" are in parallel, the axial compression of the beams is reduced by the same displacement u_{ax} . Now, by virtue of δ_P , the axial force acting on the beams is reduced which in turn allows for additional separation and a reduction of the contact pressure in the interface at the same time. This redistribution of the axial forces and the corresponding tensile and compression stresses takes place as long as the stress wave inducing F_A propagates through the lap joint.³

³Since we only measure the change of the contact area and the contact pressure in the interface and not the additional tensile stress in the bolts, this creates the impression of an unloading of the interface at larger response amplitudes.

Therefore, the simultaneous drop of the contact area and the contact pressure in the interface could be explained with a temporary transfer of potential (i.e., spring) energy from the beams to the bolts.

24.6 Conclusions and Perspectives

In this work, a new approach for dynamically measuring contact pressures in a bolted assembly was explored. This initial study focused on the capability of the new technique, electronic pressure films, to capture the transient events associated with impact hammer testing. The experiments found that significant variations in contact pressure occurred as a stress wave propagated through the interface and that the electronic pressure film could adequately resolve this effect.

Additionally, the preliminary results from these experiments indicate that several commonly held assumptions for modeling jointed structures may be invalid: that contact pressure is constant under the frustum of the bolt, that the system can be approximated to have no modal coupling, and that there is no dynamic impact internal to the interface. Instead, this research presents evidence to the contrary for each of these common assumptions. Future work must rigorously investigate these assumptions in order to develop a new approach for modeling jointed structures. In particular, by exciting the BRBS with a shaker at a frequency close to a natural frequency, the interfacial contact pressure interactions due to the mode belonging to that particular natural frequency could be isolated and investigated, thus elucidating new understanding to the physics of joint dynamics and the nature of the nonlinear coupling observed.

Acknowledgements This research was conducted at the 2017 Nonlinear Dynamics of Coupled Structures and Interfaces Summer Research Program, sponsored by Rice University.

The authors would also like to thank the “Fond Interministeriel Unique” that funds the project CLIMA and the “Bourse-Oréal UNESCO Pour les Femmes et la Science” encouraging women to pursue careers in science.

The authors would also like to thank the National Natural Science Foundation of China (Grant No.51705422).

References

1. Woo, K.L., Thomas, T.R.: Contact of rough surfaces: a review of experimental work. *Wear* **58**(2), 331–340 (1980)
2. Ovcharenko, A., Halperin, G., Etsion, I., Varenberg, M.: A novel test rig for in situ and real time optical measurement of the contact area evolution during pre-sliding of a spherical contact. *Tribol. Lett.* **23**(1), 55–63 (2006)
3. Eguchi, M., Shibamiya, T., Yamamoto, T.: Measurement of real contact area and analysis of stick/slip region. *Tribol. Int.* **42**(11), 1781–1791 (2009)
4. Dwyer-Joyce, R.S.: The application of ultrasonic NDT techniques in tribology. *Proc. Inst. Mech. Eng. J: J. Eng. Tribol.* **219**(5), 347–366 (2005)
5. Pau, M., Baldi, A.: Application of an ultrasonic technique to assess contact performance of bolted joints. *J. Press. Vessel. Technol.* **129**(1), 175–185 (2007)
6. Du, F., Hong, v., Xu, Y.: An acoustic model for stiffness measurement of tribological interface using ultrasound. *Tribol. Int.* **73**, 70–77 (2014)
7. Du, F., Li, B., Zhang, J., Zhu, Q.M., Hong, J.: Ultrasonic measurement of contact stiffness and pressure distribution on spindle–holder taper interfaces. *Int. J. Mach. Tools Manuf.* **97**, 18–28 (2015)
8. Marshall, M.B., Zainal, I., Lewis, R.: Influence of the interfacial pressure distribution on loosening of bolted joints. *Strain* **47**(s2), 65–78 (2011)
9. Fukubayashi, T., Kurosawa, H.: The contact area and pressure distribution pattern of the knee: a study of normal and osteoarthrotic knee joints. *Acta Orthop. Scand.* **51**(1–6), 871–879 (1980)
10. Dörner, F., Körblein, C.H., Schindler, C.H.: On the accuracy of the pressure measurement film in hertzian contact situations similar to wheel-rail contact applications. *Wear* **317**(1), 241–245 (2014)
11. Fregly, B.J., Sawyer, W.G.: Estimation of discretization errors in contact pressure measurements. *J. Biomech.* **36**(4), 609–613 (2003)
12. Drewniak, E.I., Crisco, J.J., Spenciner, D.B., Fleming, B.C.: Accuracy of circular contact area measurements with thin-film pressure sensors. *J. Biomech.* **40**(11), 2569–2572 (2007)
13. Brake, M.R.W.: *The Mechanics of Jointed Structures: Recent Research and Open Challenges for Developing Predictive Models for Structural Dynamics*. Springer International Publishing (2017). ISBN:9783319568164
14. Dossogne, T., Jerome, T.W., Lancereau, D.P.T., Smith, S.A., Brake, M.R.W., Pacini, B.R., Reuss, P., Schwingshackl, C.W.: Experimental assessment of the influence of interface geometries on structural dynamic response. In: *Dynamics of Coupled Structures*, vol. 4, pp. 255–261. Springer (2017)
15. Smith, S., Bilbao-Ludena, J.C., Catalfamo, S., Brake, M.R.W., Reuß, P., Schwingshackl, C.W.: The effects of boundary conditions, measurement techniques, and excitation type on measurements of the properties of mechanical joints. In: *Nonlinear Dynamics, Volume 1: Proceedings of the 33rd IMAC, a Conference and Exposition on Structural Dynamics, 2015*, pp. 415–431. Springer (2016)
16. Catalfamo, S., Smith, S.A., Morlock, F., Brake, M.R.W., Reuß, P., Schwingshackl, C.W., Zhu, W.D.: Effects of experimental methods on the measurements of a nonlinear structure. In: *Dynamics of Coupled Structures, Volume 4: Proceedings of the 34th IMAC, a Conference and Exposition on Structural Dynamics 2016*, pp. 491–500. Springer (2016)
17. Tekscan Inc.: Datasheet pressure mapping sensor 5101 (2017). [Online; accessed 16 Oct 2017]

18. Kerschen, G., Worden, K., Vakakis, A.F., Golinval, J.-C.: Past, present and future of nonlinear system identification in structural dynamics. *Mech. Syst. Signal Process.* **20**(3), 505–592 (2006)
19. Deaner, B.J., Allen, M.S., Starr, M.J., Segalman, D.J., Sumali, H.: Application of viscous and iwan modal damping models to experimental measurements from bolted structures. *J. Vib. Acoust.* **137**(2), 021012 (2015)
20. Ingenieure, V.D.: VDI 2230 part 1: systematic calculation of high duty bolted joints: joints with one cylindrical bolt. VDI-guideline. VDI-Gesellschaft Entwicklung Konstruktion Vertrieb (2003)



Chapter 25

An Improved Shape Reconstruction Methodology for Long Rod Like Structures Using Cosserat Kinematics- Including the Poisson's Effect

Mayank Chadha and Michael D. Todd

Abstract In this paper, we present an improved methodology for the global shape reconstruction of rod-like structures that capture the effect of curvature, shear, torsion, axial deformation, and Poisson's transformation. The inclusion of Poisson's effect relaxes Euler-Bernoulli's rigid cross-section assumption such that the cross-section could now undergo planar deformation (shrinking or expansion in the same plane). This scenario is particularly useful for the inflatable structures and pipelines subjected to large radial pressure.

The theory of shape sensing utilizes the concept of curve framing using Cosserat director triad also called as Cosserat kinematics. The idea is to develop an algorithm to reconstruct the global shape of the rods using the local differential geometry parameters (finite strain parameters) of the midcurve. The deformed configuration of the object lies in $\mathbb{R}^3 \times SO(3) \times \mathbb{R}$ space. The presented theory exploits localized linearization approach that helps to obtain local basis set for the approximation of the midcurve position vector and the director triad, whereas moving least square approximation is utilized to estimate the axial strain field. The uniaxial surface strain incorporating all the effects mentioned above is derived and used to develop the shape-sensing algorithm. A simulation describing the idea is presented at the end.

Keywords Shape sensing · Cosserat rod theory · Director frame · Local basis function · Scalar surface strain

25.1 Introduction

This paper extends the theory of shape sensing developed by Todd et al. [1] and Chadha and Todd [2, 3] to include Poisson's effect along with curvature, shear, torsion and axial deformation. This formulation relaxes Euler-Bernoulli's rigid cross-section. The cross-section remains planar but it can undergo deformation in the plane. The out of plane deformation due to warping is still ignored. Consideration of the Poisson's effect is beneficial in the case of pipes subjected to internal radial pressure or in case of slender inflatable objects.

This theory is geometrical exact and fully nonlinear, so it can capture large deformations. In mathematical terms, this theory involves defining the local differential geometric parameter set (called as "finite strain parameters"), estimating these parameters from the surface strain measurements, and finally using them to reconstruct the deformed configuration (that can be described as differential geometry at large). The configuration of deformable slender objects consists of the beam midcurve framed by the body-centered director triad. The initial description of this type of rod was harnessed by Cosserat and Cosserat [4] to arrive at the finite strain theory of rods and shell. Interested readers may refer to Ericksen and Truesdell [5], Chadha and Todd [6], and the references therein for a brief history and details on this subject.

The subject of shape sensing is a topic of great interest owing to its application in structural health monitoring, smart tethers, and robotic surgical and catheterization applications. Researchers have used various curve framing approaches to capture curvature effects. We maintain a body-centered frame in the unsheared cross-section (as mentioned in Todd et al. [1]) and the orthogonal director triad for a general case to capture torsion and shear (as mentioned in Chadha and Todd [2, 3]).

As in [1, 2], we focus on uniaxial surface strain values obtained from any type of multiplexed sensing approach, including fiber Bragg grating (FBG), Rayleigh backscatter, or conventional resistive strain gauge.

M. Chadha · M. D. Todd (✉)

Department of Structural Engineering, University of California San Diego, La Jolla, CA, USA
e-mail: machadha@ucsd.edu; mdtodd@ucsd.edu

The remainder of the paper is arranged as follows: Section 25.2 details the geometry of the deformed configuration of the beam and establishes various geometric relationships. Section 25.3 obtains the expression for uniaxial scalar surface strain including the Poisson's effect. Section 25.4 describes the solution approach to approximate the deformed configuration. Finally, in Sect. 25.5, we present a simulation comparing the exact deformed configuration to the predicted results followed by some conclusions.

25.2 Geometry of the Deformed Configuration of the Beam

A rod can be considered as a mathematical object described by a spatial curve in \mathbb{R}^3 (the locus of cross-sectional geometric centroid, also called midcurve) parameterized by the arclength $\xi_1 \in \mathbb{R}$, framed by a body-centered Cosserat director triad $\{\mathbf{d}_i(\xi_1)\}$. We consider that the initial unstrained configuration of the beam $\Omega_0 \subset \mathbb{R}^3$ to be straight. Section [2.1] of [2, 3] details the geometric description of the beam configuration. The inclusion of Poisson's effect does not change the position vector of the midcurve and the curve framing by the director triad $\{\mathbf{d}_i(\xi_1)\}$; all it changes is the position vector of the material point in the deformed state, which we shall explore further. As a matter of completion, we detail the necessary geometry, in same sense as section [2.1] of [2, 3].

Consider a fixed orthogonal frame $\{\mathbf{E}_i\}$. The domain of the beam is defined by the material point $\{\xi_1, \xi_2, \xi_3\}$, such that the origin of the frame $\{\mathbf{E}_i\}$ is at $\{\xi_i = 0\}$ with $i = 1 \dots 3$. Let L_0 represent the length of midcurve in the undeformed reference state Ω_0 , such that $\xi_1 \in [0, L_0]$. The position vector of any material point in the undeformed configuration Ω_0 is given by $\mathbf{R}_0(\xi_1, \xi_2, \xi_3) = \xi_i \mathbf{E}_i$.

Let us consider that the undeformed (and unstrained) configuration Ω_0 is strained and it deforms to the configuration $\Omega \subset \mathbb{R}^3$. The position vector $\boldsymbol{\varphi}(\xi_1) = \varphi_i \mathbf{E}_i$, represents the midcurve of the deformed configuration. The orientation of any cross-section in the deformed configuration Ω is defined by the set of orthogonal Cosserat director triad $\{\mathbf{d}_i(\xi_1)\}$, such that $\mathbf{d}_i(\xi_1) = d_{ij}(\xi_1) \mathbf{E}_j$. The vector $\mathbf{d}_1(\xi_1)$ is perpendicular to the cross-section and the vectors $\{\mathbf{d}_2(\xi_1), \mathbf{d}_3(\xi_1)\}$ span the cross-section of the beam at ξ_1 . Therefore, it may be interpreted that the director field $\{\mathbf{d}_i(\xi_1)\}$ framing the deformed configuration of the beam may be obtained from the fixed frame $\{\mathbf{E}_i\}$ by means of a finite rotation, or

$$\mathbf{d}_i(\xi_1) = \mathbf{Q}(\xi_1) \mathbf{E}_i. \quad (25.1)$$

Here, $\mathbf{Q}(\xi_1)$ represents family of orthogonal matrices that belongs to $SO(3)$ rotational groups. Hence, they satisfy $\mathbf{Q}\mathbf{Q}^T = \mathbf{I}$ and $\det \mathbf{Q} = 1$. The orthogonal tensor $\mathbf{Q}(\xi_1)$ is a curve on the manifold $SO(3)$. The tangent vector to this curve in $SO(3)$ is expressed as $\mathbf{Q}_{,\xi_1}$ that represents the tangent space of $SO(3)$. It can be easily obtained that $\mathbf{Q}_{,\xi_1} \mathbf{Q}^T = \mathbf{K}(\xi_1)$ such that $\mathbf{K}(\xi_1)$ is the linear space of skew symmetric matrices. Therefore, there exists an axial vector $\boldsymbol{\kappa} = \bar{\kappa}_i \mathbf{d}_i$ associated with $\mathbf{K}(\xi_1)$. Therefore, from (25.1),

$$\mathbf{d}_{i,\xi_1} = (\mathbf{Q}_{,\xi_1} \mathbf{Q}^T) \mathbf{d}_i = \mathbf{K} \mathbf{d}_i = \boldsymbol{\kappa} \times \mathbf{d}_i. \quad (25.2)$$

The vector $\boldsymbol{\kappa} = \bar{\kappa}_i \mathbf{d}_i$ represents the Darboux vector associated with the infinitesimal rotation tensor \mathbf{K} , parametrized by ξ_1 . Equation (25.2) represents the differential equation that governs the evolution of the directors and hence the cross-sections.

Let the midcurve $\boldsymbol{\varphi}(\xi_1)$ (parametrized by the undeformed arc-length) be framed by an orthogonal body centered frame $\{\mathbf{T}, \mathbf{V}, \mathbf{H}\}$ such that the vector $\{\mathbf{T}, \mathbf{V}\}$ spans the pitch angle plane and $\mathbf{T}(\xi_1)$ is the tangent vector to the midcurve. Thus, $\mathbf{H} = \mathbf{T} \times \mathbf{V}$. If there is no shearing in the beam, the triad $\{\mathbf{T}, \mathbf{V}, \mathbf{H}\}$ coincides with $\{\mathbf{d}_i\}$. Let $\theta(\xi_1)$ and $\phi(\xi_1)$ represent the pitch and yaw angle of the mid-curve. Therefore, from Fig. 25.4 of Chadha and Todd [6], with $\phi_p(\xi_1) = \theta(\xi_1)$ and $\phi_y(\xi_1) = \phi(\xi_1)$,

$$\begin{bmatrix} \mathbf{T}(\xi_1) \\ \mathbf{V}(\xi_1) \\ \mathbf{H}(\xi_1) \end{bmatrix} = \begin{bmatrix} \cos \theta(\xi_1) \cos \phi(\xi_1) & \sin \theta(\xi_1) & \cos \theta(\xi_1) \sin \phi(\xi_1) \\ -\sin \theta(\xi_1) \cos \phi(\xi_1) & \cos \theta(\xi_1) & -\sin \theta(\xi_1) \sin \phi(\xi_1) \\ -\sin \phi(\xi_1) & 0 & \cos \phi(\xi_1) \end{bmatrix} \begin{bmatrix} \mathbf{E}_1 \\ \mathbf{E}_2 \\ \mathbf{E}_3 \end{bmatrix} = \mathbf{W}_1 \begin{bmatrix} \mathbf{E}_1 \\ \mathbf{E}_2 \\ \mathbf{E}_3 \end{bmatrix}. \quad (25.3)$$

Assume that the deformed arc length coordinate is given by the parameter s . The infinitesimal length of the undeformed mid-curve $d\xi_1$ deforms to ds causing axial strain $\epsilon(\xi_1)$. If the object is subjected to shear and torsion, the orientation of the cross-section changes. The tangent vector is no longer perpendicular to the cross-section. The shearing effect is quantified by the angles $\gamma_{11}(\xi_1)$, $\frac{\pi}{2} - \gamma_{12}(\xi_1)$ and $\frac{\pi}{2} - \gamma_{13}(\xi_1)$ subtended by the directors $\mathbf{d}_1, \mathbf{d}_2$ and \mathbf{d}_3 with the tangent vector $\mathbf{T}(\xi_1) = \frac{\partial \boldsymbol{\varphi}}{\partial s}$. Hence, we note the following relations:

$$e = \frac{ds - d\xi_1}{d\xi_1}; \frac{\partial \xi_1}{\partial s} = \frac{1}{1+e}, \quad (25.4)$$

$$\boldsymbol{\varphi}_{,s} \cdot \mathbf{d}_i = \frac{1}{1+e} \boldsymbol{\varphi}_{,\xi_1} \cdot \mathbf{d}_i = \begin{cases} \cos \gamma_{1i}, & \text{when } i = 1 \\ \sin \gamma_{1i}, & \text{when } i = 2, 3 \end{cases}.$$

Therefore,

$$\boldsymbol{\varphi}_{,\xi_1} = (1+e) \cos \gamma_{11} \mathbf{d}_1 + (1+e) \sin \gamma_{12} \mathbf{d}_2 + (1+e) \sin \gamma_{13} \mathbf{d}_3 = (1+e) \mathbf{T}. \quad (25.5)$$

To define a unique relation between $\{\mathbf{T}, \mathbf{V}, \mathbf{H}\}$ and $\{\mathbf{d}_i\}$, we introduce the parameters $\alpha_1(\xi_1)$, $\alpha_2(\xi_1)$ and $\alpha_3(\xi_1)$, defined as the angles subtended by the directors \mathbf{d}_1 , \mathbf{d}_2 and \mathbf{d}_3 with the vector \mathbf{V} respectively. Therefore,

$$\begin{bmatrix} \mathbf{T}(\xi_1) \\ \mathbf{V}(\xi_1) \\ \mathbf{H}(\xi_1) \end{bmatrix} = \mathbf{W}_2 \begin{bmatrix} \mathbf{d}_1 \\ \mathbf{d}_2 \\ \mathbf{d}_3 \end{bmatrix} \quad (25.6)$$

The component of the orthogonal tensor \mathbf{Q} in Eq. (25.1) can be obtained from Eqs. (25.3) and (25.6). The component of orthogonal matrix \mathbf{W}_2 , the tensor \mathbf{Q} and the Darboux vector can be obtained as in Chadha and Todd [6]. Note that \mathbf{Q} is orthogonal if and only if the constraints on the parameters (α_i, γ_{1i}) as mentioned in Chadha and Todd [6] are satisfied. From Eqs. (25.2) and (25.5) we arrive at an important equation that governs the evolution of the system as

$$\begin{bmatrix} \boldsymbol{\varphi}_{,\xi_1} \\ \mathbf{d}_{1,\xi_1} \\ \mathbf{d}_{2,\xi_1} \\ \mathbf{d}_{3,\xi_1} \end{bmatrix} = \begin{bmatrix} 0 & (1+e) \cos \gamma_{11} & (1+e) \sin \gamma_{12} & (1+e) \sin \gamma_{13} \\ 0 & 0 & \bar{\kappa}_3 & -\bar{\kappa}_2 \\ 0 & -\bar{\kappa}_3 & 0 & \bar{\kappa}_1 \\ 0 & \bar{\kappa}_2 & -\bar{\kappa}_1 & 0 \end{bmatrix} \begin{bmatrix} \boldsymbol{\varphi} \\ \mathbf{d}_1 \\ \mathbf{d}_2 \\ \mathbf{d}_3 \end{bmatrix} \quad (25.7)$$

Note on the smoothness requirement of the midcurve

Note that unique smooth curve framing by $\{\mathbf{T}, \mathbf{V}, \mathbf{H}\}$ and hence by $\{\mathbf{d}_i\}$ requires a regular C^2 curve that can have degeneracy. Thus, this frame has a relaxed condition of existence compared to the Frenet frame that needs regular C^3 non-degenerate curves.

25.3 Kinematics of the Beam-Obtaining Uniaxial Scalar Strain

25.3.1 Strain Vector and Deformation Gradient Tensor

The position vector of any material point $\{\xi_1, \xi_2, \xi_3\}$ in the deformed configuration Ω is given by

$$\mathbf{R}(\xi_1, \xi_2, \xi_3) = \boldsymbol{\varphi}(\xi_1) + \widehat{\xi}_2 \mathbf{d}_2(\xi_1) + \widehat{\xi}_3 \mathbf{d}_3(\xi_1) \quad (25.8a)$$

where

$$\widehat{\xi}_i(\xi_1, \xi_i) = (1 - e(\xi_1) \nu) \xi_i \text{ for } i = 2 - 3, \quad (25.8b)$$

and ν represents the Poisson's ratio. Eq. (25.8b) represents Poisson's transformation of the cross-section. To obtain the deformation gradient tensor \mathbf{F} for the problem, we define the infinitesimal tangent vector $d\mathbf{R}_0 = d\xi_1 \mathbf{E}_1$ and $d\mathbf{R}$ in Ω_0 and Ω configuration. Therefore, the tensor \mathbf{F} can be obtained as,

$$\mathbf{F} = \frac{d\mathbf{R}}{d\mathbf{R}_0} = \sum_{i=1}^3 \mathbf{R}_{,\xi_i} \otimes \mathbf{E}_i \quad (25.9)$$

From Eq. (25.8a, b), we obtain the following,

$$\frac{\partial \mathbf{R}}{\partial \xi_i} = \begin{cases} \left(\boldsymbol{\varphi}_{\cdot, \xi_1} + \widehat{\xi}_2 \mathbf{d}_{2, \xi_1} + \widehat{\xi}_3 \mathbf{d}_{3, \xi_1} + \widehat{\xi}_{2, \xi_1} \mathbf{d}_2 + \widehat{\xi}_{3, \xi_1} \mathbf{d}_3 \right) & \text{when } i = 1; \\ (1 - e(\xi_1) \nu) \mathbf{d}_i, & \text{when } i = 2, 3. \end{cases} = \boldsymbol{\lambda}_i + \mathbf{d}_i. \quad (25.10a)$$

where

$$\widehat{\xi}_{i, \xi_1} = -e_{\cdot, \xi_1} \nu \xi_i \text{ for } i = 2 - 3. \quad (25.10b)$$

Using the results from Eq. (25.7), we obtain the expression of the vector parameter $\boldsymbol{\lambda}_i$ as

$$\begin{aligned} \boldsymbol{\lambda}_1 = & \left(((1 + e) \cos \gamma_{11} - 1) + \widehat{\xi}_3 \bar{\kappa}_2 - \widehat{\xi}_2 \bar{\kappa}_3 \right) \mathbf{d}_1 + \left((1 + e) \sin \gamma_{12} - \widehat{\xi}_3 \bar{\kappa}_1 + \widehat{\xi}_{2, \xi_1} \right) \mathbf{d}_2 \\ & + \left((1 + e) \sin \gamma_{13} + \widehat{\xi}_{3, \xi_1} + \widehat{\xi}_2 \bar{\kappa}_1 \right) \mathbf{d}_3; \end{aligned} \quad (25.11)$$

$$\boldsymbol{\lambda}_i = \left(\widehat{\xi}_{2, \xi_i} - 1 \right) \mathbf{d}_i = (-\nu e) \mathbf{d}_i, \quad \text{for } i = 2 \text{ and } 3.$$

Therefore, using Eqs. (25.8a, b and 25.9), we can obtain the deformation gradient tensor as,

$$\mathbf{F} = \sum_{i=1}^3 (\boldsymbol{\lambda}_i + \mathbf{d}_i) \otimes \mathbf{E}_i = \sum_{i=1}^3 \boldsymbol{\lambda}_i \otimes \mathbf{E}_i + \mathbf{Q} \quad (25.12)$$

We define the strain vector as

$$\boldsymbol{\epsilon} = \sum_{i=1}^3 \left(\frac{\partial \mathbf{R}}{\partial \xi_i} - \mathbf{d}_i \right) = \sum_{i=1}^3 \boldsymbol{\lambda}_i \quad (25.13)$$

25.3.2 The Orientation of an Arbitrary Strain Gauge in the Deformed State (Measurement Model)

Consider a strain gauge attached to a typical material point on the surface $q \equiv (\xi_2^g, \xi_3^g)$ on the cross-section $\blacksquare (\xi_1^g)$ in the undeformed configuration Ω_0 . We assume that the strain gauge is completely attached to the material. Therefore, it maintains the angle μ with the normal vector to the cross-section. In the deformed state, the unit direction vector of the strain gauge would lie on the plane spanned the $\mathbf{d}_1 - \mathbf{Q}_t$ as described in Fig. 25.1. Let $\mathbf{r}_{pq} = \widehat{\xi}_2^g \mathbf{d}_2 + \widehat{\xi}_3^g \mathbf{d}_3$ represent the vector joining the centroid of the cross-section $\blacksquare (\xi_1^g)$ to the material point q in the deformed state. The tangent vector \mathbf{Q}_t for the cross-section subjected to the Poisson's contraction can be obtained as

$$\mathbf{Q}_t = \mathbf{d}_1 \times \frac{\mathbf{r}_{pq}}{|\mathbf{r}_{pq}|} = - \left(\frac{\widehat{\xi}_3^g}{\sqrt{\widehat{\xi}_2^{g2} + \widehat{\xi}_3^{g2}}} \right) \mathbf{d}_2 + \left(\frac{\widehat{\xi}_2^g}{\sqrt{\widehat{\xi}_2^{g2} + \widehat{\xi}_3^{g2}}} \right) \mathbf{d}_3 = - \left(\frac{\xi_3^g}{\sqrt{\xi_2^{g2} + \xi_3^{g2}}} \right) \mathbf{d}_2 + \left(\frac{\xi_2^g}{\sqrt{\xi_2^{g2} + \xi_3^{g2}}} \right) \mathbf{d}_3. \quad (25.14)$$

For simplicity, we assume the cross-section to be circular with the radius r in the undeformed state. Therefore, if σ is angle subtended by the vector \mathbf{r}_{pq} with the vector \mathbf{d}_2 , $\xi_2^g = r \cos \sigma$ and $\xi_3^g = r \sin \sigma$. Therefore, we obtain $\mathbf{Q}_t = -\sin \sigma \mathbf{d}_2 + \cos \sigma \mathbf{d}_3$. Therefore, the unit direction vector of the strain gauge in the deformed configuration \mathbf{n} is given as.

$$\mathbf{n} = \cos \mu \mathbf{d}_1 + \sin \mu \mathbf{Q}_t = \cos \mu \mathbf{d}_1 - \sin \mu \sin \sigma \mathbf{d}_2 + \sin \mu \cos \sigma \mathbf{d}_3 \quad (25.15)$$

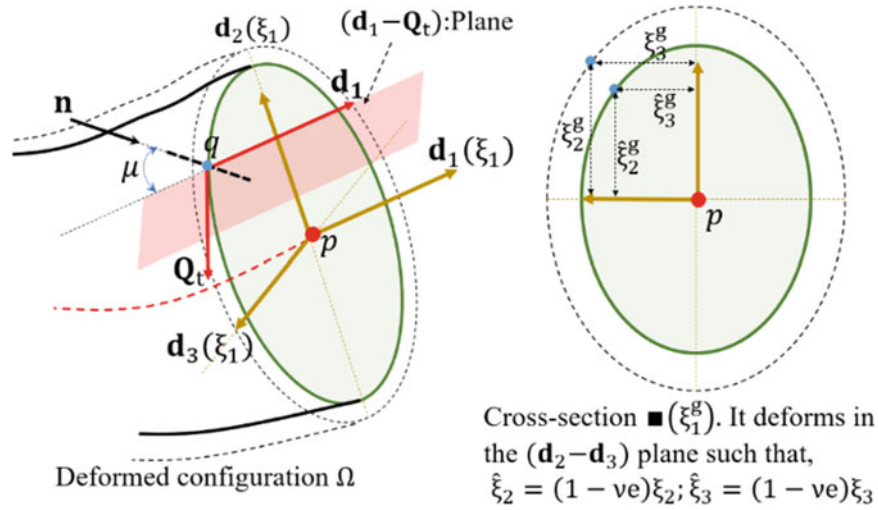


Fig. 25.1 Orientation of the strain gauge in the deformed configuration

Notice that despite the inclusion of Poisson's effect, the unit direction vector \mathbf{n} is identical to the one in Chadha and Todd [2]. This is because Poisson's effect leads to proportionate planar deformation depending on average axial strain, thereby preserving the geometric form of the cross-section.

From Eqs. (25.11, 25.13 and 25.15), and considering $\xi_2 = \xi_2^g = r \cos \sigma$, $\xi_3 = \xi_3^g = r \sin \sigma$, $\widehat{\xi}_{3,\xi_1}(\xi_3^g) = -e_{,\xi_1} v \xi_3 = -e_{,\xi_1} v r \sin \sigma$ and $\widehat{\xi}_{2,\xi_1}(\xi_2^g) = -e_{,\xi_1} v \xi_2 = -e_{,\xi_1} v r \cos \sigma$, the unit scalar surface strain ε for the strain gauge with the unit direction vector \mathbf{n} in Ω can be obtained as

$$\varepsilon = \boldsymbol{\epsilon} \cdot \mathbf{n} = [\cos \mu (((1 + e) \cos \gamma_{11} - 1) + (1 - ev) r \sin \sigma \bar{\kappa}_2 - (1 - ev) r \cos \sigma \bar{\kappa}_3) - \sin \mu \sin \sigma ((1 + e) \sin \gamma_{12} - (1 - ev) r \sin \sigma \bar{\kappa}_1) + \sin \mu \cos \sigma ((1 + e) \sin \gamma_{13} + (1 - ev) r \cos \sigma \bar{\kappa}_1)] - \sin \mu \sin \sigma (-ve) + \sin \mu \cos \sigma (-ve) \quad (25.16)$$

Interestingly there is no term containing $e_{,\xi_1}$ in Eq. (25.16). It is not hard to prove that the expression of the surface scalar strain ε for the strain gauge on $(\mathbf{d}_1 - \mathbf{Q}_t)$ plane does not have $e_{,\xi_1}$ dependence, irrespective of the shape of cross-section. Even though estimation of the parameter $e_{,\xi_1}$ is required to obtain strain vector in Eq. (25.13), but there is no need to estimate $e_{,\xi_1}$ for shape sensing. It is worth noting that the deformed configuration Ω of the beam can be described by $(\boldsymbol{\varphi}(\xi_1), \mathbf{Q}(\xi_1), \mathbf{e}(\xi_1))$ in the space $\mathbb{R}^3 \times SO(3) \times \mathbb{R}$. In fact, obtaining $e_{,\xi_1}$ at a given cross-section would involve an additional strain gauge in non-tangential plane (for instance in \mathbf{E}_2 direction in Ω_0 configuration.)

We define the following strain parameters,

$$S_1 = (1 + e) \cos \gamma_{11} - 1; \quad (25.17a)$$

$$S_2 = (1 + e) \sin \gamma_{12};$$

$$S_3 = (1 + e) \sin \gamma_{13};$$

$$S_4 = r \bar{\kappa}_1; S_5 = r \bar{\kappa}_2; S_6 = r \bar{\kappa}_3;$$

Hence,

$$e = \left((S_1 + 1)^2 + S_2^2 + S_3^2 \right)^{0.5} - 1 = S_7; \quad (25.17b)$$

Substituting Eq. (25.17a, b) into Eq. (25.16), we arrive at the equation of surface strain in terms of parameters S_i .

25.4 Solution Approach

As mentioned in the previous section that the deformed configuration belongs to $\mathbb{R}^3 \times SO(3) \times \mathbb{R}$ space, we present our solution strategy to obtain approximate configuration Ω_h that comprises of the midcurve position vector $\boldsymbol{\varphi}_h(\xi_1)$, director triad $\{\mathbf{d}_{n_i}\}$ and axial strain field $e_h(\xi_1)$. The solution to $\boldsymbol{\varphi}_h(\xi_1)$ and $\{\mathbf{d}_{n_i}\}$ is based on a localized linear basis approach, and $e_h(\xi_1)$ is estimated using moving least square approximation or equivalently, the reproducing Kernel approximation used in mesh-free methods.

25.4.1 An Approximate Solution for the Midcurve Position Vector and Director Triad

It is clear from Eq. (25.17a, b) that a minimum of 6 strain gauges across the cross-section is required to determine all the deformation parameters, the same as in Chadha and Todd [2]. Unlike Chadha and Todd [2], obtaining 6 strain parameters ($S_1 - S_6$) would involve solving a non-linear system of six simultaneous equations at a given cross-section. To obtain the approximate solution of the global deformed shape of the structure, we discretize the structure into N segments ($\bar{n} = 1, \dots, N$) with the center of each segment located at $\xi_{1\bar{n}}$. We attach 6 strain gauges at the right cross-section bounding the segment N at ξ_{1n} with $n = 1, \dots, N$. If we consider the left end to be fixed, the left cross-section of the first segment serves as the boundary condition. Thus, the scalar strain at the n^{th} cross-section and for the m^{th} strain gauge $\varepsilon_{n,m}$ can be obtained by substituting $S_i = S_{i_n}$, $\sigma = \sigma_{n,m}$ and $\mu = \mu_{n,m}$ in Eqs. (25.16 and 25.17a, b) as,

$$\varepsilon_{n,m} = \cos \mu_{n,m} (S_{1_n} + (1 - S_{7_n} \nu) \sin \sigma S_{5_n} - (1 - S_{7_n} \nu) \cos \sigma_{n,m} S_{6_n}) - \sin \mu_{n,m} \sin \sigma_{n,m} (S_{2_n} - (1 - S_{7_n} \nu) \sin \sigma_{n,m} S_{4_n} - \nu S_{7_n}) + \sin \mu_{n,m} \cos \sigma_{n,m} (S_{3_n} + (1 - S_{7_n} \nu) \cos \sigma_{n,m} S_{4_n} - \nu S_{7_n}) \quad (25.18)$$

Here, $\sigma_{n,m}$ is the angle subtended by the m^{th} strain gauge with the normal vector \mathbf{d}_1 on the cross-section of the n^{th} cross-section and S_{7_n} depends on other strain terms as per Eq. (25.17b). Note that unlike the definition of the deformed configuration of the beam in Chadha and Todd [2], here the cross-section also undergoes Poisson's transformation. Therefore, it is necessary to determine the approximate axial strain $e(\xi_1)$ along with the midcurve position vector $\boldsymbol{\varphi}(\xi_1)$ and the director triad $\{\mathbf{d}_i\}$. For the n^{th} cross-section, the discrete differential equations governing the configuration Ω is same as Chadha and Todd [2].

We use local linearization approach where the coefficients in the governing differential equation are linearized locally in each segment. We tractate a Taylor series expansion of the seven coefficients about the location of the cross-section $\xi_1 = \xi_{1n}$ to zeroth order, thereby reducing the system of differential Eq. (25.7) into a constant-coefficient system that admits exact solution, valid locally at each segment. The solution for the n^{th} segment is,

$$\boldsymbol{\varphi}_n(\xi_1) = \mathbf{A}_{n_1} \xi_1 + \mathbf{A}_{n_2} \sin\left(\frac{\xi_1 \gamma_n}{r}\right) + \mathbf{A}_{n_3} \cos\left(\frac{\xi_1 \gamma_n}{r}\right) + \mathbf{A}_{n_4} \quad (25.19a)$$

$$\mathbf{d}_{n_i}(\xi_1) = \mathbf{B}_{n_{i1}} \xi_1 + \mathbf{B}_{n_{i2}} \sin\left(\frac{\xi_1 \gamma_n}{r}\right) + \mathbf{B}_{n_{i3}} \cos\left(\frac{\xi_1 \gamma_n}{r}\right) + \mathbf{B}_{n_{i4}}, \text{ where } \gamma_n = \left(\sum_{i=4}^6 S_{i_n}^2\right)^{\frac{1}{2}} \quad (25.19b)$$

The vector constants $\mathbf{A}_{n_1} - \mathbf{A}_{n_4}$ in Eq. (25.21a) can be found as described in Appendix (A.2) of Chadha and Todd [2]. In fact, these vector constants ($\mathbf{A}_{n_1} - \mathbf{A}_{n_4}$ and $\mathbf{B}_{n_{i1}} - \mathbf{B}_{n_{i4}}$) are function of the strain parameters $S_{1_n} - S_{6_n}$ and the constants of integration. Hence, if there are N cross-sections, there are $12N$ constants of integration. Imposing continuity in each component of $\{\boldsymbol{\varphi}_n, \mathbf{d}_1, \mathbf{d}_2, \mathbf{d}_3\}$ between the segments gives $12(N - 1)$ constraints, and an appropriate boundary condition gives 12 additional conditions. The estimated value of the axial strain at the cross-section location can be obtained from Eq. (25.17b). If all the strain parameters S_{i_n} are zero (implying a point of degeneracy), then Chadha and Todd [2] showed that the solution basis has no singularity. The global approximate solution for $\boldsymbol{\varphi}_h(\xi_1)$ and $\{\mathbf{d}_{n_i}\}$ can be obtained by stitching together each of these local solutions using the Heaviside function as in Todd et al. [1].

25.4.2 Approximate Solution to the Axial Strain

Equation (25.17b) can be used to obtain the axial strain $e(\xi_{1_n})$ in the n^{th} cross-section. We approximate the axial strain field using Moving Least square approximation. We brief the approach here. Let $\mathbf{P}(\xi_1) = \{1, \xi_1, \xi_1^2, \dots, \xi_1^m\}^T$ represent set of m^{th} order polynomial basis set, ξ_{1_n} represent n^{th} location of discrete cross-section and $W(\xi_1 - \xi_{1_n})$ represent the moving weight function, then the approximate axial strain and curvature field is given as,

$$e_n(\xi_1) = \mathbf{P}^T(\xi_1) \mathbf{M}^{-1} \sum_{n=1}^N \mathbf{P}(\xi_{1_n}) e(\xi_{1_n}) W(\xi_1 - \xi_{1_n}) \quad (25.20a)$$

Where,

$$\mathbf{M} = \text{Moment matrix} = \sum_{n=1}^N \mathbf{P}(\xi_{1_n}) \mathbf{P}^T(\xi_{1_n}) W(\xi_1 - \xi_{1_n}); \quad (25.20b)$$

$$e(\xi_{1_n}) = \left((S_{1_n} + 1)^2 + S_{2_n}^2 + S_{3_n}^2 \right)^{0.5} - 1; \quad (25.20c)$$

One of the most commonly used weight function is cubic B spline, such that

$$W(\xi_1 - \xi_{1_n}) = W(z_n) = \begin{cases} \frac{2}{3} - 4z_n^2 + 4z_n^3, & \text{for } 0 \leq z_n \leq 0.5 \\ \frac{4}{3} - 4z_n + 4z_n^2 - \frac{4}{3}z_n^3, & \text{for } 0.5 \leq z_n \leq 1 \\ 0 & \text{otherwise} \end{cases}; z_n = \frac{|\xi_1 - \xi_{1_n}|}{a} \quad (25.21)$$

The term a is the support size. For m^{th} order basis set, the weight function must be spread enough to cover at least $(m + 1)$ data points. This fact is used to evaluate the support size. In a similar fashion, the approximate curvature fields $\bar{\kappa}_{h_1}$, $\bar{\kappa}_{h_2}$ and $\bar{\kappa}_{h_3}$ can be obtained.

25.5 Simulation

We simulate a 300 m long circular rod with $\nu = 0.3$ and diameter of 30.48 cm to study the effect of multiple curvatures, axial strain, Poisson's deformation, but no shear. Unlike Chadha and Todd [2] the shape sensing now depends on the material property ν . The strain value at the surface of Ω for assumed orientation of strain gauge was obtained using Eq. (25.16). The strain parameters for the given cross-section were obtained by solving the non-linear simultaneous equations in Eq. (25.18). The approximate configuration Ω_h is obtained using Eqs. (25.19a, b and 25.20a). The assumed midcurve shape bears two points of degeneracy. The algorithm is thus without any singularity. We assume the orientation of the surface strain gauges given by $\sigma_n = \left\{ \frac{\pi}{4}, \frac{\pi}{2}, \frac{3\pi}{4}, \pi, \frac{5\pi}{4}, \frac{3\pi}{2} \right\}$ and $\mu_n = \left\{ \frac{\pi}{4}, -\frac{\pi}{4}, \frac{\pi}{4}, -\frac{\pi}{4}, \frac{\pi}{4}, -\frac{\pi}{4} \right\}$.

Figure 25.2 compares the exact midcurve $\boldsymbol{\varphi}(\xi_1)$ with the approximate midcurve $\boldsymbol{\varphi}_h(\xi_1)$ and the exact orientation field $\{\mathbf{d}_i\}$ with the approximate field $\{\mathbf{d}_{h_i}\}$, solved using linearized analytical inverse approach for 5, 7, 20 and 50 discretized cross-sections. The RMS Error is mentioned on top of the plots. The RMS Error reduces exponentially with the increase in number of cross-section at which strain gauge is attached.

Figures 25.3 and 25.4 compares the exact curvature and axial strain field with the approximated fields. The approximation is obtained using Moving Least Square approximation. In this simulation, we use 2nd order shape function. The parameter $\frac{l}{a}$ in Figs. 25.3 and 25.4 represents the ratio of the undeformed length of beam and the support size chosen for the approximation. Therefore, the approximation algorithms suggested in Sect. 25.4 gives an excellent (as well as converging) reconstruction of the deformed configuration.

As explained in Chadha and Todd [2], there are three main sources of error: uncertainty in the boundary condition, noise in the strain measurements, and error due to approximation.

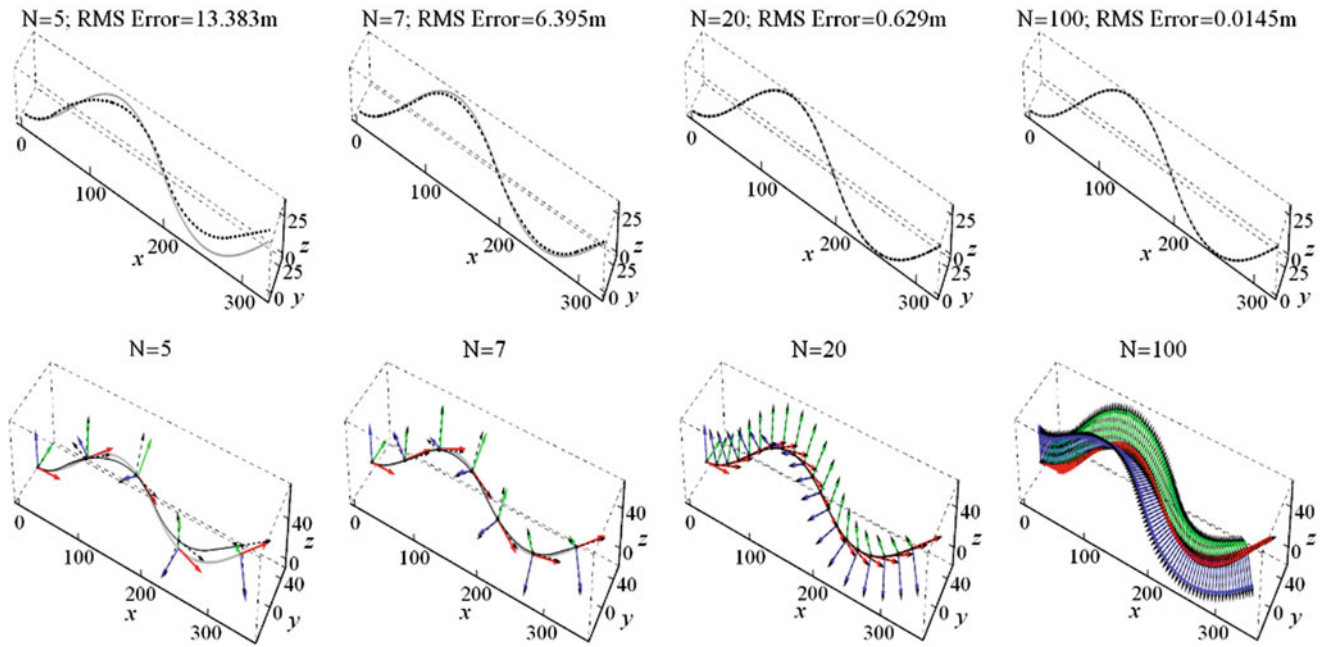


Fig. 25.2 Top plots: Comparison of exact midcurve $\varphi(\xi_1)$ (light gray solid line) and the reconstructed approximate midcurve $\varphi_h(\xi_1)$ (dashed line). Bottom Plots: Comparison of exact directors (\mathbf{d}_1 , \mathbf{d}_2 and \mathbf{d}_3 are represented by red, green and blue vectors respectively) and the predicted directors ($\{\mathbf{d}_h\}$) represented by black-dashed directors) of the object

25.6 Conclusion

In this paper, we improve the theory of shape sensing by incorporating Poisson's effect, thereby partially relaxing Euler-Bernoulli's rigid cross-section assumption such that the cross-section could undergo planar Poisson's transformation. The problem still maintains its single manifold nature where the configuration of the structure is defined by the mid-curve, director triad, and the axial strain, all being function of the undeformed arclength ξ_1 . Unlike Chadha and Todd [2] where the configuration was defined in $\mathbb{R}^3 \times SO(3)$ space, here the configuration is defined in $\mathbb{R}^3 \times SO(3) \times \mathbb{R}$ space.

We briefly defined the finite strain parameters, obtained expression for deformation gradient tensor and strain vector. Unlike [1, 2] the second and third component of an infinitesimal vector in the undeformed state are also strained due to Poisson's effect. Another observation is that the unit direction vector bears the same expression as in [2]. This is because Poisson's transformation does not change the form of the cross-section. For instance, ellipse remains ellipse Poisson's transformation except for different major and minor axis. The ratio of major to minor axis lengths remains the same.

The number of strain gauges per cross-section remains the same as in [2] but obtaining $(S_1 - S_6)$ from the scalar surface strain measurements now involves solving for 6 nonlinear simultaneous equations. The global solution to the set of differential equations obtained is determined using the continuity conditions and boundary conditions. The axial strain and the curvature fields can be estimated by a moving least squares continuous approximation. The suggested reconstruction strategy is convergent and non-singular even if the midcurve has multiple points or segment of degeneracy. The RMS error reduces exponentially with the increase in number of cross-sections.

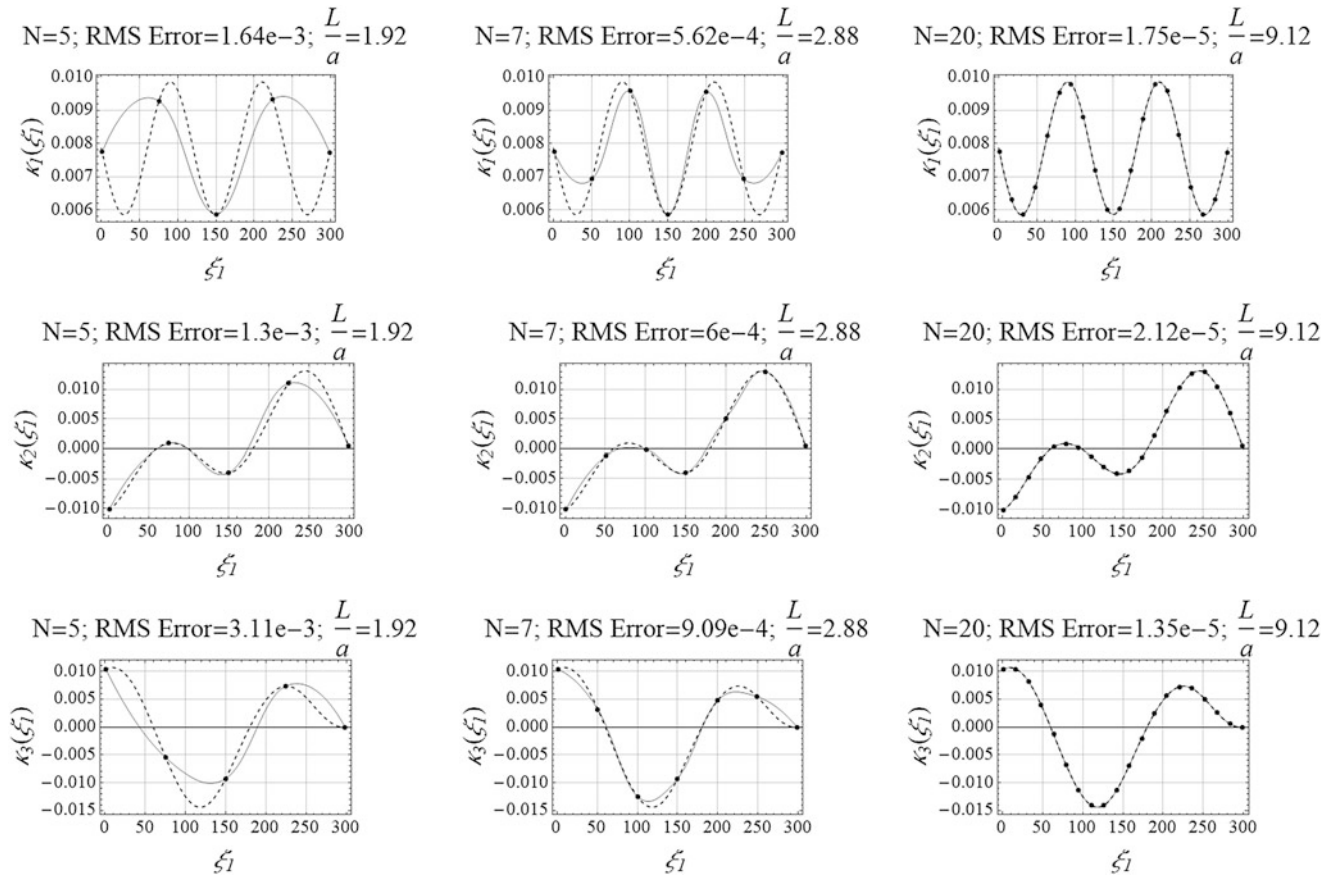


Fig. 25.3 Comparison of exact curvature terms $\kappa_i(\xi_1)$ (dashed line) and the approximate axial strain $\kappa_{ih}(\xi_1)$ (light gray solid line). The dots represent the data points obtained from the surface strain values

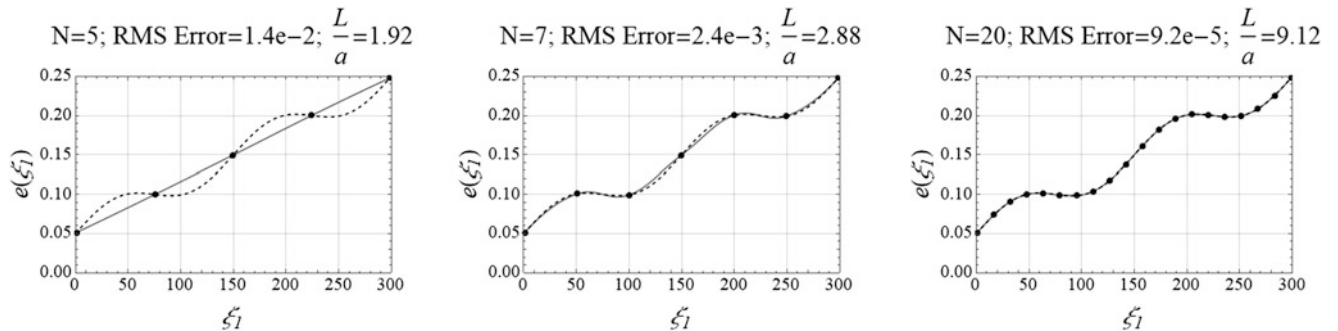


Fig. 25.4 Comparison of exact axial strain $e(\xi_1)$ (dashed line) and the approximate axial strain $e_h(\xi_1)$ (light gray solid line). The dots represent the data points obtained from the surface strain values and used for global approximation

References

1. Todd, M.D., Skull, C.J., Dickerson, M.: A local material basis solution approach to reconstructing the three-dimensional displacement of rod-like structure from strain measurements. *ASME J. Appl. Mech.* **80**(4), (2013). <https://doi.org/10.1115/1.4023023>
2. Chadha, M., Todd, M.D.: A generalized approach to reconstructing the three-dimensional shape of slender structures including the effects of curvature, shear, torsion, and elongation. *ASME J. Appl. Mech.* (2017). <https://doi.org/10.1115/1.4035785>

3. Chadha, M., Todd, M.D.: A displacement reconstruction strategy for long, slender structures from limited strain measurements and its application to underground pipeline monitoring. In: Conte, J., Astroza, R., Benzoni, G., Feltrin, G., Loh, K., Moaveni, B. (eds.) *Experimental Vibration Analysis for Civil Structures. EVACES 2017. Lecture Notes in Civil Engineering*, vol. 5, pp. 317–327. Springer, Cham (2018)
4. Cosserat, E., Cosserat, F.: *Theorie des Corps Deformable*. Herman, Paris (1909)
5. Ericksen, J.L., Truesdell, C.: Exact theory of stress and strain in rods and shell. *Arch. Ration. Mech. Analysis*. **1**, 295–323 (1958)
6. Chadha, M., Todd, M.D.: An introductory treatise on reduced balance laws of Cosserat beams. *Int. J. Solids Struct.* **126–127**, 54–73 (2017)



Chapter 26

Computing Nonlinear Normal Modes of Aerospace Structures Using the Multi-harmonic Balance Method

Christopher I. VanDamme, Ben Moldenhauer, Matthew S. Allen, and Joseph J. Hollkamp

Abstract The extreme environments that hypersonic vehicles experience during flight expose the thin structural panels to high aerodynamic pressure loading and large temperature gradients, leading to a highly nonlinear structural response. Reduced order models (ROMs) provide an efficient means to compute nonlinear response, however, the accuracy of a ROM is highly dependent on how it is made: the number of modes included within the basis set and the load scaling factors used. The authors have previously proposed to validate ROMs by computing the Nonlinear Normal Modes (NNMs) of the ROMs and using them to compare ROMs of increasing order. The NNMs are a useful metric because they are independent of a specific loading scenario, yet if the NNMs are reproduced accurately then the response to various resonant inputs will also be accurate. This framework has proven challenging to apply to curved structures because they can exhibit complex softening-hardening behavior as well as many nested internal resonance branches. The numerical integration and shooting method that has been used to compute the NNMs typically tracks all the internal resonances, and so it becomes slow and tends to require manual intervention. This work seeks to address these challenges by applying a Multi-Harmonic Balance (MHB) method rather than the shooting algorithm used previously. One attractive feature of the MHB method is the fact that one can filter out internal resonance branches from the solution by limiting the number of harmonics included. This filtering property will be explored, to ascertain the extent to which it can be used to skip internal resonances and identify the primary backbone branch of the NNMs. Particular attention will be paid to balancing the number of harmonics required to obtain an accurate primary backbone branch, including modal interactions that occur along the backbone. The method is applied to a clamped-clamped flat beam, a complex aerospace panel structure and a curved beam to demonstrate the capabilities.

Keywords Reduced order modeling · Geometric nonlinearities · Nonlinear normal modes · Finite element analysis · Structural dynamics

26.1 Introduction

In order to achieve the speed, life and efficiency demanded of next generation aircraft, it will be necessary to explore new methods of structural design. One promising approach has been to explore the nonlinear response envelope of designs. Typically aircraft structures are made to behave linearly due to the simplicity of analyzing the system and the relatively well behaved response. However, as the loading environment increases and/or the weight decreases, the amplitude of vibration increases and structures simply cannot provide the desired stiffness at an acceptable weight. If one allows the structure to behave nonlinearly, new regimes of the design space open up in which the structure automatically detunes itself from resonance as the vibration amplitude increases. On the other hand, the variety of possible responses increases drastically allowing such phenomena as softening or hardening of resonant frequency with increasing vibration amplitude, sub-harmonic resonance and jump phenomenon [1]. In the context of hypersonic vehicles in which thermal effects are also present there is the possibility of thermal buckling and dynamic snap through as well [2]. To account for these possible effects high fidelity numerical simulations must be used.

The complex nonlinear responses of aircraft structural members can be computed using the conventional finite element (FE) method, but as the size of the models increase the computational demand becomes infeasible. The conventional FE

C. I. VanDamme (✉) · B. Moldenhauer · M. S. Allen
Department of Engineering Physics, University of Wisconsin-Madison, Madison, WI, USA
e-mail: cvandamme@wisc.edu; bmoldenhauer@wisc.edu; matt.allen@wisc.edu

J. J. Hollkamp
Air Force Research Lab, Wright-Patterson AFB, OH, USA
e-mail: joseph.hollkamp@us.af.mil

method requires numerical integration over long time periods in order to properly model the responses. An alternative is to use a reduced order model (ROM) to compute the nonlinear response. A ROM can be derived from a parent FE model with either a direct or indirect approach. The direct approach requires access to the internals of the FE code (i.e., functions used to derive the element stiffness matrices) while the indirect only requires the nonlinear solution capabilities. When using the indirect method the accuracy of a ROM can vary with the number of modes included within the basis set as well as the load scaling used when approximating the nonlinear stiffness values from the parent FE model.

Significant work in the past couple of decades has focused on the development of methods to generate ROMs for geometrically nonlinear response but there has been a lack on the development of procedural methods that validate the accuracy of a ROM. The validation of a ROM is a critical step in order to have confidence in their response predictions because experience has shown that ROMs can vary widely in accuracy depending on how they are made. It is imperative that the ROM is an accurate representation of the full FE model yet it is difficult to be sure that this is true, because the structure may be subjected to a wide range of potential load cases, and computing the response of the full FEM to even one of these may be extremely expensive computationally. The conventional approach to validating a ROM is to compare the static or dynamic response of the ROM with the full order model from which it was derived. This becomes a costly procedure as the size of the parent FE model, from which the ROM is generated, increases. Additionally, since the loading environment of the hypersonic vehicles is non-deterministic, long time simulations are required to approximate the response statistics accurately. It is desirable to have validation metrics that do not directly rely on computing the nonlinear dynamic response of the full FE model over a long time window or for a variety of different loading scenarios.

One form of model validation between a ROM and a parent FE model is to compare their Nonlinear Normal Modes (NNMs). The NNMs are an ideal metric because they are independent of loading and show how the nonlinear response changes with increased amplitude of the system. This was done in [3] and found to provide strong foundation in which to evaluate a ROM. A drawback of the procedure is the requirement of computing the NNMs of a full FE model which can be computationally expensive. In [3] the NNMs were computed using shooting methods that integrate the FE model over the period of oscillation to find a periodic orbit satisfying the NNM equation. In addition a Newton-Raphson correction scheme was used to converge to a solution of the NNM which requires the generation and inversion of the Jacobian of the nonlinear equation. Both of these features increase the computational demand as the size of the FE model increases.

An alternative to comparing the NNMs of a ROM with the full FE parent model's NNM is to look at the convergence of a series of ROMs' NNMs as they are generated. Tracking how the NNMs of a reduced order model change with the addition of basis vectors or as load scaling factors are altered can provide good insight into the accuracy of the ROM. This procedure was originally proposed in [4] and applied to a flat clamped-clamped beam and a coffin shaped plate. The method was later used in [5] for a curved beam. In both cases it was found to provide a mechanism in which to evaluate the accuracy of a ROM. In the latter case, difficulties were encountered due to the presence of internal resonances, which arise due to modal coupling of the nonlinear system. The internal resonances are challenging to compute, since the step size must often be very small to resolve them, and hence it becomes difficult to compute the primary NNM backbone because so much time is spent computing these departures from the backbone. In addition when a structure is randomly excited there is currently no evidence that the internal resonances have a significant effect on the response, and so the backbone of the NNM is the primary portion of interest.

Detroux et al. [6] suggested that one could avoid having to compute a multitude of internal resonances by replacing the shooting algorithm [7] with a Harmonic Balance (HB) method. The HB method relies on approximating the periodic response of the system as a low order sum of harmonics, or Fourier coefficients. The accuracy of HB method in representing the original nonlinear system is dependent on the number of harmonics retained to approximate the periodic response. For smooth and mild nonlinear systems it has been shown that accurate response predictions can be obtained with a small number of harmonics [6, 8]. Furthermore, by limiting the number of harmonics one can limit the potential modal interactions, and filter out internal resonance branches [6]. Since the conventional shooting method performs direct integration over the period it implicitly has all of the harmonics of the system included and so it will compute all of the internal resonances branches unless the step size is chosen such that they happen to be missed.

This paper explores the use of the harmonic balance method to compute nonlinear normal modes of ROMs representing geometrically nonlinear structures. The focus is on using the HB method to determine the number of harmonics required to accurately compute the primary NNM backbone branches. Complimentary to that aim is to seek the use of the HB method's filtering property to avoid having to compute internal resonances.

The paper is organized as follows. Section 26.2 outlines the theoretical background of the harmonic balance method for computing NNMs. In Sect. 26.3 the HB method is applied to a clamped-clamped flat beam, a more complex aerospace panel structure, and a curved beam. The aerospace structure is the discovery experimental panel [9] planned for high-speed flow/structural interaction tests by the Structural Sciences Center at AFRL. The conclusions of the paper are presented in Sect. 26.4.

26.2 Theory

The geometrically nonlinear elastic FE equation of motion for an N degree-of-freedom (DOF) system can be written as

$$\mathbf{M} \ddot{\mathbf{x}} + \mathbf{C} \dot{\mathbf{x}} + \mathbf{K}\mathbf{x} + \mathbf{f}_{NL}(\mathbf{x}) = \mathbf{f}(t) \quad (26.1)$$

where \mathbf{M} , \mathbf{C} and \mathbf{K} are the mass, damping and linear stiffness matrices respectively of dimension $N \times N$. The displacement, velocity, and acceleration vectors \mathbf{x} , $\dot{\mathbf{x}}$ and $\ddot{\mathbf{x}}$ are $N \times 1$ vectors. The nonlinear restoring force term \mathbf{f}_{NL} is a function of the displacements of the system and $\mathbf{f}(t)$ is the external forcing vector. The system can be reduced using

$$\mathbf{x}(t) = \Phi_m \mathbf{q}(t) \quad (26.2)$$

where Φ_m is the $N \times m$ mass normalized mode matrix comprised of the mode vectors, ϕ_r , that are used as basis vectors in the reduction. The system is reduced down to a $m \times 1$ vector of time-dependent modal displacements $\mathbf{q}(t)$. When substituting the modal transformation presented in Eq. (26.2) into the non-linear equation of motion in Eq. (26.1) and subsequently pre-multiplying by Φ_m^T , where T is the transpose operator, the r th nonlinear modal equation becomes

$$\ddot{q}_r + c_r \dot{q}_r + \omega_r^2 q_r + \theta_r(q_1, q_2, \dots, q_m) = \phi_r^T f(x, t) \quad (26.3)$$

where the nonlinear portion of the restoring force, θ_r , is represented as a function of the modal displacements by

$$\theta_r(\mathbf{q}) = \phi_r^T \mathbf{f}_{NL}(\Phi_m \mathbf{q}) \quad (26.4)$$

In [2] it was shown that the nonlinear part of the restoring forces for a linear elastic system with geometric nonlinearities can be accurately approximated as

$$\theta_r(\mathbf{q}_1, \mathbf{q}_2, \dots, \mathbf{q}_m) = \sum_{i=1}^m \sum_{j=1}^m \mathbf{B}_r(i, j) \mathbf{q}_i \mathbf{q}_j + \sum_{i=1}^m \sum_{j=1}^m \sum_{k=1}^m \mathbf{A}_r(i, j, k) \mathbf{q}_i \mathbf{q}_j \mathbf{q}_k \quad (26.5)$$

where the nonlinear restoring force is a function of quadratic and cubic polynomials with coefficients B_r and A_r respectively for the r th nonlinear modal equation.

26.2.1 Harmonic Balance Method Applied to Computing NNMs

Nonlinear normal modes of the ROMs represented by the nonlinear modal equation in this work will be computed using the harmonic balance method. The harmonic balance method attempts to find periodic solutions of the nonlinear system by transforming the nonlinear system of equations from the time domain to the frequency domain. Looking at the undamped and unforced form of Eq. (26.3) the system becomes

$$\ddot{\mathbf{q}}(t) + \mathbf{\Lambda} \mathbf{q}(t) + \boldsymbol{\theta}(\mathbf{q}(t)) = 0 \quad (26.6)$$

where $\mathbf{\Lambda} = [\omega_r^2]$. Assuming a periodic response of the modal displacements, $\mathbf{q}(t)$, the response can be represented as a sum of Fourier coefficients truncated to the N_H^h harmonic as

$$\mathbf{q}(t) = \frac{z_0^f}{\sqrt{2}} + [h = 1] N_H \sum \left(z_s^h \sin\left(\frac{h\omega t}{v}\right) + z_c^h \cos\left(\frac{h\omega t}{v}\right) \right) \quad (26.7)$$

where the state conditions of the HB solution, the Fourier coefficients, are now

$$\mathbf{Z} = \left[z_0 \ z_C^{1T} \ z_S^{1T} \ z_C^{2T} \ z_S^{2T} \ \dots \ z_C^{N_H^T} \ z_S^{N_H^T} \right] \quad (26.8)$$

where the subscripts c and s refer to cosine and sine terms of the Fourier coefficients. The final harmonic balance equation obtained is

$$\mathbf{h}(Z, \omega) = \mathbf{A}(\omega)Z - F(Z) = 0 \quad (26.9)$$

in which the linear term, $\mathbf{A}(\omega)$, is the linear portion of the system and $F(z)$ represents the internal nonlinear force. The system is now represented as an algebraic system of equations in which Z and ω must be solved. For a more detailed derivation and explanation of the method, see [6]. In order to trace out branches of periodic orbits, NNMs, the method is combined with a numerical continuation scheme as represented in [6].

26.3 Numerical Case Studies

Three numerical case studies are presented to explore the benefit of using the HB method for its filtering property when computing NNMs of geometrically nonlinear structures.

26.3.1 Flat Beam

The first numerical study is a clamped-clamped beam with geometric nonlinearity present. This beam has been used in previous studies [2–4, 10] and has well known internal resonances. The nonlinear beam model, constructed of structural steel, was 228.6 mm (9 in.) long, with a cross section of 12.7 mm (0.5 in.) wide by 0.787 mm (0.031 in.) thick. The material properties are listed below in Table 26.1. The beam was modeled with forty B31 beam elements in Abaqus®, resulting in 117 DOF. The clamped-clamped beam NNMs were computed using 4 Mode ROM consisting of modes 1, 3, 5, and 7 of the FE model.

The first NNM of the beam was computed using the shooting method in [7] in order to compare the harmonic balance method's accuracy. The computed NNMs are presented in Fig. 26.1. The NNM computed using only one harmonic does not capture any of the internal resonances as expected but traces the primary backbone computed using shooting method. When including the first three harmonics of the system the NNM also does not identify any of the internal resonances.

After including all the harmonics up to the 4th, the 1:4 internal resonance was captured, which leaves the backbone at 120 Hz. In Fig. 26.2a the internal resonance branch is shown in detail. The 4 harmonic model predicts the start of the internal resonance branch but fails to trace the branch accurately. Once the fifth harmonic is added to the system the 1:5 internal resonance is captured at 88 Hz. Figure 26.2b shows this internal resonance in detail, and that it is very accurately tracked by the 5 harmonic HB method.

In order to understand how the accuracy of the harmonic balance changes with the number of harmonics the primary backbone solutions were isolated to compare with the shooting method. The primary backbones computed by each algorithm are presented in Fig. 26.3, revealing that the curves are nearly indistinguishable. The horizontal lines on Fig. 26.3 represent the point along the NNM backbone at which the structure has displacements of $1\times$ -, $2\times$ -, $4\times$ the beams thickness. To quantify the accuracy more rigorously, at a certain set of frequencies the error in the energy was calculated. The errors in energy were then calculated for each frequency value and are presented on the right hand side of Fig. 26.3 as a grouped bar plot. The error between the one term harmonic balance and the shooting method increases as the NNM increases in frequency but only contains an error of 4.9% at 107 Hz with a displacement of $2\times$ the thickness and 12.36% at 180 Hz with a displacement of over $4\times$ the thickness. For the 3-,4- and 5-harmonic models the error throughout the NNM curve up to 140 Hz remains below 2%. As the number of harmonics included increases the accuracy of the method is increased in comparison with the shooting method, this is shown looking at the error in energy at 180 Hz.

Table 26.1 Material properties of the clamped-clamped beam

ROM	Modulus of elasticity	Poisson's ratio	Density
Modes	$E = 204.8 \text{ GPa (29,700 ksi)}$	0.3	$\rho = 7,870 \frac{\text{kg}}{\text{m}^3} \left(7.36 \times 10^{-4} \frac{\text{lb-s}^2}{\text{in}^4} \right)$

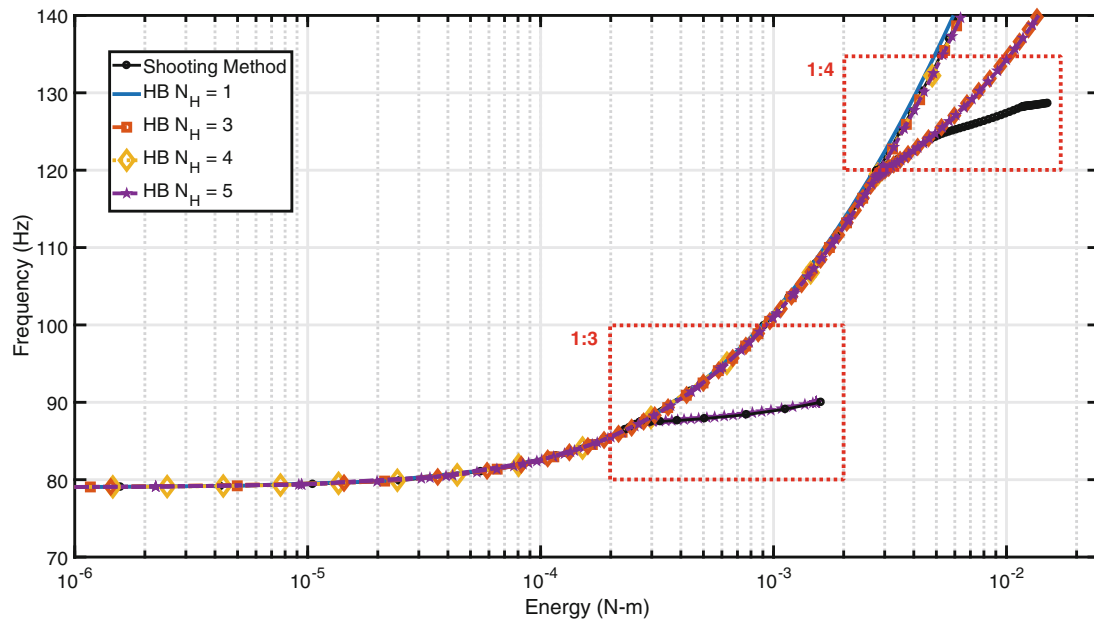


Fig. 26.1 Comparison of 1st NNM of clamped-clamped beam computed using a shooting method and using the HB method with varying numbers of harmonics

26.3.2 Discovery Experimental Panel

The second example is a significantly larger model with more complex geometry. The discovery experimental panel (DEP) FE model is shown in Fig. 26.4. The panel was modeled in Abaqus® with 8627 S4R elements resulting in a total of 52,734 DOF. This model is vastly larger than the flat beam but can be reduced down to a relatively small nonlinear ROM in order to compute the NNMs. The DEP panel is constructed of titanium 6Al-2Sn-4Zr-2Mo (Ti-6242) with uniform thicknesses of 50 mil (1.27 mm). The material properties used are defined in Table 26.2.

The DEP finite element model was reduced to a 6 mode ROM including modes 1, 2, 3, 5, 8 and 11 to compute the NNMs. The linear modes of the DEP used as basis vectors within the ROM are given in Table 26.3.

The first NNM of the DEP, as computed using the HB method with various number of harmonics, is presented in Fig. 26.5 along with the NNM computed using the shooting method. The NNM contains two internal resonance branches in the region computed, a 1:4 at 99 Hz and a 1:3 at 130 Hz. The shooting method traces both of these internal resonances.

The harmonic balance solution with only 1 harmonic included computes only the primary backbone branch of the NNM. Interestingly the 3 harmonic model also only traces the backbone of the NNM and does not continue down the 1:3 internal resonance branch. Both of these models provide comparable backbones with the shooting method results. When including harmonics 1–5, the system identifies and tracks the 1:3 internal resonance branch and the 1:4 internal resonance branch. A closer look at the 1:3 and 1:4 internal resonance branches is provided in Fig. 26.6a, b respectively in which the HB method traces both of the internal resonance branches accurately. As the harmonics included increased to 7 the system showed the same characteristics.

To depict how the shape of deformation of the panel changes throughout the NNM, the deformation shapes at the points labeled in Fig. 26.5 are presented in Fig. 26.7. Points along the primary backbone and along the internal resonance branches are shown. For reference, point B along the primary backbone branch is when the panel deflects $1\times$ the thickness of the structure.

As was done for the flat beam, the accuracy of the backbone for each HB model was quantified by computing their error relative to the Shooting Method solution. The primary backbone of the NNM of the DEP system is presented on the left hand side of Fig. 26.8 in which each model appears to provide similar results. The errors in energy for each interpolated frequency value are presented on the right hand side of Fig. 26.8. As was seen with the flat beam, the error in the one term harmonic balance solution is seen to increase as the energy of the system increases. The energy error of the 1-term harmonic balance method reaches a maximum of 10% at 354 Hz at which point it has a maximum displacement of $2\times$ the thickness of the structure. Similarly, for the 3-, 5- and 7-term harmonic balance solutions the error throughout the NNM curve up to 360 Hz also continues to increase. For each HB solution, the maximum error over the computed NNM portion decreases as the number of harmonics included increases, with the 7-term model having a maximum error of less than 2%.

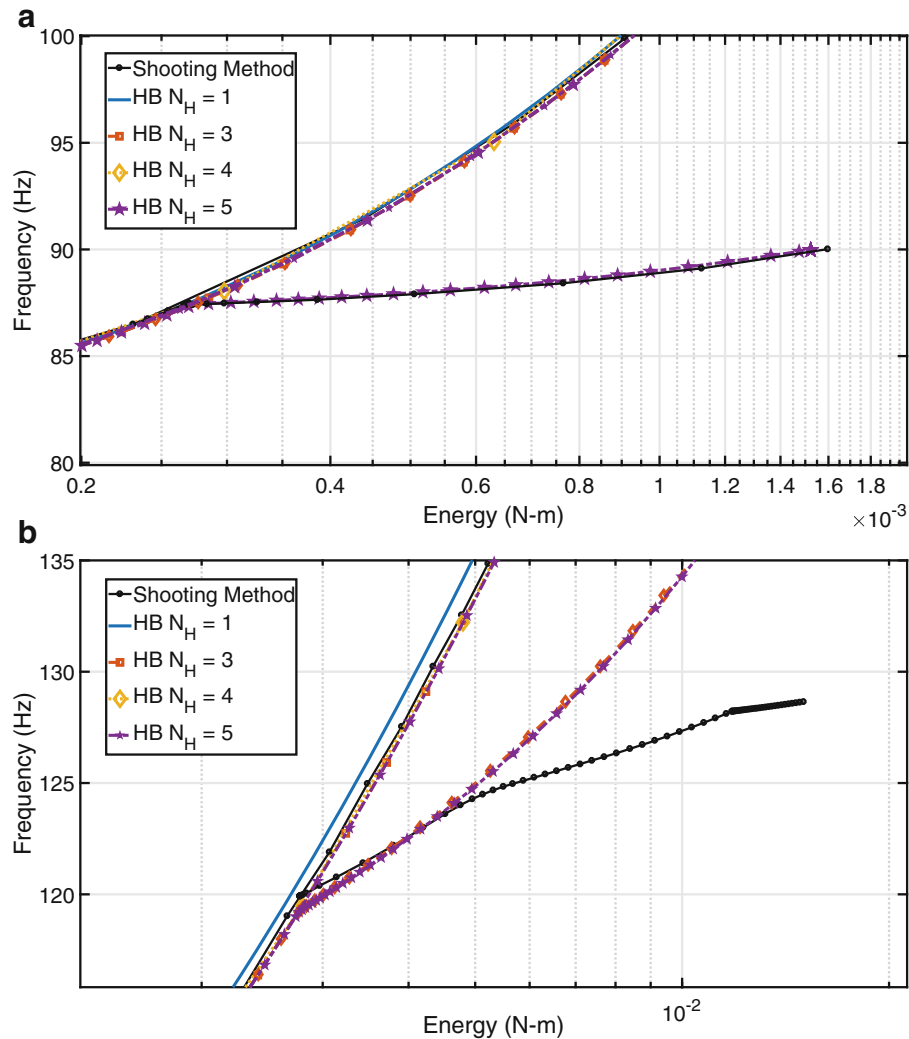


Fig. 26.2 Comparison of 1st NNM of clamped-clamped beam including shooting method results (a) zoomed in portion of Fig. 26.1 showing 1:3 internal resonance (b) zoomed in portion of Fig. 26.1 showing 1:4 internal resonance

26.3.3 Curved Beam

The last numerical example presented in this work is a curved beam model in which the system dynamics have shown to be more complex than the previously studied flat structures [11]. The curved beam geometry is presented in Fig. 26.9 with a radius of curvature of 22,860 mm (900 in.) resulting in a maximum height of 0.508 mm (0.02 in.) which is equal to the thickness of the beam. The curved beam has the same section and material properties as the flat beam and is represented by a 11-mode ICE ROM with linear modes [1–5, 7, 9, 11, 12, 14, 16] included within the basis set; this was determined to be accurate in [11].

The 1st NNM of the curved beam is presented in Fig. 26.10 in which it exhibits a softening behavior followed by hardening as the deflection approaches one thickness. The single harmonic model shows some error in describing the softening behavior, but is still quite accurate as the frequency error is only 2.5% at the lowest frequency that the NNM reaches. When at least 3 harmonics are included the softening is accurately captured. Additionally this systems contains complex internal resonance branches which become difficult to fully trace out as the number of harmonics increases. The shooting algorithm was unable to continue past the second internal resonance branch and took many restarts to get past the first branch.

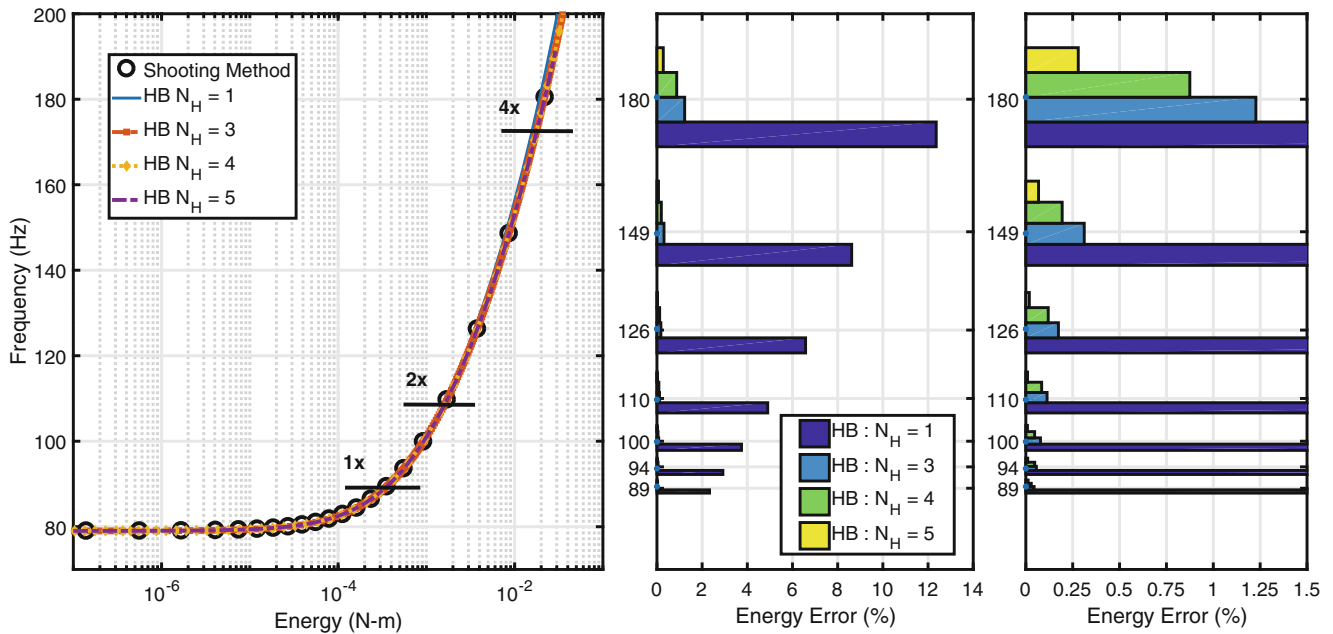


Fig. 26.3 (a) Comparison of 1st NNM isolating only the primary backbone. (b) Relative errors in energy of the HB algorithm with the shooting method at interpolated solution points. (c) Zoomed in portion of errors in energy highlighting the 3-,4-, and 5-harmonic model values

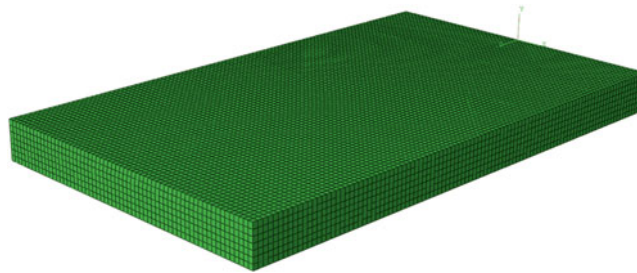


Fig. 26.4 The finite element model used for the discovery experimental panel

Table 26.2 Material properties of the discovery experimental panel

Modulus of elasticity	Poisson's ratio	Density
114.1 GPa	0.32	4,428 $\frac{\text{kg}}{\text{m}^3}$

The harmonic balance method also has difficulties continuing past some of the internal resonances when enough harmonics are included to identify them. Because of these difficulties, it becomes challenging to compare the shooting and harmonic balance solutions over the full range of frequency and energy that is of interest. Additionally, because the backbones are our primary interest, it does not seem wise to invest a lot of effort into computing complicated internal resonance branches simply to be able to compare those sections of the NNM along the backbone. This has the benefit of identifying accuracy of the model at specific frequencies or energies of interest as a function of the number of harmonics included. Convergence is identified by looking at the change in the predicted solution value with increasing number of harmonics at a specific frequency.

Figure 26.11 presents the convergence of a NNM solution for an increasing number of harmonics started from 55 and 100 Hz respectively from a 1-harmonic solution. The change in the energy of the solution is plotted as the harmonic order increases, for example with 1–3 indicating the change in energy between the 3-harmonic solution and the 1-harmonic solution. In each case there is a large change in energy from the 1 harmonic model to the 3 harmonic model. Once three harmonics are included within the system the percent energy change remains below 1%.

Table 26.3 The linear modes of DEP used within ROM showing the frequency and shape

Mode	Frequency (Hz)	Plot	Mode	Frequency (Hz)	Plot
1	96.44		5	291.59	
2	166.57		8	390.74	
3	183.73		11	478.71	

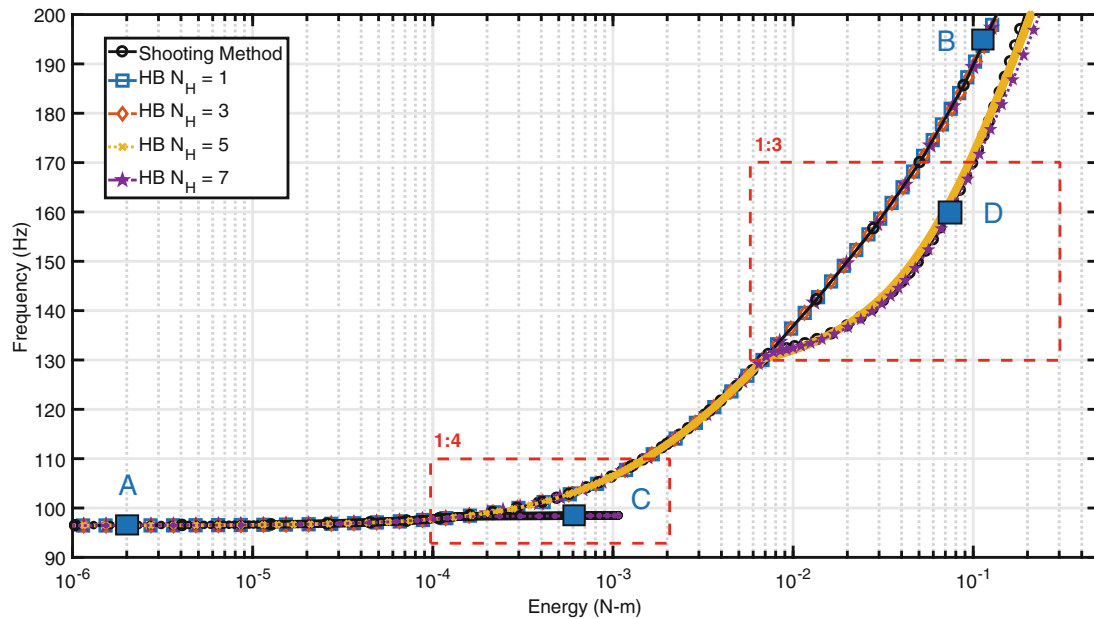


Fig. 26.5 First NNM of DEP computed using the harmonic balance method with increasing harmonics included and the shooting method

26.4 Conclusion

This work explained the use of the multi-harmonic balance method as a means of limiting the internal resonances that are computed when seeking to compute the NNMs of geometrically nonlinear reduced order models. Three geometrically nonlinear models were considered. In each case the harmonic balance method provided the ability to compute low order harmonic solutions that maintained accuracy and the ability to skip internal resonance branches. Additionally the filtering property of the harmonic balance method was found to be able to filter out the internal resonances for all three models.

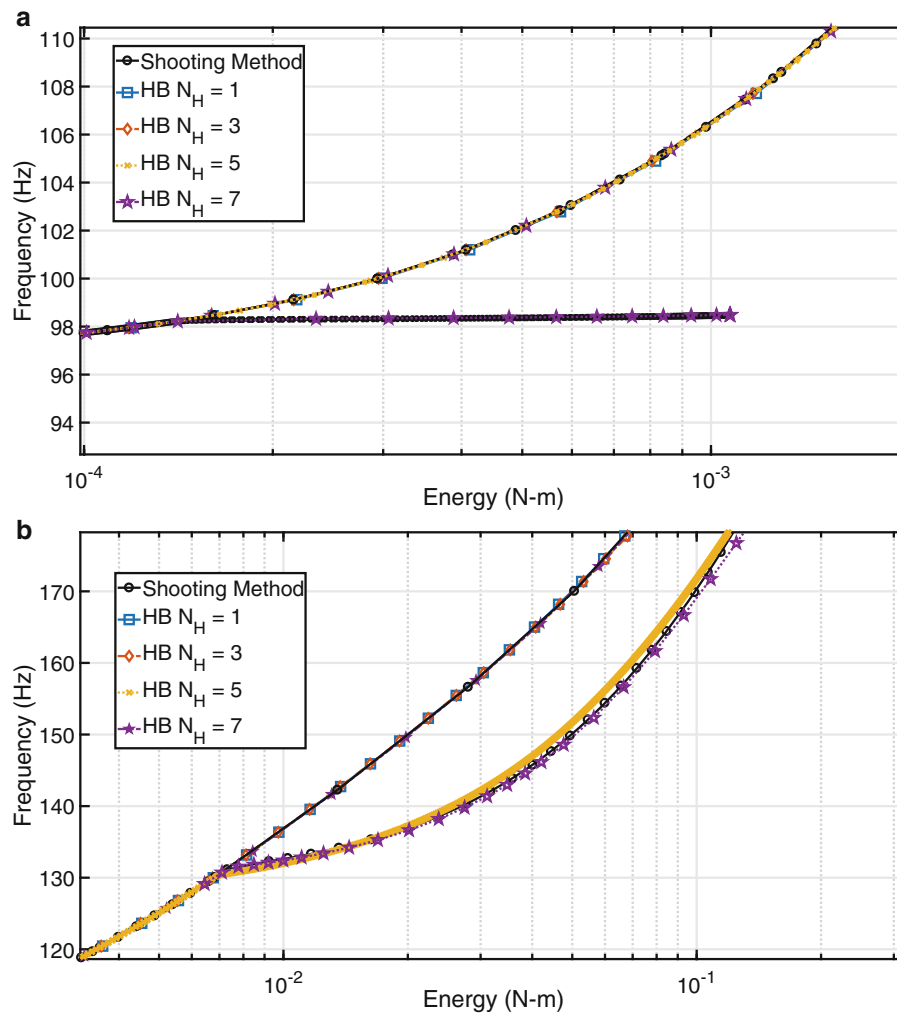


Fig. 26.6 Internal resonance branches of 1st NNM of DEP (a) 1:3 internal resonance (b) 1:4 internal resonance

In the first two cases the harmonic balance method was used with continuation to estimate the entire NNM, including the backbone of interest and some internal resonances. The accuracy of the harmonic balance solutions was established by comparing them with solutions from the shooting algorithm in [7]. For both numerical studies good accuracy was achieved using only a small number of harmonics. In the case of the clamped-clamped flat beam the error in the energy at each point in the NNM was less than 2% up to 180 Hz, at which point the solutions had displacements up to $4\times$ the thickness of the beam. Similarly, for the discovery experimental panel a low number of harmonics was required in order to maintain accurate NNM predictions. With a 3-term harmonic solution the error was less than 6% at solution points whose displacement reached 2 times the thickness of the panel. In both cases the accuracy of the harmonic balance method increased with the number of the harmonics included.

For the third numerical study, it proved problematic to compute the entire NNM branch, and so this was avoided by using the single-harmonic solution as an initial guess for higher harmonic solutions at the same fundamental frequency. Convergence was then monitored by tracking the change of solution value, energy in this work, at a desired frequency level. This methodology showed a strong convergence of relative energy change as the number of harmonics increased with a maximum change less than 1% for the curved beam model when 3 harmonics were included.

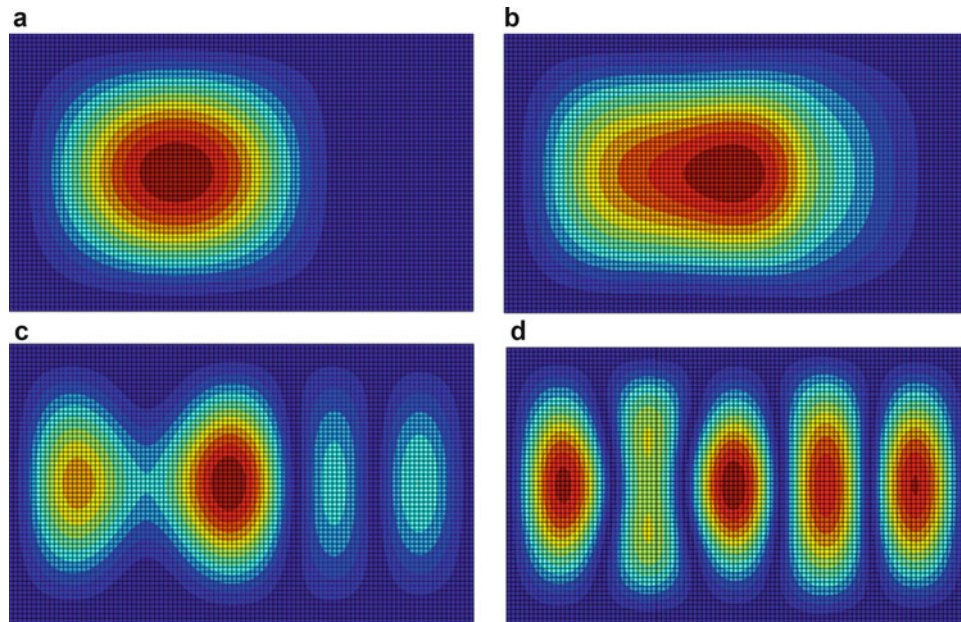


Fig. 26.7 Deformation of DEP at solution points identified in Fig. 26.5 along the NNM for the 5-term harmonic balance model. (a) Deformation at NNM1 solution point A along the primary backbone branch. (b) Deformation at NNM1 solution point B along the primary backbone branch. (c) Deformation at NNM1 solution point C along the 1:4 internal resonance branch. (d) Deformation at NNM1 solution point D along the 1:3 internal resonance branch

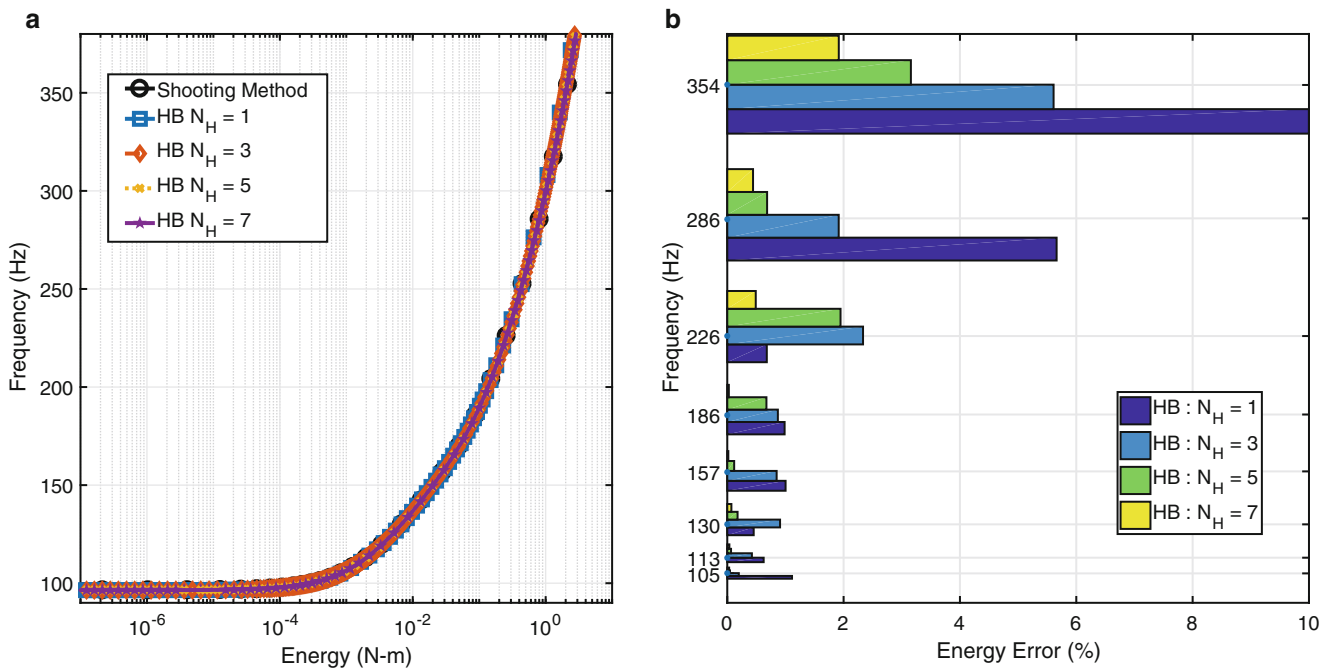


Fig. 26.8 (a) Comparison of 1st NNM isolating only the primary backbone. (b) Relative errors in energy of the HB algorithm with the shooting method at interpolated solution points

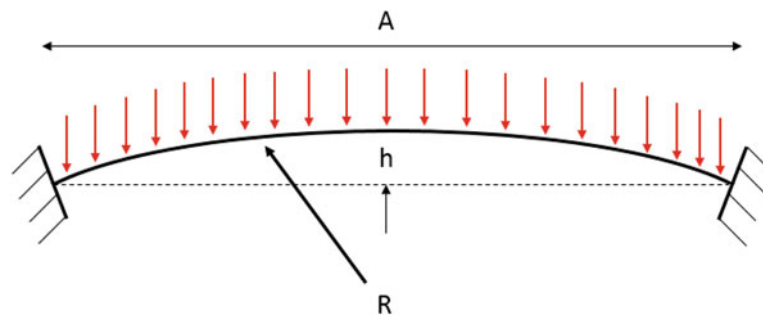


Fig. 26.9 The geometry of the curved-beam model

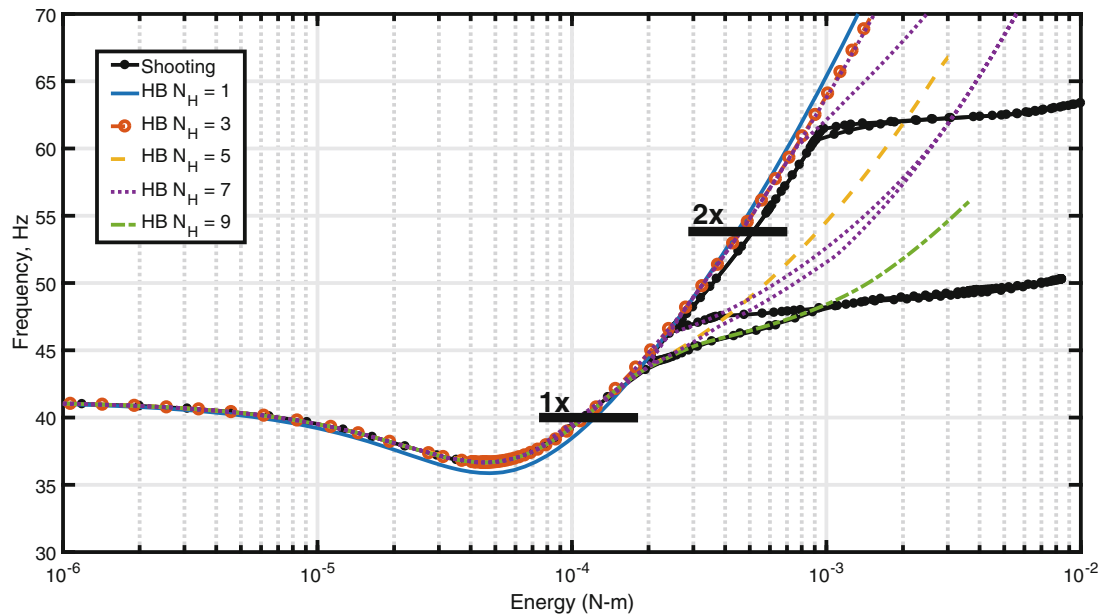


Fig. 26.10 First NNM of the curved beam computed using shooting (truth solution) and using the harmonic balance method with an increasing number of harmonics included

The extension of this work is to test it on models in which the modal coupling is stronger such as structures with larger curvature or that undergo thermally buckling. Future works will seek to exploit this to evaluate the convergence of ROMs as the number of modes in the ROM increase, or as the load levels used to construct the ROM are varied, as was done in [3]. That work showed that the NNMs are an effective metric to use when evaluating a ROM, but it can become quite challenging to use the NNMs to evaluate convergence of the ROM because many internal resonance branches had to be computed in order to estimate the backbone over the range of interest. This new approach is expected to greatly simplify that process.

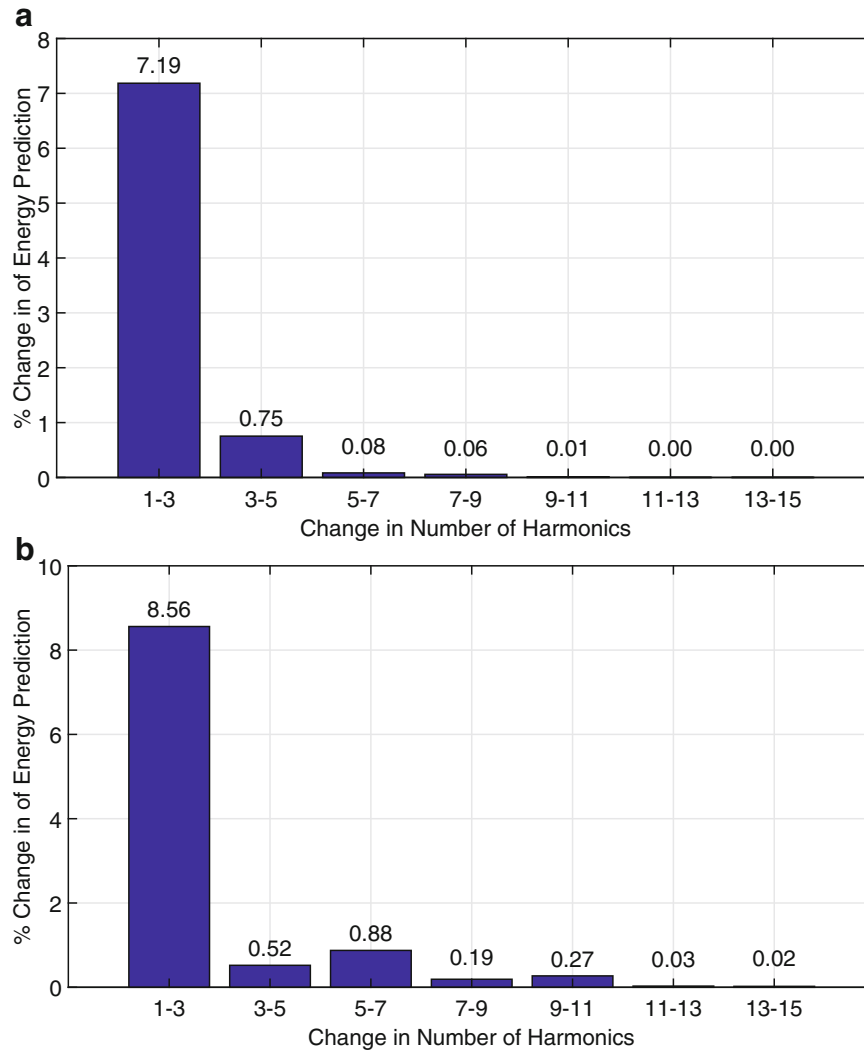


Fig. 26.11 Convergence of NNM solution energy values started from single harmonic solutions (a) Relative energy change computed at 55 Hz (b) Relative energy change computed at 100 Hz

Acknowledgements This work was supported by the Air Force Office of Scientific Research, Award # FA9550-17-1-0009, under the Multi-Scale Structural Mechanics and Prognosis program managed by Dr. Jaimie Tiley.

References

1. Mignolet, M., Przekop, A., Rizzi, S., Spottswood, M.: A review of indirect/non-intrusive reduced order modeling of nonlinear geometric structures. *J. Sound Vib.* **332**, 2437–2460 (2013)
2. Gordon, R., Hollkamp, J.: Reduced-order models for acoustic response prediction, Air Force Research Laboratory, techreport AFRL-RB-WP-TR-2011-3040 (2011)
3. Kuether, R., Deaner, B., Hollkamp, J., Allen, M.: Evaluation of geometrically nonlinear reduced-order models with nonlinear normal modes. *AIAA J.* **53**, 3273–3285 (2015)
4. Kuether, R., Allen, M.: Validation of nonlinear reduced order models with time integration targeted at nonlinear normal modes. In: *Nonlinear Dynamics, Volume 1 Conference Proceedings of the Society for Experimental Mechanics Series* (2015)
5. Damme, C.V., Allen, M.: Using NNMS to evaluate reduced order models of curved beam. In: De Clerck, J., Epp, D. S. (eds.) *Rotating Machinery, Hybrid Test Methods, Vibro-Acoustics and Laser Vibrometry. Volume 8: Proceedings of the 34th IMAC, a Conference and Exposition on Structural Dynamics 2016*, pp. 457–469. Cham (2016)
6. Detroux, T., Renson, L., Kerschen, G.: The harmonic balance method for advanced analysis and design of nonlinear mechanical systems. In: *Nonlinear Dynamics, Volume 2. Conference Proceedings of the Society for Experimental Mechanics Series* (2014)

7. Peeters, M., Virguie, R., Serandour, G., Kerschen, G., Golinval, J.C.: Nonlinear normal modes, Part II: toward a practical computation using numerical continuation techniques. *Mech. Syst. Signal Process.* **23**, 195–216 (2009)
8. Cochelin, B., Vergez, C.: A high order purely frequency-based harmonic balance formulation for continuation of periodic solutions. *J. Sound Vib.* **324**(1), 243–262 (2009)
9. Shah, P., Blades, E., Nucci, M., Schoneman, J., Berg, D., Cornish, A., Hill, T.: Nonlinear dynamic response of hypersonic vehicle skin panels using coupled fluid-thermal-structural simulation tools. In: *Proceedings of the 35th International Modal Analysis Conference* (2017)
10. Kuether, R.J., Allen, M.S.: A numerical approach to directly compute nonlinear normal modes of geometrically nonlinear finite element models. *Mech. Syst. Signal Process.* **46**(1), 1–15 (2014)
11. Damme, C.V., Allen, M.: Nonlinear normal modes of a curved beam and its response to random loading. In: *Nonlinear Dynamics, Volume 1. Conference Proceedings of the Society for Experimental Mechanics* (2017)



Chapter 27

Nonlinear Identification of an Aero-Engine Component Using Polynomial Nonlinear State Space Model

Samson B. Cooper, Koen Tiels, and Dario DiMaio

Abstract In non-linear structural dynamics, the identification of nonlinearity often requires prior knowledge or an initial assumption of the mathematical law (model) of the type of nonlinearity present in a system. However, applying such assumptions to large structures with several sources and types of nonlinearities can be difficult or practically impossible due to the individualistic nature of nonlinear systems. This paper presents the identification of an aerospace component using polynomial nonlinear state space models. As a first step, the best linear approximation (BLA), noise and nonlinear distortion levels are estimated over different amplitudes of excitation. Next, a linear state space model is estimated on the nonparametric BLA using the frequency domain subspace identification method. The nonlinear model is constructed using a set of multivariate polynomial terms in the state variables and the parameters are estimated through a nonlinear optimisation routine. The polynomial nonlinear state space models are tested and validated on measured data obtained from the experimental investigation of the Aero-Engine component.

Keywords Nonlinear systems · System identification · Black-box model · Aircraft Structures

27.1 Introduction

The levels of nonlinearities encountered during the vibration test of aerospace structures is ever increasing and becoming more significant as attested by the literature [1]. Over the last few years, evidence of nonlinear phenomena has been reported during the Ground Vibration Testing (GVT) of large aircraft structures [2–4] and it is now evident that these cases require profound investigation to understand and identify the nonlinearities observed in such test data. In addition, the use of developed linear tools and theories to perform identification on nonlinear test data often produces undesirable results or in most cases fail to predict the structural response within the acceptable levels which are required for validation and industrial certification purpose. Hence the development of effective system identification techniques applicable to nonlinear systems is a major demand by many structural dynamic engineers and researchers.

In most cases, the detection of nonlinearity from measured data can easily be achieved by using simple techniques such as the superposition principle, observation of distorted peaks at the resonances and recognition of jumps between low and high response amplitudes. After nonlinearity has been detected in measured data, identification of parametric or nonparametric models from such data is a challenging task. The last two decades have witnessed the development of several procedures and techniques for nonlinear system identification, in [5] the white-box identification process namely (Detection, Characterisation and Quantification) was revealed. The white-box approach has a great progression procedure with the advantage of implementing and integrating two or more developed techniques such as the Wavelet Transform (WT), Hilbert Transform (HT) [6], Restoring Force Surface (RFS) [7] and the Frequency Nonlinear Subspace Identification (FNSI) [8]. A drawback to this approach is that the functional forms and mathematical representation of the nonlinearities must be known in advance based on the physics law governing the dynamics of the system. In addition, this application can be difficult for large aircraft structures with multiple nonlinear sources and different individualistic nonlinear phenomena.

Another successful way of tackling nonlinear system identification is to consider black-box approaches, in this case the only available information about the system is given by the measured inputs and outputs. A black-box approach uses model structures that are adequate and rich to capture all the appropriate physics and dynamics governing the nonlinearities

S. B. Cooper (✉) · D. DiMaio

University of Bristol, Department of Mechanical Engineering, Queen's Building, University Walk, Bristol, UK
e-mail: sc14784@bristol.ac.uk

K. Tiels

Vrije Universiteit Brussel (VUB), Department of Fundamental Electricity and Instrumentation (ELEC), Brussels, Belgium

a system. Examples of black-box models available in the literature are: nonlinear autoregressive network (NARX) and nonlinear autoregressive moving average (NARMAX) with exogenous inputs models [9, 10], the Volterra models [11–13] and state space models [14–16]. Although, black-box models in most cases do not provide physical insight to the system under identification, the advantage of their flexible mathematical structure can be used to capture significant nonlinear behaviours in measured data.

Obtaining a prior knowledge of the nonlinear functional form or characterisation of large assembled structures with joints can be very challenging due to their individualistic nonlinear behaviour such as stick-slip behaviour at macro-and microscopic levels and hysteresis damping. This paper presents the nonlinear identification of a large aero-engine component using Polynomial Non-Linear State Space (PNLSS) model, in this situation a PNLSS identification is a strong method for modelling the nonlinearities observed in the experimental data of such a large aero-engine component. The method implemented in this paper uses the flexibility of the PNLSS model to experimentally investigate the nonlinear phenomena observed at certain areas of the structure without any prior assumptions. The paper starts in Sect. 27.2 with a description of the test structure and linear modal identification using low-level experimental data. The nonlinear detection, Best Linear Approximation, total distortions (noise and nonlinear distortions) observed in the test data are presented in Sect. 27.3. In Sect. 27.4, the PNLSS identification of the test data is presented while discussions and concluding remarks are described in Sect. 27.5.

27.2 Description of the Aero-Engine Casing

The test structure represented in Fig. 27.1 the casing of an aircraft engine used for powering a typical commercial aircraft. The structural configuration considered in this paper is a three-layer architecture of the aircraft engine casing without any internally attached accessories. The entire casing has structural features that are typical of a full-size assembled system e.g. multiple body sections and bolted joints, the total mass of the casing assembly is 461 kg. To address the nonlinearities observed in bolted connections, the casing was connected to a component that might introduce some nonlinearity into the dynamics of the whole assembly. The component used in this demonstration is a flat aluminium plate bolted on four stiffness shaped steel blocks. The plate is then bolted on the first cylinder of the casing very close to the excitation position as shown in Fig. 27.2a.

27.3 Experimental Setup and Linear Modal Analysis

The casing was suspended horizontally from a blue test frame using four elastic chords to support the suspension as shown in Fig. 27.2a. The test frame used in this research is classified as a Technology Research Level (TRL6) structure developed under the HITEA project while the elastic chords are used to represent a free-free boundary test condition. The experimental set-up

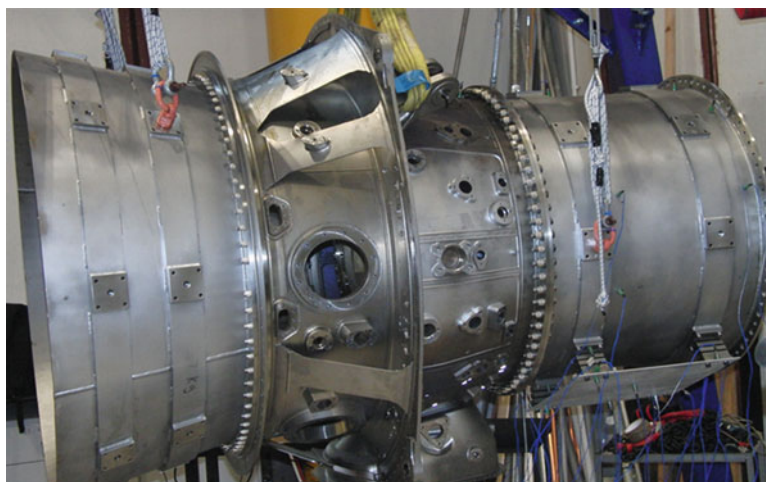


Fig. 27.1 Photograph of the Aero-engine casing and the Aluminium plate

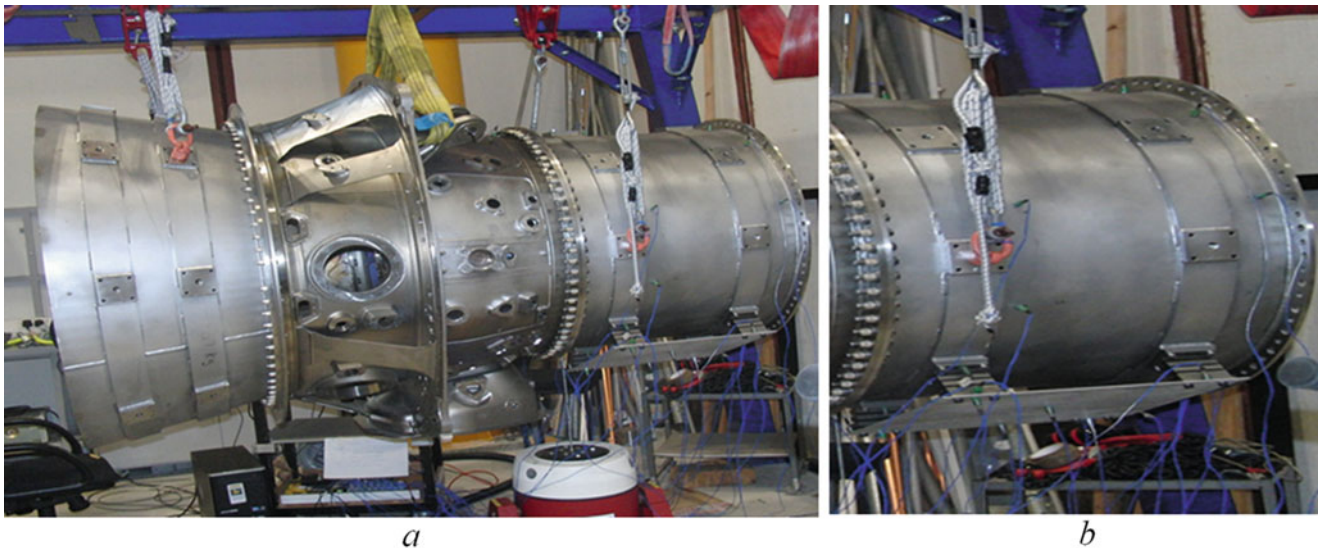


Fig. 27.2 Experimental set-up of the Engine casing suspended on a TRL-6 frame. (a) Test Set-up, (b) Instrumented section of the casing

was designed to replicate the traditional horizontal configuration of such component when attached to an aircraft. A total of 32 accelerometers was employed to instrument the structure, all of which are single-axial sensors. For this investigation, only the first subassembly section where the plate is bolted to the engine casing as illustrated Fig. 27.2b was fully instrumented, a large shaker visible in Fig. 27.2a was used to apply excitation inputs to the casing in a vertical direction.

The first stage of the experimental investigation involved conducting a set of traditional modal tests on the casing and plate assembly to obtain the natural frequencies and damping ratios at low amplitude of vibration. In addition, stepped-sine test at high excitation levels was carried out on the assembly to check for symptoms of nonlinearity that may be present in the instrumented section of the casing.

27.4 Linear Analysis of the Casing and Plate Assembly

The first measurements obtained from the experimental test comprised of several low random data which were acquired based on broadband excitation, the choice of broadband excitation was made based on its conventional use in modal testing. Broadband excitation also provides some early information on the behaviour of the structure and experimental configuration, the low level random test was performed using the Spectral Test module in LMS Test Lab. The test structure was excited near the flange connecting the inter-case (middle case) with the first case as shown in Fig. 27.2a. The structure was excited using burst random excitation ranging between 30 and 500 Hz. The Frequency Response Function (FRFs) obtained from the test were exploited to identify the linear modal parameters of the engine casing. Figure 27.3 shows a selection of the FRFs obtained from the low-level test. Before getting an insight of the nonlinear behaviour of the casing, a linear modal analysis based on the FRF's obtained from low-level random test was conducted using the PolyMAX method [17]. The applied random excitation has an RMS value of 45 N, Fig. 27.3 shows a selection of the FRFs obtained from the low-level test and Table 27.1 presents the corresponding natural frequencies and damping ratios of the casing with the plate bolted to the first cylinder.

27.5 Non-linear Detection Based on Distortions in Time-Series and FRF Measurements

Equally, to check for symptoms of nonlinear behaviour in the casing and plate assembly, stepped sine and sine-sweep tests were conducted on the assembly. The new assembly was also excited at several excitation levels covering a frequency bandwidth of 80–90 Hz. Figure 27.4 shows a selection of the FRFs and phase results obtained from the stepped sine test. In Fig. 27.4 stepped-sine FRFs and phase are presented for plate casing assembly, the test was concentrated around the first

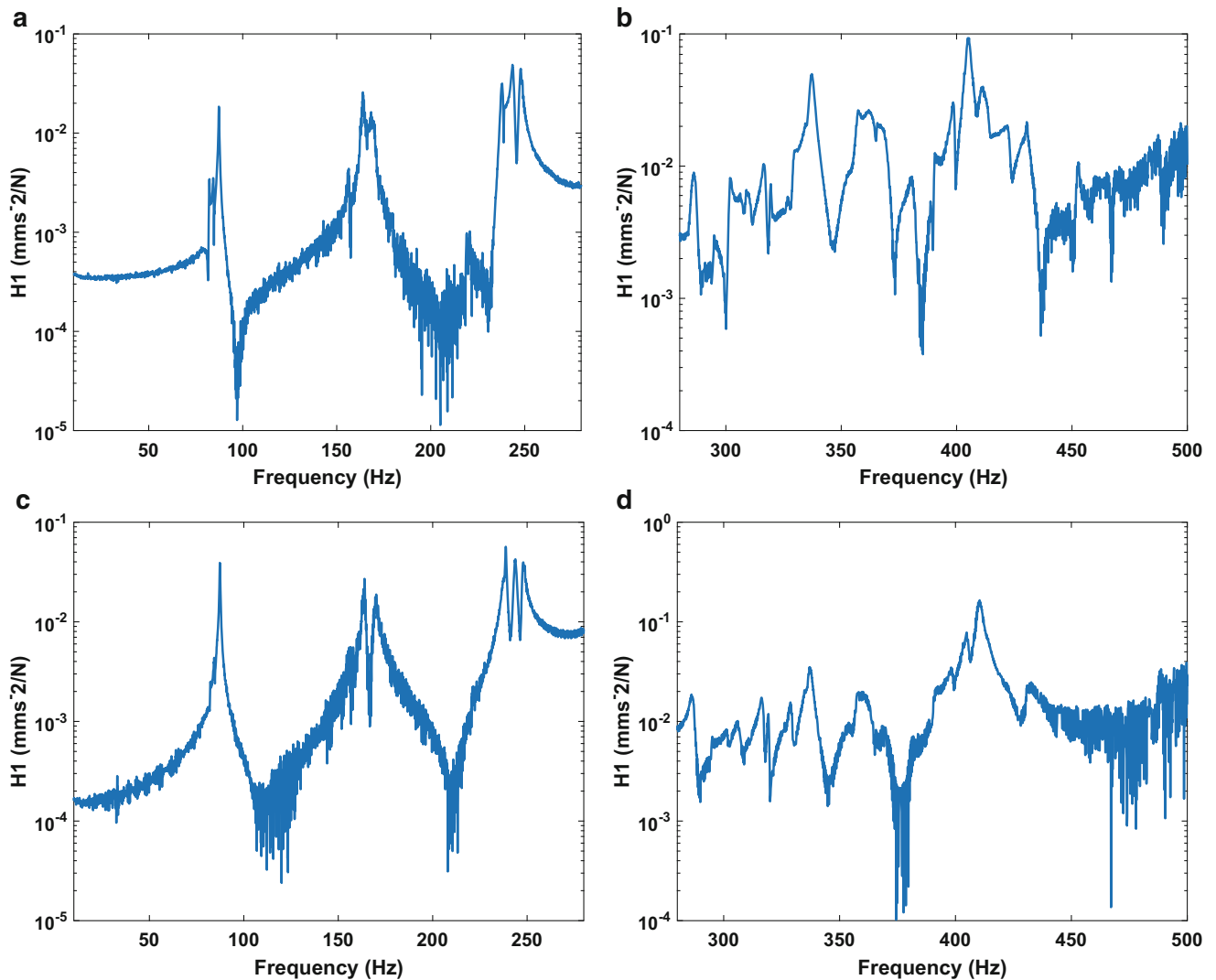


Fig. 27.3 Acceleration response function obtained from low-level broadband excitation performed on the nonlinear assembly. (a, b) (Bottom centre of the first cylinder) (c, d) (Drive point)

Table 27.1 Estimated Linear resonance frequencies and damping ratios based on low-level random data

Mode number	Natural frequency (Hz)	Damping ratio (%)	Mode number	Natural frequency (Hz)	Damping ratio (%)
1	82.17	0.29	7	169.98	0.46
2	84.34	0.19	8	172.05	0.46
3	87.17	0.09	9	179.68	0.19
4	158.42	0.13	10	237.51	0.34
5	163.41	0.39	11	238.68	0.12
6	167.29	0.57	12	243.45	0.28

three modes of the assembly ranging from the lowest (10 N) to a highest (120 N) input levels of excitation. These stepped-sine FRFs only consider the first harmonic and neglect all other higher-order harmonic components in both input and output. In Fig. 27.4a, a clear symptom of nonlinearity is observed based on the shift in frequency and maximum amplitude, most especially for the first mode around 82 Hz. The corresponding phase plot in Fig. 27.4b also shows the presence of nonlinear behaviour through the reduction observed in the phase plot as the excitation increases.

Sine-sweep test was also conducted on the plate casing assembly at multiple excitation levels to gain some insight into the time series data, the sine-sweep test was conducted to cover a frequency bandwidth of 70–93 Hz. Accelerations at selected

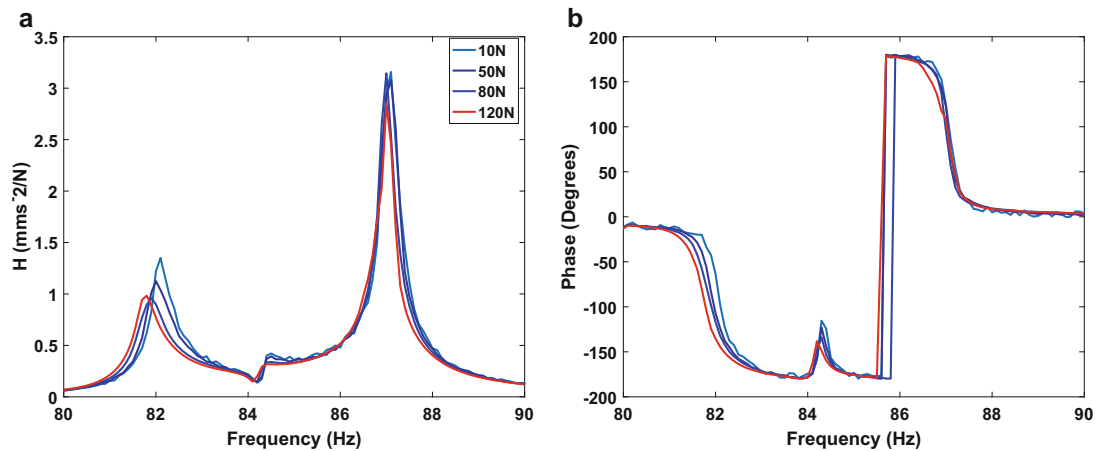


Fig. 27.4 Comparison of Stepped Sine FRFs and phase measured at several excitation levels obtained from the Stepped Sine test on the assembly

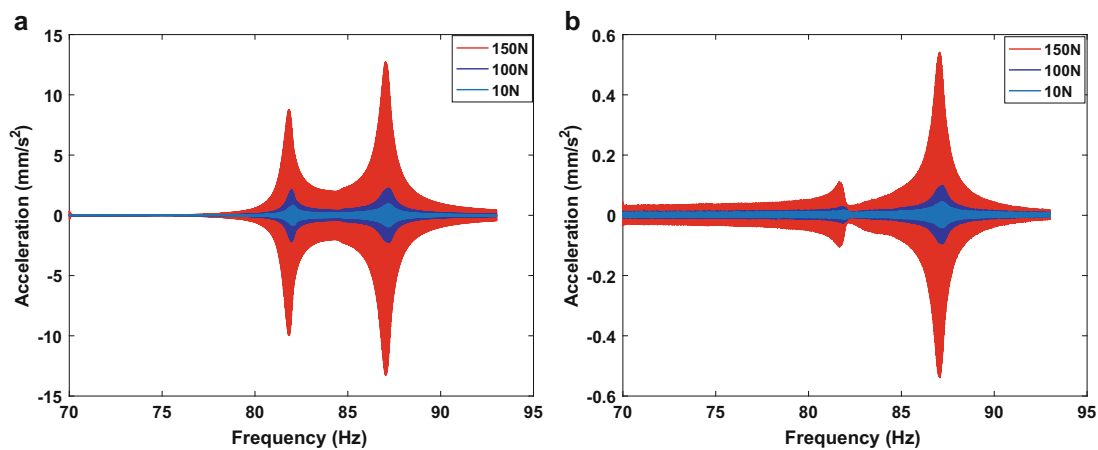


Fig. 27.5 Sine-sweep acceleration responses measured on two different locations of the nonlinear assembly. (a) (Bolted connection closest to the drive point between the casing and the plate), (b) (Drive point)

locations of the assembly were measured at 10, 80 and 120 N excitation levels. Figure 27.5a, b shows selected plots of the measured acceleration against sweep frequency for the modes of the assembly in that bandwidth.

Symptoms of nonlinearity are visible in the plots presented in Fig. 27.5 where a frequency shift is observed for both modes when the amplitude of vibration is increased. The lack of symmetry feature is also observed around the resonance peak of 82 Hz for high amplitude of vibration, this is more in Fig. 27.5b.

27.6 Identification Procedure

This section of the paper describes the identification process that was implemented in developing a nonlinear state space model for the assembly using experimental data. To obtain a PNLSS model structure it is important that the initial linear state space parameters (A, B, C, D) of the nonlinear system are first identified, in this paper the BLA approach was used in calculating these parameters from the measured data. After the calculation of these, a full nonlinear model is then built using the initial linear state space parameters as the starting point followed by an optimisation procedure to get a suitable nonlinear model structure of the test data.

27.7 Parametric and Non-parametric Analysis of the Nonlinear Distortions

This section introduces the best linear approximation (BLA) framework [18, 19] and the Local Polynomial Method (LPM) [20, 21] to estimate the BLA nonparametrically. The estimated BLA is used in the next section as an initialisation for the nonlinear model. To keep the notation simple, the single input single output case of the BLA estimation procedure is presented. A generalisation for multiple input and multiple output nonlinear systems is presented in [22, 23]. Practically the BLA of a nonlinear system for a class of input signals is defined as the linear model whose output best approximates the system's output in least-square sense [19]:

$$G_{BLA}(k) = \underset{G(k)}{\operatorname{argmin}} E_u \left\{ \|Y(k) - G(k)U(k)\|_2^2 \right\} \quad (27.1)$$

where G_{BLA} is the frequency response function (FRF) of the BLA, $E_u\{\cdot\}$ is an ensemble average over the considered class of input signals, $Y(k)$ and $U(k)$ are the discrete Fourier spectra of the output and the input at frequency line k , and G is the FRF of a linear system. Usually, the BLA framework is introduced for PISPO systems [19], which means that the response of the system to a periodic input is itself periodic with the same period length, and for (extended) Gaussian input signals [19]. With this condition obeyed, then the BLA of such system is definite to exist. The output spectrum of the system can then be written as:

$$Y(k) = G_{BLA}(k)U(k) + Y_S(k) + V(k) + T(k) \quad (27.2)$$

where the term $Y_S(k)$ accounts for nonlinear distortions, $V(k)$ accounts for additive measurement noise, and $T(k)$ accounts for leakage due to system and noise transients.

To estimate the BLA and to significantly reduce the effect of leakage, the LPM is used. The LPM exploits the smoothness over frequencies of $G_{BLA}(k)$ and $T(k)$, and the roughness over frequencies of $U(k)$, $Y_S(k)$, and $V(k)$. The basic idea of the LPM is to model the $G_{BLA}(k)$ and $T(k)$ as polynomials in a local frequency band around frequency line k :

$$Y(k+r) = G_{BLA}(k+r)U(k+r) + Y_S(k+r) + V(k+r) + T(k+r) \quad (27.3)$$

with

$$G_{BLA}(k+r) = \widehat{G}_{BLA}(k) + \sum_{s=1}^R \alpha_s r^s \quad (27.4)$$

$$T(k+r) = \widehat{T}(k) + \sum_{s=1}^R \beta_s r^s \quad (27.5)$$

for $r = -n, -n+1, \dots, 0, \dots, n-1, n$ with $n \geq R+1$. Putting all unknown coefficients $\widehat{G}_{BLA}(k)$, $\widehat{T}(k)$, $\alpha_1, \dots, \alpha_R, \beta_1, \dots, \beta_R$ in a parameter vector θ_{LPM} , and collecting all the Eq. (27.3) for $r = -n, -n+1, \dots, 0, \dots, n-1, n$ results in a linear regression formulation:

$$Y_n = K_n \theta_{LPM} + V_n \quad (27.6)$$

Solving for θ_{LPM} in least squares sense provides an estimate $\widehat{G}_{BLA}(k)$ of the FRF of the BLA. From the residuals, the LPM can also provide an estimate of the covariance matrix of the noise V_n , which in this case includes the random noise and the nonlinear distortions.

27.8 BLA Estimation of the Casing Assembly

To calculate the BLA of the casing assembly, sine-sweep input and output data sets were acquired at different excitation levels and different locations of the whole assembly. Although a sine-sweep is a deterministic signal instead of a random one, the initial linear state space and the FRF of the BLA can still be obtained using the expression given by:

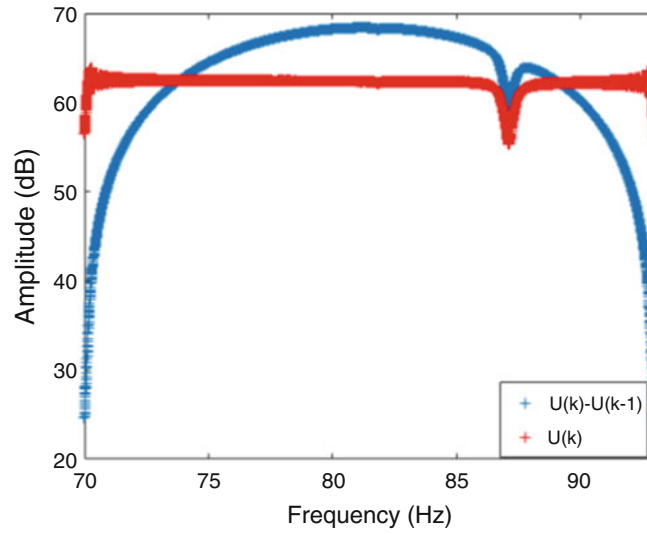


Fig. 27.6 The difference of the input spectrum ($U(k) - U(k-1)$)

$$G_{BLA}(k) = \frac{Y(k)}{U(k)} \quad (27.7)$$

at the excited frequency lines k . The fact that the spectrum $U(k)$ of a sine-sweep is not rough at all frequencies [20] could pose a challenge in the calculation, however the LPM can still be applied based on calculating the difference between the input at two consecutive frequencies i.e., ($U(k) - U(k-1)$). The results obtained from the difference in spectrum calculation is presented in Fig. 27.6, the spectrum ($U(k) - U(k-1)$) remains the same or at least within the same order of magnitude as $U(k)$ in a large part of the frequency band of interest and only become extinct to zero at 70 and 93 Hz. This means that the spectrum $U(k)$ is sufficiently rough in the frequency band of interest. Therefore, the LPM will be able to locally smooth the FRF for the BLA estimation.

With the FRFs and the BLA estimated using the expression in (27.7), a linear state space model (A B C D) is fitted on the nonparametric estimated model of the $G_{BLA}(k)$ using the frequency-domain subspace identification described in [24, 25]. The state space model is evaluated using the weighted least squares cost function:

$$V_L = \sum_{k=1}^F \epsilon_L^H(k) W_L(k) \epsilon_L(k) \quad (27.8)$$

Where F is the number of processed frequencies, superscript H represents the Hermitian transpose while the weighting function is $W_L(k)$. In this case, the inverse of the estimated total variance is used as a weighting. The model fitting error is then calculated based on the difference between the parametric and nonparametric BLA:

$$\epsilon_L = G_L(k) - G_{BLA}(k) \quad (27.9)$$

Figure 27.7 shows the corresponding estimated amplitude and phase for the parametric and nonparametric BLA along with the total (= noise + nonlinear) distortion levels at selected location of the assembly for 10 N excitation level.

An accurate fit based on a model order of 6 is observed both for the parametric and nonparametric estimation of the BLA, little discrepancies are only noticed outside the bandwidth of the start (70 Hz) and end (93) frequencies. The noise and distortion levels across the input band mostly lie averagely below 40 dB most especial for the FRF estimation illustrated in Fig. 27.7a, this proves the accuracy in the choice of 6 for the model order and the fact that the level of excitation used for this estimation is relatively low indicating that the nonlinearities are not yet active. To get an initial understanding of the of the experimental data before performing any nonlinear identification, the parametric and nonparametric BLA was also obtained from different excitation levels ranging from an RMS value of 10 N to 120 N. Figure 27.8 shows an illustration of the estimated amplitudes and total distortion levels across the different excitation levels, a slight shift in frequency and reduction in amplitude is observed in Fig. 27.8a, b as the excitation level increases. Similarly, it is evident that the total distortion (noise

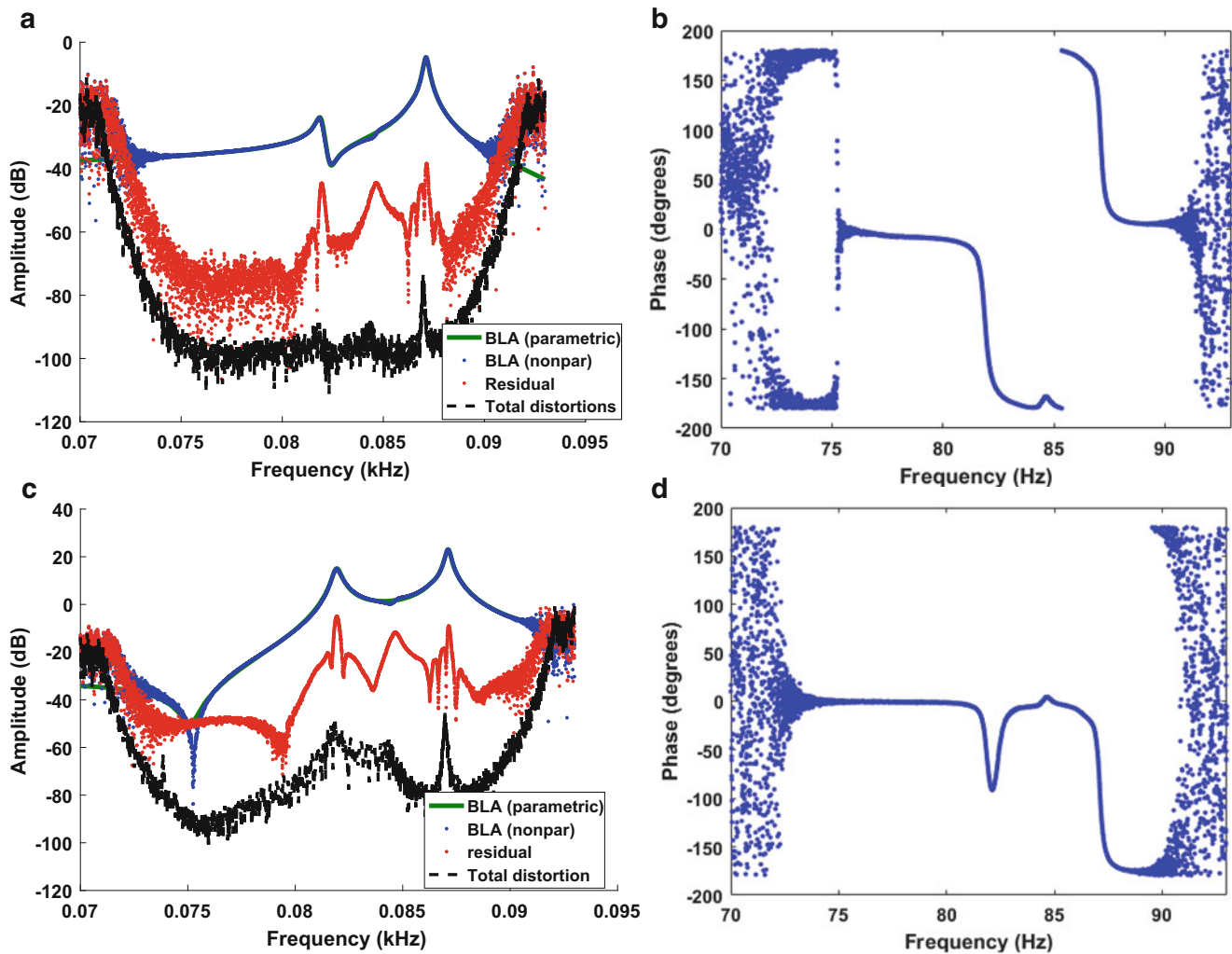


Fig. 27.7 Parametric and nonparametric BLA estimation and phase for two different output sensors on the assembly based on Sine-sweep data

+ nonlinear) distortions also affect the response of the structure. In Fig. 27.8b, d, the level of total distortions increases as the forcing changes from 10 to 120 N. The results obtained from the multiple forcing BLA estimation shows clear signs of nonlinearity in the measured data and thus require inclusion of nonlinear terms in the state space modelling.

27.9 Non-linear Identification Based on Polynomial Nonlinear State Space Models

The PNLSS model [14] structure generalizes a discrete-time linear state space model by extending the state and the output equation with polynomials in the states and the input:

$$x(t+1) = Ax(t) + Bu(t) + E\zeta(x(t), u(t)) \quad (27.10)$$

$$\hat{y}(t) = Cx(t) + Du(t) + F\eta(x(t), u(t)) \quad (27.11)$$

where the functions ζ and η are monomials with user-chosen degrees larger than one, and the matrices E and F contain the corresponding monomial coefficients. The state equation captures the dynamics since it describes how the state of the model

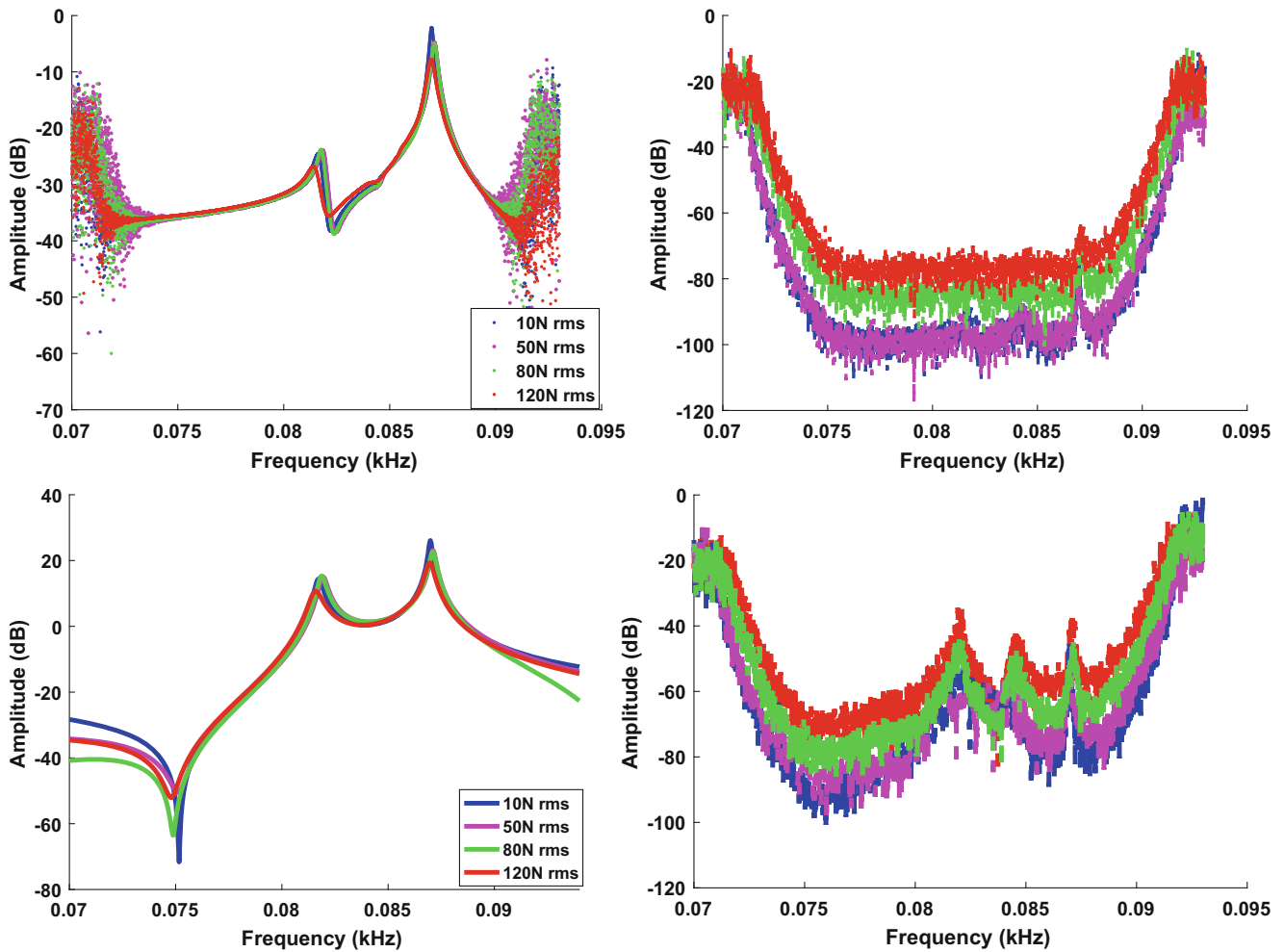


Fig. 27.8 Comparison of parametric, nonparametric BLA estimation, and total distortion for 4 different excitation levels

evolves as a function of the current state and input. Nonlinear dynamics can be captured because of the inclusion of the nonlinear terms $E \zeta$ and $F \eta$.

The parameters of the PNLSS model are the elements in the matrices A , B , C , D , E , and F . They are estimated by minimizing the difference between the measured and the modelled output in (weighted) mean-square sense. Since the modelled output is nonlinear in its parameters, the minimization problem is a nonlinear optimization problem that requires a good initial estimate of the parameters. Local optimization methods can then be used to further improve the estimate. The linear state space model estimated in the previous section is used as an initial guess for the matrices A , B , C , and D in the PNLSS model. The matrices E and F are initialised as zero matrices of the appropriate dimension. This initial estimate of the state-space model is further improved using a Levenberg-Marquardt algorithm [19, 26].

27.9.1 Identification Results Based on BLA Initialisation

The second step in the identification procedure involves identifying the appropriate nonlinear terms and parameters in matrices E and F that would capture the nonlinear dynamics in the measured data. To begin this stage, the BLA estimated in the previous section was used as an initial starting point while the PNLSS model is evaluated using a second weighted least-squares cost function in form:

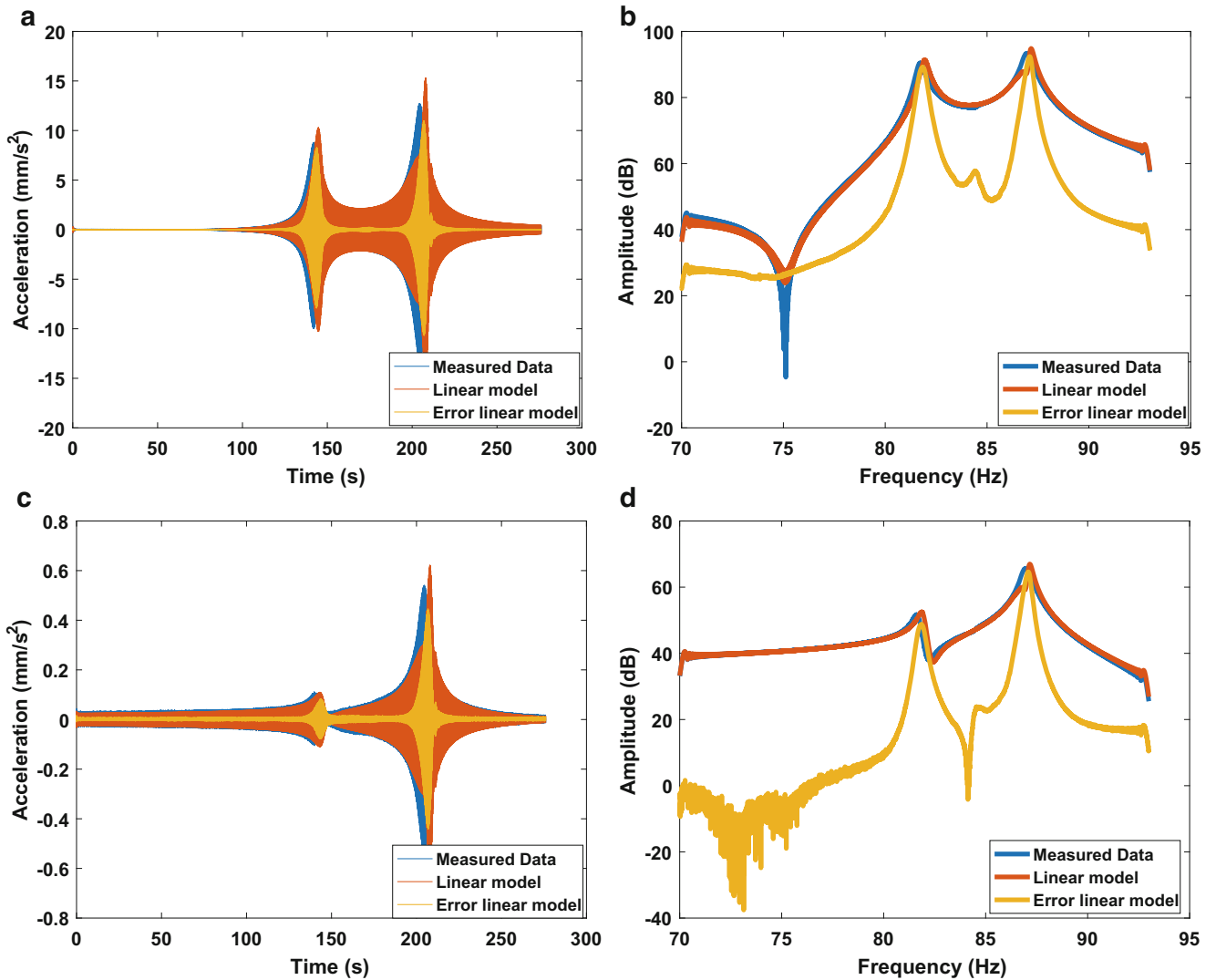


Fig. 27.9 Comparison of initial linear model against measured data for two selected location on the casing assembly. (a, b) (Time domain and frequency domain for the Bolted connection closest to the drive point between the casing and the plate), (c, d) (Time domain and frequency domain for the Drive point)

$$V_{NL} = \sum_{k=1}^F \epsilon_{NL}^H(k) W_{NL}(k) \epsilon_{NL}(k) \quad (27.12)$$

In this case all the parameters in the matrices of the of the full nonlinear model (A, B, C, D, E, F) are estimated through the minimisation of the second cost function V_{NL} . The model error is the calculated using the expression in Eq. (27.13).

$$\epsilon_{NL}(k) = Y_{NL}(k) - Y(k) \quad (27.13)$$

Where $Y_{NL}(k)$ and $Y(k)$ are the modelled and measured response. Figure 27.9 depicts the comparison between the initial results obtained from the PNLSS identification and the measured data. These results are identified based on using the BLA estimated model parameters i.e. (A, B, C, D) as initial starting values while the parameters in the E, and F matrices are set to have zero initial values.

Judging from the time and frequency domain results presented in Fig. 27.9, the results show that the initial identified linear model has a reasonable agreement with the measured data. However large errors and discrepancies are observed mainly around the resonance region which shows a clear indication that the nonlinear dynamics are not yet captured. The acceleration values at the resonance region are larger and in this case, may mean that the nonlinearities are stronger in those

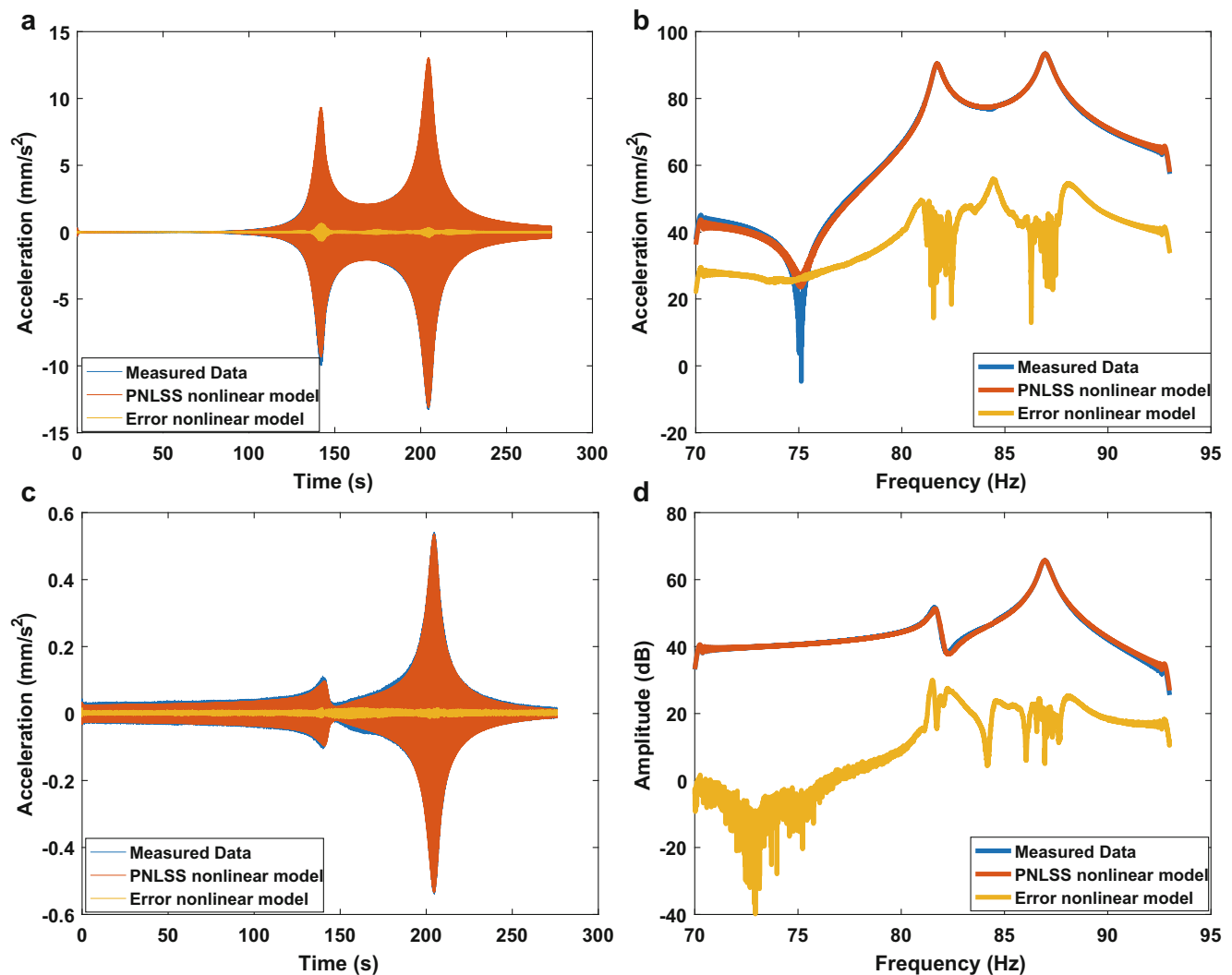


Fig. 27.10 Comparison of final identified model against measured data for two selected location on the casing assembly. (a, b) (Time domain and frequency domain for the Bolted connection closest to the drive point between the casing and the plate), (c, d) (Time domain and frequency domain for the Drive point)

section of the measured data, it therefore evident that the nonlinear behaviour that cannot be captured by a linear model and as such a full identification is required to accurately capture the nonlinear dynamics in the measured data. Similarly, the normalized Root Mean Squared (RMS) error of the linear model on the estimation dataset was 58.6%. Such a relatively high RMS percentage value is also an indication that the proposed linear model is not sufficient and thus require further identification and minimisation of the selected cost function.

To improve the results obtained based on the BLA initialisation, a full nonlinear model was developed for the final nonlinear state-space parameters (A, B, C, D, E, F) by minimising the second cost function in Eq. 27.12. The results obtained after running the second optimization are presented in Fig. 27.10. Comparing the full PNLSS results with the initial estimated results in Fig. 27.9, one can observe a great improvement between both models. The optimised PNLSS model improves on the results of the initial linear model, most especially around the resonance frequencies as shown in Fig. 27.10. This is a clear indication that the PNLSS model has successfully been able to capture a large portion of the nonlinear dynamics that was not captured in the initial model presented in Fig. 27.9.

A great improvement was also observed in the RMS percentage value after running the optimisation. Compared to the initial estimated model, a much lower RMS value of 3.2% was obtained for the PNLSS model. This a strong augmentation of about 50% between the initial and the final estimated PNLSS model. With this important improvement, it is evident that a PNLSS model that describes the nonlinear dynamics observed in the measured data has been identified without imposing any prior knowledge of the nonlinearities in the measured data.

27.10 PNLSS Model Validation

To study the validity of the identified PNLSS model, sine-sweep data sets at a lower forcing level was introduced to the PNLSS model. In this case, a comparison between the measured data and the reconstructed PNLSS model under an excitation level of 80 N was used as a validation activity. Figure 27.11 depict the results of the PNLSS model compared with experimental data at 80 N, the PNLSS results presented in Fig. 27.11 also show good agreement with the measured data. Although minor discrepancies are still observed between the PNLSS model and measured data most especially around the second resonance frequencies. However, for such a black-box application, the results are still quite impressive.

The RMS errors obtained on the for both the linear and PNLSS model on the validation data sets are 18.6% and 15.3%. It is worth stating that a price to pay for the large modelling flexibility implemented in nonlinear state space models is systematic and variance errors which are sometimes unavoidable depending on the problem which is being investigated.

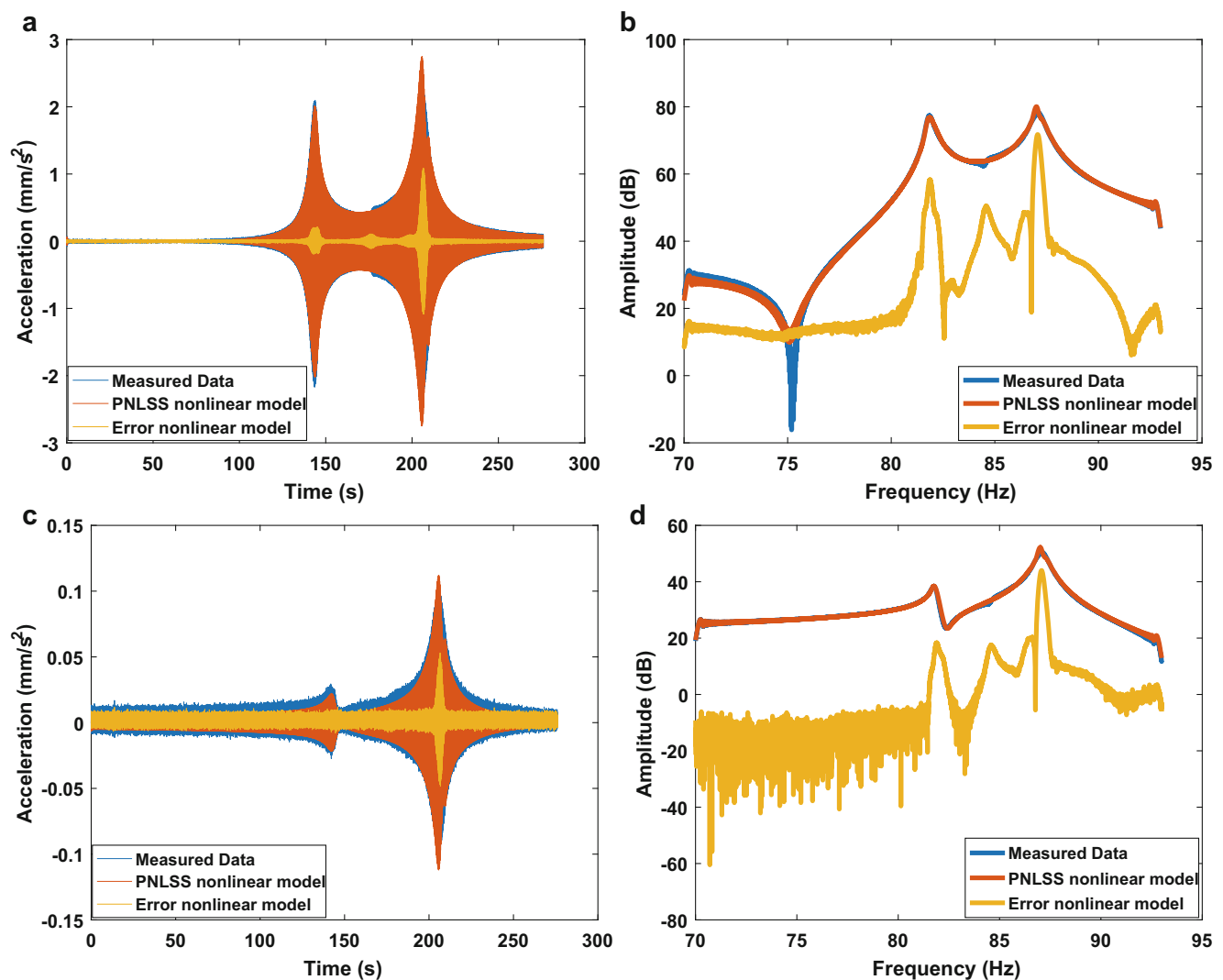


Fig. 27.11 Validation of PNLSS model against measured data for two selected location on the casing assembly. (a, b) (Time domain and frequency domain for the Bolted connection closest to the drive point between the casing and the plate), (c, d) (Time domain and frequency domain for the Drive point)

27.11 Conclusion

In this paper, a PNLSS model was used for the identification and validation of the nonlinear phenomena observed in the measured data obtained from a vibration test conducted on a large aerospace structure. The whole PNLSS model was investigated using Sine-Sweep data, the PNLSS model was initialised using the best linear approximation and a local polynomial method for local smoothing of the FRFs. Subsequently, a weighted least-squares minimisation approach was used to evaluate the PNLSS. The success of the of the PNLSS model was judged based on RMS errors between the PNLSS model and the true measured data. Based on the RMS values of 3.2% and 15.3% on the identification and validation models, one can conclude that the PNLSS method was able to successfully model the nonlinear dynamics observed in the measured data without any prior knowledge or physical insight to the nature of the nonlinearities. Finally, results presented in this paper shows the strength in using a black-box method to model the nonlinearities observed in a large aerospace structure.

References

1. Noël, J.P., Kerschen, G.: Nonlinear system identification in structural dynamics: 10 more years of progress. *Mech. Syst. Signal Process.* **83**, 2–35 (2017)
2. Noel, J.P., et al.: Nonlinear dynamic analysis of an F-16 aircraft using GVT data. In *Proceedings of the International Forum on Aeroelasticity and Structural Dynamics (IFASD)*, Bristol (2013)
3. Ahlquist, J.R., et al.: Assessment of nonlinear structural response in A400M GVT. in *Proceedings of the 28th International Modal Analysis Conference (IMAC)*. Springer, Jacksonville, Florida (2010)
4. Fuellekrug, U., Goege, D.: Identification of weak non-linearities within complex aerospace structures. *Aerosp. Sci. Technol.* **23**(1), 53–62 (2012)
5. Kerschen, G., et al.: Past, present and future of nonlinear system identification in structural dynamics. *Mech. Syst. Signal Process.* **20**(3), 505–592 (2006)
6. Feldman, M.: Hilbert transform in vibration analysis. *Mech. Syst. Signal Process.* **25**(3), 735–802 (2011)
7. Masri, S.F., et al.: Identification of the state equation in complex non-linear systems. *Int. J. Non Linear Mech.* **39**(7), 1111–1127 (2004)
8. Noel, J.P.: A Frequency-domain approach to subspace identification of nonlinear systems. In: *Aerospace and Mechanical Engineering*, p. 160. University of Liege, Liege (2014)
9. Chen, Q., et al.: Genetic algorithm with an improved fitness function for (N)ARX modelling. *Mech. Syst. Signal Process.* **21**(2), 994–1007 (2007)
10. Peng, Z.K., et al.: Feasibility study of structural damage detection using NARMAX modelling and nonlinear output frequency response function based analysis. *Mech. Syst. Signal Process.* **25**(3), 1045–1061 (2011)
11. Khan, A.A., Vyas, N.S.: Non-linear parameter estimation using Volterra and Wiener theories. *Sound Vib.* **221**, 805–821 (1998)
12. Khan, A.A., Vyas, N.S.: Nonlinear bearing stiffness parameter estimation in flexible rotor-bearing systems using Volterra and Wiener approach. *Probab. Eng. Mech.* **16**, 137–157 (2000)
13. Tawfiq, I., Vinh, T.: Contribution to the extension of modal analysis to non-linear structure using volterra functional series. *Mech. Syst. Signal Process.* **17**(2), 379–407 (2003)
14. Paduart, J., et al.: Identification of nonlinear systems using polynomial nonlinear state space models. *Automatica.* **46**(4), 647–656 (2010)
15. Noël, J.P., et al.: A nonlinear state-space approach to hysteresis identification. *Mech. Syst. Signal Process.* **84**, 171–184 (2017)
16. Svensson, A., Schön, T.B.: A flexible state–space model for learning nonlinear dynamical systems. *Automatica.* **80**, 189–199 (2017)
17. Peeters, B., et al.: The PolyMAX frequency-domain method: a new standard for modal parameter estimation. *Shock. Vib.* **11**(3–4), 395–409 (2004)
18. Schoukens, J., Dobrowiecki, T., Pintelon, R.: Parametric and nonparametric identification of linear systems in the presence of nonlinear distortions-A frequency domain approach. *IEEE Trans. Autom. Control.* **43**(2), 176–190 (1998)
19. Pintelon, R., Schoukens, J.: *System Identification: A Frequency Domain Approach*. Wiley-IEEE Press, Piscataway (2012)
20. Schoukens, J., et al.: Nonparametric preprocessing in system identification: a powerful tool. *Eur. J. Control.* **15**(3–4), 260–274 (2009)
21. Pintelon, R., et al.: Estimation of nonparametric noise and FRF models for multivariable systems—Part I: theory. *Mech. Syst. Signal Process.* **24**(3), 573–595 (2010)
22. Dobrowiecki, T.P., Schoukens, J.: Linear approximation of weakly nonlinear MIMO systems. *IEEE Trans. Instrum. Meas.* **56**(3), 887–894 (2007)
23. Pintelon, R., et al.: Estimation of nonparametric noise and FRF models for multivariable systems—Part II: extensions, applications. *Mech. Syst. Signal Process.* **24**(3), 596–616 (2010)
24. Pintelon, R.: Frequency-domain subspace system identification using non-parametric noise models. *Automatica.* **38**, 1295–1311 (2002)
25. Mckelvey, T., Akcay, H., Ljung, L.: Subspace-based multivariable system identification from frequency response data. *IEEE Trans. Autom. Control.* **41**(7), 960–979 (1996)
26. Marquardt, D.W.: An algorithm for least-squares estimation of nonlinear parameters. *Soc. Ind. Appl. Math.* **11**(2), 431–441 (1963)

Chapter 28

Curved Structures That Can Elastically Snap-Through



Lawrence N. Virgin, Yue (Susan) Guan, and Raymond H. Plaut

Abstract Curved structures, such as beams, arches and panels are capable of exhibiting snap-through buckling behavior when loaded laterally. However, the propensity to maintain a stable snapped-through equilibrium position (in addition to the nominally unloaded equilibrium configuration) after the load is removed depends on certain geometric properties. A number of clamped arches are used to illustrate the relation between geometry (thickness, span, initial deflection) and the corresponding equilibrium configuration(s). The finite element method and an elastica analysis compare well with a number of specifically-shaped arches produced using a 3D printer.

Keywords Nonlinear mechanics · Elastica · Snap-through · Co-existing equilibria · 3D printing

28.1 Introduction

In the classic sinusoidal arch [1], and similarly for other shapes, the arch needs a certain rise (for given span) to have a stable inverted equilibrium shape under no load. A symmetric arch with pinned boundary conditions will exhibit an unambiguous snapped-through (inverted) position, given sufficient perturbation. However, with clamped boundary conditions it is apparent that for some arches a stable snapped-through configuration is possible whereas for others the initial shape is the *only* stable equilibrium [2]. It is therefore natural to ask: for which initial shapes can a clamped symmetric arch-like structure maintain a partially snapped-through equilibrium (that is, without the need for any kind of external applied force or constraint to maintain the position)?

This presentation uses a specific mathematical form to describe an initial shape. The resulting (highly nonlinear) equilibrium equations are solved and their stability is assessed. The stability assessment is then related back to the parameters associated with the initial shape. An additional FEA is conducted and the results compared to those from the elastica analysis.

Additive manufacturing is used to produce a variety of prescribed shaped arches (with built-in ends) that span the critical boundary between shapes with just a single stable equilibrium and those that possess a stable snapped-through equilibrium.

28.2 The Geometry

The shapes of the symmetric arches considered here can be conveniently prescribed in arc-length coordinates by

$$\theta_0(s) = (1 - 2s)\beta + cs(1 - s)(1 - 2s), \quad (28.1)$$

where s is the arc length, and c and β (the end angle) are positive constants. These shapes are somewhat similar to ones analyzed in Ref. [3] for shallow extensible arches. The arc-length description is useful in terms of the end angle, but the correspondence to conventional shapes in Cartesian coordinates (for 3D printing purposes) is not simple.

L. N. Virgin (✉) · Y. (Susan) Guan

Department of Mechanical Engineering and Materials Science, Duke University, Durham, NC, USA
e-mail: l.virgin@duke.edu

R. H. Plaut

Department of Civil and Environmental Engineering, Virginia Tech, Blacksburg, VA, USA

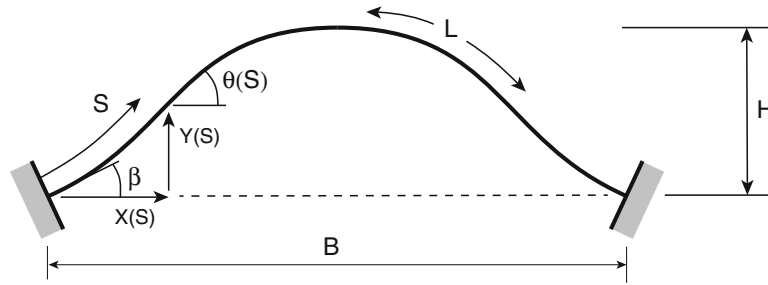


Fig. 28.1 The initial geometry of a class of symmetric geometries

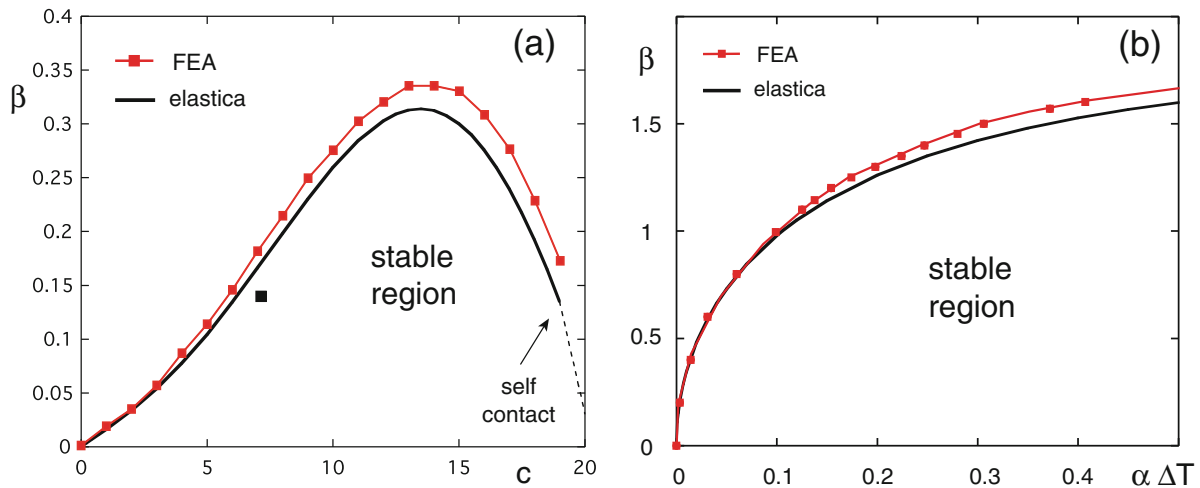


Fig. 28.2 Parameter space separated into regions of stable inverted equilibria labeled ‘stable region’ and where only the initial equilibrium is stable, (a) based on shape, (b) based on thermal loading for an initially circular arch

The form of Eq. 28.1 is shown schematically in Fig. 28.1 in an initially stable equilibrium configuration. Various techniques are then used to establish whether specific shapes are capable of exhibiting another (typically snapped-through) equilibrium configuration. The shape is parameterized by c and β , and the results will be presented in these terms, but they relate directly to the practical shape parameters of length L , horizontal separation of the boundary conditions B , and the central arch rise H .

28.3 Theoretical Results

28.3.1 Analysis Based on Shape

For an elastica analysis, the governing partial differential equations for this system can be set-up, non-dimensionalized, and solved using a shooting technique with Mathematica. The initial solution consists of satisfying the equilibrium conditions, and the stability is assessed using the frequencies of small-amplitude vibrations. This numerical approach is used for many combinations of c and β , and Fig. 28.2a shows the parameter space, indicating the region of more than one stable equilibrium configuration. A finite element analysis using ABAQUS was also performed and the line separating the region of multiple stable equilibria shows a close correspondence with the elastica analysis [2].

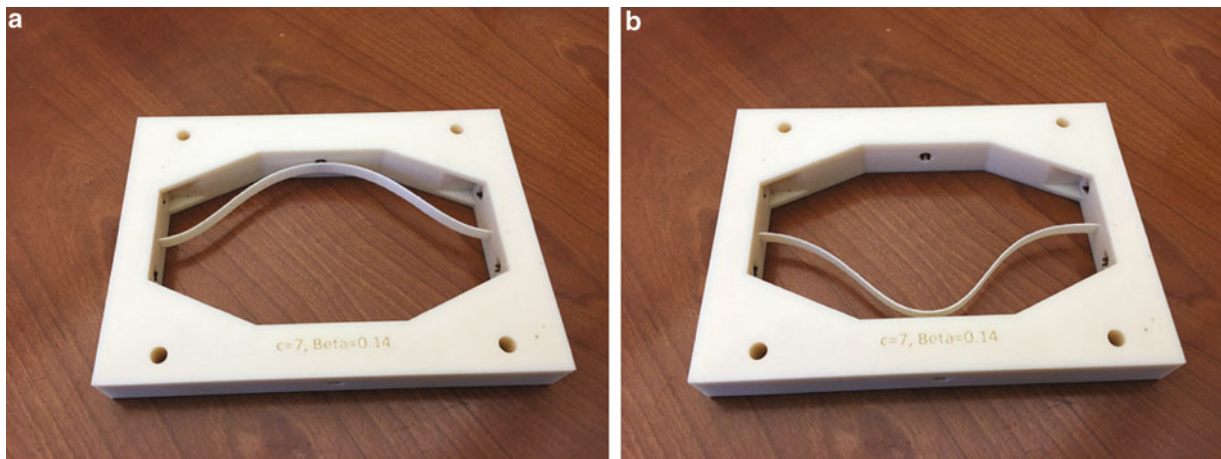


Fig. 28.3 (a) A specific arch shape as printed, (b) the same arch in its inverted equilibrium configuration

28.3.2 Thermal Loading

Similar analyses were performed in which a thermal loading parameter was introduced for the specifically circular arch ($c = 0$). Again, the parameter space is shown to consist of regions in which only the initial equilibrium configuration is stable and those where other equilibria are realizable (stable), see Fig. 28.2b. The results of FEA again support the elastica analysis. It is interesting to note that the slow *cooling* of the arch can result in a sudden loss of stability if the transition boundary is crossed [4] such that there is a loss of stability of the inverted equilibrium configuration.

28.4 Some 3D Printed Shapes

A 3D printer was used to produce arches of certain shapes corresponding to specific parameter values within Fig. 28.2a, and an example is shown in Fig. 28.3. This arch is capable of exhibiting a stable snapped-through equilibrium (part b) in addition to the initial equilibrium (part a). Since the parameters corresponding to this shape are given by $c = 7$ and $\beta = 0.14$, it corresponds, as expected, to a point within the stable region (and indicated by the black data point in Fig. 28.2a).

28.5 Concluding Remarks

This study considers slender, symmetric, elastic arches, whose ends are clamped, and can be described in relatively simple mathematical terms. Both elastica and FEA analyses are conducted to determine if a given geometry is capable of displaying a stable (typically partially inverted) equilibrium configuration, in addition to the initial shape. A 3D printer is used to produce shapes that confirm the results of these analyses.

References

1. Fung, Y.-C., Kaplan, A.: Buckling of low arches or curved beams of small curvature, Technical note 2840, National Advisory Committee for Aeronautics (1952)
2. Virgin, L.N., Guan, Y., Plaut, R.H.: On the geometric conditions for multiple stable equilibria in clamped arches. *Int. J. Non Linear Mech.* **92**, 8–14 (2017)
3. Hsu, C.S.: Equilibrium configurations of a shallow arch of arbitrary shape and their dynamic stability character. *Int. J. Non Linear Mech.* **3**, 113–136 (1968)
4. Virgin, L.N., Wiebe, R., Spottswood, S.M., Eason, T.G.: Sensitivity in the structural behavior of shallow arches. *Int. J. Non Linear Mech.* **58**, 212–221 (2014)



Chapter 29

Experimental Analysis of Non-Linear Damping Performance in Composites Materials Thanks to Local Transduction-Dissipation Phenomenon

Mathieu Chevalier, Camille Bessaguet, Luis Quiroga-Cortès, Eric Dantras, and Guilhem Michon

Abstract This paper describes the influence of a passive vibration damping concept on the dynamic response of high performance composites. The analysis of hysteresis loops and frequency response function of cantilever beams shows non-linear effects and high dissipative performances. These results are associated with the damping materials' properties.

Keywords Composites · Piezoelectric · Damping · Hysteresis loops · Vibration

Enhancement of dynamic mechanical and vibroacoustic responses of primary structures is a topic of great interest in aerospace applications. The objective is to improve payload comfort and structures reliability. In addition, Organic Matrix Composites (OMC) become more competitive versus metallic solutions. On the one hand, these solutions provide advantageous rigidity/weight and resistance/weight ratios, ability to manufacture complex shapes with reduced amount of fasteners that contribute to weight reductions. On the other hand, it induces drawbacks such as the decrease of damping capacity and the increase of vibration levels.

The current counter strategies consist in ensuring structures reliability by active control, design modifications, add-on extrinsic macroscopic elements, in order to adapt the dynamic response. But these solutions increase the overall mass of targeted structures.

For real weight and cost reductions, it is proposed to study embedded passive damping concepts. The objective is to bring this functionality at materials' level in high performance polymers and organic matrix composites while maintaining mechanical performances. In this context, the integration of passive damping functionality in high performance composites is studied.

The concepts consist in adding piezoelectric and electrically dissipative particles at material scale in order to add a new contribution – the local transduction-dissipation [1–3] – to overall damping generally obtained thanks to structural, stick-slip and viscous contributions [4]. To reach this ambitious objective, R&D activities target the most promising concepts, taking into account realistic manufacturing processes. In the same time, a scale-up methodology is implemented in order to assess the dynamic response and damping properties from coupons to more complex systems (Fig. 29.1).

To understand physical dissipative properties of the studied concept requires identification of hysteresis loops in the strain-stress representation [5]. These are measured with shear tests thanks to a specific Dynamic Mechanical Analysis system. They highlight strong non-linear effects, frequency and amplitude dependency [6] (Fig. 29.2).

Finally, dynamic tests are performed on cantilever sandwich beams including the proposed damping solution in a constrained layer configuration, embedded on an electrodynamic shaker for several excitation amplitudes. Frequency sweeps show non-linear effects and high dissipative performances (Fig. 29.3).

M. Chevalier (✉) · C. Bessaguet · L. Quiroga-Cortès
Institut de Recherche Technologique (IRT) Saint Exupéry, Toulouse, France
e-mail: mathieu.chevalier@irt-saintexupery.com

E. Dantras
Physique des Polymères, Institut Carnot CIRIMAT, Université Paul Sabatier, Toulouse, France

G. Michon
Institut Supérieur de l'Aéronautique et de l'espace, Institut Clément Ader, Toulouse, France

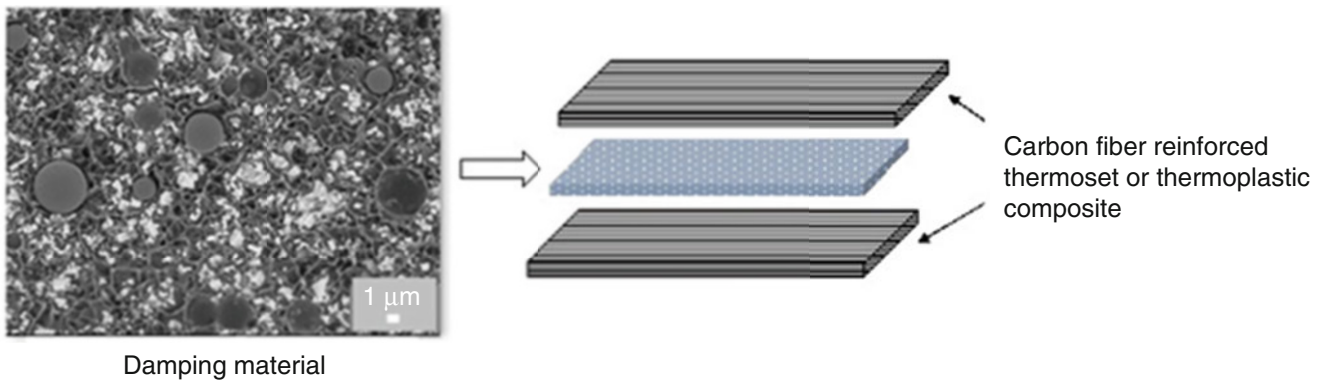


Fig. 29.1 Constrained Layer Damping configuration (CLD)

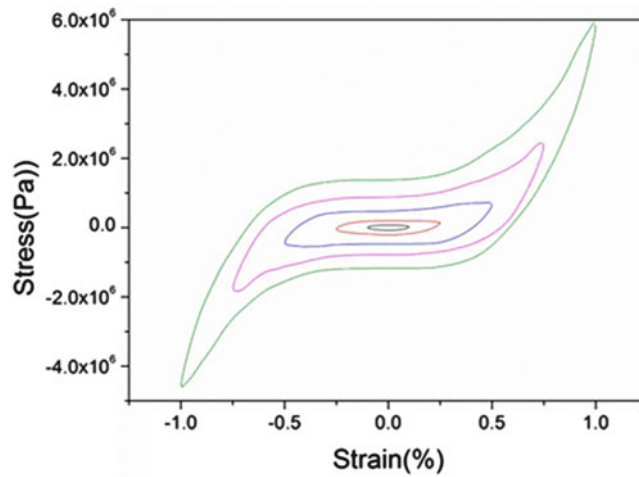


Fig. 29.2 Measured hysteresis loops for strain rate between 0.25% and 1%

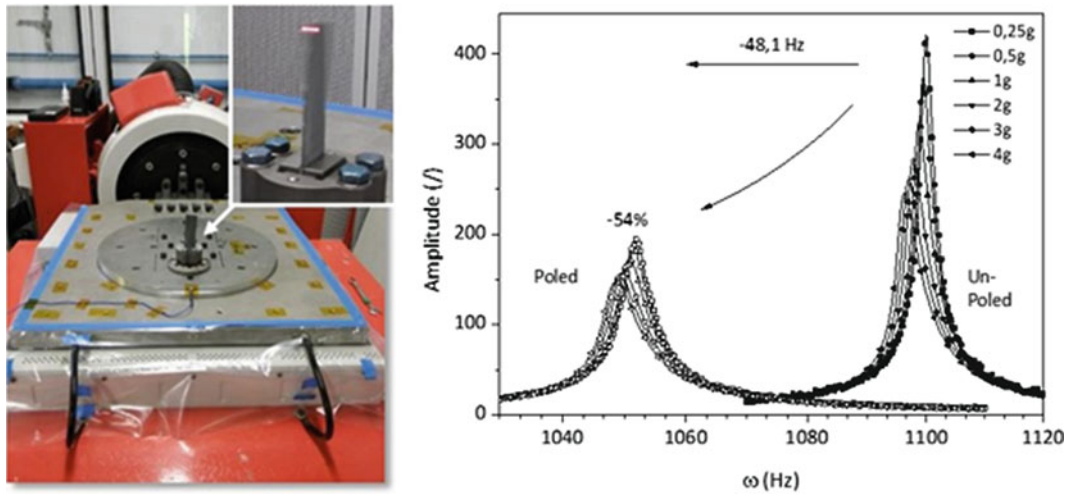


Fig. 29.3 Test set up configuration on the electrodynamic shaker (left) and frequency response function for the second mode of a cantilever beam for un-poled and poled versions (right)

This damping concept highlights an increase of the dissipated energy thanks to hysteresis loops analysis. This behavior is related to the response of a dynamic structure with an important decrease of the resonance mode amplitude for the 2nd bending mode. Further investigation will be devoted to multiscale understanding and modeling of the material contribution to damping performances.

References

1. Hori, M., Aoki, T., Ohira, Y., Yano, S.: New type of mechanical damping composites composed of piezoelectric ceramics, carbon black and epoxy resin. *Compos. Part A*. **32**, 287–290 (2001)
2. Carponcin, D., Dantras, E., Michon, G., Dandurand, J., Aridon, G., Levallois, F., Cadiergues, L., Lacabanne, C.: New hybrid polymer nanocomposites for passive vibration damping by incorporation of carbon nanotubes and lead zirconate titanate particles. *J. Non-Cryst. Solids*. **409**, 20–26 (2015)
3. Bessaguet, C., Dantras, E., Lacabanne, C., Chevalier, M., Michon, G.: Piezoelectric and mechanical behavior of NaNbO₃/PEKK lead-free nanocomposites. *J. Non-Cryst. Solids*. **459**, 83–87 (2017)
4. Barbier, C., Dendievel, R., Rodney, D.: Role of friction in the mechanics of nonbonded fibrous materials. *Phys. Rev. E*. **80**, 1–5 (2009)
5. Piollet, E., Poquillon, D., Michon, G.: Dynamic hysteresis modelling of entangled cross-linked fibres in shear. *J. Sound Vib.* **383**, 248–264 (2016)
6. Al-Bender, F., Symens, W., Swevers, J., Van Brussel, H.: Theoretical analysis of the dynamic behavior of hysteresis elements in mechanical systems. *Int. J. Non. Linear. Mech.* **39**, 1721–1735 (2004)



Chapter 30

Subspace-Based Identification of a Distributed Nonlinearity in Time and Frequency Domains

D. Anastasio, S. Marchesiello, J. P. Noël, and G. Kerschen

Abstract Nonlinear system identification has become of great interest during the last decades. However, a common and shared framework is not present yet, and the identification may be challenging, especially when real engineering structures are considered with strong nonlinearities. Subspace methods have proved to be effective when dealing with local nonlinearities, both in time domain (TNSI method) and in frequency domain (FNSI method). This study reports an improvement for both methods, as a first attempt to account for distributed nonlinearities, which is still an open question in the research community. A numerical beam under moderately large oscillations that exhibits geometric nonlinearity is considered. The object of the identification process is to exploit its behavior through the correct identification of the parameters that define the nonlinearity. Results show a high level of confidence between the two methods, and suggest that a more complete analysis of distributed nonlinear phenomena can be conducted based on these approaches.

Keywords Nonlinear system identification · Subspace identification · Distributed nonlinearity · Geometric nonlinearity · Nonlinear beam

30.1 Introduction

Identification of nonlinear dynamical systems has been thoroughly investigated in recent years. The number of methods developed is large and, generally, no method exists to be adopted for any type of nonlinearity, system complexity or exciting force [1]. However, a basic distinction on the nature of the nonlinearity can be done between local nonlinearities (clearances, loosing connections, . . .) and distributed nonlinearities. A few examples of distributed nonlinearities are material (or constitutive), inertia, geometric [2]. In particular, the geometric nonlinearity is associated with large deformations in solids, resulting in nonlinear strain-displacement relations. This case has become frequent during the last years, due to a continual interest to expand the performance envelope of structures, which brings the need for designing lighter, more flexible, and consequently, more nonlinear structural elements [3, 4]. In this framework, system identification plays a key role as a tool to gather information about the dynamics of the system.

This study refers to a simple nonlinear beam under large transversal oscillations, which bring geometric nonlinearity. This should be considered as a first attempt to identify distributed nonlinearities, which is still an open point in the research community. Two methods are used, both based on subspace identification [5]: TNSI (Time Nonlinear Subspace Identification) [1, 6] and FNSI (Frequency Nonlinear Subspace Identification) [7, 8]. The main difference between TNSI and FNSI is the domain in which they work, which is time for the first and frequency for the second. They both proved to be effective in the identification of local nonlinearities [9], thus an extension to a case of distributed nonlinearity is here suggested.

D. Anastasio (✉) · S. Marchesiello
Department of Mechanical and Aerospace Engineering, Politecnico di Torino, Torino, Italy
e-mail: dario.anastasio@polito.it

J. P. Noël
Space Structures and Systems Laboratory, Department of Aerospace and Mechanical Engineering, University of Liège, Liège, Belgium

G. Kerschen
Mechanical Engineering, S3L, Quartier Polytech, University of Liege, Department of Aerospace, Liege, Belgium

30.2 Beam Under Large Lateral Oscillations

A 2D Euler-Bernoulli beam with large lateral deflection is considered. The governing equation is [2]:

$$\mu \frac{\partial^2 w}{\partial t^2} + EI \frac{\partial^4 w}{\partial x^4} - \frac{EA}{2L} \left(\int_0^L \left(\frac{\partial w}{\partial x} \right)^2 dx \right) \frac{\partial^2 w}{\partial x^2} = f(t) \delta(x - x_F) \quad (30.1)$$

Where μ is the linear mass, E is the Young's Modulus, I is the moment of inertia, A is the section, L is the length, x_F is the forcing position and w is the lateral displacement. The third term in Eq. (30.1) expresses the nonlinearity, and can be seen as a variable axial load generated by the lateral movement. The solution to Eq. (30.1) can be found applying the modal transformation expressed in Eq. (30.2).

$$w(x, t) = \sum_{j=1}^{\infty} \phi_j(x) \eta_j(t), \quad \phi_j = j^{\text{th}} \text{ eigenmode}, \quad \eta_j = j^{\text{th}} \text{ modal coordinate} \quad (30.2)$$

The mode shapes ϕ_j depend on the boundary conditions at the ends of the beam, and analytic expressions are available for the most common ones. A set of N equations is obtained substituting Eq. (30.2) in Eq. (30.1) considering N modes, as expressed in Eq. (30.3). The nonlinear part of the equation is approximated considering $P \leq N$ nonlinear terms.

$$m_j \ddot{\eta}_j + k_j \eta_j - \frac{EA}{2L} \sum_{r=1}^P (c_{1,r}^{nl} \eta_r^2) c_{2,j}^{nl} \eta_j = Q_j \quad j = 1, \dots, N \quad (30.3)$$

Where $Q_j = \phi_j^T f$ are the modal forces, m_j is the modal mass, k_j is the modal stiffness and $c_{1,r}^{nl}, c_{2,j}^{nl}$ are the nonlinear coefficients. These depend on the boundary conditions, and can be generally expressed as:

$$c_{1,r}^{nl} = \int_0^L \phi_r'(x) dx, \quad c_{2,j}^{nl} = \int_0^L \phi_j(x) \phi_j''(x) dx \quad (30.4)$$

These coefficients are the objective of the identification process implemented in the following example.

30.3 Nonlinear System Identification

TNSI and FNSI are applied to a numerical clamped-clamped beam under large lateral oscillations, whose characteristics are reported in Table 30.1. The methodology here explained can be applied also considering other boundary conditions which verify the hypothesis of self-adjoint operators for mass, stiffness and damping. The goal of the identification process is to extract the modal parameters of the underlying linear system and the coefficients that express the nonlinearity.

The numerical test is performed applying a periodic random excitation to the beam and measuring the response in 10 points by numerical integration. Also, a reasonable amount of Gaussian noise is added to the response. The identification is performed on the modal equations, thus a first low-excitation test is performed to extract the linear mode shapes of the beam, called ϕ^{exp} . It should be noticed that an analytical expression of the eigenmodes is not needed, assuming that a linear test can be performed on the structure. The experimental modal coordinates can be expressed as:

$$\eta^{\text{exp}} = \text{pinv}(\phi^{\text{exp}}) w^{\text{exp}} \quad (30.5)$$

Once the modal coordinates are extracted, the identification can be performed starting from Eq. (30.3) and remembering that both TNSI and FNSI treat the nonlinear force as a feedback. One of the advantages of the presented methodology is that the set of N equations are linearly independent, which means that the identification can be performed on each mode separately. This speeds up the calculations, as avoids the computation of huge matrices due to high model orders. An exemplary result of the identification considering the first 3 modes is depicted in Fig. 30.1. Both the FRF and the nonlinear coefficients are well identified, which proves the goodness of the adopted methodology.

Table 30.1 Characteristics of the beam

Length (mm)	L	300
Section (mm ²)	$b \cdot h$	30 • 1
Young's Modulus (GPa)	E	200

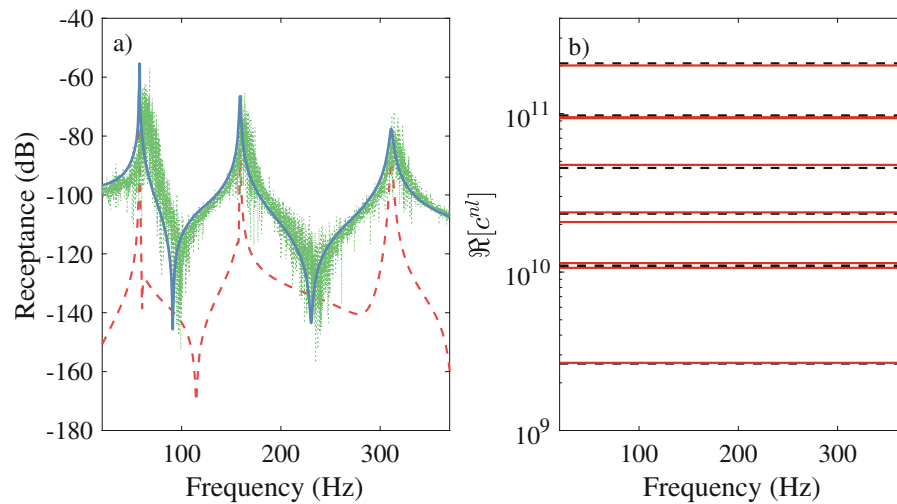


Fig. 30.1 Results of the identification. (a) Blue line: driving point receptance of the identified underlying linear system; red dashed line: residue with the analytical linear receptance; green dotted line: nonlinear FRF distortion. (b) Red lines: real part of the identified nonlinear coefficients; black dashed lines: true nonlinear coefficients

References

1. Marchesiello, S., Garibaldi, L.: A time domain approach for identifying nonlinear vibrating structures by subspace methods. *Mech. Syst. Signal Process.* **22**, 81–101 (2008)
2. Nayfeh, A.H., Pai, P.F.: *Linear and Nonlinear Structural Mechanics*. Wiley-Interscience, New York (2004)
3. Amabili, M., Paidoussis, M.: Review of studies on geometrically nonlinear vibrations and dynamics of circular cylindrical shells and panels, with and without fluid–structure interaction. *Appl. Mech. Rev.* **56**, 349–381 (2003)
4. Kerschen, G., Worden, K., Vakakis, A.F., Golinval, J.C.: Past, present and future of nonlinear system identification in structural dynamics. *Mech. Syst. Signal Process.* **20**, 505–592 (2006)
5. Van Overschee, P., De Moor, B.: *Subspace Identification for Linear Systems: Theory-Implementation-Applications*. Kluwer Academic Publishers, Dordrecht (1996)
6. Marchesiello, S., Fasana, A., Garibaldi, L.: Modal contributions and effects of spurious poles in nonlinear subspace identification. *Mech. Syst. Signal Process.* **74**, 111–132 (2016)
7. Noël, J.P., Kerschen, G.: Frequency-domain subspace identification for nonlinear mechanical systems. *Mech. Syst. Signal Process.* **40**, 701–717 (2013)
8. De Filippis, G., Noël, J.P., Kerschen, G., Soria, L., Stephan, C.: Model reduction and frequency residuals for a robust estimation of nonlinearities in subspace identification. *Mech. Syst. Signal Process.* **93**, 312–331 (2017)
9. Noël, J.P., Marchesiello, S., Kerschen, G.: Subspace-based identification of a nonlinear spacecraft in the time and frequency domains. *Mech. Syst. Signal Process.* **43**, 217–236 (2014)



Chapter 31

Reduced Order Modelling for Non-linear Rotating Systems in ALE Formulation with Contact

Tim Weidauer and Kai Willner

Abstract One approach for the simulation of rotating systems is the *Arbitrary-Lagrangian-Eulerian* (ALE) finite element formulation, which is well-established in the field of rolling contact mechanics for tires. With this formulation the rotational motion is handled from an Eulerian viewpoint and thus can be separated from the occurring Lagrangian deformation of the finite element mesh. In this context of (non-linear) systems undergoing gyroscopic and/or contact forces, e.g., for tires or disc brakes, model reduction techniques such as the *Second order modal truncation*, the *Krylov subspace technique* and the *Craig-Bampton method* are employed and analysed in their applicability.

Keywords Gyroscopic system · ALE · Non-linear dynamics · Model order reduction · Contact

31.1 Introduction

Despite the constant increase of computational capabilities of today's hardware configurations reduced order modelling is still an important topic as at the same time the complexity of the systems to be simulated increases as well. Thus it is still a challenging necessity to reduce a system's dimension, while keeping its dynamic properties intact. In the following the well-known methods of reduced order modelling *Second order modal truncation*, the *Krylov subspace technique* and the *Craig-Bampton method* are discussed in the context of linear and non-linear gyroscopic mechanical systems, which are formulated utilizing an *Arbitrary-Lagrangian-Eulerian* (ALE) approach.

31.2 Model Order Reduction

The general concept of reduced order modelling in structural mechanics focusses on finding a low-dimensional subspace \mathcal{K} , spanned by a set of $q \ll n$ basis vectors, gathered in the columns of a transformation matrix $\mathbf{T} \in \mathbb{R}^{n \times q}$ in order to approximate a full-sized solution vector $[\bullet] \in \mathbb{R}^n$ via

$$[\bullet] \approx \mathbf{T} [\bullet]_r \quad \text{with} \quad [\bullet]_r \in \mathbb{R}^q. \quad (31.1)$$

This way degrees of freedom (DoF) of minor importance of the spatially discretized structure are neglected and a reduced order model (ROM) is built. More general for fields like control engineering this goal can be formulated as finding a suitable approximation of low order for the full-sized system output to a specific input. There exist several methods for this purpose, which all rely on a coordinate transformation as in (31.1). The main difference between these methods lies in the way the basis vectors in \mathbf{T} are determined. Out of these a brief outline of the *Second order modal truncation*, *Krylov subspace techniques* and the *Craig-Bampton substructuring technique* is given in Sects. 31.2.1 and 31.2.2. For deeper insight into the technicalities it is referred to the respective references.

T. Weidauer (✉) · K. Willner
Friedrich-Alexander Universität Erlangen-Nürnberg, Erlangen, Germany
e-mail: tim.weidauer@fau.de

31.2.1 Linear Systems

The motion of a linear undamped non-gyroscopic system with dimension n in second order form is described by

$$\mathbf{M}\ddot{\mathbf{y}} + \mathbf{K}\mathbf{y} = \mathbf{f} \quad (31.2)$$

with mass matrix $\mathbf{M} = \mathbf{M}^\top$, stiffness matrix $\mathbf{K} = \mathbf{K}^\top$ and forcing \mathbf{f} . It can be expressed as the superposition of the n system's eigenmodes $\tilde{\mathbf{y}}_j$ gathered in the modal column matrix $\tilde{\mathbf{Y}}$ and the modal coordinates $\hat{\mathbf{y}}(t)$ via

$$\mathbf{y}(t) = \tilde{\mathbf{Y}}\hat{\mathbf{y}}(t). \quad (31.3)$$

The eigenmodes $\tilde{\mathbf{y}}_j$ and the respective eigenfrequencies ω_j stem from the eigenproblem and its determinant

$$(-\omega_j^2\mathbf{M} + \mathbf{K})\tilde{\mathbf{y}}_j = \mathbf{0} \quad \Leftrightarrow \quad \det(-\omega_j^2\mathbf{M} + \mathbf{K}) = 0 \quad (31.4)$$

with the exponential ansatz $\mathbf{y}(t) = \tilde{\mathbf{y}} e^{i\omega t}$. For the case with no or at most proportional damping, e.g., Rayleigh damping of the form

$$\mathbf{D} = \alpha\mathbf{M} + \beta\mathbf{K}, \quad (31.5)$$

$\tilde{\mathbf{y}}_j \in \mathbb{R}^n$ holds and thus $\tilde{\mathbf{Y}} \in \mathbb{R}^{n \times n}$ is a real square matrix, [1].

In the case of (axi-)symmetric structures like discs so-called *double modes* $\tilde{\mathbf{y}}_j \equiv \tilde{\mathbf{y}}_{j+1} \in \mathbb{R}^n$, i.e., multiple modes with the same eigenfrequency $\omega_j = \omega_{j+1}$, exist. When applied to the structure, the corresponding eigenvectors define the same deformation pattern in different orientations on the symmetric structure. Free vibration at the eigenfrequency ω_j may then occur in any pattern orientation possible by linear combination of the eigenvectors $\tilde{\mathbf{y}}_j$ and $\tilde{\mathbf{y}}_{j+1}$, [2]. Section 31.4 discusses the role of double modes in the context of gyroscopic systems.

31.2.1.1 Second Order Modal Truncation

Most of the time only a fraction $q \ll n$ of the system's modes contribute to the answer (31.3) under (arbitrary) excitation, which allows for truncation of the modal basis to only these q eigenvectors and build a reduced, rectangular modal matrix $\tilde{\mathbf{Y}}_r \in \mathbb{R}^{n \times q}$. Using this reduced form in the coordinate transformation (31.3) yields the approximation

$$\mathbf{y}_r(t) = \tilde{\mathbf{Y}}_r\hat{\mathbf{y}}(t), \quad (31.6)$$

which when applied to the system's equation (31.2) and pre-multiplication with $\tilde{\mathbf{Y}}_r^\top$ gives a decoupled reduced system equation

$$\underbrace{\tilde{\mathbf{Y}}_r^\top \mathbf{M} \tilde{\mathbf{Y}}_r}_{\tilde{\mathbf{M}}_r \in \mathbb{R}^{q \times q}} \ddot{\hat{\mathbf{y}}} + \underbrace{\tilde{\mathbf{Y}}_r^\top \mathbf{K} \tilde{\mathbf{Y}}_r}_{\tilde{\mathbf{K}}_r \in \mathbb{R}^{q \times q}} \hat{\mathbf{y}} = \tilde{\mathbf{Y}}_r^\top \mathbf{f} \quad (31.7)$$

of dimension q . The modes which should be kept as basis vectors in the reduced basis depend on several aspects. The local distribution of the excitation in modal coordinates as well as the comparison of the excitation frequency range with the system's modal characteristics can be used as a criterion. Usually the modes corresponding to the lowest eigenfrequencies are of interest, [1]. In prevision of Sect. 31.5.1.1 it is mentioned here that in case of a symmetric undamped non-gyroscopic system with double modes $\tilde{\mathbf{y}}_j \equiv \tilde{\mathbf{y}}_{j+1}$ an increase in accuracy of the reduction procedure by accounting for *both* representatives of the modal double pair instead of *just one* depends directly on the load case. If for example two double mode partners are considered in the basis, where one is oriented in such a way that the forcing is located in its modal node, it will not contribute to the system's answer and thus can be dismissed from the reduced order basis.

One disadvantage of this reduction approach lies in the fact that the frequency response curves in the reduced state generally do not match the original system's at $\hat{\Omega} = 0$ rad/s, i.e., the constant component is missed in the reduced order model. This cannot be fixed in a sensible way by adding additional modes to the basis and is exceptionally inconvenient

when the reduced model is only needed for a dynamic time integration step. If it starts from a static load step computed for the full model, the deflection from the previous step will be missed as an initial condition for the time integration.

31.2.1.2 Second Order Krylov Subspace Method

Methods based on Krylov subspaces belong to the most common reduction methods for linear time-invariant systems of large scale in the field of circuit simulation or control engineering in general, [3]. In [4] the technique was first introduced for multiple-input multiple-output (MIMO) systems of first order in state-space and then investigated and modified by many others like [5]. In structural dynamics the equations of motion are formulated in a simplified form

$$\begin{aligned} \dot{\mathbf{x}} &= \mathbf{A} \mathbf{x} + \mathbf{b} \\ \begin{Bmatrix} \dot{\mathbf{y}} \\ \ddot{\mathbf{y}} \end{Bmatrix} &= \begin{bmatrix} \mathbf{0} & \mathbf{I} \\ \mathbf{M}^{-1}\mathbf{K} & \mathbf{M}^{-1}\mathbf{D} \end{bmatrix} \begin{Bmatrix} \mathbf{y} \\ \dot{\mathbf{y}} \end{Bmatrix} + \begin{Bmatrix} \mathbf{0} \\ \mathbf{f} \end{Bmatrix}, \end{aligned} \quad (31.8)$$

with $\mathbf{x} \in \mathbb{R}^{2n}$ as the state-space vector, the system matrix $\mathbf{A} \in \mathbb{R}^{2n \times 2n}$ and the external loading vector $\mathbf{b} \in \mathbb{R}^{2n}$ as system input. The complex transfer matrix \mathbf{H} and the frequency response curve \mathbf{q}_0 describe the system's input-output behaviour with

$$\mathbf{H}(\hat{\Omega}) = (i\hat{\Omega}\mathbf{I} - \mathbf{A})^{-1} \Leftrightarrow \mathbf{q}_0(\hat{\Omega}) = \mathbf{H}\mathbf{b}_0, \quad (31.9)$$

where \mathbf{b}_0 denotes the complex coefficients of the harmonic excitation $\mathbf{b}(t)$ with its frequency $\hat{\Omega}$ in its complex form

$$\mathbf{b}(t) = \mathbf{b}_0 e^{+i\hat{\Omega}t} + \bar{\mathbf{b}}_0 e^{-i\hat{\Omega}t}. \quad (31.10)$$

The reduction method aims at matching the so-called *moments* between the original system and its low order approximation, where these moments correspond to the coefficients of the Taylor series expansion of the transfer function $\mathbf{H}(\hat{\Omega})$ respectively $\mathbf{q}_0(\hat{\Omega})$ about a certain frequency point of interest $\hat{\Omega}$. At low frequencies of excitation the system's behaviour is represented by the moments about $\hat{\Omega} = 0 \text{ rad/s}$, whereas the high frequency range is characterized by the moments about $\hat{\Omega} \rightarrow \infty$ as expansion point. In the latter case the moments are then called *Markov parameters*. Like the modal truncation the method relies on a projection from the original high dimensional system space to a low dimensional subspace, here a *First order Krylov subspace*, by means of a transformation matrix $\mathbf{T} \in \mathbb{R}^{2n \times q}$, where the orthonormal basis vectors spanning the subspace are most commonly calculated by employing the *Arnoldi* or the *Lanczos algorithm*, see [6] and [7].

The requirement of *first order* equations of motion is an inconvenience in structural dynamics where mainly finite element approximations relying on *second order* forms are employed. For this reason [8, 9] and others focus on preserving the second order structure of mechanical systems as in (31.2) by extending the concept in [4] to *Second Order Krylov Subspaces*, while retaining the number of matched system moments and Markov parameters. This approach is applied here to linear systems of structural dynamics under gyroscopic influence. The extended subspaces are defined as

$$\mathcal{K}(\mathbf{A}_1, \mathbf{A}_2, \mathbf{G}_1) = \text{colspan}\{\mathbf{P}_0, \mathbf{P}_1, \dots, \mathbf{P}_{q_1-1}\}, \quad (31.11)$$

$$\text{where } \begin{cases} \mathbf{P}_0 = \mathbf{G}_1, \mathbf{P}_1 = \mathbf{A}_1 \mathbf{P}_0, \\ \mathbf{P}_i = \mathbf{A}_1 \mathbf{P}_{i-1} + \mathbf{A}_2 \mathbf{P}_{i-2}, \quad i = 2, 3, \dots \end{cases} \quad (31.12)$$

with $\mathbf{A}_1, \mathbf{A}_2 \in \mathbb{R}^{n \times n}$ and $\mathbf{G}_1 \in \mathbb{R}^{n \times m}$. The m columns of \mathbf{G}_1 are called starting vectors, the matrices \mathbf{P}_i are called basic blocks – both of which are used for the extended *Second Order Arnoldi Algorithm* in [9] for finding the orthogonal basis vectors collected in the transformation matrix \mathbf{T} . Applied to damped, non-gyroscopic second order systems with a single starting vector $-\mathbf{K}^{-1}\mathbf{f}$ (equivalent to the deformation under static loading) the corresponding load-dependent subspace reads

$$\mathcal{K}(-\mathbf{K}^{-1}\mathbf{D}, -\mathbf{K}^{-1}\mathbf{M}, -\mathbf{K}^{-1}\mathbf{f}). \quad (31.13)$$

In case of a Rayleigh damped system this subspace is equivalent to its first order version spanned by basis vectors out of the classical Arnoldi scheme, see [3]. As this paper focusses on introducing gyroscopic effects in Sect. 31.5 violating the Rayleigh condition (31.5) the second order form (31.13) above is employed. Additionally it is mentioned here that in the

described way only the *one-sided* version of the reduction method is realized, when a skew-symmetric system matrix \mathbf{G} is included later in the equations. As the system will no longer be symmetric a distinction between an *input* and a separate *output* Krylov subspace, i.e., a *two-sided* technique, is necessary to sustain the same number of matched moments.

31.2.2 Craig-Bampton Method for Non-linear Systems

The relationships in Sect. 31.2.1 are no longer valid in the presence of non-linearities in a system. Formulation (31.2) is not applicable anymore and instead the equations of motion are of the form

$$\mathbf{M}\ddot{\mathbf{y}} + \mathbf{k}_{nl}(\dot{\mathbf{y}}, \mathbf{y}) = \mathbf{f}. \quad (31.14)$$

There exist many types of non-linearities, which differ in the way how their contribution in \mathbf{k}_{nl} is computed. In this paper contact non-linearities will be considered, while also employing a geometrically non-linear ALE formulation, which demands a special treatment in Sect. 31.5.2.2 compared to the standard Craig-Bampton technique described below.

The Craig-Bampton substructuring method is a popular method for building reduced order models of systems which are non-linear due to contacting interfaces. The DoFs of these interfaces are gathered in a specific set \mathbf{y}_b of *boundary degrees of freedom*, while all other DoFs belong to the set of *inner degrees of freedom* \mathbf{y}_i . This way the equations of motions are partitioned,

$$\begin{bmatrix} \mathbf{M}_{bb} & \mathbf{M}_{bi} \\ \mathbf{M}_{ib} & \mathbf{M}_{ii} \end{bmatrix} \begin{Bmatrix} \ddot{\mathbf{y}}_b \\ \ddot{\mathbf{y}}_i \end{Bmatrix} + \begin{bmatrix} \mathbf{K}_{bb} & \mathbf{K}_{bi} \\ \mathbf{K}_{ib} & \mathbf{K}_{ii} \end{bmatrix} \begin{Bmatrix} \mathbf{y}_b \\ \mathbf{y}_i \end{Bmatrix} = \begin{Bmatrix} \mathbf{f}_b \\ \mathbf{f}_i \end{Bmatrix}, \quad (31.15)$$

and a coordinate transformation

$$\mathbf{y} = \begin{Bmatrix} \mathbf{y}_b \\ \mathbf{y}_i \end{Bmatrix} = \begin{bmatrix} \mathbf{I} & \mathbf{0} \\ \tilde{\mathbf{Y}}_c & \tilde{\mathbf{Y}}_n \end{bmatrix} \begin{Bmatrix} \mathbf{y}_b \\ \hat{\mathbf{y}}_i \end{Bmatrix} = \tilde{\mathbf{Y}}_{CB} \hat{\mathbf{y}} \quad (31.16)$$

is applied. The special feature of the transformation matrix $\tilde{\mathbf{Y}}_{CB}$ lies in the preservation of \mathbf{y}_b as physical coordinates in the reduced order subspace, i.e., the contact computations can still be performed in the truncated state as all interface DoFs can still be addressed directly. $\tilde{\mathbf{Y}}_c$ and $\tilde{\mathbf{Y}}_n$ denote the column matrices of *coupling modes* and *inner modes*. The first-mentioned contains the system's answers to static uniform deflections of its boundary degrees of freedom \mathbf{y}_b (one at a time), while the latter consists of a selection of q *inner* linear modes $\tilde{\mathbf{y}}_i$ of the system under the condition of a temporarily fixed interface, i.e., $\mathbf{y}_b = \mathbf{0}$. Mathematically they are described by

$$\tilde{\mathbf{Y}}_c = -(\mathbf{K}_{ii})^{-1} \mathbf{K}_{ib} \quad (31.17)$$

and

$$\tilde{\mathbf{Y}}_n = [\tilde{\mathbf{y}}_{i,1}, \dots, \tilde{\mathbf{y}}_{i,q}] \quad (31.18)$$

with the inner eigenproblem

$$(-\omega_{ij}^2 \mathbf{M}_{ii} + \mathbf{K}_{ii}) \tilde{\mathbf{y}}_{i,j} = \mathbf{0}. \quad (31.19)$$

The size of the reduction basis and thus the accuracy of the reduced order model are controlled by the number q of inner modes $\tilde{\mathbf{y}}_{i,1\dots q}$ considered in the projection (31.16). For further insight it is referred to [10].

31.3 ALE Formulation with Contact Mechanics

For the numerical analysis of rolling contact the *Arbitrary Lagrangian-Eulerian* (ALE) formulation is a well-established tool. It is briefly outlined here and later employed for the integration of gyroscopic influences into the systems in Sect. 31.5. Details can be found in [11].

31.3.1 Kinematic Framework

The basic principle of ALE relies on the introduction of an arbitrarily moved *reference configuration* $\mathcal{X}(\mathcal{B})$, which coincides neither with the material nor the spatial configuration $\mathbf{X}(\mathcal{B})$ and $\mathbf{x}(\mathcal{B})$. This leads to a decomposition

$$\mathbf{x}(\mathcal{B}) = \boldsymbol{\phi}(\mathbf{X}, t) = \underbrace{\hat{\boldsymbol{\phi}}(\mathcal{X}(\mathbf{X}, t), t)}_{\text{ref.config.}} \quad \text{with } \mathbf{X} = \mathbf{X}(\mathcal{B}). \quad (31.20)$$

of the general particle motion $\boldsymbol{\phi}(\mathbf{X}, t)$ into a (prescribed) rigid body movement $\mathcal{X}(\mathbf{X}, t)$ and the deformation $\hat{\boldsymbol{\phi}}(\mathcal{X}, t)$. Mathematically this is realized by means of a multiplicative split of the material deformation gradient

$$\mathbf{F} = \hat{\mathbf{F}} \cdot \mathbf{R}. \quad (31.21)$$

\mathbf{R} constitutes the rigid body motion from an Eulerian point of view, i.e., a perspective observing a *fixed* location in space and watching the motion of an *arbitrary* particle coinciding with that location at the given moment. $\hat{\mathbf{F}}$ then describes the deformation in standard Lagrangian material manner *relative* to that moving reference configuration. This way the mesh does not have to account for the rotational displacements in \mathbf{R} and only for true deformation in $\hat{\mathbf{F}}$. Instead convective terms in the momentum and continuity equations are considered. In this context the material time derivative of a function f consists of a relative and a convective part

$$\left. \frac{\partial f}{\partial t} \right|_{\mathbf{x}} = \left. \frac{\partial f}{\partial t} \right|_{\mathcal{X}} + \text{Grad}f \cdot \mathbf{w} \quad \text{with} \quad \text{Grad}f = \frac{\partial f}{\partial \mathcal{X}}, \quad (31.22)$$

where \mathbf{w} denotes the constant guiding velocity applied to the ALE mesh. In terms of the velocity \mathbf{v} with the displacements $\boldsymbol{\varphi}$ the split in the material time derivative yields

$$\mathbf{v} = \left. \frac{d\boldsymbol{\varphi}}{dt} \right|_{\mathbf{x}} = \left. \frac{d\boldsymbol{\varphi}}{dt} \right|_{\mathcal{X}} + \text{Grad}\boldsymbol{\varphi} \cdot \mathbf{w} = \hat{\mathbf{v}} + \mathbf{c} \quad (31.23)$$

with relative velocity $\hat{\mathbf{v}}$ and convective velocity \mathbf{c} . In case of stationary motion the relative velocity $\hat{\mathbf{v}}$ vanishes, which means that the steady state behaviour is independent of time and comes down to a problem in space. Thus all time derivatives can be replaced by spatial gradients.

As per [11] derivation of the equations of motion with respect to the reference configuration $\mathcal{X}(\mathcal{B})$ yields

$$\int_{\mathcal{X}(\mathcal{B})} \hat{\boldsymbol{\rho}} \hat{\mathbf{v}} \cdot \delta\boldsymbol{\varphi} \, d\hat{V} = - \int_{\mathcal{X}(\mathcal{B})} \hat{\mathbf{P}} : \text{Grad}\delta\boldsymbol{\varphi} \, d\hat{V} + \int_{\mathcal{X}(\mathcal{B})} \hat{\boldsymbol{\rho}} \hat{\mathbf{b}} \cdot \delta\boldsymbol{\varphi} \, d\hat{V} + \int_{\partial, \mathcal{X}(\mathcal{B})} \hat{\mathbf{t}} \cdot \delta\boldsymbol{\varphi} \, d\hat{A} \quad (31.24)$$

with virtual displacements $\delta\boldsymbol{\varphi}$, the first Piola-Kirchhoff stress tensor $\hat{\mathbf{P}}$, the external applied volume load $\hat{\mathbf{b}}$ and the external applied surface load $\hat{\mathbf{t}}$. The inertia term on the left can be reformulated for avoiding second order gradients which required C^1 -continuous shape functions in the finite element method. While limiting the formulation at the same time to *stationary* motion [11] gives

$$\int_{\mathcal{X}(\mathcal{B})} \hat{\boldsymbol{\rho}} \hat{\mathbf{v}} \cdot \delta\boldsymbol{\varphi} \, d\hat{V} = - \int_{\mathcal{X}(\mathcal{B})} \hat{\boldsymbol{\rho}} \hat{\mathbf{c}} \cdot (\text{Grad}\delta\boldsymbol{\varphi} \cdot \mathbf{w}) \, d\hat{V} + \int_{\partial, \mathcal{X}(\mathcal{B})} \hat{\boldsymbol{\rho}} \delta\boldsymbol{\varphi} \cdot \mathbf{c} \, \hat{\mathbf{n}} \, d\hat{A}. \quad (31.25)$$

The first term describes the virtual work by the centrifugal forces and the surface integral expresses the impulse flux over the boundary of the domain $\partial\mathcal{X}(\mathcal{B})$. The latter vanishes at natural boundaries of rotating systems, as the unit normal $\hat{\mathbf{n}}$ pointing outward of the body is always perpendicular to the (tangential) guiding velocity \mathbf{w} . Finally linearization and discretization of (31.24) with (31.25) lead to the incremental finite element equation

$$\left[{}^t\mathbf{K} - \mathbf{W} \right] \left[\Delta\tilde{\boldsymbol{\varphi}} \right] = \left[{}^{t+\Delta t}\mathbf{f}_{\text{ext}} + {}^t\mathbf{f}_{\ominus} - {}^t\mathbf{f}_{\text{int}} \right] \quad (31.26)$$

for the stationary ALE problem for rotating structures. Solving for the nodal displacement increments $\Delta\tilde{\boldsymbol{\varphi}}$ the tangential stiffness matrix ${}^t\mathbf{K}$ at increment t and the symmetric ALE inertia matrix \mathbf{W} have to be computed as well as the right hand side. Here ${}^{t+\Delta t}\mathbf{f}_{\text{ext}}$ and ${}^t\mathbf{f}_{\text{int}}$ denote the external and internal forces, while ${}^t\mathbf{f}_{\ominus}$ stands for the nodal forces caused by inertia effects. For the complete modal description of the system and computation of its transient behaviour later on additionally the discretized forms of the mass, damping and gyroscopic matrix \mathbf{M} , \mathbf{D} and \mathbf{G} are needed, see [12].

31.3.2 Contact Mechanics

So far no contact influences were accounted for in (31.26), but can be easily added in case of frictionless normal contact. It is introduced here via *Zero-Thickness (ZT) elements* formulated with a penalty approach, see [13] and [14]. However adding frictional tangential contact in an ALE system poses a challenge, as concepts like the mentioned penalty approach rely on the slip quantity for computing the contact sticking conditions. This slip relation, i.e., the relative deformation between two material particles, is not directly at hand here as an ALE observer does not track a particle's history. This paper is limited to the case of only normal contact, but approaches for frictional contact in ALE formulation can be found in [11] or [15].

31.4 Dynamics of Gyroscopic Systems

In this section a brief discussion of gyroscopic influences on the dynamics of rotating symmetric structures like discs is given. Focus is laid on the eigenvectors and frequencies. For further insight [16, 17] and [18] are recommended.

31.4.1 Eigenvectors as Travelling Waves

Starting from an undamped non-gyroscopic system (31.2) with geometric symmetry, real single modes $\tilde{\mathbf{y}}_k \in \mathbb{R}^n$ with the corresponding eigenvalues $\lambda_k = +i\omega_k$ next to real double modes $\tilde{\mathbf{y}}_j \equiv \tilde{\mathbf{y}}_{j+1} \in \mathbb{R}^n$ with $\lambda_{j,j+1} = +i\omega_j$ where $k + j = n$ occur. For both types also their ‘‘conjugated complex’’ equivalents $\bar{\tilde{\mathbf{y}}}_k \in \mathbb{R}^n$ and $\bar{\tilde{\mathbf{y}}}_j \equiv \bar{\tilde{\mathbf{y}}}_{j+1} \in \mathbb{R}^n$ with their eigenvalues $\bar{\lambda}_k = -i\omega_k$ and $\bar{\lambda}_{j,j+1} = -i\omega_j$ are (real) eigenvectors of the system, which is obvious for this case due to the fact that they coincide as real vectors. The double modes are of more interest here for they may not be invariant when considering the same system under rotational velocity $\Omega \neq 0$,

$$\mathbf{M}\ddot{\mathbf{y}} + \mathbf{G}(\Omega)\dot{\mathbf{y}} + \mathbf{K}\mathbf{y} = \mathbf{0} \quad \text{with} \quad \mathbf{G}(\Omega) = -\mathbf{G}(\Omega)^{\text{T}}. \quad (31.27)$$

In (31.27) gyroscopic influences in the gyroscopic matrix $\mathbf{G}(\Omega)$ split the pairs of both the formerly real double modes and their ‘‘conjugate’’ counterparts in the quadruple $\{\tilde{\mathbf{y}}_j \equiv \tilde{\mathbf{y}}_{j+1}, \bar{\tilde{\mathbf{y}}}_j \equiv \bar{\tilde{\mathbf{y}}}_{j+1}\} \in \mathbb{R}^n$ into two separate, now *complex* modes $\{\tilde{\mathbf{y}}_j^+, \tilde{\mathbf{y}}_j^-\} \in \mathbb{C}^n$ and $\{\bar{\tilde{\mathbf{y}}}_j^+, \bar{\tilde{\mathbf{y}}}_j^-\} \in \mathbb{C}^n$ as new eigenvectors of the gyroscopic system.¹ In this complex state their real parts are no longer proportional to the imaginary parts, which is why every degree of freedom possesses its own phase although so far there is no damping, $\mathbf{D} = \mathbf{0}$, in the system. In the sense of the rotational velocity Ω these complex modes can be interpreted as a pair of forward $(\bullet)^+$ and backwards $(\bullet)^-$ travelling waves of deformation $\tilde{\mathbf{y}}_j^{\pm}$ on the structure instead of phase-shifted

¹This stands in agreement with the fact that the spectrum of eigenvalues and thus the eigenvectors for quadratic eigenvalue problems are (at least) symmetric about the real axis.

still-standing vibrations. The waves' travelling velocities correspond to the associated eigenfrequencies in the gyroscopic state, which are discussed in the next section.

31.4.2 Frequency Split

The split of double modes similarly affects the eigenvalues λ_j and thus the eigenfrequencies ω_j of the rotating system, where $\Re(\lambda_j) = 0$ holds for real system matrices $\mathbf{M} = \mathbf{M}^\top$, $\mathbf{G} = -\mathbf{G}^\top$ and $\mathbf{K} = \mathbf{K}^\top$. This phenomenon can be illustrated by Eqs. (31.28), (31.29), (31.30), (31.31), (31.32) and (31.33). After pre-multiplication of the gyroscopic eigenproblem

$$(-\omega_j^2 \mathbf{M} + i\omega_j \mathbf{G}(\Omega) + \mathbf{K}) \tilde{\mathbf{y}}_j = \mathbf{0} \quad (31.28)$$

with $\tilde{\mathbf{y}}_j^{\text{H}}$, where $(\bullet)^{\text{H}}$ denotes the hermitian transpose, one finds

$$-\omega_j^2 \tilde{\mathbf{y}}_j^{\text{H}} \mathbf{M} \tilde{\mathbf{y}}_j + i\omega_j \tilde{\mathbf{y}}_j^{\text{H}} \mathbf{G} \tilde{\mathbf{y}}_j + \tilde{\mathbf{y}}_j^{\text{H}} \mathbf{K} \tilde{\mathbf{y}}_j = \mathbf{0}, \quad (31.29)$$

where the dependence on Ω is not explicitly stated anymore but still accounted for. After substituting

$$\begin{cases} \tilde{\mathbf{M}}_j = \tilde{\mathbf{y}}_j^{\text{H}} \mathbf{M} \tilde{\mathbf{y}}_j, \\ \tilde{\mathbf{G}}_j = \tilde{\mathbf{y}}_j^{\text{H}} \mathbf{G} \tilde{\mathbf{y}}_j \\ \tilde{\mathbf{K}}_j = \tilde{\mathbf{y}}_j^{\text{H}} \mathbf{K} \tilde{\mathbf{y}}_j \end{cases} \quad \text{with } \Re(\tilde{\mathbf{G}}_j) = 0 \text{ as } \tilde{\mathbf{G}}_j = -\bar{\tilde{\mathbf{G}}}_j, \quad (31.30)$$

solving for ω_j yields the real solutions

$$\omega_j^\pm = \pm \sqrt{\left(i \frac{\tilde{\mathbf{G}}_j}{2\tilde{\mathbf{M}}_j}\right)^2 + \omega_{0,j}^2} + i \frac{\tilde{\mathbf{G}}_j}{2\tilde{\mathbf{M}}_j}, \quad (31.31)$$

where the Rayleigh quotient

$$\omega_{0,j}^2 = \frac{\tilde{\mathbf{K}}_j}{\tilde{\mathbf{M}}_j} \quad (31.32)$$

of the non-gyroscopic undamped system was used. By means of (31.31) the eigenfrequencies in dependence of the eigenvectors can be calculated. With fixed integer j the square root term is fully constant, where the second term is only constant in its magnitude, but changes its sign when it comes to $\tilde{\mathbf{y}}_j \in \{\tilde{\mathbf{y}}_j^+, \tilde{\mathbf{y}}_j^-, \bar{\tilde{\mathbf{y}}}_j^+, \bar{\tilde{\mathbf{y}}}_j^-\}$. Thus Eq. (31.31) can be summarized to

$$\omega_j^\pm := \omega_{\Omega,j} \pm \Delta\omega_j \quad (31.33)$$

with

$$\omega_{\Omega,j} := + \sqrt{\left(i \frac{\tilde{\mathbf{G}}_j}{2\tilde{\mathbf{M}}_j}\right)^2 + \omega_{0,j}^2} \quad \text{and} \quad \Delta\omega_j := i \frac{\tilde{\mathbf{G}}_j}{2\tilde{\mathbf{M}}_j}. \quad (31.34)$$

$\omega_j^\pm > 0$ denotes the split eigenfrequencies corresponding to the gyroscopic modes $\{\tilde{\mathbf{y}}_j^+, \tilde{\mathbf{y}}_j^-\}$ respectively $\{\bar{\tilde{\mathbf{y}}}_j^+, \bar{\tilde{\mathbf{y}}}_j^-\}$ stemming from the former double mode $\tilde{\mathbf{y}}_j \equiv \tilde{\mathbf{y}}_{j+1}$. Due to this frequency shift it is now possible that modes appear in different order when sorted according to eigenfrequency. For moderate rotational velocities it can be seen from (31.31) and (31.33) that the split happens linearly when the quadratic term in the square root term can be neglected, hence $\omega_{\Omega,j} \approx \omega_{0,j}$. In the case of $\Omega = 0$ rad/s Eq. (31.31) deflates to the standard Rayleigh quotient (31.32) for undamped non-gyroscopic systems. Equation (31.33) then yields $\omega_j^\pm = \omega_0$, i.e., the forward and backward travelling waves $\tilde{\mathbf{y}}_j^+$ and $\bar{\tilde{\mathbf{y}}}_j^-$ become real again and

possess the same velocity ω_j in opposite directions. Superposition then gives the known non-gyroscopic mode $\tilde{\mathbf{y}}_j$ of the non-rotating system in form of a still-standing vibration.

31.5 Application

In the following two simple gyroscopic systems including a linear elastic steel disc² rotating at velocity Ω will serve as examples for testing the introduced techniques in Sect. 31.2 on ALE models. It will be investigated how the reduction methods are able to handle the phenomenons due to gyroscopic influences of Sect. 31.4 and how they work in the ALE frame described in Sect. 31.3. Firstly the linear methods are evaluated on the freely rotating system and its transient behaviour. Secondly normal contact will be introduced which leads to a non-linear gyroscopic system.

31.5.1 Rotating Disc Under Forcing Excitation

At first the spinning disc under forcing excitation \mathbf{f} is analysed. Some light Rayleigh damping³ as in (31.5) is introduced to avoid high frequency transients in the time domain. The inner circumference is fully restrained resulting in a linearized ALE finite element model

$$M\ddot{\mathbf{y}} + \left(D + G(\Omega) \right) \dot{\mathbf{y}} + \left(K_L - W(\Omega) \right) \mathbf{y} = \mathbf{f} \quad (31.35)$$

of $n = 1152$ degrees of freedom with skew-symmetric $G(\Omega) = -G(\Omega)^T$ and otherwise symmetric system matrices. The system is examined for small lateral deformation such that the geometric non-linearity of the ALE formulation is considered negligible and the stiffness matrix is kept constant, i.e., $K_L = K|_{\varphi=0} = \text{const.}$

Figure 31.1 shows the first five modes of the still-standing disc, $\Omega = 0 \text{ rad/s}$, with the eigenfrequencies

$$\omega_{1,2} = 4298 \text{ rad/s}, \quad \omega_3 = 5239 \text{ rad/s}, \quad \omega_{4,5} = 5930 \text{ rad/s}. \quad (31.36)$$

The frequencies indicate two pairs of real double out-of-plane bending modes $\tilde{\mathbf{y}}_1 \equiv \tilde{\mathbf{y}}_2$ and $\tilde{\mathbf{y}}_4 \equiv \tilde{\mathbf{y}}_5$ at $\omega_{1,2}$ and $\omega_{4,5}$. The deformation patterns are characterized by their circumferential wave numbers $\tilde{n}_{1,2} = 1$ and $\tilde{n}_{4,5} = 2$ leading to one respectively two nodal non-oscillating diameters on the disc. A single mode $\tilde{\mathbf{y}}_3$ is found at ω_3 which is rotationally invariant about the rotation axis.

In the rotating state with $\Omega = 50 \text{ rad/s}$ the eigenfrequencies of the double modes are split and given as

$$\omega_1^\pm \approx \omega_{1,2} \pm \tilde{n}_{1,2} \cdot \Omega = \begin{cases} 4248 \text{ rad/s} \\ 4348 \text{ rad/s} \end{cases} \quad \text{and} \quad \omega_2^\pm \approx \omega_{4,5} \pm \tilde{n}_{4,5} \cdot \Omega = \begin{cases} 5830 \text{ rad/s} \\ 6030 \text{ rad/s} \end{cases}, \quad (31.37)$$

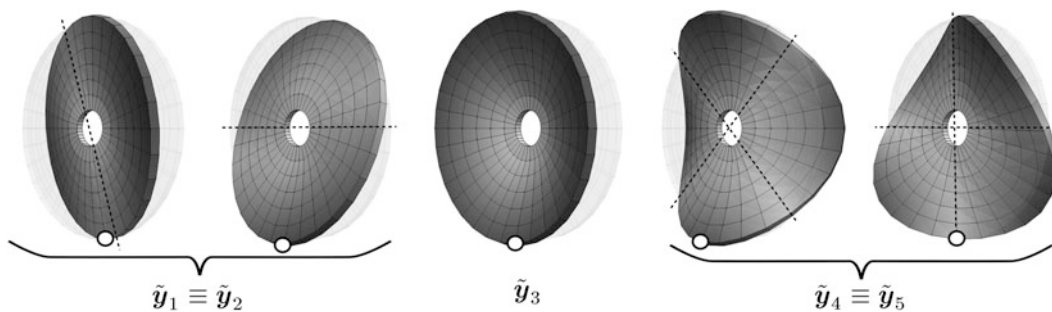


Fig. 31.1 First five disc modes for $\Omega = 0 \text{ rad/s}$ with nodal diameters and positioning of excitation

²Inner/outer diameter $d_i = 50 \text{ mm}$ and $d_a = 300 \text{ mm}$, thickness $t = 10 \text{ mm}$, Young's modulus $E = 2.1 \cdot 10^5 \text{ MPa}$, Poisson ratio $\nu = 0.3$.

³ $\alpha = 0$, $\beta = 1 \cdot 10^{-6}$.

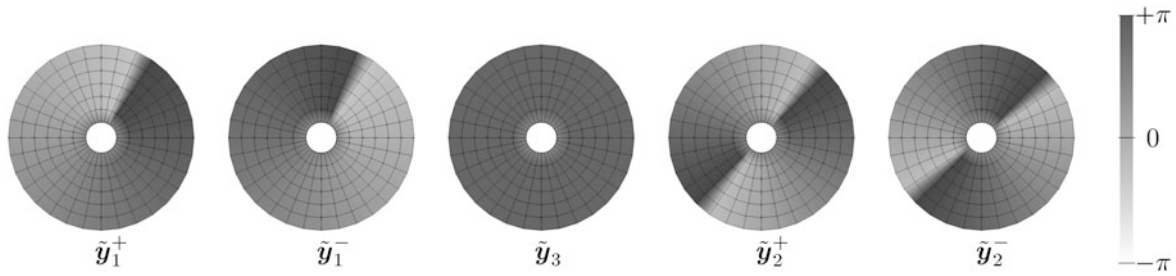


Fig. 31.2 Phase of first five (complex) disc modes in lateral direction for $\Omega = 50 \text{ rad/s}$

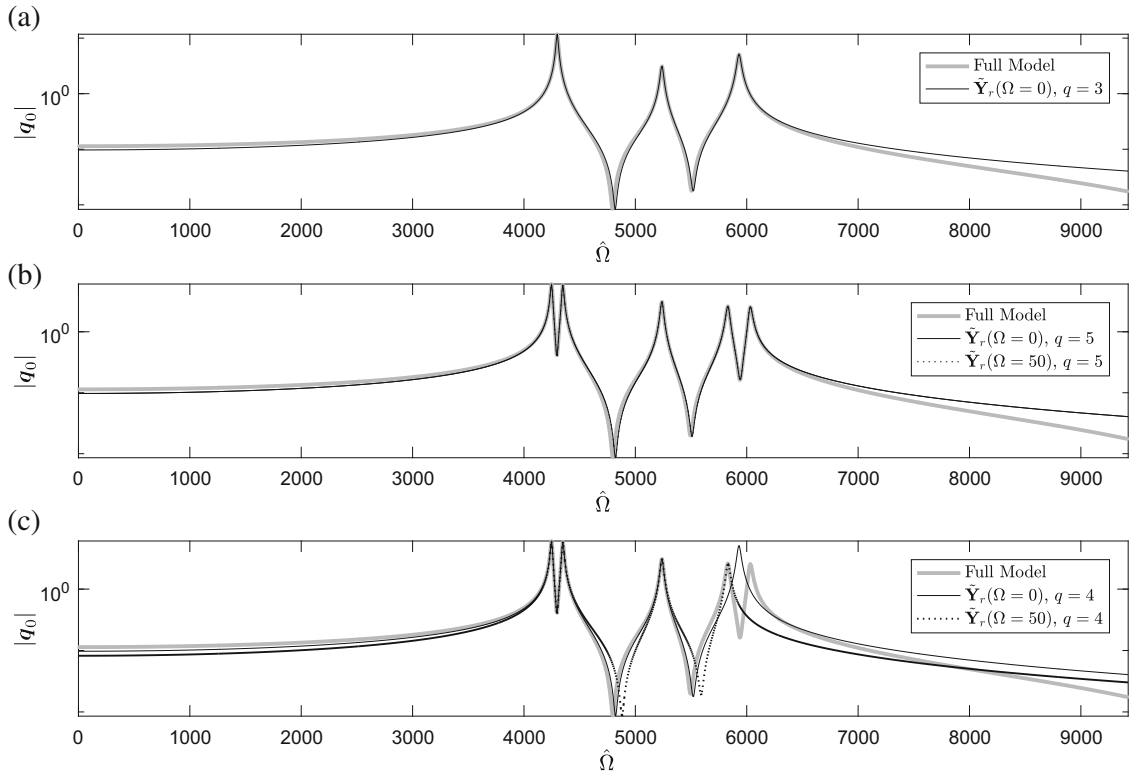


Fig. 31.3 Frequency response functions of full and modally truncated models:

- (a) $\Omega = 0 \text{ rad/s}$, $\tilde{\mathbf{Y}}_{r,\Omega=0} = [\tilde{\mathbf{y}}_2, \tilde{\mathbf{y}}_3, \tilde{\mathbf{y}}_4] \in \mathbb{R}^{n \times 3}$
- (b) $\Omega = 50 \text{ rad/s}$, $\tilde{\mathbf{Y}}_{r,\Omega=0} \in \mathbb{R}^{n \times 5}$ and $\tilde{\mathbf{Y}}_{r,\Omega=50} \in \mathbb{C}^{n \times 5}$
- (c) $\Omega = 50 \text{ rad/s}$, $\tilde{\mathbf{Y}}_{r,\Omega=0} \setminus \tilde{\mathbf{y}}_5 \in \mathbb{R}^{n \times 4}$ and $\tilde{\mathbf{Y}}_{r,\Omega=50} \setminus \tilde{\mathbf{y}}_2^+ \in \mathbb{C}^{n \times 4}$

whereas ω_3 of the single mode remains unchanged independent of Ω . In the same way the double modes are split to $\{\tilde{\mathbf{y}}_1^+, \tilde{\mathbf{y}}_1^-\} \in \mathbb{C}^n$ and $\{\tilde{\mathbf{y}}_2^+, \tilde{\mathbf{y}}_2^-\} \in \mathbb{C}^n$ while the third mode $\tilde{\mathbf{y}}_3 \in \mathbb{R}^n$ stays real as it was before. Figure 31.2 illustrates the phase of the DoFs in lateral direction for the modes of the gyroscopic state. It can be seen that for the double modes the phase changes continuously from $-\pi$ to $+\pi$ over the discs circumference, where the wave numbers \tilde{n}_j describe how often this phase change occurs per circulation. As stated before the real and imaginary parts of the modes are no longer proportional and no nodal diameters exist anymore. Having said that $\tilde{\mathbf{y}}_3$ as single mode shows a constant phase angle for all degrees of freedom as it is real and all nodes deform in the same lateral direction.

In the following example the system is statically deformed in the first load step by a static force $\mathbf{f} = \hat{\mathbf{f}} = 1 \text{ kN}$ located on the 6 o'clock position parallel to the rotation axis. In this state the force starts oscillating, $\mathbf{f} = \hat{\mathbf{f}} \cos(\hat{\Omega}t)$ with $\hat{\Omega} = 5000 \text{ rad/s}$, and for $\Omega = 0 \text{ rad/s}$ the grey shaded frequency response function (FRF) $|q_0|$ in Fig. 31.3a is obtained. Three resonance peaks, corresponding to the eigenfrequencies in (31.36), can be found. Because of the forcing position mode $\tilde{\mathbf{y}}_5$ is not excited and the third peak stems solely from $\tilde{\mathbf{y}}_4$. Under rotation the grey shaded FRF alters to Fig. 31.3b with its peaks according to (31.37).

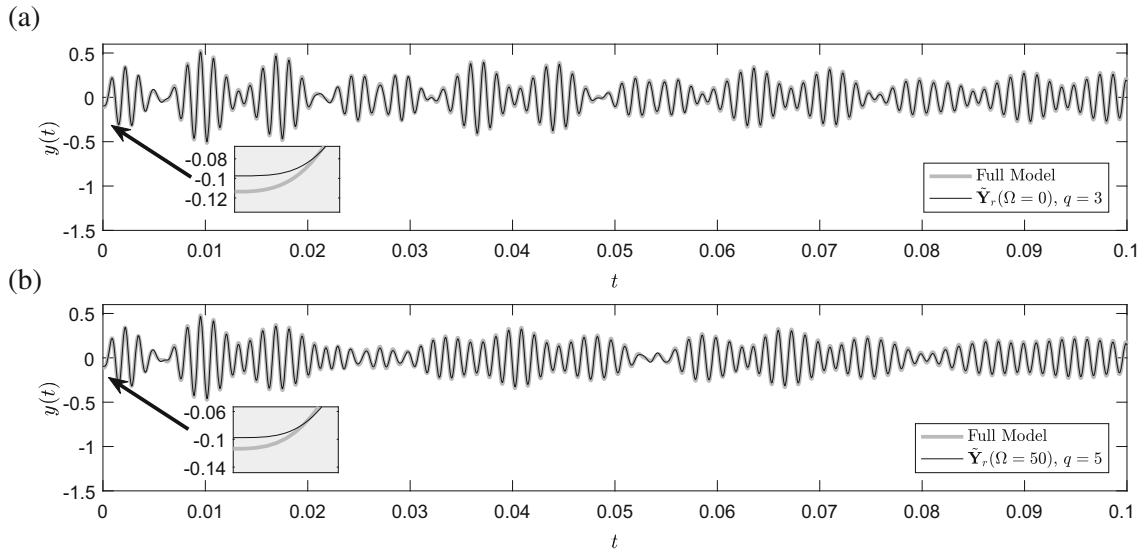


Fig. 31.4 System responses at excitation point of full and modally truncated models:

- (a) $\Omega = 0 \text{ rad/s}$, $\tilde{\mathbf{Y}}_{r,\Omega=0} = [\tilde{\mathbf{y}}_2, \tilde{\mathbf{y}}_3, \tilde{\mathbf{y}}_4] \in \mathbb{R}^{n \times 3}$
 (b) $\Omega = 50 \text{ rad/s}$, $\tilde{\mathbf{Y}}_{r,\Omega=50} \in \mathbb{C}^{n \times 5}$

Finally Fig. 31.4a, b show the still-standing and the rotating full system's response to the excitation in the time domain which will be used as references for judging the quality of the reduced order models. They were computed by a linear Newmark time integration procedure.

31.5.1.1 ROM by Second Order Modal Truncation

For the non-rotating disc a small reduced order basis of $q = 3$ is found for a suitable reduction as can be seen in Fig. 31.3a. Modes $\tilde{\mathbf{y}}_2$, $\tilde{\mathbf{y}}_3$ and $\tilde{\mathbf{y}}_4$ are considered. The constant component at $\hat{\Omega} = 0 \text{ rad/s}$ is not matched exactly, thus the initial condition of the previous static load step is missed. This effect can also be seen in the time domain in Fig. 31.4a together with some transients at the beginning of the time interval which are damped out later on as the system converges to its steady state response. Addition of a sensible number of further modes to the reduced order basis improves the approximation of the constant component slightly, but cannot reproduce it accurately.

When applying the modal truncation from Sect. 31.2.1.1 to the gyroscopic model (31.35), the projections $\tilde{\mathbf{Y}}_r^\top [\bullet] \tilde{\mathbf{Y}}_r$ of the gyroscopic system's matrices $[\bullet] \in \{\mathbf{M}, \mathbf{D}, \mathbf{G}, \mathbf{K}, \mathbf{W}\}$ have to be determined. At this point it is now appealing to use the eigenvectors of the non-rotating system for $\Omega = 0 \text{ rad/s}$ in a basis $\tilde{\mathbf{Y}}_{r,\Omega=0} \in \mathbb{R}^{n \times q}$ rather than the (split) eigenvectors in basis $\tilde{\mathbf{Y}}_{r,\Omega \neq 0} \in \mathbb{C}^{n \times q}$ in the gyroscopic state. They are easier to compute numerically from the standard second order form (31.2) as there is no need for a state space representation for incorporating velocity-proportional coefficients in \mathbf{D} or \mathbf{G} . Additionally this way offers a reduced order basis independent of the rotational velocity Ω . Either way the projection yields for both types of standard or gyroscopic eigenvectors the common decoupled expressions for \mathbf{M} , \mathbf{D} and \mathbf{K} as they are known from modal theory when for the gyroscopic case the pre-multiplication is performed with the *hermitian* transpose $\tilde{\mathbf{Y}}_r^H$ instead of $\tilde{\mathbf{Y}}_r^\top$. The same projection procedure is necessary for the skew-symmetric gyroscopic matrix \mathbf{G} and for the ALE matrix \mathbf{W} . The first-mentioned cannot be decoupled by the suggested projection using the real non-gyroscopic eigenvectors, but only when the (complex) gyroscopic modes from (31.28) are used in $\tilde{\mathbf{Y}}_r$. It then becomes a diagonal but *purely imaginary* matrix $\tilde{\mathbf{G}} = \tilde{\mathbf{Y}}_r^H \mathbf{G} \tilde{\mathbf{Y}}_r$ with null entries on the main diagonal where single mode eigenvectors like $\tilde{\mathbf{y}}_3$ were used in the transformation matrix, see Eq. (31.30).⁴ Additionally the projection of the ALE matrix \mathbf{W} is necessary, which shows to be of no difficulty as

⁴Alternatively *bi-modal decoupling*, using the left and right eigenvectors and their transposed forms, or working in complex coordinates for decoupling is possible, [1] and [16].

it is symmetric and decouples to a real diagonal matrix with both kind of eigenvectors just as the standard system matrices. In that way the modal truncation procedure is ALE compatible and the approach can be further pursued.

Despite the uncoupling hurdles of \mathbf{G} , it was first of all confirmed that both types of eigenvectors are suitable for truncating the gyroscopic system, [1]. At the same time it was found that special attention has to be laid on the (split) double modes. Figure 31.3c shows that in both cases of $\tilde{\mathbf{Y}}_{r,\Omega=0}$ and $\tilde{\mathbf{Y}}_{r,\Omega=50}$ the approximation of the frequency response curves for a gyroscopic system suffers from neglect of such a double mode partner – even if it stems from the non-gyroscopic eigenproblem and is not split up. In the shown example $\tilde{\mathbf{y}}_5$ respectively $\tilde{\mathbf{y}}_2^+$ were excluded from the projection. For the non-gyroscopic basis the missing column vector results in the original unsplit double mode peak in the spectrum, where for the gyroscopic basis this exclusion leads to matching only the first peak. Only when *both* partners are considered, the split up frequency behaviour is matched as in Fig. 31.3b. This stands opposed to still-standing systems, where the double mode partners may hold redundant or obsolete information for the projection depending on their orientation w.r.t. the excitation. In the shown example mode $\tilde{\mathbf{y}}_5$ can be neglected in the still-standing case for Fig. 31.3a as it is (not) excited in its nodal diameter, but has to be considered in the gyroscopic case in the form of $\tilde{\mathbf{y}}_2^+$ to map the second one of the split peaks at ω_2^+ . In that way the gyroscopic influences double the order of the reduced basis when it comes to double modes as nodal diameters no longer exist in the complex modes. Each split peak in the spectrum demands its own split or unsplit basis vector. In line with this fact the resonance peaks in the gyroscopic state need a reduced order basis of $q = 5$ for sufficiently matching the system's behaviour in this range, where both the still-standing and gyroscopic basis succeed in equal measure, see solid black and dotted curves in Fig. 31.3b. Meanwhile the constant component is missed by both even when all five (split) modes are considered.

As a last point the influence of numerical inaccuracies, when the gyroscopic basis $\tilde{\mathbf{Y}}_{r,\Omega=50}$ is used for projection, should be mentioned. Doing so may lead to weakly complex projections of the system matrices and equally complex solution vectors with small imaginary parts of negligible size with respect to the expected real solution. Again considering *both* double mode eigenvectors serves as remedy here for lowering the imaginary parts.

31.5.1.2 ROM by Krylov Subspace Technique

The modal truncation is compared to the Krylov subspace technique from Sect. 31.2.1.2. The Krylov basis is computed including the gyroscopic influences and the linearized ALE finite element formulation (31.35). Thus the subspace reads

$$\mathcal{K}(-\mathbf{Q}^{-1}\mathbf{C}, -\mathbf{Q}^{-1}\mathbf{M}, -\mathbf{Q}^{-1}\mathbf{f}). \quad (31.38)$$

with $\mathbf{C}(\Omega) = \mathbf{D} + \mathbf{G}(\Omega)$ and $\mathbf{Q}(\Omega) = \mathbf{K}_L - \mathbf{W}(\Omega)$ spanned by a number of q basis vectors gathered in \mathbf{T} . Although these basis vectors are not eigenvectors of the system, they are still denoted here in the same way by $\tilde{\mathbf{y}}_j$. The first five of them computed for $\Omega = 0 \text{ rad/s}$ are shown in Fig. 31.5. As for the modal truncation it is possible to consider both the Krylov vectors of the rotating or non-rotating system for reduction, which show to be alike for small rotational velocities Ω . Either way the reduced order basis remains purely real under gyroscopic influences contrary to the modal basis in Sect. 31.5.1.1. In the following the gyroscopic Krylov vectors of subspace (31.38) are employed.

Figure 31.6 shows several frequency response functions of the still-standing and rotating system computed in the full or reduced model. For $\Omega = 0 \text{ rad/s}$ a basis $\mathbf{T}_{\Omega=0}$ of at least $q = 5$ Krylov vectors is needed as seen from Fig. 31.6a. For $q = 4$ the FRF is not accurately approximated. In conclusion a pair of *two* Krylov vectors is necessary here for accurately mapping *one* double mode resonance peak. The single mode at ω_3 demands only a single basis vector. Under rotation with $\Omega = 50 \text{ rad/s}$

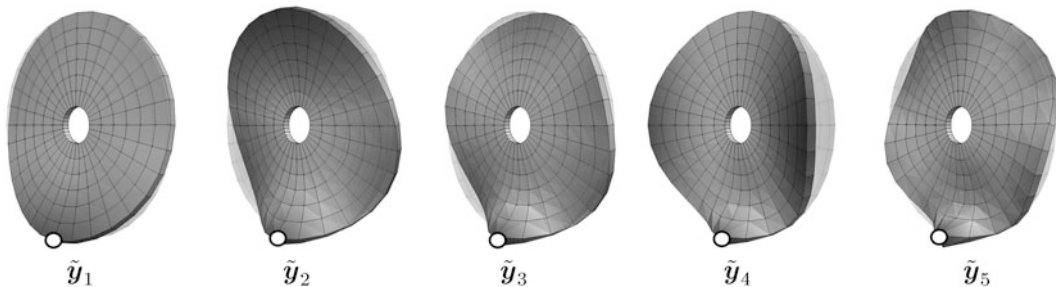


Fig. 31.5 First five Krylov vectors for $\Omega = 0 \text{ rad/s}$ with loading at 6 o'clock position

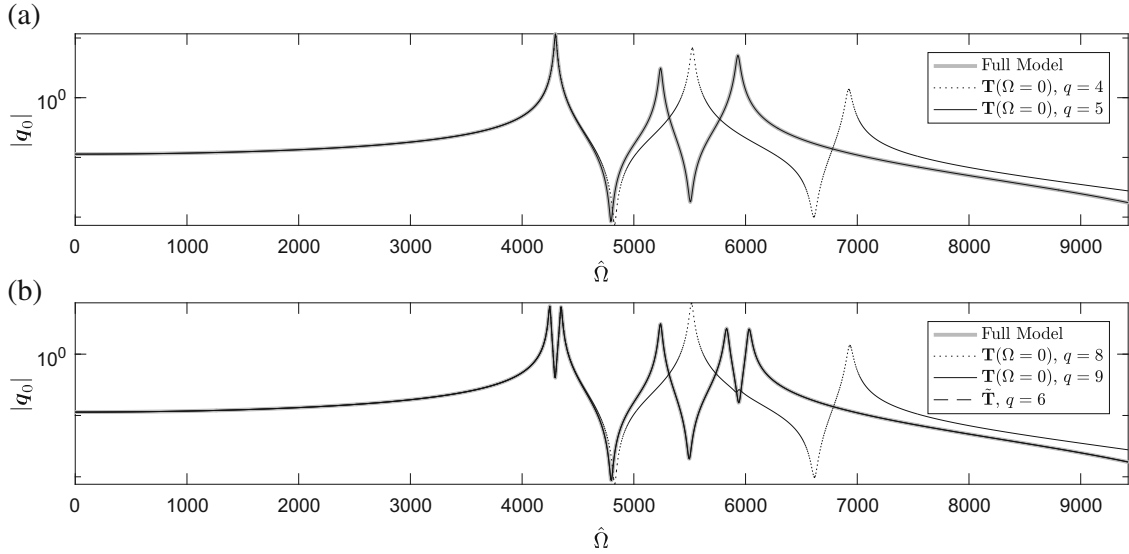


Fig. 31.6 Frequency response functions of full and truncated models in Krylov subspace:

- (a) $\Omega = 0 \text{ rad/s}$: $T_{\Omega=0} \in \mathbb{R}^{n \times 4}$ and $T_{\Omega=0} \in \mathbb{R}^{n \times 5}$
 (b) $\Omega = 50 \text{ rad/s}$: $T_{\Omega=0} \in \mathbb{R}^{n \times 8}$, $T_{\Omega=0} \in \mathbb{R}^{n \times 9}$ and $\tilde{T} = [T | \tilde{Y}_r] \in \mathbb{C}^{n \times 6}$ with $T = T_{\Omega=0} \in \mathbb{R}^n$ and $\tilde{Y}_r = \tilde{Y}_{r,\Omega=50} \in \mathbb{C}^{n \times 5}$

the double mode peaks in Fig. 31.6b are split up, which is why the number of necessary basis vectors is doubled again for these resonances. In this state a minimal set of $q = 9$ vectors is necessary. This relation can also be seen from comparison of the dotted curves in Fig. 31.6a, b for $q = 4$ and $q = 8$, which are congruent. In consideration of these facts the Krylov technique performs worse than the modal truncation procedure in this example as roughly double the number of basis vectors is needed, especially as soon the system enters its gyroscopic state.

Despite the higher order bases the Krylov technique offers the inherent advantage that the static deflection of the system due to loads as input is automatically part of the built subspace as it serves as starting vector in the Arnoldi algorithm. This way it is made sure that the constant component in the frequency range at $\hat{\Omega} = 0 \text{ rad/s}$ is accurately reproduced by the reduced order model and thus no offset from the original system's answer is found in Fig. 31.7a, b for $\Omega = 0 \text{ rad/s}$ or $\Omega = 50 \text{ rad/s}$. To combine the best of modal truncation and Krylov subspaces one could introduce the first Krylov vector into the modal basis of the modal truncation, although this way the orthogonality of the basis is lost. Nevertheless, the reduced order model profits from the accuracy of the (split) eigenvectors and is still able to reproduce the static component as the Krylov method does. Doing so an optimal basis of $q = 6$ is found for the rotating disc, consisting of the static system response together with four gyroscopic split eigenmodes and one single mode – see the dashed line in Fig. 31.6b, which is congruent to the full model's curve.

31.5.2 Rotating Disc with Normal Contact

31.5.2.1 Full System

Finally as a short example for a gyroscopic non-linear system the same disc from Sect. 31.5.1 is considered, but a small block with a ZT element on the 12 o'clock position is added. In a static displacement controlled step the block is pressed against the disc, causing a small deflection of 1 mm via frictionless normal contact, see Sect. 31.3.2 for references. For the subsequent dynamic step the block is pulled back to its initial position instantaneously, thus acting as a stop for the rebounding disc and causing an impact in the steadily rotating body. The non-linear finite element equation reads

$$M\ddot{y} + \left(D + G(\Omega) \right) \dot{y} + k_{nl}(y, \Omega) = f \quad (31.39)$$

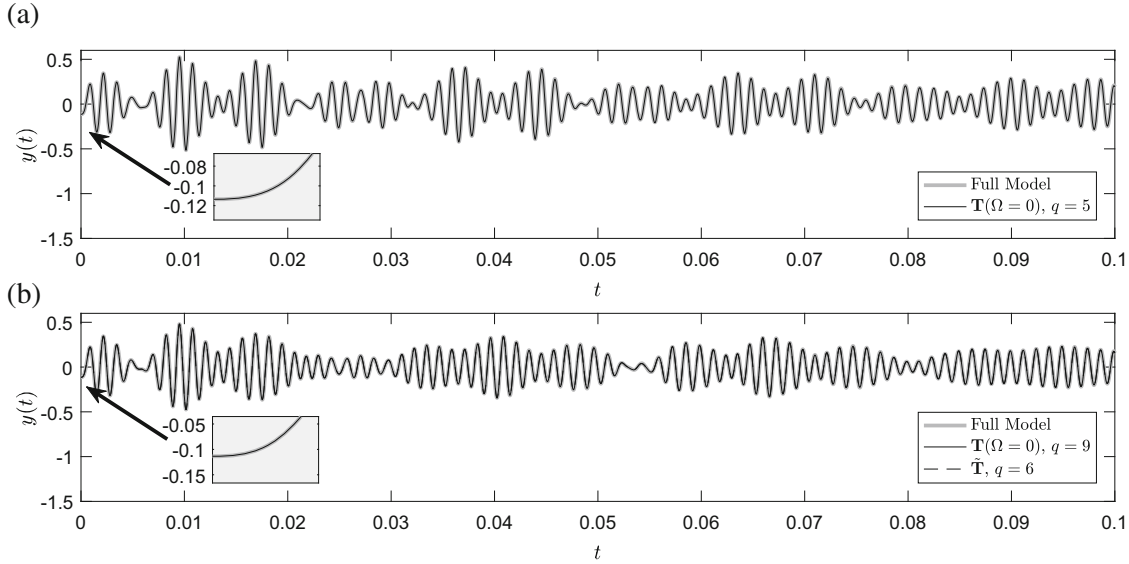


Fig. 31.7 System responses at excitation point of full and truncated models in Krylov subspace:

(a) $\Omega = 0 \text{ rad/s} : T_{\Omega=0} \in \mathbb{R}^{n \times 5}$

(b) $\Omega = 50 \text{ rad/s} : T_{\Omega=0} \in \mathbb{R}^{n \times 9}$ and $\tilde{T} = [T | \tilde{Y}_r] \in \mathbb{C}^{n \times 6}$ with $T = T_{\Omega=0} \in \mathbb{R}^{n \times n}$ and $\tilde{Y}_r = \tilde{Y}_{r, \Omega=50} \in \mathbb{C}^{n \times 5}$

from which a ROM by means of the Craig Bampton substructuring technique in Sect. 31.2.2 is built. In Fig. 31.8 the details of the contact situation together with the rotational ALE flow with $\Omega = 500 \text{ rad/s}$ are shown. The thick grey shaded graph in Fig. 31.11 gives the full model's answer to the described load case in the time domain.

31.5.2.2 ROM by Craig-Bampton Substructuring Technique

For reducing the gyroscopic system (31.39) the insight of Sect. 31.5.1.1 is helpful as the Craig Bampton technique also relies on the (inner) modal behaviour of the system. The reduced order basis is built accordingly to Eqs. (31.16), (31.17), (31.18) and (31.19) where damping and gyroscopic influences are neglected temporarily and $\mathbf{K}_L = \mathbf{K}(\boldsymbol{\varphi} = \mathbf{u}_s)$ of the statically displaced state \mathbf{u}_s is employed as tangent stiffness matrix. The set of boundary DoFs \mathbf{y}_b contains the nodal DoFs of the contact element together with the remaining DoFs of the single block, which are addressed by the displacement control during the load steps. With this in mind the non-gyroscopic inner modes $\tilde{\mathbf{y}}_{i,j}$ and coupling modes $\tilde{\mathbf{y}}_{c,j}$ can be computed, both of which are real and depicted in parts in Figs. 31.9 and 31.10.

In the course of the basis computations the fixed interface strategy for the inner eigenproblem destroys the system's geometrical symmetry, hence no double modes are found anymore. Mode pairs $\{\tilde{\mathbf{y}}_{i,1} \tilde{\mathbf{y}}_{i,2}\}$ and $\{\tilde{\mathbf{y}}_{i,3} \tilde{\mathbf{y}}_{i,4}\}$ could be interpreted as degenerated double modes with wave numbers $\tilde{n}_{1,2} = 1$ and $\tilde{n}_{3,4} = 2$, but differ significantly in their eigenfrequencies $\omega_{i,j}$ with

$$\omega_{i,1} = 4612 \text{ rad/s}, \omega_{i,2} = 4859 \text{ rad/s}, \omega_{i,3} = 5685 \text{ rad/s}, \omega_{i,4} = 8037 \text{ rad/s}, \omega_{i,5} = 12185 \text{ rad/s}. \quad (31.40)$$

When solving the inner eigenproblem in its gyroscopic ALE version with $\mathbf{Q}(\Omega) = \mathbf{K}_L - \mathbf{W}(\Omega)$ complex inner modes $\tilde{\mathbf{y}}_{i,j}$ are attained as expected. Nevertheless, the orderly phase change over the disc's circumference for the range $[-\pi, +\pi]$ as in Fig. 31.2 for the linear case is lost. The occurring phases in the DoFs are clumped in a smaller band, which alters the modes less complex than for the unrestrained case. However, proportionality in their real and imaginary parts is still not obtained and each (single) mode $\tilde{\mathbf{y}}_{i,j}$ is influenced differently by the gyroscopic effects. This way the double mode interplay is not present here, meaning the travelling waves in the sense of Sect. 31.4.1 are hindered in their propagation or do not exist at all. In this state these modes could not be employed successfully in creating a robust Craig-Bampton ROM yielding real-valued solution vectors. For this reason only the real, non-gyroscopic inner modes $\tilde{\mathbf{y}}_{i,j}$ are used in the projection matrix $\tilde{\mathbf{Y}}_{CB}$ in the following.

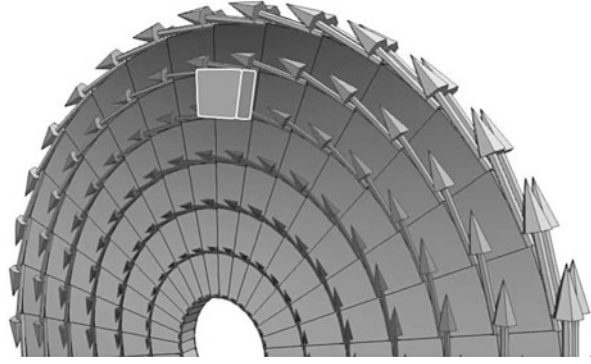


Fig. 31.8 Contact situation with rotational ALE flow

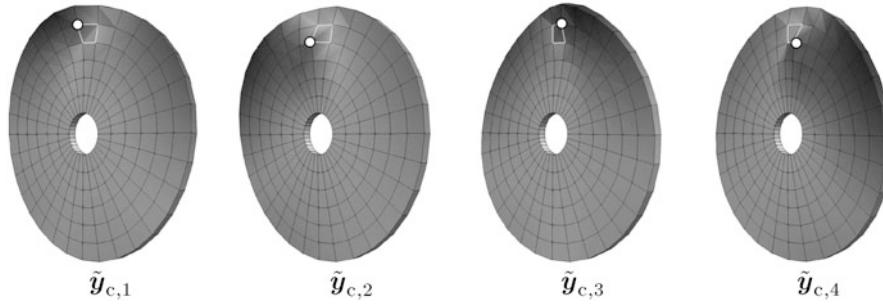


Fig. 31.9 Static coupling modes for $\Omega = 0 \text{ rad/s}$ with uniform displacement in lateral direction at contact DoFs

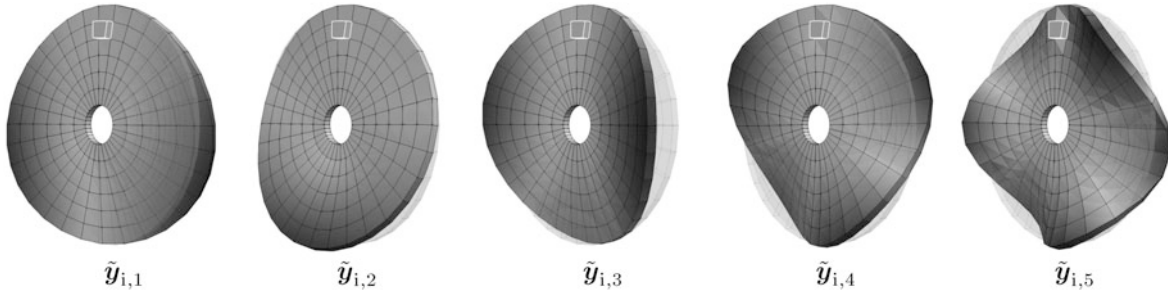


Fig. 31.10 First five inner modes for $\Omega = 0 \text{ rad/s}$ with fixed contact interface at 12 o'clock position

After the basis is computed the restriction of $\mathbf{K} = \mathbf{K}_L$ is lifted and a fully non-linear Newmark time integration with a Newton-Raphson algorithm is performed. It accounts for both the geometric non-linearities of the ALE formulation and the normal contact in lateral direction. As the present reduction procedure only preserves the contacting DoFs in their physical form for the Newmark timesteps, a transformation back into the physical configuration space is necessary for the evaluation of the geometric non-linearity contributions in \mathbf{k}_{nl} for each Newton iteration. Compared to the standard Craig-Bampton method this raises the computational effort significantly and calls for *hyper reduction methods* such as *ECSW*, see [19]. Despite this fact, reduced order models capable of reproducing the essential system dynamics could be built, see Fig. 31.11. Two bases of 20 coupling modes $\tilde{\mathbf{y}}_{c,j}$ plus 80 or 100 inner modes $\tilde{\mathbf{y}}_{i,j}$ were used, i.e., $\tilde{\mathbf{Y}}_{CB} \in \mathbb{R}^{n \times 100}$ or $\tilde{\mathbf{Y}}_{CB} \in \mathbb{R}^{n \times 120}$. For $y_{cb} = 0$ at $t = 0.32 \text{ ms}$ the first impact between the contact partners occurs, which induces the complex trajectory $y_{cb}(t)$ with follow-up impacts for the DoFs in the contact interface.

A structure's answer to a sudden contact interaction is a challenging case to approximate by means of a ROM. The thin grey shaded and black results of Fig. 31.11 show fast oscillations in contrast to the full model's almost smooth graph. This deviation can be explained by the impacts in the contact area, which represent a broadband excitation for the structure. A large number of eigenmodes is excited and the system's answer consists of their superpositionend eigenfrequencies. For the full model these frequencies smoothen each others amplitudes, yielding an overall clean graph with relatively slow oscillatory behaviour. In the reduced model many of these high frequencies are neglected by the projection, which is why the

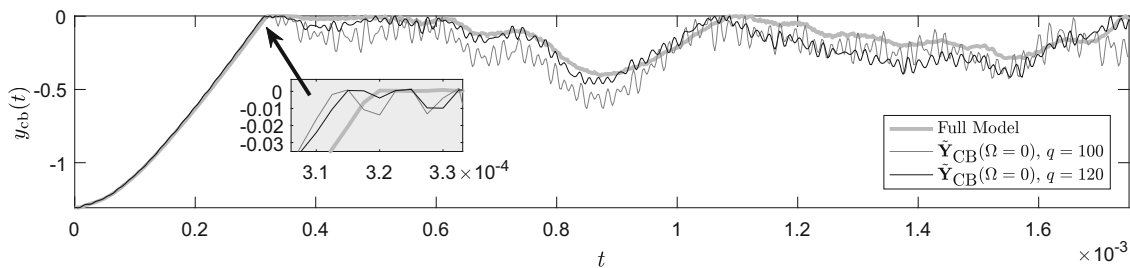


Fig. 31.11 System responses of lateral contact DoF of full model and Craig-Bampton models with $\Omega = 500 \text{ rad/s}$, $\tilde{\mathbf{Y}}_{\text{CB},\Omega=0} \in \mathbb{R}^{n \times 100}$ and $\tilde{\mathbf{Y}}_{\text{CB},\Omega=0} \in \mathbb{R}^{n \times 120}$

compensation worsens and the system's answer seems more fluttery. The smoothing of amplitudes can only be achieved by considering a larger reduced order basis allowing for a higher frequency content in the system's output. A comparison of the graphs for $\tilde{\mathbf{Y}}_{\text{CB},\Omega=0} \in \mathbb{R}^{n \times 100}$ and $\tilde{\mathbf{Y}}_{\text{CB},\Omega=0} \in \mathbb{R}^{n \times 120}$ confirms this observation. Additionally it can be seen from Fig. 31.11 that the first impact happens earlier for the reduced models, indicating a stiffer behaviour with a faster rebound than the full model. This is a known effect of model reduction decreasing the number of system DoFs. Overall applicability of the Craig-Bampton technique for gyroscopic ALE models could be confirmed, where a higher degree of discretization in the full model should allow for a bigger gain in reduction savings.

31.6 Conclusion

In this paper linear and non-linear gyroscopic finite element systems were analysed and how they can be handled by a selection of methods of reduced order modelling. The *Second order modal truncation*, *Second order Krylov subspaces* and the *Craig-Bampton substructuring technique* were applied, where the rotational motion was introduced by a geometrically non-linear ALE formulation. With all of these methods reduced order models of a spinning disc with or without contact could be built, preserving the system's dynamics in the rotating state. The gyroscopic influences alter the system's modal behaviour, which was discussed by means of the eigenvectors and eigenfrequencies of geometrically symmetric structures. As a future topic the application of model order reduction to real-life models, such as disc brakes or rolling tires, in ALE formulation is a remaining challenge, especially when frictional tangential contact is considered. For these complex examples the use of hyper reduction approaches, e.g., the ECSW method, promises computational savings, avoiding costly back transformations of the equations to full system size.

References

1. Gasch, R., Knothe, K., Liebich, R.: *Strukturodynamik: Diskrete Systeme und Kontinua*. Springer, Berlin (2012)
2. Ewins, D.J.: *Modal Testing: Theory, Practice and Application*, 2nd edn. Research Studies Press, Baldock/Philadelphia (2000); Previous edition (1995)
3. Salimbahrami, B.: *Structure preserving order reduction of large scale second order models*. PhD thesis, Lehrstuhl für Regelungstechnik, Technische Universität München (2005)
4. Villemagne, C.D., Skelton, R.E.: Model reductions using a projection formulation. *Int. J. Control.* **46**(6), 2141–2169 (1987)
5. Freund, R.W.: Krylov-subspace methods for reduced-order modeling in circuit simulation. *J. Comput. Appl. Math.* **123**(1), 395–421 (2000)
6. Arnoldi, W.E.: The principle of minimized iterations in the solution of the matrix eigenvalue problem. *Q. Appl. Math.* **9**(1), 17–29 (1951)
7. Lanczos, C.: An iteration method for the solution of the eigenvalue problem of linear differential and integral operators. *J. Res. Natl. Bur. Stand. B* **45**, 255–282 (1950)
8. Lohmann, B., Salimbahrami, B.: Reduction of second order systems using second order Krylov subspaces. *IFAC Proc. Vol.* **38**(1), 614–619 (2005). 16th IFAC World Congress
9. Salimbahrami, B., Lohmann, B.: Order reduction of large scale second-order systems using Krylov subspace methods. *Linear Algebra Appl.* **415**(2), 385–405 (2006). Special Issue on Order Reduction of Large-Scale Systems
10. Bampton, M.C.C., Craig, R.R., Jr.: Coupling of substructures for dynamic analyses. *AIAA J.* **6**, 1313–1319 (1968)
11. Nackenhorst, U.: The ALE-formulation of bodies in rolling contact: theoretical foundations and finite element approach. *Comput. Methods Appl. Mech. Eng.* **193**(39), 4299–4322 (2004)

12. Nackenhorst, U.: Rollkontaktdynamik, Numerische Analyse der Dynamik rollender Körper mit der Finite Elemente Methode. Habilitation, Institut für Mechanik, Universität der Bundeswehr Hamburg (2000)
13. Willner, K.: Kontinuums- und Kontaktmechanik: Synthetische und Analytische Darstellung. Springer, Berlin/Heidelberg (2003)
14. Geisler, J., Willner, K.: Modeling of jointed structures using zero thickness interface elements. *PAMM* **7**(1), 4050009–4050010 (2007)
15. Ziefle, M., Nackenhorst, U.: Numerical techniques for rolling rubber wheels: treatment of inelastic material properties and frictional contact. *Comput. Mech.* **42**(3), 337–356 (2008)
16. Genta, G.: Dynamics of Rotating Systems. Mechanical Engineering Series. Springer, New York (2005)
17. Bryan, G.H.: On the beats in the vibrations of a revolving cylinder or bell. *Proc. Camb. Philos. Soc.* **7**(3), 101–114 (1890)
18. Joubert, S.V., Fedotov, I., Pretorius, W., Shatalov, M.: On gyroscopic effects in vibrating and axially rotating solid and annular discs. In: 2007 International Conference – Days on Diffraction, pp. 89–94 (2007)
19. Farhat, C., Avery, P., Chapman, T., Cortial, J.: Dimensional reduction of nonlinear finite element dynamic models with finite rotations and energy-based mesh sampling and weighting for computational efficiency. *Int. J. Numer. Methods Eng.* **98**(9), 625–662 (2014)



Chapter 32

Damage Precursor Indicator for Aluminum 7075-T6 Based on Nonlinear Dynamics

Robert A. Haynes, Ed Habtour, Todd C. Henry, Daniel P. Cole, Volker Weiss, Antonios Kotsos, and Brian Wisner

Abstract In this work, a damage precursor indicator for aluminum 7075-T6 is proposed based on the nonlinear dynamics of a cantilevered beam system. A shouldered beam specimen is used to move the region of highest stress away from the clamped end. The beam is subject to harmonic base excitation in a uniaxial shaker. Fatigue damage accumulates in the beam with damage forming most quickly in the region of highest stress. By monitoring the tip deflection, changes in the natural frequency and response to a given excitation are correlated to fatigue life. Despite the absence of large-scale cracks, detectable changes in the nonlinear dynamics are discovered. The nonlinear dynamic parameters are estimated capturing the change in the forward and backward nonlinear sine sweeps. These changes could lend themselves to being a trackable damage precursor. The presence of microstructural precursors are confirmed using nanoindentation.

Keywords Fatigue Damage Precursors · Nonlinear Dynamics · Vibration · Structural Health Monitoring · Micromechanics

32.1 Introduction

Army vehicles are subject to significant vibratory loads, which have the potential to cause damage such as cracks in the structure. A visual inspection is typically performed to identify cracks in the airframe. The inspections cause the aircraft to be taken out of service for long periods of time. The U.S. Army Research Laboratory is researching methods for detecting and identifying damage precursors [1–3]. In this way, early signs of degradation can be detected, and prognostics can be conducted to provide a meaningful estimate of when a structural component will no longer be able to perform its primary function, i.e. carry load. This supports the Army’s “Zero-Maintenance Aircraft” concept.

Previous work has established that structural changes, such as compliance, damping, and nonlinear dynamics, are detectable and can be linked to damage precursors [4, 5]. This work extends the previous work to investigate aluminum 7075-T6 and include additional microscopy for identifying the damage precursors.

32.2 Experimental Approach

Three aluminum 7075-T6 cantilevered beams are subject to vibratory loads at the clamped end. The beams are nominally 150 mm long by 12.0 mm wide by 1.64 mm thick (6" by 0.5" by 1/16"). Nominally 25.4 mm (1") of beam length is inserted into a clamp consisting of two hardened steel plates with pass-through holes bolted onto the expansion head of the shaker, resulting in a nominal cantilevered length of 125 mm (5"). The bolts are torqued to 11 N-m. The shaker is a Data Physics V400LT, and the controller is a Data Physics 901. A PCB 352A24 and a PCB 352A21 accelerometer are attached to the clamp as close to the beam root as practical and a PCB 352A21 accelerometer is attached to the tip of the beam. The PCB 352A24 accelerometer on the clamp is used to control the shaker. The wire for the tip accelerometer is taped to the specimen to prevent interference. See Fig. 32.1 for a photograph of the setup.

R. A. Haynes (✉) · E. Habtour · T. C. Henry · D. P. Cole · V. Weiss
US Army Research Laboratory, Aberdeen Proving Ground, Aberdeen, MD, USA
e-mail: robert.a.haynes43.civ@mail.mil

A. Kotsos · B. Wisner
Drexel University, Philadelphia, PA, USA

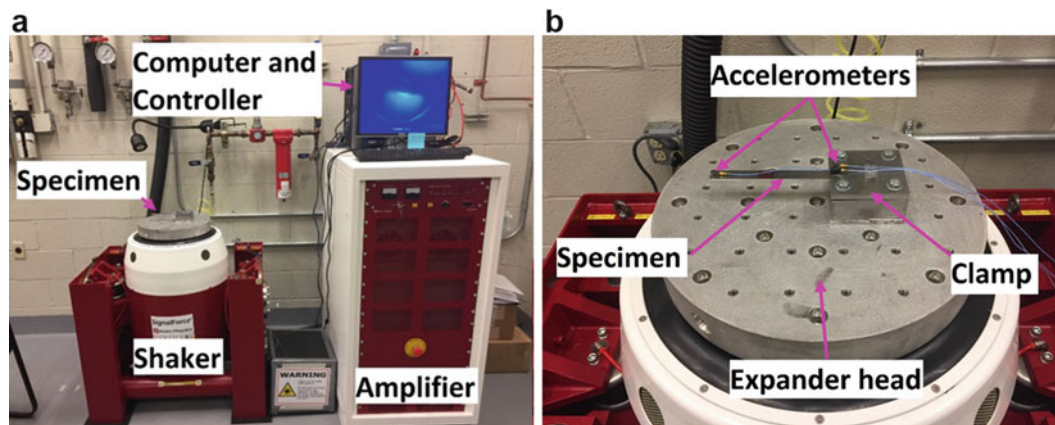


Fig. 32.1 Shaker setup (a) all components; (b) close-up of shaker head with specimen in clamp

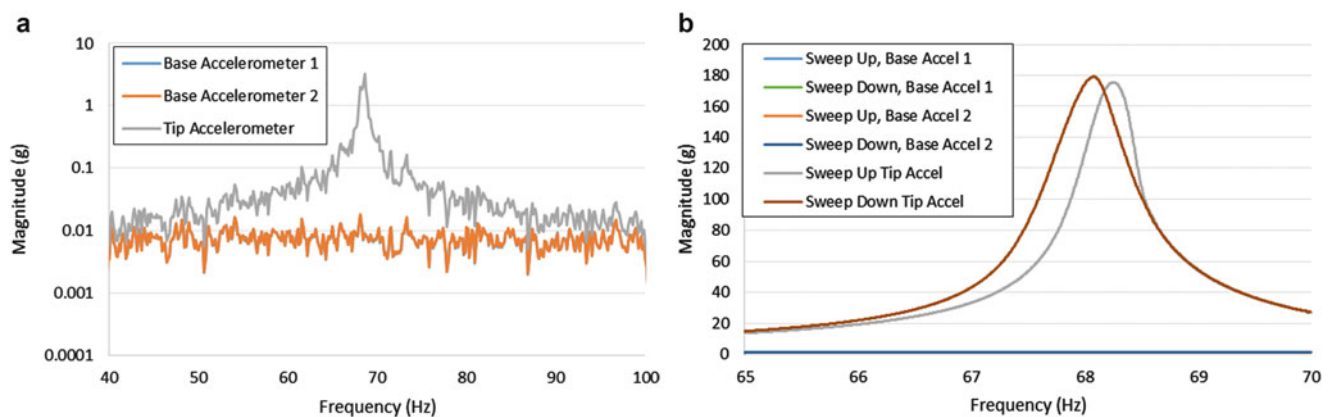


Fig. 32.2 Representative responses for a pristine beam (a) subject to broadband random excitation, and (b) subject to sine sweep

Prior to testing, a wide-band (40–100 Hz) low-amplitude ($0.0025 \text{ g}^2/\text{Hz}$) random excitation is commanded to the shaker to determine the approximate natural frequency. Next, both up and down sine sweeps in a 5 Hz range around the natural frequency are conducted at a rate of 0.075 Hz/s and a 1 g excitation to more accurately determine the natural frequency as well as measure the tip response. See Fig. 32.2 for a representative random excitation and a sine sweep response.

The beams are excited near their natural frequency using either sine or random excitation to induce fatigue damage. The first beam is subject to a 1 g sine excitation for 1,400,000 cycles at its natural frequency as determined by the preceding up sine sweep. The natural frequency of the pristine beam is 66.5 Hz. After the stated number of cycles, a narrow-band (5 Hz), high-amplitude ($0.5 \text{ g}^2/\text{Hz}$) random excitation around the natural frequency is used to excite the base to continue the fatigue damage; in this case the load was applied for a predetermined amount of time before pausing the test to measure the natural frequency and tip response and to check bolt tightness. The second and third beams are only subject to narrow-band (5 Hz), high-amplitude ($0.5 \text{ g}^2/\text{Hz}$) random excitation around the natural frequency to create the fatigue loading. Fatigue loading is continued until complete fracture of the beam is observed as evidenced by separation of the cantilevered section from the clamped section under slight touch. For all beams, the test is paused at predetermined cycle intervals to measure the natural frequency and tip response using the same technique as described previously. Each time the test is paused, the bolt tightness is checked with a torque wrench.

The second and third beams exhibited a fatigue life of approximately 4 h when subject to the narrow-band (5 Hz), high-amplitude ($0.5 \text{ g}^2/\text{Hz}$) random excitation around the natural frequency. This was used as the basis for fatiguing three more beams to 25%, 50%, and 75% of their expected fatigue life, or 1, 2, and 3 h. of narrow-band (5 Hz), high-amplitude ($0.5 \text{ g}^2/\text{Hz}$) random excitation around the natural frequency, respectively. Upon completion of the loading, the beams were sectioned at the location of highest stress and 20 mm along the cantilevered length direction from the location of highest

stress. The resulting section was cut again along the length direction to form three approximately equal sections. The sections were potted in phenolic resin to expose an interior face formed by the length-thickness directions (L-t), a face formed by the length-width directions (L-w) that was part of the upper surface of the beam, and a face formed by the width-thickness directions (w-t) corresponding to the plane of highest bending stresses. The potted specimens were polished to 50 nm to prepare for nanoindentation, atomic force microscopy, and electron backscattering diffraction.

Nanoindentation studies were performed using a Hysitron TI-950 Triboindenter with a diamond Berkovich tip (tip radius of curvature ~ 150 nm). Arrays of 25 indents spaced approximately 5 μm apart were performed at multiple locations throughout the beam. Tests were performed in load control. Scanning probe microscopy tests were run with an Asylum MFP-3D atomic force microscope (AFM). Platinum-silicide coated AFM probes were used for the measurements; the probes had a natural frequency, radius of curvature, and spring constant of approximately, 75 kHz, 25 nm, and 5 N/m, respectively. Topography, phase, and scanning Kelvin probe microscopy (SKPM) scans were performed in AC mode using typical scan rates of 1 Hz.

32.3 Nonlinear Dynamic Parameter Development

To track the health state of the structures exposed to vibratory loads, we focus on monitoring the change in the kinematic stiffness coefficient, k_n . The high amplitude, low rate sine-sweep base excitation amplifies the nonlinear terms at the bifurcation point, which make it possible to extract indicators sensitive to fatigue build up. Changes in the geometric stiffness, structural compliance, and natural frequency are estimated from the dynamic bifurcation. The nonlinear changes in the material microstructure and kinematic stiffness (geometric nonlinearity) necessitate the following steps: (1) obtain the viscous damping, (2) extract the initial natural frequency, and (3) calculate the linear and nonlinear stiffness coefficients after each experiment. These steps are essential since the material elastic constants, E , the geometric properties, and the modal characteristics are contained in the dynamic model parameters.

The equation of motion for the nonlinear system can be expressed as follows [6]:

$$m_s \ddot{x} + 2\zeta m \omega_n \dot{x} + k_l x + m_n (x^2 \ddot{x} + x \dot{x}^2) + k_n x^3 = F \cos(\omega_f t) \quad (32.1)$$

The dot superscript denotes the time derivative, and x is the displacement. The distributive mass and the nonlinear inertial coefficient are m_s , and m_n , respectively. The fundamental frequency and forcing frequencies are ω_n and ω_f , respectively. The structural damping coefficient and linear structural stiffness are ζ and k_l , respectively. F is the magnitude of the forcing function. The structural stiffness can be expressed in terms of m_s and ω_n , as follows:

$$k_l = m_s \omega_n^2 \quad (32.2)$$

The coefficient k_n is also referred to as cubic spring constant, or Duffing parameter [7]. The next step is to apply the method of averaging to equation of motion. The displacement can be expressed as follows:

$$x = A(t) \cos(\omega_f t + \phi) = A \cos \gamma \quad (32.3)$$

where $A(t)$ is the beam deflection amplitude as a function of t , but we drop t for brevity. The phase shift is ϕ . The displacement first time derivative is:

$$\dot{x} = -A \omega_f \sin \gamma + \dot{A} \cos \gamma - \dot{\phi} A \sin \gamma \quad (32.4)$$

The displacement first temporal derivative can be reduced to:

$$\dot{x} = -A \omega_f \sin \gamma \quad (32.5)$$

The displacement second temporal derivative becomes:

$$\ddot{x} = -A\omega_f^2 \cos \gamma \quad (32.6)$$

Substituting Eqs. (32.3), (32.5), and (32.6) into Eq. (32.1) and integrating over one period yields the following:

$$\left[\left(\frac{k_l}{m_s} - \omega_f^2 \right) A - \frac{m_n}{2m_s} \omega_f^2 A^3 + \frac{k_n}{m_s} \frac{3}{4} A^3 \right]^2 + 4\xi^2 \omega_n^2 A^2 \omega_f^2 = \left(\frac{F}{m_s} \right)^2 \quad (32.7)$$

Since the state assessment is based on dynamic the bifurcation of the structure, the forcing frequency is replaced with maximum peak frequency, ω_p , and A is replaced with the peak displacement, A_p , at the bifurcation. The nonlinear inertial can be neglected since it tends to be extremely small [8]. For free vibration Eq. (32.7) reduces to:

$$\frac{k_n}{m_s} = \frac{4}{3A_p^2} \left(\omega_p^2 - \frac{k_l}{m_s} \right) \quad (32.8)$$

The above equation is used to estimate the global nonlinear stiffness. To extract the change in the material elastic constant at the region of stress concentration, the beam flexural mode shape, $Y(x)$, is employed to calculate both k_l and k_n [8]. For a continuous structure, the structural stiffness is [6]:

$$k_l = k_{ld} + k_{lu} = \int_0^{x_d} EIY''^2 dx + EI \int_{x_d}^L Y''^2 dx \quad (32.9)$$

The nonlinear geometric stiffness coefficient [7]:

$$k_n = k_{nd} + k_{nu} = 2 \int_0^{x_d} EI(Y'Y'')^2 dx + 2EI \int_{x_d}^L (Y'Y'')^2 dx \quad (32.10)$$

where, the prime is the spatial derivative and I is the moment of inertia. It can be assumed that the stress concentration will occur near the beam clamped end. The first integrals in k_{ld} and k_{nd} are the stiffness coefficient in the damaged region from $x = 0$ (beam root) to x_d . From x_d to L , the beam is assumed to be undamaged, and linear and nonlinear stiffness coefficients are k_{lu} , and k_{nu} , respectively. Substituting k_l and k_n into Eq. (32.8) yields:

$$\omega_p^2 m_{eff} - k_{lu} - \frac{3A_p^2}{4} k_{nu} = E_d \int_0^{x_d} IY''^2 ds + \frac{3A_p^2}{2} E_d \int_0^{x_d} I(Y'Y'')^2 ds \quad (32.11)$$

The elastic constant for the damaged region, E_d becomes:

$$E_d = \frac{\omega_p^2 m_{eff} - k_{lu} - \frac{3A_p^2}{4} k_{nu}}{\int_0^{x_d} IY''^2 ds + \frac{3A_p^2}{2} \int_0^{x_d} I(Y'Y'')^2 ds} \quad (32.12)$$

32.4 Results and Discussion

The response at the peak frequency and the peak frequency for the first beam are plotted in Fig. 32.3 along with the difference in peak magnitude between the up and down sweeps. Note that cycles is converted to approximate time based on the pristine natural frequency; the sine loading accounts for the first 350 min and the random loading is the remainder of the time. Note the initial increase in magnitude for approximately the first 100 min, suggesting a slight decrease in the damping or an increase in the compliance of the material. This is followed by a decrease in the magnitude, suggesting an increase in material damping or decrease in compliance. After approximately 300 min, an erratic behavior is observed, perhaps the result of large scale damage. The frequency follows a similar response, except on a much smaller scale; while the initial increase in magnitude is 12% and 9% for the sweeps up and down, respectively, the frequency only increases by 0.53% and 0.34%

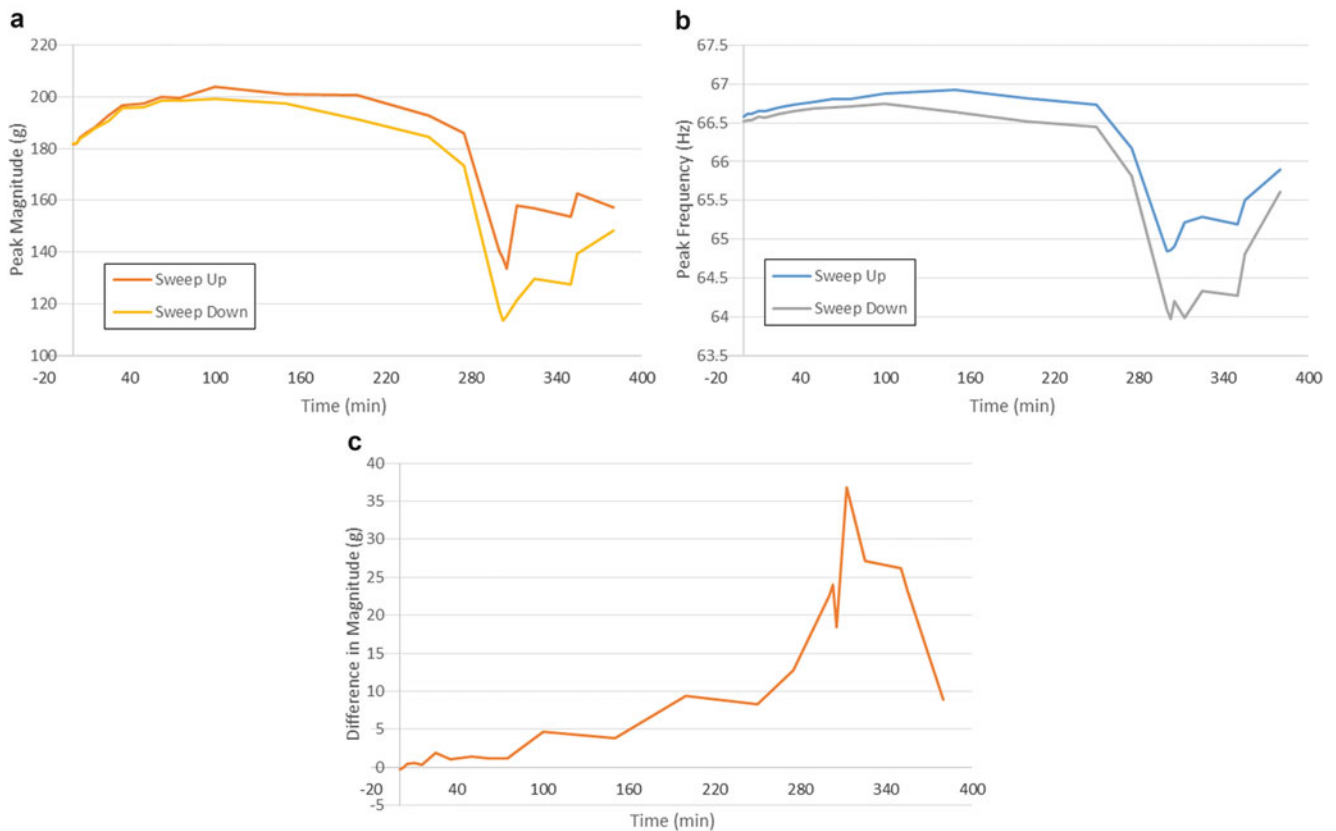


Fig. 32.3 Response for the first beam with fatigue life: (a) magnitude response, (b) natural frequency, (c) difference in magnitude for up and down sweeps

for the sweeps up and down, respectively. Until the erratic behavior is seen, the difference in peak magnitude for the sweeps up and down grows demonstrates a clear upward trend, suggesting it could be a useful damage precursor indicator.

Before switching from the sine to the random loading, i.e. after 1.4 million cycles, a stepped sine dwell was performed in addition to the random excitation and up and down sweeps. The benefit of the stepped dwell is that it allows the beam response to stabilize at a given frequency such that the steady-state response becomes apparent; what is typically observed is an initial large response followed by a sudden drop in the response after a few seconds. The results are plotted in Fig. 32.4. Note that because of the duration of each dwell in the stepped dwell, multiple magnitude points can be extracted at a given frequency; this is most evident near the natural frequency where the response can vary as much as 64 g between the initial response and the steady state response. Several interesting features regarding the magnitude of the response are evident in this plot. First, all tests match well at frequencies away from the natural frequency, i.e. less than 64 Hz and greater than 66 Hz. Second, the sweep down and the stepped dwell match closely, even near the natural frequency. Third, the stepped dwell shows the largest overshoot near the natural frequency. At the natural frequency, the stepped dwell overshoot matches the sweep down peak magnitude; however, the response drops significantly ($\sim 50\%$) over time. Fourth, the sweep up exhibits a significant unstable region where the response remains large, even though the sweep down and stepped dwell exhibit a much lower response. This large response may be driven by the dynamics immediately preceding that instance in time. The unstable nature of this region is made clear by the sharp drop in response and subsequent ringdown that starts at about 65 Hz. Fifth, the unsymmetric nature of all response curves is evidence of the nonlinearities in the system, most likely caused by the presence of damage.

The response at the peak frequency and the peak frequency for the second beam are plotted in Fig. 32.5 along with the difference in peak magnitude between the up and down sweeps. Five data points are recorded with an average time between breaks in the test of 45 min; failure occurred between 180 and the next planned test break at 240 min. Trends similar to the first beam are observed in that for both magnitude and frequency, there exists an initial increase followed by a decrease until failure. The magnitude demonstrates much greater sensitivity to the evolving damage state in that the observed increase in magnitude is 7.0% and 7.4% for the sweeps up and down, respectively, while the increases in frequency are less than 0.1% for both sweeps up and down. The difference in magnitude does not show a clear trend for this beam.

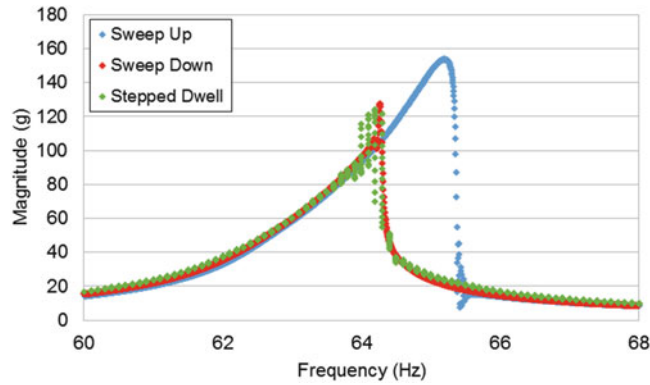


Fig. 32.4 Sweep up and down and stepped dwell responses

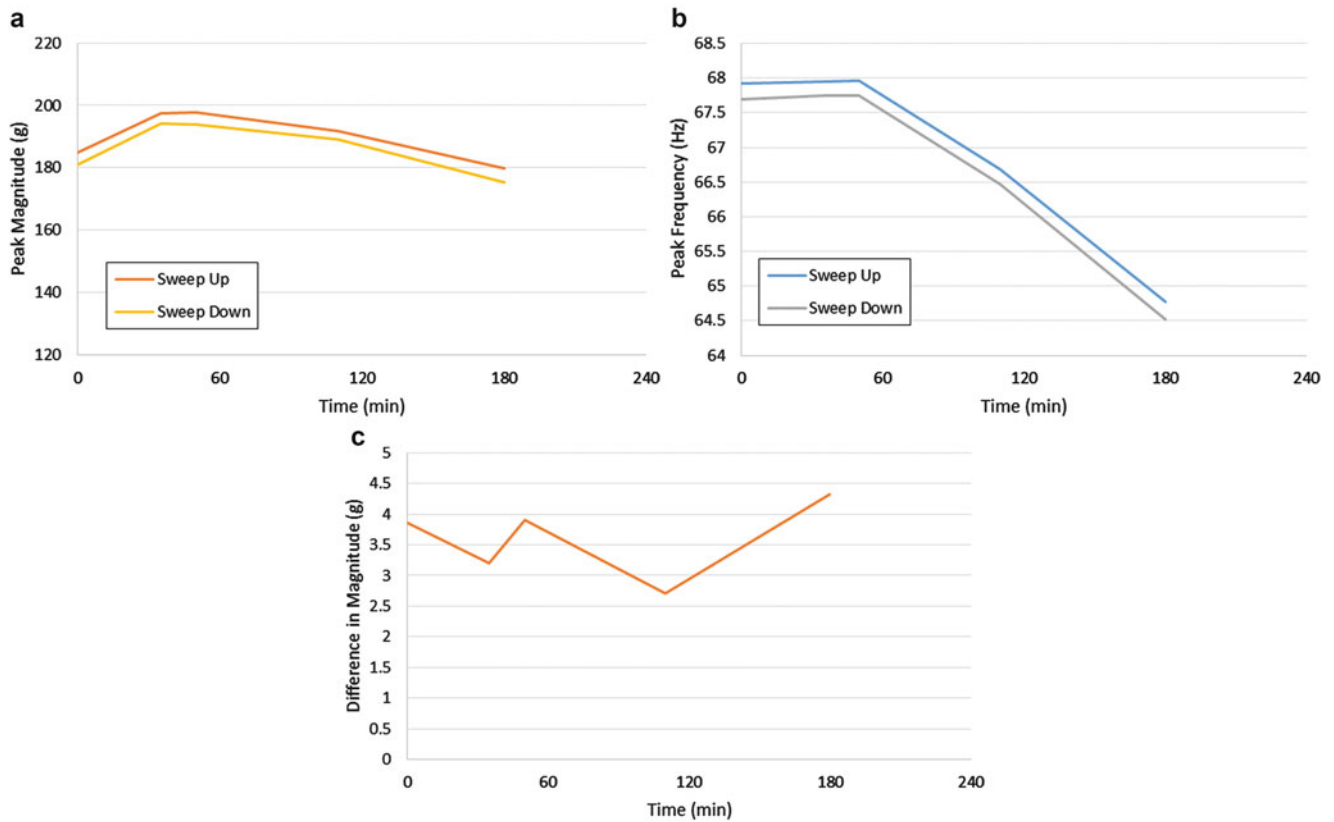


Fig. 32.5 Response for the second beam with fatigue life: (a) magnitude response, (b) natural frequency, (c) difference in magnitude for up and down sweeps

The response at the peak frequency and the peak frequency for the third beam are plotted in Fig. 32.6 along with the difference in peak magnitude between the up and down sweeps. The test break interval is chosen to be 15 min, providing 17 data points from pristine to failure. Again, the same overall trends in magnitude and frequency are observed. The increase in magnitude is 16% and 12% for the sweeps up and down, respectively, while the increases in frequency are 0.14% for both sweeps up and down. The general upward trend in difference in peak magnitude between the up and down sweeps is also observed, particularly beginning at 50% of life. Figure 32.7 is a photograph of the fracture surface of the third beam, which is typical of fatigue fracture.

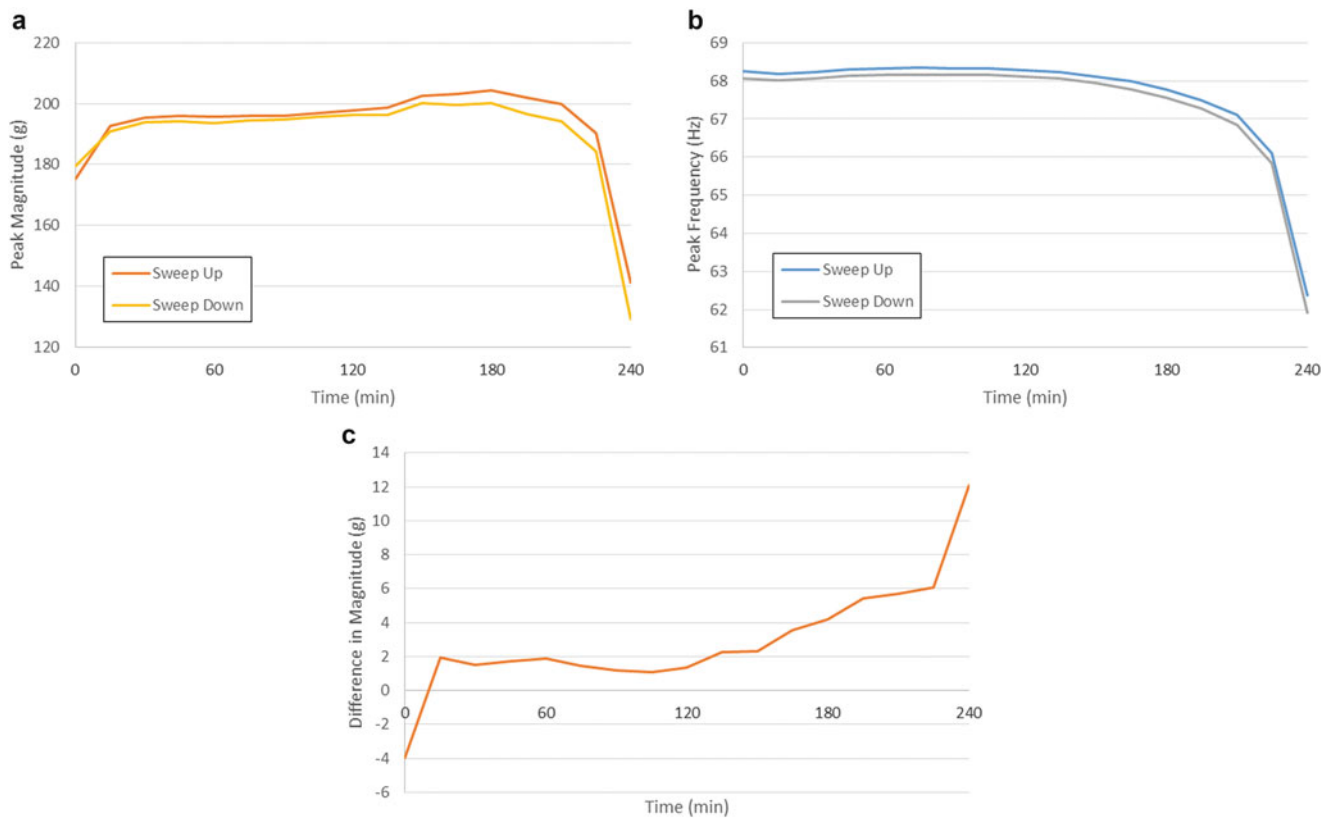


Fig. 32.6 Response for the third beam with fatigue life: (a) magnitude response, (b) natural frequency, (c) difference in magnitude for up and down sweeps



Fig. 32.7 Fracture surface of the third beam

The estimation of the global nonlinear stiffness and its change versus normalized fatigue life percentage are plotted in Fig. 32.8 using Eq. (32.8). The change in the global nonlinear stiffness is also sensitive to damage build up especially at the early stage in fatigue. Dynamic bifurcation amplified the change in k_n , which made it possible to use as a health state indicator. The elastic constant in the stress concentration region ($x_d \rightarrow 0$) is estimated using Eq. (32.12) and plotted as a function of fatigue life in Fig. 32.9. The results shown is for the average E_d from $0 < x_d < 1$ cm.

Figure 32.10 shows typical nanoindentation force-displacement responses, in this case performed on the L-w face of the specimen fatigued to approximately 25% of life. Note that with increasing distance from the clamping location, there is a decrease in the maximum indentation depth and an increase in the residual indent depth. This trend suggests a decrease in plastic work with fatigue damage. Figure 32.11 shows the results of nanoindentation tests on the beam from the L-t face near the cantilever clamped end for specimens fatigued to 25%, 50%, and 75% of fatigue life. The data are normalized by the average indentation response on the same cross-section of an Al 7075-T6 control specimen. The 0-mm position indicates testing areas along the neutral axis of the beam. The specimens all showed a significant compliance effect with respect to the control; the specimen cycled to 50% of life demonstrated an indentation response roughly half the stiffness of the control. There also appears to be a relative compliance effect for each specimen near the beam surfaces, which are

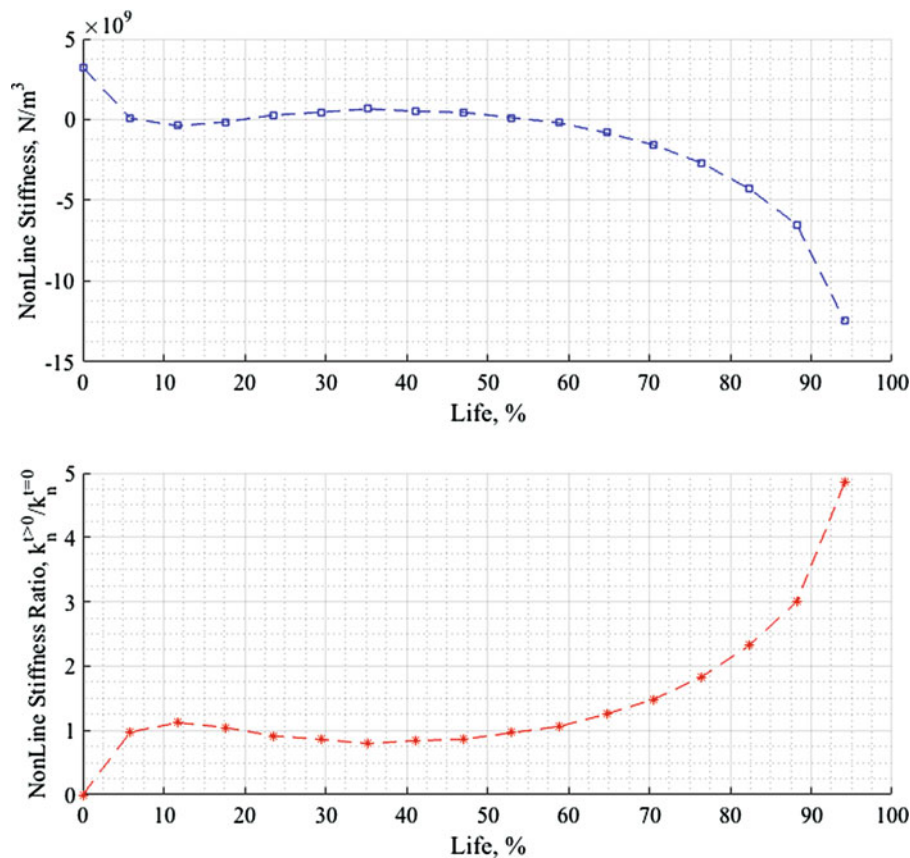


Fig. 32.8 Change in the global nonlinear stiffness due to fatigue build up

locations of relatively high stress and thus likely experienced greater degradation. Variations in local mechanical behavior of the specimens is likely affected by the microstructural evolution due to fatigue, but the indentation response may also be complicated by variations in residual stress, which was not accounted for in this study. Future studies will include tests on the other cross sections of the beam at various positions relative to the clamped end.

The results of the AFM tests are displayed in Fig. 32.12 and include SKPM maps ($10\ \mu\text{m} \times 10\ \mu\text{m}$) overlaid onto the corresponding topography scans. The SKPM images measure the difference in the electronic work function between the tip material (i.e. PtSi) and the sample. The technique has previously been used to characterize variations in the dislocation density in stainless steels (Wang *et al.*, Proc. Mater. Sci. 3, 1736–1741 (2014)). Figure 32.12a, b displays SKPM maps of an Al7075-T6 control and a failed Al7075-T6 cantilever near the beam root (i.e. where the specimen was fixed, and a region exposed to the maximum stress). The average potential difference between the tip and sample surface is dependent on several factors, including surface roughness, tip geometry, and elemental and microstructural variations. Figure 32.10c displays a SKPM map on a single crystal Aluminum (100) reference sample, which was used to calibrate the tip for Aluminum. The data appear to show a trend between the average work function difference on single crystal Al (885 mV), control Al 7075 (510 mV), and the failed Al 7075 specimen (–1015 mV). In addition, smaller electric potential domains appear to exist on the 7075 surface which may be indicative of grain fragmentation.

Finally, to capture changes in the grain structure, electron backscattering diffraction was performed on the L-t face of the 75% fatigued specimen. Two scans were performed and are provided in Fig. 32.13: Fig. 32.13a is from near the corner formed by the upper surface and the length position furthest from the clamping location, taken to be representative of a control specimen, and Fig. 32.13b is from near the corner formed by the upper surface and the clamping location. Long horizontal grains are indicative of the rolling direction during manufacturing, which is along the length of the beam. The line technique was used to estimate the presence of grain breakup; five vertical lines were drawn on each image, and the number of grain boundaries crossing each line was counted. The control scan has an average of 36.4 grain boundaries, while the scan from the highest damage area has an average of 43.2 grain boundaries, 19% more than the control.

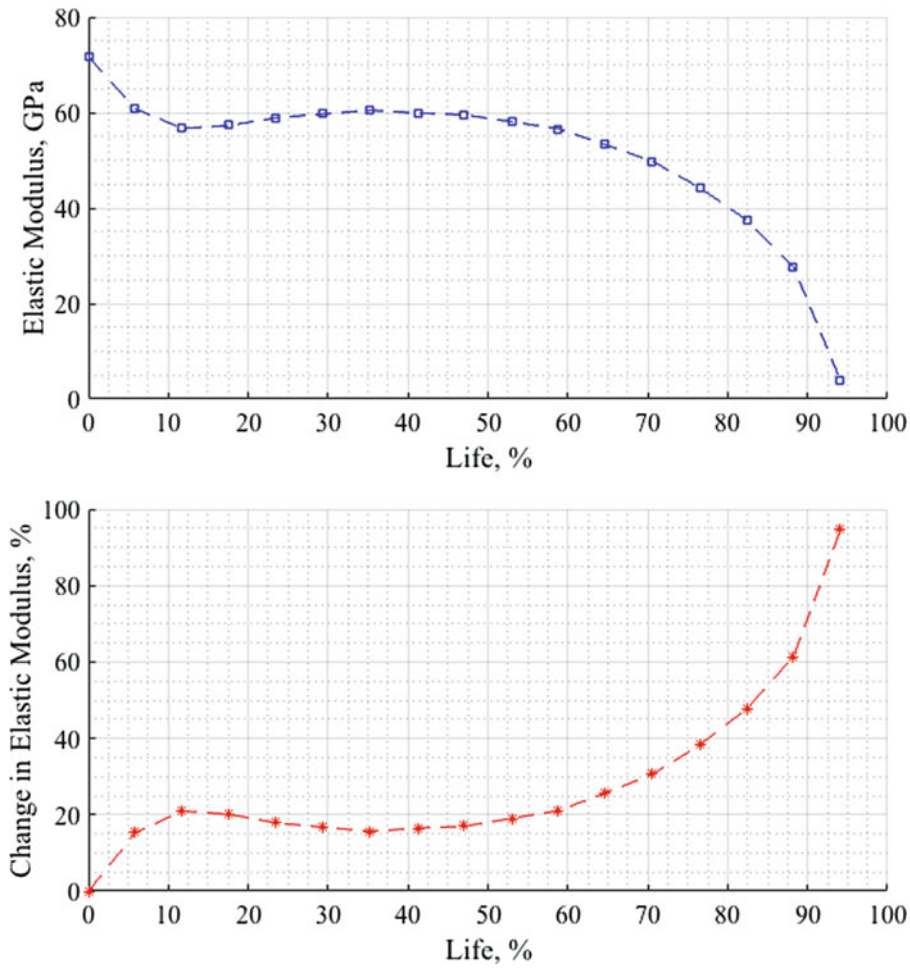


Fig. 32.9 Average elastic modulus near the beam root from the clamping point out 1 cm

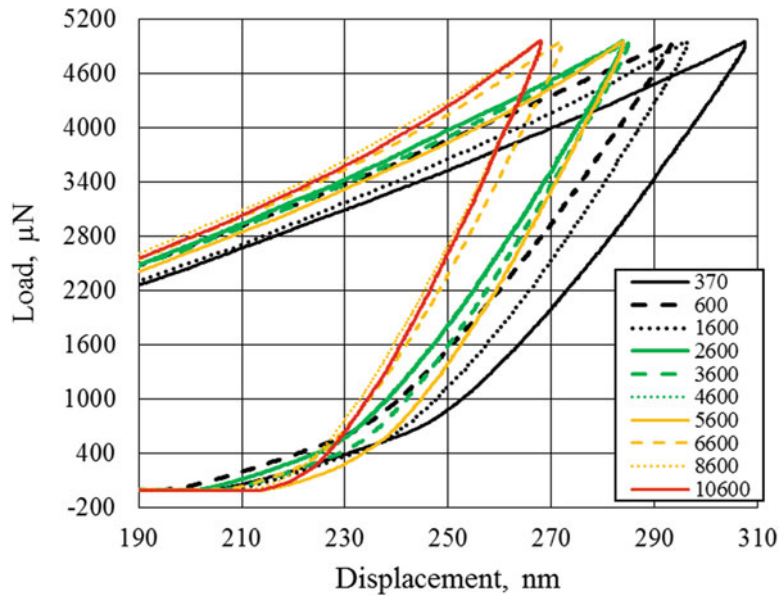


Fig. 32.10 Nanoindentation results displaying the variation in maximum indent depth (h_{max}) and residual indent depth (h_f) for various positions along the cantilever surface from the clamping location; units are μm

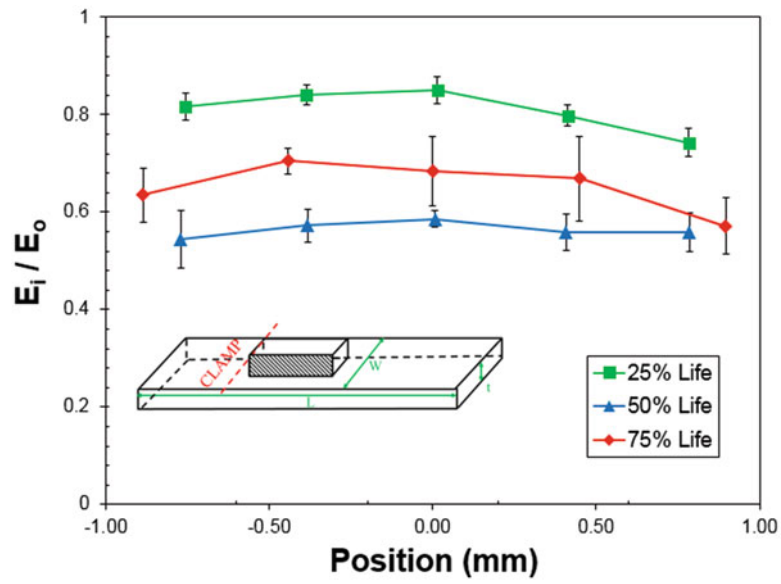


Fig. 32.11 Normalized indentation results on the beam cross-section at various stages of fatigue life as a function of thickness position

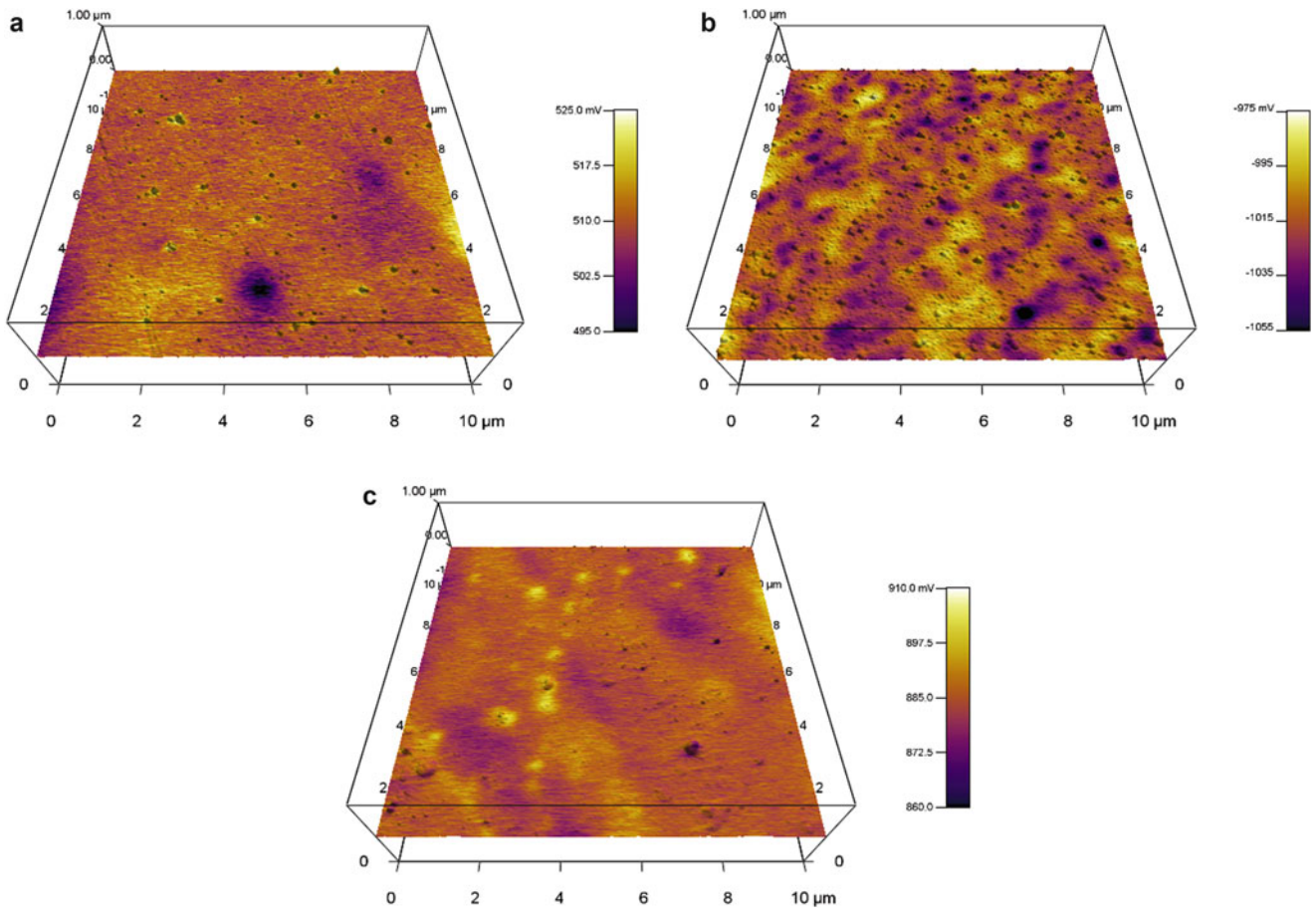


Fig. 32.12 Atomic force microscopy (AFM) maps of (a) aluminum 7075 control, (b) Al 7075 fatigued, (c) Al (100) single crystal reference. Plots show scanning kelvin probe microscope images overlaid onto AFM height maps

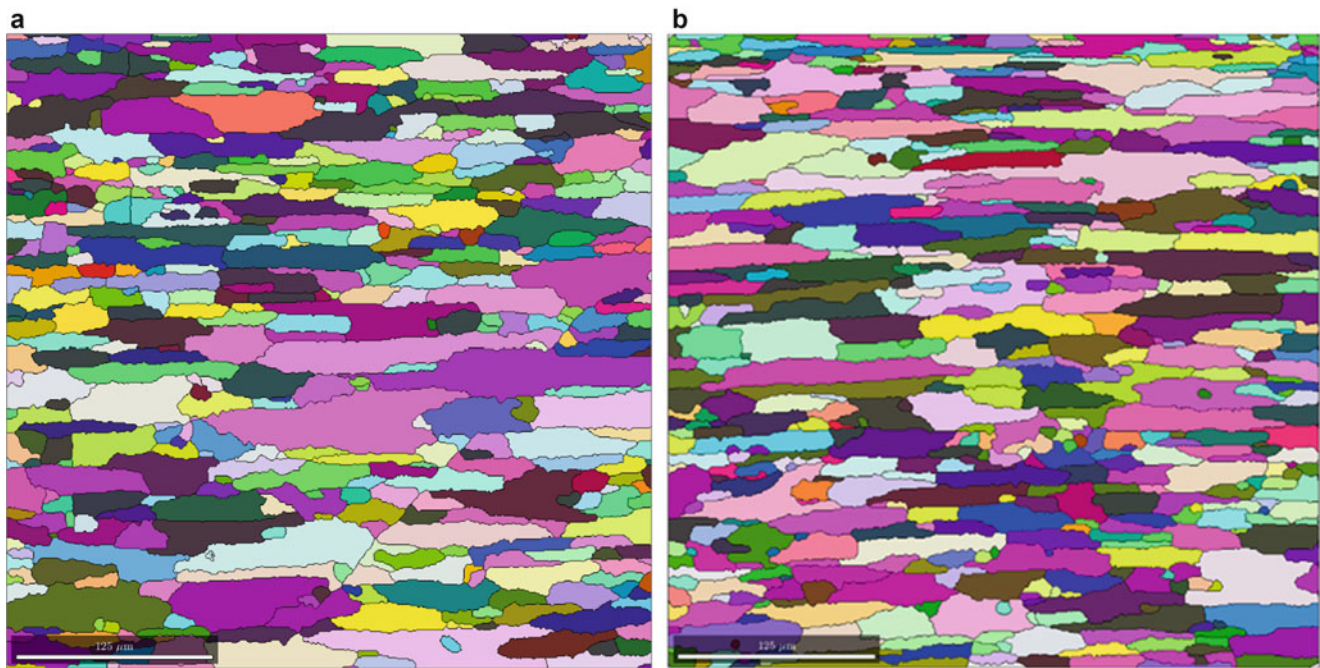


Fig. 32.13 Electron backscattering diffraction results from (a) a location away from the area of highest stresses and (b) a location near the highest stresses

32.5 Conclusions and Future Work

Changes in the response of a structure at its natural frequency shows promise as an indicator of fatigue damage. These changes are detectable before large scale damage would be present and are evidence of damage precursors. Of greatest immediate interest is the difference between the responses from up and down sweeps that appears to grow with damage state, which grows due to the growing presence of nonlinear dynamics as damage evolves. Future work will test more specimens to determine repeatability of the results. Additionally, the local electrical and mechanical signatures of the specimens at various stages of fatigue life will be compared to the global dynamic behavior of the beams, and additional microscopy will be used to observe the microstructural changes.

References

1. Weiss, V., Ghoshal, A.: On the search for optimal damage precursors. *Struct. Health Monit.* **13**(6), 601–608 (2014)
2. Haile, M.A., Hall, A.J., Yoo, J.-H., Coatney, M.D., Myers, O.J.: Detection of damage precursors with embedded magnetostrictive particles. *J. Intell. Mater. Syst. Struct.* **27**(12), 1567–1576 (2015)
3. Henry, T.C., Haynes, R.A., Cole, D.P., Haile, M.A., Coatney, M.D., Weiss, V.: Tapered test specimen for rapid damage precursor identification. In *Proceedings of the ASME 2017 Conference on Smart Materials, Adaptive Structures, and Intelligent Systems*, Snowbird, UT, 18–20 Sept 2017
4. Curadelli, R.O., Riera, J.D., Ambrosini, D., Amani, M.G.: Damage detection by means of structural damping identification. *Eng. Struct.* **30**(12), 3497–3504 (2008)
5. Habtour, E., Cole, D.P., Riddick, J.C., Weiss, V., Roberson, M., Sridharan, R., Dasgupta, A.: Detection of fatigue damage precursor using a nonlinear vibration approach. *Struct. Control. Health Monit.* **23**(12), 1442–1463 (2016)
6. Cole, D.P., Habtour, E., Sano, T., Fudger, S.J., Grendahl, S.M., Dasgupta, A.: Local mechanical behavior of steel exposed to nonlinear harmonic oscillation. *Exp. Mech.* **57**(7), 1027–1035 (2017)
7. Balachandran, B., Magrab, E.B.: *Vibrations*, 2nd edn. Cengage Learning, Toronto (2009)
8. Habtour, E., Cole, D.P., Stanton, S.C., Sridharan, R., Dasgupta, A.: Damage precursor detection for structures subjected to rotational base vibration. *Int. J. Non Linear Mech.* **82**, 49–58 (2016)



Chapter 33

Application of Control-Based Continuation to a Nonlinear System with Harmonically Coupled Modes

L. Renson, D. A. W. Barton, and S. A. Neild

Abstract The objective of this study is to demonstrate the applicability of control-based continuation to systems with multiple degrees of freedom. Experimental demonstration is performed on a nonlinear structure comprising harmonically coupled modes. The design of the feedback controller used to stabilise unstable periodic solutions is discussed. The response of the system is then traced out for constant forcing frequencies and amplitudes. System identification is performed to analyse the stability of the underlying, uncontrolled system and detect the presence of limit-point and Neimark-Sacker bifurcations.

Keywords Control-based continuation · Multiple degrees of freedom · Harmonic coupling · Experimental bifurcation analysis · Closed-loop identification

Nonlinear structures can exhibit very complicated dynamic behaviours that have no equivalent in linear systems. Take, for example, modal interactions which can lead to energy transfers between modes with well-separated, non-commensurate natural frequencies [1]. One of the most important manifestation of nonlinearity is the presence of bifurcations. In the frequency response of a nonlinear structure, bifurcations correspond to boundaries in forcing frequency where the structural response changes stability. Bifurcations can also mark regions where multiple, stable responses coexist and where sudden ‘jumps’ between these sometimes qualitatively and quantitatively different regimes of motion can occur. Characterising experimentally the dynamics and, in particular, the bifurcations of nonlinear structures is therefore a challenging task.

Control-based continuation (CBC) is a method that allows to explore the dynamics of a physical system directly during experimental tests. CBC relies on feedback control to reach and stabilise periodic responses of the tested specimen, and uses the principle of numerical continuation to track their evolution as parameters (for instance, forcing frequency/amplitude) are varied[2]. The stability of the response and the size of its basin of attraction are a priori unimportant to the method (provided the controller has been properly designed), so that CBC can be viewed as a general and systematic approach to perform controlled, nonlinear experiments. CBC was successfully used to trace out nonlinear frequency responses, nonlinear normal modes[3] and limit-point bifurcation curves[4] of several simple systems subjected to external harmonic excitations.

As of now, the experimental demonstration of CBC has been limited to simple experiments where tested specimens can be considered as single-degree-of-freedom (SDOF) nonlinear oscillators. This study shows, for the first time, that the method is also applicable to systems with multiple degrees of freedom (MDOF).

The tested structure is presented in Fig. 33.1a. It is a cantilever beam whose free-end is attached to two linear springs. The displacements of the beam tip lead to large displacements of the springs in the direction transverse to their natural direction of elongation, leading to nonlinear geometric effects. The natural frequencies of the structure are adjusted by adding a localised mass (magnet) at the first antinode of the second-bending mode such that the frequency ratio between the first two natural frequencies is close to and larger than 3.

Previous applications of the CBC method have considered a proportional plus derivative output feedback controller to stabilise the periodic responses of the tested structure. Proportional and derivative gains were estimated manually and kept constant. However, in the present case, such manual tuning is impractical due the MDOF character of the structure and the presence of strong harmonic couplings between the first two modes. To design the controller, a linear state-space model of the structure is first identified using a low-amplitude random excitation and linear subspace identification algorithms. The identified model is restricted to the first two modes of the system. Based on this model, a Luenberger state observer and a full-state feedback controller are designed using standard pole-placement methods.

L. Renson (✉) · D. A. W. Barton · S. A. Neild
Faculty of Engineering, University of Bristol, Bristol, UK
e-mail: l.renson@bristol.ac.uk

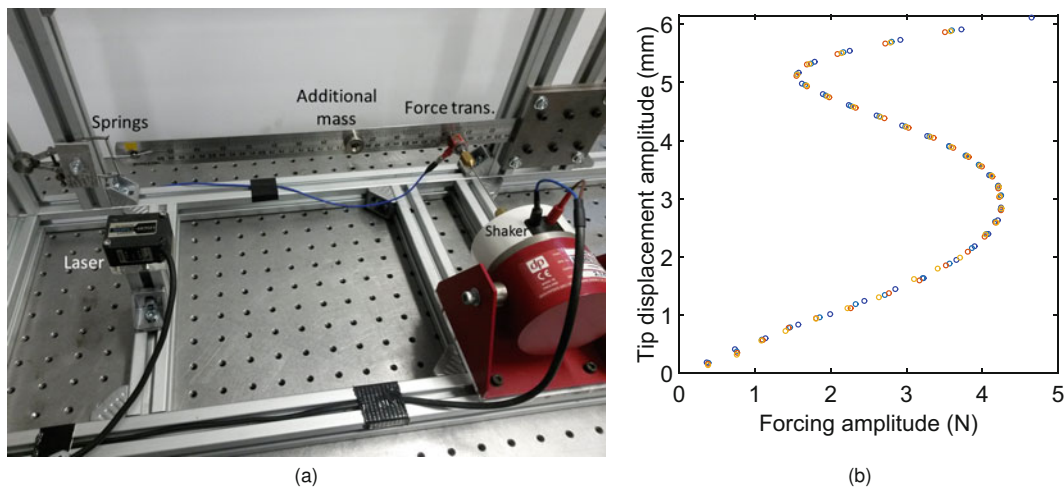


Fig. 33.1 (a) Multi-degree-of-freedom system investigated in this study. (b) Forced response of the structure obtained using CBC. The excitation frequency is kept constant (13 Hz) and the excitation amplitude is considered as the continuation parameter. Different colours correspond to results obtained with different continuation parameters

Figure 33.1b shows the response of the structure to harmonic excitation. The forcing frequency is fixed to 13 Hz and experimental continuation is carried out considering the forcing amplitude as the free parameter. The continuation is performed for different step-size parameters to show the reproducibility of the results. Interestingly, the use of a linear model and a linear controller is sufficient to successfully apply CBC in the range of forcing frequencies and forcing amplitudes considered.

The stability of the underlying uncontrolled system of interest is not directly apparent due to the presence of the stabilising feedback controller used in the CBC method. However, the stability properties of the uncontrolled dynamics can be recovered using system identification techniques[5]. Specifically, the behaviour of a nonlinear system can be approximated around a periodic response by a linear time-periodic (LTP) model. The stability of such linear model can be analysed and used to infer the local stability of the nonlinear system. In this study, random input-output data are collected for every periodic orbit and linear techniques for closed-loop identification are exploited to identify the LTP linearisation of the nonlinear system.

References

1. Renson, L., Noël, J.P., Kerschen, G.: Complex dynamics of a nonlinear aerospace structure: numerical continuation and normal modes. *Nonlinear Dyn.* **79**, 1293–1309 (2015)
2. Sieber, J., Krauskopf, B.: Control based bifurcation analysis for experiments. *Nonlinear Dyn.* **51**(3), 365–377 (2008)
3. Renson, L., Gonzalez-Buelga, A., Barton, D.A.W., Neild, S.A.: Robust identification of backbone curves using control-based continuation. *J. Sound Vib.* **367**, 145–158 (2016)
4. Renson, L., Barton, D.A.W., Neild, S.A.: Experimental tracking of limit-point bifurcations and backbone curves using control-based continuation. *Int. J. Bifurcation Chaos* **27**(1), 1730002 (2017)
5. Barton, D.A.W.: Control-based continuation: bifurcation and stability analysis for physical experiments. *Mech. Syst. Signal Process.* **84**(B), 54–64 (2017)



Chapter 34

Numerically Assessing the Relative Significance of Nonlinear Normal Modes to Forced Responses

T. L. Hill, S. A. Neild, and A. Cammarano

Abstract Nonlinear normal modes, which describe the unforced, undamped responses of nonlinear systems, are often used for understanding the dynamic behaviour of nonlinear structures in engineering. As such, a key property of nonlinear normal modes (NNMs) is that they relate to the dynamic behaviour of the system when forcing and damping are applied. Previous work has shown that an extremely large number of NNMs may be predicted for relatively simple systems; however only a small number of these NNMs have a meaningful influence on the forced and damped dynamics. As such, a method for determining which NNMs are significant (i.e., strongly relate to the forced dynamics) and which are not is crucial for the use of NNMs as a tool for understanding nonlinear systems.

As shown in the literature, NNMs only relate to the forced dynamics in the presence of a mechanism for energy transfer between resonating components of the system. Whilst this provides an understanding of the mechanism, computing which NNMs exhibit this property requires detailed analytical analysis. In this paper, we discuss a numerical approach for determining the degree of significance, with respect to the forced responses, of the NNMs. Such an approach removes the need for analytical investigation and provides an efficient and practical approach to determining the significance of the NNMs.

Keywords Nonlinear normal modes · Nonlinear structural dynamics · Backbone curves · Energy balancing · Nonlinear beam

34.1 Introduction

Nonlinear normal modes are a tool that have been studied extensively and put to great practical use [1–7]. The definition of a nonlinear normal mode (NNM) has seen many evolutions since the original work of Rosenberg [8, 9], including the extension to include nonconservative effects by Shaw and Pierre [10–12]. Another line of development has considered the conservative responses of nonlinear systems, and the current definition of this type of NNM is *any periodic motion of the underlying conservative system* [13]. These conservative responses are of interest as it has been shown that they relate to the forced responses of the system [14]. This not only allows the complex forced responses to be reduced to a simpler set of conservative responses [15], but also aids in the detection of features such as isolas [16–18]. However, recent work has highlighted that not all NNMs relate to the forced responses [19].

As described in [20], a very large number of NNMs may exist in a relatively simple nonlinear system. It is therefore crucial to understand which of these are significant (i.e., relate to the forced responses) and which do not. It was also highlighted in [20] that the significant NNMs are *phase-locked*, whilst the remaining responses are termed *phase-unlocked* and only correspond to the forced responses when the damping is extremely small. It was demonstrated that this is due to the degree of coupling (i.e., the amount of energy that may be transferred) between the modes, and that this is related to the phase-locking property. Specifically, a phase-locked NNM is able to transfer a large amount of energy via the fundamental components of the response, whilst phase-unlocked responses can only transfer a small amount of energy via the harmonics.

T. L. Hill (✉) · S. A. Neild
Department of Mechanical Engineering, University of Bristol, Bristol, UK
e-mail: tom.hill@bristol.ac.uk

A. Cammarano
School of Engineering, University of Glasgow, Glasgow, UK

The ability to transfer energy is critical, as a forcing rarely provides precisely the correct amount of energy to each mode, and hence the system must “correct” for this by transferring the energy internally [14]. If it is unable to achieve this, then the response cannot be close to the NNM. Distinguishing between phase-locked and phase-unlocked NNMs is therefore an effective way of determining the significance of NNMs. However, phase-locking is a property that is determined analytically [19], and this analytical process becomes algebraically expensive for large and complex systems. Therefore an alternative method for determining significance will allow this insight to be more widely applicable.

In [21], a numerical extension of the energy-balancing technique, introduced in [22], was used to compute the damping level required to observe each of the NNMs, given a forcing at a single harmonic. Whilst this approach is computationally cheap, it only accounts for a specific form of excitation. It is therefore difficult to separate the phenomena that are inherent to the NNMs from those that arise from this specific forcing configuration.

In [20], time-domain numerical simulations were used to simulate the case where the external forcing precisely matched the damping on a specific NNM. When this is the case, the response is precisely equal to that of the NNM, i.e., the forcing has no effect on the response. A perturbation in the form of a time-delay was then applied to the forcing on one of the modes. The response of the system was then allowed to reach steady-state, and the relative change in the response (in terms of the phase between the modes) was measured. This revealed that the phase-locked NNMs exhibited little change in phase, compared to the delay of the forcing, whilst the phase-unlocked NNMs exhibited a large change. Whilst this further demonstrates the importance of the phase in the energy transfer mechanisms, these simulations are computationally expensive.

In this paper an alternative, computationally-cheap, technique is discussed. This is based on the time-delay in the forcing, as discussed in [20]. However, rather than performing a time-domain integration, this approach considers the instantaneous demand for energy transfer between the modes. This demand must be met by the response, and the larger the demand, the further from the NNM response the system will be pushed. It is found that the phase-unlocked NNMs have a very high energy transfer demand, given a small delay in the forcing. This suggests that they are highly sensitive to such perturbations, providing further explanation as to why they are rarely observed.

After introducing a nonlinear beam model and its NNMs, used as a motivating example throughout this paper, the method for determining the energy transfer demand is presented. These results are then validated using a time-domain integration approach to observe the effects of the energy demand.

34.2 The Nonlinear Dynamics of a Pinned-Pinned Beam

34.2.1 A Nonlinear Pinned-Pinned Beam

Throughout this paper, the pinned-pinned beam, previously studied in [20, 21], will be considered. This beam has a length of $L = 500$ mm, and has a linear torsional spring, of stiffness $\hat{k} = 10$ N m rad⁻¹, at one end. This torsional spring leads to an asymmetry in the system. The depth and height of the beam are 30 and 1 mm respectively, and it is made from a material with a density and Young’s modulus given by $\rho = 7800$ kg m⁻³ and $E = 2 \times 10^{11}$ N m⁻². A schematic of this beam is shown in Fig. 34.1.

In this paper, the vertical deflection of the beam – written $w(x, t)$, where x is the distance along the beam and t is time – is sufficiently large that the dynamic tension along the length of the beam is significant (note that tension is zero when there is no deflection). This dynamic tension leads to nonlinearity at large displacements.

The nonlinear equation of motion of a pinned-pinned beam with dynamic tension is derived in [23]. With the addition of the force due to the torsional spring, this equation of motion is written

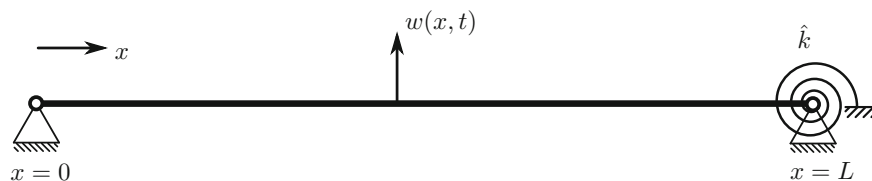


Fig. 34.1 A schematic of the pinned-pinned beam with a torsional end spring

$$\rho\hat{A}\frac{\partial^2 w(x,t)}{\partial t^2} + EI\frac{\partial^4 w(x,t)}{\partial x^4} - \left[\frac{E\hat{A}}{2L} \int_0^L \left(\frac{\partial w(x,t)}{\partial x} \right)^2 dx \right] \frac{\partial^2 w(x,t)}{\partial x^2} + \delta(x-L)\hat{k}\psi(L,t) = 0, \quad (34.1)$$

where \hat{A} and I denote the cross-sectional area and second moment of area respectively. Additionally, δ represents the Dirac delta function and $\psi(x,t)$ represents the rotation of the beam. Note that this equation of motion is conservative – i.e., it does not contain any damping or external forcing. The first and second terms in Eq. (34.1) represent the inertia and linear stiffness of the beam respectively; the third term captures the nonlinear stiffening of the beam due to the dynamic axial tension; and the final term represents the conservative force exerted on the beam by the torsional spring.

As described in [24], the vertical displacements of the beam may be described using the underlying linear modal coordinates

$$w(x,t) = \sum_{i=1}^{\infty} \theta_i(x)q_i(t), \quad (34.2)$$

where θ_i and q_i represent the modeshape and modal displacement of the i th linear mode respectively. The modeshapes are found using

$$\theta_i(x) = \left[\frac{1}{2} - \frac{EI}{\hat{k}L} \sin^2(\beta_i) - \frac{1}{2} \left(\frac{\sin(\beta_i)}{\sinh(\beta_i)} \right)^2 \right]^{-\frac{1}{2}} \left[\sin\left(\frac{\beta_i}{L}x\right) - \frac{\sin(\beta_i)}{\sinh(\beta_i)} \sinh\left(\frac{\beta_i}{L}x\right) \right], \quad (34.3)$$

where β_i is found from

$$\cot(\beta_i) - \coth(\beta_i) + 2EI\frac{\beta_i}{\hat{k}L} = 0. \quad (34.4)$$

As detailed in [24], the Galerkin method may be applied to Eq. (34.1), alongside Eq. (34.2), to find the modal equation of motion of the beam, written

$$\ddot{\mathbf{q}} + \mathbf{\Lambda}\mathbf{q} + \mathbf{N}_q(\mathbf{q}) = 0, \quad (34.5)$$

where: \mathbf{q} is a vector of modal displacements, i.e., the i th element of \mathbf{q} is q_i ; $\mathbf{\Lambda}$ is a diagonal matrix whose i th leading diagonal element is the square of i th linear natural frequency, ω_{ni}^2 ; and \mathbf{N}_q is a vector of nonlinear terms, expressed as a function of the linear modal displacements. The i th linear natural frequency may be computed using

$$\omega_{ni}^2 = \frac{EI}{\rho\hat{A}} \left(\frac{\beta_i}{L} \right)^4. \quad (34.6)$$

The dynamics of interest in this paper can be captured by considering the first two modes, i.e., the deflection of the beam is approximated to

$$w(x,t) \approx \theta_1(x)q_1(t) + \theta_2(x)q_2(t). \quad (34.7)$$

Using this, the terms in the modal equation of motion, Eq. (34.5), are written

$$\mathbf{q} = \begin{pmatrix} q_1 \\ q_2 \end{pmatrix}, \mathbf{\Lambda} = \begin{bmatrix} \omega_{n1}^2 & 0 \\ 0 & \omega_{n2}^2 \end{bmatrix}, \mathbf{N}_q = \begin{pmatrix} \alpha_1 q_1^3 + 3\alpha_2 q_1^2 q_2 + \alpha_3 q_1 q_2^2 + \alpha_4 q_2^3 \\ \alpha_2 q_1^3 + \alpha_3 q_1^2 q_2 + 3\alpha_4 q_1 q_2^2 + \alpha_5 q_2^3 \end{pmatrix}, \quad (34.8)$$

where α_k denote the nonlinear coefficients, which are computed using

$$\begin{aligned} \alpha_1 &= \frac{-E}{2L^2\rho} \left[\int_0^L \theta_1' \theta_1' dx \right] \left[\int_0^L \theta_1'' \theta_1 dx \right], \alpha_2 = \frac{-E}{2L^2\rho} \left[\int_0^L \theta_1' \theta_1' dx \right] \left[\int_0^L \theta_1'' \theta_2 dx \right], \\ \alpha_3 &= \frac{-E}{2L^2\rho} \left\{ 2 \left[\int_0^L \theta_1' \theta_2' dx \right] \left[\int_0^L \theta_2'' \theta_1 dx \right] + \left[\int_0^L \theta_2' \theta_2' dx \right] \left[\int_0^L \theta_1'' \theta_1 dx \right] \right\}, \end{aligned} \quad (34.9)$$

Table 34.1 The linear natural frequencies and nonlinear parameters for the beam considered here

ω_{n1}	ω_{n2}	α_1	α_2	α_3	α_4	α_5
[rad s ⁻¹]		($\times 10^{10}$)				
125.91	418.41	8.81	-1.31	34.70	-5.12	133.63

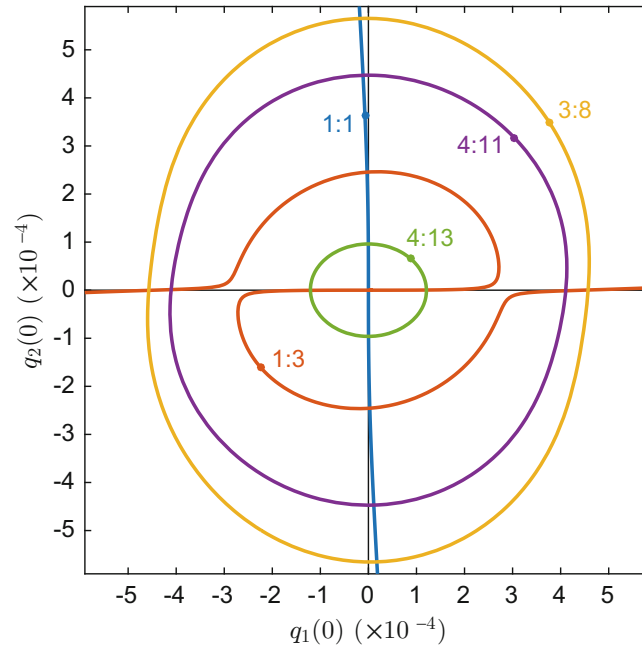


Fig. 34.2 Five nonlinear normal mode branches of the two-mode beam model. These are shown in the projection of the initial modal displacements, $q_1(0)$ against $q_2(0)$. The labels denote the ratio between the frequencies of the fundamental components of the two modes, and the dots on the branches mark the responses that are represented in Fig. 34.3

$$\alpha_4 = \frac{-E}{2L^2\rho} \left[\int_0^L \theta_2' \theta_2' dx \right] \left[\int_0^L \theta_2'' \theta_1 dx \right], \alpha_5 = \frac{-E}{2L^2\rho} \left[\int_0^L \theta_2' \theta_2' dx \right] \left[\int_0^L \theta_2'' \theta_2 dx \right],$$

where θ_i' and θ_i'' denote the first and second derivative of θ_i , with respect to x , respectively. After using Eq. (34.3) to compute the modeshapes, θ_1 and θ_2 , for the set of physical parameters considered here, the linear natural frequencies and nonlinear parameters may be found using Eqs. (34.6) and (34.9). These are listed in Table 34.1, and are the same as those considered in [20, 21].

34.2.2 The Nonlinear Normal Modes of a Pinned-Pinned Beam

The nonlinear normal modes of this structure have previously been examined in [20, 21]. For completeness, they are now presented here. The definition of a nonlinear normal mode (NNM) is that of any periodic motion of the underlying unforced and undamped system [13]. These periodic responses have neighbouring solutions, which respond at a different frequency. The loci of these solutions form branches which are referred to here as *NNM branches*.

Five NNM branches of the example system are shown in Fig. 34.2, represented in the projection of the initial displacements of the two modes: $q_1(0)$ against $q_2(0)$. The initial velocities are zero, i.e., $\dot{q}_1(0) = \dot{q}_2(0) = 0$. These branches have been computed using the numerical continuation software AUTO-07p [25], using initial conditions found analytically using a normal form approximation [26]. The labels for the branches represent the ratios between the fundamental components of the two modes, i.e., a 1:3 response consists of a first mode that is dominated by a harmonic at a frequency of 1ω and second mode dominated by a harmonic at frequency 3ω . Note that we define $\omega = 2\pi T^{-1}$, where T is the period of the response. It has previously been observed [20] that the 1:1 and 1:3 branches are *phase-locked* (and hence are strongly related to the forced responses) whilst the 3:8, 4:11 and 4:13 branches are *phase-unlocked*.

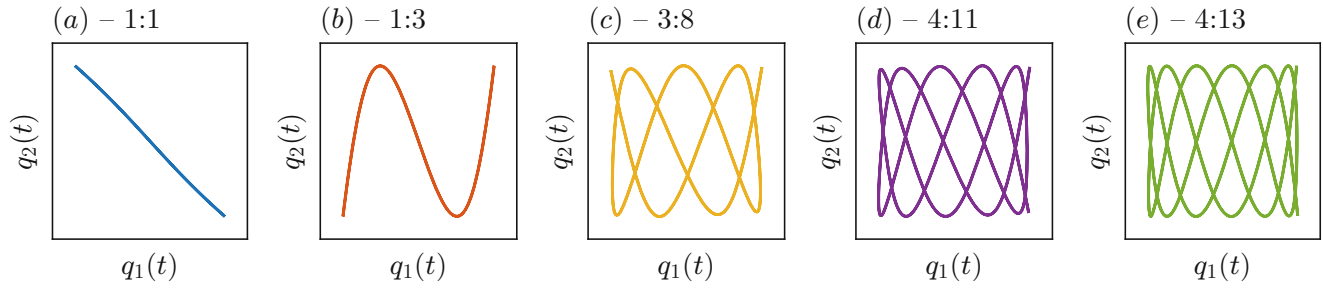


Fig. 34.3 The time-parameterised responses of five NNMs, whose branches are shown in Fig. 34.2. These are represented in the projection of the first modal displacement, $q_1(t)$, against the second modal displacement, $q_2(t)$. The title of each panel denotes the ratio between the frequencies of the fundamental components of the two modes (corresponding to the labels in Fig. 34.2)

The dots on the NNM branches shown in Fig. 34.2 correspond to individual NNM responses which are shown, parameterised in time, in Fig. 34.3. These five responses demonstrate how the complexity of these responses varies, with the phase-locked responses (3:8, 4:11 and 4:13) exhibiting the most complex behaviour. It is important to note that these responses only represent a small number of phase-locked NNM branches for this system, and for the region of initial conditions shown here, additional branches may be found if higher frequency ratios are considered. Additionally, these are computed numerically, and hence are not an artefact of analytical approximations. This demonstrates the complexity that may arise from a simple, 2-DOF system with cubic nonlinearities. Furthermore, this highlights the need for a method of distinguishing which of these responses are needed to understand the forced responses of the system. Specifically, a computationally- and algebraically-cheap method for determining the relative significance of NNMs, for a range of different forcing conditions, is required.

34.3 Energy Transfer Due to a Phase Shift in Forcing

34.3.1 The Relationship Between Energy and Phase

As in [20], we now consider the effect of introducing a delay to an *ideal forcing* – i.e., a forcing that precisely matches the damping of an NNM. The modal equations of motion for this case may be written

$$\ddot{q}_1 + \zeta_1 \dot{q}_1 + \omega_{n1}^2 q_1 + N_{q1}(\mathbf{q}) = f_1(t) = \zeta_1 \dot{\bar{q}}_1, \quad (34.10a)$$

$$\ddot{q}_2 + \zeta_2 \dot{q}_2 + \omega_{n2}^2 q_2 + N_{q2}(\mathbf{q}) = f_2(t) = \zeta_2 \dot{\bar{q}}_2. \quad (34.10b)$$

where ζ_i represents the coefficient of the linear modal damping term for the i th mode, and \bar{q}_i represents the *target* response in the i th mode – in this case, the NNM of interest. Note that no delay is introduced in the above equations, and hence the solutions that satisfy these will correspond to the target response precisely, i.e., $q_i = \bar{q}_i$.

The net energy lost due to damping in the i th mode, during one period of motion, may be written

$$E_{Di} = \int_0^T (\zeta_i \dot{q}_i) \dot{q}_i dt. \quad (34.11)$$

If the modal velocities are expressed as an infinite summation of the harmonics components, i.e.,

$$\dot{q}_i = \sum_{j=0}^{\infty} V_{i,j} \cos(j\Omega t - \phi_{i,j}), \quad (34.12)$$

then the net damping energy may be written

$$E_{Di} = \zeta_i \int_0^T \left[\sum_{j=0}^{\infty} V_{i,j} \cos(j\Omega t - \phi_{i,j}) \right]^2 dt, \quad (34.13a)$$

$$= \frac{1}{2} \zeta_i \sum_{j=0}^{\infty} V_{i,j}^2 \int_0^T 1 + \cos(2j\Omega t - 2\phi_{i,j}) dt, \quad (34.13b)$$

$$= \frac{\pi}{\Omega} \zeta_i \sum_{j=0}^{\infty} V_{i,j}^2, \quad (34.13c)$$

where $T = 2\pi\Omega^{-1}$ has been used.

Now, if a small delay, τ_i , is introduced to the ideal forcing term in the i th mode then, using Eq. (34.12), this term may be written

$$f_i(t + \tau_i) = \sum_{j=0}^{\infty} V_{i,j} \cos(j\Omega(t + \tau_i) - \phi_{i,j}), \quad (34.14)$$

where it has been assumed that the response is equal to the target response, i.e., $q_i = \bar{q}_i$.

As such, the net energy *gained* due to a delayed forcing over one period of motion is given by

$$E_{Fi} = \int_0^T f_i(t + \tau_i) \dot{q}_i(t) dt, \quad (34.15a)$$

$$= \int_0^T \left[\zeta_i \sum_{j=0}^{\infty} V_{i,j} \cos(j\Omega(t + \tau_i) - \phi_{i,j}) \right] \left[\sum_{j=0}^{\infty} V_{i,j} \cos(j\Omega t - \phi_{i,j}) \right] dt, \quad (34.15b)$$

$$= \zeta_i \sum_{j=0}^{\infty} V_{i,j}^2 \int_0^T \cos(j\Omega t + j\Omega\tau_i - \phi_{i,j}) \cos(j\Omega t - \phi_{i,j}) dt, \quad (34.15c)$$

$$= \frac{\pi}{\Omega} \zeta_i \sum_{j=0}^{\infty} V_{i,j}^2 \cos(j\Omega\tau_i). \quad (34.15d)$$

The critical difference between phase-locked and phase-unlocked responses is their ability to transfer energy between the modes. This energy transfer is required in order to account for the difference in the net energy input due to forcing and the net energy removed due to damping (noting that these two values are equal when the forcing is ideal). As such, the energy that must be transferred is given by

$$E_{Ti} = E_{Fi} - E_{Di} = \left[\frac{\pi}{\Omega} \zeta_i \sum_{j=0}^{\infty} V_{i,j}^2 \cos(j\Omega\tau_i) \right] - \left[\frac{\pi}{\Omega} \zeta_i \sum_{j=0}^{\infty} V_{i,j}^2 \right], \quad (34.16a)$$

$$= \frac{\pi}{\Omega} \zeta_i \sum_{j=0}^{\infty} V_{i,j}^2 [\cos(j\Omega\tau_i) - 1], \quad (34.16b)$$

$$= -2 \frac{\pi}{\Omega} \zeta_i \sum_{j=0}^{\infty} V_{i,j}^2 \left[\sin\left(\frac{1}{2}j\Omega\tau_i\right) \right]^2. \quad (34.16c)$$

Assuming that τ_i is small, and that higher harmonics are negligible, the transferred energy may be approximated by

$$E_{Ti} \approx -\tau_i^2 \frac{\pi}{2} \Omega \zeta_i \sum_{j=0}^{\infty} V_{i,j}^2 j^2. \quad (34.17)$$

This highlights an important property of the application of a small delay to a forcing – regardless of the direction of the delay (i.e., the sign of τ_i), the net energy input to the mode is always negative. As such, the net energy input to the *system* is always negative, and hence an NNM response can never be sustained. Instead, the system will be forced to a lower-energy solution.

To account for this energy loss, a scaling factor ϵ is introduced to increase the amplitude of the forcing, such that the forcing energy is now given by

$$E_{Fi} = (1 + \epsilon) \frac{\pi}{\Omega} \zeta_i \sum_{j=0}^{\infty} V_{ij}^2 \cos(j\Omega\tau_i). \quad (34.18)$$

Therefore, the transferred energy must now be equal to

$$E_{Ti} = \left[(1 + \epsilon) \frac{\pi}{\Omega} \zeta_i \sum_{j=0}^{\infty} V_{ij}^2 \cos(j\Omega\tau_i) \right] - \left[\frac{\pi}{\Omega} \zeta_i \sum_{j=0}^{\infty} V_{ij}^2 \right], \quad (34.19a)$$

$$= \frac{\pi}{\Omega} \zeta_i \sum_{j=0}^{\infty} V_{ij}^2 [\cos(j\Omega\tau_i) - 1 + \epsilon \cos(j\Omega\tau_i)], \quad (34.19b)$$

$$\approx -\tau_i^2 \frac{\pi}{2} \Omega \zeta_i \sum_{j=0}^{\infty} V_{ij}^2 j^2 + \epsilon \frac{\pi}{\Omega} \zeta_i \sum_{j=0}^{\infty} V_{ij}^2, \quad (34.19c)$$

$$= -\tau_i^2 \bar{E}_{Ti} + \epsilon E_{Di}, \quad (34.19d)$$

where small angle approximations have again been assumed, and where

$$\bar{E}_{Ti} = \frac{\pi}{2} \Omega \zeta_i \sum_{j=0}^{\infty} V_{ij}^2 j^2. \quad (34.20)$$

We require that the total transferred energy into the system is zero, i.e., $E_{T1} + E_{T2} = 0$. Using Eq. (34.19), this may be written

$$\tau_1^2 \bar{E}_{T1} - \epsilon E_{D1} + \tau_2^2 \bar{E}_{T2} - \epsilon E_{D1} = 0, \quad (34.21)$$

and hence ϵ is given by

$$\epsilon = \frac{\tau_1^2 \bar{E}_{T1} + \tau_2^2 \bar{E}_{T2}}{E_{D1} + E_{D2}}. \quad (34.22)$$

If the two small delays, τ_1 and τ_2 , are the same magnitude, i.e., $\tau_1^2 = \tau_2^2 = \tau^2$, then the energy transferred by the forcing and damping for the i th mode may therefore be written

$$E_{Ti} = \tau^2 \left[-\bar{E}_{Ti} + \frac{\bar{E}_{T1} + \bar{E}_{T2}}{E_{D1} + E_{D2}} E_{Di} \right]. \quad (34.23)$$

As $E_{T1} + E_{T2} = 0$, it follows that $E_{T1} = -E_{T2}$, hence:

$$|E_{Ti}| = \tau^2 E'_{Ti}, \quad (34.24)$$

where

$$E'_{Ti} = \left| \frac{\bar{E}_{T1} E_{D2} - \bar{E}_{T2} E_{D1}}{E_{D1} + E_{D2}} \right|. \quad (34.25)$$

Hence, Eq. (34.24) represents the amount of energy that must be transferred between the modes, given a small delay to the ideal forcing. It can be seen that this scales linearly with the square of the delay, and hence E'_{Ti} describes the rate of this energy transfer.

Note that this assumes that there is no change in the response as a result of the forcing. This is clearly not the case, as the change in the forcing will inevitably change the response. However, if the delay is small, and the damping is small (such that the nonconservative terms are small in comparison to the inertial and stiffness terms), this will be approximately correct for the first period of motion. The energy transfer rate, E'_{Ti} , therefore provides a metric to indicate the relationship between the delay in the forcing and the required energy transfer between the modes for an NNM (with an assumed damping model).

34.3.2 Energy-Phase Relationships for the NNMs of the Example System

Figure 34.4 shows how the energy transfer rate, E'_{Ti} , varies for five NNM branches of the two-mode beam model. These branches are shown in terms of the initial displacements of the modes, as used previously in Fig. 34.2. The energy transfer rate is represented using a color scale, which varies logarithmically. Additionally, the energy transfer rate is scaled using the square of the period T^2 . This is equivalent to measuring the rate of energy transfer with respect to δ , where $\tau = \delta T$, and accounts for the change in period between the NNMs. The values of E'_{Ti} have been found using Eq. (34.25), where the terms \bar{E}_{Ti} and \bar{E}_{Di} are computed by numerically integrating the time-domain solutions of the NNMs. The damping model that has been assumed is $\zeta_i = 2\zeta\omega_{ni}$, where $\zeta = 1\% = 0.01$.

Figure 34.4 clearly shows that the 1:1 NNM branch has a very low energy transfer rate. This shows that a perturbation in the forcing delay will require very little energy to be transferred between the modes. Similarly, the portion of the 1:3 branch near $q_1(0) = q_2(0) = 0$ has a very low transfer rate, and the portions of the 1:3 branch that cross the 3:8 and 4:11 branches are also low. These correspond to the observations made in [20] that these branches are phase-locked and strongly attractive to the forced responses. The “loop” region of the 1:3 response, however, exhibits a larger energy transfer rate. A similar loop region is observed in other structures [17], where it is not followed by the forced response, and thus is not considered to be significant. Furthermore, the presence of this region can cause the forced response to *split*, and an isolated forced response to emerge [17].

The phase-unlocked branches (3:8, 4:11 and 4:13) all have very high energy transfer rates. This demonstrates that a relatively small delay will lead to a very high energy transfer demand. Furthermore, it is known that the coupling between

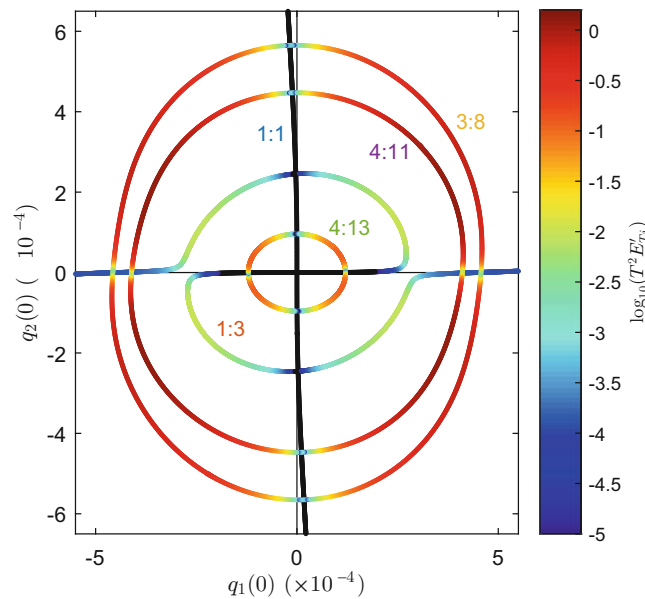


Fig. 34.4 The energy transfer rate for the five nonlinear normal mode branches of the two-mode beam model. These are shown in the projection of the initial modal displacements, $q_1(0)$ against $q_2(0)$, and the energy transfer rate is represented by a colour scale. The colour scale varies logarithmically, and the energy is scaled using the square of the period T^2

the modes is weak, and hence this demand is difficult to meet [20]. It can be seen that, in the vicinity of the crossing points with the phase-locked branches, the energy transfer rates become lower. This is due to the convergence of the responses, and at the points where the branches meet, the responses are identical.

34.4 Settling Time After a Delay

The previous section considers the effect of a forcing delay on a response that is precisely that of an NNM. As previously discussed, this is an approximation, as the true response would diverge from the NNM. As such, we now consider the effect of the forcing delay over time.

If the delay applied to the forcing is equal for both modal components, i.e., $\tau_1 = \tau_2 = \tau$, then it can be assumed that the responses will converge to the target NNM response, with an equal delay, i.e., $q_i(t) = \bar{q}_i(t + \tau)$. The time taken to converge back to this solution gives an indication of the amount of energy that must be transferred in order to account for the forcing delay.

Figure 34.5 shows the five NNM branches, with the convergence time represented by a colour scale. The delay that is applied to each mode is $\tau = 10^{-4}T$ and the system is initiated on the target NNM response. The system is then simulated for one period of motion, and the end conditions are compared to the initial conditions to provide a convergence error, e , where

$$e = \max \left\{ \frac{|q_1(T) - q_1(0)|}{\max |q_1|}, \frac{|\dot{q}_1(T) - \dot{q}_1(0)|}{\max |\dot{q}_1|}, \frac{|q_2(T) - q_2(0)|}{\max |q_2|}, \frac{|\dot{q}_2(T) - \dot{q}_2(0)|}{\max |\dot{q}_2|} \right\}. \quad (34.26)$$

The solution is deemed to have converged when $e < 10^{-5}$. Until convergence is reached, the system is simulated, one period at a time. The convergence time shown in Fig. 34.5 represents the total time taken to satisfy this convergence criterion. The black dots represent unstable responses, i.e., responses that do not converge to the target NNM. As such, these responses do not have an associated convergence time.

Comparing Figs. 34.4 and 34.5 shows that a high energy transfer rate corresponds to a high convergence time. As previously discussed, this is to be expected as a large amount of transferred energy will take longer to correct, particularly when the mechanism for energy transfer between the modes is weak.

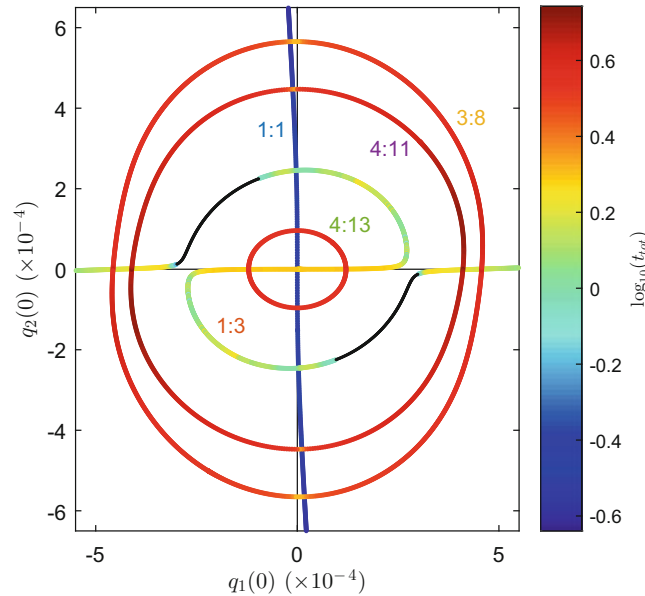


Fig. 34.5 The convergence time for the five NNM branches of the two-mode beam model. These are shown in the projection of the initial modal displacements, $q_1(0)$ against $q_2(0)$, and the convergence time is represented by a colour scale. The black dots represent unstable responses, which do not converge to the target NNM over time

34.5 Conclusions

This paper has introduced the concept of *energy transfer rate* for nonlinear normal modes. This describes the rate at which energy must be transferred between the underlying linear modes of a nonlinear system, given a time-delay perturbation to a perfect forcing (i.e., a forcing that allows the system to respond precisely on an NNM). It is demonstrated that the energy transfer rate relates to the significance of an NNM, and a high rate means that the response is unlikely to be observed in a typical forced response. This is verified by considering the time taken for an NNM response to converge to a steady-state response, given a time-delay perturbation in a perfect forcing. It is seen that responses with a high energy transfer rate are seen to correspond to high convergence times. The key feature of the energy transfer rate is the efficiency of its computation. This provides significant advantage when compared to existing approaches which rely on expensive simulations, or analytical derivations.

References

- Rand, R.H.: A direct method for non-linear normal modes. *Int. J. Non Linear Mech.* **9**(5), 363–368 (1974)
- Montaldi, J., Roberts, M., Stewart, I.: Existence of nonlinear normal modes of symmetric hamiltonian systems. *Nonlinearity* **3**(3), 695 (1990)
- Lewandowski, R.: On beams membranes and plates vibration backbone curves in cases of internal resonance. *Meccanica* **31**(3), 323–346 (1996)
- Nayfeh, A.H., Chin, C., Nayfeh, S.A.: Nonlinear normal modes of a cantilever beam. *J. Vib. Acoust.* **117**(4), 477–481 (1995)
- Gendelman, O.V.: Bifurcations of nonlinear normal modes of linear oscillator with strongly nonlinear damped attachment. *Nonlinear Dyn.* **37**(2), 115–128 (2004)
- Touzé, C., Amabili, M.: Nonlinear normal modes for damped geometrically nonlinear systems: application to reduced-order modelling of harmonically forced structures. *J. Sound Vib.* **298**(4), 958–981 (2006)
- Cammarano, A., Hill, T.L., Neild, S.A., Wagg, D.J.: Bifurcations of backbone curves for systems of coupled nonlinear two mass oscillator. *Nonlinear Dyn.* **77**(1–2), 311–320 (2014)
- Rosenberg, R.M.: Normal modes of nonlinear dual-mode systems. *J. Appl. Mech.* **27**, 263–268 (1960)
- Rosenberg, R.M.: The normal modes of nonlinear n-degree-of-freedom systems. *J. Appl. Mech.* **29**(1), 7–14 (1962)
- Shaw, S., Pierre, C.: Non-linear normal modes and invariant manifolds. *J. Sound Vib.* **150**(1), 170–173 (1991)
- Shaw, S., Pierre, C.: Normal modes for non-linear vibratory systems. *J. Sound Vib.* **164**(1), 85–124 (1993)
- Haller, G., Ponsioen, S.: Nonlinear normal modes and spectral submanifolds: existence, uniqueness and use in model reduction. *Nonlinear Dyn.* **86**(3), 1493–1534 (2016)
- Kerschen, G., Peeters, M., Golinval, J.C., Vakakis, A.F.: Nonlinear normal modes, part I: a useful framework for the structural dynamicist. *Mech. Syst. Signal Process.* **23**(1), 170–194 (2009). Special Issue: Non-linear structural dynamics
- Hill, T.L., Cammarano, A., Neild, S.A., Wagg, D.J.: Interpreting the forced responses of a two-degree-of-freedom nonlinear oscillator using backbone curves. *J. Sound Vib.* **349**, 276–288 (2015)
- Hill, T.L., Cammarano, A., Neild, S.A., Wagg, D.J.: Out-of-unison resonance in weakly nonlinear coupled oscillators. *Proc Royal Soc Lond A Math Phys Eng Sci* **471**, 2173 (2014)
- Hill, T.L., Neild, S.A., Cammarano, A.: An analytical approach for detecting isolated periodic solution branches in weakly nonlinear structures. *J. Sound Vib.* **379**, 150–165 (2016)
- Shaw, A.D., Hill, T.L., Neild, S.A., Friswell, M.I.: Periodic responses of a structure with 3:1 internal resonance. *Mech. Syst. Signal Process.* **81**, 19–34 (2016)
- Detroux, T., Noël, J., Kerschen, G., Virgin, L.N.: Experimental study of isolated response curves in a two-degree-of-freedom nonlinear system. In: *Proceedings of the International Modal Analysis Conference* (2016)
- Hill, T.L., Neild, S.A., Cammarano, A., Wagg, D.J.: The influence of phase-locking on internal resonance from a nonlinear normal mode perspective. *J. Sound Vib.* **379**, 135–149 (2016)
- Hill, T.L., Cammarano, A., Neild, S.A., Barton, D.A.W.: Identifying the significance of nonlinear normal modes. *Proc. R. Soc. Lond. A Math. Phys. Eng. Sci.* **473**, 2199 (2017)
- Hill, T., Neild, S., Cammarano, A., Barton, D.: The significance of nonlinear normal modes for forced responses. In: *Nonlinear Dynamics*, vol. 1, pp. 135–142. Springer (2017)
- Hill, T., Cammarano, A., Neild, S., Wagg, D.: An analytical method for the optimisation of weakly nonlinear systems. *Proc. EURO DYN* **2014**, 1981–1988 (2014)
- Wagg, D.J., Neild, S.A.: Beams. In: *Nonlinear Vibration with Control. Solid Mechanics and Its Applications*, vol. 218, pp. 261–312. Springer, Dordrecht (2015)
- Hill, T.L.: Modal interactions in nonlinear systems. PhD thesis, University of Bristol (2016)
- Doedel, E.J., with major contributions from Champneys, A.R., Fairgrieve, T.F., Kuznetsov, Y.A., Dercole, F., Oldeman, B.E., Paffenroth, R.C., Sandstede, B., Wang, X.J., Zhang, C.: AUTO-07P: Continuation and Bifurcation Software for Ordinary Differential Equations. Concordia University, Montreal (2008). Available at: <http://cmvl.cs.concordia.ca/>
- Neild, S.A., Champneys, A.R., Wagg, D.J., Hill, T.L., Cammarano, A.: The use of normal forms for analysing nonlinear mechanical vibrations. *Philos. Trans. R. Soc. Lond. A Math. Phys. Eng. Sci.* **373**, 2051 (2015)

Chapter 35

Direct Frequency Domain Identification of Time Varying Systems



Lee Mazurek and Richard Christenson

Abstract The following paper presents a frequency domain method to perform time varying linear identification of deterministic non-linear systems and provides an empirical example to illustrate the application of the method for a nonlinear structural dynamic system. The proposed method employs the Kronecker product form of convolution matrices to enable the least mean squares solution of arbitrarily structured cross frequency coupled responses. The mathematical framework allows for solution of different parts of the time varying frequency response depending upon information known about the system. Definitions of time varying coherence, cross and autospectra are derived, and are shown to be equivalent to conventional definitions when simplified to the linear time invariant form. These methods are applied to a physical beam damper system with observed nonlinear behavior tested at the University of Connecticut in order to identify an accurate time varying frequency domain model of the nonlinear system. The new model shows improved coherence relative to a standard linear time invariant model.

Keywords Linear time varying system identification · Time frequency analysis

35.1 Background

The broad theoretical framework of time frequency analysis extends conventional time invariant spectral analysis by simultaneously representing signal power at instantaneous frequency and time [1, 2]. These time frequency spectra have been employed in literature to perform time varying system identification [2–4]. Time frequency transfer functions have many terms, which can lead to problems with ill conditioned matrix inverses, so many practitioners make assumptions about the type of admissible solution. Therefore previous methods have generally assumed candidate time varying basis functions to describe a set of data.

Definitions of coherence (a measure of model to data fit quality) for time varying systems have been proposed based on time frequency distributions or time varying basis functions. Definitions of coherence based on time-frequency distributions result in compromises associated with negative power terms which make their application difficult. Examples of coherence definitions based directly on the time frequency distribution include coherence calculated using spectrograms [5] and coherence calculated using the correlation matrix square root [6]. Others have extended the classical definition of coherence [7] by using time varying or non-linear [8] basis functions. Time varying basis functions have also been used to perform coherence analysis for medical applications [9–11].

The difficulties of ill conditioning and previous knowledge of time varying basis functions may be partially overcome by factoring convolution systems into component models (impulse responses) and time variation (or basis functions) [12]. This approach allows for selected component models or time variation to be independently solved for if sufficient data is available. The current paper employs the discrete Fourier matrix [13] to transform structured convolution matrices from the time domain to frequency domain. This has the benefit of orthogonalizing some parts of the convolution system under certain conditions. The factored convolution structure is represented using components of frequency response, and input frequency variation. These components lend themselves to classical coherence analysis by using time varying basis functions to synthesize new effective input channels.

L. Mazurek · R. Christenson (✉)
Civil & Environmental Engineering, University of Connecticut, Storrs, CT, USA
e-mail: rchrste@engr.uconn.edu

35.2 Mathematical Methods

The following equations represent the time varying discrete convolution equation using a structured matrix. By representing the convolution equation as a matrix, linear algebra and structured matrix theory [13–15] may be used to facilitate the derivation process. The derivations lead to a solution for the frequency response or its time variation given input, output, and associated convolution structure.

Equation (35.1) defines the time varying convolution matrix to be the matrix that reproduces the same output, y , given an input, x , as the time varying discrete convolution sum.

$$y = [H]_C \cdot x := \forall n : y(n) = \sum_m \mathcal{H}(m, n-m) \cdot x(n-m) \quad (35.1)$$

The Kronecker identity is used to transform Eq. (35.1) to

$$\text{vec}(y) = (x^T \otimes I_y) \cdot T \cdot \text{vec}(H \cdot v) \quad (35.2)$$

where $\text{vec}(y)$ represents the columns of y stacked as a vector, \otimes designates the Kronecker product, variable T represents a sample shifting matrix, H represents models, and v represents their variation over input samples. The purpose of this transformation is to express the components of the convolution model and the convolution structure independently [12]. The sample shifting matrix T is given in Eq. (35.3), which is composed of the unit sample shift matrix S , raised to increasing powers. Note that the unit shift matrix is circular, which will allow the Fourier transform matrix to orthogonalize the resulting convolution structure for the linear time invariant case.

$$T = \begin{bmatrix} S^0 & 0_y & 0_y & \cdots & 0_y \\ 0_y & S^1 & 0_y & \cdots & 0_y \\ 0_y & 0_y & S^2 & \cdots & 0_y \\ \vdots & \ddots & \ddots & \ddots & 0_y \\ 0_y & 0_y & 0_y & 0_y & S^{N_x} \end{bmatrix} \quad S = \begin{bmatrix} 0 & 0 & 0 & \cdots & 1 \\ 1 & 0 & 0 & \cdots & 0 \\ 0 & 1 & 0 & \cdots & 0 \\ \vdots & \ddots & \ddots & \ddots & 0 \\ 0 & 0 & 0 & 1 & 0 \end{bmatrix} \quad (35.3)$$

The above equations are transformed from the time domain to the frequency domain using the Fourier matrix [13]. The Fourier matrix is shown in Eq. (35.4), where N_x indicates the number of input samples. The matrix multiplied by its conjugate transpose (inverse Fourier matrix) is identity. The Fourier matrix has the attractive property that it represents the eigenvalues of a circulant matrix. The linear time invariant convolution matrix is circulant, when constructed with the circular shift operator shown above.

$$\mathcal{F}_{pq} = \frac{(e^{-i2\pi \cdot p \cdot q / N_x})}{\sqrt{N_x}} \quad \text{for} \quad \begin{cases} 0 \leq p \leq (N_x - 1) \\ 0 \leq q \leq (N_x - 1) \end{cases} \quad (35.4)$$

$$\mathcal{F} \cdot \mathcal{F}^* = I \quad (35.5)$$

The time domain convolution matrix shown in Eq. (35.1) is shown in the frequency domain using the Fourier matrix as

$$\mathcal{F}y = \mathcal{F}[H]_C \mathcal{F}^* \cdot \mathcal{F}x \quad (35.6)$$

where $\mathcal{F}y$ represents output samples in the frequency domain, $\mathcal{F}x$ represents input samples in the frequency domain, and $\mathcal{F}[H]_C \mathcal{F}^*$ represents the fully coupled frequency response function. The Fourier matrix is further factored into Eq. (35.2) to yield Eq. (35.7), and then the resulting convolution structure is simplified to yield Eq. (35.8).

$$\text{vec}(\mathcal{F}y) = ((\mathcal{F}x)^T \otimes I_y) \cdot (\mathcal{F}^* \otimes \mathcal{F}) \cdot T \cdot ((\mathcal{F} \otimes \mathcal{F}^*) \cdot \text{vec}(\mathcal{F}H \cdot v \mathcal{F}^*)) \quad (35.7)$$

$$\text{vec}(\mathcal{F}y) = ((\mathcal{F}x)^T \otimes I_y) \cdot T_{ff} \cdot \text{vec}(\mathcal{F}H \cdot v \mathcal{F}^*) \quad \text{where} \quad T_{ff} = (\mathcal{F}^* \otimes \mathcal{F}) \cdot T \cdot (\mathcal{F} \otimes \mathcal{F}^*) \quad (35.8)$$

The forward convolution Eq. (35.8) can be factored using Kronecker identities into two different forms to independently expose the frequency responses, $\mathcal{F}H$, and their frequency variation, $v\mathcal{F}^*$, as shown in Eqs. (35.9) and (35.10).

$$vec(\mathcal{F}y) = ((\mathcal{F}x)^T \otimes I_y) \cdot C_{v\mathcal{F}^*} \cdot vec(\mathcal{F}H) \quad \text{where } C_{v\mathcal{F}^*} = T_{ff} \cdot (v\mathcal{F}^{*T} \otimes I_H) \quad (35.9)$$

$$vec(\mathcal{F}y) = ((\mathcal{F}x)^T \otimes I_y) \cdot C_{\mathcal{F}H} \cdot vec(v\mathcal{F}^*) \quad \text{where } C_{\mathcal{F}H} = T_{ff} \cdot (I_x^T \otimes \mathcal{F}H) \quad (35.10)$$

Solutions for the frequency response or frequency variation are developed by employing the left Moore-Penrose pseudo-inverse to yield Eqs. (35.11) and (35.12). The result is that, if input, output, and variation are known, then the frequency response can be found as shown:

$$vec(\mathcal{F}H) = (C_{v\mathcal{F}^*}^* ((\overline{\mathcal{F}x}\mathcal{F}x^T) \otimes I_y) C_{v\mathcal{F}^*})^{-1} \cdot (C_{v\mathcal{F}^*}^* \cdot (\overline{\mathcal{F}x} \otimes I_y) \cdot vec(\mathcal{F}y)) \quad (35.11)$$

where $\overline{\mathcal{F}x}\mathcal{F}x^T$ is the instantaneous auto-spectrum matrix, $C_{v\mathcal{F}^*}^* ((\overline{\mathcal{F}x}\mathcal{F}x^T) \otimes I_y) C_{v\mathcal{F}^*}$ and $C_{v\mathcal{F}^*}^* \cdot (\overline{\mathcal{F}x} \otimes I_y) \cdot vec(\mathcal{F}y)$ represent the auto and cross spectrum matrices respectively for the selected convolution structure. The auto-spectrum matrix is diagonal when $v\mathcal{F}^*$ is a vector with one at zero Hertz and zeros everywhere else ([1 0 0 ... 0]). This case reproduces spectra used in conventional linear time invariant system identification.

Alternately, if input, output and candidate frequency responses are known, the frequency variation can be found as shown:

$$vec(v\mathcal{F}^*) = (C_{\mathcal{F}H}^* ((\overline{\mathcal{F}x}\mathcal{F}x^T) \otimes I_y) C_{\mathcal{F}H})^{-1} \cdot (C_{\mathcal{F}H}^* \cdot (\overline{\mathcal{F}x} \otimes I_y) \cdot vec(\mathcal{F}y)) \quad (35.12)$$

Coherence may be assessed using standard multiple input single output methods [7] once the frequency response function, or input frequency variation are identified using test data. The following section of this paper shows how inputs and outputs are mapped through the convolution structure to form new equivalent inputs and outputs compatible with traditional assessment methods. The Fourier matrix is omitted for brevity. To generate the same expressions in the frequency domain, substitute $v\mathcal{F}^*$ for v , $\mathcal{F}H$ for H , $\mathcal{F}y$ for y , $\mathcal{F}x$ for x and T_{ff} for T .

The discussion of coherence is broken into three sections which provide different forms of equivalent input and output for the coherence Eq. (35.13). Event coherence is used in this discussion to indicate the power average coherence for an entire dataset. This definition is useful because it results in the same relative predicted power as the convolution model defined above. The definitions for output coherence and input output coherence constrain their assessment to selected terms of the data. The distinction between these definitions is similar to the distinction between ordinary and multiple coherence, where ordinary coherence to multiple inputs does not necessary sum to the same answer as multiple coherence to those same inputs.

$$\gamma^2 = (S_{xx} \cdot S_{yy})^{-1} \cdot S_{xy} \cdot S_{xy}^H \quad \text{where } S_{ab} = E[a \cdot b^H] \quad (35.13)$$

The time varying convolution process is shown in Eq. (35.14) and broken up into equivalent outputs and inputs in Eqs. (35.15) and (35.16). The Kronecker products and sample shifting matrix have the effect of generating a number of new effective inputs. The output in this case is every sample listed independently for an entire event or test record. Part (a) of the equations shows equivalent inputs and outputs to assess coherence for a model, $vec(H)$, and part (b) show the equivalent inputs and outputs to assess coherence for variation, $vec(v)$.

$$(a) \quad vec(y) = (x^T \otimes I_y) \cdot T \cdot (v^T \otimes I_H) \cdot vec(H) \quad (b) \quad vec(y) = (x^T \otimes I_y) \cdot T \cdot (I_x^T \otimes H) \cdot vec(v) \quad (35.14)$$

$$(a) \quad \tilde{y} = vec(y)^T \quad (b) \quad \tilde{y} = vec(y)^T \quad (35.15)$$

$$(a) \quad \tilde{x} = ((x^T \otimes I_y) \cdot T \cdot (v^T \otimes I_H))^T \quad (b) \quad \tilde{x} = ((x^T \otimes I_y) \cdot T \cdot (I_x^T \otimes H))^T \quad (35.16)$$

The coherence definition may be constrained in order to examine the relationship to a single output by using an output selection vector, n_i . The output selection vector is defined to be a vector of same length as the variable it is multiplied by that is composed of zeros except for at the index, i , where it is one. Equations (35.17, 35.18, and 35.19) show the equivalent

inputs and outputs using a particular selection vector. Equation (35.19a) shows the projection to generate new inputs for the model coherence assessment, and Eq. (35.19b) shows the projection for input variation coherence assessment.

$$\tilde{y} = n_i y \quad (35.17)$$

$$\tilde{x} = Ax \quad (35.18)$$

$$(a) \ A = (I_v \otimes H^T) \cdot T^T \cdot (I_x \otimes n_i^T) \quad (b) \ A = (v \otimes I_H) \cdot T^T \cdot (I_x \otimes n_i^T) \quad (35.19)$$

The following Eqs. (35.20, 35.21, and 35.22) show the equivalent transformed inputs and outputs for assessing coherence of a single output sample to single input sample. Equation (35.22a) shows the transformation for model coherence assessment, and Eq. (35.22b) shows the transformation for variation coherence assessment.

$$\tilde{y} = n_i y \quad (35.20)$$

$$\tilde{x} = n_i x \quad (35.21)$$

$$(a) \ A = (v \otimes I_H) \cdot T^T \cdot (n_j^T \otimes n_i^T) \quad (b) \ A = (I_v \otimes H^T) \cdot T^T \cdot (n_j^T \otimes n_i^T) \quad (35.22)$$

35.3 Experimental Methods

A physical experiment was conducted in order to illustrate frequency domain identification of time varying systems. The system under test includes a lightly damped beam coupled to a viscous damper and electrodynamic shaker. The experimental setup, conducted at the University of Connecticut Structures Research Lab, is shown in Fig. 35.1 (from Ref. [12]). The steel beam is 9.1 m long, with a 0.15 m² cross section and 6.3 mm wall thickness, with a damper 3.7 m from its base.

The vibration test hardware employed in this experiment is the same as that used in Ref. [12], and is repeated here. The electrodynamic shaker is an LDS model V408 located 2.4 m from the base of the beam. The connection between the damper and beam was instrumented with a 208C01 load cell, and the beam was instrumented at the damper attachment position with a PCB 393C seismic accelerometer (5% bandwidth 0.025–800 Hz). Matlab Simulink with Quanser D/A drove the shaker using a consumer grade voltage amplifier, and a DataPhysics A/D system was used to record time series at 256 Hz.

The forces employed in this experiment were intentionally set to operate the damper at lower than its specified velocity operating point so that it would undergo time varying behavior. The Taylor Devices damper used in this experiment (model 1 × 2D-2C) is specified for 440 N/(m/s) at a velocity of 0.25 (m/s), and was operated at approximately 0.035 (m/s) rms. The system was excited at the shaker location with an underlying tone designed to alter the operating point of the damper in a repeatable way, and superimposed Gaussian noise. The resulting force at the damper is shown in Fig. 35.2.

The test signal consisted of a 512 s record of a 10 N tone at 1 Hz with a bandlimited 1.4 N RMS broadband signal superimposed. The signal was used to generate the cross and auto-spectra to solve for time varying filters using Eqs. 35.11 and 35.12. The coherence was then calculated using the methods shown in Eqs. 35.19a and 35.22a. A band limited derivative at 100 Hz was digitally applied to the numerator of the force per acceleration filter to convert it to a force per velocity to improve numerical conditioning and plot dynamic range.

35.4 Results

The load cell and accelerometer time series corresponding to Fig. 35.2 were post-processed in order to illustrate frequency domain identification of time varying systems. The following examples vary in terms of which parts of the convolution structure are assumed and which are solved for. The first example involves the solution of frequency response function

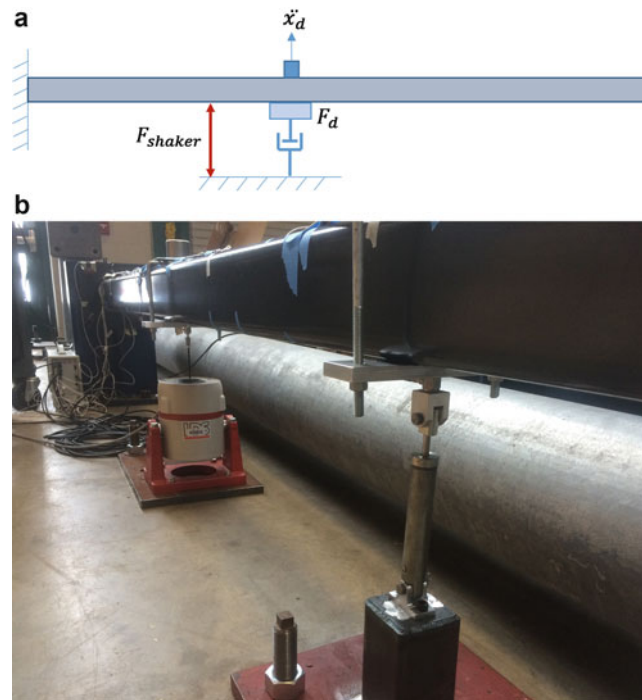


Fig. 35.1 Experimental beam damper system. (a) Notional schematic of test setup. (b) Photo of test setup (Source: Reproduced from Ref. [12])

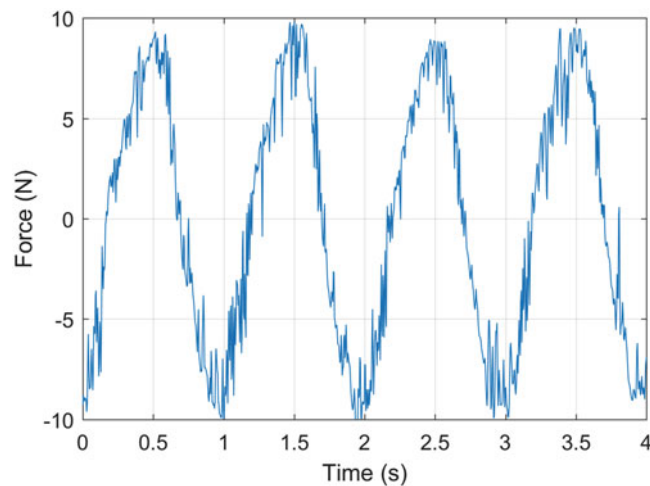


Fig. 35.2 Force at damper

models, given candidate bases of time variation. The second example involves the solution of bases of time variation given frequency response function candidate models. The last example illustrates multiple ways to assess coherence depending upon the assumed convolution structure.

The frequency response models, FH, were solved for using Eq. (35.11). The input acceleration and output force time series were transformed to the frequency domain in ensembles synchronous with one tonal period of the excitation waveform. A rectangular window was employed for ensemble estimates due to non-linearity associated with other windowing types. The assumed bases of time variation allow for the input to be modulated by up to five wavelengths of a sine or cosine within the 1 Hz excitation period. Figure 35.3 shows the dominant components of the model and compares them to linear approximations. The three linear approximations of the measured impedance shown include a stiffness line representing locked behavior at low amplitudes, a damping line representing behavior at the manufacturer specified operating point, and the linear time invariant frequency response identified for the event using conventional system identification methods. The damping and stiffness line were previously identified [12] as reasonable approximations of the most linear operating regimes

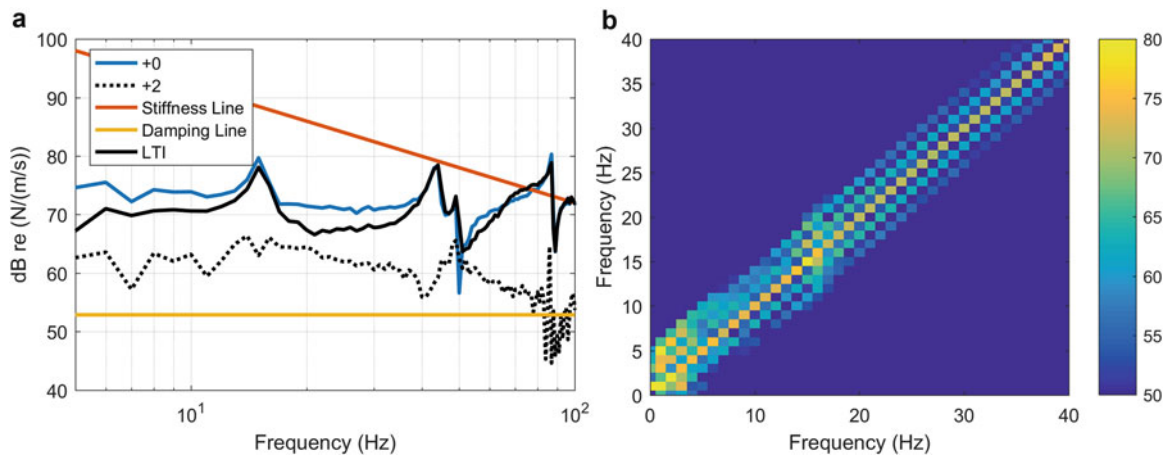


Fig. 35.3 Identified model components (left) and coupled frequency response function (right) given assumed frequency variation

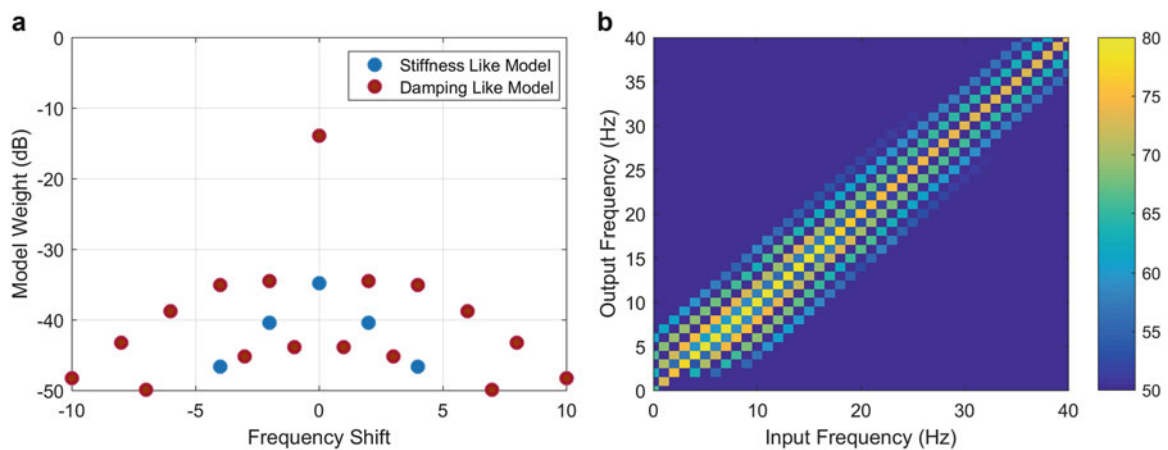


Fig. 35.4 Solved variation (left) and resulting coupled frequency response function (right)

of the damper. Time varying model components are shown in this plot including the +0 component which represents input frequencies which couple to the same output frequency, and the +2 (times 1 Hz shift) component which represents input frequencies that couple to shifted output frequencies. The plot in the right pane of Fig. 35.3 shows the input to output relationship, $F[H]_c F^*$, resulting from the solved for model components and the assumed basis of variation. The +0 and +2 model components shown in the left pane appear as diagonal lines on the center and shifted by 2 Hz respectively in the right pane.

The frequency variation, νF^* , was solved for using Eq. (35.12). The assumed models were frequency response functions similar to the stiffness line (lowest input operating point) and damping line (manufacturer specified operating point) in Fig. 35.3. Figure 35.4 shows the frequency variation (left pane) for the stiffness model and damping model. The 0 term represents input frequencies which couple directly to the same output frequency, and the ± 2 and 4 terms represent the candidate models at shifted frequencies. The plot in the right pane of Fig. 35.4 shows the input to output relationship, $F[H]_c F^*$, resulting from the solved for frequency variation and the assumed model components. The frequency modulation of the model results in a number of off-diagonal coupling terms, indicating that input at one frequency couples to another.

The coherence was solved for using Eqs. (35.17, 35.18, 35.19a, 35.20, 35.21, and 35.22a) for multiple input to single output and single input to output coupling respectively. The left pane of Fig. 35.5 shows coherence assuming that more than one input frequency couple to each output frequency, up to the number prescribed by the convolution structure. Employing multiple input frequencies to predict one output frequency accounts for predicting 5–10% more of the output signal power than the linear time invariant model. The right pane of Fig. 35.5 shows single input frequency to single output frequency coherence. The plot shows input at single frequencies predicts output signal power at multiple frequencies.

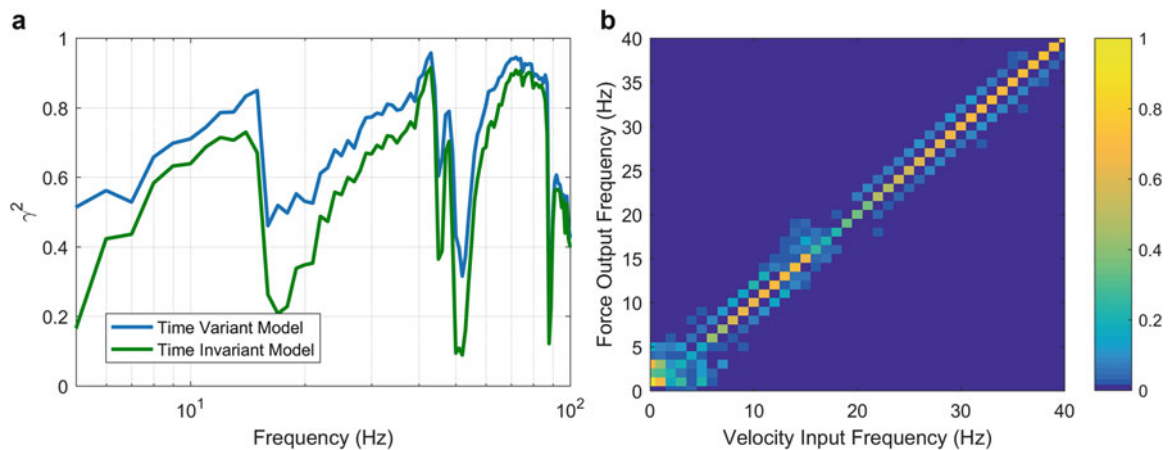


Fig. 35.5 Output coherence (left) and input to output coherence (right)

35.5 Discussion

The experimental results for the coupled beam damper system show time varying frequency domain behavior at the selected identification operating point shown in Fig. 35.2. For the results shown, time varying behavior is manifested as identified model or variation terms with a non-zero shift between input and output frequency, or an increase in coherence when these terms are included in a candidate convolution structure. Figures 35.3, 35.4, and 35.5 represent different mathematical strategies for understanding time varying frequency domain behavior discussed in this paper.

Assumed frequency variation is used to solve for a frequency response model shown in Fig. 35.3, which represents an example application of Eq. (35.11). The model was assumed to have variation at up to ± 5 times the frequency of the fundamental period of the excitation waveform (1 Hz), resulting in 11×256 model terms being identified. Note that the 0, or auto-frequency, component shown in Fig. 35.3 is similar to the linear time invariant model identified using conventional methods. However, the figure shows a term varying up and down over the cycle at two times the frequency of the fundamental.

Assumed frequency response is used to solve for frequency variation shown in Fig. 35.4, which represents an example application of Eq. (35.12). The convolution system was assumed to have two candidate frequency response models, resulting in 2×256 variation terms being identified. This analysis expresses the variation relative to known models and provides insight into how each component changes with time. The resulting frequency coupled response functions shown in Figs. 35.3 and 35.4 are similar, but show differences at low frequencies (below 15 Hz). The differences may be partly due to constraints imposed by the assumed convolution structure, or may be due to low frequency windowing artifacts [7] related to the aperiodic noise probe super-imposed on the tone.

Coherence analysis of the recorded data provides insight into the relative benefit of frequency varying terms in a convolution model. Output coherence (Fig. 35.5) shows some added benefit to include varying model terms to help predict output signal power. The single input to single output frequency coherence plot is indicative of time varying terms to try including in a candidate convolution model. These terms are normalized to one, and consequently provide a differently weighted input output coupling map than as shown in Figs. 35.3 and 35.4. The threshold of importance for modeling these terms will depend upon the individual analyst's objectives.

35.6 Conclusions

The mathematical framework presented in this paper was successfully applied to identify the frequency domain behavior of a deterministic non-linear dynamic system. The framework allows for the solution of frequency variation or frequency response models depending on the known information about the identified system. The two different identification methods were demonstrated using experimental data. Results show the combined response to be composed of stiffness and damping-like characteristics in different proportions, which vary over the cycle of the applied forcing function. Future work is required in order to improve aspects of test design, such as designing the most effective waveforms for system identification, and finding their optimal duration, such that the statistical variance of the measured frequency responses is kept to an acceptable limit.

References

1. Cohen, L.: Time Frequency Analysis. Prentice Hall, NJ (1994)
2. Boashash, B.: Time-Frequency Signal Analysis and Processing. Academic Press, London (2015)
3. Xia, X., Qian, S.: Convergence of an iterative time-variant filtering based on discrete Gabor transform. *IEEE Trans. Signal Process.* **47**(10), 2895–2899 (1999)
4. Hlawatsch, F., Auger, F.: Time-frequency methods for non-stationary statistical signal processing. In: *Time-Frequency Analysis: Concepts and Methods*, pp. 279–320. Wiley, London (2008)
5. White, L.B., Boashash, B.: Cross spectral analysis of nonstationary processes. *IEEE Trans. Inf. Theory.* **36**, 830–835 (1990)
6. Matz, G., Hlawatsch, F.: Time frequency coherence analysis of non-stationary random processes. In: *Proceedings on the Tenth IEEE Workshop on Statistical Signal and Array Processing* (2000)
7. Bendat, J., Piersol, A.: *Random Data: Analysis and Measurement Procedures*, 4th edn. Wiley, Hoboken, NJ (2010)
8. Bendat, J.: *Nonlinear System Techniques and Applications*. Wiley, New York (1998)
9. Zhao, H., Sheng, L., Zou, R., Ju, K., Chon, K.: Estimation of time-varying coherence function using time-varying transfer functions. *Ann. Biomed. Eng.* **33**(11), 1582–1594 (2005)
10. Orini, M., Bailon, R., Mainardi, L., Laguna, P.: Characterization of dynamic interactions between cardiovascular signals by time-frequency coherence. *IEEE Trans. Biomed. Eng.* **59**(3), 663–673 (2012)
11. Keissar, K., Davrath, L., Akselrod, S.: Coherence analysis between respiration and heart rate variability using continuous wavelet transform. *Philos. Trans. R. Soc.* **367**, 1393–1406 (2009)
12. Mazurek, L., Harris, M., Christenson, R.: Kronecker product formulation for system identification of discrete convolution filters. In: Caicedo, J., Pakzad, S. (eds.) *Dynamics of Civil Structures Conference Proceedings of the Society for Experimental Mechanics Series*, vol. 2. Springer, Cham (2017)
13. Davis, P.: *Circulant Matrices*, 2nd edn. American Mathematical Society, Providence, RI (2012)
14. Laub, A.: *Matrix Analysis for Scientists & Engineers*. Society of Industrially Applied Mathematics, Philadelphia, PA (2005)
15. Kailath, T., Sayed, A.: *Fast Reliable Algorithms for Matrices with Structure*. Society of Industrially Applied Mathematics, Philadelphia, PA (1999)

Chapter 36

Reduced-Order Modelling for Investigating Nonlinear FEM Systems



I. Tartaruga, S. A. Neild, T. L. Hill, and A. Cammarano

Abstract Modern finite element (FE) packages are capable of capturing nonlinear behaviour in extremely complex structures. However, due to the scale of these models, full dynamic analysis is often prohibitively expensive. An alternative approach is to use the FE models to derive reduced-order models (ROMs) which capture the dynamic behaviour of interest at a significantly lower computational cost. An automatic identification of the stated ROMs is powerful and desirable when parametric, sensitivity and uncertainty analysis is of interest. The authors implemented in Matlab a strategy to automatically compute the reduced order model and investigate the effects of parametric variation exchanging information with FEM software. In the strategy it is adopted the Applied Modal Force (AMF) approach, where a force is applied to the FE model and the resulting displacements are used to identify coefficients of the ROM, as is done in the ICE method. The developed techniques are presented in the paper and validated considering a crossed beam structure modelled in Abaqus.

Keywords Nonlinear dynamics · Reduced order model · Finite element model · Nonlinear normal mode · Parametric variation

Nomenclature

$[M]$	physical mass matrix
$[K]$	physical stiffness matrix
$[\Phi]$	matrix of eigenvector
$[\Phi_T]$	truncated $[\Phi]$
$\overline{[M]}$	modal mass matrix
$\overline{[K]}$	modal stiffness matrix
$\overline{[M]}_T$	truncated $\overline{[M]}$
$\overline{[K]}_T$	truncated $\overline{[K]}$
$\{x\}$	vector of physical coordinates
$\{q\}$	vector of modal coordinates
$\{q\}_T$	truncated $\{q\}$
$\{f_{nl}\}$	vector of physical generalized nonlinear forces
$\overline{\{f_{nl}\}}$	vector of modal generalized nonlinear forces
$\overline{\{f_{nl}\}}_T$	truncated $\overline{\{f_{nl}\}}$
$\{F\}$	vector of physical generalized linear forces
$\overline{\{F\}}$	vector of modal generalized linear forces
$\overline{\{F\}}_T$	truncated $\overline{\{F\}}$
R	number of retained modes in the reduction
Tol_m	tolerance adopted for retaining more modes

I. Tartaruga (✉)
Department of Engineering Mathematics, University of Bristol, Bristol, UK
e-mail: irene.tartaruga@bristol.ac.uk

S. A. Neild · T. L. Hill
Department of Mechanical Engineering, University of Bristol, Bristol, UK

A. Cammarano
School of Engineering, University of Glasgow, Glasgow, UK

Tol_f	tolerance adopted for identifying the input set
$\{C\}_p$	vector of scale factors
t_R	referential thickness
S_f	scale factor adopted to rescale the input set
V_f	scale factor adopted to rescale the input set
S	scale factor

36.1 Introduction

The development of techniques able to investigate and deal with dynamic systems that exhibit nonlinearities has been of interest for academic researchers for decades. Recently, industrial interest has also been growing rapidly due to the desire to design lighter and hence more flexible structures [1, 2]. The industrial interest has pushed and motivated even more researchers to enhance already developed methodologies and conceive new strategies. Of particular interest is the possibility of dealing with nonlinearities in the real world; such an ambition requires a suitable modelling of the systems and phenomena of interest and an exchange of information between numerical and experimental analyses. The modelling needs to suit the aim of the research, which can require higher accuracy for specific aspects, such as stability analysis, coupling effects, modal interactions, resonances. The challenge in the analysis of nonlinearities is the often increased complexity in the modelling. In such a scenario, it is significant to identify and adopt techniques that are able to retain sufficient information from the real physics of a system/phenomena of interest reducing the degree of complexity allowing the investigation of nonlinear effects in a realistic time. Developing techniques able to reduce the complexity of a system, researchers have faced the problem of understanding what dynamics are to be retained for the system of interest, the limits and the effects of the assumptions and simplifications [3–7]. In the last two decades, reduced order modelling strategies, as well as identification techniques, have been widely considered in engineering fields to deal with nonlinearities in numerical and experimental systems, respectively [8–18]. In the development of reduced order models, Enforced Modal Displacement (EMD) and Applied Modal Force (AMF) techniques have been widely considered. To the best of the author's knowledge, the nonlinear reduced order model techniques still lacks robustness and automatization. The lack of robustness arises from the sensibility of the values of the coefficients adopted in reduced order models to the variation of the criteria adopted for the reduction. The criteria are in terms of: which set of static forces and modes to adopt for the reduction. The lack of automatization is due to the difficulty of performing uncertainty and sensitivity analysis. This paper will cover mainly progression in terms of automatization showing the effects of considering different modes. It presents the developed Matlab code that allows the application of EMD and AMF techniques. The developed code allows the interchange of information with finite element analysis (FEA) programs (such as Abaqus or Nastran) in an automatic environment, if either EMD or AMF technique is adopted. The code allows parametric studies and investigation of the effect of asymmetry. In the paper, a crossed beam modelled in Abaqus will be considered and the investigation of nonlinear behaviour will be done using backbone curves or nonlinear normal modes (NNM) [19], system characteristics recently adopted to investigate nonlinearities [2, 20–24].

36.2 Methodology

The techniques considered here are based on the reduced order model concept applied to FE model and have been implemented in Matlab. The most general equation for a FE model is the following

$$[M] \{\ddot{x}\} + [K] \{x\} + \{f_{nl}(x)\} = \{F\} \quad (36.1)$$

Where $[M]$, $[K]$, $\{\ddot{x}\}$, $\{x\}$, $\{f_{nl}(x)\}$ and $\{F\}$ are the matrices of inertia and stiffness, vector of generalised states-acceleration and states, vector of generalised nonlinear force and linear force.

For reduction purpose, Eq. 36.1 needs to be projected in a space where further information can be adopted by the user to reduce the order of the system of interest. The reduction is in terms of the degrees of freedom, acting forces and nonlinearities due to inherent characteristics of the system or interaction with the environment, external to the system itself. The EMD and the AMF project the equations in the linear modal space, this is accomplished using the matrix of linear eigenvectors $[\Phi]$ for the projection. The physical states are then projected and $x = [\Phi] q$; to complete the projection the Eq. 36.1 is premultiplied by $[\Phi]^T$. The two steps to project the physical space to the modal one are presented in Eq. 36.2

$$\begin{aligned} [\Phi]^T ([M] [\Phi] \{\ddot{q}\} + [K] [\Phi] \{q\} + \{f_{nl}\} ([\Phi] \{q\})) &= [\Phi]^T \{F\} \\ [\overline{M}] \{\ddot{q}\} + [\overline{K}] \{q\} + \{\overline{f_{nl}}(\{q\})\} &= \{\overline{F}\} \end{aligned} \quad (36.2)$$

In Eq. 36.2, $[\overline{M}]$, $[\overline{K}]$ and $\{\overline{f_{nl}}\}$ are the modal mass and stiffness matrices and the nonlinear force vector projected in the modal space. $\{q\}$ is the vector of modal coordinates.

All the coefficients in Eq. 36.2 are known except the nonlinear one. In fact, the modal matrices can be derived from FEM software. At this point three main questions need to be answered to continue the reduction of the original physical systems:

1. how to describe the nonlinear modal force ($\{\overline{f_{nl}}\}$) in terms of the modal coordinates if the nonlinear force $\{f_{nl}(x)\}$ is not analytically known.
2. how many modes and which one to retain, i.e. how to truncate the modal projection.
3. how to define the analysis to be accomplished to identify coefficients characterizing the reduced order model

36.2.1 Nonlinear Modal Force

The first point, the description of the nonlinear modal force ($\{\overline{f_{nl}}\}$), is generally [1, 5, 7, 25] accomplished considering quadratic and cubic nonlinear terms as it follows

$$\begin{aligned} ([\Phi]^T \{f_{nl}\} ([\Phi] \{q\}))_m &= (\{\overline{f_{nl}}\} (\{q\}))_m = \\ &= \sum_i \sum_j \sum_k (A_{ijk})_m q_i q_j q_k + \sum_i \sum_j (B_{ij})_m q_i q_j \end{aligned} \quad (36.3)$$

Where the indexes i, j, k and m refer to the modal coordinates whose number R is given by truncation, i.e. if R is the number of retained modes, then $i, j, k, m = 1 \dots R$.

When dealing with FEM models that present geometric nonlinearities, the use of the quadratic and cubic terms is a sensible choice, as demonstrated [1, 18].

The coefficients A_{ijk} and B_{ij} need to be identified, the process for the identification is the key step that differentiates the Applied Modal Force (AMF) and Enforced Modal Displacement (EMD) techniques. Both the techniques adopt static responses, a set of static physical force (F) and static physical deformation (x) are adopted as input in the analysis if the AMF and EMD techniques are adopted, respectively. Figure 36.1 shows two flow charts describing how the identification of the coefficients A_{ijk} and B_{ij} in Eq. 36.3 is accomplished. The input set (in terms of force F or deformation x) is considered and the static response obtained (in terms of deformation x or force F). Then the truncation is accomplished, and the known modal and stiffness reduced matrices are obtained. Using the static input and responses the coefficients adopting in the description of the nonlinear terms can be also obtained; the least square methods together with constraints due to energy consideration [18] is used. The number of considered static responses need to be at least equal to the sum of the considered quadratic and cubic terms.

36.2.2 Truncation

A crucial point when a reduced order method is adopted is the selection of modes to be retained. Most of the time there is not a clear knowledge of the modes that significantly affect the responses of interest, such as stability analysis. Ideally, the modal participation characterizing the responses of interest should be adopted to identify the modes to be retained; unfortunately this is not easily available especially in the presence of numerical systems with many degrees of freedom and experimental systems. In the present application, the modes are selected iteratively without considering the actual solutions. This is because the main point we want to underline is that the efficiency of modal reduction techniques is dictated by the number of evaluations of the actual system of interest. Having selected the first set of modes, the truncated equations projected in the modal space is obtained (Eq. 36.4).

$$[\overline{M}]_T \{\ddot{q}\}_T + [\overline{K}]_T \{q\}_T + \{\overline{f_{nl}}\} (\{q\})_T = \{\overline{F}\}_T \quad (36.4)$$

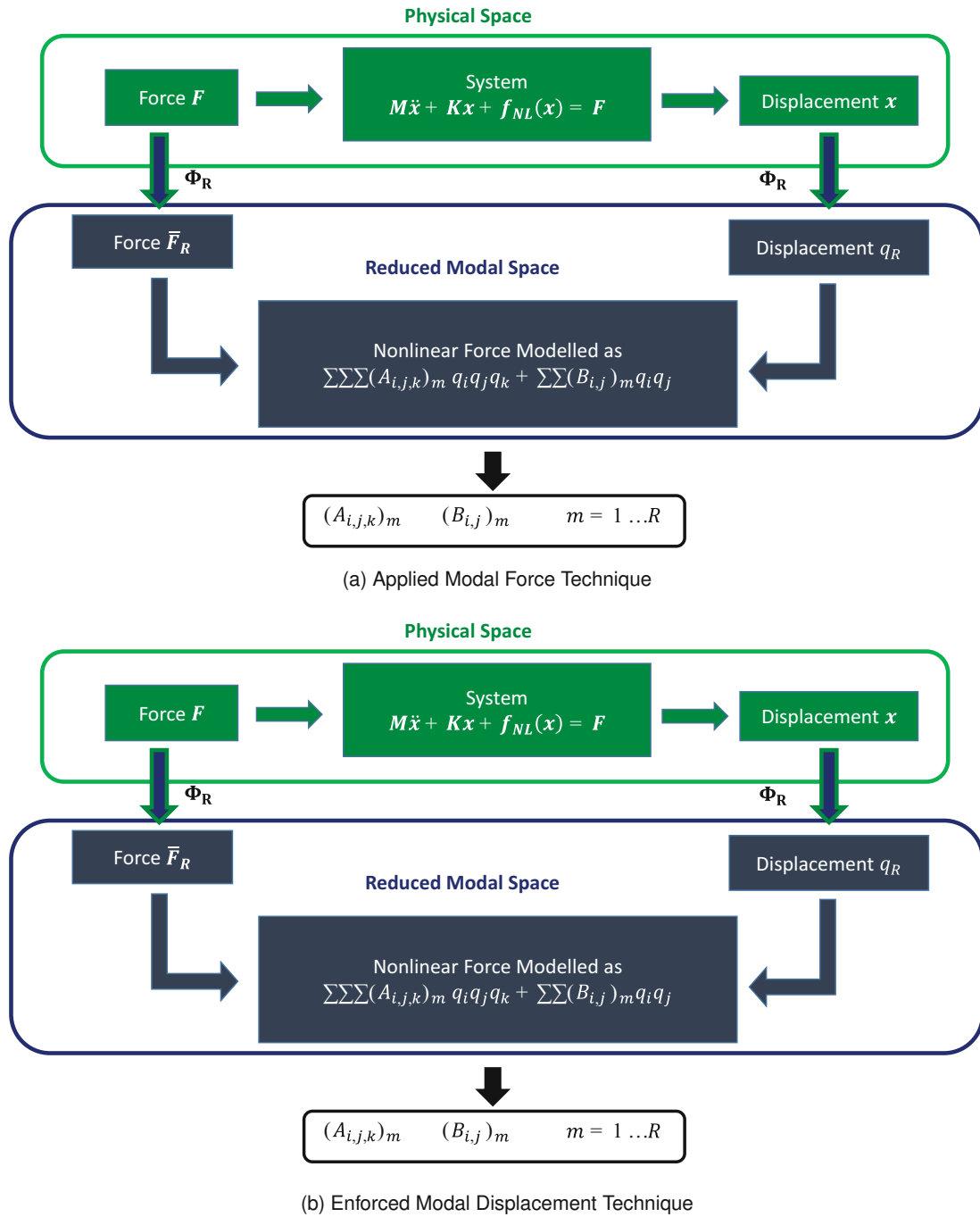


Fig. 36.1 Flow chart describing how the coefficients adopted in the assumed expression for the nonlinear terms in the reduced order model are obtained. Two techniques are presented. (a) Applied Modal Force technique. (b) Enforced Modal Displacement technique

Then, additional modes can be added using the AMF (EMD) if some components of the reconstructed modal displacement (modal forces) has some ‘importance’ compared to the components related to the retained modes. The ‘importance’ is weighted fixing some tolerances. For the sake of clarity, the steps required for finding additional modes to be included is here shown both for the AMF (Eq. 36.5) and the EMD (Eq. 36.6) methods. The physical static response ($\{x^*\}$ and $\{F^*\}$) for the AMF – Eq. 36.5 and EMD – Eq. 36.6) is first obtained using the initial set of modes ($\{q^*\}_T$), then it is projected in the modal space and inspection of the components is possible. Having fixed a tolerance Tol_m , the mode k could be included if $|\{q^*\}_k| > \min(|\{q^*\}_T|) \cdot Tol_m$ or $|\bar{F}_k^*| > \min(|\{\bar{F}^*\}_R|) \cdot Tol_m$ having adopted the AMF or the EMD method, respectively.

$$\{q^*\} = [\Phi]^{-1} \{x^*\} = [\Phi]^T [M] \{x^*\} \quad (36.5)$$

$$\{\bar{F}^*\} = [\Phi] \{F^*\} \quad (36.6)$$

The process has been automatized considering as stopping criteria the total number of allowable retained modes; modes are retained until the maximum allowable number is reached.

36.2.3 Coefficient Identification

The last issue that needs to be dealt with is the definition of the static analysis to be run in order to obtain the responses to be used for the identification of the coefficients A_{ijk} and B_{ij} . The key point in the selection is to find out the way of exciting the nonlinearities of the structure of interest without involving non-physical conditions, i.e. exceeding the breaking limit of the structure. It has been recognised that a close solution for the stated issue is a challenge and, to the best of the authors' knowledge, a solution has not been yet identified. Considering the AMF and the EMD, a referential thickness of the structure of interest (t_R) is considered and the set of input force or displacement are consequently defined. In particular, the adopted formula for a single physical input (force – Eq. 36.7 or displacement – Eq. 36.8) are

$$\{F\}_p = [M] [\Phi]_T \{C\}_p \quad (36.7)$$

$$\{x\}_p = [\Phi]_T \{C\}_p \quad (36.8)$$

Where

- the sub-index p is varying from 1 to the total number of considered input set. The number of input set needs to be at least equal to the number of unknown coefficients. However, as it is well known in regression analysis, the number of training points needs to be large enough to capture the behaviour of interest whilst avoiding overfitting [26]. Having assumed the nonlinear terms to be expressed as shown in Eq. 36.3, the dimension of the input set has been here fixed to the same one adopted by Hollkhampt et al. [5, 25, 27], i.e.

$$2n + 2(n!/(n-2)!) + 4/3(n!/(n-3)!) \quad (36.9)$$

This number is automatically obtained following the definition of the scale factor $\{C\}_p$, which follows. It is always greater than the number of unknown coefficients per mode and this is enough to determine the values of the coefficients because the input set is projected in the modal space, thus the dimension of each modal input set is equal to Eq. 36.9.

- $\{C\}_p$ is a column vector of considered scale factor and has the size equal to the number of retained modes. The values of the components are selected in a specific way. The k th component refers to one specific of the retained mode since, in determining the input set (Eqs. 36.7 and 36.8), $\{C\}_p$ multiplies the truncated matrix of eigenvector $[\Phi]_T$. The basic value $C_{p,k}$ is given as follows

$$C_{p,k} = \begin{cases} t_R / \max_{disp}(|\Phi_k|) \cdot \omega_k^2 & \text{if AMF} \\ t_R / \max_{disp}(|\Phi_k|) & \text{if EMD} \end{cases} \quad (36.10)$$

where $[\Phi]_k$ and ω_k are the eigenvector and the linear frequency (rad/s) related to the k th retained mode. \max_{disp} states for the maximum value among the generalized coordinates that are displacements.

Both positive and negative values of the stated scale factor are considered. Single or combinations of modal shapes are considered to define the input set, a maximum of 3 modal shapes are considered [5, 25, 27]. Using the expressions for $\{C\}_{p,k}$ previously introduced, this can be accomplished giving values different from zero to three of the total number of components of $\{C\}_p$. Moreover, the coefficients $C_{p,k}$ need to be divided by the number of modes considered in the combination to define the p th input set.

For the sake of clarity, three examples of scale vectors $\{C\}_p$ considering the AMF technique are here shown. A total of five modes are retained.

1st set C_1 only the second mode is selected, $C_1 = [0, C_{1,2}, 0, 0, 0]'$

2nd set C_2 the second and fourth mode are selected, $C_2 = [0, C_{2,2}, 0, C_{2,4}, 0]' \cdot 1/2$

3rd set C_3 the second, third and fifth mode are selected $C_3 = [0, C_{3,2}, C_{3,3}, 0, C_{3,5}]' \cdot 1/3$

Having defined the input set, the coefficients can be determined adopting the least square methods and additional constraints due to energy considerations [5, 25, 27].

The literature shows that the set of referential thickness (t_R) adopted is often not the one that gives accurate reduced order model [14], thus scale factors need to be adopted to modify the referential thickness. It is important to notice at this point that changing the scale factors, the results are different and this is due to two different reasons if the AMF or the EMF are adopted:

AMF the modes are differently excited since different is the value of the scale factors

EMD the assumption in terms of the nonlinear terms is not correct and thus also the EMD is exciting differently the modes depending on the adopted scale factor

Moreover, if very high frequency modes are adopted, then the input set can acquire excessively large values in some components if the AMF is used (as it is apparent looking at Eq. 36.10), and this has not been previously discussed to the best of the authors' knowledge.

In the method presented here, a strategy is adopted to define the scale factor avoiding excessively large values for the input force if the AMF is adopted and reaching the desired maximum displacement. The stated strategy consists of three main steps:

1. given the modes to be retained a starting input set is defined as shown in Eq. 36.10
2. just for the AMF. Among the modes of interest, defined the low frequency mode of interest; the input set are divided into the set related to low frequency modes and high frequency modes, these are here labelled as $\{IS_{low}\}$ and $\{IS_{high}\}$. Then divide the components of the input set related to forces from those linked to moments ($\{IS_{low/high_F}\}$, $\{IS_{low/high_M}\}$. Reduce by a scale factor S_f the input set $\{IS_{high_F}\}$ and $\{IS_{high_M}\}$ until all the components are less than the maximum component assumed by the input set $\{IS_{low_F}\}$ and $\{IS_{low_M}\}$, respectively.
3. the last step is conceived in order to be sure that the excitation is actually reaching the maximum desired amplitude in the displacement response. This can be accomplished by comparing the actual response and the predicted maximum static linear modal displacement, which is obtained once the input set has been defined ($[\Phi]_T \{C\}_p$). If the static nonlinear response is less (greater) than the predicted linear modal displacement then the input set need to be increased (on decreased). This last step must be done iteratively until the static nonlinear response is within the allowed tolerance $\pm Tol_m$. The adopted method to update the input set is using the following scale factor $V_f(k)$ at the k th iteration

$$V_f(k) = \begin{cases} V_f(k-1)/S & \text{if } == 1 \\ |(V_f(k-1) - |V_f(k-1) - V_{f_{store}}(i)|/S)| & \text{otherwise} \end{cases} \quad (36.11)$$

$$V_f(k) = \begin{cases} V_f(k-1)S & \text{if } == 1 \\ |(V_f(k-1) + |V_f(k-1) - V_{f_{store}}(i)|/S)| & \text{otherwise} \end{cases} \quad (36.12)$$

where i is the index counting the input set that gives a convergent solution in Abaqus.

The flow chart in Fig. 36.2 summarizes the steps characterizing the developed code in Matlab for the identification of reduced order models. The mode selection, coefficient identification and iterative strategies previously introduced are part of the steps presented in Fig. 36.2. The code can be used to perform iterative analyses if an iterative variation of parametric values or system configuration is of interest. In fact, the main input for the method (in the circular shape box) is the desired configuration for the system. The code is able to update the input file required by the FEM software in order to fulfil the requirement of the user.

36.3 Test Case

The developed strategy presented in Sect. 36.2 is applied here to a crossed beam structure. The structure reproduce a physical system present in our lab and has been modelled in Abaqus (Fig. 36.3 and has 405 nodes and 404 B31 elements).

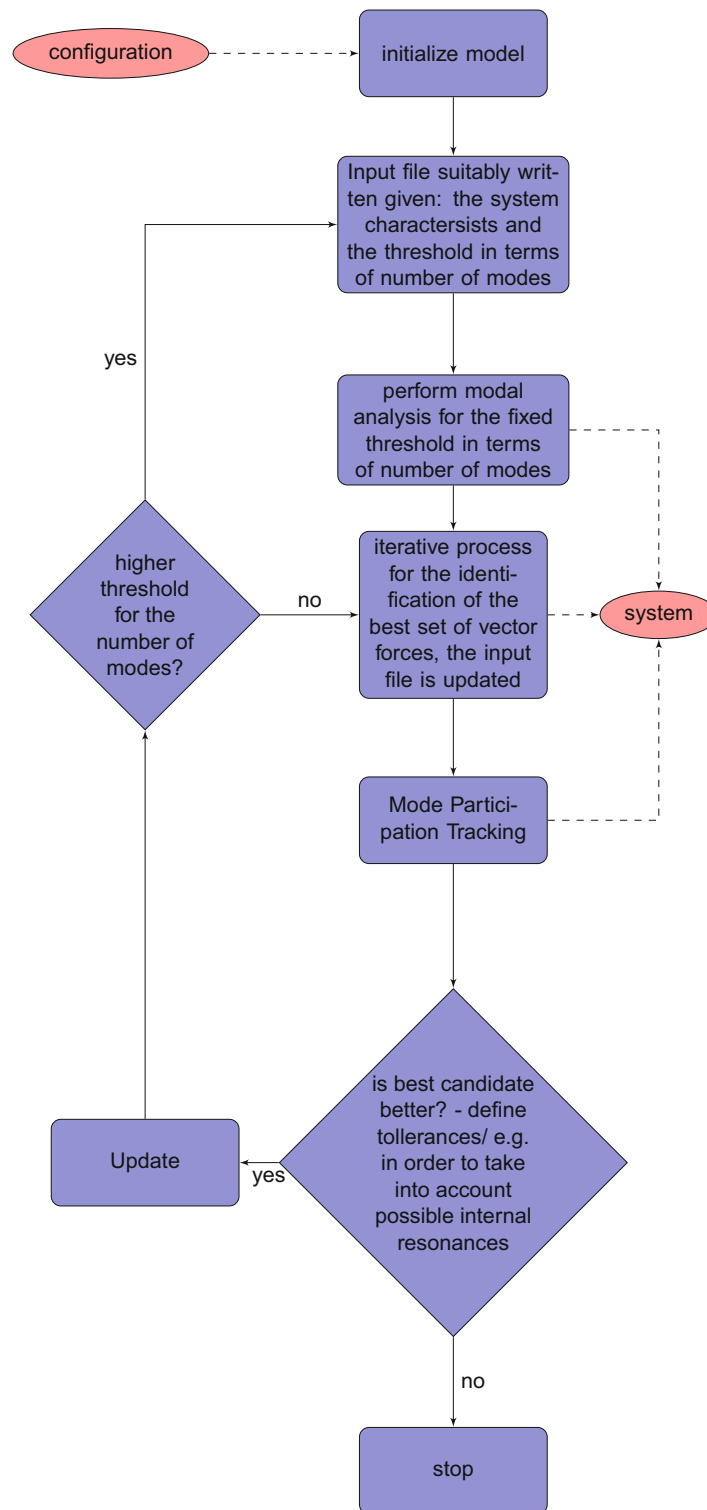


Fig. 36.2 Flow chart of the developed strategies coded in Matlab

Looking at Fig. 36.3, it is apparent that there are three beams, two crossing. The reason for the small crossing beam is purely due to reproduce the physical system, whose has a small crossing beam used for applying forces, as closely as possible. Moreover, along the main crossing beam there are masses that can be moved along the span and this is made possible in

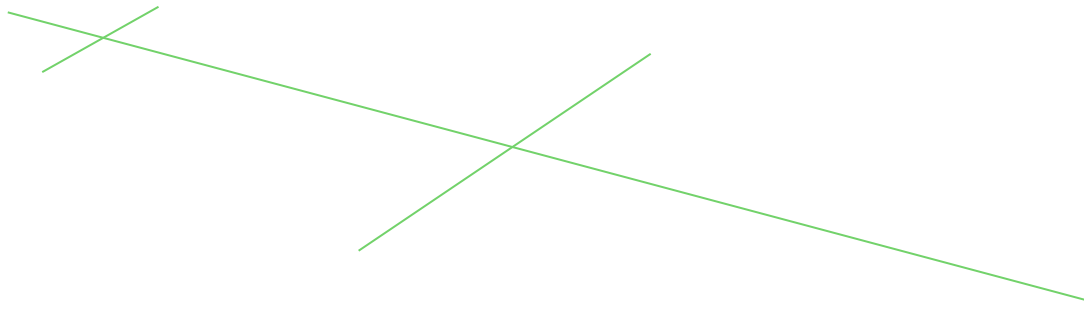


Fig. 36.3 Crossed beam structure modelled in Abaqus

Table 36.1 Elements and properties featuring the crossed beam system

<i>Part</i>	<i>Number of elements</i>
Main beam	247
Main crossed beam	102
Secondary crossed beam	43
Masses – main crossed beam	12
<i>Part</i>	<i>Total length</i>
Main beam	1 m
Main crossed beam	0.44 m
Secondary crossed beam	0.097 m
Masses – main crossed beam	0.164 m
<i>Part</i>	<i>Crossed section, dimensions</i>
Main beam	Rectangular, (0.0127, 0.0064) m
Main crossed beam	Circular, 0.00595 m
Secondary crossed beam	Rectangular, (0.015, 0.015) m
Masses – main crossed beam	Circular, 0.01995 m
<i>Part</i>	<i>Material</i>
Main beam	Steel
Main crossed beam	Steel
Secondary crossed beam	Steel
Masses – main crossed beam	Steel

Abaqus by changing the element nodes. Table 36.1 summarizes the number of elements and properties featuring each part of the modelled crossed beam. Regarding the crossed section, the dimensions are referred to the sides or to the diameter if the crossed section is rectangular or circular, respectively.

The features of the steel material are a density equal to 7850 kg/m^3 , an Elastic modulus equal to $2.1 \cdot 10^{11} \text{ Pa}$ and a poisson ratio of 0.3.

Regarding the border conditions, the ends of the main beam allows a translation in the x direction and are supported by two axial springs whose stiffness is $1.85 \cdot 10^6 \text{ kg m}$.

Finally, there are two further points that need to be covered:

- the position of the crossing beams with respect to the main beam: the main and secondary crossing beam are crossing the main beam at 0.164 and 0.097 m starting from the end more near to the secondary small crossing beam.
- the position of the masses along the main crossed beam: the set of masses is distributed on both the side of the main crossing beam, six on each side and the user can decide where to position them. In what it follows, the six mass elements are next to each other and are moved simultaneously. We will refer to the node of the first of the six set elements to identify the position of the set at each side of the crossing beam. Figures 36.4 and 36.5 in Sect. 36.4 show the crossed beam model created in Matlab, the masses are the red points along the crossed beam.

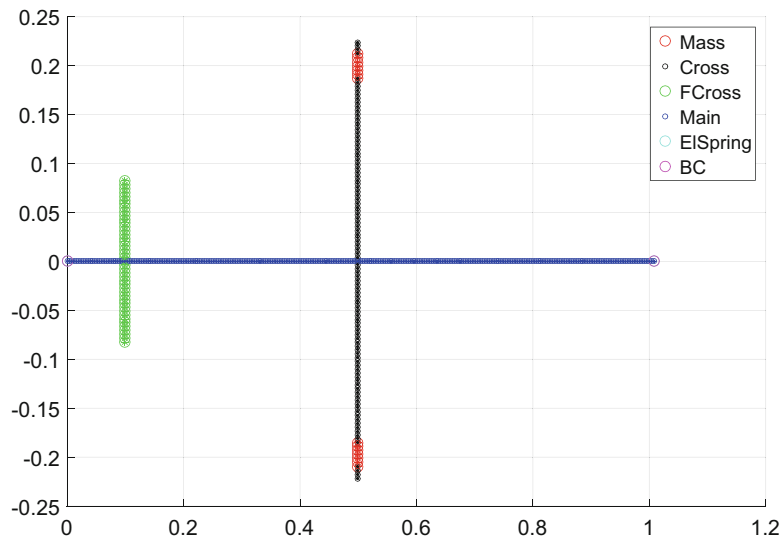


Fig. 36.4 Example of a symmetric configuration

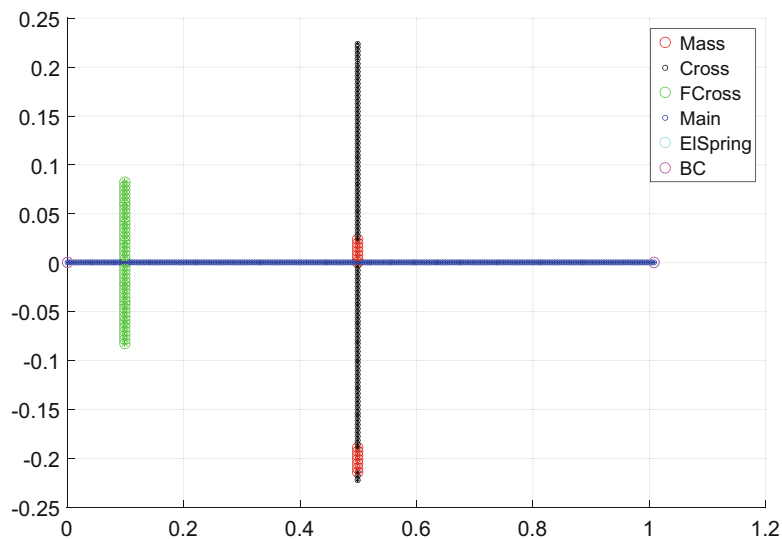


Fig. 36.5 Example of asymmetric configuration having fixed the position on one side at the 49th elements counting from the main beam structure

36.4 Results

The results presented here, cover the investigation of the effect of parametric variation on the linear and nonlinear behaviour of the crossed beam introduced in Sect. 36.3. To such end, linear modal frequencies and nonlinear normal modes [19–21] are considered. These have been obtained using the reduced order models determined following the strategy discussed in Sect. 36.2 and using the COCO software¹ for performing numerical continuation. Before showing and discussing the results, the values for the constant factors adopted in the strategy are here given (Table 36.2).

¹COCO, <https://sourceforge.net/p/cocotools/wiki/Home/>, date accessed October, 2016.

Table 36.2 Values adopted for constants featuring the strategy adopted for reduced order modelling under parameter variation

Constant	Value
Tol_f	0.5
t_R	0.05
S_f	1.5
S	2

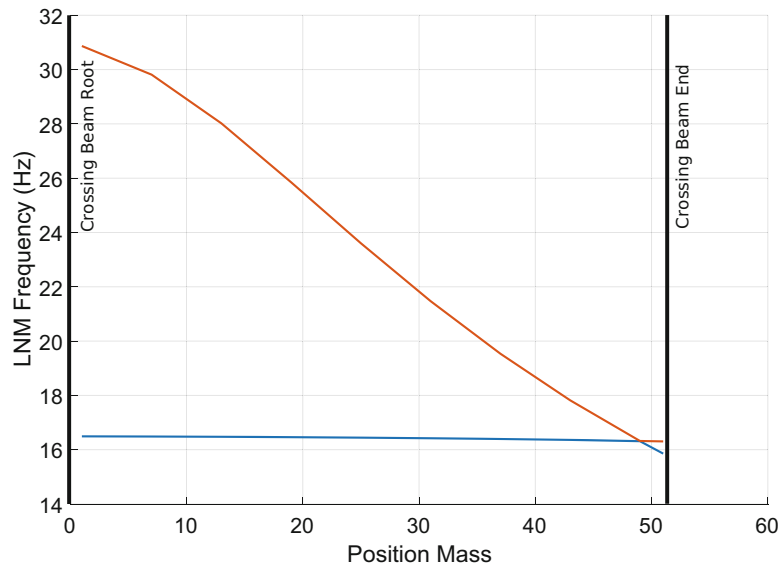


Fig. 36.6 Variation of linear modal frequency if the position of the additional masses is varied symmetrically

The analysis that has been performed and is presented here considers a symmetric and asymmetric parametric variation in terms of the mass elements along the main crossing beam. In particular, the following cases are shown and discussed.

Case a 2 modes are retained, the mass elements are varied symmetrically from the root of the main crossing beam until the end – Fig. 36.4

Case b 2 modes are retained, the mass elements are varied asymmetrically, the set of the masses is kept at a fixed position on one side of the crossing beam – Fig. 36.5

36.4.1 Case a

Having retained the first two modes, the first parametric variation considered is symmetric. In particular, the set of masses is varied symmetrically in both the side of the crossed beam. The strategy presented in Sect. 36.2 has given the possibility of analysing the main effects of the stated parametric variation on linear and nonlinear behaviour. Figure 36.6 shows the variation of the linear modal frequency of the two retained modes as the set of six masses is moved symmetrically along the main crossing beam from the main beam towards the end.

Looking at Fig. 36.6, it is apparent that the two linear frequencies converge as the set of masses approach the 49th position. In particular, the first -lower frequency (second – higher frequency) have a flexional (torsional) modal shape until the position 49 is reached, then a switch in the modal shape occurs.

For each symmetrical configuration, the strategy discussed in Sect. 36.2 is adopted to identify the coefficients characterizing the nonlinear terms and the reduced order models. Figures 36.7 and 36.8 show the first and second NNMs projected in the first and second mode respectively. Different positions for the set of masses are considered and are specified in the legend of the figures. Since the configuration is symmetric, there are neither modal interactions or internal resonances; the amplitude of the first (second) modal coordinate is dominant considering the first (second) NNM. Moreover, as could have been expected from the variation of the linear modal frequencies (Fig. 36.6), the NNMs present a change of variation when the set of masses reaches the position 49. The first NNM presents a slight increment (decrease) in amplitude (frequency) just before the position 49 is reached. Reaching the position 49 the amplitude of the first NNM is suddenly increasing and after the stated position the increment (decrease) in amplitude (frequency) is much more apparent. Similar consideration can be

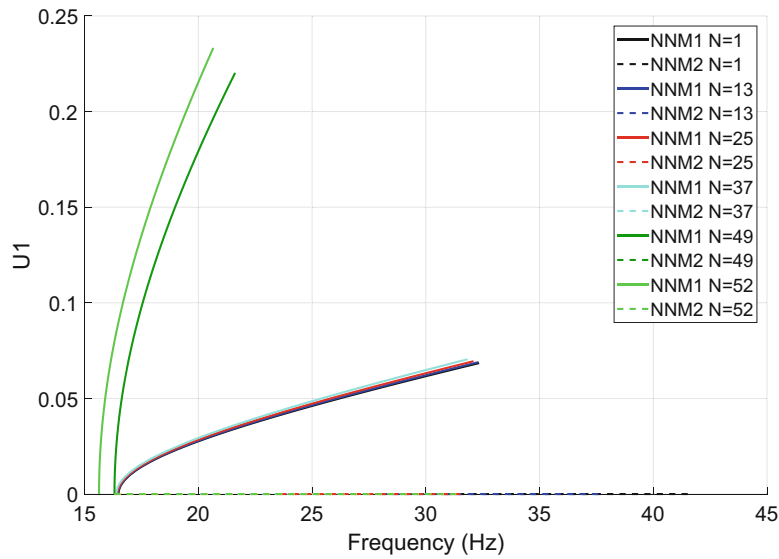


Fig. 36.7 Nonlinear normal modes projected in the first mode obtained retaining the first two modes adopting the AMF for a set of symmetric configuration. The set of masses start at N position – defined in the legend – counted starting from the main beam

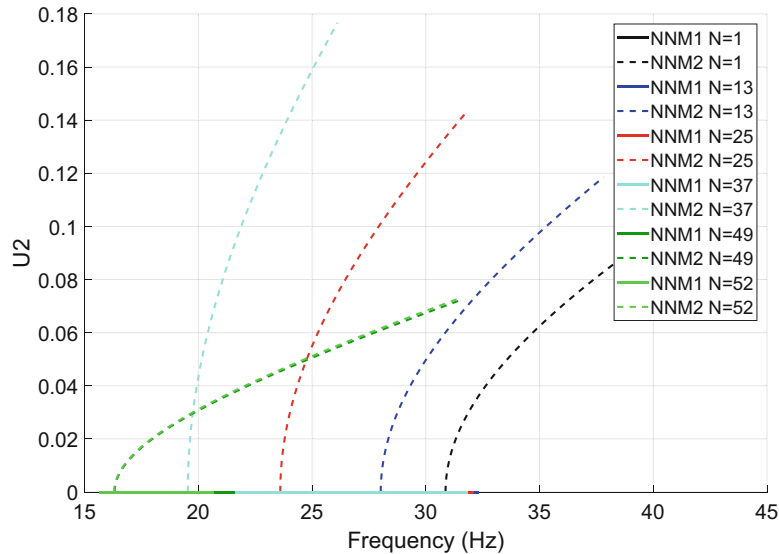


Fig. 36.8 Nonlinear Normal Modes projected in the first mode obtained retaining the first two modes adopting the AMF for a set of symmetric configuration. The set of masses start at N position – defined in the legend – counted starting from the main beam

done for the second NNM, the amplitude (frequency) is apparently increasing (decreasing) until the position 49 is reached. At such a position a sudden decrease in amplitude occurs and after such a position, the amplitude and frequency do not change significantly. The stated inversion of behaviour is linked to the change of modal shape of the normal mode. The first (second) mode presents a switch of modal behaviour; from being predominantly flexional (torsional) becomes predominantly torsional (flexional).

36.4.2 Case b

As for the symmetric case, the first two modes have been considered and effects of the asymmetric stated parametric variation on linear and nonlinear behaviour have been investigated looking at nonlinear normal modes. The set of masses is varied asymmetrically changing the position of the masses just on one side of the crossed beam. Figures 36.9 and 36.10 shows the

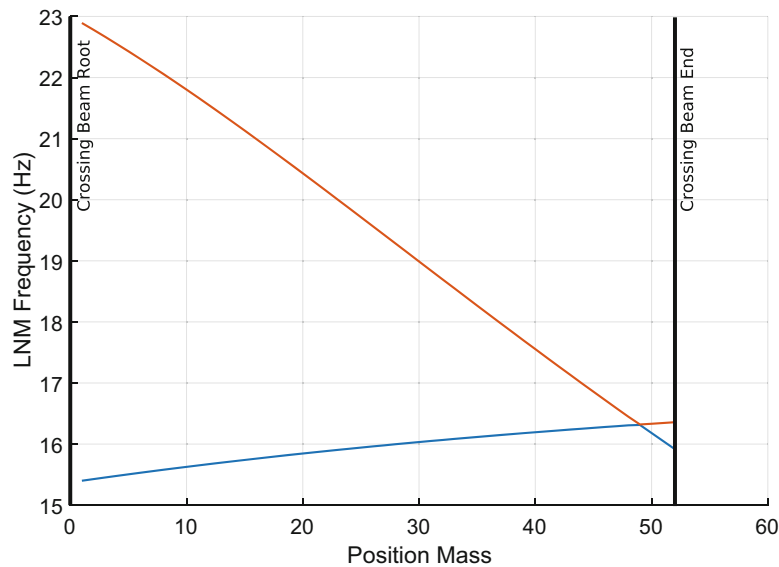


Fig. 36.9 Variation of linear modal frequency if the position of the additional masses is varied asymmetrically, keeping one set of masses fixed at the 49th position on one side

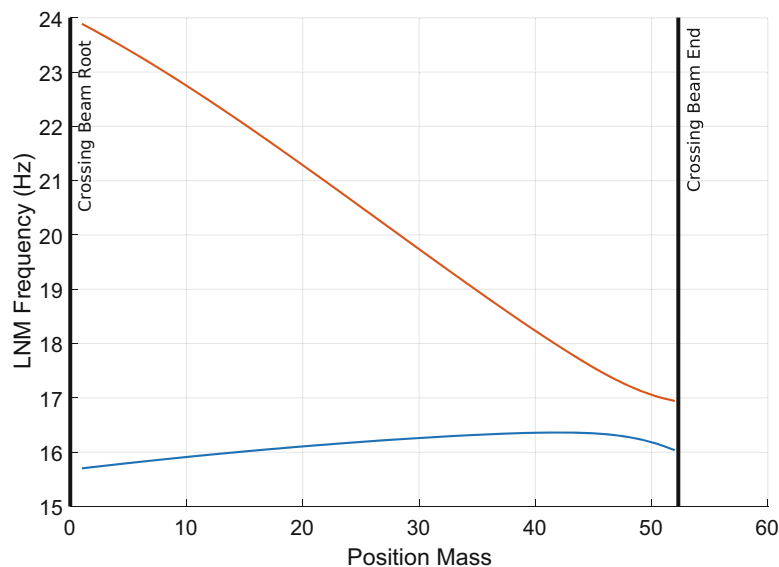


Fig. 36.10 Variation of linear modal frequency if the position of the additional masses is varied asymmetrically, keeping one set of masses fixed at the 43th position on one side

variation of the linear modal frequency of the two retained modes having fixed the set of masses on one side of the main crossing beam at the 49th (Fig. 36.9) and 43th (Fig. 36.10) position.

Looking at Fig. 36.9, and comparing with Fig. 36.6, it is possible to conclude that the considered asymmetry affects the linear frequencies making them closer, thus a possible modal interaction is expected. Moreover, there is a significantly higher decrease in the frequency of the second mode, when predominantly torsional, and a slight higher decrease in the frequency of the first mode, when predominantly flexional.

It is of interest noting that if the fixed position on one side of the main crossing beam is not the 49 the frequencies keep a larger difference between each other. For instance, this is shown in Fig. 36.10 where the linear modal frequencies are obtained having fixed one set of masses at the position 43 along the crossing beam.

As done for the symmetric configuration, NNMs are obtained after having determined the reduced order models. Figures 36.11 and 36.12 show the NNMS projected in the first and second modal coordinate, respectively. Different asymmetric configurations have been considered, having fixed the set of masses at the position 49 on one side of the

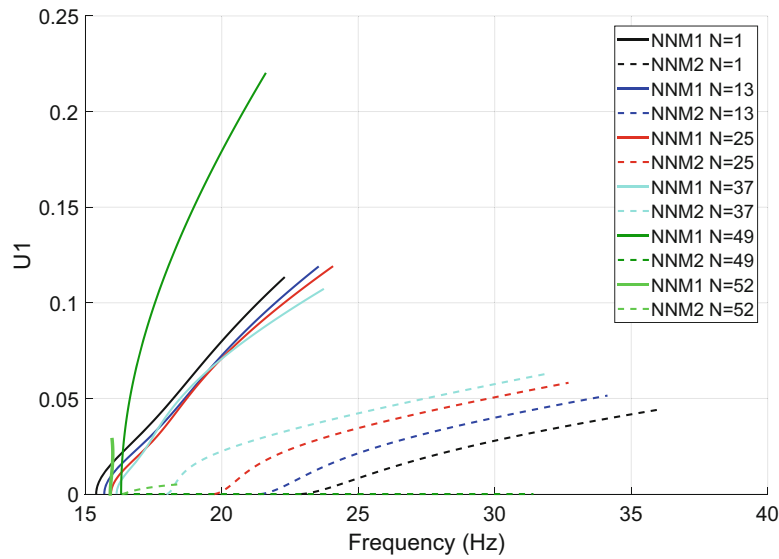


Fig. 36.11 Nonlinear normal modes projected in the first mode retaining the first two modes adopting the AMF for a set of asymmetric configuration. On one side of the crossed beam the set of masses is fixed at the 49th position. On the other side the set of masses starts at the N position – defined in the legend – counted starting from the main beam

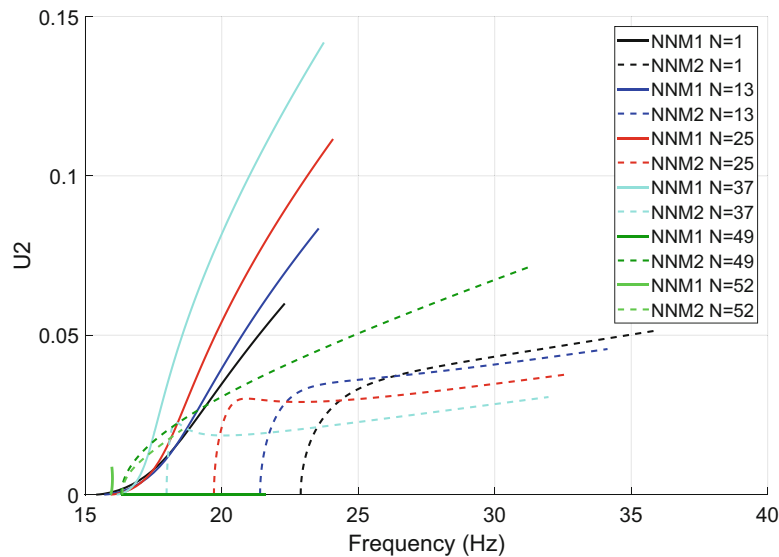


Fig. 36.12 Nonlinear normal modes projected in the second mode retaining the first two modes adopting the AMF for a set of asymmetric configuration. On one side of the crossed beam the set of masses is fixed at the 49th position. On the other side the set of masses starts at the N position – defined in the legend – counted starting from the main beam

crossing beam. The position of the set of masses on the other side of the crossing beam is specified in the legend of each figure. A different behaviour is shown if compared to the NNMs obtained for the symmetric configuration. The asymmetry causes modal interaction and this is apparent looking at the NNMs projected both in the first and second modal coordinate; the amplitude of the second (first) modal coordinate have a significant amplitude if compared to the first (second) modal coordinate for the first (second) NNM. Moreover, for each modal coordinate, at a fixed frequency, the amplitude of the two NNMs are very close to each other.

Finally the occurrence of modal interactions for all asymmetric configurations has been checked looking at the modal shape. This can be shown investigating the ratio between the first and the second (second and first) modal coordinate for the second (first) NNM. Figures 36.13 and 36.14 show the stated ratio for the first and second NNM, respectively. The ratio is plotted as the frequency changes and for the different asymmetric configurations adopted for testing the code and identifying the reduced order model. As for the NNM, the position of the ‘moving’ set of masses is specified in the legend. Moving

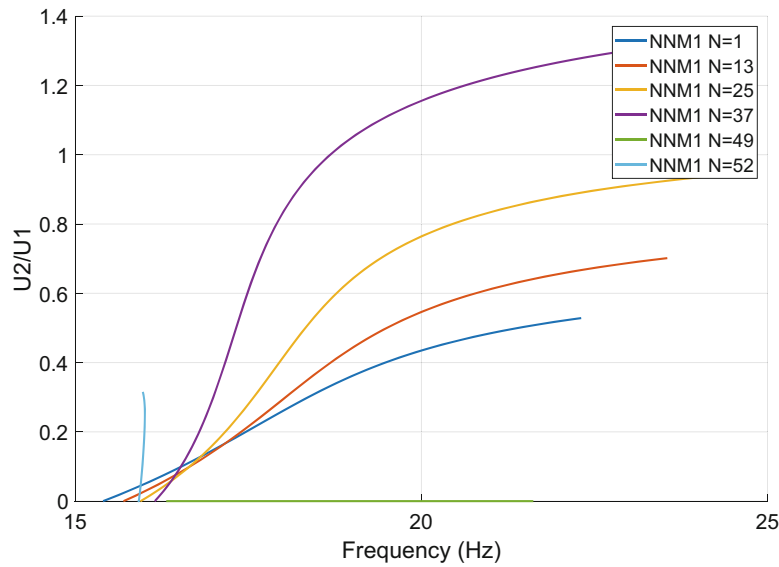


Fig. 36.13 Amplitude of the second mode over the first one along the first backbone curves

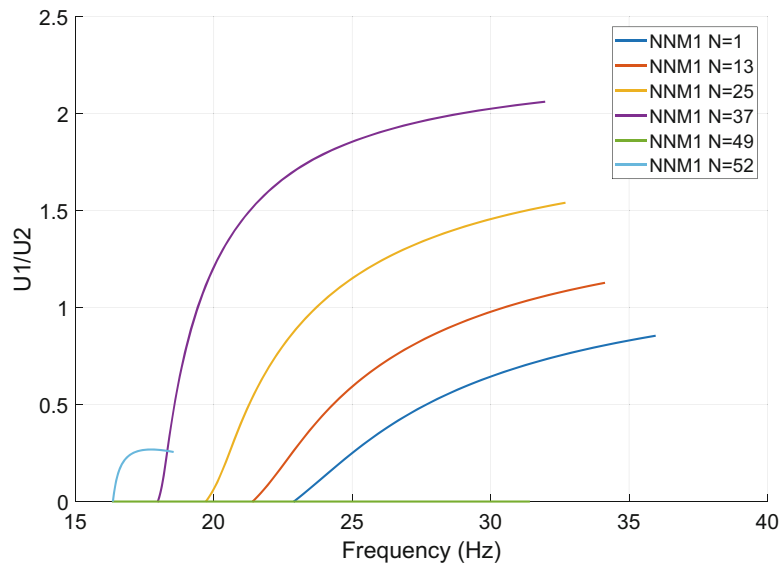


Fig. 36.14 Amplitude of the first mode over the second one along the second backbone curves

the set of masses along the main crossing beam, from the main beam until the position 49 (at which the set of masses on the other side of the crossing beam is fixed) the modal interaction increases. When the position 49 is reached, the modal interaction disappears and is slightly present again moving further than the position 49. Note that if the ratio between the modal coordinates is greater than 1 it means that the second (first) mode is prevalent in the modal shape of the first (second) NNM.

36.5 Conclusions

A strategy for performing nonlinear modal reduction using either the applied modal force (AMF) or the enforced modal displacement (EMD) has been presented. The technique is conceived with the aim of using it in an automatic environment. It has been implemented in a Matlab environment and allows the automatic exchange of information with the FEM software,

Abaqus. The conceived strategy allows the investigation of the effects of parametric variation on linear and nonlinear behaviour of the system of interest. The validation considers a crossed beam structure modelled in Abaqus and the presented results have been obtained using the AMF technique. Symmetric and asymmetric configurations have been investigated. The results reveal that modal interaction occurs only in the presence of asymmetric configurations and disappears when the systems is in a symmetric configuration. These results are encouraging and the potential for such an automatic environment for modal reduction in the presence of parameter variation is powerful. Further investigation needs to be done in terms of the assumptions made for the description of the nonlinear terms, i.e. considering only quadratic and cubic terms, and of the modal participation. Moreover, comparison with the results obtained using the EMD technique and validation of the identified nonlinear normal modes will be covered in the future steps of our research.

References

1. McEwan, M.I., Wright, J.R., Cooper, J.E., Leung, A.Y.T.: A combined modal/finite element analysis technique for the dynamic response of a non-linear beam to harmonic excitation. *J. Sound Vib.* **243**(4), 601–624 (2001)
2. Detroux, T., Renson, L., Masset, L., Kerschen, G.: The harmonic balance method for bifurcation analysis of large-scale nonlinear mechanical systems. *Comput. Methods Appl. Mech. Eng.* **296**, 18–38 (2015)
3. Przekop, A., Guo, X., Rizzi, S.A.: Alternative modal basis selection procedures for reduced-order nonlinear random response simulation. *J. Sound Vib.* **313**, 4005–4024 (2012)
4. Kuether, R.J., Allen, M.S.: Validation of nonlinear reduced order models with time integration targeted at nonlinear normal modes. *Nonlinear Dyn.* **1**, 363–375 (2016)
5. Kuether, R.J., Allen, M.S., Hollkhamp, J.J.: Modal substructuring of geometrically nonlinear finite-element models. *AIAA J.* **54**(2), 691–702 (2016)
6. Kuether, R.J., Allen, M.S., Hollkhamp, J.J.: Modal substructuring of geometrically nonlinear finite element models with interface reduction. *AIAA J.* **55**(5), 1695–1706 (2017)
7. VanDamme, C.I., Allen, M.S.: Using NNMs to evaluate reduced order models of curved beam. In: De Clerck, J., Epp, D.S. (eds.) *Rotating Machinery, Hybrid Test Methods, Vibro-Acoustics & Laser Vibrometry*, vol. 8, pp. 457–469. Springer International Publishing, Cham (2016)
8. Spottswood, S.M., Allemang, R.J.: Identifying nonlinear parameters for reduced order models. Part I: an analytical comparison. In: *IMAC-XXIV: Conference & Exposition on Structural Dynamics* (2006)
9. Fujimoto, K., Scherpen, J.M.A.: Balanced realization and model order reduction for nonlinear systems based on singular value analysis, *SIAM J. Control Optim.* **48**(7), 4591–4623 (2010)
10. Rizzi, S.A., Przekop, A.: The effect of basis selection on static and random acoustic response prediction using a nonlinear modal simulation. *J. Sound Vib.* **313**, 4005–4024 (2012)
11. Rizzi, S.A., Przekop, A.: System identification-guided basis selection for reduced-order nonlinear response analysis. *J. Sound Vib.* **315**, 467–485 (2008)
12. VanDamme, C.I., Allen, M.S.: Evaluating NLRMs' ability to predict dynamic snap through of a curved beam in a random loading environment. In: *58th AIAA/ASCE/AHS/ASC Structures, Structural Dynamics, and Materials Conference*, Grapevine, 9–13 Jan 2017
13. Guerin, L.C.M., Kuether, R.J., Allen, M.S.: Considerations for indirect parameter estimation in nonlinear reduced order models. *Nonlinear Dyn.* **1**, 327–342 (2016)
14. Kuether, R.J., Deaner, B.J., Hollkhamp, J.J., Allen, M.S.: Evaluation of geometrically nonlinear reduced-order models with nonlinear normal modes. *AIAA J.* **53**(11), 3273–3285 (2015)
15. Kuether, R.J., Brake, M.R., Allen, M.S.: Evaluating convergence of reduced order models using nonlinear normal modes. *Model Valid. Uncertain. Quantif.* **3**, 287–300 (2014)
16. Allen, M.S., Kuether, R.J., Deaner, B.J., Sracic, M.W.: A numerical continuation method to compute nonlinear normal modes using modal reduction. In: *53rd AIAA/ASME/ASCE/AHS/ASC Structures, Structural Dynamics and Materials Conference*, Honolulu (2012)
17. Chang, Y.-W., Wang, X., Capiez-Lernout, E., Mignolet, M.P., Soize, C.: Reduced order modelling for the nonlinear geometric response of some curved structures. In: *AAAF-AIAA. International Forum on Aeroelasticity and Structural Dynamics*, Paper IFASD-2011-185, Paris, pp. 1–19, June 2011
18. Gordon, R.W., Hollkamp, J.J.: *Reduced-order models for acoustic response prediction*, Final report (2011)
19. Serandour, G., Peeters, M., Kerschen, G., Golinval, J.C.: Computation of nonlinear normal modes, part II: numerical continuation in AUTO. In: *ENOC-2008*, Saint Petersburg (2008)
20. Hill, T.L., Neild, S.A., Cammarano, A.: An analytical approach for detecting isolated periodic solution branches in weakly nonlinear structures. *J. Sound Vib.* **379**, 150–165 (2016)
21. Hill, T.L., Neild, S.A., Cammarano, A., Wagg, D.J.: An analytical approach for detecting isolated periodic solution branches in weakly nonlinear structures. *J. Sound Vib.* **379**, 135–149 (2016)
22. Noël, J., Detroux, T., Masset, L., Kerschen, G., Virgin, L.: Isolated response curves in a base-excited, two-degree-of-freedom, nonlinear system. In: *Proceedings of the ASME 2015 International Design Engineering Technical Conferences & Computers and Information in Engineering Conference*, Boston (2015)

23. Kuether, R., Renson, L., Detroux, T., Grappasonni, C., Kerschen, G., Allen, M.: Nonlinear normal modes, modal interactions and isolated resonance curves. *J. Sound Vib.* **351**, 299–310 (2015)
24. Detroux, T., Habib, G., Masset, L., Kerschen, G.: Performance, robustness and sensitivity analysis of the nonlinear tuned vibration absorber. *Mech. Syst. Signal Process.* **60–61**, 799–809 (2015)
25. Hollkamp, J.J., Gordon, R.W., Spottswood, S.M.: Nonlinear modal models for sonic fatigue response prediction: a comparison of methods. *J. Sound Vib.* **284**, 1145–1163 (2005)
26. Forrester, A., Sbester, A., Keane, A.: *Engineering Design via Surrogate Modelling: A Practical Guide*. Wiley, Chichester (2008)
27. Hollkamp, J.J., Gordon, R.W.: Reduced-order models for nonlinear response prediction: implicit condensation and expansion. *J. Sound Vib.* **318**, 1139–1153 (2008)



Chapter 37

Nonlinear Forced Response of a Composite Fan Blade Actuated by Piezoelectric Patches: Simulation and Testing

Antoine Mabilia, Claude Gibert, Fabrice Thouverez, and Edouard De Jaeghere

Abstract This paper deals with a correlation between simulation and test results of woven composite fan blades excited by 18 piezoelectric actuators. A nonlinear simulation including friction at blade attachment is performed on the reduced system in which the piezoelectric actuators are condensed on their internal potential Degrees Of Freedom before being integrated in the simulation. The results of the correlation are interesting, especially for the first bending mode despite a difference in the sliding phase of the contact.

Keywords Simulation/test correlation · Piezoelectric actuators · Nonlinear simulation · Friction at blade attachment · Model reduction

37.1 Introduction

Bladed disks are key parts of turbojet engines. It is essential to understand and control their vibrations to ensure they don't lead to their early fatigue failure. Latest fan blades technological developments, including shape (wide-chord blade) or material (composite material) evolutions, have allowed to increase by-pass ratio and reduce greatly the whole turbojet mass. However, these evolutions imply changes in fan dynamic behavior and sensitivity to vibrations. The PHARE#1 (standing for: Rotating machinery Platform for control of Environmental Risks) facility has been developed in the perspective of mastering bladed disks vibratory phenomena. PHARE#1 is a research engine test rig allowing full-scale vacuum tests at nominal speed. To provide the necessary forces for modal testing, 18 piezoelectric patches actuate each of the 18 woven composite fan blades. A test campaign on clamping jaws has been conducted on the 18 blades in order to validate the actuator behavior on each blade and calibrate the nonlinear numerical model of the blade and the piezoelectric actuators in a stationary configuration.

Piezoelectric applications have been used in several works on bladed disks vibrations, particularly in the vibration reduction thematic on rotating subscale composite fan blades [1] or stationary full-scale composite fan blades [2]. Piezoelectric patches have also been employed to actuate High Pressure Compressor (HPC) blades to study friction rings damping [3], friction damping on blade attachments [4] or Coriolis effect [5]. More recently, piezoelectric Macro-Fiber Composites (MFC) actuators have been bonded on a rotating bladed disk for aeroelastic investigations [6].

This paper contains a description of the experimental set-up of a woven composite fan blade in clamping jaws and actuated by piezoelectric patches. The numerical models of the blade and the clamping jaws are presented and the nonlinear dynamic simulation is detailed with special care for the condensation of internal potential Degrees Of Freedom (DOFs). To conclude this paper, a correlation between experimental and simulation results is proposed. For reasons of confidentiality, all axes of the graphs on this paper will be normalized.

A. Mabilia (✉)
École Centrale de Lyon, LTDS, UMR CNRS 5513, Écully, France

Safran Aircraft Engines, Moissy-Cramayel, France
e-mail: antoine.mabilia@doctorant.ec-lyon.fr

C. Gibert · F. Thouverez
École Centrale de Lyon, LTDS, UMR CNRS 5513, Écully, France

E. De Jaeghere
Safran Aircraft Engines, Moissy-Cramayel, France

37.2 Experimental Set-Up

37.2.1 General Description

The structure tested through this test rig is a woven composite fan blade with a titanium leading edge at full scale (Fig. 37.1a), similar to the blades used in the latest generation of turbojet. The blade is inserted into the clamping jaws whose mass is about 150 kg. Clamping jaws is representative of the ones found on a fan disk. To isolate the system from the ground, elastic suspensions are placed under the clamping jaws. The blade is wedged into the jaws by means of a wedge tightened by screws evenly distributed along its length. A tightening torque is applied to all screws with a torque wrench, always following the same tightening scheme in order to guarantee a good repeatability. The contact pressure between the blade and the jaws is representative of the centrifugal effect of the blade in a disk for a given fan speed. A metallic foil is inserted into the contact interfaces between the blade and the jaws to approach rotational test conditions.

37.2.2 Test-Rig Excitation System

Piezoelectric patches are distributed over the pressure and suction side of the blade in order to actuate the blade. The piezoelectric actuators chosen for this application are made of Lead Zirconate Titanate (PZT 5H). The dimension of the active part of the piezoelectric patches is 45.97 mm long, 38.1 mm wide and 254 μm thick. These patches are a good compromise between flexibility (to fit the blade shape) and excitation power (high piezoelectric coefficient d_{31}). The patches are bonded to the blades with a specific glue for aeronautics. The bonding process uses a vacuum bag in order to improve the gluing of the actuators on the curved surfaces of the blades.

Piezoelectric patches are most effective when positioned in blade's greater strain areas [1]. A preliminary study was carried out to determine the number of piezoelectric patches to be installed and their position on the blade (Fig. 37.2). As the aim is to study the influence of several parameters on the blade dynamics, the patches positioning results from a compromise between the maximum strain zones of the different targeted modes (first bending mode: 1B, second bending mode: 2B and first torsion mode: 1T) for different fan rotation speeds (Fig. 37.2). It has been shown that, as rotation speed increase, dynamic strain distribution changes [1]. Eighteen piezoelectric actuators were finally bonded to the blade: 8 on the suction side and 10 on the pressure side divided into two groups (Fig. 37.2). The piezoelectric patches are wired in parallel to deliver the same voltage at all the actuators.

A linear power amplifier specially designed for this application of 1500 W for 18 channels (one for each blade of the fan) amplified the control signal emitted by the generation device and its associated software (Fig. 37.1b).

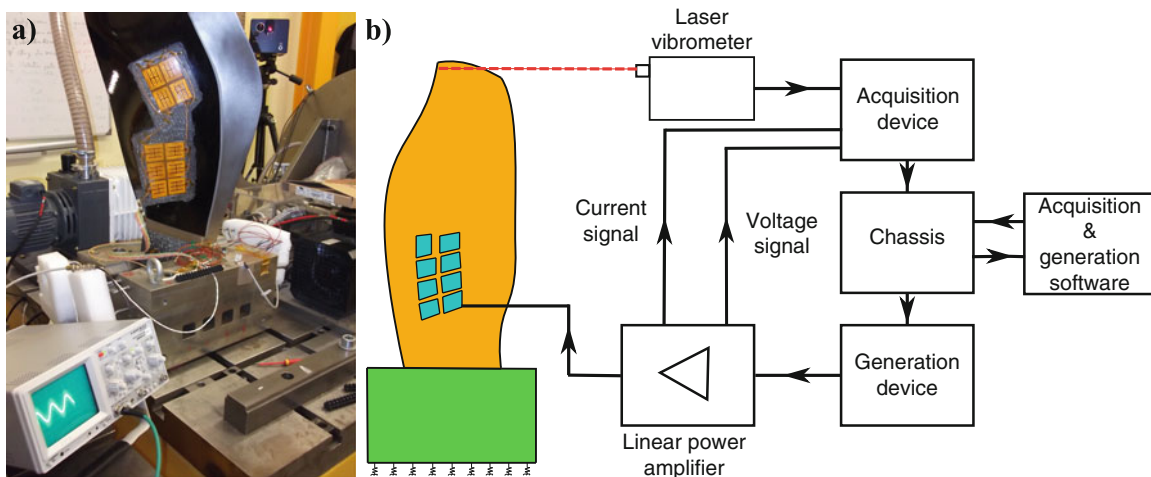


Fig. 37.1 (a) Illustration of the experimental set-up (b) Diagram of the experimental set-up

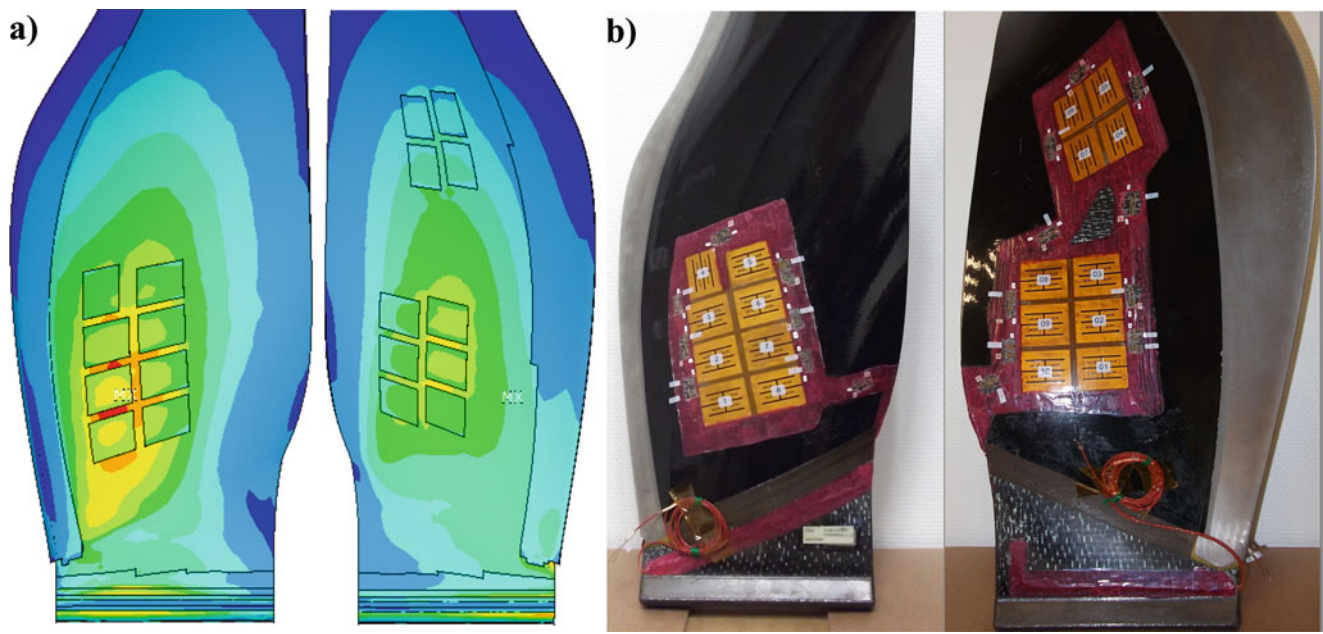


Fig. 37.2 (a) Pressure side and suction side strain maps for the first bending mode (b) Illustrations of the blade equipped with piezoelectric actuators

37.2.3 *Vibration Measurement*

Vibration measurement is performed using a POLYTEC PSV400 laser vibrometer (Fig. 37.1). Vibration displacements are measured at a point on the tip of the suction side near the leading edge along a normal direction to the blade surface (Fig. 37.1). The current and voltage distributed by the amplifier are also monitored and saved during the tests.

37.2.4 *Experimental Protocol*

A wide band excitation of the structure using a random signal is generated in order to identify the resonance frequencies of the first three modes of the structure (Fig. 37.3a). Stepped sines are then performed to obtain the forced responses of each targeted mode and for several excitation amplitude ranges (Fig. 37.3b). All tests are performed under standard temperature and pressure conditions.

A particular attention is needed in the choice of the stepped sine excitation signal parameters in order to avoid spurious distortions of the estimated forced responses.

37.3 Numerical Simulation

37.3.1 *Numerical Modeling*

The finite element software ANSYS has been used to model the fan blade and the clamping jaws. The Finite Element Model (FEM) is composed of 70,674 nodes for 212,022 DOFs. The different layers of the composite material are represented with orthotropic material characteristics and a particular orientation of the elements according to the weaving of the zone. The contact between the blade and the jaws is modelled with specific surface-to-surface contact elements. The metallic foil is not represented in the numerical model.

The clamping jaws' thrust wedge is included in the FEM. The wedge is clamped on the clamping jaws' base nodes. In order to simulate the thrust forces transmitted by the wedge to the blade due to the tightening of the thrust screws, an equivalent thermal expansion coefficient is added to the wedge's material characteristics. This thermal expansion coefficient

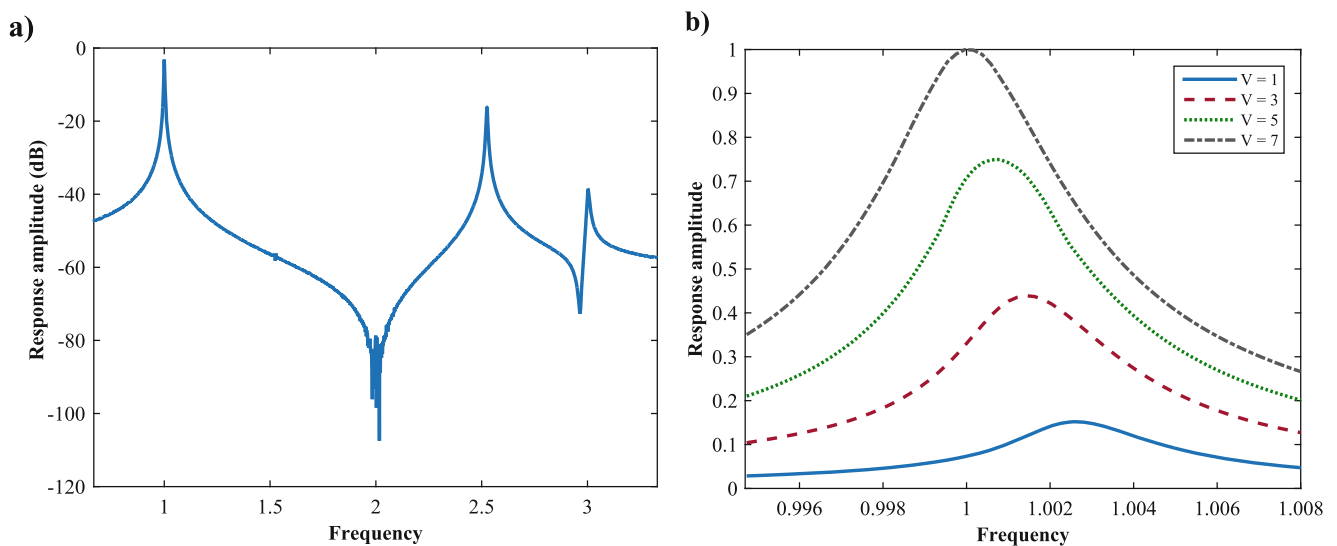


Fig. 37.3 (a) Response to a wide band excitation (b) Forced response of the first bending mode for several excitation

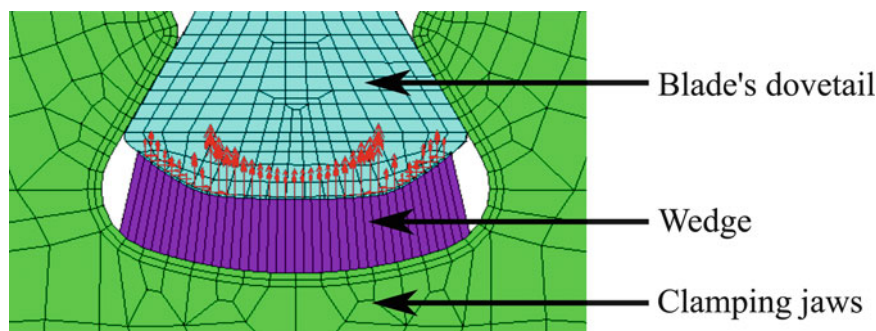


Fig. 37.4 Contact force distribution of the wedge on the blade

is uniaxial along the thrust axis. A uniform thermal field is then imposed on the wedge in order to expand it and simulate its thrust under the blade. This thermal expansion is recalibrated to obtain a thrust force representative of a certain rotation speed. The contact between the wedge and the blade is supposed to be a sliding contact. Modelling the thrust force thanks to the wedge dilatation maintains the static equilibrium in the whole system, which is important because the clamping jaws are suspended. In addition, this approach provides a more accurate representation of the contact forces distribution between the blade and the wedge (Fig. 37.4).

Multiple springs connect the bottom face's nodes of the clamping jaws to the ground along the three nodal directions in order to represent the elastic suspension used to isolate the system from the ground (Fig. 37.1). The springs' stiffness are adjusted with respect to the resonance frequencies of the system suspension modes obtained in tests (the highest suspension mode frequency is 11% of the lowest resonance frequency). To prove the good isolation of the system from the ground, a modal analysis of the free system was carried out. The difference between the resonance frequencies of the two analyses is less than 0.8% for the 6 first modes: the boundary conditions of the testing set-up is then considered acceptable.

Piezoelectric actuators are modelled with quadratic hexahedral elements including piezoelectric capabilities [7]. The actuators are positioned as precisely as possible in relation to their real position while coinciding with the meshing of the blade. The bonding between the actuators and the blade is assumed to be perfect: the actuators' base nodes are merged with the blade's outer nodes. The actuators are meshed with two elements in the thickness. The FEM contains 5355 piezo-mechanical nodes for 21,420 piezo-mechanical DOFs (3 mechanical DOFs and 1 tension DOF per node). To take account of the polarization direction of the actuators, each element coordinate system is oriented along the actuator's polarization direction, i.e. through the thickness of the actuator.

37.3.2 Condensation of Piezoelectric Actuator Potential DOFs

A numerical simulation involving piezoelectric elements contains mechanical and voltage unknowns. The presence of these voltage unknowns does not allow to solve the problem like a standard elastic vibration problem. It is therefore interesting to condense these voltage unknowns in order to solve a general vibration problem (37.1). In particular, the actuators action on the system would appear as an external force whose magnitude is proportional to the applied voltage, whereas the system stiffness would be purely elastic.

$$M\ddot{\mathbf{x}}(t) + C\dot{\mathbf{x}}(t) + K\mathbf{x}(t) = \mathbf{f}^{ext}(t) \quad (37.1)$$

With M , C , K commonly referred as the mass, viscous damping and linear stiffness matrices respectively, \mathbf{f}^{ext} the vector of external load applied to the system and \mathbf{x} the displacement vector of all DOFs.

Starting from the linear law of piezoelectricity [8], early works [9] proposed a first discretized formulation of the piezoelectric problem coupled between displacement and voltage unknowns (37.2). This work considers the direct and reverse effects of piezoelectricity. This formulation has been used in many studies, particularly those dealing with piezoelectric shunt [10, 11].

$$\left(-\omega^2 \begin{bmatrix} \mathbf{M}_u & 0 \\ 0 & 0 \end{bmatrix} + i\omega \begin{bmatrix} \mathbf{C}_u & 0 \\ 0 & 0 \end{bmatrix} + \begin{bmatrix} \mathbf{K}_u & \mathbf{K}_{u\psi} \\ -\mathbf{K}_{u\psi}^T & \mathbf{K}_\psi \end{bmatrix} \right) \begin{Bmatrix} \mathbf{u} \\ \boldsymbol{\psi} \end{Bmatrix} = \begin{Bmatrix} \mathbf{f}^{ext} \\ \mathbf{q} \end{Bmatrix} \quad (37.2)$$

In the above equation, \mathbf{u} and $\boldsymbol{\psi}$ are the displacement and potential vectors of the piezoelectric actuators, respectively. \mathbf{M}_u , \mathbf{C}_u and \mathbf{K}_u are the mechanical mass, viscous damping and stiffness matrices respectively. $\mathbf{K}_{u\psi}$ is the electromechanical coupling matrix and \mathbf{K}_ψ is the dielectric stiffness matrix. \mathbf{f}^{ext} is the external mechanical load and \mathbf{q} the electrical charge vector.

In the case where piezoelectric elements have the form of patches containing very thin lower and upper electrodes, recent works [2] propose to define the potential vector in the following form (37.3):

$$\{\boldsymbol{\psi}\} = \{\boldsymbol{\psi}_+ \boldsymbol{\psi}_{int} \boldsymbol{\psi}_-\}^T \quad (37.3)$$

The subscripts \bullet_+ , \bullet_- are standing for the nodes of the upper and lower electrodes respectively and \bullet_{int} is standing for the nodes located between the two electrodes.

The Eq. (37.2) can be rewritten as follows (37.4):

$$\left(-\omega^2 \begin{bmatrix} \mathbf{M}_u & 0 & 0 & 0 \\ 0 & 0 & 0 & 0 \\ 0 & 0 & 0 & 0 \\ 0 & 0 & 0 & 0 \end{bmatrix} + i\omega \begin{bmatrix} \mathbf{C}_u & 0 & 0 & 0 \\ 0 & 0 & 0 & 0 \\ 0 & 0 & 0 & 0 \\ 0 & 0 & 0 & 0 \end{bmatrix} + \begin{bmatrix} \mathbf{K}_u & \mathbf{K}_{u\psi_+} & \mathbf{K}_{u\psi_{int}} & \mathbf{K}_{u\psi_-} \\ -\mathbf{K}_{u\psi_+}^T & \mathbf{K}_{\psi_+} & \mathbf{K}_{\psi_+\psi_{int}} & \mathbf{K}_{\psi_+\psi_-} \\ -\mathbf{K}_{u\psi_{int}}^T & \mathbf{K}_{\psi_+\psi_{int}}^T & \mathbf{K}_{\psi_{int}} & \mathbf{K}_{\psi_{int}\psi_-} \\ -\mathbf{K}_{u\psi_-}^T & \mathbf{K}_{\psi_+\psi_-}^T & \mathbf{K}_{\psi_{int}\psi_-}^T & \mathbf{K}_{\psi_-} \end{bmatrix} \right) \begin{Bmatrix} \mathbf{u} \\ \boldsymbol{\psi}_+ \\ \boldsymbol{\psi}_{int} \\ \boldsymbol{\psi}_- \end{Bmatrix} = \begin{Bmatrix} \mathbf{f}^{ext} \\ \mathbf{q}_+ \\ 0 \\ \mathbf{q}_- \end{Bmatrix} \quad (37.4)$$

The potential $\boldsymbol{\psi}_-$ is wired to the ground of the amplifier: $\{\boldsymbol{\psi}_-\} = \{0\}$ and so $\{\boldsymbol{\psi}_+\} = \{\mathbf{v}\}$ with \mathbf{v} the potential difference vector between the upper and lower electrodes. Moreover, charges of the two electrodes are opposite in sign: $\{\mathbf{q}_+\} = -\{\mathbf{q}_-\} = \{\mathbf{q}\}$. The matrix system is also converted to a symmetrical matrix system (37.5) by reversing the sign of the charge equation.

$$\left(-\omega^2 \begin{bmatrix} \mathbf{M}_u & 0 & 0 \\ 0 & 0 & 0 \\ 0 & 0 & 0 \end{bmatrix} + i\omega \begin{bmatrix} \mathbf{C}_u & 0 & 0 \\ 0 & 0 & 0 \\ 0 & 0 & 0 \end{bmatrix} + \begin{bmatrix} \mathbf{K}_u & \mathbf{K}_{u\psi_+} & \mathbf{K}_{u\psi_{int}} \\ \mathbf{K}_{u\psi_+}^T & -\mathbf{K}_{\psi_+} & -\mathbf{K}_{\psi_+\psi_{int}} \\ \mathbf{K}_{u\psi_{int}}^T & -\mathbf{K}_{\psi_+\psi_{int}}^T & \mathbf{K}_{\psi_{int}} \end{bmatrix} \right) \begin{Bmatrix} \mathbf{u} \\ \mathbf{v} \\ \boldsymbol{\psi}_{int} \end{Bmatrix} = \begin{Bmatrix} \mathbf{f}^{ext} \\ -\mathbf{q} \\ 0 \end{Bmatrix} \quad (37.5)$$

To reduce the number of potential unknowns, internal potentials are condensed to obtain the Eq. (37.6). Since no inertia is associated to the internal potential DOFs, the achieved condensation is exact.

$$\left(-\omega^2 \begin{bmatrix} \mathbf{M}_u & 0 \\ 0 & 0 \end{bmatrix} + i\omega \begin{bmatrix} \mathbf{C}_u & 0 \\ 0 & 0 \end{bmatrix} + \begin{bmatrix} \mathbf{K}_u^* & \mathbf{K}_{uv}^* \\ \mathbf{K}_{uv}^{*T} & \mathbf{K}_v^* \end{bmatrix} \right) \begin{Bmatrix} \mathbf{u} \\ \mathbf{v} \end{Bmatrix} = \begin{Bmatrix} \mathbf{f}^{ext} \\ -\mathbf{q} \end{Bmatrix} \quad (37.6)$$

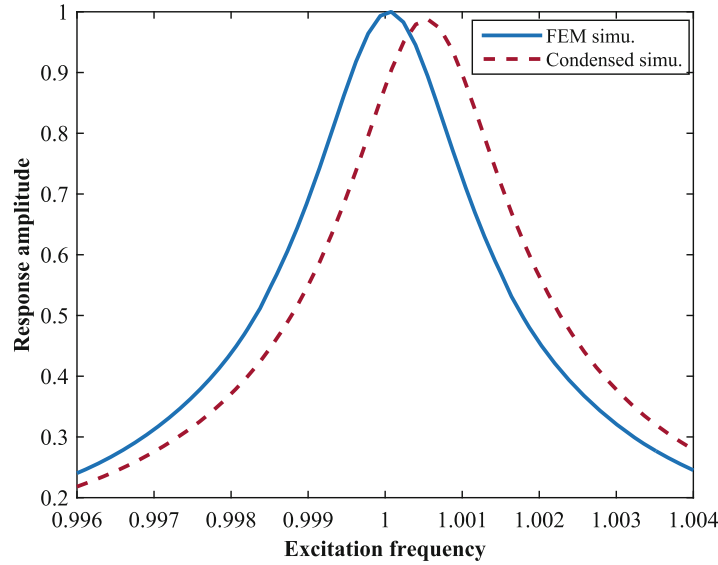


Fig. 37.5 Comparison between FEM simulation and condensed simulation for the 1B mode

With:

$$[\mathbf{K}_u^*] = [\mathbf{K}_u + \mathbf{K}_{u\psi_{int}} \mathbf{K}_{\psi_{int}}^{-1} \mathbf{K}_{u\psi_{int}}^T] \quad (37.7)$$

$$[\mathbf{K}_{uv}^*] = [\mathbf{K}_{u\psi_+} - \mathbf{K}_{u\psi_{int}} \mathbf{K}_{\psi_{int}}^{-1} \mathbf{K}_{\psi_+ \psi_{int}}^T] \quad (37.8)$$

$$[\mathbf{K}_v^*] = [-\mathbf{K}_{\psi_+} + \mathbf{K}_{\psi_+ \psi_{int}} \mathbf{K}_{\psi_{int}}^{-1} \mathbf{K}_{\psi_+ \psi_{int}}^T] \quad (37.9)$$

The linear amplifier used during the tests imposes the voltage at the piezoelectric actuators' terminals. The system (37.6) can be decoupled and the actuator forces appear as external forces proportional to the applied voltage in the Eq. (37.10). The Eq. (37.11) can be used to obtain the charge vector of the upper electrode in function of the displacement vector and the potential vector.

$$(-\omega^2 \mathbf{M}_u + i\omega \mathbf{C}_u + \mathbf{K}_u^*) \mathbf{u} = \mathbf{f}^{ext} - \mathbf{K}_{uv}^* \mathbf{v} \quad (37.10)$$

$$\mathbf{K}_{uv}^{T*} \mathbf{u} + \mathbf{K}_v^* \mathbf{v} = -\mathbf{q} \quad (37.11)$$

To validate the achieved condensation and some of the hypothesis formulated, a comparison between the linear forced response of the complete system, condensed on the internal potential DOFs, and the linear forced response of this same system with all the potential DOFs is carried out (Fig. 37.5). The simulation without condensation is solved through a finite element software, whereas the condensed simulation is reduced using the Craig-Bampton method before being solved with the Harmonic Balance Method [12]. Both methods are described in the following paragraph.

The frequency and amplitude deviations observed in Fig. 37.5 are respectively 0.06% and 1.2%. Condensation performances are equivalent for 2B and 1T modes. These deviations are due to the information loss during the reduction step. The method of internal potential DOFs condensation can therefore be considered reliable and will be used in the remaining part of the article.

Table 37.1 Summary table of the different condensations and reductions

Condensation or reduction step	Number of remaining DOFs	Percentage of reduced or condensed DOFs (%)
FEM model	231,513 DOFs	0
Condensation of potential DOFs	226,158 DOFs	2.3
CMS reduction	2869 DOFs	98.8
Condensation on relative interface displacements	1456 DOFs	99.4

37.3.3 Reduction and Resolution of the System

Since the complete model has a very large amount of DOFs, it is necessary to reduce the model before solving the general equation. In this reduction approach, a substructuring method is employed: a Component Mode Synthesis (CMS) with fixed interfaces (also known as Craig-Bampton reduction method [13]). The structure is divided into two substructures: the blade and the clamping jaws connected together by means of each substructure's contact nodes. All the contact DOFs between the clamping jaws and the blade are considered as master DOFs, i.e. 1428 DOFs for each substructure to which must be added an observation node (3 DOFs) chosen at the laser vibrometer sighting point. To complete these master DOFs, 25 natural vibration modes are chosen to represent the blade dynamics and 15 for the clamping jaws. The number of natural modes selected is determined by means of a frequency criterion so only the modes involved in the frequency range of the study are retained.

Since the non-linearity type of the system is dry friction, another condensation step can be performed to reduce the number of DOFs of the system: a condensation on the non-linear relative interface displacements [14]. The condensation consists in pairing the contact nodes of each substructure and thus resolving the system only on relative displacements, which means dividing the number of contact DOFs by two. A summary table of the different condensations and reductions performed in this work is presented in Table 37.1.

The general discretized equation of nonlinear dynamics (37.12) is solved in the frequency domain using the Harmonic Balance Method (HBM) [15]. The general principle of the HBM is to seek solutions in the form (37.13)

$$\mathbf{M}\ddot{\mathbf{x}}(t) + \mathbf{C}\dot{\mathbf{x}}(t) + \mathbf{K}^{pl}\mathbf{x}(t) + \mathbf{f}_{nl}(\mathbf{x}, \dot{\mathbf{x}}) = \mathbf{f}^{extpl}(t) = -\mathbf{K}_{uv}^{pl*} \mathbf{v}(t) \quad (37.12)$$

With \mathbf{f}_{nl} a term of nonlinear forces. The subscript \bullet^{pl} refers to the preloaded matrices and vectors. The mass matrix \mathbf{M} includes the \mathbf{M}_u matrix, the viscous damping matrix \mathbf{C} includes the \mathbf{C}_u matrix and the stiffness matrix \mathbf{K}^{pl} includes the \mathbf{K}_u^{pl*} matrix. The external load vector \mathbf{f}^{extpl} is equal to $-\mathbf{K}_{uv}^{pl*} \mathbf{v}$ since there are no other loads than those of the piezoelectric actuators.

$$\mathbf{x}(t) = \mathbf{a}_0 + \sum_{k=1}^{N_h} (\mathbf{a}_k \cos(k\omega t) + \mathbf{b}_k \sin(k\omega t)) \quad (37.13)$$

\mathbf{a}_0 is the constant term of the Fourier decomposition, \mathbf{a}_k and \mathbf{b}_k are the coefficient of the Fourier decomposition and N_h is the number of harmonics retained in the HBM resolution.

Substituting (37.13) into the general Eq. (37.12), and projecting on the basis of harmonic functions with respect to the adapted scalar product (37.14) lead to the general equation of the HBM (37.15)

$$\forall (f, g) \in (\mathbf{C}([0, T]))^2, \quad \langle f | g \rangle = \frac{2}{T} \int_0^T f(t)g(t)dt \quad (37.14)$$

$$\mathbf{Z}(\omega) \mathbf{x}_h + \mathbf{f}_h(\mathbf{x}_h, \omega) = \mathbf{f}_h = -\mathbf{K}_{uv}^{pl*} \mathbf{v}_h \quad (37.15)$$

The subscript \bullet_h is standing for the Fourier coefficient vectors. The dynamic stiffness matrix \mathbf{Z} is built as follows (37.16).

$$\mathbf{Z} = \begin{bmatrix} 2\mathbf{K} & & & \\ & \mathbf{Z}_1 & & \\ & & \ddots & \\ & & & \mathbf{Z}_{N_h} \end{bmatrix} \text{ and } \mathbf{Z}_k = \begin{bmatrix} \mathbf{K}^{pl} - (k\omega)^2 \mathbf{M} & k\omega \mathbf{C} \\ -k\omega \mathbf{C} & \mathbf{K}^{pl} - (k\omega)^2 \mathbf{M} \end{bmatrix}, \forall k \in [1, N_h] \quad (37.16)$$

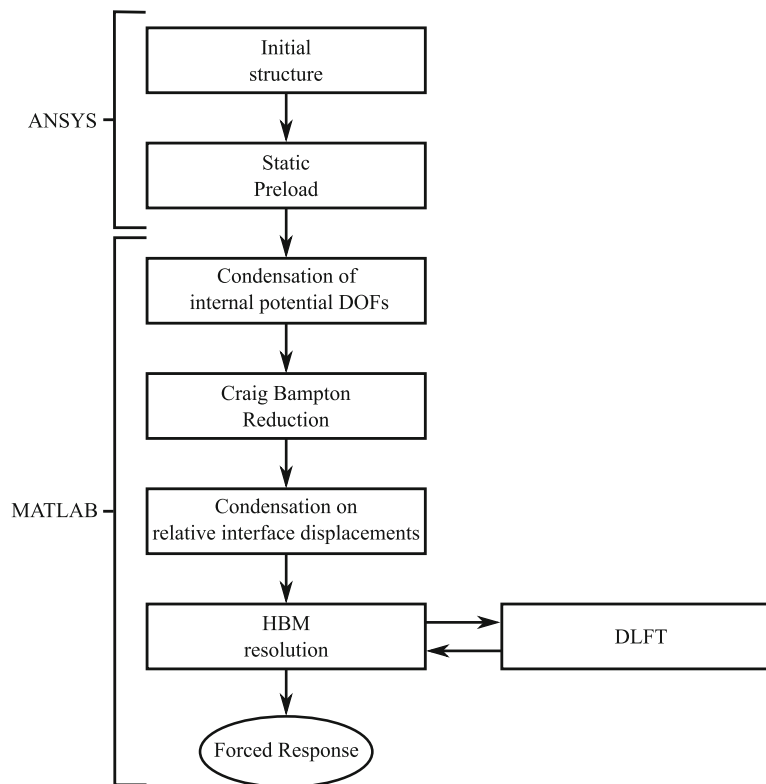


Fig. 37.6 Flowchart of the calculation procedure

The nonlinear forces are computed by means of the Dynamic Lagrangian mixed Frequency-Time method (DLFT) [16] which is using an alternating frequency-time domain procedure to calculate the nonlinear steady state response to periodic excitations of structures subject to dry friction.

The resolution of the algebraic equation system (37.15) is approached using an iterative Newton-Raphson solver and more precisely with a trust-region algorithm [17] implemented in Matlab's *fsolve* function. To accelerate the system resolution, the Jacobian matrix of the system is calculated analytically in the solver [18].

A flowchart summarizing the calculation procedure is given in Fig. 37.6.

37.3.4 Influence Studies on Resolution Parameters

Two influence studies have been conducted on the resolution parameters N_{it} which is standing for the number of time steps in the evaluation of non-linear forces in the time domain in the DLFT [16] $N_{it} = T / \Delta t$ (T is the period of the temporal non-linear forces and Δt is the time step) and N_h . Both parameters influence the precision of the frequency response.

As expected, the higher the number of harmonics retained, the more precise the frequency response is (Fig. 37.7a). The same observation can be made for the number of time steps (Fig. 37.7b). However, the simulation time is highly dependent to the value of these parameters. Taking this into account, the N_h parameters will be set to three. Noticing that even harmonics do not influence the forced response, it would be interesting to exclude them in the resolution in order to reduce computing time. For parameter N_{it} , Fig. 37.7b) displays very strong oscillations at resonance for a low discretization ($N_{it} = 8$), these oscillations decrease as N_{it} increases. These oscillations at resonance tend to disappear from $N_{it} = 32$. The N_{it} value will be fixed to 32 in the following paper.

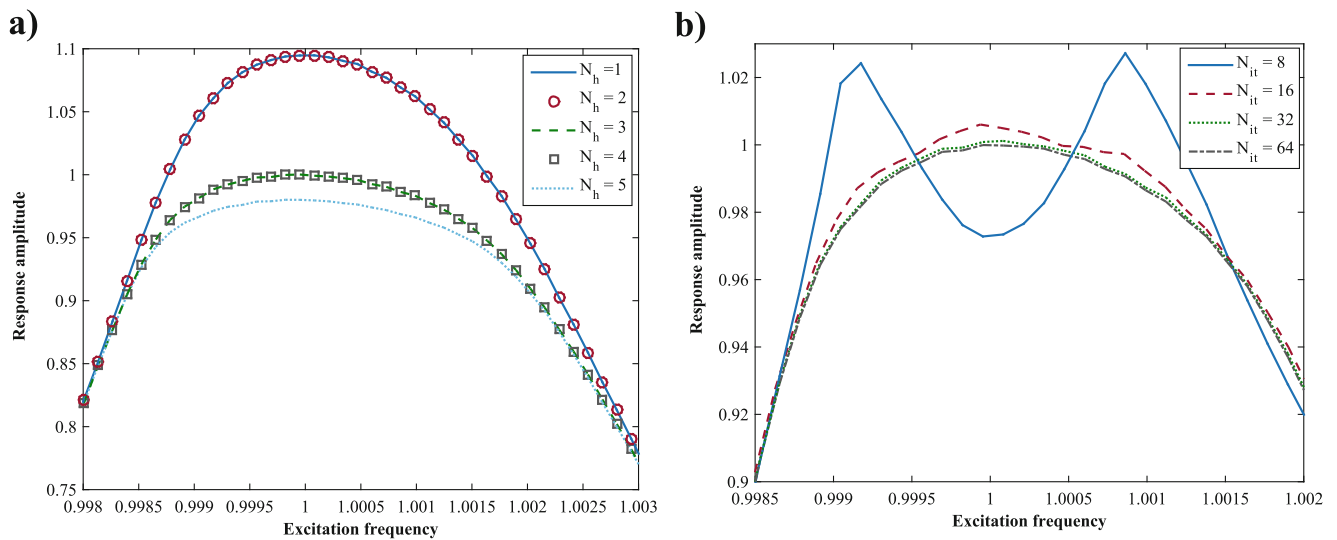


Fig. 37.7 (a) Influence study on the number of harmonics with $N_{it} = 32$ (b) Influence study on the number of discretization intervals with $N_h = 3$

Table 37.2 Deviations between test and simulation results for a linear problem

Deviations from test results (in %)		1B mode (%)	2B mode (%)	1T mode (%)
Resonance frequency	Deviations from reference blade	-0.17	+0.50	-0.30
	Standard deviations of the 18 blades tested	1.13	0.96	1.16
Displacement amplitude	Deviations from reference blade	+0.23	+0.17	+34
	Standard deviations of the 18 blades tested	12.83	18.54	46.26

37.4 Correlation Between Test and Simulation Results

The results of a single blade (among the 18 blades tested) are taken into account to achieve the following correlations.

37.4.1 Correlation on the Linear Simulations

A first correlation is performed on the main linear modal parameters, namely the natural frequency, the displacement amplitude and the damping for low amplitude excitations (Table 37.2). It is assumed that tests performed at low excitation levels provide a good approximation of the modal parameters of the linear underlying system.

The correlation between test and simulation results for a linear problem is quite good compared to the dispersions of these modal parameters on the 18 blades tested (Table 37.2). To correlate the resonance frequencies from linear simulations to the ones from tests, the clamping jaws' mass has been adjusted to approach its actual mass. The piezoelectric coefficient d_{31} has been adjusted in order to compare numerical and experimental resonance amplitude.

The displacement amplitude of the first torsion mode is a difficult parameter to correlate since it strongly depends on the measurement direction of the laser as well as the precision of the actuator position on the blade. These strong dependencies result in a large deviation. Moreover, a large deviation of the 1T displacement amplitude is observed on the other blades tested. The deviation can be up to 46% of the average displacement amplitude.

The structural damping is determined by frequency smoothing using an approximation by a linear frequency response function on the experimental frequency response. Nonlinear identification methods of modal parameters exist [19], however the nonlinearities of the system are weak enough to use a linear method. This structural damping has been included in the simulation as modal damping.

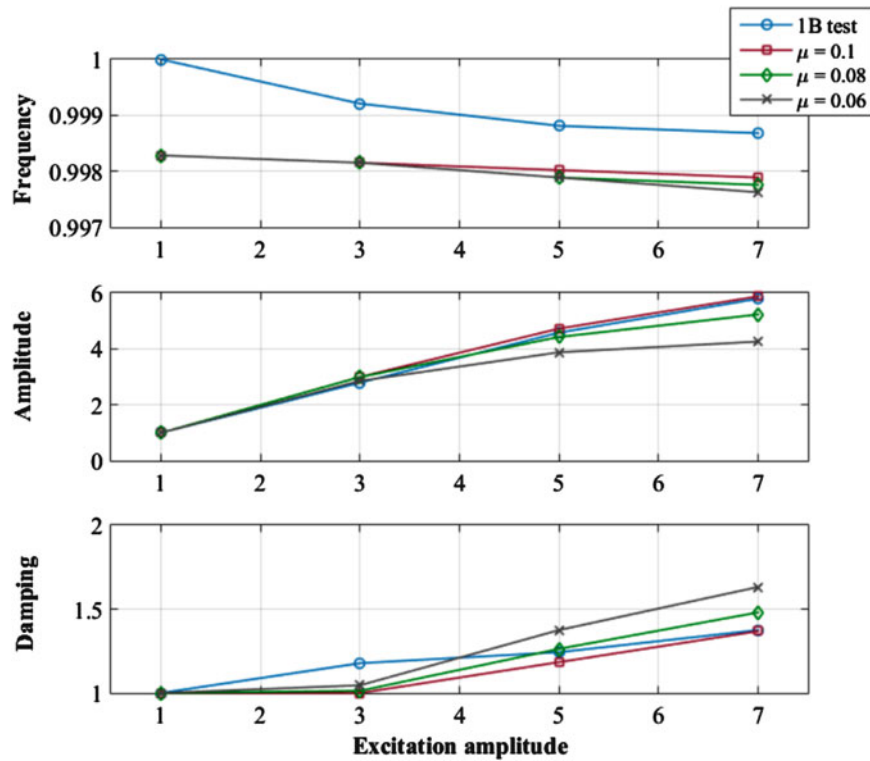


Fig. 37.8 Resonance frequency, response amplitude at resonance and damping in function of excitation amplitude for several friction coefficients for the 1B mode compared to test results

37.4.2 Influence Study on Friction Coefficient μ

In systems including friction non-linearity, the friction coefficient μ is a delicate parameter to predict. Therefore, a sensitivity study is required to calibrate this parameter (Fig. 37.8).

As illustrated by the Fig. 37.8, $\mu = 0.1$ is the best compromise between damping and response amplitude. However, it seems that the simulation and test results are not in the same sliding phase, this will be discussed in the next paragraph. In the remaining part of the paper, the friction coefficient will be set to $\mu = 0.1$.

37.4.3 Correlation for the Three Targeted Modes

Figures 37.9 and 37.10 represent the test/simulation correlation on the 1B, 2B and 1T modes.

A good correlation on the response amplitudes and the damping can be observed between simulations and tests for the first bending mode and this for different excitation levels (Fig. 37.9b). However, the frequency shift on the simulation results is very small compared to the frequency shift obtained experimentally. This frequency shift difference can be interpreted as a difference in the sliding phase in the numerical and experimental results. The Fig. 37.9a) shows that the values of the resonance frequency and damping are equal for excitation amplitudes of one and three. The contact is then stuck for this two excitation amplitudes while a sliding phenomenon can be assumed from an excitation amplitude of 3 on the experimental results.

The experimental and numerical results of the 2B mode (Fig. 37.10a) confirm this theory. Vibration amplitudes being significantly lower than 1B amplitudes, the contact remains stuck for every excitation amplitudes simulated which is demonstrated by a constant resonance frequency and a constant damping for each amplitude. It is therefore expected for vibration amplitudes to be greater in simulations than in tests for the 2B mode.

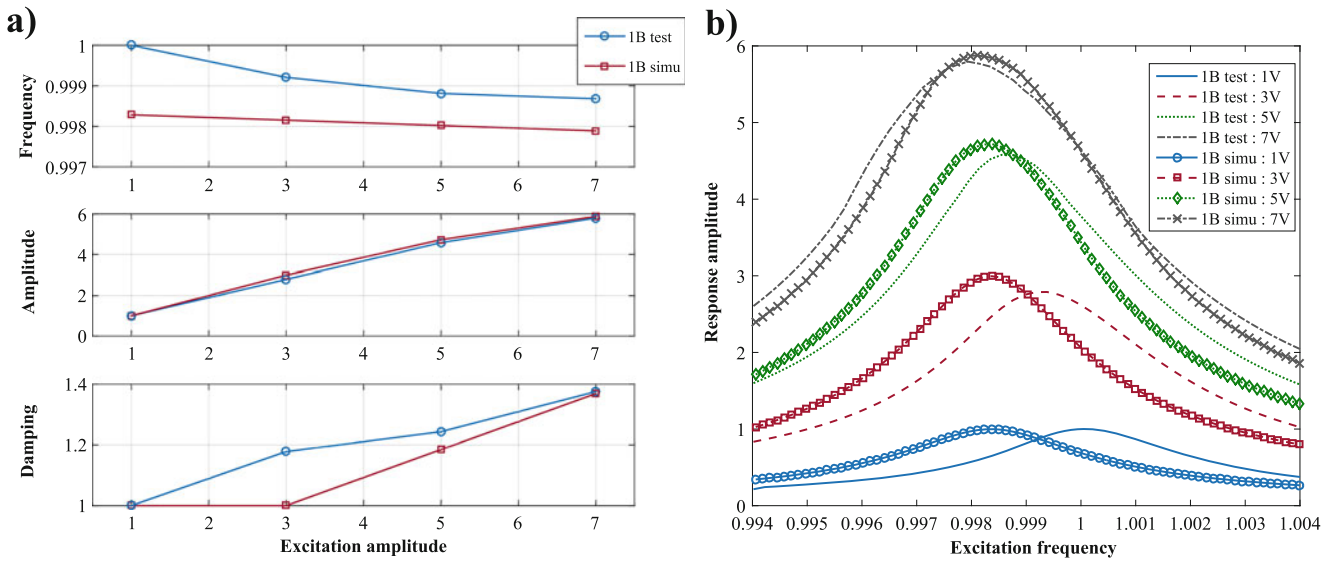


Fig. 37.9 (a) Resonance frequency, response amplitude at resonance and damping in function of excitation amplitude for the 1B mode compared to test results (b) Comparison between simulation and test forced responses for multiple excitation amplitudes

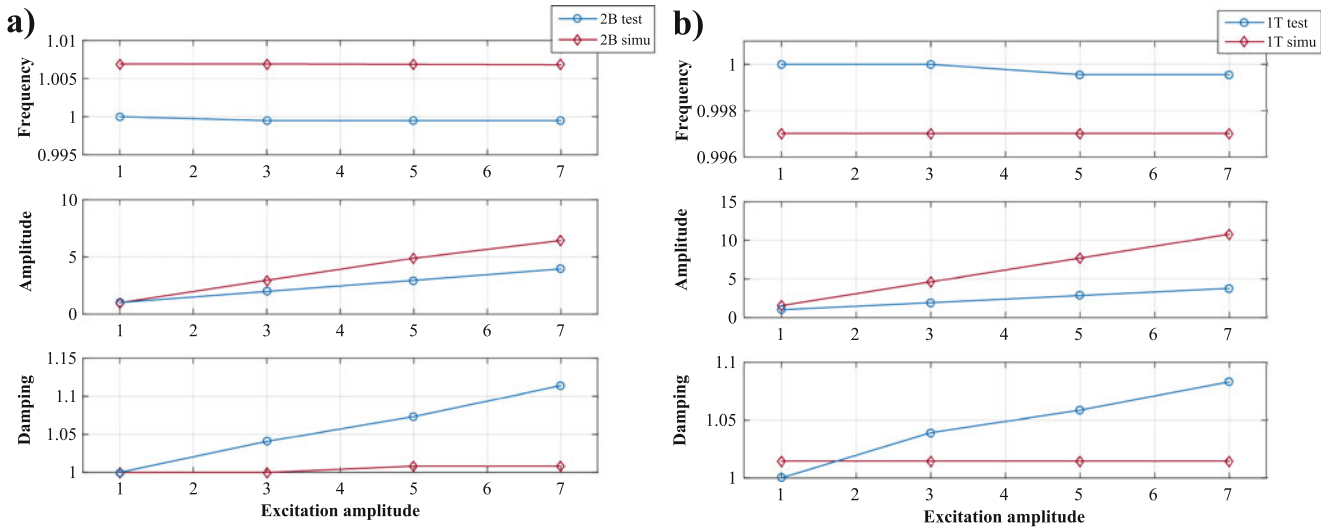


Fig. 37.10 (a) Resonance frequency, response amplitude at resonance and damping in function of excitation amplitude for the 2B mode compared to test results (b) Resonance frequency, response amplitude at resonance and damping in function of excitation amplitude for the 1T mode compared to test results

The same applies for the 1T mode (Fig. 37.10b): the contact remains stuck for every excitation amplitudes simulated. The deviation between the experimental and numerical response amplitudes is far more significant for the 1T mode than for the 2B mode which is due to the already large deviation between linear simulations and low amplitude excitation tests.

Several elements can explain this difference in the sliding phase. First and certainly the dominant factor: a large uncertainty is present in the calculation of the wedge thrust force. This calculation is proportional to the friction coefficient of the screw thread on the borehole thread. Like all friction coefficients, this one is complicated to estimate what introduces a significant uncertainty in the calculation of the thrust force and therefore in the contact force between the blade and the clamping jaws. Secondly, the contact interface has been fitted with foils, however the hypothesis of not taking them into account in the modelling was retained. Foils can act as a third element in contact on interfaces, with their own displacements and forces, and can thus influence the evaluation of nonlinear friction forces.

37.5 Conclusion

In the perspective of a test campaign with a complete fan in rotation in vacuum, these tests performed on clamping jaws allowed to experiment and evaluate the efficiency of the excitation system by piezoelectric actuators, which will also be used during rotational tests. In addition, a correlation between experimental and numerical results could be carried out in order to calibrate our finite element model of the blade but also our non-linear resolution tools in stationary conditions. The piezoelectric actuators could also be modelled and integrated into the non-linear numerical simulation thanks to a condensation technique of internal potentials DOFs presented in this paper. The integration of piezoelectric elements in our nonlinear mechanical model allows to quantify the excitation in the structure and thus to estimate consistent nonlinear responses. An interesting comparison between simulations and test results has been performed. The correlation of linear modal parameters (resonance frequency, resonance amplitude and damping) between linear simulations and low amplitude excitation tests is quite good for the three targeted modes. The correlation between test results and nonlinear simulation including friction at blade attachment is satisfactory but a difference in the sliding phase does not allow a perfect correlation. This difference in the sliding phase has a more important influence on the correlation of results for the 2B and 1T modes that provide less satisfactory correlations. The large uncertainty in the calculation of wedge thrust forces could explain these deviations and the sliding phase difference.

However, these uncertainties will be clarified during the rotating test campaign. Indeed, the centrifugal load is expected to be more accurately defined on the PHARE#1 test rig than the thrust force of the screws on the clamping jaws. Moreover, tests without foils are scheduled in order to evaluate their influence.

Acknowledgments The authors are grateful to Safran Aircraft Engines for providing the financial support allowing to carry out this study. The PHARE#1 test-rig was set up as part of the French Future Investment Program (10-EQPX-0043) and implemented by the French National Research Agency (ANR).

References

- Duffy, K.P., Choi, B.B., Provenza, A.J., Min, J.B., Kray, N.: Active piezoelectric vibration control of subscale composite fan blades. *J. Eng. Gas Turbines Power.* **135**(1), 011601-011601-7 (2012)
- Thierry, O., De Smet, O., Deü, J.-F.: Vibration reduction of a woven composite fan blade by piezoelectric shunted devices. *J. Phys. Conf. Ser.* **744**, 012164 (2016)
- Laxalde, D., Gibert, C., Thouverez, F.: Experimental and numerical investigations of friction rings damping of Blisks. *ASME Turbo Expo.* **2008**, GT2008-G50862 (2008)
- Charleux, D., Gibert, C., Thouverez, F., Dupeux, J.: Numerical and experimental study of friction damping blade attachments of rotating bladed disks. *Int J Rotating Mach.* **2006**, 1–13 (2006)
- Gibert, C., Kharyton, V., Thouverez, F., Jean, P.: On forced response of a rotating integrally bladed disk: predictions and experiments. *ASME Turbo Expo.* **2010**, 1103–1116 (2010)
- Belz, J., May, M., Siemann, J., Seume, J.R., Voigt, C., Böhmer, H., Grüber, B.: Excited blade vibration for Aeroelastic investigations of a rotating Blisk using piezo-electric macro fiber composites. *ASME Turbo Expo.* **2013**, V07BT33A011 (2013)
- ANSYS Inc. Coupling – Piezoelectrics. Theory reference for the Mechanical APDL and Mechanical Applications (12.0), Chapter 11.3 (April 2009)
- IEEE Standard on Piezoelectricity. *ANSI/IEEE Std 176–1987* (1988)
- Allik, H., Hughes, T.J.R.: Finite element method for piezoelectric vibration. *Int. J. Numer. Methods Eng.* **2**, 151–157 (1970)
- Thomas, O., Deü, J.-F., Ducarne, J.: Vibrations of an elastic structure with shunted piezoelectric patches: efficient finite element formulation and electromechanical coupling coefficients. *Int. J. Numer. Methods Eng.* **80**(2), 235–268 (2009)
- Sénéchal, A., Thomas, O., Deü J.-F.: Optimization of shunted piezoelectric patches for vibration reduction of complex structures: application to a turbojet fan blade. *ASME 2010 International Design Engineering Technical Conferences and Computers and Information in Engineering Conference*, pp. 695–704. 1 Jan 2010
- Joannin, C., Chouvion, B., Thouverez, F., Ousty, J.-P., Mbaye, M.: A nonlinear component mode synthesis method for the computation of steady-state vibrations in non-conservative systems. *Mech. Syst. Signal Process.* **83**, 75–92 (2017)
- Bampton, M.C.C., Craig Jr., R.R.: Coupling of substructures for dynamic analyses. *AIAA J.* **6**(7), 1313–1319 (1968)
- Laxalde, D., Thouverez, F.: Complex non-linear modal analysis for mechanical systems: application to turbomachinery Bladings with friction interfaces. *J. Sound Vib.* **322**, 1009–1025 (2009)
- Grolet, A., Thouverez, F.: On a new harmonic selection technique for harmonic balance method. *Mech. Syst. Signal Process.* **30**, 43–60 (2012)
- Nacivet, S., Pierre, C., Thouverez, F., Jezequel, L.: A dynamic Lagrangian frequency–time method for the vibration of dry-friction-damped systems. *J. Sound Vib.* **265**(1), 201–219 (2003)
- Conn, A., Gould, N., Toint, P.: Trust Region Methods. *MOS-SIAM Series on Optimization*. Society for Industrial and Applied Mathematics (2000)
- Laxalde, D., Salles, L., Blanc, L., Thouverez, F.: Non-linear modal analysis for bladed disks with friction contact interfaces. *ASME Turbo Expo.* **2008**, 457–467 (2008)
- Gibert, C.: Fitting measured frequency response using non-linear modes. *Mech. Syst. Signal Process.* **17**(1), 211–218 (2003)



Chapter 38

Locating Nonlinearity in Mechanical Systems: A Dynamic Network Perspective

J. P. Noël, M. Schoukens, and P. M. J. Van den Hof

Abstract Though it is a crucial step for most identification methods in nonlinear structural dynamics, nonlinearity location is a sparsely addressed topic in the literature. In fact, locating nonlinearities in mechanical systems turns out to be a challenging problem when treated nonparametrically, that is, without fitting a model. The present contribution takes a new look at this problem by exploiting some recent developments in the identification of dynamic networks, originating from the systems and control community.

Keywords Nonlinear structural dynamics · Nonlinear system identification · Nonlinearity location · Best linear approximation · Dynamic networks

38.1 Introduction

The identification of linear dynamic networks has attracted increasing attention over the past few years. An example of linear network is displayed in Fig. 38.1. It consists of three nodes, where the signal $w_i(t)$ measured at node i is the sum of the applied reference signal $r_i(t)$, the noise signal $v_i(t)$ and the outputs $y_{i,k}(t)$ of the linear blocks $G_{i,k}(j\omega)$ that point towards it. The majority of the contributions in the field has so far dealt with obtaining consistent estimates of linear block dynamics under different noise assumptions [1–3]. In a recent study [4], some research attention has eventually been turned to the detection and location of nonlinearities in networks using linear approximation techniques.

Approximating nonlinear systems for topology detection is not a new idea and various approaches exist [5, 6], but a common thread is the definition of an optimality criterion for the approximation that holds within a given class of systems and under a certain class of excitation signals. In the present work, the Best Linear Approximation (BLA) of Volterra nonlinear systems is exploited, assuming Gaussian excitation signals [7]. Applying the BLA to mechanical systems has already proved successful for nonlinearity detection [8, 9]. In this contribution, by interpreting mechanical systems as dynamic networks and following the methodology introduced in Ref. [4], and described in Sect. 38.2, we extend the use of the BLA in structural dynamics to nonlinearity *location*. A demonstration on a three-degree-of-freedom system is proposed in Sect. 38.3.

38.2 Methodology

The key assumption to a proper application of the BLA framework is that noise must only corrupt output measurements [7]. This prevents one from directly calculating the BLA from node to node in a dynamic network setting. To circumvent this issue, a three-step methodology is followed, leading a rigorous nonlinearity detection and location procedure.

J. P. Noël (✉)

Space Structures and Systems Laboratory, Department of Aerospace and Mechanical Engineering, University of Liège, Liège, Belgium
e-mail: jp.noel@uliege.be; jp.noel@ulg.ac.be

M. Schoukens · P. M. J. Van den Hof

Control Systems Group, Technical University of Eindhoven, Eindhoven, The Netherlands
e-mail: m.schoukens@tue.nl; p.m.j.vandenhof@tue.nl

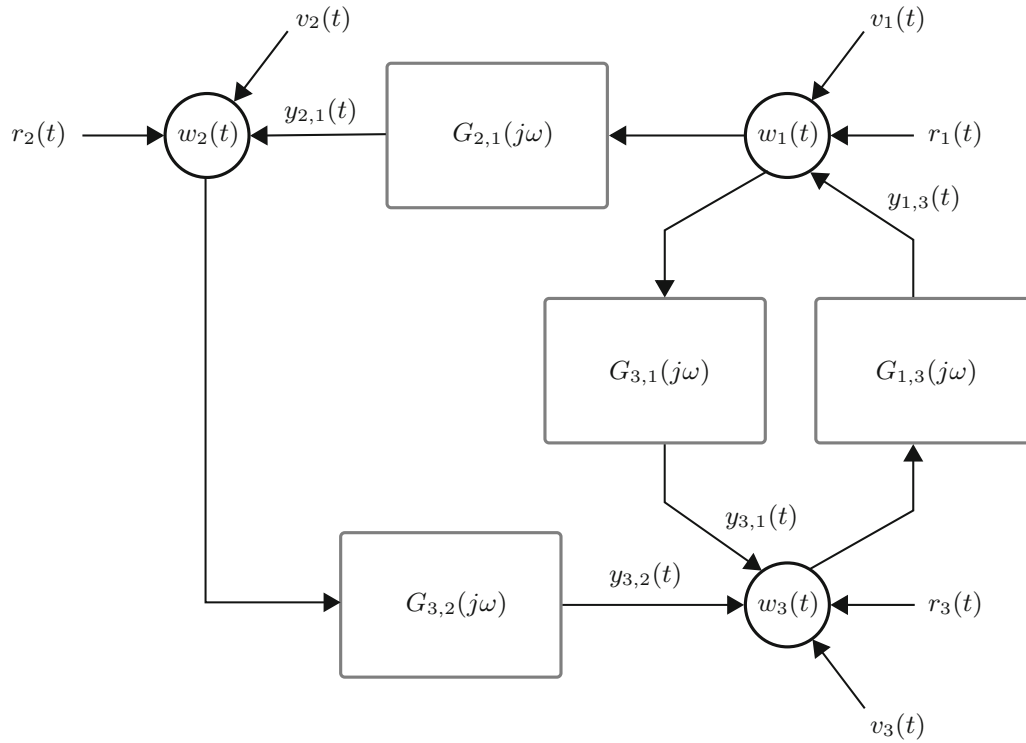


Fig. 38.1 An example of a linear dynamic network with three nodes and four linear dynamic blocks

38.2.1 Step 1: BLA Analysis from References to Nodes

The first step consists in calculating a multi-input, multi-output (MIMO) BLA from all references to all nodes. It is defined from reference k to node i as the transfer function $S_{BLA}^{i,k}(j\omega)$ providing the best linear approximation of the nonlinear network dynamics in least-squares sense, i.e.

$$S_{BLA}^{i,k}(j\omega) = \arg_{S^{i,k}} \min_{E_{r,v}} \left\{ \sum_{i=1}^{n_w} \left| w_i(j\omega) - \sum_{k=1}^{n_r} S_{i,k}(j\omega) r_k(j\omega) \right|^2 \right\}. \quad (38.1)$$

The expectation $E_{r,v} \{\bullet\}$ is taken with respect all possible realisations of the reference signal r_k and noise signal v_i , within the considered signal class. In Eq. (38.1), reference and node signals are assumed to be zero-mean.

Equation (38.1) allows one to calculate a noise-free linear approximation $\bar{w}_i(j\omega)$ of the node signal $w_i(j\omega)$ that writes

$$\bar{w}_i(j\omega) = \sum_{k=1}^{n_r} S_{BLA}^{i,k}(j\omega) r_k(j\omega). \quad (38.2)$$

38.2.2 Step 2: BLA Analysis from Nodes to Nodes

A second MIMO BLA analysis is carried out in between nodes, considering as inputs the noise-free node signals from Eq. (38.2), and taking into account the direct contributions of the references. This results in BLA estimates $G_{BLA}^{i,k}(j\omega)$ from node i to node k of the form

$$G_{BLA}^{i,k}(j\omega) = \arg_{G^{i,k}} \min_{E_{r,v}} \left\{ \sum_{i=1}^{n_w} \left| w_i(j\omega) - \sum_{k=1}^{n_r} S_{i,k}(j\omega) r_k(j\omega) \right|^2 \right\}. \quad (38.3)$$

Node signals can now be simulated using the node-to-node linear approximate description $G_{BLA}^{i,k}(j\omega)$ of the network dynamics, leading to the relation

$$\bar{w}_i(j\omega) = r_i(j\omega) + \sum_{k=1, \neq i}^{n_w} G_{BLA}^{i,k}(j\omega) w_k(j\omega). \quad (38.4)$$

38.2.3 Step 3: Residual Analysis and Nonlinearity Location

By comparing the simulated node signals $\bar{w}_i(j\omega)$ and the corresponding measurements $w_i(j\omega)$ over multiple periods and realisations, a residual analysis can be conducted. Let P and M be the number of measured periods and realisations of the network signals, and $\bar{w}_i^{[m,p]}(j\omega)$ and $w_i^{[m,p]}(j\omega)$ be the simulated and measured node signals over period p of realisation m , respectively. The variances of the total distortions σ_t^2 , noise distortions σ_n^2 and nonlinear distortions σ_{nl}^2 in the residual are then separated following the expressions [10]

$$\sigma_t^2(j\omega) = \frac{1}{P} \frac{1}{M-1} \sum_{p=1}^P \sum_{m=1}^M \left(e_i^{[m,p]}(j\omega) - \frac{1}{P} \sum_{m=1}^M e_i^{[m,p]}(j\omega) \right)^2; \quad (38.5)$$

$$\sigma_n^2(j\omega) = \frac{1}{M} \frac{1}{P-1} \sum_{m=1}^M \sum_{p=1}^P \left(e_i^{[m,p]}(j\omega) - \frac{1}{P} \sum_{p=1}^P e_i^{[m,p]}(j\omega) \right)^2; \quad (38.6)$$

$$\sigma_{nl}^2(j\omega) = \sigma_t^2(j\omega) - \sigma_n^2(j\omega), \quad (38.7)$$

where

$$e_i^{[m,p]}(j\omega) = \bar{w}_i^{[m,p]}(j\omega) - w_i^{[m,p]}(j\omega). \quad (38.8)$$

The comparison along the frequency axis of the three variance levels $\sigma_t^2(j\omega)$, $\sigma_n^2(j\omega)$ and $\sigma_{nl}^2(j\omega)$ provides a quantitative way of detecting and locating nonlinearities in any network arrangement of linear dynamic subsystems.

38.3 Application to a Three-Degree-of-Freedom Mechanical System

The present section illustrates the methodology described in Sect. 38.2 considering the three-mass system of Fig. 38.2. The physical parameters and modal properties of the system are listed in Tables 38.1 and 38.2, respectively. A cubic spring is introduced between mass 3 and the ground. Multisine excitations are applied to the three masses, and displacements

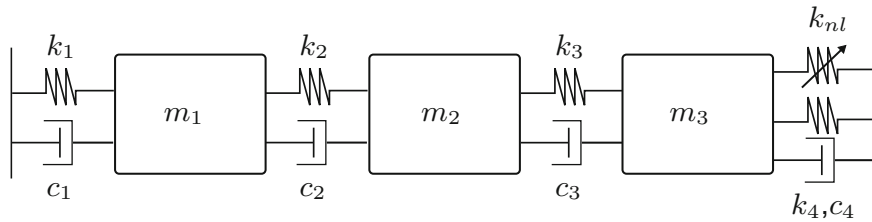


Fig. 38.2 A three-mass system with one cubic spring connecting mass 3 to the ground

Table 38.1 Physical parameters of the three-mass system

Parameter	Value
m_1	1 kg
m_2	0.8 kg
m_3	1.2 kg
k_1	20 10^3 N/m
k_2	35 10^3 N/m
k_3	50 10^3 N/m
k_4	80 10^3 N/m
k_{nl}	1 10^8 N/m ³
c_{1-4}	8 Ns/m

Table 38.2 Linear modal properties of the three-mass system

Mode	Frequency (Hz)	Damping ratio (%)
1	25.0	2.0
2	44.8	2.7
3	64.8	3.4

are processed as output data. Multisines are periodic signals with a user-defined amplitude spectrum and randomly-chosen phases [11]. In this application, they excite the system in the 5–100 Hz band with a root-mean-square amplitude of 50 N. Response signals are generated using a nonlinear Newmark integration algorithm with a sampling frequency of 5000 Hz, and numerical experiments are repeated over 10 periods and 30 realisations with 8192 measured samples per period. The resulting displacement time signals are corrupted with white Gaussian noise with a signal-to-noise ratio of 40 dB.

The result of the residual analysis performed through Eqs. (38.5), (38.6), (38.7) and (38.7) is shown in Fig. 38.3. The spectra of the signals $\bar{w}_i(t)$ and the noise levels are displayed using grey and black lines, respectively. The total and nonlinear distortions are plotted using orange crosses and blue squares, respectively. It is easily concluded from these three graphs that mass 3 in Fig. 38.3c is the only node in the system connected to a nonlinear element. For masses 1 and 2 in Fig. 38.3a, b, the observed total distortion level is fully explained by the noise disturbances, implying that they are not directly connected to a nonlinearity.

38.4 Conclusions and Perspectives

This contribution introduced an original methodology to locate nonlinearities in mechanical systems using random excitation signals. The proposed technique is fully nonparametric, i.e. it requires no estimation of parameters. It relies on the use of the Best Linear Approximation (BLA) of the nonlinear dynamics taking place in between the masses of the considered system, interpreted as a network arrangement of nodes. Its graphical outcome is a frequency-domain plot per measurement location comparing the amplitude of the nonlinear and the noise distortions, and hence enabling the user to assess quantitatively and systematically the impact of nonlinearity across the tested structure. Further developments in this research will focus on relaxing the current need for multi-input, multi-output experiments, through the concatenation of data measured sequentially in single-input conditions.

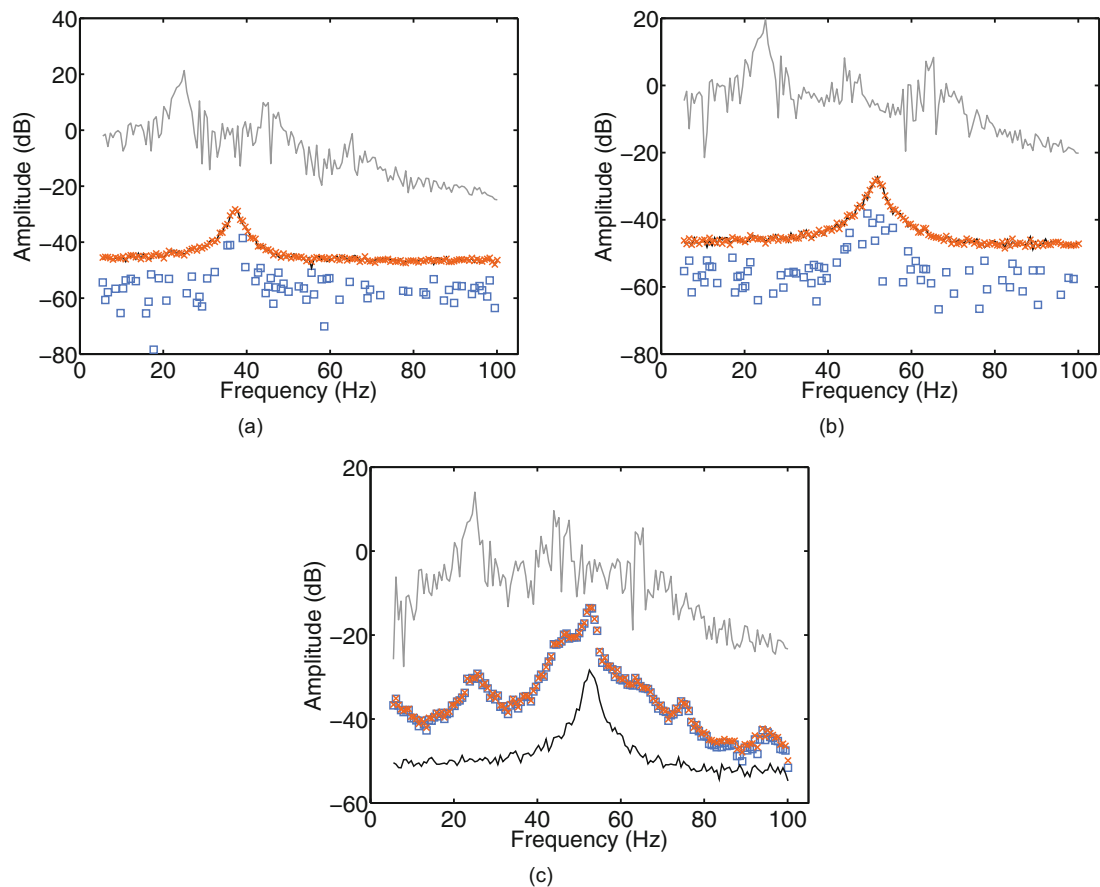


Fig. 38.3 Locating nonlinearity in the three-mass system. (a–c) mass 1–3. The spectra of the signals $\bar{w}_i(t)$ and the noise levels are displayed using grey and black lines, respectively. The total and nonlinear distortions are plotted using orange crosses and blue squares, respectively

Acknowledgements The author J.P. Noël is a Postdoctoral Researcher of the *Fonds de la Recherche Scientifique – FNRS* which is gratefully acknowledged.

References

1. Van den Hof, P., Dankers, A., Heuberger, P., Bombois, X.: Identification of dynamic models in complex networks with prediction error methods – basic methods for consistent module estimates. *Automatica* **49**, 2994–3006 (2013)
2. Dankers, A., Van den Hof, P., Bombois, X., Heuberger, P.: Errors-in-variables identification in dynamic networks – consistency results for an instrumental variable approach. *Automatica* **62**, 39–50 (2015)
3. Weerts, H.H., Van den Hof, P., Dankers, A.G.: Identification of dynamic networks with rank-reduced noise. *IFAC PapersOnLine* **50**(1), 10562–10567 (2017)
4. Schoukens, M., Van den Hof, P.: Detecting and quantifying nonlinearity in dynamic networks. *Automatica* (2017, in review)
5. Schoukens, J., Pintelon, R., Rolain, Y., Schoukens, M., Tiels, K., Vanbeylen, L., Van Mulders, A., Vandersteen, G.: Structure discrimination in block-oriented models using linear approximations: a theoretic framework. *Automatica* **53**, 225–234 (2015)
6. Schoukens, M., Tiels, K.: Identification of block-oriented nonlinear systems starting from linear approximations: a survey. *Automatica* **85**, 272–292 (2017)
7. Schoukens, J., Vaes, M., Pintelon, R., Linear system identification in a nonlinear setting. *IEEE Control Syst.* **36**(3), 38–69 (2016)
8. Wernholt, E., Gunnarsson, S.: Estimation of nonlinear effects in frequency domain identification of industrial robots, *IEEE Trans. Instrum. Meas.* **57**(4), 856–863 (2008)
9. Vaes, M., Schoukens, J., Peeters, B., Debillé, J., Dossogne, T., Noël, J., Grappasonni, C., Kerschen, G.: Nonlinear ground vibration identification of an F-16 aircraft – part 1: fast nonparametric analysis of distortions in FRF measurements. In: *Proceedings of the International Forum on Aeroelasticity and Structural Dynamics (IFASD)*, Saint Petersburg (2015)
10. Schoukens, J., Swevers, J., Pintelon, R., Van der Auweraer, H.: Excitation design for FRF measurements in the presence of non-linear distortions. *Mech. Syst. Signal Process.* **18**, 727–738 (2004)
11. Pintelon, R., Schoukens, J.: *System Identification: A Frequency Domain Approach*. IEEE Press, Piscataway (2001)

Chapter 39

Tracing a Prescribed Force-Displacement Curve Using Topology Optimization



Jongsuh Lee, Thibaut Detroux, and Gaetan Kerschen

Abstract The objective of this study is to develop an optimization methodology to trace a prescribed force-displacement curve. For this purpose, we employ the topology optimization to find the layout of a structure that minimizes the difference from the predefined force-displacement curve. In addition, we propose a constraint that is necessary for the initial design of the structure to escape from its inherent nonlinearities. The effectiveness of the proposed method is verified by performing a simulation with a thin plate.

Keywords Force-displacement curve · Topology optimization · Hardening and softening nonlinearities · Slope constraint

39.1 Introduction

The generalized Hook's law is not valid if a structure is under large deformation, meaning that the force-displacement (F-D) curve exhibits nonlinear behavior due to geometric nonlinearity. Geometric nonlinearities can be of the softening or hardening types, i.e., variations of displacement with respect to increasing external force is decreased or increased, respectively [1]. For instance, a thin plate is governed by the hardening nonlinearity in general [1, 2]. In the present, we propose a methodology to find the layout of a structure that traces a predefined F-D curve in which softening, hardening, or both nonlinearities are involved. If the nonlinearity in the prescribed F-D curve differs from the inherent nonlinearity in the initial design—for instance, the softening nonlinearity for a thin plate—it may seem impossible to find a layout that thoroughly follows the prescribed curve in the optimization problem. Therefore, we take the slope of the curve into account as well as the values of the prescribed F-D curve in order to adapt to the nonlinearities on the curve. The slope is involved in the optimization problem as a constraint. Simulation is performed to verify the proposed method, in which a thin plate is used. In the simulation, the St. Venant-Kirchhoff model [3] is used to describe the behavior of the material. The purpose of the simulation in this work is to find the layout of the structure that exhibits a softening behavior.

39.2 Optimization Formulas

To find a structural layout tracing a given F-D curve, the following optimization formulation was considered:

$$\text{Min}_{\rho} c = \sum_i^N [u(f_i) - u_i^*]^2 \quad (39.1)$$

$$\text{st} : \theta_i^{\min} \leq s(f_i) \leq \theta_i^{\max}, \quad i = 1, N \quad \text{where } s(f_i) = \left. \frac{df}{du} \right|_{f=f_i} \quad (39.2)$$
$$V_{\min} \leq \frac{V(\rho)}{V_0} \leq V_{\max}, \quad 0 < \rho_e < 1$$

J. Lee · T. Detroux

Space Structures and Systems Laboratory (S3L), University of Liège, Department of Aerospace and Mechanical Engineering, Liège, Belgium
e-mail: jongsuh.lee@ulg.ac.be

G. Kerschen (✉)

Mechanical Engineering, S3L, Quartier Polytech, University of Liege, Department of Aerospace, Liege, Belgium
e-mail: g.kerschen@uliege.be

In this formula, u and u^* denote the displacement when the external force f is applied and the prescribed displacement at the corresponding force f , respectively. N is the number of load steps and ρ is the design variable. In Eq. (39.1), c is a scalar objective function measuring the sum of the differences between the actual displacement u and the target displacement u^* for N steps of given loads. Equation (39.2) shows defined constraints. Here, s represents a slope on the F-D curve at external force f and it is bounded by two prescribed values: θ^{\min} and θ^{\max} . V_{\min} and V_{\max} are prescribed minimum and maximum volume fraction values.

39.3 Simulation

The proposed method is demonstrated on a thin plate. The initial layout used in the optimization problem and its essential and natural boundary conditions are depicted in Fig. 39.1a. The total number of elements is 6000 (25×240).

Figure 39.1b shows three F-D curves that are measured from the initial design layout (■ ▼ ■), prescribed (★), and measured from the optimized layout (○). The curve measured from the initial layout looks like a straight line, but it is slightly curved upward, meaning that the initial design behaves with the hardening nonlinearity. The prescribed (target) curve depicts the softening nonlinearity. Therefore, in the optimization process, the inherent nonlinearity must be converted from hardening to softening, and the slope constraint in Eq. (39.2) helps this conversion. Figure 39.1c shows the optimized layout, and the measured F-D curve from this layout is plotted in Fig. 39.1b. It agrees well with the prescribed curve.

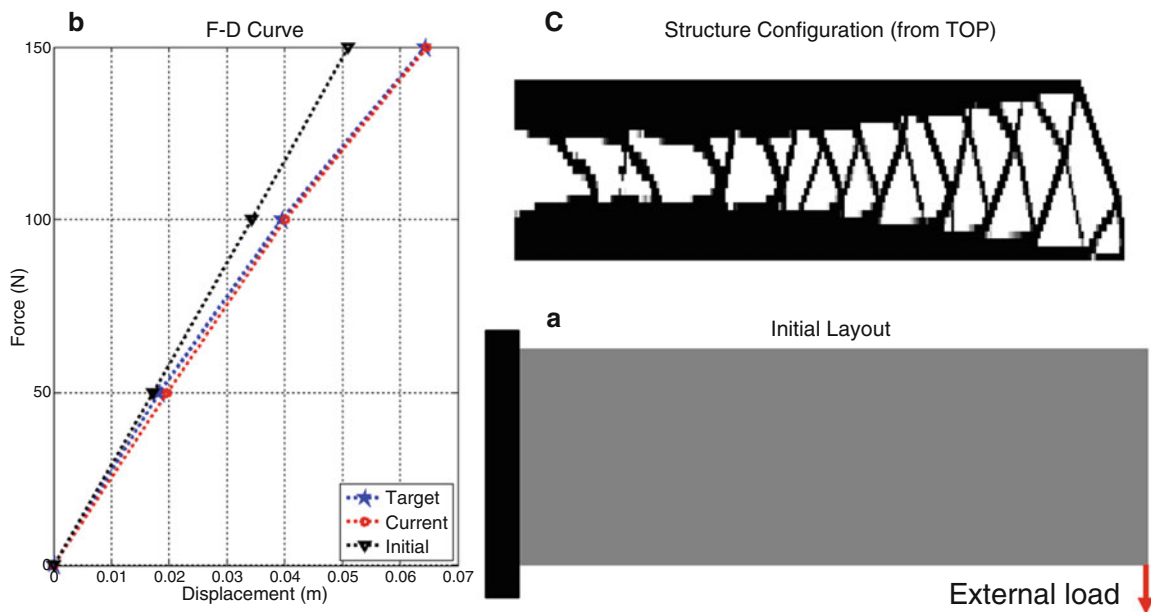


Fig. 39.1 (a) Initial design layout and its essential and natural boundary conditions; (b) three F-D curves measured from the initial layout (■ ▼ ■), prescribed (★) in the optimization problem, and measured from the optimized layout (○); (c) optimized layout from the topology optimization

39.4 Conclusion

This study introduced an optimization methodology to find a structural layout that traces a prescribed curve, in which the slope of the prescribed F-D curve is involved. The effectiveness of the proposed approach was demonstrated by a simulation in which a thin plate is employed and the softening behavior is set as a target curve.

Acknowledgement This work was fully supported by the European Commission of Marie Curie COFUND (600405). The author T. Detroux is a Postdoctoral Researcher of the *Fonds de la Recherche Scientifique – FNRS* which is gratefully acknowledged.

References

1. Reddy, J.N.: Theory and Analysis of Elastic Plates and Shells, 2nd edn. CRC Press, London (2007)
2. Lee, J., Detroux, T., Kerschen, G.: Harmonic balance computation of the nonlinear frequency response of a thin plate. In: 24th International Congress on Sound and Vibration (ICSV24), London (2017)
3. Kim, N.: Introduction to Nonlinear Finite Element Analysis. Springer, Gainesville (2015)



Chapter 40

Model Updating of a Wing-Engine Structure with Nonlinear Connections

Mingming Song, Ludovic Renson, Jean-Philippe Noël, Babak Moaveni, and Gaetan Kerschen

Abstract This paper investigates the performance of a Bayesian model updating approach using nonlinear normal modes (NNMs). The proposed approach is applied to a wing-engine structure tested in the laboratory. The structure response to a broadband input excitation is measured experimentally. The structure NNMs are then extracted from the measured data by combining a frequency-domain nonlinear subspace identification method with numerical continuation technique. An initial finite element model of the wing-engine structure is built in Matlab and its linear stiffness parameters and the coefficients of the local nonlinearities are selected as the updating parameters. The joint posterior probability distribution of the model parameters is estimated based on their prior distribution and the likelihood function which is defined as a Gaussian distribution of error function. The error function in this study is defined as the difference between model-predicted and identified NNMs at different energy levels. The calibrated model is then used to predict the structure response (NNMs and time history), taking into account model parameters uncertainties and modeling errors. The model predictions are compared with a set of experimental results that were not used in the calibration process and only considered for validation purpose.

Keywords Bayesian model updating · System identification · Nonlinear normal modes · Uncertainty propagation · Modeling error

The wing-engine structure shown in Fig. 40.1 is tested in a laboratory and its response to broadband input excitation is measured experimentally. Previous investigations [1] showed that the structure exhibits evident nonlinearity and a 5:1 modal interaction between the first and fourth modes of the structure. The nonlinear normal modes (NNMs) of the structure are identified following the two-step, phase separation method proposed in Ref. [2]. First, a frequency-domain nonlinear subspace identification (FNSI) method is exploited to identify a state-space model of the tested structure. Second, a shooting and pseudo-arclength continuation method [3] is used to compute the structure NNMs.

A finite element (FE) model of the wing-engine structure is built in Matlab for the purpose of model updating. The Bayesian model updating framework using NNMs is applied to the FE model of the wing-engine structure. This study represents the first application of this method to experimental data. The linear stiffness parameters and the coefficients of the local nonlinearities are selected as the updating parameters. The error function is defined as the difference between model-predicted and identified NNMs at different energy levels and assumed to follow a zero-mean Gaussian distribution. The error function is then utilized to derive the likelihood function of the updating parameters based on identified NNMs. According to Bayes' theorem, the posterior distribution function is proportional to the product of likelihood function and the prior function:

$$p(\boldsymbol{\theta}|\mathbf{d}) \propto p(\mathbf{d}|\boldsymbol{\theta})p(\boldsymbol{\theta}) \quad (40.1)$$

M. Song · B. Moaveni (✉)
Department of Civil and Environmental Engineering, Tufts University, Medford, MA, USA
e-mail: babak.moaveni@tufts.edu

L. Renson
Department of Engineering Mathematics, University of Bristol, Bristol, UK

J.-P. Noël
Space Structures and Systems Laboratory, Department of Aerospace and Mechanical Engineering, University of Liege, Liege, Belgium

G. Kerschen
Mechanical Engineering, S3L, Quartier Polytech, University of Liege, Department of Aerospace, Liege, Belgium



Fig. 40.1 The tested wing-engine structure

in which $\boldsymbol{\theta}$ denotes the updating parameters, \mathbf{d} refers to the measured data, $p(\boldsymbol{\theta}|\mathbf{d})$ is the posterior distribution function, $p(\mathbf{d}|\boldsymbol{\theta})$ is the likelihood function, $p(\boldsymbol{\theta})$ is the prior function. By assuming an uninformative prior function $p(\boldsymbol{\theta})$ (uniform distribution), the posterior distribution function will be proportional to the likelihood function which can be derived as:

$$L(\boldsymbol{\theta}|\mathbf{d}) = \prod_{i=1}^{N_m} \frac{1}{(2\pi)^N \sigma_{\lambda_i}^N \sigma_{\phi_i}^{NN_s}} \exp \left[-\frac{1}{2} \sum_{j=1}^N \left(\sum_{i=1}^{N_m} \frac{(\lambda_i(\boldsymbol{\theta}) - \tilde{\lambda}_i^j)^2}{\sigma_{\lambda_i}^2 (\tilde{\lambda}_i^j)^2} + \sum_{i=1}^{N_m} \frac{\|\phi_i(\boldsymbol{\theta}) - \gamma_i \tilde{\phi}_i^j\|^2}{\sigma_{\phi_i}^2 \|\gamma_i \tilde{\phi}_i^j\|^2} \right) \right] \quad (40.2)$$

in which N is the number of datasets, N_m is the number of modes, N_s is the mode shape components, $\lambda = \omega^2$ where ω is circular frequency, ϕ is mode shape, σ_{λ} and σ_{ϕ} is the standard deviation of λ and mode shapes respectively, γ is mode shape scaling factor.

Markov Chain Monte Carlo (MCMC) algorithms (Metropolis-Hastings and Transitional MCMC) are used to sample the derived posterior distribution function and evaluate the maximum-a-posteriori (MAP) estimator $\hat{\boldsymbol{\theta}}^{MAP}$. This Bayesian model updating approach is also performed to calibrate another FE model with significant modeling errors for the purpose of verification and comparison. The two calibrated models are then used to predict the structure response (NNMs and time history) by accounting for model parameters uncertainties and modeling errors. The model predictions are then compared with a set of experimental results which were not used in the calibration process and only considered for validation purpose.

References

1. Renson, L., Noël, J., Barton, D., Neild, S., Kerschen, G.: Nonlinear phase separation testing of an experimental wing-engine structure. In: Rotating Machinery, Hybrid Test Methods, Vibro-Acoustics & Laser Vibrometry, vol. 8, pp. 115–117. Springer (2017)
2. Noël, J.-P., Renson, L., Grappasonni, C., Kerschen, G.: Identification of nonlinear normal modes of engineering structures under broadband forcing. Mech. Syst. Signal Process. **74**, 95–110 (2016)
3. Peeters, M., Vigué, R., Sérandour, G., Kerschen, G., Golinval, J.C.: Nonlinear normal modes, Part II: toward a practical computation using numerical continuation techniques. Mech. Syst. Signal Process. **23**, 195–216 (2009)



Chapter 41

Modal Analysis of Axially Deforming Rods with Isolated Lap Joints

D. Dane Quinn

Almost every modern engineering structure incorporates some form of mechanical interface, a connection between two otherwise separate mechanical structures. Complex machines and structures such as automobiles, bridges, aircraft, rockets, etc. rely heavily on these interfaces; however, high-fidelity numerical analysis of such connected structures is currently extremely difficult and computationally expensive due to the disparate length and time scales of the interface as compared to those characterizing the overall structure.

This work describes recent developments in the reduced order modeling of structures with isolated interfaces. In particular, the response of the mechanical system with interfaces can be described in terms of the corresponding monolithic system, with the addition of isolated contributions of the interface that are assumed to be small compared to those that are derived from the monolithic system. As a result, the underlying modal structure of the monolithic system can be used to describe the response of the jointed structure. Further, the contributions from the interface can be described in terms of a physically motivated reduced-order model, so that nonlinear damping and mode coupling are an integral part of the observed response. This approach is applied to study the dynamic response of axially deforming lap joints. The results show that the reduced-order model is capable of reproducing experimentally observed characteristics of the system, including mode coupling and softening effects with increasing excitation. Further, the model easily incorporates both transient and the forced response of the system.

Consider a uniform rod of length $\ell = 1$ that contains an internal joint located in the interval $x \in (x_1, x_2) = (0.45, 0.55)$ with a uniform frictional intensity at the interface [4]. Outside of the isolated joint interval the system is described by the equations of motion for the axial vibrations of a linearly elastic rod. However, within the isolated joint region microslip can occur due to the presence of the interface, and the governing equations are no longer linear within this region. The development of reduced order model for an elastic rod with a single interface, together with an expansion in terms of the modes of the monolithic system was developed previously in [3]. The response of the rod $u(s, \tau)$ can be expanded in terms of the spatial functions $\phi_j(s)$ as

$$u(s, \tau) = \sum_{j=1}^{\infty} A_j(\tau) \phi_j(s), \quad (41.1)$$

leading to modal equations of the form

$$\frac{\partial^2 A_i}{\partial \tau^2}(\tau) + \lambda_i \frac{\partial A_i}{\partial \tau}(\tau) + \omega_i^2 A_i(\tau) = \hat{f}_i(\tau) + \delta Q[\Delta(\tau)] (\phi_i(s_2) - \phi_i(s_1)), \quad (41.2)$$

where ω_i is modal frequency corresponding to the eigenmode $\phi_i(s)$, λ_i is the i th modal damping coefficient, and $\hat{f}_i(\tau)$ is the modal forcing. If $Q_i^{\mathcal{J}}(t)$ represents the axial tension in the jointed structure at $x = x_i$ and $Q_i^{\mathcal{M}}(t)$ is the axial tension in the monolithic structure at $x = x_i$, then this deviatoric force is defined as $\delta Q_i(t) = Q_i^{\mathcal{J}}(t) - Q_i^{\mathcal{M}}(t)$.

D. Dane Quinn (✉)

Department of Mechanical Engineering, The University of Akron, Akron, OH, USA
e-mail: quinn@uakron.edu

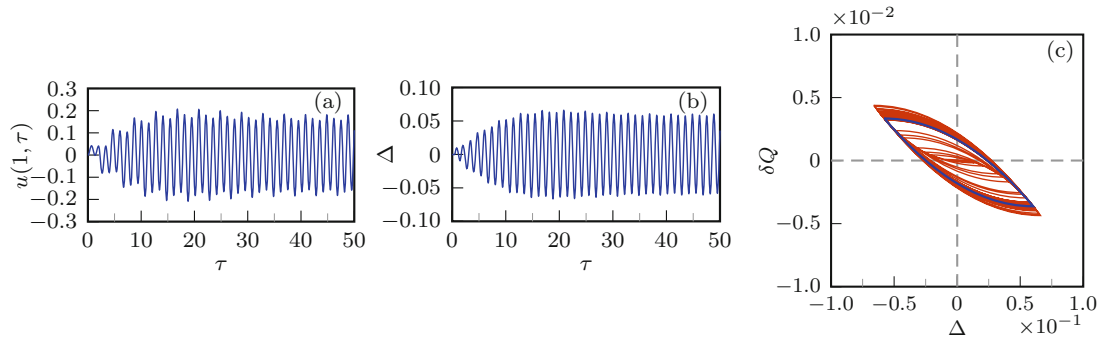


Fig. 41.1 Forced response ($F_0 = 0.1$, $\Omega = 3\pi/2$); (a) $u(1, \tau)$, (b) $\Delta(\tau)$, (c) hysteretic curve

Note that this description requires that the interface force $\delta Q_i(t)$ be known, and the above equation provides the response of the structure outside the interfacial region. In [3] a reduced-order model for δQ_i was developed based on the hysteretic response of a continuum interfacial element developed by [2], with $\delta Q_2 = -\delta Q_1 \equiv \delta Q$. This deviatoric force is obtained from a specified unidirectional backbone curve together with Masing's hypotheses, so that δQ is a hysteretic function of $d(t)$, expressed as $\delta Q(t) = \delta Q[d(t)]$. While the equation governing each mode given in Eq. (41.2) appears decoupled from the remaining modes, they are in fact coupled together through Δ , the displacement across the interface. Retaining a finite N modes, this can be written as

$$\Delta(\tau) = \sum_{j=1}^N A_j(\tau) (\phi_j(s_2) - \phi_j(s_1)), \quad (41.3)$$

leading to a system of N coupled equations of motion to determine the modal displacements $A_i(\tau)$, $i = 1, \dots, N$.

If the nondimensional linear density and axial rigidity are defined as $\rho \equiv 1$ and $EA \equiv 1$, then the modal frequencies ω_i and mode shapes $\phi_i(s)$ are determined to be

$$\omega_i = \frac{(2i-1)\pi}{2}, \quad \phi_i(s) = \sqrt{2} \sin(\omega_i s), \quad i = 1, 2, \dots \quad (41.4)$$

The modal damping coefficient for each mode is assumed to be $\lambda_i = 0.005$ and the simulations are carried out using the lowest $N = 16$ modes of the system. Finally, a single-frequency excitation applied to the end of the bar at $s = 1$ of the form $F(\tau) = F_0 \sin \Omega \tau$.

The modal equations given in Eqs. (41.2) and (41.3) can be numerically integrated to determine the response of the system. The forced response of the rod is illustrated when excited at the frequency of the second mode ($\Omega = \frac{3\pi}{2}$). In Fig. 41.1a the displacement at the end of the rod ($s = 1$) is shown as a function of time, while the displacement across the interface, located across the interval $s \in (0.45, 0.55)$ is shown in Fig. 41.1b—both are dominated by the second mode. Finally, the hysteretic curve between the interfacial force δQ and the corresponding displacement Δ is shown in Fig. 41.1c. Note that in this figure the final cycle of the integration is emphasized with the heavier curve.

The modal filtered frequency response functions (FRFs) for the system are shown in Figs. 41.2 and 41.3 for the lowest three modes, corresponding to $A_i(\tau)$, $i = 1, 2, 3$. In the absence of the interface each of the modal FRF curves would be decoupled, however, as the amplitude of the excitation increases (F_0) significant evidence of mode coupling is observed. As seen in Fig. 41.2a, for low forcing amplitude ($F_0 = 0.01$) the modes show little coupling—when the system is excited near the resonant frequency of the lowest mode ($\Omega = \frac{\pi}{2}$) the remaining modes are only slightly affected. However, as the excitation amplitude increases ($F_0 = 0.1$ in Fig. 41.2b and $F_0 = 0.20$ in Fig. 41.2b) the non-resonant modes exhibit significant peaks in their response due to the coupling between modes provided by the interface. This behavior can be clearly observed in Fig. 41.3a, which focuses on modes 1 and 2 in the neighborhood of the lowest natural frequency of the rod in the absence of the interface (cf. Eq. (41.4)).

In addition to the mode coupling, the presence of the interface introduces significant nonlinearity in the response, easily observed in the FRF of the second mode. As seen in Fig. 41.3b, as the forcing amplitude of the excitation varies from $F_0 = 0.01$ to $F_0 = 0.20$ the response curve of this mode exhibits behavior characteristic of a softening nonlinearity with increased damping. The peak of the response curve moves to lower excitation frequencies and has a lower amplitude. We

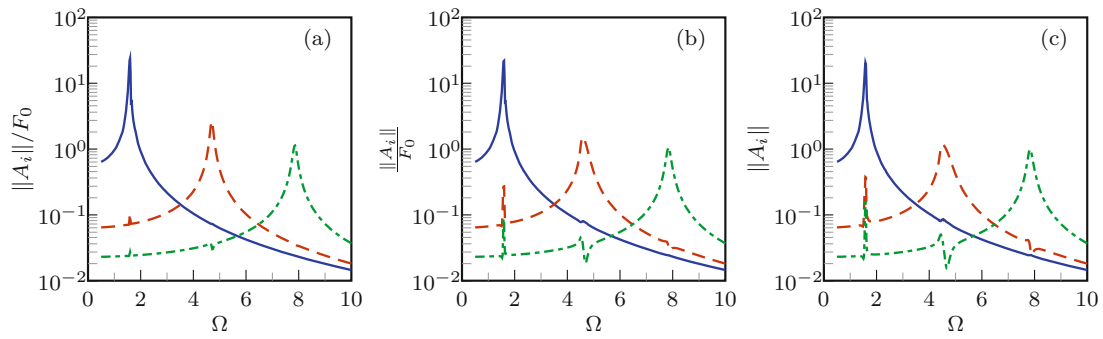


Fig. 41.2 Frequency response function; (a) $F_0 = 0.01$, (b) $F_0 = 0.10$, (c) $F_0 = 0.20$

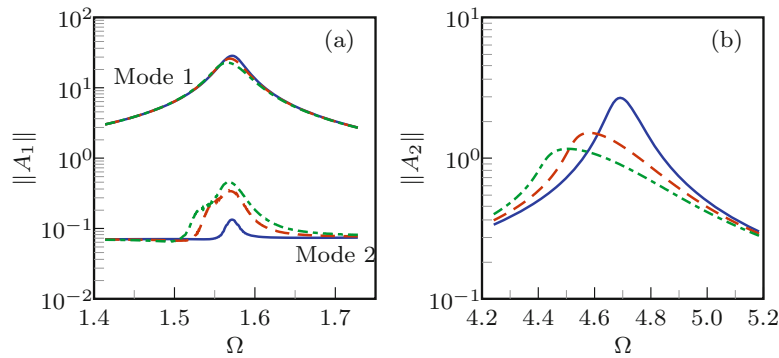


Fig. 41.3 Frequency response function, — $F_0 = 0.01$, - - $F_0 = 0.10$, - · - $F_0 = 0.20$; (a) modes 1 and 2, near $\Omega = \frac{\pi}{2}$, (b) mode 2 near $\Omega = \frac{3\pi}{2}$

note however that the model for the interface does not explicitly contain terms that would normally be associated with a stiffness nonlinearity, such as a cubic component, nor does it contain explicit nonlinear damping components. Rather, the observed behavior arises naturally from the microslip model used in this formulation as is characterized by the hysteretic behavior illustrated in Fig. 41.1c. Finally, the effect of the interface varies from mode to mode. The apparent changes in mode 2 seen in Fig. 41.3b are much more pronounced than those observed in Fig. 41.3a for mode 1. This is consistent with the work of [1] in which identified interface parameters varied significantly between modes.

References

1. Lacayo, R.M., Deaner, B.J., Allen, M.S.: A numerical study on the limitations of modal Iwan models for impulsive excitations. *J. Sound Vib.* **390**, 118–140 (2017)
2. Miller, J.D., Quinn, D.D.: A two-sided interface model for dissipation in structural systems with frictional joints. *J. Sound Vib.* **321**(1–2), 201–219 (2009)
3. Quinn, D.D.: Modal analysis of jointed structures. *J. Sound Vib.* **331**(1), 81–93 (2012)
4. Quinn, D.D., Segalman, D.J.: Using series-series Iwan-type models for understanding joint dynamics. *J. Appl. Mech.* **72**, 778–784 (2005)



Chapter 42

Identification of Nonlinear Viscoelastic Parameters Based on an Enhanced Oberst Beam Method

Kévin Jaboviste, Emeline Sadoulet Reboul, Nicolas Peyret, Gaël Chevallier, C. Arnould, and E. Collard

Abstract This work deals with payload vibration insulation in aeronautic applications. The main objective is to design stabilization devices for optical devices. To achieve this goal, polymer materials have been used because they provide damping and flexibility in order to isolate the optical devices from vibrations and shocks. This kind of material exhibit a mechanical behavior that strongly dependent on the temperature, the strain amplitude and the frequency. The purpose of this paper is to give a new identification method of the viscoelastic parameters based on the Oberst beam test. The aim is to carry out the dependence of the elastomer mechanical properties on the strain amplitude. By coupling this test with Dynamic Mechanical Analysis, it is possible to obtain the mechanical behavior of viscoelastic material according to the strain amplitude and the frequency. To achieve this goal, the experiment derived from the Oberst beam set-up and ASTM E756-05. The time response signal is post-processed using nonlinear unconstraint optimization method in order to identify the instantaneous frequency and damping ratio of the first eigenmode. Then, it is possible to recover the storage modulus and the loss factor of the polymer according to the strain amplitude using a finite element model of the setup. Finally, the identified frequency and amplitude dependent models are taken into account to carry out numerical simulations on the whole mechanical device.

Keywords Elastomer · Damping · Nonlinear · Oberst · Characterization

42.1 Introduction

Viscoelastic materials are commonly recognized as efficient passive damping systems, and are widely used in many applications such as automotive, marine or aerospace. Viscoelasticity is studied since many years by many authors, for citing just a few of them: Ferry [4], Caputo and Mainardi [2], Lakes [8], Chevallier and Vinh [3]. The viscoelastic behavior can be described by the relaxation function or the creep function that express the delay between the applied force and the displacement. This behavior depends on several parameters such as the frequency, the temperature, the preload and the amplitude.

Our study focus on the amplitude dependency that is especially strong for the elastomer containing fillers such as carbon black. This characteristic is mainly led by two phenomenons. The Mullins effect [11] represents a softening effect observed for the first excitation cycle on a sample of elastomer containing fillers such as carbon black. The second effect, named Fletcher-Gent or Payne effect [5, 12] express the dependency of the dynamics properties such as storage modulus on the amplitude of the applied strain. This effect is observed under cyclic loading conditions with small strain amplitudes. Origin of the Payne effect is not clearly defined but it is a reversible phenomenon due to a continuous breaking and reforming Van-der-Walls forces between carbon black particle [6].

K. Jaboviste (✉)

Department of Applied Mechanics, Université Bourgogne Franche-Comté FEMTO-ST Institute, Besançon, France

Thales Optronique SAS, Elancourt Cedex, France

e-mail: kevin.jaboviste@femto-st.fr

E. S. Reboul · G. Chevallier

Department of Applied Mechanics, Université Bourgogne Franche-Comté FEMTO-ST Institute, Besançon, France

N. Peyret

Quartz – Supméca, Saint-Ouen, France

C. Arnould · E. Collard

Thales Optronique SAS, Elancourt Cedex, France

Several experimental studies have been carried out to characterize this behavior such as tension-compression, bending and shearing tests. These experiments are usually realized thanks to viscoanalyzer using different sample holders in order to lead Dynamic Mechanical Analysis (DMA). The DMA is mainly used to characterize the mechanical behavior of a sample (here an elastomer) according to the frequency, the temperature and the strain amplitude. However, the range where the data are obtained is restricted by the experimental set-up (testing machine, sample holder and sample association). In fact, each set-up exhibit a confidence interval of measurements defined by a minimum and a maximum in frequency, temperature and strain amplitude ranges.

There are other ways to characterize the dynamic behavior of elastomer. One of these tests is the famous Oberst beam method [1] used to extract the storage modulus and the loss factor of the tested material. Practically, the sample is glued directly on a steel blade or sandwiched between two steel blades. This association form an “hybrid” beam which is clamped at one of its ends and free at the other. The Frequency Response Function (FRF) of this beam is carry out thanks to an accelerometer and an excitation signal realized by a hammer shock, a shaker or a magnetic exciter. Then, this response is compared with the FRF of an uniform steel beam to retrieve the storage modulus and the loss factor of the sample. This approach only allows the identification of these mechanical parameters in the neighbourhood of the resonance frequencies. It is an important drawback of the Oberst method. However, several ways exists to expand the characterization range of the parameters. One can cite the work of Hillstrom et al. [7] and Liao and Wells [9, 10] for example.

42.2 Enhanced Oberst Beam Method

Despite the numerous studies based on the Oberst beam method to identify the storage modulus and the loss factor of viscoelastic material according to the frequency, it seems that no approach, using this method, has been developed to characterize these mechanical parameters according to the strain amplitude. In order to investigate this possibility, a sandwich cantilever beam has been designed with a filled silicon containing black carbon sample (Fig. 42.1a).

The geometry of the elastomer sample has been chosen to obtain a uniform shearing strain rate. A known displacement is applied to the cantilever beam to reach the desire strain rate. One can notice that the design of the beam bounds the range of measuring strain rate. The beam is released into its natural first mode of vibration. The measured acceleration coupled with an appropriate post-treatment and an identification method based on the Least-Squares method using a sliding window allow us to extract the instantaneous frequency and the damping ratio of the first eigenmode (Fig. 42.1b). Then, using a parametric study on the Finite Element Model (FEM) of the experimental set-up to determine the evolution of the first eigenfrequency according to the storage modulus of the sample, it is possible to retrieve the storage modulus and the loss factor of the silicon according to the strain amplitude. The dependency of the storage modulus according to the strain rate is the famous Payne effect. Finally, it is possible to take into account this behavior law in a finite element model of a damper composed of

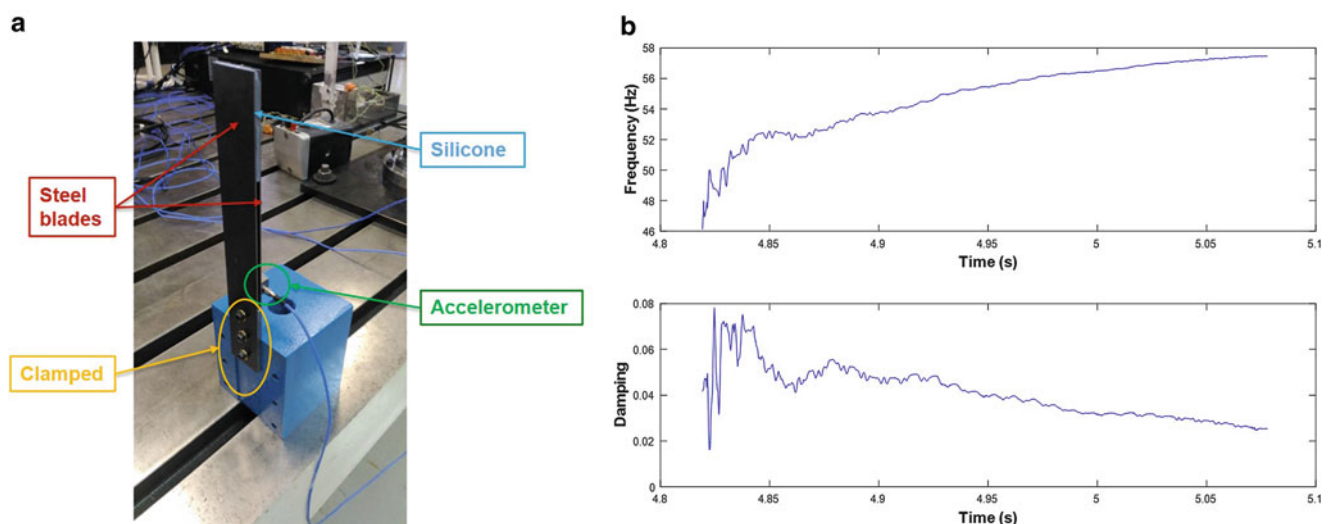


Fig. 42.1 Experimental set-up of the cantilever beam and identification results. (a) Experimental set-up of the sandwich cantilever beam. (b) Identified instantaneous frequency and damping ratio of the sandwich beam first mode

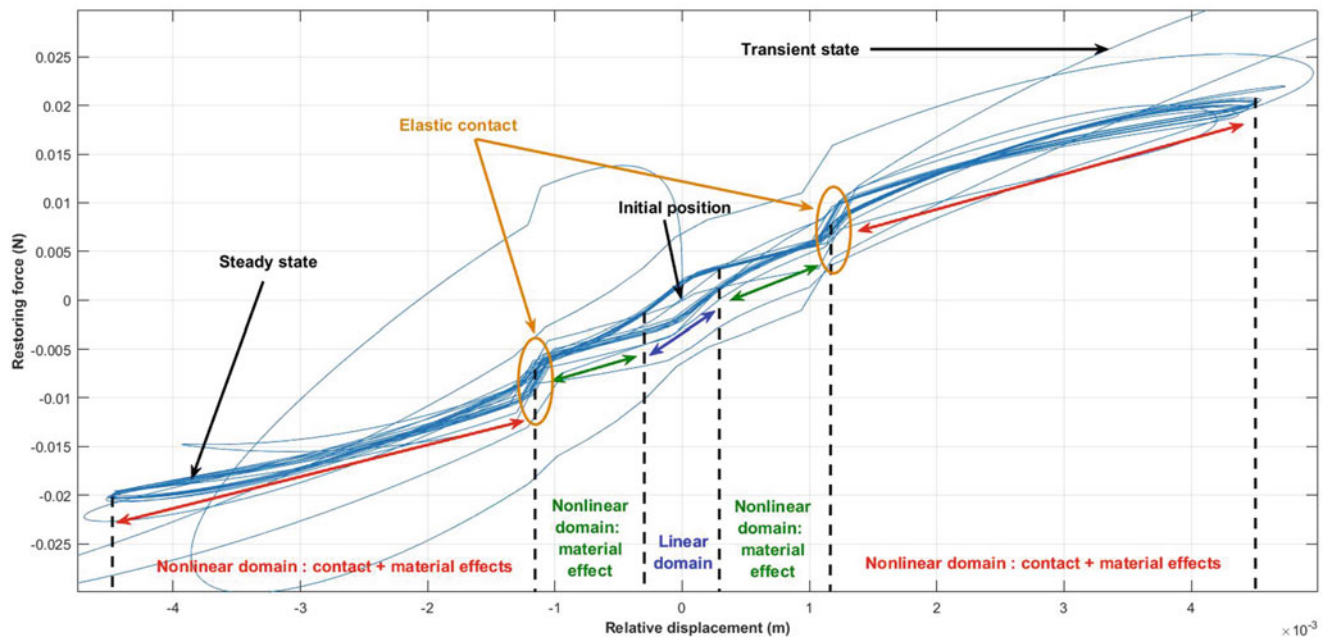


Fig. 42.2 Restoring force of a passive damper system made up of elastomer parts subject to Payne effect and an elastic stop

elastomer parts in order to drive non-linear simulations. From the industrial point of view, it could be interesting to observe and quantify the different non-linearity phenomena involved in the dynamic behavior of the passive damping systems to refine the defined dynamic modeling of this kind of devices and to improve their design cycle. For example, the RFS (Restoring Force Surface) method allows us to evaluate the non-linearities participation in the neighborhood of a chosen eigenmode as shown Fig. 42.2.

42.3 Conclusion

In this study, a framework is proposed to identify the storage modulus and the loss factor dependency of viscoelastic material according to the strain amplitude. This approach is based on the Oberst beam method. Instead of carry out the frequency response function of a sandwich cantilever beam, a chosen displacement is applied at the free end of this one and suddenly released in order to measure the free vibration response. Thanks to an identification method based on the Least-Squares method using a sliding window, the instantaneous frequency and the damping ratio of the first eigenmode are extracted. By coupling the modified Oberst beam method and a Finite Element Model of the experimental set-up, it is finally possible to retrieve the dependency of the storage modulus according to the strain rate and modeling the Payne effect. Thus, non-linear numerical simulations on passive damper systems using elastomer subject to the Payne effect can be carried out and correctly predict the dynamic behavior of the whole structure.

References

1. ASTM E756-98: Standard test method for measuring vibration-damping properties of materials. Am. Soc. Test. Mater. (1998)
2. Caputo, M., Mainardi, F.: Linear models of dissipation in anelastic solids. *La Rivista del Nuovo Cimento* (1971–1977) **1**(2), 161–198 (1971)
3. Chevalier, Y., Tuong, J.V.: *Mechanical Characterization of Materials and Wave Dispersion*. Wiley, New York (2013)
4. Ferry, J.D.: *Viscoelastic Properties of Polymers*. Wiley, New York (1980)
5. Fletcher, W.P., Gent, A.N.: Nonlinearity in the dynamic properties of vulcanized rubber compounds. *Rubber Chem. Technol.* **27**(1), 209–222 (1954)
6. Fröhlich, J., Niedermeier, W., Luginsland, H.D.: The effect of filler-filler and filler-elastomer interaction on rubber reinforcement. *Compos. A Appl. Sci. Manuf.* **36**(4), 449–460 (2005)

7. Hillström, L., Mossberg, M., Lundberg, B.: Identification of complex modulus from measured strains on an axially impacted bar using least squares. *J. Sound Vib.* **230**(3), 689–707 (2000)
8. Lakes, R.S.: *Viscoelastic Solids*. CRC Press (1998)
9. Liao, Y., Wells, V.: Estimation of complex modulus using wave coefficients. *J. Sound Vib.* **295**(1), 165–193 (2006)
10. Liao, Y., Wells, V.: Estimation of complex Young's modulus of non-stiff materials using a modified Oberst beam technique. *J. Sound Vib.* **316**(1), 87–100 (2008)
11. Mullins, L.: Softening of rubber by deformation. *Rubber Chem. Technol.* **42**(1), 339–362 (1969)
12. Payne, A.R., Whittaker, R.E.: Low strain dynamic properties of filled rubbers. *Rubber Chem. Technol.* **44**(2), 440–478 (1971)



Chapter 43

A General Framework for Time Domain Finite Element Analysis of Viscoelastically Damped Structures

J.-F. Deü and L. Rouleau

Abstract The purpose of this work is to present a general framework for the computation of time responses of viscoelastically damped systems, by using recurrence formulas involving internal variables into a time discretization scheme. The most common viscoelastic models are studied, and especially the four-parameter fractional derivative model. After presenting the numerical methodology adapted to the representation of the constitutive behavior, the proposed approach is applied to the computation of time responses of structures treated with constrained viscoelastic layers.

Keywords Viscoelasticity · Damped structures · Time domain analysis · Finite element · Fractional derivative model

43.1 Introduction

The use of constrained viscoelastic materials has been regarded as a convenient strategy to reduce noise and vibrations in many types of industrial applications. Many of the modeling approaches which have been developed to account for the frequency- and temperature- dependency on the mechanical properties of viscoelastic materials are adapted to analysis in the frequency domain. Some issues, such as the presence of local nonlinearities in the system, cannot be appropriately dealt with in the frequency domain. However, while the use of viscoelastic models is quite straightforward in the frequency domain, some difficulties arise from their application in the time domain. The main objective of this work is thus to present a general framework for the computation of time responses of viscoelastically damped systems. Among the broad variety of viscoelastic models presented in the literature, the generalized Maxwell model (GMM), the Golla-Hughes-McTavish model (GHM) [1], the Anelastic Displacement Field model (ADF) [2] and the fractional derivative model (FDM) [3], which are the most commonly used, are under study in this work.

43.2 Integration of the Viscoelastic Models and Finite Element Implementation

In the GMM, GHM and ADF model, internal variables can be introduced to obtain an augmented coupled matrix system which is used to compute the time response of the viscoelastically damped structure [4]. With this strategy, the system matrices are frequency-independent but the size of the matrix system largely exceeds the original size of the problem (the increase in the number of degree of freedom to be solved being directly proportional to the number of series considered for the viscoelastic model). Moreover, in the case of the GMM and ADF model, the mass matrix of the augmented matrix system is singular. A state-space first-order representation is thus required to compute the structural time response. This procedure doubles the size of the matrix system to solve at each time step, and increases even further the computational cost of such approaches.

J.-F. Deü (✉) · L. Rouleau

Structural Mechanics and Coupled Systems Laboratory, Conservatoire national des arts et métiers, Paris, France
e-mail: jean-francois.deu@cnam.fr; lucie.rouleau@cnam.fr

Another strategy is to apply the concept of dissipation variables in conjunction with a time discretization scheme [5, 6]. It consists in transforming the stress-strain relation into a two-step recurrence formula involving internal variables. In [5], the convolution representation of the constitutive law is approximated by second-order schemes. This leads to second-order accurate recurrence formulas which allow the computation of updated internal variables at each time step. This method is limited to a particular class of relaxation functions, consisting in a linear combination of functions which possess the semi-group property [5]. Therefore, it is applicable only to the GMM and ADF models, whose relaxation functions consist in a linear combination of exponentials in the time-domain (Prony series).

We propose in this work a general framework for the computation of time responses of viscoelastically damped systems by using two-step recurrence formulas involving internal variables in the time discretization scheme. For the four models under study, a recurrence formula is obtained for the computation of the internal dissipation variables at each time step. For viscoelastic models with a time-domain representation (GMM and ADF), the internal variables can be directly obtained from the expression of the time-domain expressions of the relaxation modulus in the form of Prony series. For viscoelastic models which have only a frequency-domain representation (GHM and FDM), internal variables can be identified from the expression of the relaxation modulus in the Fourier-Laplace domain. These internal variables are solutions of integer or fractional differential equations in time which can be solved by using appropriate numerical discretization schemes, i.e. backward Euler method for the GHM and Grünwald-Letnikov approximation for the FDM. In this last case, recurrence formula updating the internal variables requires the storage of their memory [6].

Using the recurrence formulas obtained for the four models under study, the computational strategy is implemented in the general context of finite element method with time-stepping method. In particular, a modified Newmark algorithm is used. Its implementation leads to a two stages recurrence formula at each time step. The first stage is the calculation of a modified external load taking into account the dissipation due to the viscoelastic model, and the second one is the updating of the internal dissipation variables.

43.3 Numerical Example

The implementation of each viscoelastic model is tested on the simple example of a cantilever sandwich beam with viscoelastic core and symmetrical faces subjected to a transverse triangular impulse at its free end (see Fig. 43.1). The structure is modeled using sandwich finite elements. All the details concerning this numerical example are given in [6]. The frequency dependency of the Young modulus is modeled by one of the four viscoelastic models investigated in this work. The parameters of the models have been identified so that the corresponding master curves are similar (for the models with series representation, i.e. GMM, GHM and ADF, 8 series were considered leading to a relative error inferior to 1% between each model).

The time response of the sandwich beam to the transverse load is computed with a time step of 0.25 ms for each viscoelastic model implemented. The results are presented in Fig. 43.2. A good correlation is observed between the four models, which validates the implementation of the models in the time-domain.

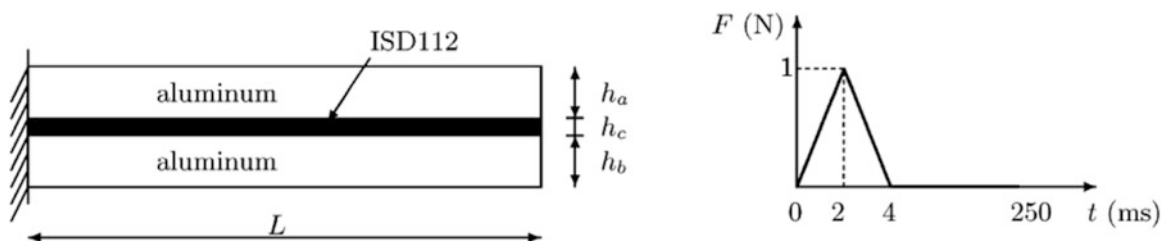


Fig. 43.1 Sandwich structure and triangular impulse imposed at the free end of the beam. (From [6])

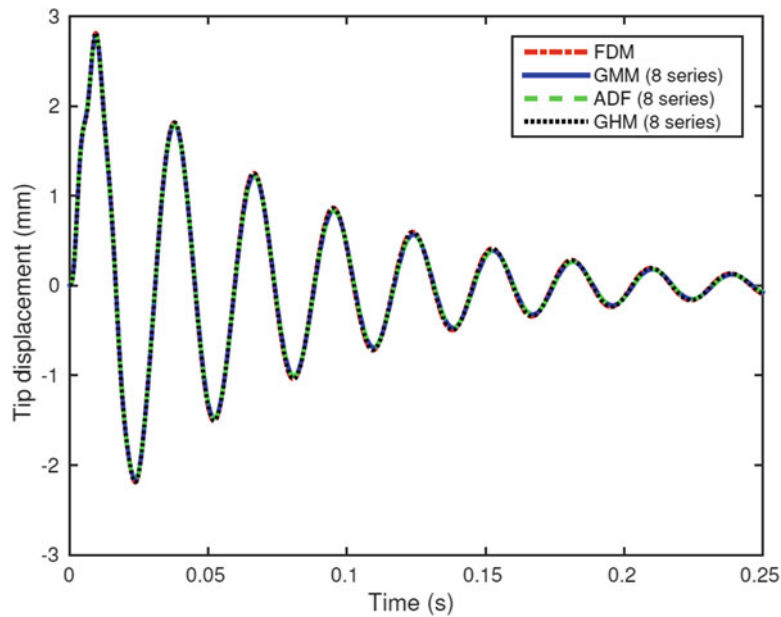


Fig. 43.2 Time response of the sandwich beam for each viscoelastic model implemented

43.4 Conclusions

A general framework for the computation of time responses of viscoelastically damped systems was proposed in this work, by using two-step recurrence formulas involving internal variables in the time discretisation scheme. The generalised Maxwell model, the anelastic displacement field model, the Golla-Hughes-McTavish model and a four-parameter fractional derivative model were implemented within a modified Newmark scheme to compute the time response of sandwich structures subjected to a transient load. It is shown that by identifying properly the models' parameters, the results obtained with each models are similar. These results prove the effectiveness of the proposed methodology. The evolution of the error in amplitude and in period needs to be investigated further, as well as the order of convergence of numerical schemes.

References

1. Golla, D.F., Hughes, P.C.: Dynamics of viscoelastic structures – a time domain finite formulation. *J. Appl. Mech.* **52**, 897–906 (1985)
2. Lesieutre, G.A., Bianchini, E.: Time domain modeling of linear viscoelastic using anelastic displacement fields. *J. Vib. Acoust.* **117**, 424–430 (1995)
3. Bagley, R.L., Torvik, P.J.: A theoretical basis for the application of fractional calculus to viscoelasticity. *J. Rheol.* **27**, 201–210 (1983)
4. Vasques, C.M.A., Moreira, R.A.S., Dias Rodrigues, J.: Viscoelastic damping technologies – part I: modeling and finite element implementation. *J. Adv. Res. Mech. Eng.* **1**, 76–95 (2010)
5. Simo, J.C., Hughes, T.J.R.: *Computational Inelasticity*. Springer, Beijing (1998)
6. Galucio, A.C., Deü, J.-F., Ohayon, R.: Finite element formulation of viscoelastic sandwich beams using fractional derivative operators. *Comput. Mech.* **33**, 282–291 (2004)



Chapter 44

Nonlinear Structural, Inertial and Damping Effects in an Oscillating Cantilever Beam

Michal Raviv Sayag and Earl H. Dowell

Abstract The nonlinear oscillations of a cantilever beam are studied with a theoretical computational model and the results are compared to experimental results obtained in a previous study. In order to explore the various possible nonlinear effects, the cantilevered beam is oscillated by the clamped base in a harmonic motion. Frequency sweeps are conducted in the vicinity of the first and second resonance frequencies of the beam to produce tip displacements of the order of the beam's length. Three types of nonlinear effects are included in the model and discussed: Inertial, structural, and fluid damping nonlinearities.

Comparison of results from the computational model to previously conducted experiments near the first natural frequency shows reasonable to good agreement, suggesting that this model could be effective in describing large amplitude oscillations. Based on the success of this experimental/computational correlation, a computational study near the second resonant mode suggests that nonlinear inertial effects at a higher resonance frequency have a greater effect on both peak amplitude and the frequency at which it is achieved. For the first resonant mode the effects of nonlinear inertia and nonlinear stiffness are offsetting and hence the peak resonant frequency is little changed from that predicted by linear theory and only a very modest hysteresis is observed. However for the second resonant mode, because the nonlinear inertia effect dominates relative to the nonlinear stiffness effect, there is a greater shift in the peak resonant frequency from its linear value and a more substantial hysteresis is observed.

Keywords Nonlinear · Dynamics · Beam · Theory · Experiment

Nomenclature

E	Young's modulus
f	Frequency in Hz
I	Moment of inertia
L	Beam length
m	Mass per length unit
$q = 1/2w'$	Dynamic pressure of the fluid
T	Kinetic energy
U	Potential energy
w	Transverse displacement
W	Displacement amplitude
x	Coordinate along the beam
ζ	Damping coefficient
ρ	Density
σ	Yield stress
Ψ_i	Spacial functions
ω	Natural frequency in rad/s

M. Raviv Sayag · E. H. Dowell (✉)
Department of Mechanical Engineering Materials Science, Duke University, Durham, NC, USA
e-mail: earl.dowell@duke.edu

44.1 Introduction

The dynamic oscillations of cantilevered beams have long been a source of interest in many scientific and engineering applications. The Bernoulli-Euler theory has been generally accepted to describe small amplitude oscillations, but becomes inadequate when the large amplitudes occur.

With recent developments in the aeronautical industry, the large amplitude beam oscillations are utilized in different applications such as flapping UAVs [1, 2] and wind harvesting mechanisms [3–5]. The need to predict large amplitude oscillations accurately has encouraged new models to be developed and studied [6–16]. This exploration has led some researchers to the conclusion that the linear viscous damping model, widely used due to its simplicity, is deficient when used in nonlinear model of the beam deflection [16–18].

Ozcelic et al. [15] conducted a numerical and experimental study of a flapping slender beam. It was found that while good agreement was reached using viscous damping in a wide range of frequencies up to 1.3 times the first resonance frequency, this was not the case near the primary and secondary harmonic regions. In a following study, Ozcelic and Attar [17] suggested four distinct linear and nonlinear models for the damping force on an oscillation beam. The coefficients for each model were chosen empirically to minimize error near the secondary resonant peak. A damping model based on the third power velocity provided the best prediction of strain response, of the four. Anderson et al. [18] found that including a quadratic damping model improved the agreement between their theory and experiment. In the studies in [17] and [18] a physical source for the nonlinear damping was not proposed.

In a previous study by the authors [16], a nonlinear model was suggested to describe the response of a cantilever beam to a harmonic base excitation, and compared to experiments. While good agreement between numerical and experimental results was observed, the damping coefficient calculated from experiments varied with excitation amplitude. This led the authors to suggest a nonlinear damping model based on the aerodynamic drag force acting on the beam during oscillation. The initial study showed promising agreement between experiments and the drag induced damping model. It was also found in the study that while nonlinear inertia and stiffness effects arise near the first resonance frequency, these effects are mostly mutually offsetting when combined into the full nonlinear model, leading to a small change in effective resonance frequency and amplitude.

The current study is focused on two aspects of the nonlinear model for cantilever beam oscillations. In the first section the suggested nonlinear fluid damping model is discussed. The effect of the structural (linear) damping and drag coefficient for the nonlinear fluid damping model are studied, and computational results are compared to experiments conducted during the previous study [16] for the first resonant frequency. In the second part of the study the full nonlinear model is used to simulate beam deflection near the second natural frequency of the beam. The partial nonlinearities and their effect on the complete nonlinear model are investigated, and effects that were not as readily visible near the first natural frequency are discussed.

Finally the very interesting work of Luongo et al. [19] and Lenci et al. [20] should be mentioned. In their theoretical/computational work they study the effects of various axial constraints. In the numerical examples it appears they deal with a case of beam fixed at both ends in the transverse direction, but free to move axially [19, 20]. In any event their deformations are much smaller than those considered here.

44.2 Theoretical Background

44.2.1 The Equation of Motion

The equation of motion for an inextensible beam can be developed from the potential energy U_b and kinetic energy T_b . For a cantilever beam with a point mass at the free tip undergoing harmonic displacement at the clamped tip, the kinetic and potential energy are defined as follows:

$$U_b = \frac{1}{2} \int_0^L EI \left(\frac{\partial^2 w}{\partial x^2} \right)^2 \left[1 + \left(\frac{\partial w}{\partial x} \right)^2 \right] dx \quad (44.1)$$

$$T_b = \frac{1}{2} \int_0^L m_{tot} \left[(\dot{x} + \dot{w}_b)^2 + \left(\frac{\partial w}{\partial \xi} \frac{\partial^2 w}{\partial \xi \partial t} d\xi \right)^2 \right] dx \quad (44.2)$$

where the total mass of the system is constructed of both the uniform beam mass as well as the tip mass contribution at $x = L$.

$$m_{tot} = m_b + m_{tip}\delta(x - L) \quad (44.3)$$

Using a Rayleigh-Ritz approach and Lagrange's equation, and following a process described in Tang and Dowell [6] and extended in Sayag and Dowell [16], a nonlinear equation for the beam's motion is achieved.

$$M_{bi}\ddot{q}_i + M_{ti}2\zeta\omega_i\dot{q}_i + M_{bi}\omega_i^2q_i = -F_{wb} - F_{BN} - F_{BM} - F_{m_{tip}} \quad (44.4)$$

The terms on the left hand side of Eq. (44.4) represent the linear, unforced, unloaded part of the equation. A linear term for viscous damping is included in this equation as a simplified model of dissipation. The left hand side of the equation represents external loads as well as internal nonlinear forces acting on the beam: F_{wb} is a load due to the harmonic motion of the clamped base, F_{BN} and F_{BM} are the nonlinear structural and inertial forces respectively and $F_{m_{tip}}$ is the load generated by a point mass at the free tip of the beam. A detailed description of how these forces are calculated is presented in the appendix.

44.2.2 Damping

For a beam oscillating in any fluid medium, it is reasonable to assume that interaction of the structure with surrounding fluid will cause some energy dissipation. While this may be negligible for small amplitude oscillations, the effect could be more notable when deflections are large enough to be considered nonlinear.

In a previous study by the authors [16] this additional dissipation of energy was described as a drag force acting on the beam due to its rapid motion through the fluid medium. This force is defined by the shape and dimensions of the cross section, as well as the dynamic pressure.

$$D = C_D \cdot q \cdot b \cdot \text{sign}(\dot{w}) \quad (44.5)$$

The generalized force for the fluid damping can therefore be computed and added to the equation of motion:

$$F_{FD_i} = \frac{1}{2}C_D\rho_{air}\dot{q}_i^2 \cdot \text{sign}(\dot{q}_i) b \int_0^L \psi_i^3(x) dx \quad (44.6)$$

This force is most significant when the oscillation frequency is close to resonance, and under this circumstance the motion of the beam can be closely described by a single mode shape. An instantaneous fluid damping coefficient can be defined by comparing the generalized force caused by drag to the viscous damping term of a single mode from Eq. (44.4), and solving for an equivalent ζ . The damping coefficient corresponding with the drag force is presented in Eq. (44.7). This time dependent coefficient is computed at each frequency using the dominant mode shape.

$$\zeta_{FD_i} = \frac{C_D \rho_{air}\dot{q}_i \cdot \text{sign}(\dot{q}_i) \int_0^L \psi_i^3(x) dx}{4 \omega_i \rho h \int_0^L \psi_i^2(x) dx} \quad (44.7)$$

44.3 Experimental System

Numerical simulations conducted for the full nonlinear model were compared with experiments conducted during a previous study. A short description of the experimental system is provided below. More information about the system can be found in Sayag and Dowell [16]. A thin aluminum beam is mounted on a BK 4809 vibration shaker. The beam is clamped to the shaker at the centerline, effectively creating two opposite cantilevered beams. This was done in order to minimize rotational instability of the shaker caused by the large amplitude oscillations of the beam. The shaker is driven by a sine signal generated by a Labview Virtual Instrument (VI), and amplified by a BK 2718 power amplifier. The frequency, w_0 , and amplitude, W_0 , of the sine signal are controlled by the VI, allowing a frequency sweep at a desired rate. The beam response was measured using three PCB 352C22 miniature piezoelectric accelerometers. The mass of each accelerometer is 0.5 g. Two

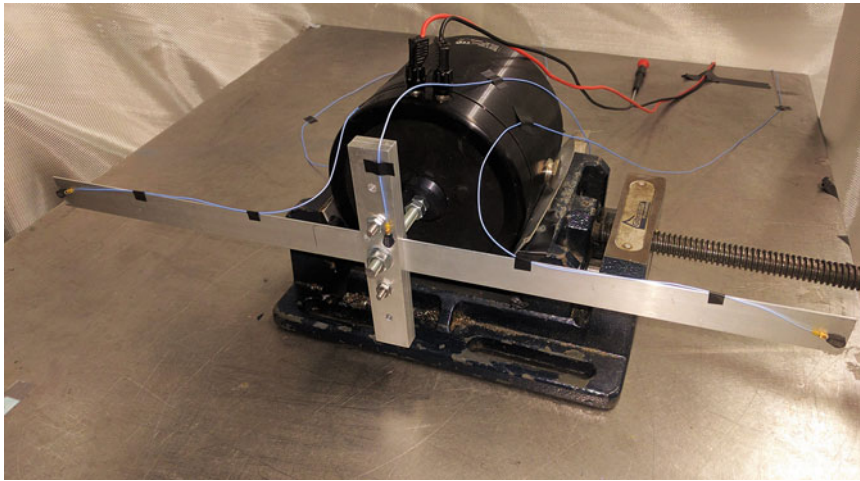


Fig. 44.1 Experimental system: shaker, two sided beam and three accelerometers

Table 44.1 Beam dimensions

Beam name	b (mm)	h (mm)	L (mm)
Beam1/beam2	25.4	1.5	254

Table 44.2 Beam material properties

Property	Symbol	Value	Units
Density	ρ	2680	kg/m ³
Young modulus	E	52.6	GPa
Yield stress	σ_y	241	MPa

accelerometers were placed at the two free beam tips, while a third was attached to the mounting system, near the base of the beam. All accelerometers were connected to a PCB 441A101 signal conditioner. A picture of the shaker, mounting system, two sided beam and three accelerometers is presented in Fig. 44.1.

All beams were made of 6061 Aluminum, which was chosen due its high yield stress to Young modulus ratio. The beam dimensions were chosen to allow for large deflections while keeping the maximal stress below the yield point. The beam dimensions are listed in Table 44.1. All numerical simulations were conducted using the same beam dimensions. The length of each cantilever beam, L , is the distance between the edge of the mounting system and the tip of the beam. The material properties of the beam are listed in Table 44.2.

44.4 Results and Discussion

Numerical simulations were conducted for a beam with material properties and dimensions described in the experimental system. A nominal value of $\zeta_{st} = 0.006$ was chosen for structural damping determined from experimental results for a low amplitude oscillation test. Since the cross section of the beam is rectangular, a drag coefficient of a flat plate facing oncoming flow was chosen as a nominal value of $C_d = 2$.

Numerical simulations were conducted for an increasing or decreasing frequency sweep with increments of 0.1–0.5 Hz, for each run. The amplitude of base displacement was chosen to either be a constant value for an entire numerical simulation, or a combination of specific amplitude per frequency that was observed during experiments. An example of the two possible base displacement input methods is presented in Fig. 44.2. The blue curve displays a base displacement input that does not change in amplitude as input frequency is increased. The yellow curve presents an input amplitude that depends on the instantaneous frequency. This base amplitude was measured during an experimental run. The goal of such simulations was to recreate, as accurately as possible, the oscillations observed during an experiment.

Figure 44.3 presents the calculated tip displacement amplitudes for both simulation presented in Fig. 44.2, as well as the measured tip displacement amplitude during the corresponding experiment. Although the resonance frequency measured for both tips of the experimental system is identical, this frequency varies slightly from that calculated numerically. This deviation is likely caused by a small variation in material properties reported by the manufacturer, as explained in previous work [16].

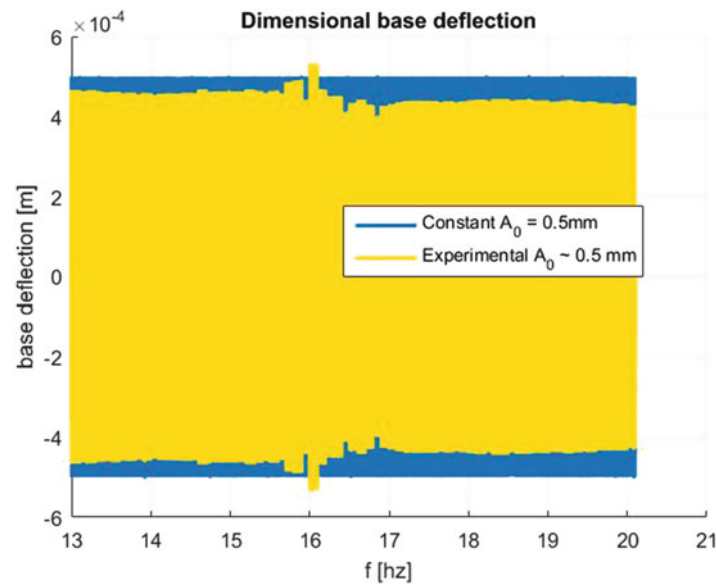


Fig. 44.2 Dimensional base displacement vs. frequency during numerical simulations

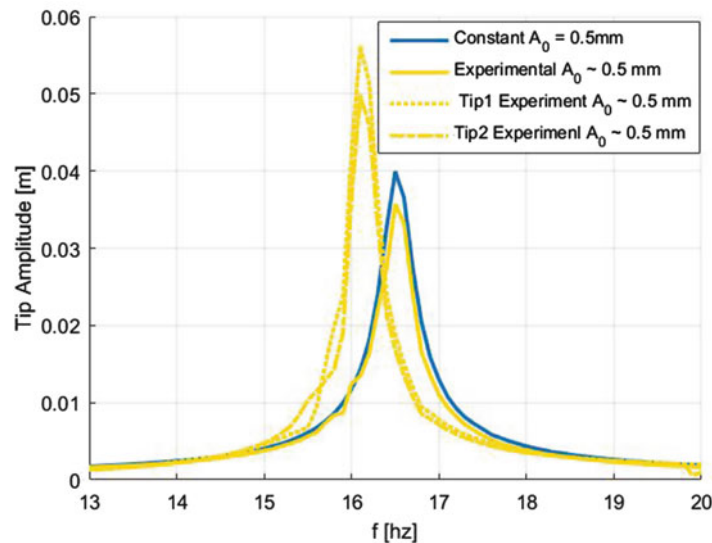


Fig. 44.3 Tip displacement amplitude vs. frequency during numerical simulations and matching experiment

The total instantaneous damping coefficient was also calculated and recorded for each step during the calculation. Figure 44.4 displays the damping coefficient for the two calculated cases described above. The structural damping coefficient in both cases was set to $\zeta_{st} = 0.006$, therefore the total damping remains above that value for the entire frequency sweep. The increased tip velocity in frequencies close to resonance cause the fluid (nonlinear) component of the damping to become more prominent, and therefore increase the total instantaneous damping significantly. A more in depth discussion of the total damping is included in the next section.

44.4.1 Effect of Structural Damping and Drag Coefficient on Computational Results

A sensitivity test for the effect of structural damping and drag coefficient was performed by creating numerical simulations for the beam described above with a wide range of base displacement values. Figure 44.5 presents the maximal tip displacement observed during a numerical run, for a range of different base displacement values and drag coefficients. For this figure

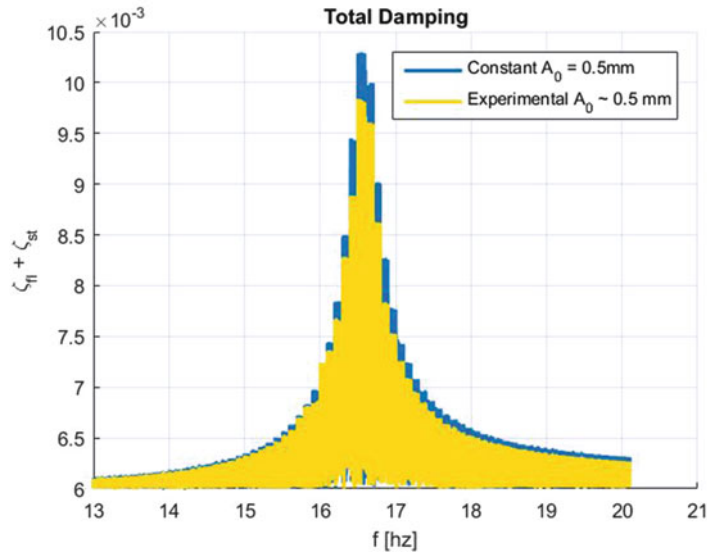


Fig. 44.4 Total instantaneous damping vs. frequency during numerical simulations

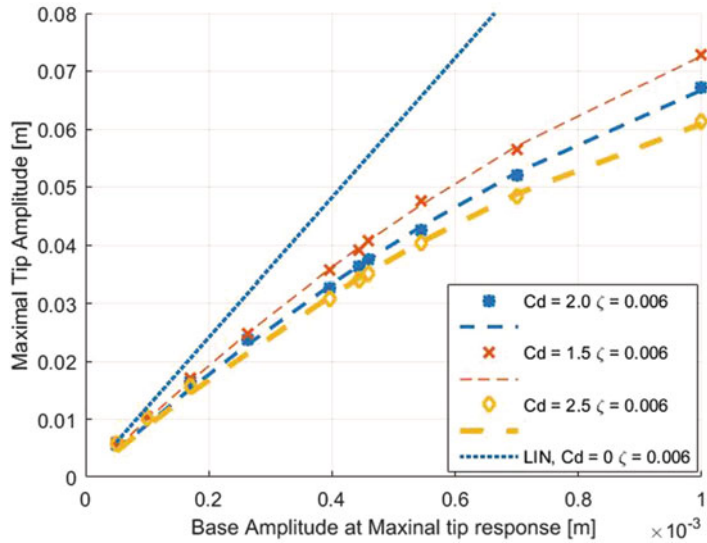


Fig. 44.5 Tip displacement amplitude vs. base displacement amplitude at resonance, $\zeta_{st} = 0.006$, $C_d = 1.5-2.5$. Markers are computed results. Curves are fitted to data to show trend. Linear model computation with no fluid damping is presented for comparison

the structural (linear) damping was kept as the nominal value of $\zeta_{st} = 0.006$. A purely linear calculation with structural damping only is also presented, for reference. For small values of base displacement (around 0.1 mm) nonlinear effects are insignificant; The structural damping is most dominant, and drag induced fluid damping is barely noticeable. This causes the tip displacement for all three cases presented here to produce very similar results to the linear case at resonance. As base amplitude increases, the velocity of the beam during deflection becomes greater, causing an increase in the fluid component of damping. The connection between base amplitude and tip amplitude for each value of C_d is well described by a second order concave function, as presented in Fig. 44.5. Base displacement was kept at an amplitude of 1 mm or less to insure that stress in the beam does not exceed yield stress, where material weakening effects (that are not represented in the model) might take place.

Figure 44.6 presents the peak in transfer function between tip and base amplitude for each base amplitude that was simulated. At low base amplitudes these peak values come close to the transfer function achieved by the linear model, presented here as a horizontal line, for comparison. As base displacement increases nonlinear effects become more pronounced, reduce tip amplitude, causing a reduction in peak transfer function values.

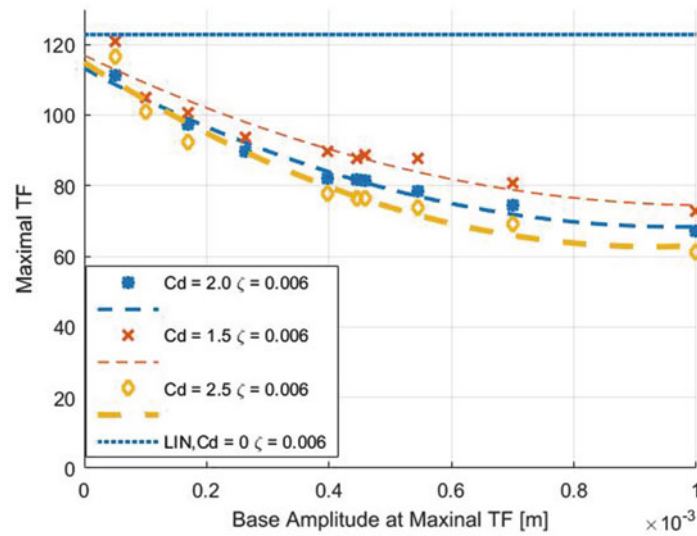


Fig. 44.6 Tip displacement to base displacement transfer function vs. base displacement amplitude at resonance, $\zeta_{st} = 0.006$, $C_d = 1.5$ – 2.5 . Markers are computed results. Curves are fitted to data to show trend. Linear model computation with no fluid damping is presented for comparison

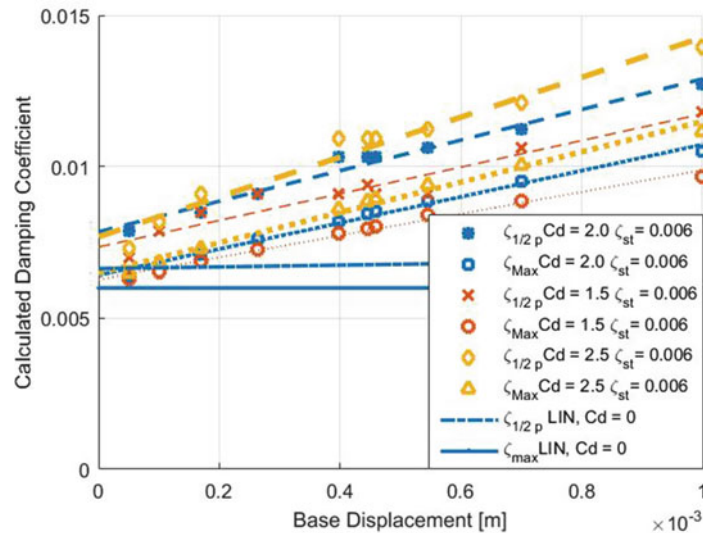


Fig. 44.7 Damping coefficient vs. base displacement amplitude at resonance, $\zeta_{st} = 0.006$, $C_d = 1.5$ – 2.5 . $\zeta_{1/2p}$ is calculated using the half power method. ζ_{max} is maximal instantaneous combined damping (structural and fluid). Linear computation with no fluid damping is presented for comparison

Figure 44.7 presents the damping coefficient for the previously discussed cases, derived in two ways: ζ_{max} is the maximal instantaneous total damping coefficient for a single numerical simulation. It represents a combination of structural damping, and the *instantaneous* fluid damping, caused by drag. This coefficient was detected while the base was oscillated at the frequency which caused maximal tip deflection, and when the beam's velocity was highest. By contrast, $\zeta_{1/2p}$ is the damping coefficient calculated using the half power method, according to the transfer function between tip and base displacement from the full numerical simulation.

It is seen that for every run presented in this plot, the damping coefficient calculated using the half power method is notably higher than the maximum damping recorded during the run. This can be explained by the variation of total damping presented in Fig. 44.4. The rapid drop in total damping surrounding the resonance frequency causes a change in the shape of the Tip-to-Base transfer function compared to a case with purely linear damping. The maximum damping is well described by a quadratic function that approaches the structural damping as base excitation goes to zero. While the half power method produced an inaccurate coefficient for the linear computation, it is easily seen that this error in $\zeta_{1/2p}$ is greater for the full nonlinear computation, and increases as base displacement (and total damping) increases. This affirms that the half power method is not suitable for accurately predicting damping in *nonlinear* systems, and particularly systems with nonlinear damping.

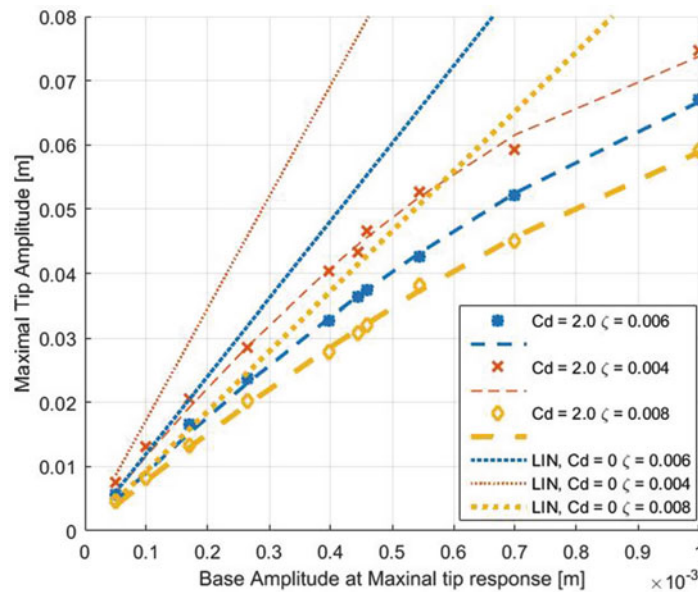


Fig. 44.8 Tip displacement amplitude vs. base displacement amplitude at resonance, $\zeta_{st} = 0.004\text{--}0.008$, $C_d = 2.0$

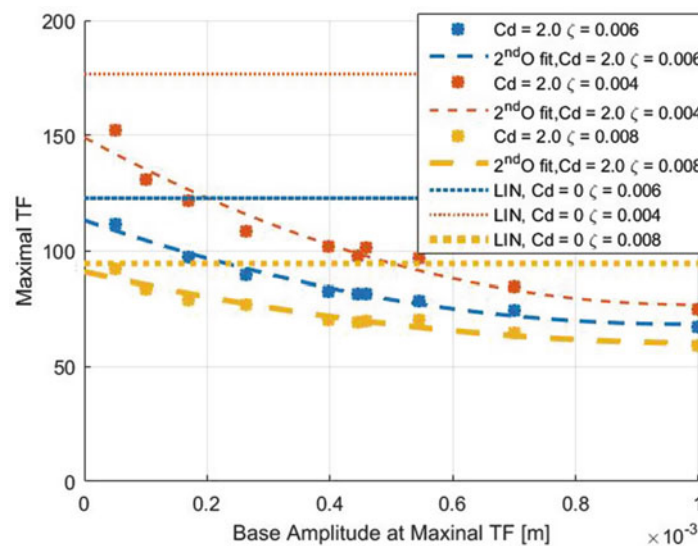


Fig. 44.9 Tip displacement to base displacement transfer function vs. base displacement amplitude at resonance, $\zeta_{st} = 0.004\text{--}0.008$, $C_d = 2.0$

A sensitivity test was also performed for the structural damping ζ_{st} using the same range of base displacements. Figures 44.8, 44.9, and 44.10 present the tip displacement amplitude, peak *transfer* function value, and calculated damping coefficient vs. base displacement for a constant drag coefficient of $C_d = 2.0$ and a varying structural damping coefficient of $\zeta_{st} = 0.004\text{--}0.008$. Results computed using the linear model are presented for all ζ_{st} values, where available.

Tip amplitude values versus base displacement for the linear models follow a linear trend, as expected and seen in Fig. 44.7. Computations with lower structural damping produce higher tip displacement. For the nonlinear model computation, all results follow a parabolic curve. Close examination of the curves reveals that as the structural damping increases, the discrepancy between the linear and nonlinear computation decreases. For a base displacement of 0.4 mm and $\zeta_{st} = 0.004$, a tip displacement of almost 69 mm is observed for the linear computation, compared to only 41 mm for the nonlinear computation. This is a reduction of about 40% in tip amplitude. Increasing the structural damping to $\zeta_{st} = 0.008$ yields a linear tip displacement of 37 mm, versus 28 mm for the nonlinear case. This is a reduction of only 24%. As base displacement increases, these variations only increase in size, causing the curve with the lowest structural damping, $\zeta_{st} = 0.004$, to drift further away from its linear counterpart. This is likely due to a fine balance that is achieved between the structural and fluid

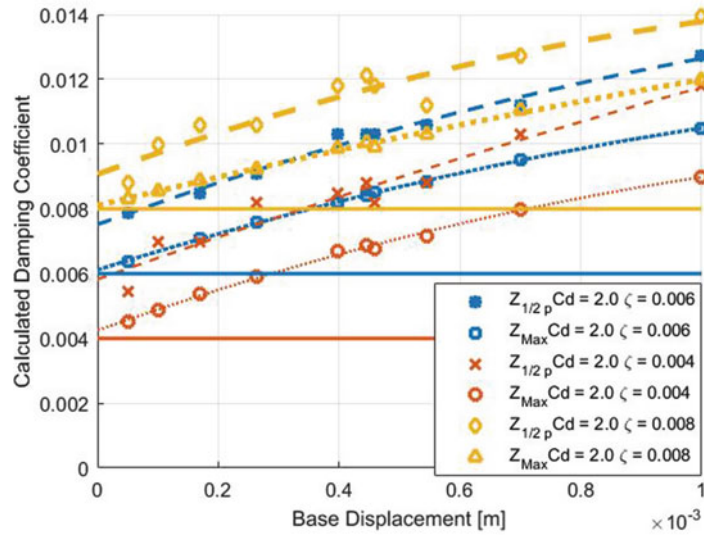


Fig. 44.10 Damping coefficient vs. base displacement amplitude at resonance, $\zeta_{st} = 0.004\text{--}0.008$, $C_d = 2.0$

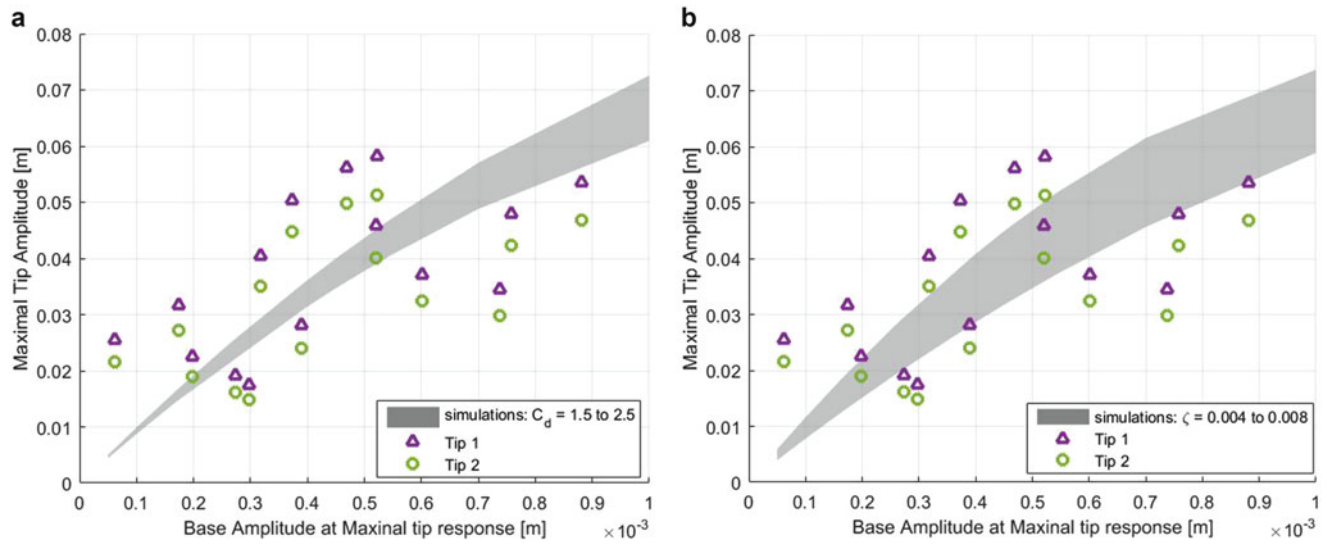


Fig. 44.11 Tip displacement amplitude vs. base displacement amplitude at resonance. Markers are experimental results. Shaded area represents simulations using (a) $\zeta_{st} = 0.006$, $C_d = 1.5\text{--}2.5$ or (b) $\zeta_{st} = 0.004\text{--}0.008$, $C_d = 2.0$

damping. For a large structural damping, the beam is restricted to smaller displacements and low velocity, preventing fluid damping from reaching high values and greatly affecting the results. As structural damping decreases, beam displacement and velocity increase, allowing for greater fluid damping to take place. Since fluid damping is only present in the nonlinear model, the more dominant it becomes, the greater the difference between the linear and nonlinear models.

Similarly, the transfer functions presented in Fig. 44.9 show the best agreement between linear and nonlinear computations for the highest structural damping and lowest base displacement, and an increasing difference as either base displacement increases, or structural damping decreases.

Figure 44.11 shows two types of damping coefficients, calculated coefficient using half power method, and maximal instantaneous total damping, for various levels of ζ_{st} . For all levels of structural damping, maximal instantaneous damping approaches the structural base value for small base displacements, as discussed previously. The inherent difference between instantaneous and calculated (half power) damping coefficient is increased as structural damping is decreased. This is due to fluid damping becoming more and more dominant, causing the nonlinearities in the system to grow, and thus decreasing the reliability of the half power method.

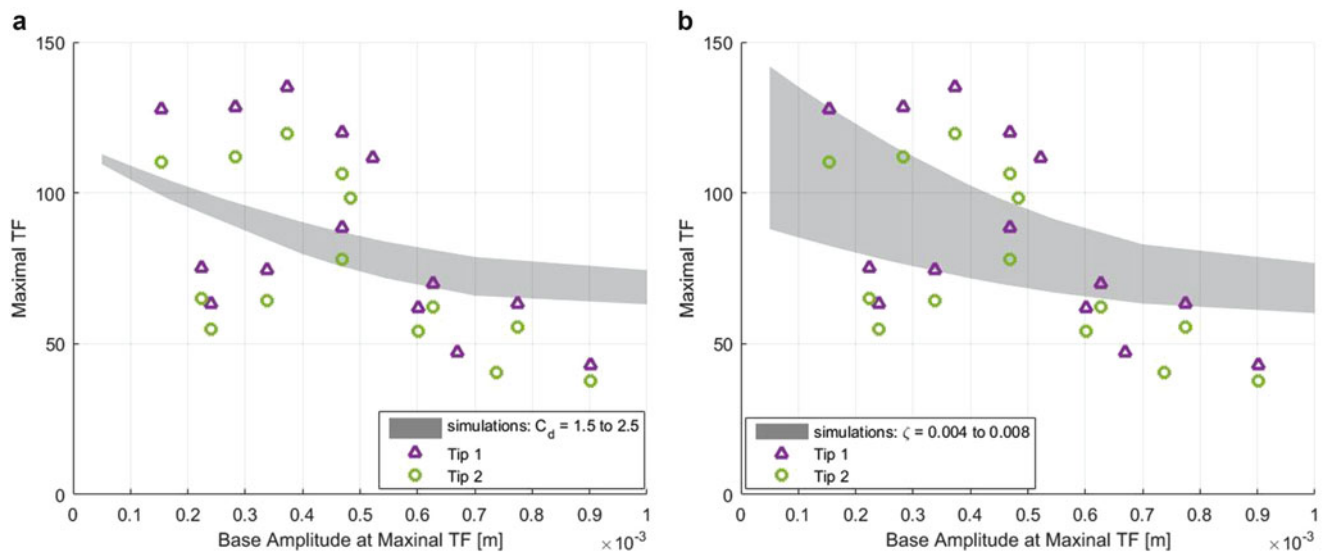


Fig. 44.12 Tip displacement to base displacement transfer function vs. base displacement amplitude at resonance. Markers are experimental results. Shaded area represents simulations using (a) $\zeta_{st} = 0.006$, $C_d = 1.5\text{--}2.5$ or (b) $\zeta_{st} = 0.004\text{--}0.008$, $C_d = 2.0$

44.4.2 Comparing Experimental and Computational Results

In order to assess whether variation in structural and fluid damping can explain the results observed in the experimental system, results from the numerical study were compared to results from experimental runs performed using the system described in Sect. 44.4. In each figure a range of simulated results for a single varying parameter (C_d or ζ_{st}) is presented as a shaded area, while the other parameter is held at a constant value. Experimental results from both tips of the two sided system are presented as discrete points. Some variation between the two tips are observed in most plots. Some possible reasons for these variations are calibration errors of the measurement instruments, or small beam asymmetries. While special considerations were taken to prevent the beam from ever reaching the yield stress during experiments, the repeated oscillatory motion during the full set of experiments may have caused some material fatigue. No indication of deformation or change in system properties were observed in a static test performed post experiment, but these fatigue effects cannot be completely ruled out.

Maximal tip displacement, transfer function at resonance, and measured damping coefficient are all presented versus the corresponding base displacement in Figs. 44.11, 44.12, and 44.13 respectively. The general trend lines produced by the computational model and experimental results in Fig. 44.11 are similar, however a fair amount of scatter is observed in the experimental results. This scatter may reflect in part the difficulty of the measurements in determining the peak response of the tip deflection for systems with relatively low damping, as the one used here. Additionally, uncertainties in material properties, as well as structural damping coefficient and fluid drag coefficient can contribute to the differences between theory and experiment.

The peak transfer function presented on Fig. 44.12 does not show improved agreement between experiment and the numerical model, since the same challenge in locating the exact peak tip amplitude affects results in the same manner described above. It is noted, however, that variation in structural damping (ζ_{st}) increases the range of results more for low base amplitudes, while changes in fluid damping (C_d) have a larger effect on the range of results for high base amplitudes.

This is consistent with observations made according to Figs. 44.5, 44.6, 44.7, 44.8, 44.9, and 44.10. For the specific range of C_d and ζ_{st} tested in this work, variation in structural damping produced a much larger range of results than variation in fluid damping. This is likely due to the fact that even at large base displacement, the added damping caused by drag was only comparable to the structural damping in near resonance frequencies, as seen in Fig. 44.4.

The damping coefficient presented in Fig. 44.13 is calculated using the half power method. While this method is normally used for linear systems and is less suitable for nonlinear systems, this is currently the best method to estimate damping effects consistently on a nonlinear system from both experiments and computational simulation data. Maximal instantaneous damping is not presented since such results could not be obtained from experiments. Interestingly, agreement between the two tips, as well agreement in trend between experiments and simulations is far better for the damping coefficient than it was for tip displacement or transfer function. This may be due to damping being a global property of the system, calculated using measurements from a range of frequencies, as opposed to peak tip amplitude and transfer function, which are local spatial and temporal properties.

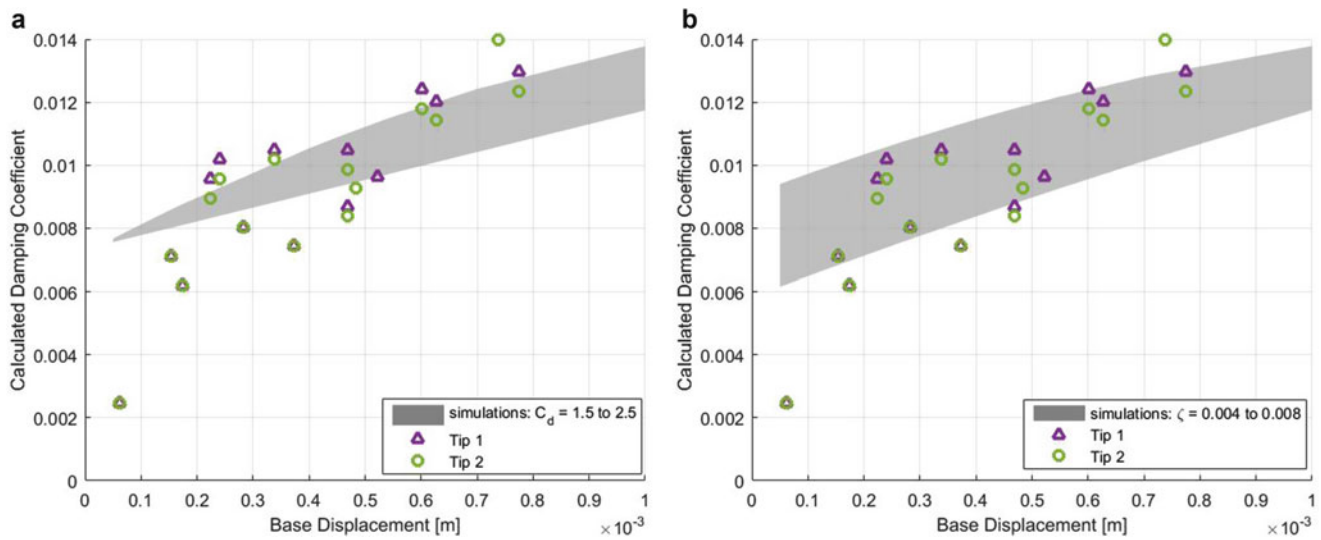


Fig. 44.13 Damping coefficient vs. base displacement amplitude at resonance. Markers are experimental results. Shaded area represents simulations using (a) $\zeta_{st} = 0.006$, $C_d = 1.5$ – 2.5 or (b) $\zeta_{st} = 0.004$ – 0.008 , $C_d = 2.0$

44.4.3 Nonlinear Effects and Hysteresis Near Second Natural Frequency

Another interesting aspect of the study was to examine how the different components of the nonlinear model affect the beams motion. As it turns out, these differences are greater for the second beam mode than the first beam mode previously studied. Figure 44.14 presents the tip deflection of the beam derived from the computer simulation using four versions of the nonlinear model: Nonlinear Damping only (NLD) – a fluid damping term is added to the linear model; Nonlinear Inertia (NLI) – the nonlinear inertia term, as well as fluid damping, are added to the linear model; Nonlinear Stiffness (NLS) – nonlinear stiffness and fluid damping terms are included in the model; Full nonlinear model (FNL) – all the above mentioned nonlinear terms are included in the model. More information about the various nonlinear terms can be found in Sect. 44.3 and in Sayag and Dowell [16]. Tip response in the vicinity of the first natural frequency, with a base displacement of 1.2 mm is presented in Fig. 44.14a, while the displacement near second resonance frequency with a base amplitude of 1.0 mm is presented in Fig. 44.14b. It is important to note that near the second resonance frequency, the stress at the root of the beam exceeds the yield stress for the type of aluminum used in the experimental study [16]. This could lead to variations in material properties that are not currently represented in the theoretical model. Since this section of the study does not include comparison to experiments, these material effects are neglected, and only the nonlinear effects mentioned above are discussed.

It is seen in Fig. 44.14a that the nonlinear inertia term and nonlinear stiffness term each have a small and opposite effect on the maximum response amplitude and frequency. When the two terms are combined into the full nonlinear model, the effect on both amplitude and frequency is reduced significantly, leading to a tip displacement very similar to the one achieved from linear computation with fluid damping added. Increasing base displacement further might emphasize the slight differences between the models, however this will certainly effect material properties in the experimental model and perhaps lead to failure in the structure.

Near the second resonance frequency, presented in Fig. 44.14b, a slightly lower base amplitude was used. The dimensional tip displacement amplitude is greatly reduced compared to the first resonance frequency, due to both the excitation amplitude and the shape of the dominant mode. Each nonlinear term effects the beams motion in a very similar manner to that observed near the first mode, but the effect is greatly magnified. For example: The NLI model produces a tip amplitude extremum that is about half of the NLD amplitude, at a frequency 98.5 Hz, which is 5.5 Hz below the peak observed using the NLD model. Near the first resonance frequency, the reduction in peak amplitude was about 2.5%, with a frequency variation of about 0.5 Hz. Recall that near the first resonant frequency the total nonlinear effect on the resonant frequency was modest because of the offsetting effects of nonlinear stiffness and inertia. By contrast the total nonlinear effects near the second resonant frequency are more evident because the nonlinear inertia effect is dominant and the nonlinear stiffness effect is less prominent. It is seen in Fig. 44.14b that the FNL computation greatly resembles the results using the NLI model. This indicates that for this range of frequencies, and perhaps higher frequencies as well, the nonlinear inertia has a greater effect on the motion of the beam than nonlinear stiffness.

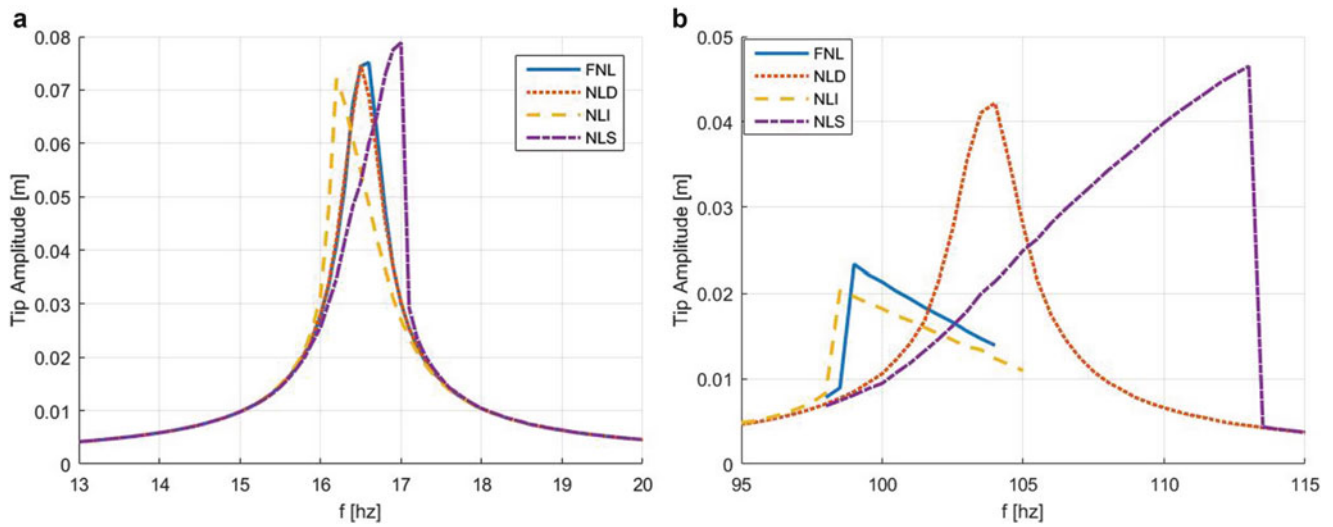


Fig. 44.14 Dimensional tip displacement vs. excitation frequency near first and second resonance frequencies: partial and full nonlinear models. (a) ω_1 , $A_0 = 1.2$ mm; (b) ω_2 , $A_0 = 1.0$ mm

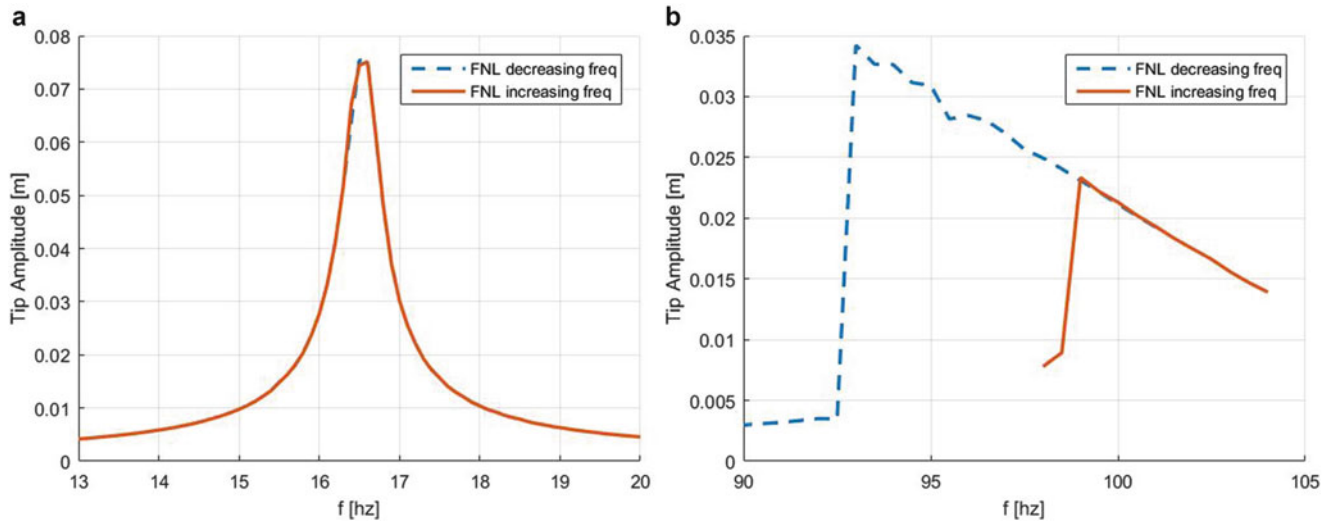


Fig. 44.15 Dimensional tip displacement vs. excitation frequency near first and second resonance frequencies: full nonlinear model, increasing and decreasing frequency sweep. (a) ω_1 , $A_0 = 1.2$ mm; (b) ω_2 , $A_0 = 1.0$ mm

The tip displacement for the FNL model for both increasing and decreasing frequency sweep is presented in Fig. 44.15. Near the first resonant frequency, presented in Fig. 44.15a, there is no significant difference between the two computations. This is consistent with the previous statements that nonlinear inertia and stiffness effects are mutually canceling in this range of frequencies, therefore no hysteresis is observed. Near the second resonant frequency, presented in Fig. 44.15b, the FNL model, which had proved to be greatly affected by the various nonlinear terms, produced a significant variation in peak amplitude and frequency depending on whether the sweep frequency was increasing or decreasing.

44.5 Summary and Conclusions

It has been widely appreciated that a cantilevered beam has very distinct and different nonlinearities from that of a beam clamped (or at least fixed) at both ends. In the latter case the dominant nonlinearity arises from the tension created by the axial extension induced by the bending of the beam. However for a cantilevered (or free-free) beam the beam is virtually inextensible and indeed a theory based upon the assumption of inextensibility provides a very good model for such a beam. However the deflection that gives rise to the nonlinearity is on the order of the beam length for a cantilevered beam, while

by contrast the nonlinearity of a beam clamped at both ends is evident when deflections are only on the order of the beam thickness.

Because the deflections are much larger for a cantilevered beam when nonlinearities come into play the mathematical model is necessarily different and the physical effects are as well. For cantilevered beams stiffness and inertial nonlinearities are both important and indeed their two effects near the first resonance frequency are offsetting to a substantial degree so that the frequency at peak response is relatively little changed from the value predicted by linear theory. However the amplitude of the peak response is modestly changed and perhaps unexpectedly recent work shows that nonlinear damping (which is likely due to fluid drag forces) may be important as well. So the cantilevered beam may exhibit nonlinear damping, inertia and stiffness.

In the present paper several themes are addressed building on the earlier work of Sayag and Dowell [16] and others. All three nonlinear effects are included in the mathematical model and a systematic comparison with the results of earlier experiments [16] is made. Both the mathematical model and the physical experiments show similar trends and quantitative agreement is fair to good. Indeed with the results of this systematic correlation study between theory and experiment in hand, several possible sources of scatter or uncertainty in the experimental data have been identified. These include the modeling of structural and fluid damping with the former being hard to control in an experiment. Ideally the experiments would be repeated in a vacuum chamber which of course makes the experiment more difficult and will require a more elaborate experimental apparatus.

Also in this study the second resonant mode has been studied as well as the first resonant mode. While inertia effects and stiffness effects are substantially offsetting for the first resonant mode, the nonlinear inertia effect is more dominant than the nonlinear stiffness effect for the second resonant mode. It is hypothesized that this will also be true for yet higher resonant modes. This is worthy of further study. Of course it takes higher force levels to bring the higher resonant modes into the nonlinear range.

It likely is significant that the global nonlinear properties of the beam response measured experimentally, i.e. natural frequency and damping as a function of base excitation, show less variation among the experimental measurements and are in better agreement with the theory computational model than the local nonlinear property i.e. tip deflection as a function of base deflection.

There are other possible directions for future work and there is not space here to mention them all. But two are offered as being particularly attractive from both a conceptual and application point of view. One would be to study a free-free beam and the other would be to study a plate rather than a beam. For initial work on these topics see the paper by McHugh and Dowell [7].

Nonlinear Terms of the Computational Model

The internal nonlinear loads and external forces acting on the beam during large amplitude oscillations are presented below. More information about these terms can be found at Tang and Dowell [6] and Sayag and Dowell [16].

$$F_{w_b} = \left[m_b \int_0^L \psi_i dx + m_{tip} \psi_0(L) \right] \ddot{w}_b$$

$$F_{BN} = \sum_j \sum_k \sum_l P A_{ijkl} (q_j q_k q_l)$$

$$F_{BM} = \sum_j \sum_k \sum_l [M A_{ijkl} + m_{tip} N_{ijkl}(L)] (q_j \dot{q}_k \dot{q}_l + q_j q_k \ddot{q}_l)$$

$$F_{m_{tip}} = m_{tip} \psi_i(L) \sum_j \psi_j(L) \ddot{q}_j$$

Here M_{bi} is the generalized mass of the beam only, while M_{ti} also includes the tip mass. The following definitions are used:

$$m_{bi} = \int_0^L \psi_i^2 dx$$

$$m_{ti} = m_{bi} + m_{tip} \psi_i(L)$$

$$N_{ijkl} = \int_0^x \psi'_i \psi'_j d\zeta \int_0^x \psi'_k \psi'_l d\zeta$$

$$M_{ijkl} = \int_0^L m_b N_{ijkl} dx$$

$$P A_{ijkl} = \int EI (\psi''_i \psi''_j \psi'_k \psi'_l + \psi'_i \psi'_j \psi'_k \psi'_l) dx$$

References

1. Gordnier, R.E., Chimakurthi, S.K., Cesnik, C.E., Attar, P.J.: High-fidelity aeroelastic computations of a flapping wing with spanwise flexibility. *J. Fluids Struct.* **40**, 86–104 (2013)
2. Chang, K., Chaudhuri, A., Rue, J., Haftka, R., Ifju, P., Tyler, C., Ganguly, V., Schmitz, T.: Improving the fabrication process of micro-air-vehicle flapping wings. *AIAA J.* **53**(10), 3039–3048 (2015)
3. Dunnmon, J., Stanton, S., Mann, B., Dowell, E.: Power extraction from aeroelastic limit cycle oscillations. *J. Fluids Struct.* **27**(8), 1182–1198 (2011)
4. Challa, V.R., Prasad, M., Shi, Y., Fisher, F.T.: A vibration energy harvesting device with bidirectional resonance frequency tunability. *Smart Mater. Struct.* **17**(1), 015035 (2008)
5. Erturk, A., Inman, D.J.: An experimentally validated bimorph cantilever model for piezoelectric energy harvesting from base excitations. *Smart Mater. Struct.* **18**(2), 025009 (2009)
6. Tang, D., Zhao, M., Dowell, E.H.: Inextensible beam and plate theory: computational analysis and comparison with experiment. *J. Appl. Mech.* **81**(6), 061009 (2014)
7. Dowell, E., McHugh, K.: Equations of motion for an inextensible beam undergoing large deflections. *J. Appl. Mech.* **83**(5), 051007 (2016)
8. Heris, N., Marinca, V.: Explicit analytical approximation to large-amplitude non-linear oscillations of a uniform cantilever beam carrying an intermediate lumped mass and rotary inertia. *Meccanica.* **45**(6), 847–855 (2010)
9. Das, D., Sahoo, P., Saha, K.: A numerical analysis of large amplitude beam vibration under different boundary conditions and excitation patterns. *J. Vib. Control.* **18**(12), 1900–1915 (2012)
10. Novozhilov, V.V.: *Foundations of the Nonlinear Theory of Elasticity*. Graylock Press, Rochester, NY (1953)
11. Qian, Y., Lai, S., Zhang, W., Xiang, Y.: Study on asymptotic analytical solutions using ham for strongly nonlinear vibrations of a restrained cantilever beam with an intermediate lumped mass. *Numer. Algorithms.* **58**(3), 293–314 (2011)
12. Qaisi, M.I.: Application of the harmonic balance principle to the nonlinear free vibration of beams. *Appl. Acoust.* **40**(2), 141–151 (1993)
13. Pillai, S., Rao, B.N.: On nonlinear free vibrations of simply supported uniform beams. *J. Sound Vib.* **159**(3), 527–531 (1992)
14. Azrar, L., Benamar, R., White, R.: Semi-analytical approach to the non-linear dynamic response problem of s–s and c–c beams at large vibration amplitudes Part i: general theory and application to the single mode approach to free and forced vibration analysis. *J. Sound Vib.* **224**(2), 183–207 (1999)
15. Ozcelik, O., Attar, P.J., Altan, M.C., Johnston, J.W.: Experimental and numerical characterization of the structural dynamics of flapping beams. *J. Sound Vib.* **332**(21), 5393–5416 (2013)
16. Sayag, M.R., Dowell, E.H.: Linear versus nonlinear response of a cantilevered beam under harmonic base excitation: theory and experiment. *J. Appl. Mech.* **83**(10), 101002 (2016)
17. Ozcelik, O., Attar, P.J.: Effect of non-linear damping on the structural dynamics of flapping beams. *Int. J. Non Linear Mech.* **65**, 148–163 (2014)
18. Anderson, T.J., Nayfeh, A.H., Balachandran, B.: Experimental verification of the importance of the nonlinear curvature in the response of the cantilever beam. *J. Vib. Acoust.* **118**, 21–27 (1996)
19. Luongo, A., Rega, G., Vestroni, F.: On nonlinear dynamics of planar shear indeformable beams. *J. Appl. Mech.* **53**, 619–624 (1986)
20. Lenci, S., Clementi, F., Rega, G.: A comprehensive analysis of hardening/softening behavior of a shearable planar beams with whatever axial boundary constraint. *Mecannica.* **51**, 2589–2606 (2016)



Chapter 45

Reduced Order Modeling of Structures with Preloaded Bolted Joints by the Use of Trial Vector Derivatives

Wolfgang Witteveen and Florian Pichler

Abstract In case of preloaded jointed structures, both, the result quality of the overall vibrations and of the local stress distribution inside the joints may depend on an accurate consideration of the nonlinear contact and friction forces between the contact surfaces. In this paper the adaption of a trial vector derivative based method to preloaded bolted joints is presented. Two advantages of this method can be reported: First, a fast convergence with respect to the number of additional joint modes, and second, reduced computational cost for the joint mode generation. The potential of the method is demonstrated using a bolted piston rod bearing cap.

Keywords Multibody simulation · Model order reduction · Preloaded structures · Joint contact

45.1 Introduction

Complex mechanical structures are commonly an assembly of several substructures which are connected by different types of joints. Several types of joints like bolted joints, interference fits and others lead to prestressed structures due to mounting forces. For the dynamics of jointed structures inside a multibody simulation special joint modes based on trial vector derivatives [1] have been introduced in the last years. In this contribution a special consideration of the deformation caused by the preload is presented. The theory of these specialized joint modes is presented in Sect. 45.2 and in Sect. 45.3 an application of this method to a bolted piston rod bearing cap is investigated.

45.2 Theory

Component mode synthesis (CMS) [2, 3] has become an established tool for integration of flexible bodies into multibody simulations. In this method the $(n_{FE} \times m)$ reduction basis

$$\Phi = [\Phi_S \Phi_V] \quad (45.1)$$

is a combination of s trial vectors collected in Φ_S which are basically static deformation shapes due to forces at the interface nodes and v vibration mode shapes collected as columns in the matrix Φ_V . This reduction basis is used to approximate the nodal DOFs $\mathbf{x} \approx \sum_{i=1}^m \phi_i q_i = \Phi \mathbf{q}$, where \mathbf{q} holds the $m = v + s$ time varying scaling factors q_i . Both types of trial vectors are a function of the stiffness matrix of the structure. Hence, for structures including nonlinear and state-dependent contact and friction forces the stiffness matrix $\mathbf{K}_{nl}(\mathbf{x})$ and consequently the trial vectors become state-dependent. For the trial vector ϕ_i this dependency can be approximated by a Taylor series expansion around a reference configuration as (see [4])

$$\phi_i(\mathbf{q}) = \phi_i|_{\hat{\mathbf{q}}} + \sum_{j=1}^m \frac{\partial \phi_i}{\partial q_j} \Big|_{\hat{\mathbf{q}}} (q_j - \hat{q}_j) + \text{terms of higher order}, \quad (45.2)$$

W. Witteveen (✉) · F. Pichler
University of Applied Sciences Upper Austria – Wels Campus, Wels, Austria
e-mail: wolfgang.witteveen@fh-wels.at

with $\hat{\mathbf{q}} = [\hat{q}_1 \cdots \hat{q}_m]^\top$ being the scaling factors at the reference configuration. For many structures the undeformed state ($\hat{\mathbf{q}} = \mathbf{0}$) is a good choice but also a certain preload state ($\hat{\mathbf{q}} = \mathbf{q}_{\text{PL}}$) might be a possible choice for the reference configuration.

In Eq. (45.2), the term $\frac{\partial \phi_i}{\partial q_j}$ denotes the first order *trial vector derivative* (TVD) of the i -th trial vector with respect to the j -th modal coordinate. For both types of trial vectors the TVD can be computed along

$$\mathbf{K}_{\hat{\mathbf{q}}} \frac{\partial \phi_i}{\partial q_j} \Big|_{\hat{\mathbf{q}}} = - \frac{\partial \mathbf{K}_{\hat{\mathbf{q}}}}{\partial q_j} \phi_i \Big|_{\hat{\mathbf{q}}} \quad (45.3)$$

whereby all inertia-related terms are neglected and $\mathbf{K}_{\hat{\mathbf{q}}} = \mathbf{K}_{nl}(\hat{\mathbf{q}})$ denotes the stiffness matrix at the chosen reference state. For contact problems TVDs are not symmetric, which leads to the number of possible TVDs being $(2m^2)$. In order to obtain a smaller subspace as the one spanned by all TVDs, proper orthogonal decomposition (POD) [5] is applied to compute the joint modes $\phi_{J,i}$ which are finally used for an extension of the reduction basis (see [1])

$$\Phi = [\Phi_{\text{CMS}} \cdots \phi_{J,i} \cdots] \quad i = 1, \dots, g. \quad (45.4)$$

The number TVDs depends with $2m^2$ on the square of the size of the CMS reduction basis m . For industrial applications with $m > 100$ the number of static computations can become quite huge ($> 10^4$). To overcome this bottleneck, a specialized computation of joint modes for preloaded structures is outlined in the following. More details can be found in [4].

In case of preloads the deformations can be assumed to be small around the preload state and not around $\hat{\mathbf{q}} = \mathbf{0}$. Therefore, the Taylor series expansion has to be built around $\hat{\mathbf{q}} = \hat{\mathbf{q}}_{\text{PL}}$ with $\mathbf{x}_{\text{PL}} = \Phi \hat{\mathbf{q}}_{\text{PL}}$. For the practical application of such a Taylor series expansion some difficulties occur in combination with commercial FE software (see [4] for details). Hence, in [4] so-called preload modes (PLMs) are introduced. The $(n_{\text{FE}} \times 1)$ PLM $\phi_{\text{PL},i}$ is basically the static deformation shape due to the preload force $\mathbf{f}_{\text{PL},i}$ considering full nonlinear contact

$$\mathbf{K}_{nl} \phi_{\text{PL},i} = \mathbf{f}_{\text{PL},i} \quad i = 1, \dots, p. \quad (45.5)$$

These PLMs are collected in the $(n_{\text{FE}} \times p)$ matrix Φ_{PL} and the $(n_{\text{FE}} \times r)$ reduction basis with $r = m + p$ trial vectors can be written as $\Phi = [\Phi_{\text{CMS}} \ \Phi_{\text{PL}}]$. Since the reference state is dominated by the PLMs, not all TVDs are of same relevance for the quality of the extended reduction basis. Consequently, the POD based computation of joint modes can be performed using only TVDs related to the preload mode. Since the most important information should be covered by the PLM related derivatives $\left[\frac{\partial \phi_{\text{PL}}}{\partial q_{\text{PL}}} \cdots \frac{\partial \phi_i}{\partial q_{\text{PL}}} \cdots \frac{\partial \phi_{\text{PL}}}{\partial q_i} \cdots \right]$, the joint modes computed with these derivatives should yield high quality results which are comparable to the results using all possible TVDs. Furthermore, it is assumed that the space spanned by PLM related TVDs is more specific concerning the interesting joint deformation, and hence the specialized joint modes should lead to a faster convergence. Moreover, this approach has the advantage that the number of TVDs which need to be computed is much lower $(2(p^2 + 2pm) \ll 2(m+p)^2)$. This fact is of practical relevance since the computation of all TVDs is a time and memory consuming task for industrial applications with many trial vectors in the CMS reduction basis. From an engineering point of view, it is easy to imagine that the derivatives $\frac{\partial \phi_{\text{PL}}}{\partial q_i}, \frac{\partial \phi_i}{\partial q_{\text{PL}}}$ are most important since they describe the change of a deformation according to the preload state, and the change of the preload state with respect to a dynamic deformation.

45.3 Numerical Example

The joint modes computed with PLM related derivatives are investigated on a bolted piston rod bearing cap of a single cylinder engine. A schematic drawing of the multibody system can be found in Fig. 45.1. The model consists of a crankshaft, a piston and a flexible piston rod with a bolted bearing cap and is excited with a prescribed rotation of the crankshaft. The parameters of the model are identical to the parameters used in [4].

45.3.1 Dynamic Convergence Analysis

For the piston rod bearing cap a dynamic convergence analysis was performed. The crankshaft is actuated by a prescribed motion and the system is simulated for $T = 0.3$ s. The motion is prescribed with a smoothed step using a Haversine function where the rotational end speed of $n_c = 10,000 \text{ min}^{-1}$ is reached after 0.25 s. As convergence criteria, the Euclidean norm

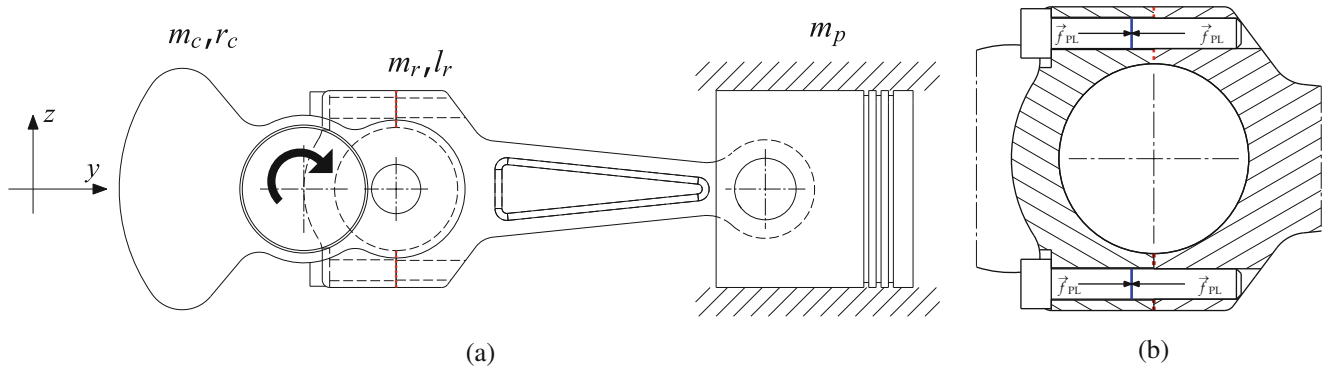


Fig. 45.1 Single cylinder with flexible bolted piston rod. (a) Schematic draft of MBS model. (b) Screw preload modeling

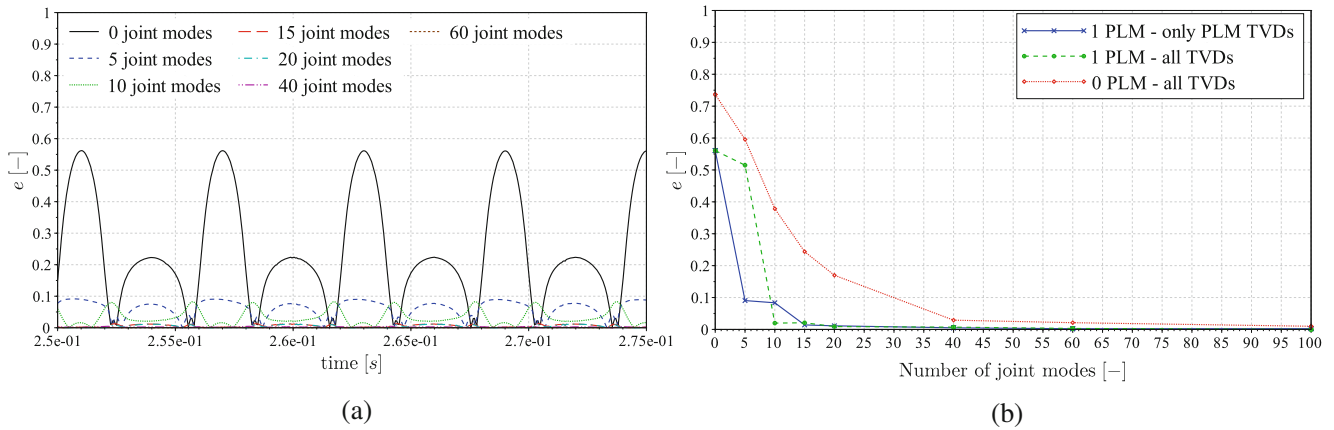


Fig. 45.2 Dynamic convergence study. (a) 1 PLM – only PLM TVDs. (b) Max. error of different joint modes

of the vector containing the normal gaps of all contact pairs $|\mathbf{g}_c|_2$ is used. In Fig. 45.2, the curves for the three compared reduction bases are shown in the left column. In the right column of this figure the absolute values of an error defined by

$$e = \frac{|\mathbf{g}_c|_2(100) - |\mathbf{g}_c|_2(x)}{|\mathbf{g}_c|_2(100)} \quad (45.6)$$

is depicted. Where $|\mathbf{g}_c|_2(100)$ denotes the solution with 100 joint modes, which is considered as a reference solution.

The figure shows that even under high dynamical loads, the use of the PLM leads to substantially better convergence. In case a PLM is considered, the methods considering only PLM derivatives or all TVDs lead nearly to the same convergence. The method using all TVDs reaches an error e below 4% at 10 joint modes, and the method using only PLM derivatives reach this limit at 15 joint modes. For both methods the solution shows a high level of accuracy at 15 joint modes, by which the error e stays below 4%. Without the PLM this 4% limit is reached at 40 joint modes.

45.4 Conclusion

A specialized computation of joint modes for preloaded structures based on PLM derivatives has been outlined. The numerical investigations confirm, that these specialized joint modes lead to a supreme convergence and result quality. It should be mentioned, that for other types of structures the convergence of specialized joint modes might even be better (see [4]). In the latter mentioned work also possible limitations of the specialized joint modes are investigated and discussed. Furthermore, the computational effort for generating the joint modes using only PLM related derivatives is much lower. For the considered example only 146 static load-cases need to be computed instead of 2738 static load-cases required for the joint modes using all TVDs.

References

1. Pichler, F., Witteveen, W., Fischer, P.: A complete strategy for efficient and accurate multibody dynamics of flexible structures with large lap joints considering contact and friction. *Multibody Sys. Dyn.* **40**(4), 407–436 (2017)
2. Craig, R.R.: A review of time-domain and frequency-domain component mode synthesis method. In: *Proceedings of the Joint Mechanics Conference on Combined Experimental/Analytical Modeling of Dynamic Structural Systems*, pp. 1–30 (1985)
3. Qu, Z.-Q.: *Model Order Reduction Techniques with Applications in Finite Element Analysis*. Springer, London (2004)
4. Pichler, F., Witteveen, W., Fischer, P.: Reduced order modeling of preloaded bolted structures in multibody systems by the use of trial vector derivatives. *J. Comput. Nonlinear Dyn.* **12**(5), 051032–051032–12 (2017)
5. Volkwein, S: Model Reduction Using Proper Orthogonal Decomposition, URL: <http://www.math.uni-konstanz.de/numerik/personen/volkwein/teaching/POD-Vorlesung.pdf>, cited 03.2018



Chapter 46

Towards the Development of a Model for Nonlinear Elements in Machine Tools

Steven M. Whitican, Charles Van Karsen, and Jason Blough

Abstract Machine tool structures contain a number of joints which provide for rotation or translation of connected structural elements. These joints add significant nonlinearity to the system thus making overall performance difficult to predict. Linear guides have been identified as a particular connection which exhibit significant nonlinearity. Linear guides are thus very difficult to accurately model into a dynamic simulation. Linear guideways have predominantly replaced box ways in industrial machinery to facilitate linear directional motion. As opposed to box ways which are scraped to obtain the most contact area possible, linear guides depend on theoretical contact patches between the guide, rail, and rolling element train. Linear guides exhibit complicated dynamics, the accurate prediction of which is necessary for a high-fidelity model of a machine tool. A fixture was developed to study linear guides. This paper highlights some of the properties of linear guides and begins the process of creating a model by studying the form of the nonlinearity using the Acceleration Surface Method (ASM). Future work will involve the comparison of the derived model against other popular linear guide models and the parameterization of the model found here.

Keywords Acceleration surface method · Machine tools · Joints · Restoring force surface · Nonlinear modes

46.1 Introduction

Accurate predictive dynamic models of a machine tools are difficult to construct. Nonlinear joints and variation of linear substructures and engineering materials add to the difficulty of build a robust mode of a machine tool. A commonly used design element which aggravates modeling complication are linear guides. Linear guides facilitate linear motion of the machine tool axes. There are two types on the market today which are commonly used for machine axes under heavy load: guides with ball rolling elements and guides with cylindrical rolling elements. It is typical that rolling elements recirculate through a path internal to the block facilitating cooling and distribution of lubricant. An example of the recirculation pathway is shown in Fig. 46.1.

Lubrication may be applied to the linear guides by the machine to maintain the most standard and consistent state. Guides feature wipers in both directions of travel to minimize contaminant entering the rolling set. Linear guides may be developed with a number of preloads built into the rolling sets. The higher the preload, the greater the static stiffness of the assembly and the more force is required to initiate motion. It is not known how preload effects damping at this point. This information is also of paramount interest for the best application of the guides and results will be shown in future work.

Existing modeling methodology utilizes a linear spring to represent the guide's stiffness. The stiffness used for this parameter may be defined experientially or based upon manufacturer recommendations. The manufacturer recommendations for stiffness are derived from calculations using Hertzian contact theory. Figure 46.2 shows a sample output of supplier calculation. This data may be enough for statically sizing the guides. Supplier calculations capture the elastic nature of the guides, but reveal nothing about frequency and energy dependence or absorption. These are the critical features of the guide which must be understood to build a robust model.

Linear guide behavior was studied in modal tests of a standard production CNC machine. Four guides carry an axis unit and the response was measured on either side of the linear guide joint by excitation at the spindle housing utilizing a servo-hydraulic shaker. Responses were then compared to aid in the understanding of dynamic behavior of the guides.

S. M. Whitican (✉)
MAG Automotive LLC, Sterling Heights, MI, USA
e-mail: steven.whitican@mag-ias.com

C. Van Karsen · J. Blough
Michigan Technological University, Houghton, MI, USA

Fig. 46.1 Example of the recirculation pathway within a linear guide containing ball rolling elements [1]

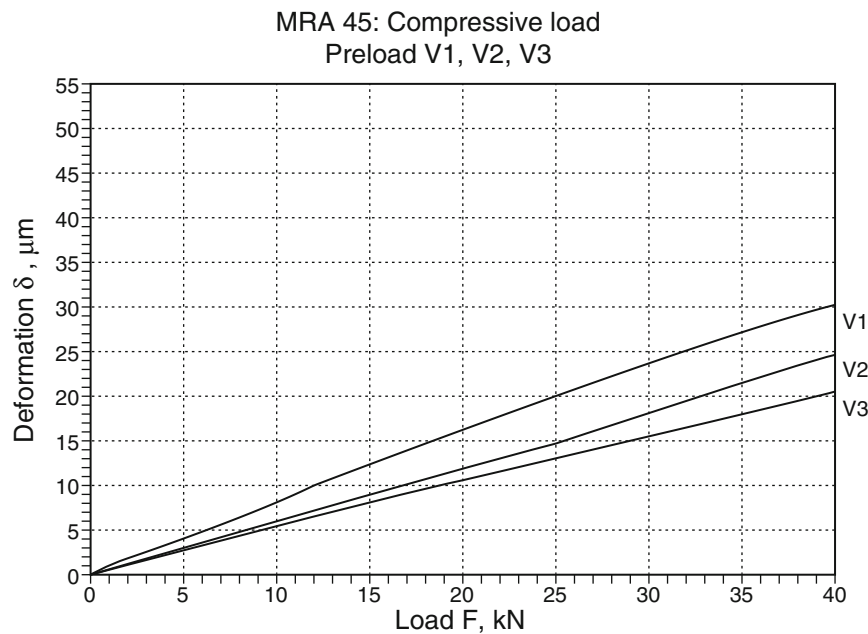
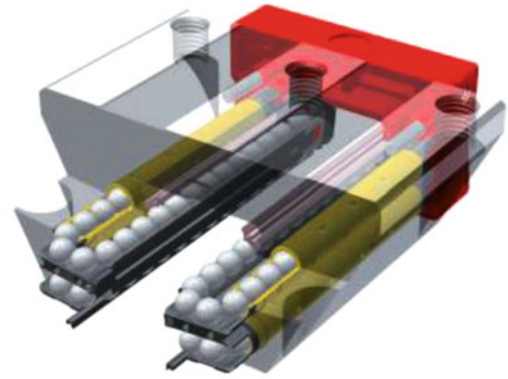


Fig. 46.2 Example computed stiffness characteristic for a linear guide [1]

The maximum normalized difference was computed across the guide and the results are shown in Fig. 46.3. If the linear assumption were valid, one would expect the value to be zero for all frequencies. This is the case out to approximately 380 Hz except at structural resonance indicating the linear assumption is *somewhat* valid for low frequencies. The linear assumption is also *somewhat* valid when not operating at or near a machine structural resonance. The linear assumption completely falls apart at frequencies greater than 380 Hz.

Though linear guides have been previously tested and models proposed, there has not been any testing to the levels done in this work. The testing performed herein is representative of the loading the guides would see during ordinary machining operations. A new model is needed which can capture the frequency and energy dependence of the guides yielding a more accurate and predictive machine tool model. Guides also need to be investigated to see in which applications the model holds. Do the guides exhibit the same nonlinear form and parameters in all applications? The form of the nonlinearity is studied in this paper with the help of the Acceleration Surface Method (ASM).

46.2 Methodology

A brief history of ASM is necessary. ASM derives itself from the Restoring Force Surface Method (RFS). The Restoring Force Surface (RFS) method was developed for nonlinear SDOF systems by Marsi and Caughey. The method is derived in detail in [2]. A generalization of the procedure for MDOF systems involves the use of modal parameters as opposed to physical parameters [3]. The process has not been used industrially for reasons to be detailed below.

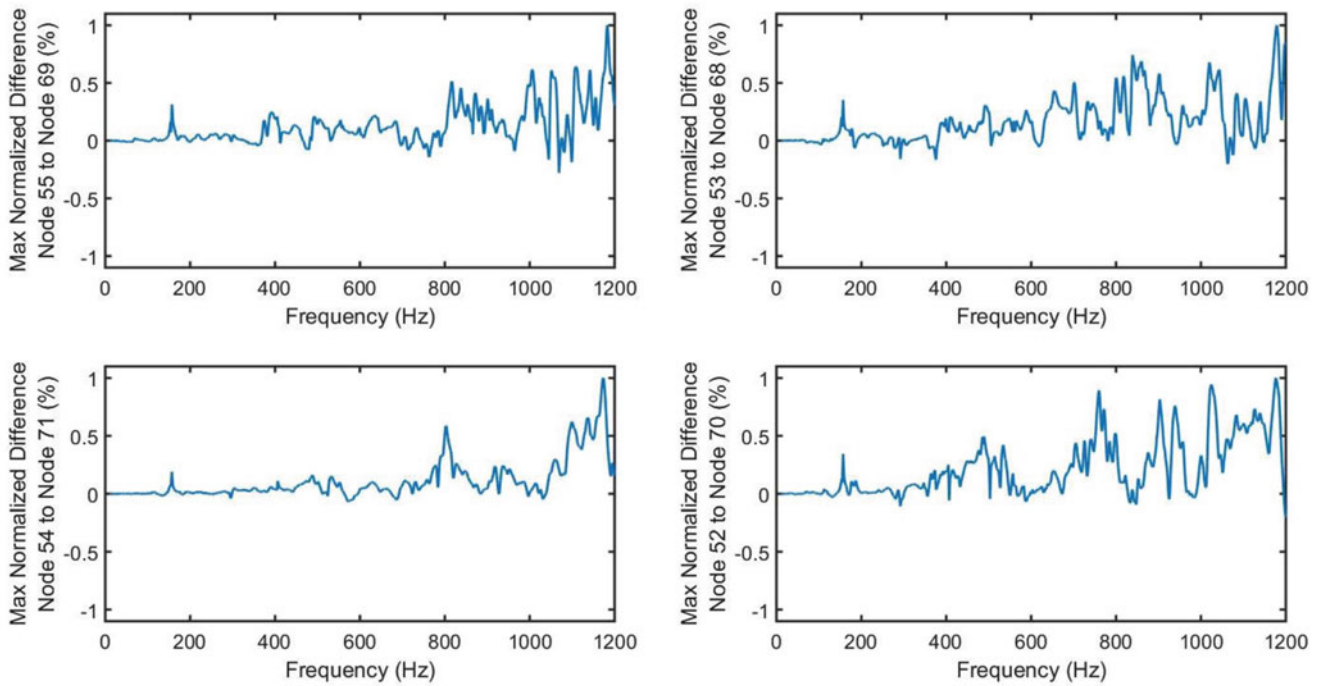


Fig. 46.3 Max normalized difference comparison for all corners of the lateral axis of a CNC machine

RFS finds its basis in Newton's second law. To account for the nonlinearity in an otherwise linear system an additional term included which maps the nonlinearity over the displacement, velocity plane. A full derivation of the method may be found in [3].

The computation of a fully parametrized model using the Restoring Force Surface method relies on the correct determination of modal mass. Unfortunately, this is still a very errant task for experimentalists. Computation of modal mass is influenced heavily by measurement noise and very difficult for flexible modes of vibration. One particular method for computation of modal mass which was developed for use with the RFS method by Al-Hadid and Wright may be found in [4]. This method involves monotonic testing just above and below resonance, plotting results in a stiffness/mass plane, and finding where the lines from the two frequency levels cross. This was found with analytical data to be very accurate. The method, however, (unautomated) is clunky and time consuming. The method also has the detractor that special testing is required for its implementation.

To that end, if the modal mass, or system mass in the case of a single degree of freedom system, is set to unity the *form* of the nonlinearity may be determined. The mass is used as a scaling factor for the form of the nonlinearity [5]. For use with ASM the mass set to unity thus the nonlinearity may not be quantified. The typical RFS procedure involves the fitting of Chebyshev or polynomial to the surface. This is not possible without the mass to provide the appropriate scale.

Further, the RFS methodology as originally stated would compute restoring force surfaces between a particular degree of freedom and ground. Nodes are not all typically connected to ground making this method unhandy for practical flexible systems. To extend RFS as a means to determine the form of a nonlinearity across a joint Dossogue et al. [3] generalized the methodology further into ASM. ASM may be used to create a visual aid for determining the form of a nonlinearity. ASM is successful in identifying stiffness and damping nonlinearities in many cases [6–8]. Data for generation of the acceleration surface may be entirely collected and processed from accelerometers with no *a priori* information. The acceleration surface method is particularly helpful for establishing and identifying nonlinearity across joints as it involves relative measurements from one side of the joint to the next. ASM is computed by means of Eq. (46.1) [3].

$$g_i(q_i - q_j, \dot{q}_i - \dot{q}_j) \approx -m_{i,i}\ddot{q}_i \quad (46.1)$$

For every measurement instance, a relative displacement and velocity are calculated. These values are plotted against the acceleration taken to be the prime side of the joint. It is noteworthy that for the acceleration surface to come out correctly, proper filtering is an absolute necessity.

In this work ASM will be used to define the form of the nonlinearity inherent to the linear guides. This work will involve decomposition of the response signal into its fundamental and harmonics and the acceleration surface computed for each.

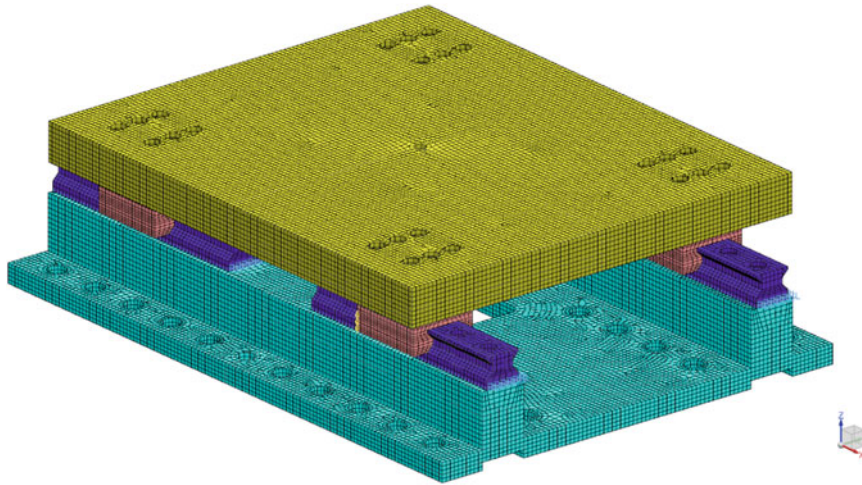


Fig. 46.4 Test fixture utilized in work to establish models of linear guides

46.3 Development of Test Fixture

A test fixture was constructed to study the linear guides. A FEM of the fixture is shown in Fig. 46.4. Linear guides are typically applied in denominations of four or six. The test fixture was designed to accommodate four guides. The fixture was also developed to avoid too much variability such as a top plate with complicated or uncertain geometry and material quality (indicative of a machine axis).

The test fixture allowed for application and physical connection of a servo-hydraulic shaker. The shaker was screwed between the fixed base and the upper plate so loads could be applied with compressive, tensile, or no static preload.

Per guide manufacturer recommendations the screws were tightened using a torque wrench. The screws connecting the rails to the lower weldment were torqued to 95 Nm. The screws connecting the trucks to the upper weldment were torqued to 50 Nm [9]. The guides were also lubricated with grease per the manufacturer.

46.4 Collection of Data

Using a servo-hydraulic shaker, this fixture is capable of studying guides under compressive, tensile, or lateral loading out to the shaker's maximum frequency usable of approximately 1250 Hz. There was difficulty realized in achieving a uniform input spectra as the shaker system's frequency response begins to roll off at approximately 300 Hz and the modes of interest lie between 463 and 1 kHz. Figure 46.5 shows the input spectrum for the 1 kN sweep. This sweep was controlled using the analog on the dual-loop master controller. The roll-off of the shaker system is evident in the figure.

For the purpose of this initial work, the guides were tested vertically. The excitation was placed at the center of the plate so equal loading would be observed on all four guides. This was done with future modeling of the guides in mind. For future work, the excitation will be moved to better excite the shell modes and transverse modes of the plate piece.

The test fixture was mounted on a stiff cast iron cube to provide the most 'fixed' boundary condition achievable. The servo-hydraulic shaker was screwed down to cast cube to facilitate tensile static preloading of the guides. The servo-hydraulic shaker system in use has the capacity to apply a full array of static preloads from compressive to tensile. Table 46.1 lists the loading to which the guides were subjected. The purpose of the various loading scheme was to track how response of the guides varies with different loading schemes. For example, if the guides are purposed to carry a heavy headstock or fixture assembly they may be preloaded in compression. If they are used to hang machine structure from a wall, the guides will be exposed to both tensile and compressive static preloads dependent on where they are in the assembly.

Various excitation regimes were attempted on the structure including impact, sine-dwell, swept sine, and periodic random. Burst random techniques were used for the measurement of response at the described excitation levels and determine the modes which present for further study. Slow sine sweeps were finally performed to acquire integrable time histories for use in computing the acceleration surface and studying the nonlinear modes.

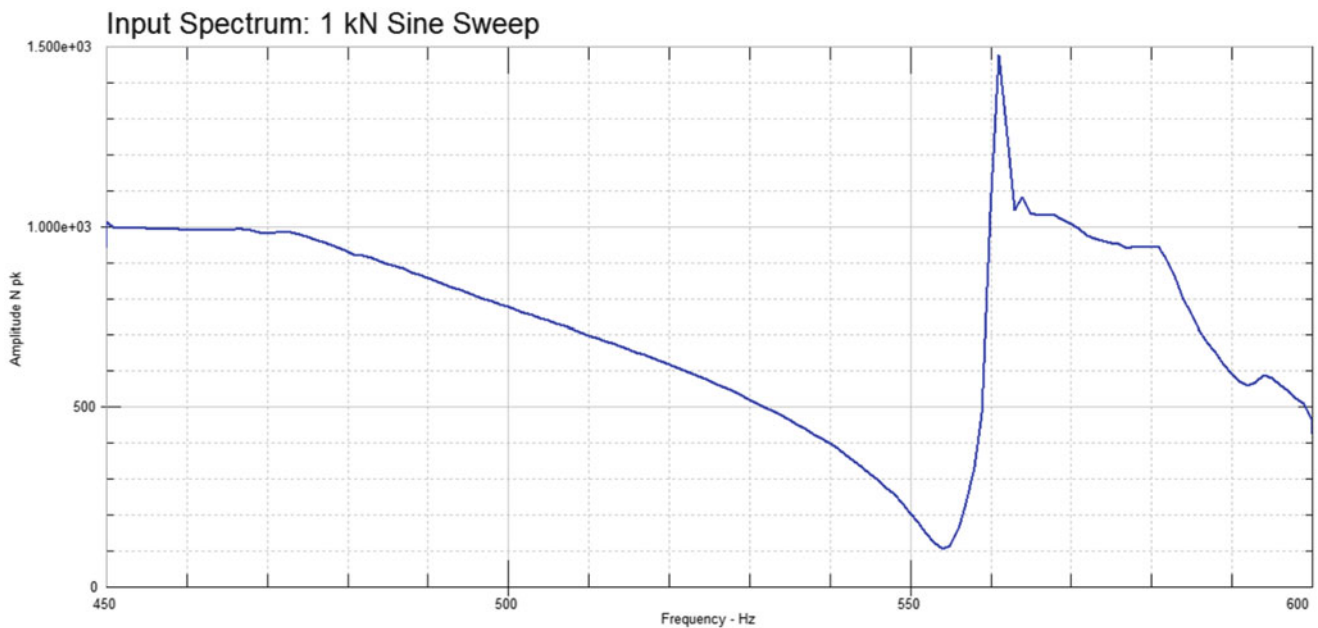


Fig. 46.5 Input spectrum: 1 kN sine sweep

Table 46.1 Static/dynamic loading test summary

Static (N)	Dynamic (N RMS)	
-3000	500	2000
-1000	500	2000
0	500	2000
1000	500	2000
3000	500	2000

The structure was instrumented with 39 triaxial accelerometers. Measurements were made predominantly across the linear guides for use in calculation of the acceleration surface. Accelerometers were also placed to pick up the flexible modes of the top plate. Measurements were made in duplicate across guides to confirm results. In addition to the truck and rail, mating components were also instrumented to determine the influence of the screwed joints.

Figure 46.6 compares the FRFs for varying static preloads and excitation levels. Burst random excitation was utilized for the computation of these FRFs. The responses show that the guides experience a softening as loading increases. Five modes were extracted from the test data. Their shapes correlated well with the shapes calculated by FEA. The shapes are reported in Figs. 46.7, 46.8, 46.9, 46.10, and 46.11.

A closer look at the response at first bending is shown in Fig. 46.12. As excitation levels increase, the natural frequency shifts lower and the compliance increases. This would indicate that any looseness in the preloaded guides is taken up with the higher dynamic loading and application of static preload. The minimum excitation level, 500 N RMS, represents the highest natural frequency at the first two modes evident in the responses. As excitation levels increase the natural frequencies decrease until saturation.

46.5 Results

The acceleration surface method was used to determine the form of the nonlinearity. Acceleration surfaces were computed from sine-sweep data taken with a very slow slew rate. The acceleration surface computed for the 553 Hz mode is shown in Fig. 46.13. Results from computation of the stiffness and damping curves are shown respectfully in Figs. 46.14 and 46.15. At the outset, these curves are very difficult to interpret. The form of the nonlinearity is very sophisticated, and a simple model is not evident.

To help make sense of the acceleration surface, the physical meaning behind the damping curve is shown in Fig. 46.16. Figure 46.16 depicts the motions of the two DOFs included in the ASM calculations with respect to one another on a per-

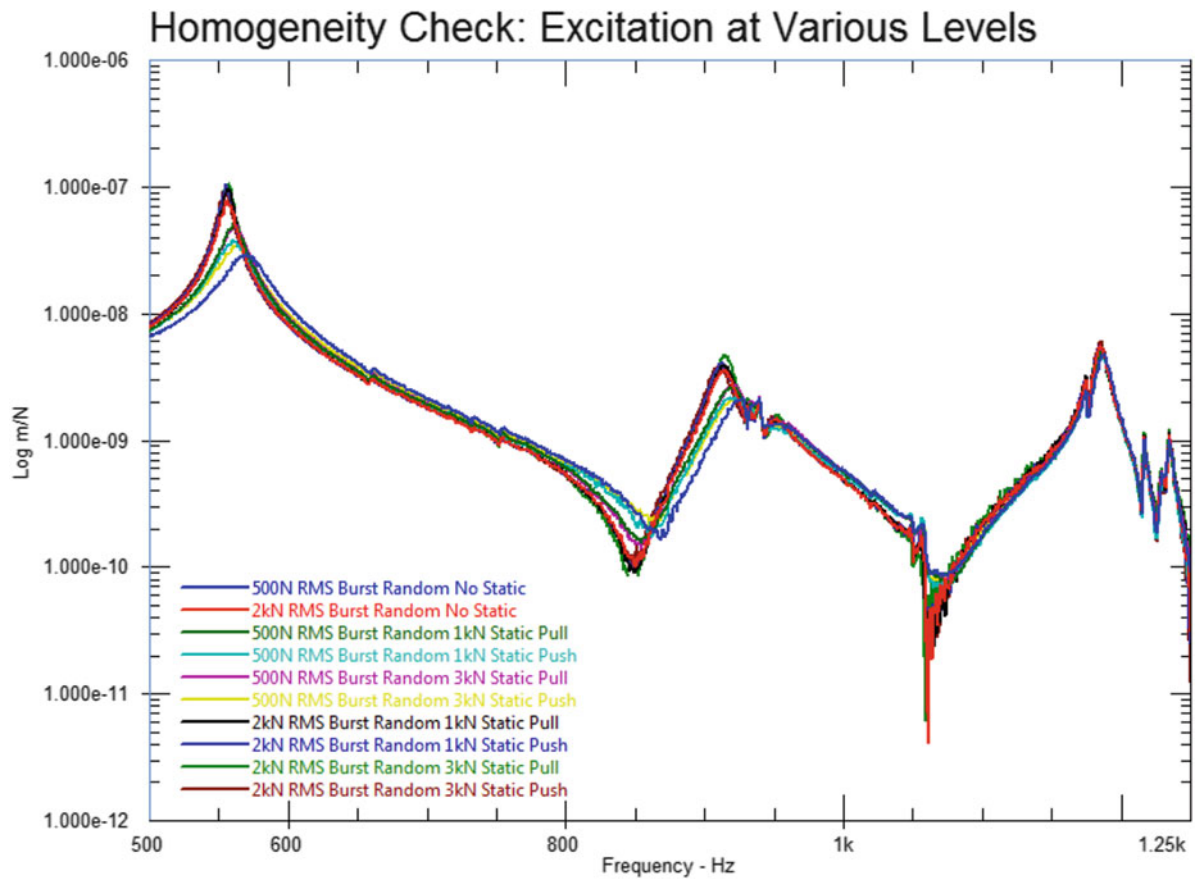


Fig. 46.6 Comparison of FRFs, varying static preload and dynamic excitation

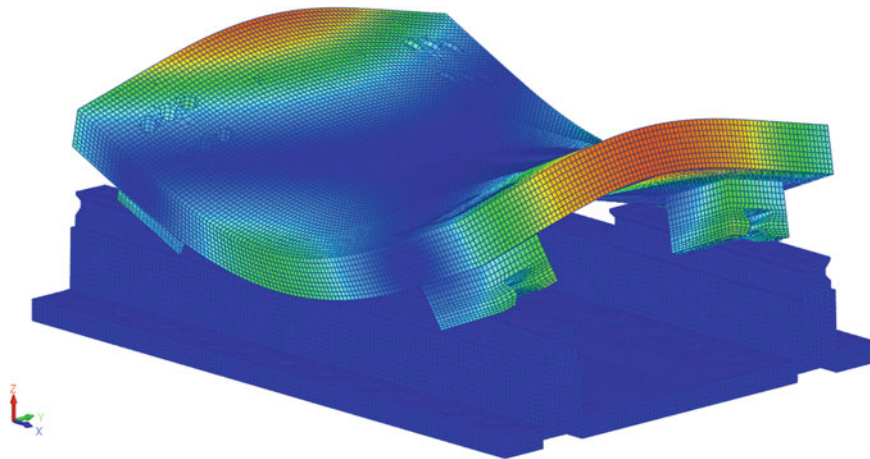


Fig. 46.7 913 Hz 1% damping (measured)

quadrant basis. Acceleration is considered only on the prime DOF. ASM does not involve computation of relative acceleration along with relative displacement and velocity. There are four cases that can be derived by studying the systems represented in Fig. 46.16.

Case I: Acceleration is negative while relative velocity is positive. This case involves x_2 moving away from x_1 . DOF x_1 accelerates downwards, but for this case to be relevant, $\dot{x}_2 > \dot{x}_1$. Case I represents a tensile load across the joint.

Case II: Both acceleration and relative velocity are positive indicating x_1 moves away from x_2 . This motion begins with the reversal of x_1 and DOF x_1 accelerates upwards. Case II represents a tensile load across the joint.

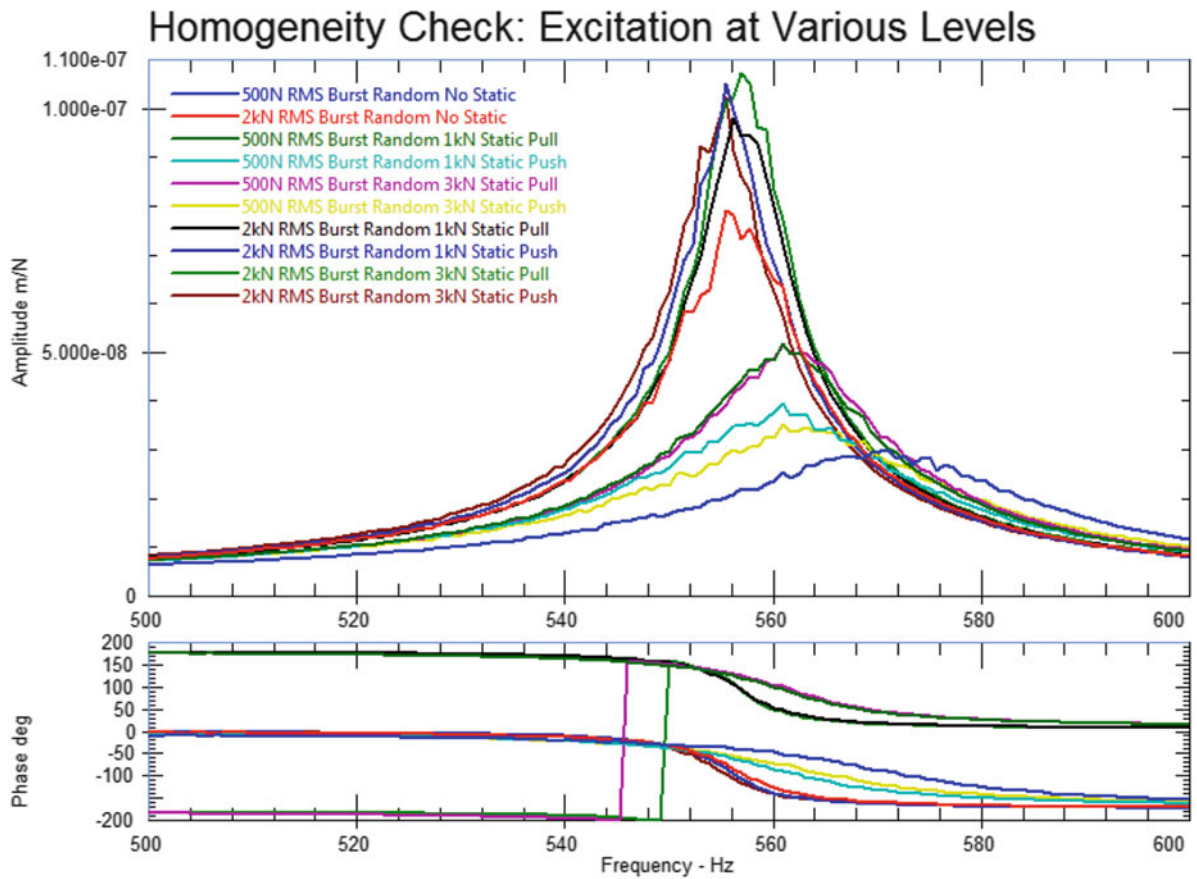


Fig. 46.8 Close-up of plate bending mode: comparison of FRFs with varying static preload and dynamic excitation

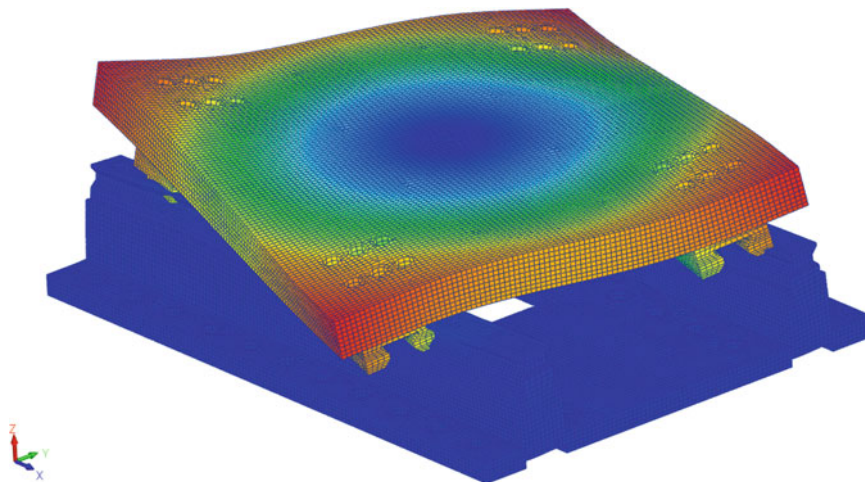


Fig. 46.9 463 Hz, 1.3% damping (measured)

Case III: Acceleration is positive while relative velocity is negative, this indicates the continued motion of x_1 up wards, x_2 reverses direction and begins to approach x_1 . Case III represents a compressive load across the joint.

Case IV: Acceleration and relative velocity are both negative indicating x_1 and x_2 move towards one another. Case IV represents a compressive load across the joint.

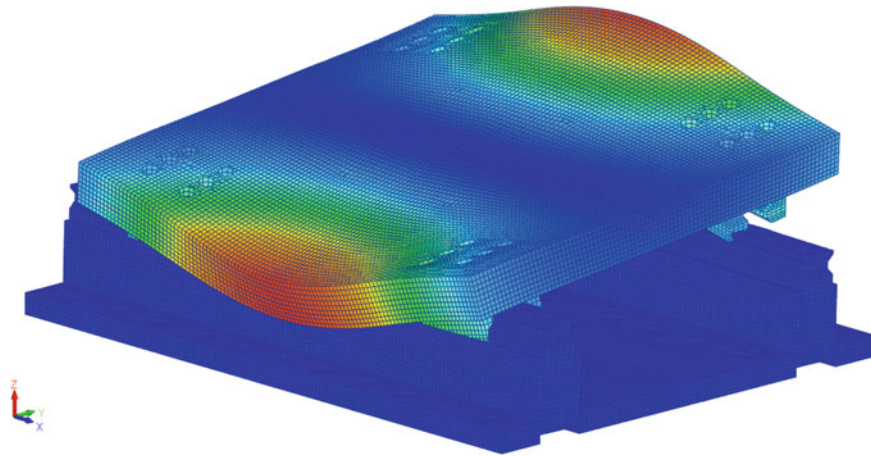


Fig. 46.10 556 Hz 0.8% damping (measured)

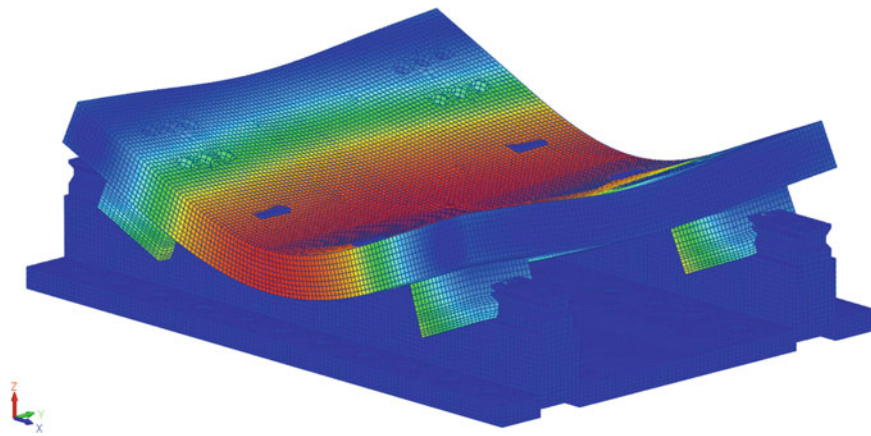


Fig. 46.11 804 Hz 0.8% damping (measured)

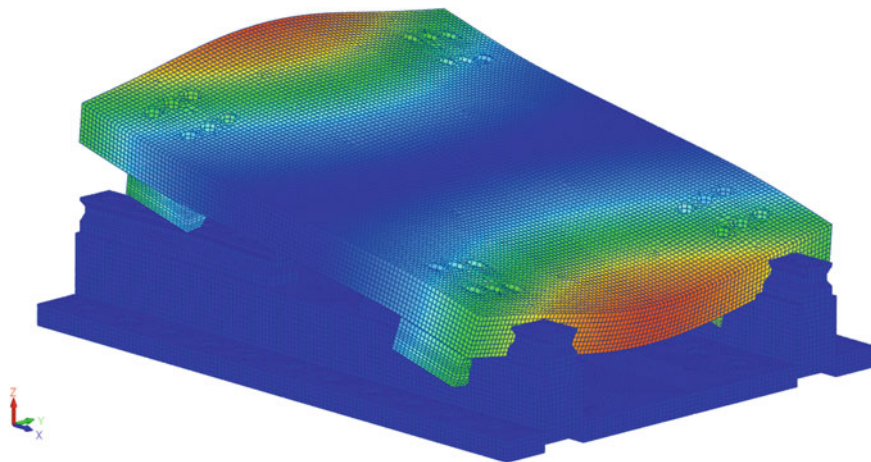


Fig. 46.12 873 Hz 0.2% damping (measured)

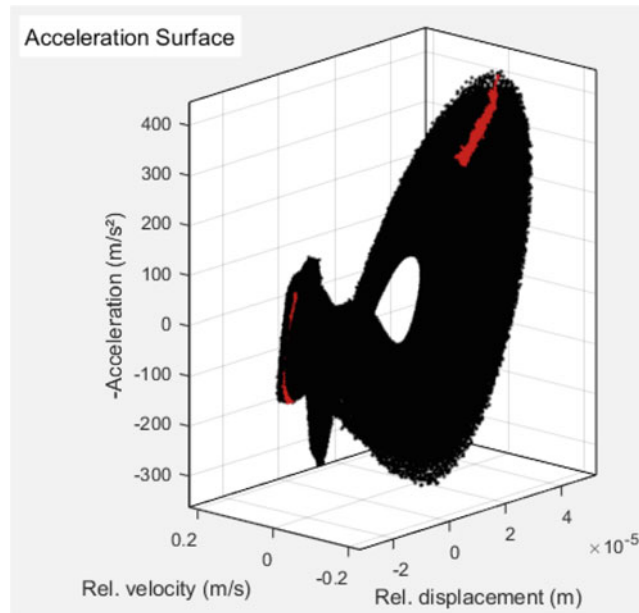


Fig. 46.13 Acceleration surface, 553 Hz bending mode [10]

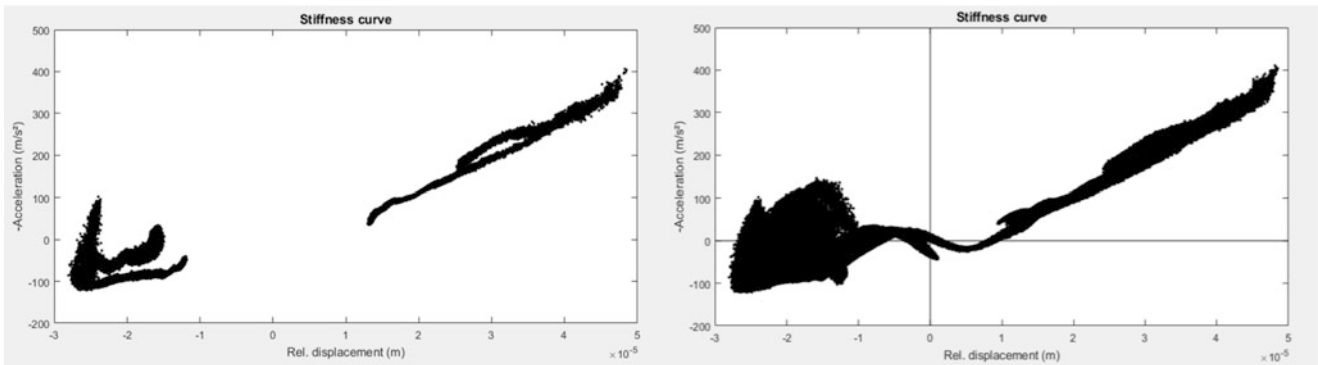


Fig. 46.14 Stiffness curve, 1 kN sine sweep with no static preload [10]

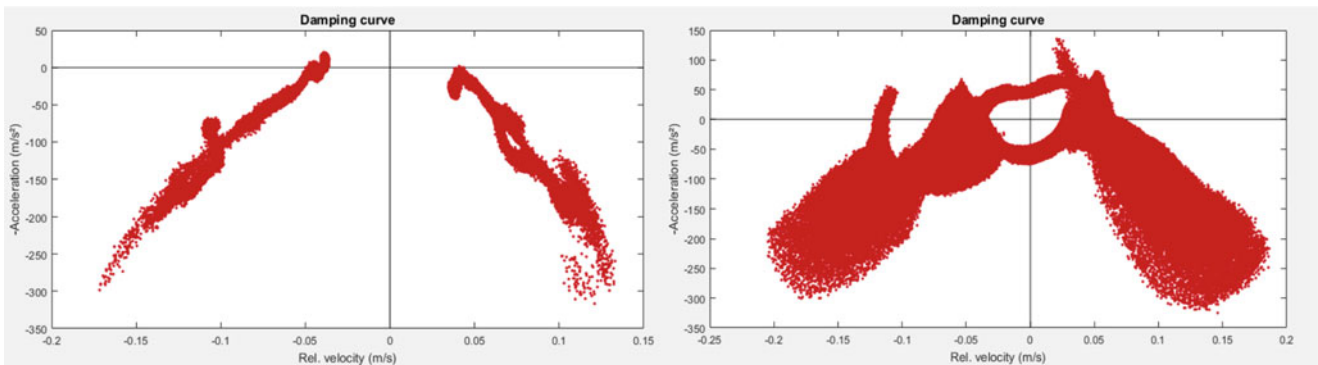


Fig. 46.15 Damping curve, 1 kN sine sweep with no static preload [10]

46.5.1 Study of Acceleration Surface: Full Content Data

Applying these developed cases to the guide assembly, when relative displacement is negative the truck encroaches on the rail. This motion involves the assembly in compression. When relative displacement is positive, the truck pulls away from the rail, thus the assembly is in tension.

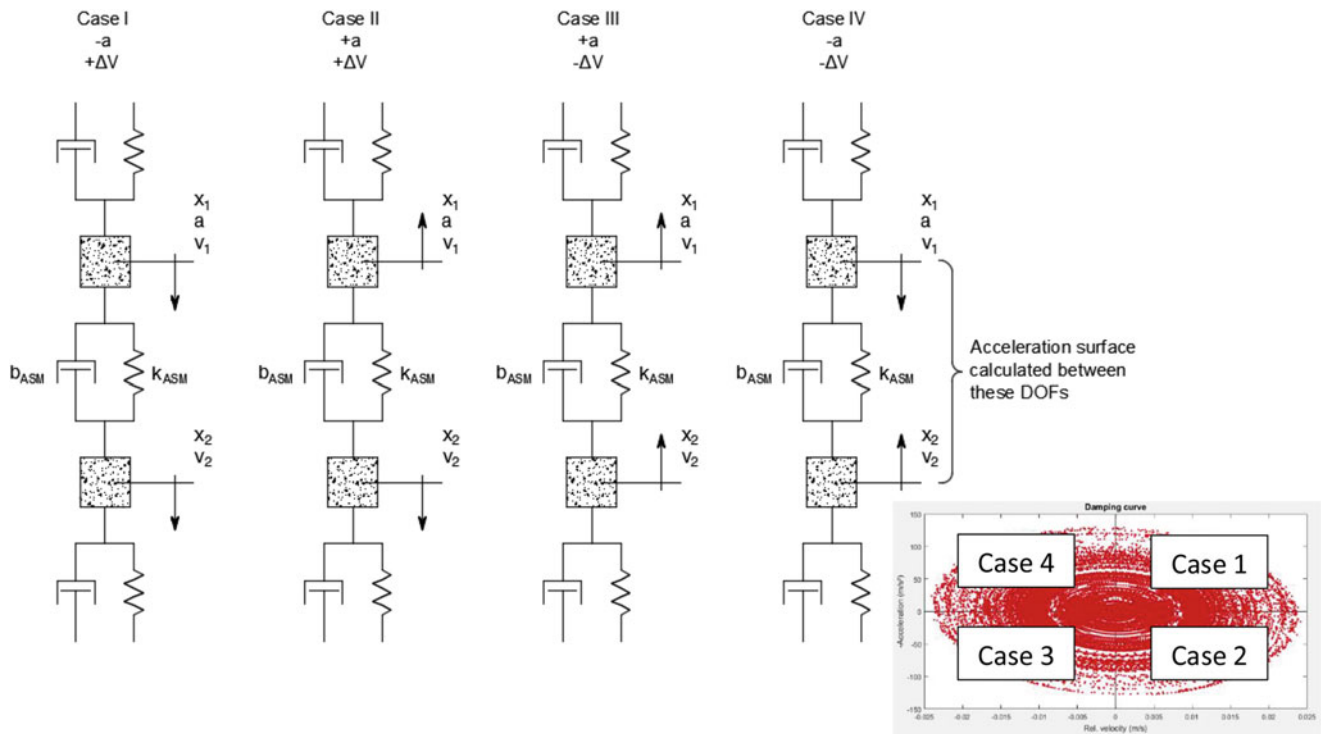


Fig. 46.16 Physical interpretation of damping curve: relative motions

The stiffness characteristic of the joint is evident by studying the acceleration surface. During the portion of the orbit where the truck pulls away from the guide (when the guide is in tension) the acceleration surface represents what is expected of a linear mode. The surface is flat and confined to a plane. The surface is inclined at an angle representative of a linear stiffness. Linear behavior of the assembly makes sense when considering the compliance of elastic elements when the truck is in tension.

In tension, the rolling element train is able to slide on the rails, leveraging the sides of the guide open. Further investigation is necessary to determine what drives this portion of the orbit. For a predictive model, the behavior of the elastic elements must be defined in order to quantify how much of the acceleration surface is indicative of opening of the guide and how much by the Hertzian contact regime in the rolling element train.

The compression cycle is significantly more involved. The truck is less likely to distort in the compression cycle, so the bulk of the acceleration surface will be defined by Hertzian contact and viscous effects of the lubrication over the contact surface. How Hertzian contact affects the shape of the acceleration surface will be investigated in future work.

An attempt may be made to create a model form for the stiffness and damping curves. The left hand images of Figs. 46.14 and 46.15 show respectively the stiffness and damping curves on a plane through the origin. The right hand images represent the stiffness and damping curves with more of the surrounding surface projected to the origin plane. Simply studying the left hand stiffness plot may lead to the assumption that the nonlinearity may be represented by a bi-linear stiffness. Studying the right hand stiffness plot reveals there is significantly more uncertainty associated with the model of the guide in compression. As more of the surface is projected to the characteristic plane, it is also evident that there is some bounce-back in the stiffness characteristic before the guide transitions into compression.

The characteristics of the damping curve are significantly more difficult to explain. Immediately on the origin plane, the damping curve is represented by two disconnected lines. Further investigation needs to be performed to understand how various damping phenomena manifest themselves in the acceleration surface.

46.5.2 Investigation of Harmonics

A property separating linear modes from nonlinear modes is their ability to excite system harmonics. The driving point response was investigated for harmonic content. A set of data was selected immediately surrounding and including the bending mode frequency (approximately 556 Hz). The Fast Fourier Transform (FFT) of this subset of data was calculated.

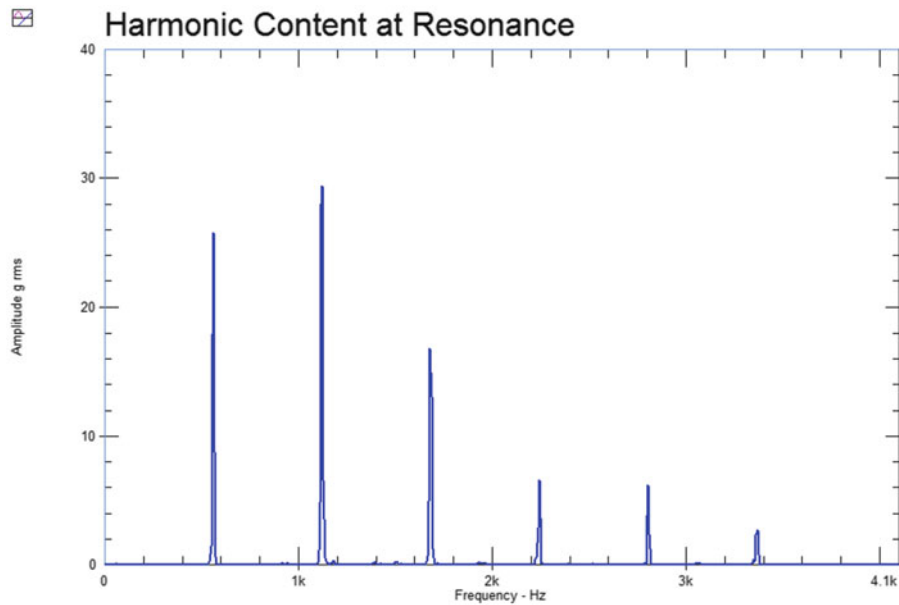


Fig. 46.17 Harmonic content at main resonance. Monotonic input produces multiple harmonics at driving point

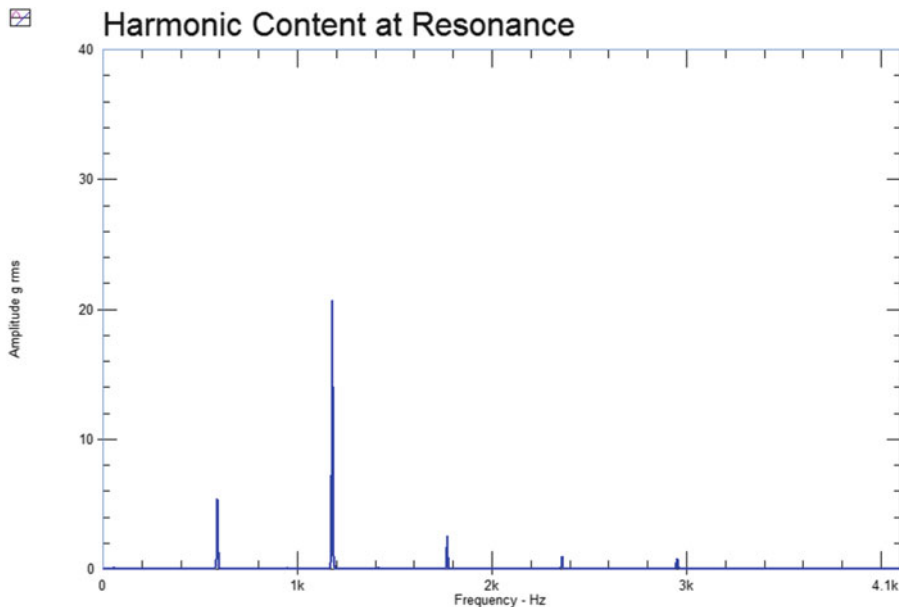


Fig. 46.18 Harmonic content at resonance, monotonic input produces monotonic response

The results of the FFT computation are shown in Fig. 46.17. It is evident that in addition to the fundamental, there are five harmonics present in this dataset. The FFT of a set of data at a linear resonance of the structure is shown in Fig. 46.18. At the linear mode, there is significantly less harmonic content, as would be expected.

Bandpass filtering was subsequently performed on the data around resonance to extract relevant data from the fundamental and first two harmonics so each bandwidth could be processed through ASM independently. Results from computation of the acceleration surface with filtering about the fundamental and first two harmonics is shown in Fig. 46.19. By neglecting the higher order terms, the stiffness and damping curves are significantly cleaner.

Uncertainty is realized as the level of the harmonic increases. Analysis of the fundamental yields a definite model form. The first harmonic also yields a semi-clear model form, however at the level of the second harmonic the model representative of the stiffness curve cannot be visually determined. The extents of the stiffness curve no longer reach as high of values as computed in Fig. 46.14.

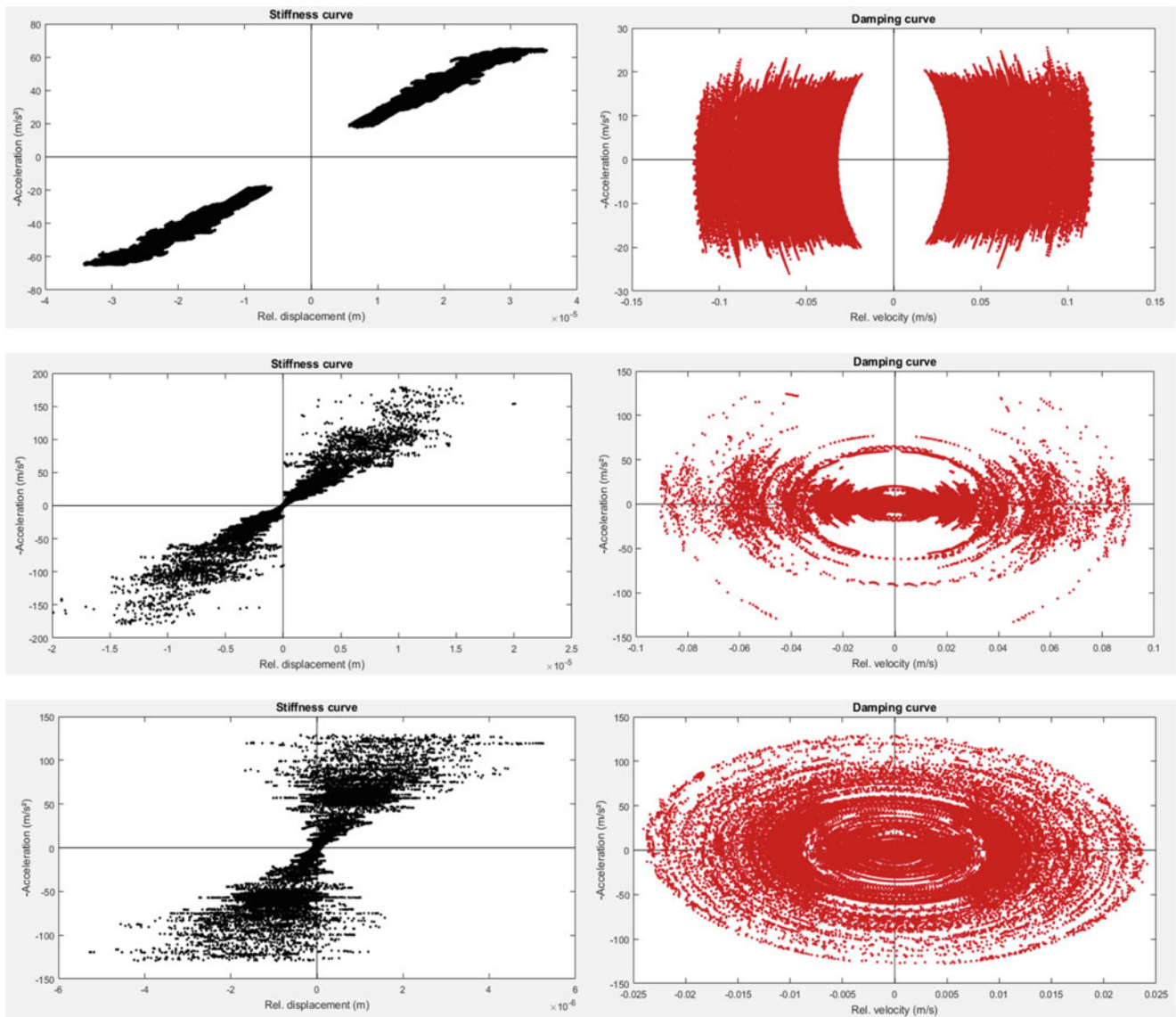


Fig. 46.19 ASM analysis of resonance at fundamental and harmonics [10]

It is expected that if a viable solution to model this nonlinearity were to make a sum of the harmonic components, one of the harmonic components would lend itself to the bi-linear stiffness. Each harmonic component investigated however, is symmetrical when investigated with ASM. Whether it is possible to combine harmonically filtered acceleration curves to build a model will be investigated in future work.

The filtering process has also linearized the damping curves. The damping curves shown in Fig. 46.19 are much more representative of what is expected of a linear system, as they bisect the plane as a horizontal line or ellipse with major and minor axes lying on the relative velocity and acceleration axis respectfully.

46.6 Conclusion

This work reviews the creation of a test bench to study linear guides. Linear guides are machine elements which facilitate translational motion of the constituent axes of a machine tool. There is significant complication in the modeling of linear guides due to the inherent complexity of their dynamics. Guides exhibit elastic effects from carriages and trackways, possess elements which exhibit Hertzian contact, and possess viscous effects due to their lubrication.

ASM was used to determine the form of the nonlinearity. It was found that proper filtering is necessary for accurate results when using ASM. The nonlinearity may take on numerous forms, the merits of which will be investigated in future works. Neglecting effects in the damping curve, the joint may take on a bi-linear stiffness. The bi-linear stiffness model would not account for advanced damping effects. Harmonic filtering was done as well to understand the contribution to the acceleration surface from each harmonic component of the response.

Further investigation will be made into the linear guides by exciting them in different locations, making static stiffness measurements, investigating different internal preload values, and ultimately making measurements on various guide series (i.e. 25–55 size long and short). Acceleration surfaces will also be calculated for other modes to determine which characteristics are observed for which distortion of the assembly.

Acknowledgements The author would like to thank Xcite for selling a servo-hydraulic shaker to a distance learning PhD student making this work possible, m+p International for the use of their software and VXI system to acquire data, Gaetan Kerschen at University of Liege for corresponding and assisting with technical details, the co-authors: Chuck Van Karsen and Jason Blough for assisting in interpretation of the data, and MAG Automotive LLC (A FFG Company) for providing facilities for testing.

References

1. Schneeberger: MONORAIL and AMS Product Catalog. Schneeberger, Roggwil (2017)
2. Worden, K., Tomlinson, G.: Nonlinearity in Structural Dynamics: Detection, Identification, and Modeling. CRC Press, London (2000)
3. Tilàn, D., Noël, J.-P., Grappasonni, C., Kerschen, G., Peeters, B., Debille, J., Vaes, M., Schoukens, J.: Nonlinear ground vibration identification of an F-16 aircraft – Part 2: understanding nonlinear behavior in aerospace structures using sine-sweep testing. In: Proceedings of the International Forum on Aeroelasticity and Structural Dynamics (2015)
4. Al-Hadid, M., Wright, J.: Estimation of mass and modal mass in the identification of non-linear single and multi degree of freedom systems using the force-state mapping approach. Mech. Syst. Signal Process. **6**(4), 383–401 (1992)
5. Kerschen, G.: Interviewee. NI2D Questions: ASM [Interview]. 16 Oct 2017
6. Noël, J.P., Renson, L., Kerschen, G., Peeters, B., Manzato, S., Debille, J.: Nonlinear dynamic analysis of an F-16 aircraft using GVT data. In: Proceedings of the International Forum on Aeroelasticity and Structural Dynamics (2013)
7. Noël, J.-P., Kerschen, G.: Nonlinear system identification in structural dynamics: 10 more years of progress. Mech. Syst. Signal Process. **83**, 2–35 (2017)
8. Kerschen, G., Lenaerts, V., Golinval, J.-C.: VTI Benchmark: application of the restoring force surface method. Mech. Syst. Signal Process. **17**(1), 189–193 (2003)
9. Schneeberger: MONORAIL Application Catalog. Schneeberger, Roggwil (2017)
10. Nolisys: NI2D. Nolisys, Liege. <http://www.nolisys.com/> (2017)

Chapter 47

Nonlinear Characterization of a Machine Tool Energy Absorber



Steven M. Whitican, Charles Van Karsen, and Jason Blough

Abstract Energy absorbers are used frequently in industrial machinery. The use of energy absorbers allows for the design of a lighter structure while still maintaining the requisite dynamic stiffness for effective operation. A standard energy absorber used on a CNC machine is investigated in this paper. The absorber is connected to a rigid mass to establish fixed boundary conditions at the joint face. Numerous dynamics tests are performed on the absorber and the Acceleration Surface Method applied to assist in the comprehension of the form of the nonlinearity.

Keywords Nonlinear dynamics · Acceleration surface · Restoring force surface · Damping · Machine tool

47.1 Introduction

Faster and more economical machine tools necessitate lighter structures. There are a number of methods used to develop machine tool structures lighter without sacrificing quality, rigidity, and dynamic stiffness. These methods ideally add to the energy absorption of the structure. Available methods include the use of composite materials, mineral casting, and porous aluminums [1]. Unfortunately, the cost of some more exotic solutions is prohibitive for machine tool manufacturers, particularly if a machine is not in high production. The application of Tuned Vibration Absorbers (TVA) can also aid in development of a structure which is light but dynamically very stiff. Proper utilization of a TVA will dramatically increase chatter free depth of cut potential [2]. Assuming the workpiece and fixturing are capable of handling the enhanced loading from the static portion of the cut, part processing time can be reduced dramatically. Modeling of a tuned vibration absorber can be a challenge due to the inherent nonlinearities [3]. The TVA of concern for this work, shown in Fig. 47.1, has a mass suspended by polymer pucks in shear. Natural frequency of the TVA may be set by adjusting preload on the pucks with the jam-nutted socket head cap screws. The steel pressure plates enforce uniform load across the face of the PVC pucks.

A standard 10 kg absorber is used for the purpose of this investigation. The pressure screws preload the shear pucks, tuning the absorber to a natural frequency of approximately 160 Hz. The absorber is tuned by repetitive impact testing. For the duration of the impact testing, the absorber is mounted to a massive cast iron cube. This cube and mounting are also used as the test fixtures for the absorber in this work.

The cast iron cube is considered a fixed base. The instrumentation scheme is developed to establish the form of the nonlinearity which is exhibited by the absorber with use of the Acceleration Surface Method (ASM). For the purpose of this work, the mode of interest is the damper mass oscillating up and down (in the z -direction per Fig. 47.1). Other modes were studied for thoroughness, but not desired for inclusion in the end result.

It is worth noting that the support structure, or halo, for the absorber mass is not exceptionally stiff. Though the halo modes may interact slightly with the lower-frequency modes at which the damper is effective, the major flexible modes of the halo are not present until more than ten times the fundamental frequency of the absorber. Due to the significant separation of halo flexible modes from rigid body absorber modes, the halo modes are not considered in the subsequent analysis.

S. M. Whitican (✉)
MAG Automotive LLC, Sterling Heights, MI, USA
e-mail: steven.whitican@mag-ias.com

C. Van Karsen · J. Blough
Michigan Technological University, Houghton, MI, USA

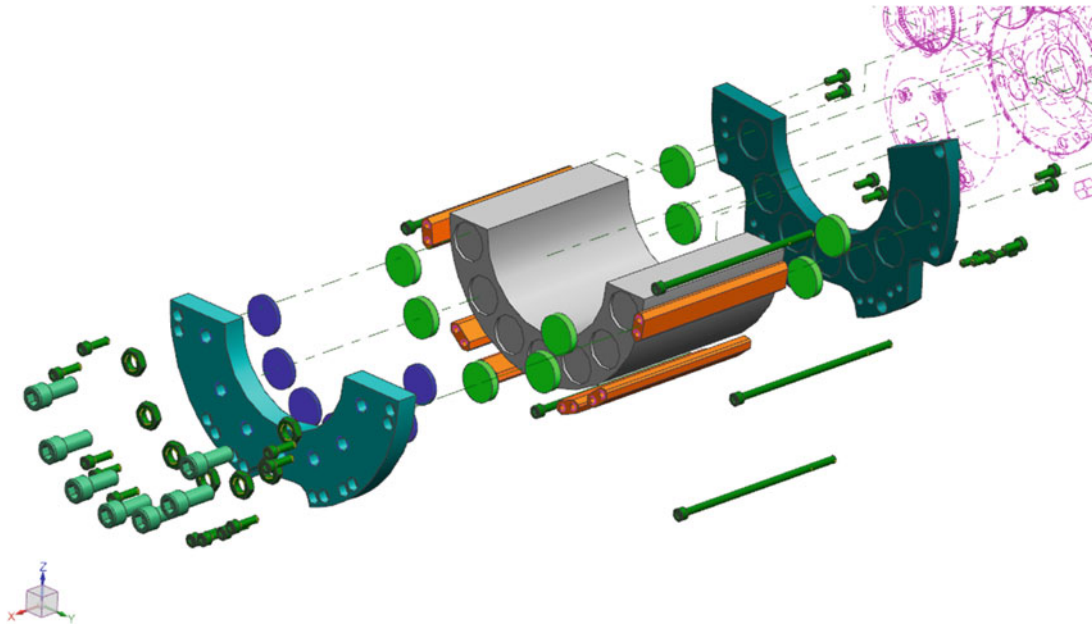


Fig. 47.1 Exploded view of tuned vibration absorber (TVA)

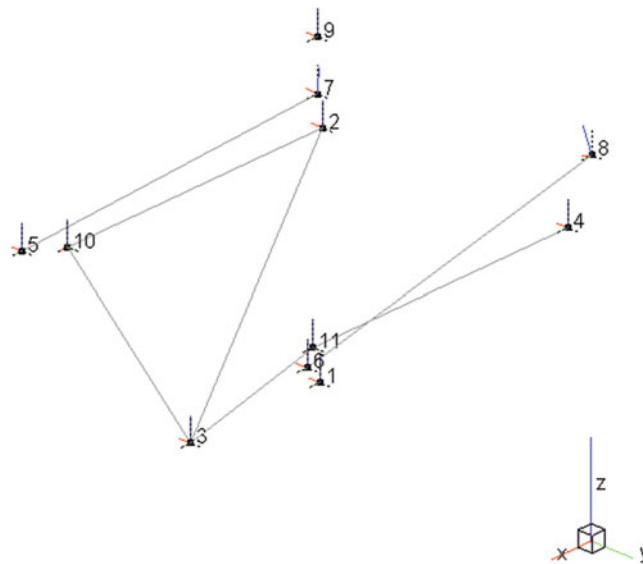


Fig. 47.2 Modal model of the TVA

47.2 Collection of Data

To fully understand the mode shapes of the damper, the mass was fully instrumented to capture the motions of the mass in all six degrees of freedom. Due to the significant weight and stiffness of the absorber as well as the lower frequency modes targeted for study, mass loading was not believed to be a concern. The halo was also instrumented in order to measure at what frequency it begins exhibit flexible modes. The cast iron base to which the TVA was mounted was also instrumented to determine relative motion and quantify the success of the fixed boundary condition.

In practice, the absorber mounts to the rear of a machine tool spindle to enhance depth of cut potential during boring and milling operations. The TVA is thus mounted to the most flexible portion of the CNC structure. Figure 47.2 shows a modal model of the damper. The complete test setup is shown in Fig. 47.3.

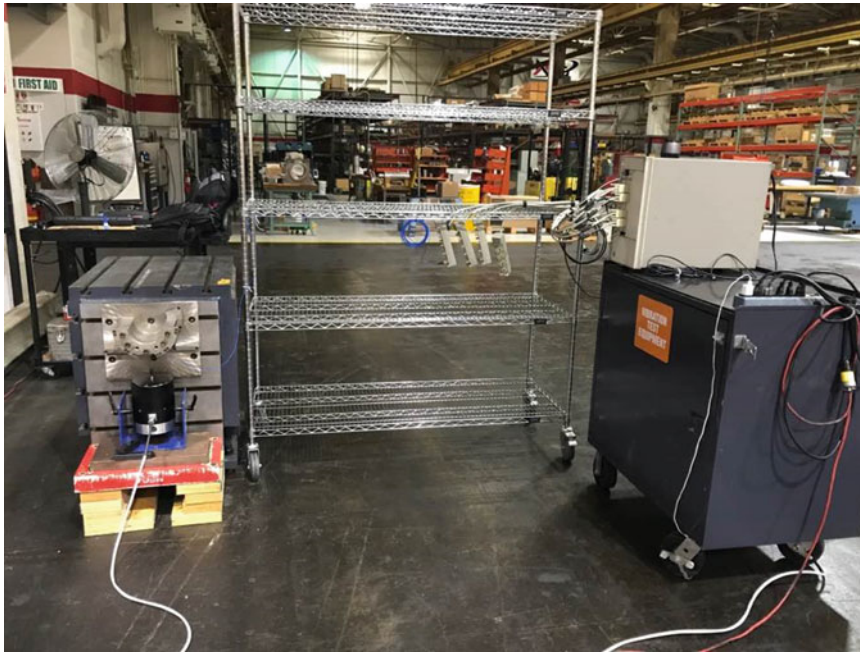


Fig. 47.3 Setup to test vibration absorber with fixed boundary condition

Table 47.1 Excitation levels and extracted linear parameters for dominant mode

	Natural freq (Hz)	Damping ratio (%)
10 N	166.2	10.3
50 N	163.7	10.6
75 N	157.8	8.5
100 N	155.8	9.7
100 N rev.	158.6	11.7
75 N rev.	158.9	11.7
50 N rev.	161.2	11.9
10 N rev.	168.2	11.8

Instrumentation consisted of a combination of 10 and 100 mV/g accelerometers and a 100 lbf piezoelectric load cell. A 100 lbf shaker was set up directly beneath the center of the absorber mass. Other directions were not considered for excitation. The TVA is effective in the vertical direction so instrumentation focused on capturing characteristics of vertical modes for future modeling.

This absorber has been in production for some time, so its frequency response is well known based on impact tests performed for tuning. This study was the first attempt made to understand the dynamic characteristics of the TVA in detail. A number of excitation regimes were utilized to facilitate full understanding of the absorber, of most interest are the results obtained from swept sine testing as data from the sweeps was used for ASM computation.

The bandwidth of 50–350 Hz was selected for detailed testing with slow sine sweeps to include the nonlinear modes. The slewing rate for this testing was 15 Hz/min. A precursory study of the FRFs taken at various levels shows that the nonlinearity is softening. Kerschen found that for studying a softening nonlinearity, reverse sine sweeps yield the best data [4]. Excitation levels used in testing of the absorber are listed in Table 47.1.

The excitation was force controlled by software to several levels: 10, 50, 75, and 100 N. Power Spectral Density of several of the sweeps is shown in Fig. 47.4. It is evident from the plots that the input level was well controlled. FRFs collected during forward sweep testing are shown in Fig. 47.5 and during the reverse sweep are shown in Fig. 47.6.

Extracted linear modal parameters are also shown in Table 47.1. Frequency decreases markedly with input load while damping is relatively unaffected. The compliance FRFs in Figs. 47.5 and 47.6 show that the damper also becomes weaker as energy is added. There is no decrease in appreciable dynamic stiffness between the 10 and 50 N sweeps, however as load is increased from 75 to 100 N, dynamic stiffness decreases significantly. This could be attributed to the polymer pucks in shear unseating in their respective cavities.

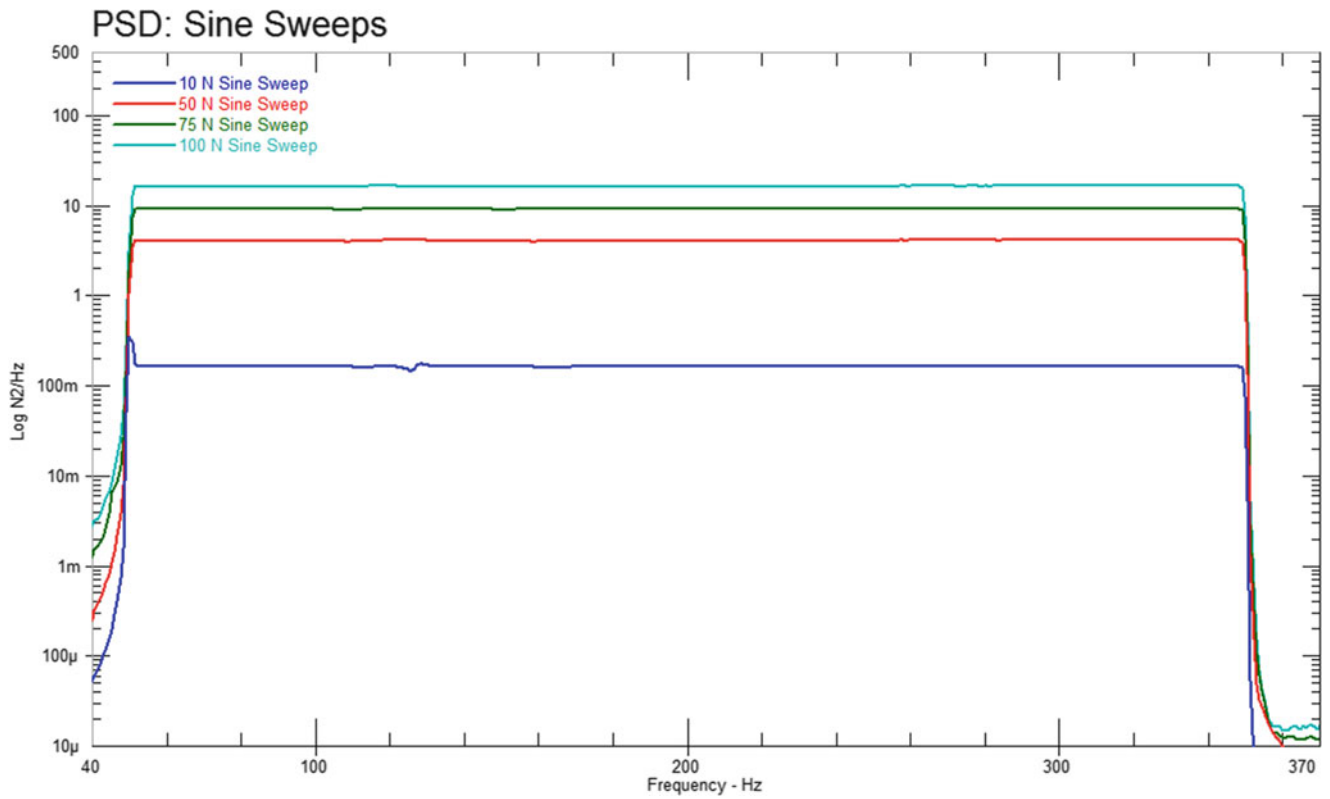


Fig. 47.4 Input power spectral density (PSD) for sine sweeps

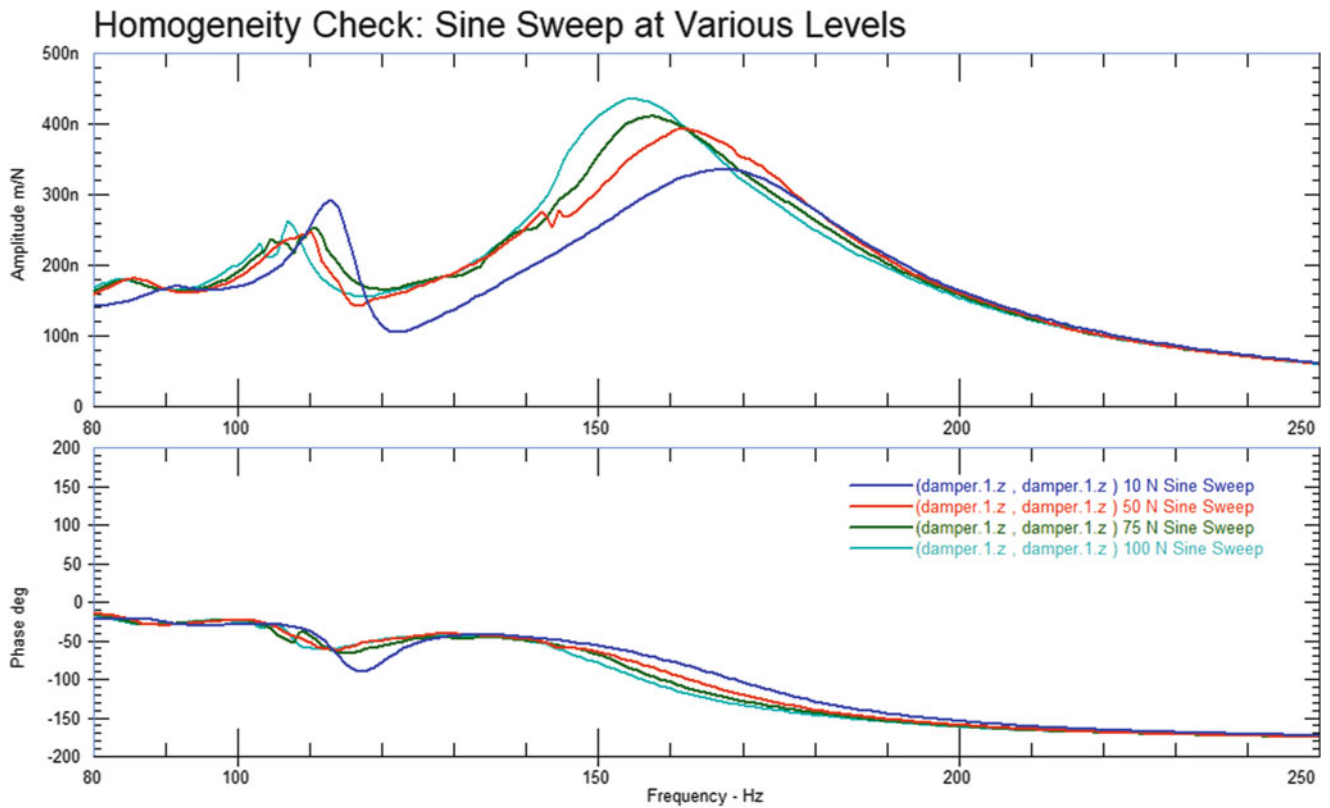


Fig. 47.5 Homogeneity check using forward sine sweep. These responses show a softening behavior

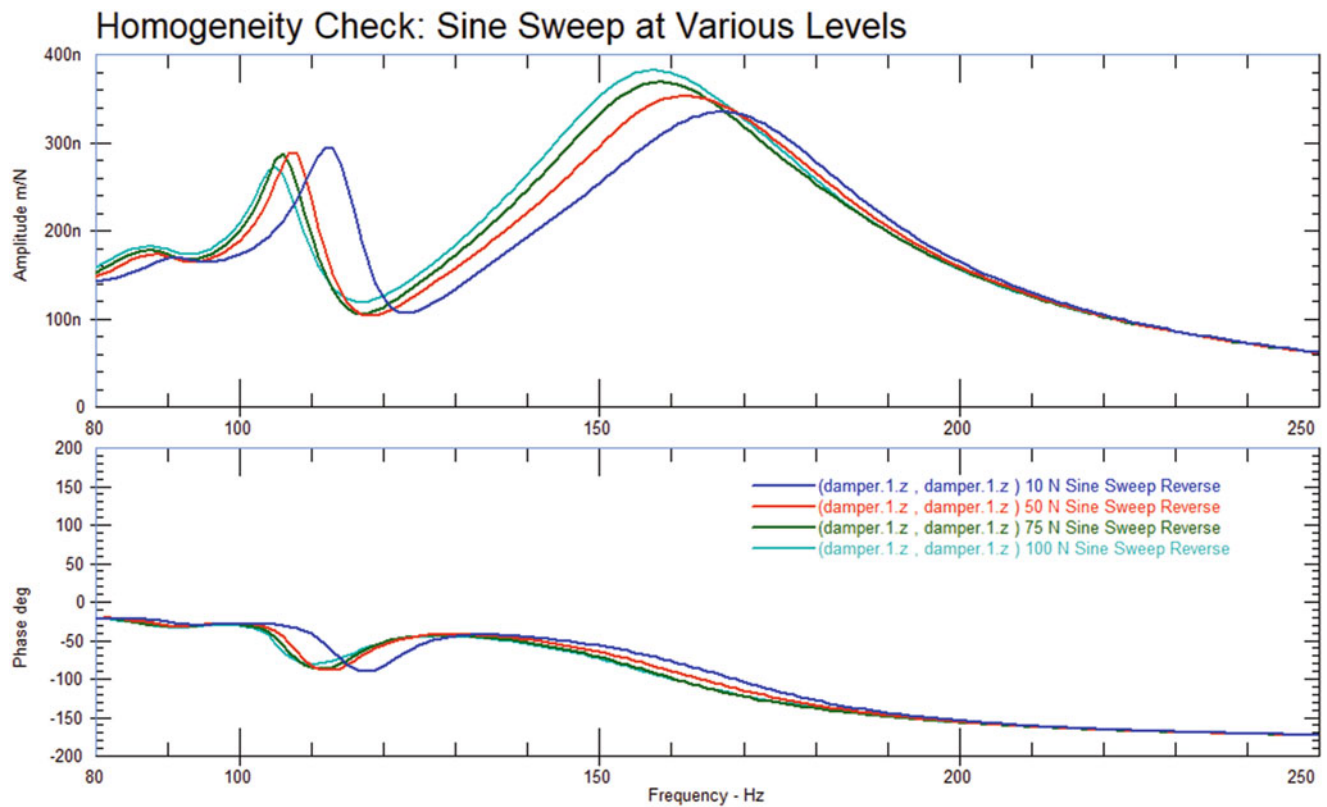


Fig. 47.6 Homogeneity check using reverse sine sweep. These responses show a softening behavior

Mode shapes extracted for this study explained and shown in Table 47.2. Three modes are of particular interest for further study, two of which are determined to behave in a nonlinear fashion.

47.3 Results

Results from the 100 N sine sweep are herein investigated as they may be utilized to reveal the form of the nonlinearity. From the data shown above in Figs. 47.5, 47.6, and 47.7 it is clear that the *dominant* nonlinearity in this system is softening. However, close examination of the data shows that there are in fact two nonlinear modes participating in the response which are close in frequency. The first is a sub-mode to the fundamental and exhibits a hardening characteristic. The stiffness characteristic for the sub-mode ($f_n = 125$ Hz) is shown in Fig. 47.8 while the stiffness characteristic of the fundamental mode is shown in Fig. 47.9.

The nonlinearity depicted in Fig. 47.8 could be represented by two models depending on the paradigm of the analyst performing the computations. The first and simplest model would represent the stiffness curve it as cubically stiffening. The extremities of the stiffness curve do not show any evidence of reaching saturation. This model may not be robust. The cubically stiffening model would represent the PVC puck material in shear. As this mode shape involves the tipping of the mass over its longitudinal axis, the pucks are further compressed and relieved as energy input the system increases. The cubically stiffening model would not account for the hysteresis loop about the origin displayed in Fig. 47.8. Depending on the desired accuracy of the model, capturing the loop may not be necessary. Study would have to be performed if the bit of system memory contained therein is necessary for construction of the TVA model.

A piecewise linear model would be more accurate, and physically representative of what is occurring with the restoring force: the pucks, at this mode. The piecewise linear model could take into account the change in stiffness as the pucks deform in compression and they overflow their pockets, creating a larger diameter of contact area which is pre-stressed. Pucks are made of a PVC material of approximately 80 durometer. The material is free to flow, and when compressed, it will overflow the pocket, making larger radial contact with the surrounding halo. When overflow occurs, the restoring force of the pucks

Table 47.2 Details and descriptions of various extracted mode shapes

Mode number	Frequency	Shape description	Shape
1	78.4	RBM rocking of damper mass about y-axis	
2	107.8	RBM translation of entire assembly z-direction	
3	130.6	RBM rocking of damper mass y & z axes	
4	155.8	RBM translation of damper mass z-axis	
5	179.1	RBM rocking of damper mass -y & z axes	

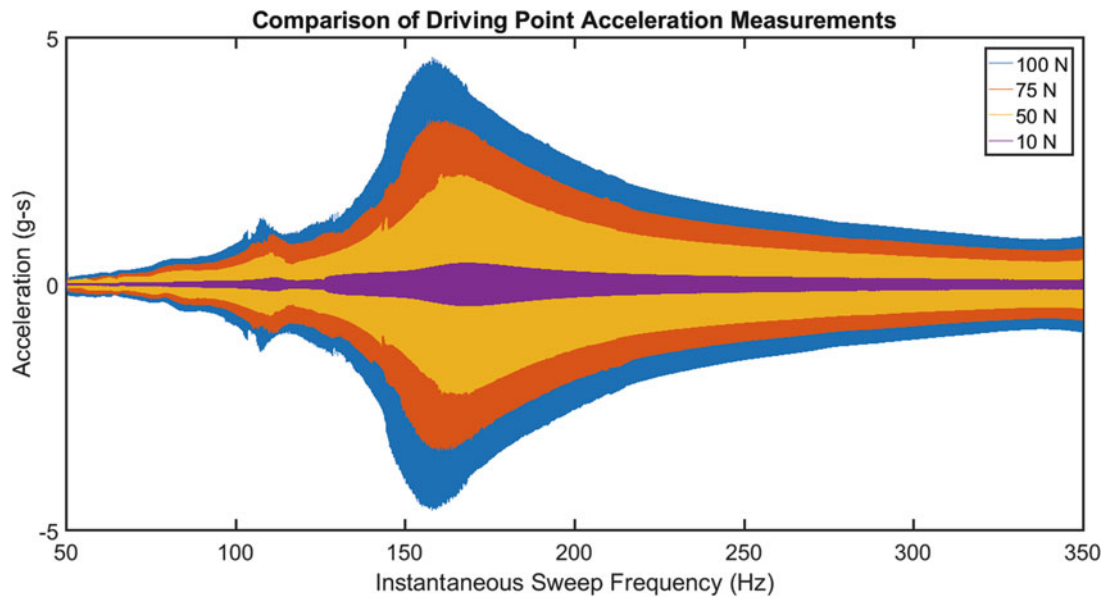


Fig. 47.7 Comparison of driving point time-domain measurement over various excitation levels. The resonance is observed to be softening with higher energies

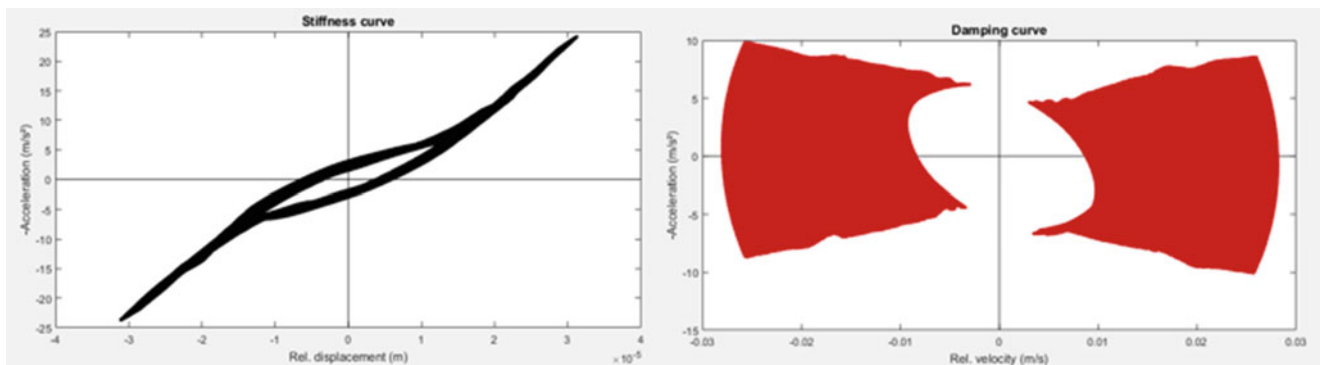


Fig. 47.8 A nonlinear mode just below the fundamental mode exhibits a hardening nonlinearity and has some indicators of hysteresis [5]

should increase from two effects. First, enough displacement is observed in the TVA that stress stiffening effects should be semi-prevalent. It is known that the PVC material is susceptible to stress stiffening effects as this concept is how the damper is tuned. Second, the physical diameter of the pucks has been observed to increase as much as 6% when the mass is pried upon giving way to higher contact regions and larger stiffness.

Figure 47.9 shows that the softening nonlinearity eventually saturates at its extremities. Further testing is required to determine if this is the case. This stiffness curve would be representative of a cubically softening nonlinearity. Considering the design of the damper, this may again be attributed to the method with which the pucks are retained. The pucks are held radially by means of a milled pocket. The pocket has minimal clearance with the pucks. For this mode, the damper mass moves vertically, thus trapping the PVC puck faces. The puck circumference is free to distort. It is expected that the puck loses its circular form at higher energies and is subject to pulling from its pocket. This would entail a puck with a more oval-shaped contact region and thus a less stiff connection.

47.4 Conclusions

RFS and ASM have been proven on simulated data in numerous instances. ASM has been used successfully in a number of practical applications to define the nonlinear rules governing a joint and to facilitate estimation of nonlinear parameters. This paper provided a case study of ASM on practical data. ASM helped to define the nonlinear behavior of a machine tool energy

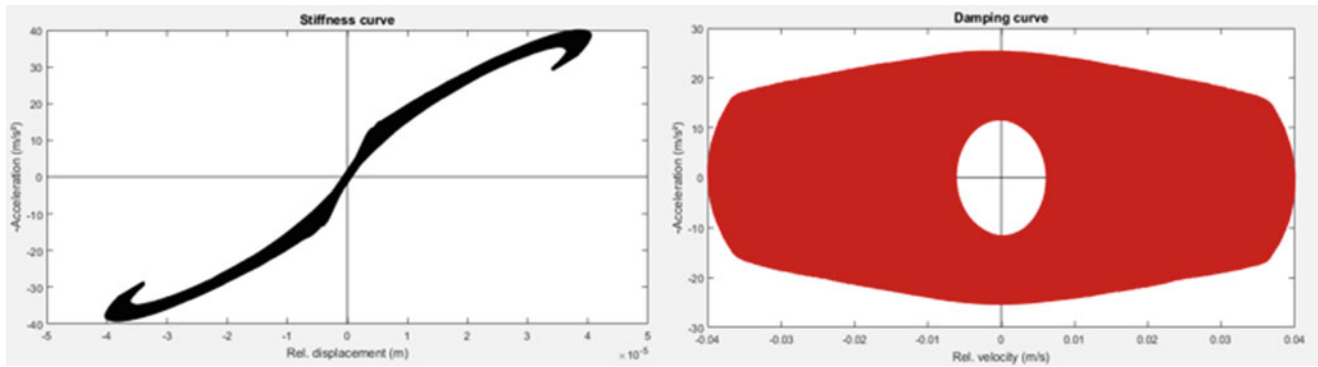


Fig. 47.9 The fundamental mode which defines the response exhibits a softening nonlinearity [5]

absorber. The absorber was found to have two nonlinear modes in the bandwidth of concern. The first identified nonlinear mode exhibits very minor participation and is a hardening nonlinearity. The second nonlinear mode has high damping and is the mode that defines the system response. This mode was found to be softening. As there is no *a priori* knowledge as to the form of the nonlinearities, physical reasoning was used to explain why each mode exhibited its respective behavior. Further work will concentrate on development and application of a model of the absorber for use in machine performance simulations.

Acknowledgements The author would like to thank m+p International for the use of their software and VXI system to acquire data, Gaetan Kerschen at University of Liege for corresponding and assisting with technical details, the co-authors: Chuck Van Karsen and Jason Blough for assisting in interpretation of the data, and MAG Automotive LLC (A FFG Company) for providing facilities for testing.

References

1. Möhring, H.-C., et al.: Materials in machine tool structures. *CIRP Ann. Manuf. Technol.* **64**(2), 725–748 (2015)
2. Muma, J., et al.: Chatter suppression techniques in metal cutting. *CIRP Ann. Manuf. Technol.* **65**(2), 452–808 (2016)
3. Habib, G., Kerschen, G., Stepan, G.: Chatter mitigation using the nonlinear tuned vibration absorber. *Int. J. Non Linear Mech.* **91**, 103–112 (2017)
4. Tilàn, D., Noël, J.-P., Grappasonni, C., Kerschen, G., Peeters, B., Debille, J., Vaes, M., Schoukens, J.: Nonlinear ground vibration identification of an F-16 aircraft – Part 2: understanding nonlinear behavior in aerospace structures using sine-sweep testing. In: *Proceedings of the International Forum on Aeroelasticity and Structural Dynamics* (2015)
5. Nolisys: *NI2D*. Nolisys, Liege. <http://www.nolisys.com/> (2017)

Chapter 48

Tutorial: Bolted Joints and Tribomechadynamics



M. R. W. Brake

Abstract The mechanics of jointed structures is a challenging research area that necessitates collaboration from multiple disciplines. Traditionally, jointed structures have been studied in isolation by three major fields – structural dynamics, contact mechanics, and tribology. The foundation of the field of tribomechadynamics is in the notion that collaboration between these three fields is necessary to advance the state-of-the-art for joint modeling. In this tutorial, the state-of-practice, state-of-the-art, and cutting edge research for joint mechanics is presented.

Keywords Joint mechanics · Tribomechadynamics · Structural dynamics · Contact mechanics · Tribology

48.1 Introduction

The primary function of a joint in an engineering structure is to connect two separate substructures. This function, however, introduces a secondary function in which the joint changes the dynamics of an assembled system. With a sufficiently large excitation, a joint will cause the resonant frequencies to decrease and the damping ratios to increase for each mode. In some systems, the excitation necessary to see this nonlinear dynamic behavior is well outside of the operating regime for the system; however, for other systems, the nonlinear dynamics of the interface can result in a 5% change in frequency and a 200% change in damping ratio for a typical range of excitations. State-of-the-art techniques can predict the *linear* stiffness of a joint reasonably well (to within 10%); however, the frequency shift exhibited as the joint is exercised by larger forces as well as the amplitude dependent damping is beyond predictive capabilities. Consequently, the prediction of damping in structures (not just from joints) is the least well characterized part of a model in structural dynamics despite it being critical to the prediction and understanding of the behavior of a structure [1]. Therefore, the goal of joint mechanics research is to understand what excitation regimes will result in a linear joint behavior or a nonlinear joint behavior, and to be able to make meaningful predictions for the stiffness and damping introduced by a jointed interface.

Friction and mechanical joints have been investigated for, conservatively, 4000 years. Evidence in ancient hieroglyphics indicate that even in 2000 BC there was an understanding of the effects of lubrication in frictional system. Despite this, *predicting* the response of an assembled structure remains an elusive goal. One reason for this is that friction is, inherently, multidisciplinary in nature. To more fully understand the fundamentals of friction and its role in assembled structure, it is necessary to study tribology, contact mechanics, and structural dynamics amongst other fields.

Tribology, contact mechanics, and structural dynamics are three sub-disciplines of mechanical engineering that are each concerned with the study of interfaces in mechanical systems. Despite this, these three sub-disciplines have remained separate due to length scale considerations, solution techniques, and response metrics. As a result, common problems solved within one of these sub-disciplines rarely affects research within the other sub-disciplines. To address this, the field of Tribomechadynamics was founded to bridge the scales from the nano- and micro-structural characterizations of tribology to the macroscale modeling of structural dynamics. The goal of this new field is three fold: to develop predictive models of jointed structures that can be used to affect the design phase of a product, to predict the degradation of an interface over time due to wear/fretting, and to enable the optimization of jointed structures to reduce weight, be wear resistant, or have advantageous properties.

M. R. W. Brake (✉)
William Marsh Rice University, Houston, TX, USA
e-mail: brake@rice.edu

48.2 Experimental Considerations

Until recently, it was difficult to discern trends in experimental data for jointed structures as the influence of the nonlinearities within a system were smaller than the experimentally measured variability [7, 8, 12, 33]. Recent experimental programs have shown that by developing a strictly controlled experimental procedure that minimizes operator-to-operator induced experimental variability, the nonlinear characteristics of a jointed structure can be accurately characterized. With this perspective, recent research has focused on the role of interfacial geometry [12] and contact pressure [28] on the dynamics of jointed structures. Aiding this effort has been the development of a set of benchmark structures (for instance, the Brake-Reuß beam [7, 8, 33], the Gaul resonator and the dumbbell apparatus [15, 32], and many others [25]). In addition, the development of nonlinear system identification techniques have allowed for a more sophisticated treatment of experimental data in order to characterize the response of a jointed structure [2, 11, 13, 19, 20]. With this high pedigree of data now available, the foundation exists for the modeling of jointed structures:

48.3 State of Practice

There are three common methods for modeling jointed interfaces in practice: linear springs, Coulomb friction, and Jenkins elements. These three common methods represent incremental increases in complexity and fidelity for modeling a jointed interface.

48.3.1 *Linear Spring Models*

A linear spring approach neglects all dissipation within a joint. If viscous damping is added in parallel to the linear spring, introducing a Kelvin-Voigt viscoelastic model, this would be fairly representative of a joint in the linear regime [36]. Alternatively, a more common practice is to use modal damping to represent the dissipation seen in the linear regime of a joint's response [10]. These models, fundamentally, do not capture the correct physics for energy dissipation within a joint. Instead, they are the coarsest method to model a structure and are only applicable to linear systems in which the joint is not appreciably exercised.

48.3.2 *Coulomb Friction*

A second approach is to use high fidelity modeling and Coulomb friction between the two surfaces in an interface. It is tempting to think that a sufficient refinement of the interface will result in a converged model that can accurately predict the energy dissipation measured in an experiment; however, Coulomb friction has been shown to not be applicable to joint mechanics [32] as the three major assumptions behind Coulomb friction all break down (i.e. friction is linearly proportional to normal force, independent of contact area, and independent of damping). While this approach may be satisfactory for low consequence applications, the lack of conservatism in predictions made using Coulomb friction models can result in potential failures for high consequence applications, which should be avoided at all cost.

48.3.3 *Jenkins Elements*

The Jenkins element [14, 18], also known as an elastic slider, is a spring in series with a Coulomb friction element. The presence of the spring allows for phenomena such as microslip (i.e. the sliding of one portion of the interface while the remainder of the interface remains stuck) and interfacial stiffness to be represented in a coarse manner. One challenge with using a Jenkins element approach is that calibration can be prohibitively expensive when there are hundreds or thousands of contact pairs within an interface [21]. Nonetheless, of the three state-of-practice methods, this is the most suitable to capturing both the linear and nonlinear dynamic behavior of a jointed interface.

48.4 State of Art

As with all methods to be discussed, current approaches to modeling jointed interfaces are not predictive. Instead, the parameters within a model must be calibrated to match existing experimental data. In some instances, this can result in a prohibitively expensive analysis [21], and in all instances to date, this still cannot yield a model that is accurate for more than several modes of a structure. Several state-of-the-art approaches attempt to more accurately describe a jointed structure's behavior:

48.4.1 Iwan Models

The Iwan model, most commonly put forth in [30], attempts to describe the hysteretic behavior of a joint using a single nonlinear degree of freedom. Internal to an Iwan model is a finite set of Jenkins element that each have their own set of properties governing their stiffness and transition to slipping. This “whole joint” modeling approach is designed to capture both the amplitude dependent damping and stiffness of a joint. While there have been several perturbations on the Iwan model [17] since its application to joints (e.g. [6, 26, 34]), these models are not yet predictive. Typically, Iwan models take several parameters for their description, which usually include [30] the tangential stiffness of the interface, the force necessary to induce macroslip (i.e. the rigid body motion between two surfaces), and descriptions of how the dissipation changes with excitation amplitude. In general, these parameters are not straight forward to measure, which has resulted in the Iwan model not being widely adopted. Three recent extensions of the Iwan model are worth noting: modal Iwan models [26] (in which an Iwan model is fit to each mode for a quasi-linear response), the five parameter Iwan model [34] (in which the ratio of static and dynamic sliding is found to allow more flexibility in fitting experimental data), and the RIPP model [6] (which is an analytical representation of an Iwan element to allow for improved numerical properties and solution).

48.4.2 Bouc-Wen Models

Iwan models belong to a larger family of models termed Masing models [22, 29, 31]. A second category of Masing models, termed Bouc-Wen models [4, 35], are also hysteretic models. Unlike Iwan models, which are described as a series of elastic sliders, the Bouc-Wen models are described as a set of differential equations. It is hypothesized that any Iwan model can be represented as a Bouc-Wen model, and vice versa. The appeal of Bouc-Wen models is that they have more flexibility in representing other features of jointed interfaces (such as evolution over time [3]). However, very little work has been done to apply Bouc-Wen models to jointed structures [16]. Directly assessing the suitability of Bouc-Wen models to jointed structures, [23] compared a Coulomb friction model (assumed to be the “truth” data), Jenkins elements, and a Bouc-Wen model and found that the Bouc-Wen model was only capable of representing the hysteresis loop in an aggregate manner, whereas the Jenkins models are able to reproduce the hysteresis loop from the FEA simulations at all points throughout a loading cycle. The Bouc-Wen model was also found to exhibit a delay in the onset of macroslip and decrease in contact stiffness.

48.5 Concluding Remarks

As researchers seek to find a method to represent a jointed structure more accurately and to predict the response, there are several open areas of research:

48.5.1 The Surrogate System Hypothesis

The Surrogate System Hypothesis [5, 9] states that a surrogate structure that contains the same joint as the system of interest can be used to deduce the properties of the joint. These properties, once accounting for the properties of the surrogate structure, can then be substituted directly into the system of interest as a spatially discrete joint model (as opposed to a modal model). The surrogate structure itself could be a system that is significantly easier or cheaper to manufacture than the application system. Ongoing work is seeking to validate this hypothesis and to determine its domain of applicability.

48.5.2 Coupled Normal Contact

Recent work has demonstrated that the normal contact within an interface is not constant [28], and, in fact, clapping mode behavior can be found even in tightly clamped lap joints. Most existing models, however, do not allow for flexibility within an interface. Thus, the next generation of joint models must include the local kinematics, particularly the coupling between normal and tangential contact. The three dimensional friction elements [24, 27] are a step in this direction; however, they must be extended to include hysteretic damping.

References

1. Akay, A.: Research needs and open questions in vibration energy transport and dissipation. Technical report. National Science Foundation (2016, Forthcoming)
2. Allen, M.S., Mayes, R.L.: Estimating degree of nonlinearity in transient responses with zeroed early-time fast fourier transforms. *Mech. Syst. Signal Process.* **24**, 2049–2064 (2010)
3. Barber, T.T., Noori, M.N.: Modeling general hysteresis behavior and random vibration application. *ASME J. Vib. Acoust. Stress Reliab. Des.* **108**, 411–420 (1986)
4. Bouc, R., Forced vibration of mechanical systems with hysteresis. In: *Proceedings of the Fourth Conference on Non-Linear Oscillation*, Prague (1967)
5. Brake, M.R.W. (ed.): *The Mechanics of Jointed Structures*. Springer (2017)
6. Brake, M.R.W.: A reduced Iwan model that includes pinning for bolted joint mechanics. *Nonlinear Dyn.* **87**, 1335–1349 (2017)
7. Brake, M.R., Reuß, P., Segalman, D.J., Gaul, L.: Variability and repeatability of jointed structures with frictional interfaces. In: *32nd International Modal Analysis Conference (IMAC XXXII)*, Orlando (2014)
8. Catalfamo, S., Smith, S.A., Morlock, F., Schwingshackl, C., Reuß, P., Brake, M.R.W.: Effects of experimental methods on the measurement of a nonlinear system. In: *34th International Modal Analysis Conference (IMAC XXXIV)*, Orlando (2016)
9. Cooper, S.B., Rosatello, M., Mathis, A., Johnson, K., Brake, M.R.W., Allen, M.S., Ferri, A.A., Roettgen, D.R., Pacini, B.R., Mayes, R.L.: Effect of far-field structure on joint properties. In: *35th International Modal Analysis Conference (IMAC XXXV)*, Garden Grove (2017)
10. Deane, B.J., Allen, M.S., Starr, M.J., Segalman, D.J., Sumali, H.: Application of viscous and Iwan modal damping models to experimental measurements from bolted structures. *ASME J. Vib. Acoust.* **137**, 021012 (2015)
11. Dossogne, T., Noël, J.P., Kerschen, G.: Robust subspace identification of a nonlinear satellite using model reduction. In: *34th International Modal Analysis Conference (IMAC XXXIV)*, Orlando (2016)
12. Dossogne, T., Jerome, T.W., Lancerau, D.P.T., Smith, S.A., Brake, M.R.W., Pacini, B.R., Reuss, P., Schwingshackl, C.W.: Experimental assessment of the influence of interface geometries on structural response. In: *35th International Modal Analysis Conference (IMAC XXXV)*, Garden Grove (2017)
13. Feldman, M.: Hilbert transform in vibration analysis. *Mech. Syst. Signal Process.* **25**, 735–802 (2011)
14. Gaul, L., Nitsche, R.: Friction control for vibration suppression. *Mech. Syst. Signal Process.* **14**, 139–150 (2000)
15. Gaul, L., Nackenhorst, U., Willner, K., Lenz, J.: Nonlinear vibration damping of structures with bolted joints. In: *12th International Modal Analysis Conference (IMAC XII)*, Honolulu (1994)
16. Ismail, M., Ikhouane, F., Rodellar, J.: The hysteresis Bouc-Wen model, a survey. *Arch. Comput. Meth. Eng.* **16**, 161–188 (2009)
17. Iwan, W.D.: A distributed-element model for hysteresis and its steady state dynamic response. *ASME J. Appl. Mech.* **33**, 893–900 (1966)
18. Jenkins, G.M.: Analysis of the stress-strain relationships in reactor grade graphite. *Br. J. Appl. Phys.* **13**, 30–32 (1962)
19. Kerschen, G., Worden, K., Vakakis, A.F., Golinval, J.C.: Past, present and future of nonlinear system identification in structural dynamics. *Mech. Syst. Signal Process.* **20**, 505–592 (2006)
20. Kurt, M., Chen, H., Lee, Y.S., McFarland, D.M., Bergman, L.A., Vakakis, A.F.: Nonlinear system identification of the dynamics of a vibro-impact beam: numerical results. *Arch. Appl. Mech.* **82**, 1461–1479 (2012)
21. Lacayo, R.M., Pesaresi, L., Fochler, D., Groß, J., Brake, M.R.W., Schwingshackl, C.: A numerical round robin to predict the dynamics of an experimentally-measured brake-reuss beam. In: *35th International Modal Analysis Conference (IMAC XXXV)*, Garden Grove (2017)
22. Masing, G.: Self-stretching and hardening for brass. In: *Proceedings of the Second International Congress for Applied Mechanics*, pp. 332–335 (1926)
23. Oldfield, M., Ouyang, H., Mottershead, J.E.: Simplified models of bolted joints under harmonic loading. *Comput. Struct.* **84**, 25–33 (2005)
24. Petrov, E.P., Ewins, D.J.: State-of-the-art dynamic analysis for non-linear gas turbine structures. *Proc. Inst. Mech. Eng. G: J. Aerosp. Eng.* **218**, 199–211 (2004)
25. Peyret, N., Dion, J.L., Chevallier, G., Argoul, P.: Micro slip induced damping in planar contact under constant and uniform normal stress. *Int. J. Appl. Mech.* **2**, 281–304 (2010)
26. Roettgen, D.R., Allen, M.S.: Nonlinear characterization of a bolted, industrial structure using a modal framework. *Mech. Syst. Signal Process.* **84**, 152–170 (2017)
27. Schwingshackl, C.W., Di Maio, D., Sever, I., Green, J.S.: Modeling and validation of the nonlinear dynamic behavior of bolted flange joints. *ASME J. Eng. Gas Turbines Power* **135**, 122504–1–8 (2013)
28. Seeger, B., Butaud, P., Du, F., Baloglu, V., Brake, M.R.W., Schwingshackl, C.W.: In situ measurements of interfacial contact pressure during impact hammer tests. In: *36th International Modal Analysis Conference (IMAC XXXVI)*, Orlando (2018)
29. Segalman, D.J.: An initial overview of Iwan modeling for mechanical joints. Technical report SAND2001-0811. Sandia National Laboratories, Albuquerque (2001)

30. Segalman, D.J.: A four-parameter Iwan model for lap-type joints. *ASME J. Appl. Mech.* **72** 752–760 (2005)
31. Segalman, D.J., Starr, M.J.: Iwan models and their provenance. In: *ASME International Design Engineering Technical Conferences IDETC/CIE, Chicago* (2012)
32. Segalman, D.J., Gregory, D.L., Starr, M.J., Resor, B.R., Jew, M.D., Lauffer, J.P., Ames, N.M.: *Handbook on dynamics of jointed structures*. Technical report SAND2009-4164. Sandia National Laboratories, Albuquerque (2009)
33. Smith, S.A., Bilbao-Ludena, J.C., Catalfamo, S., Brake, M.R.W., Reuß, P., Schwingshackl, C.: The effects of boundary conditions, measurement techniques, and excitation type on measurements of the properties of mechanical joints. In: *33rd International Modal Analysis Conference (IMAC XXXIV), Orlando* (2015)
34. Wang, X.Q., Mignolet, M.P.: Stochastic Iwan-type model of a bolted joint: formulation and identification. In: *32nd International Modal Analysis Conference (IMAC XXXII), Orlando* (2014)
35. Wen, Y.K.: Method for random vibration of hysteretic systems. *ASCE J. Eng. Mech. Div.* **102**, 249–263 (1976)
36. Yang, J.N., Lei, Y., Pan, S., Huang, N.: System identification of linear structures based on Hilbert-Huang spectral analysis. Part 1: normal modes. *Earthq. Eng. Struct. Dyn.* **32**, 1443–1467 (2003)